

THIS REPORT HAS BEEN DELIMITED
AND CLEARED FOR PUBLIC RELEASE
UNDER DOD DIRECTIVE 5200.20 AND
NO RESTRICTIONS ARE IMPOSED UPON
ITS USE AND DISCLOSURE.

DISTRIBUTION STATEMENT A

APPROVED FOR PUBLIC RELEASE;
DISTRIBUTION UNLIMITED.

UNCLASSIFIED

AD

AD859702

PRELIMINARY DESIGN REPORT
OF LOW VOLUMETRIC FLOW TURBINE

K. E. Nichols
Project Manager

J. D. Baird
Project Engineer

June 13, 1969

STATEMENT #3 UNCLASSIFIED

Each transmittal of this document outside the agencies of the
U.S. Government must have prior approval of *Deputy Director*

Prepared for: U. S. Army Engineers Reactor Group
R & T Division
Fort Belvoir, Virginia
Contract No. DAAK02-69-C-0266

Prepared by: Barber-Nichols/Engineering Company
6325 West 55th Avenue
Arvada, Colorado 80002

UNCLASSIFIED

OCT 6 1969

E 83

UNCLASSIFIED

AD

PRELIMINARY DESIGN REPORT
OF LOW VOLUMETRIC FLOW TURBINE

K. E. Nichols
Project Manager

J. D. Baird
Project Engineer

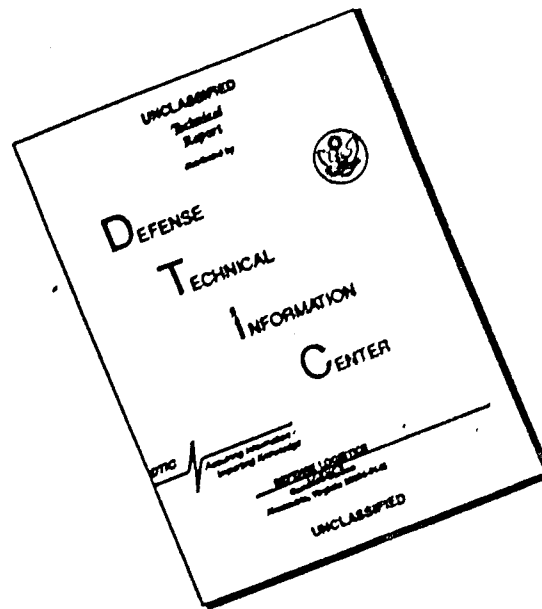
June 13, 1969

Prepared for: U. S. Army Engineers Reactor Group
R & T Division
Fort Belvoir, Virginia
Contract No. DAAK-2-69-C-0266

Prepared by: Barber-Nichols/Engineering Company
6325 West 55th Avenue
Arvada, Colorado 80002

UNCLASSIFIED

DISCLAIMER NOTICE



THIS DOCUMENT IS BEST QUALITY AVAILABLE. THE COPY FURNISHED TO DTIC CONTAINED A SIGNIFICANT NUMBER OF PAGES WHICH DO NOT REPRODUCE LEGIBLY.

FORWARD

This preliminary design of a low volumetric flow turbine was made under Contract No. DAAK02-69-C-0266 issued by the U. S. Army Engineers Reactor Group, R & T Division, Fort Belvoir, Virginia.

The authors wish to acknowledge the contribution to this preliminary design made by Messrs R. Barber, J. Lobach, W. Vining, and H. Welz of Barber-Nichols Engineering Company, and Messrs W. Shapiro and R. Colsher of Franklin Institute Research Laboratories (FIRL).

TABLE OF CONTENTS

	Page
<u>FOREWORD</u>	i
<u>TABLE OF CONTENTS</u>	ii
<u>LIST OF FIGURES AND TABLES</u>	vi
<u>SYMBOLS</u>	x
 1.0 <u>INTRODUCTION</u>	 1
2.0 <u>DESCRIPTION</u>	1
3.0 <u>DISCUSSION</u>	7
3.1 <u>AERO-THERMODYNAMIC ANALYSIS</u>	8
3.1.1 <u>Aerodynamic System Description</u>	8
3.1.2 <u>Performance Evaluation</u>	8
3.1.2.1 <u>Preliminary Evaluation of Seal Losses</u>	9
3.1.2.2 <u>Wheel Disk Friction</u>	13
3.1.2.3 <u>Turbine Efficiency</u>	16
3.1.3 <u>Performance Optimization</u>	19
3.2 <u>HEAT TRANSFER ANALYSIS</u>	23
3.2.1 <u>Main Body of Disk</u>	23
3.2.1.1 <u>Local Heat Transfer Coefficient</u>	23
3.2.1.2 <u>Disk Friction</u>	26
3.2.1.3 <u>Circulation Flow</u>	26
3.2.1.4 <u>Means of Cooling</u>	28
3.2.1.5 <u>Turbine Disk Heat Transfer Analysis</u>	30
3.2.2 <u>Disk Shroud and Seal Area</u>	33
3.2.3 <u>Nozzle and Blade Area</u>	33
3.2.4 <u>Turbine Housing</u>	34
3.2.5 <u>Shaft and Bearing Area</u>	35
3.3 <u>VIBRATION ANALYSIS</u>	36
3.3.1 <u>Blade and Shroud Vibration</u>	36
3.3.2 <u>Turbine Disk Vibration</u>	36
3.3.3 <u>Rotor Dynamics</u>	39
3.4 <u>STRESS ANALYSIS</u>	42
3.4.1 <u>Turbine Blades and Shroud</u>	43
3.4.2 <u>Disk Stress Analysis</u>	45
3.4.3 <u>Turbine Casing</u>	45

TABLE OF CONTENTS

	Page
3.5 MECHANICAL DESIGN	47
3.5.1 Discussion of Controlled Leakage Seal	47
3.5.1.1 Choice of Sectored Concept	49
3.5.1.2 Problem Areas	49
3.5.1.3 Interface Geometries considered	51
3.5.1.3.1 Hydrostatic	57
3.5.1.3.2 Rolling Diaphragm	57
3.5.2 Journal Bearings	59
3.5.3 Thrust Bearings	59
3.5.4 Thrust Load Balance	59
3.5.5 Steam Wetness	59
4.0 INVESTIGATIONS	61
5.0 DESIGN PARAMETERS	63
6.0 DESIGN	77
6.1 AERO THERMODYNAMIC DESIGN ANALYSIS	78
6.1.1 Turbine Rotor Design	78
6.1.2 Rotor Blade Design	78
6.1.3 Turbine Nozzle Design	84
6.2 HEAT TRANSFER ANALYSIS	87
6.2.1 Main Body of Disk	87
6.2.1.1 Local Heat Transfer Coefficient	87
6.2.1.2 Disk Friction	88
6.2.1.3 Circulation Flow	92
6.2.1.4 Means of Cooling	92
6.2.1.5 Turbine Disk Heat Transfer Analysis	93
6.2.2 Disk Shroud and Seal Area	100
6.2.3 Nozzle and Blade Area	101
6.2.4 Turbine Housing	104
6.2.5 Shaft and Bearing Area	107
6.3 VIBRATION ANALYSIS	109
6.3.1 Turbine Blade Design	110
6.3.2 Disk Vibration	112
6.3.3 Rotor Dynamics	115
6.4 STRESS ANALYSIS	118
6.4.1 Turbine Blade and Shroud Stress	119

TABLE OF CONTENTS

	Page
6.4.2 Turbine Disk Design	127
6.4.3 Turbine Casing	135
6.4.3.1 Inlet Casing	138
6.4.3.2 Cover Exit End	140
6.5 MECHANICAL DESIGN	142
6.5.1 Design and Performance	142
6.5.1.1 Steady-State Performance of the Hydrostatic Primary Seal	143
6.5.1.2 Steady-State Performance of Hydrostatic Secondary Seal	149
6.5.1.3 Dynamic Performance	154
6.5.1.4 Bearing Performance	164
7.0 CALCULATIONS	179
7.1 AERO-THERMODYNAMIC ANALYSIS	180
7.2 HEAT TRANSFER ANALYSIS	193
7.2.1 Disk Heat Transfer Coefficients	194
7.2.1.1 Evaluate Disk Friction	194
7.2.1.2 Evaluate Local Skin Friction	196
7.2.1.3 Evaluation of Film Coefficient	197
7.2.2 Cooling Water Heat Transfer Coefficient	198
7.2.2.1 Disk Shroud Cooling	198
7.2.2.2 Tip Cooling	199
7.2.3 Blade and Nozzle Heat Transfer Coefficient	201
7.2.4 Seal Analysis	204
7.2.5 Temperature Calculations	208
7.3 VIBRATION CALCULATIONS	221
7.3.1 Turbine Blade Vibration Calculations	222
7.3.2 Disk Vibration Calculation	224
7.3.3 Rotor Dynamics Calculation	224
7.4 STRESS CALCULATIONS	227
7.4.1 Shroud and Blade Stress Calculations	228
7.4.2 Turbine Disk Stress Analysis	234
7.4.3 Casing Calculations	237
7.4.3.1 Inlet Casing Stress Calculations	237
7.4.3.2 Exit Casing Stress Calculations	240

TABLE OF CONTENTS

	Page
7.5 ANALYTICAL METHODS	244
7.5.1 Pad Configuration	244
7.5.2 Pressure Distribution	244
7.5.3 Film Thickness	244
7.5.4 Hydrostatic and Hybrid Analysis	246
7.5.5 Bearing Forces and Moments	248
7.5.6 Dynamics	248
7.5.7 Solution Procedure	249
7.5.8 Program Descriptions	250
7.5.8.1 Bearing and Seal Systems Steady State	251
7.5.8.2 Bearing and Seal Systems Dynamics	253
7.5.9 Nomenclature (4 Pages)	255
8.0 <u>PREDICTED PERFORMANCE</u>	259
8.1 DESIGN POINT PERFORMANCE	259
8.2 OFF DESIGN PERFORMANCE	260
9.0 <u>RECOMMENDATIONS</u>	263
9.1 GENERAL RECOMMENDATIONS	263
9.2 FIRL'S RECOMMENDATIONS	263
10.0 <u>DRAWINGS</u>	265
11.0 <u>REFERENCES</u>	266
12.0 <u>APPENDIX</u>	269
12.1 STEADY STATE PERFORMANCE OF RAYLEIGH STEP PRIMARY SEAL	269
12.2 FLOW CALCULATIONS BETWEEN SEGMENTS	269
12.3 DYNAMIC PLOTS	273
12.4 FORCE BALANCE AND INERTIA COMPUTATIONS	301
13.0 DD FORM 1473	

LIST OF FIGURES AND TABLES

Figure 2.0.1	Schematic of Turbine Concept
Figure 2.0.2	Turbine Efficiency vs. Specific Speed
Figure 3.1.1	Conceptual Seal Configuration - LVF Turbine Design
Figure 3.1.2	Effect of Seal Clearance and Length on Turbine Efficiency
Figure 3.1.3	Variation of Turbine Efficiency with Inlet Seal Spacing
Figure 3.1.4	Variation of Maximum Turbine Efficiency with Velocity Ratio and Nozzle Angle
Figure 3.1.5	Variation of Maximum Efficiency with Velocity Ratio and Rotor Exit Angle
Figure 3.2.1	Sketch of Turbine Cross Section
Figure 3.2.2	Comparison of Disk Friction Data (Two Sides Immersed)
Figure 3.3.1	Turbine Blade Vibration Modes
Figure 3.3.2	Diametral Modes
Figure 3.3.3	Bearing Spacing Design
Figure 3.3.4	Shaft Vibration Mode
Figure 3.4.1	Critical Dimensions of Shroud and Blade Used in Stress Analysis
Figure 3.5.1	Seal Sector Face Configuration
Figure 3.5.2	Sector Seal Configuration - Load vs. Film Thickness
Figure 3.5.3	Sector Seal Configuration - Flow vs. Film Thickness
Figure 3.5.4	Sector Seal Configuration - Horsepower Loss vs. Film Thickness
Figure 3.5.5	Pressure Distribution Across Seal at Sector Middle
Figure 3.5.6	Rolling Diaphragm Seal
Figure 5.0.1	Cycle Efficiency vs. Turbine Inlet Pressure
Figure 5.0.2	Cycle Efficiency vs. Turbine Inlet Pressure
Figure 5.0.3	Turbine Wheel Diameter vs. Inlet Pressure

LIST OF FIGURES AND TABLES

- | | |
|--------------|--|
| Figure 5.0.4 | Stage-1 Nozzle Exit Steam Wetness vs. Inlet Pressure |
| Figure 5.0.5 | Design Point Selection Parameters |
| Figure 5.0.6 | LVFT Stage Performance
Horsepower vs. Exhaust Pressure |
| Figure 5.0.7 | LVFT Stage Performance
Tangential Velocity vs. Exhaust Pressure |
| Figure 5.0.8 | LVFT Stage Performance
Exhaust Wetness vs. Isentropic Expansion |
| Figure 6.1.1 | Effect of Trailing Edge Thickness on Blade Performance |
| Figure 6.1.2 | Pitch Line Profile
Rotor Blades LVF Turbine |
| Figure 6.1.3 | Rotor Blade Flow Characteristics Developed along
Pitch Line |
| Figure 6.1.4 | Pitch Line Profile
Stator Blade LVF Turbine |
| Figure 6.1.5 | Stator Blade Flow Characteristics Developed along
Pitch Line |
| Figure 6.2.1 | Variation of LVF Turbine Disk and Shroud Film
Coefficient as a Function of Radius |
| Figure 6.2.2 | Distribution of Heat Added to Gas due to Disk Friction
One Side of Disk Only |
| Figure 6.2.3 | Disk Thermal Model |
| Figure 6.2.4 | Turbine Housing Temperature Distribution |
| Figure 6.3.1 | Frequency of Excitation Force |
| Figure 6.3.2 | Module of Solid Disk Assumed for Stress Analysis |
| Figure 6.4.1 | Loads on Blade and Shroud |
| Figure 6.4.2 | Tabulation of Stress in Blade and Shroud |
| Figure 6.4.3 | Elastic Model of Shroud and Blade |
| Figure 6.4.4 | Elastic Stress in Turbine Disk at 12,000 rpm |

LIST OF FIGURES AND TABLES

- Figure 6.4.5 Temperature Distribution in Turbine Disk
- Figure 6.4.6 Tabulation of Disk Stress and Deflection at 12,000 rpm
- Figure 6.4.7 Steam Turbine Disk Materials
 (in order of ascending cost) (2 Pages)
- Figure 6.4.8 Properties of Ductile Iron 60-45
- Figure 6.4.9 Tabulation of Stress and Deflection in Casing
- Figure 6.4.10 Stress Analysis of LVFT Casing
- Figure 6.5.1 Nomenclature and Dimensions of Hydrostatic Primary Seal
- Figure 6.5.2 Orifice-Fed Sectored Seal Performance vs. Film Thickness at Design Operation
- Figure 6.5.3 Orifice-Fed Sectored Seal Moments, CP vs. Film Thickness at Design Operation
- Figure 6.5.4 Orifice-Fed Sectored Seal - Performance vs. Angular Tilt at Design Operation
- Figure 6.5.5 Orifice-Fed Sectored Seal - Moments, CP vs. Angular Tilt at Design Operation
- Figure 6.5.6 Orifice-Fed Sectored Seal - Performance vs. Angular Tilt at Design Operation
- Figure 6.5.7 Orifice-Fed Sectored Seal Moments, CP vs. Angular Tilt at Design Operation
- Figure 6.5.8 Sizing Orifice for Steam Secondary Seal
- Figure 6.5.9 Secondary Seal Performance as a Function of Axial Clearance
- Figure 6.5.10 Seal Sector Nomenclature
- Figure 6.5.11 BN - Seal Dynamic Performance at Design Operation, 24-Segment Orifice-Fed Step Seal, Case 10, two Degrees of Freedom, Wheel Y - Nutation
- Figure 6.5.12 BN - Seal Dynamic Performance At Design Operation, 24-Segment Orifice-Fed Step Seal, Case 10, Two Degrees of Freedom, Wheel X - Nutation

LIST OF FIGURES AND TABLES

- Figure 6. 5. 13 BN - Seal Dynamic Performance at Design Operation, 24-Segment Orifice-Fed Step Seal, Case 10, Two Degrees of Freedom, Seal Translation
- Figure 6. 5. 14 BN - Seal Dynamic Performance at Design Operation, 24-Segment Orifice-Fed Step Seal, Case 10, Two Degrees of Freedom, Seal Y - Rotation
- Figure 6. 5. 15 BN - Seal Dynamic Performance at Design Operation, 24-Segment Orifice-Fed Step Seal, Case 10, Two Degrees of Freedom, Seal Leakage
- Figure 6. 5. 16 BN - Seal Dynamic Performance at Design Operation, 24-Segment Orifice-Fed Step Seal, Case 10, Two Degrees of Freedom, Seal Y - Moment
- Figure 6. 5. 17 Tilting Pad Journal Bearing - Single Bearing Performance vs. Eccentricity Ratio
- Figure 6. 5. 18 Tilting Pad Journal Bearing - Single Bearing Performance vs. Eccentricity Ratio
- Figure 6. 5. 19 Tilting Pad Journal Bearing - Single Bearing Performance vs. eccentricity Ratio
- Figure 6. 5. 20 Tilting Pad Journal Bearing - Single Bearing Flow vs. Change in Temperature
- Figure 6. 5. 21 Tilting Pad Journal Bearing - Single Bearing Flow vs. Change in Temperature
- Figure 6. 5. 22 Tilting Pad Journal Bearing - Single Bearing Flow vs. Change in Temperature
- Figure 6. 5. 23 Tilting Pad Thrust Bearing - Opposed Pair Bearing Load vs. Pivot Clearance
- Figure 6. 5. 24 Tilting Pad Thrust Bearing - Opposed Pair Bearing, FHP vs. Pivot Clearance
- Figure 6. 5. 25 Tilting Pad Thrust Bearing - Opposed Pair Bearing, Minimum Clearance vs. Pivot Clearance
- Figure 6. 5. 26 Tilting Pad Thrust Bearing - Opposed Pair Bearing, Flow vs. Change in Temperature
- Figure 7. 1. 1 Symbols and Nomenclatures (3 Pages)

LIST OF FIGURES AND TABLES

- Figure 7.1.2 Design Point Calculations
- Figure 7.1.3 LVF Turbine Thermodynamic Cycle and Velocity Diagrams
- Figure 7.1.4 Gas Incidence Angle vs. Loss Coefficient for Round and Sharp-Nosed Turbine Blades
- Figure 7.2.1 Heat Transfer Program - List of Symbols
- Figure 7.2.2 Disk Heat Transfer Analysis, Node Conductances, (2 Pages)
- Figure 7.2.3 Turbine Housing Heat Transfer Analysis, Conductor Values, (3 Pages)
- Figure 7.2.4 Heat Transfer Analysis, Computer Program Flow Diagram, (4 Pages)
- Figure 7.3.1 Pitch Line Profile Rotor Blade - LVF Turbine
- Figure 7.3.2 Axial Vibration of Turbine Disks LVFT - Two Nodal Diameters
- Figure 7.4.1 Exit Casing Elastic Model
- Figure 8.1.1 Variation of Turbine Efficiency with Velocity Ratio
- Figure 12.1.1 Side-Fed Rayleigh-Step Sectored Seal Steady-State Performance
- Figure 12.1.2 Side-Fed Rayleigh-Step Sectored Seal Steady-State Performance
- Figure 12.1.3 Side-Fed Rayleigh-Step Sectored Seal Steady-State Performance
- Figure 12.3.1 BN-Seal Dynamic Performance at Design Operation, 24-Segment Orifice-Fed Seal, Case 1, One Degree of Freedom, Wheel Y - Nutation
- Figure 12.3.2 BN-Seal Dynamic Performance at Design Operation, 24-Segment Orifice-Fed Seal, Case 1, One Degree of Freedom, Wheel X - Nutation
- Figure 12.3.3 BN-Seal Dynamic Performance at Design Operation, 24-Segment Orifice-Fed Seal, Case 1, One Degree of Freedom, Seal Translation

LIST OF FIGURES AND TABLES

- Figure 12.3.4 BN-Seal Dynamic Performance at Design Operation,
24-Segment Orifice-Fed Seal, Case 1, One Degree
of Freedom, Seal Leakage
- Figure 12.3.5 BN-Seal Dynamic Performance at Design Operation,
24-Segment Orifice-Fed Seal, Case 1, One Degree
of Freedom, Minimum Clearance
- Figure 12.3.6 BN-Seal Dynamic Performance at Design Operation,
24-Segment Orifice-Fed Seal, Case 1, One Degree
of Freedom, Fluid Film Force
- Figure 12.3.7 BN-Seal Dynamic Performance at Design Operation,
24-Segment Orifice-Fed Seal, Case 1, One Degree
of Freedom, Seal Y - Moment
- Figure 12.3.8 BN-Seal Dynamic Performance at Design Operation,
12-Segment Side-Fed Step Seal, Case 2, One Degree
of Freedom, Wheel X - Nutation
- Figure 12.3.9 BN-Seal Dynamic Performance at Design Operation,
24-Segment Orifice-Fed Seal, Case 2, One Degree
of Freedom, Wheel Y - Nutation
- Figure 12.3.10 BN-Seal Dynamic Performance at Design Operation,
12-Segment Side-Fed Step Seal, Case 2, One Degree
of Freedom, Seal Translation
- Figure 12.3.11 BN-Seal Dynamic Performance at Design Operation,
12-Segment Side-Fed Step Seal, Case 2, One Degree
of Freedom, Minimum Clearance
- Figure 12.3.12 BN-Seal Dynamic Performance at Design Operation,
12-Segment Side-Fed Step Seal, Case 2, One Degree
of Freedom, Seal Leakage
- Figure 12.3.13 BN-Seal Dynamic Performance at Design Operation,
12-Segment Side-Fed Step Seal, Case 2, One Degree
of Freedom, Fluid Film Force
- Figure 12.3.14 BN-Seal Dynamic Performance at Design Operation,
12-Segment Side-Fed Step Seal, Case 2, One Degree
of Freedom, Seal Y - Moment
- Figure 12.3.15 BN-Seal Dynamic Performance, Case 3, Rotation
- Figure 12.3.16 BN-Seal Dynamic Performance, Case 3, Translation

LIST OF FIGURES AND TABLES

- Figure 12.3.17 BN-Seal Dynamic Performance Case 4, Translation
- Figure 12.3.18 BN-Seal Dynamic Performance Case 5, Rotation
- Figure 12.3.19 BN-Seal Dynamic Performance, Case 5, Translation
- Figure 12.3.20 BN-Seal Dynamic Performance at Design Operation,
12-Segment Side-Fed Step Seal, Case 9, Two Degrees
of Freedom, Wheel X - Nutation
- Figure 12.3.21 BN-Seal Dynamic Performance at Design Operation,
12-Segment Side-Fed Step Seal, Case 9, Two Degrees
of Freedom, Wheel Y - Nutation
- Figure 12.3.22 BN-Seal Dynamic Performance at Design Operation,
12-Segment Side-Fed Step Seal, Case 9, Two Degrees
of Freedom, Seal Translation
- Figure 12.3.23 BN-Seal Dynamic Performance at Design Operation,
12-Segment Side-Fed Step Seal, Case 9, Two Degrees
of Freedom, Seal Y - Rotation
- Figure 12.3.24 BN-Seal Dynamic Performance at Design Operation,
12-Segment Side-Fed Step Seal, Case 9, Two Degrees
of Freedom, Seal Leakage
- Figure 12.3.25 BN-Seal Dynamic Performance at Design Operation,
12-Segment Side-Fed Step Seal, Case 9, Two Degrees
of Freedom, Minimum Clearance
- Figure 12.3.26 BN-Seal Dynamic Performance at Design Operation,
12-Segment Side-Fed Step Seal, Case 9, Two Degrees
of Freedom, Fluid Film Force
- Figure 12.3.27 BN-Seal Dynamic Performance at Design Operation,
12-Segment Side-Fed Step Seal, Case 9, Two Degrees
of Freedom, Seal Y - Moment

TABULATIONS

- Table 6.2.1 Summary of Seal Friction and Leakage Data
- Tabulation 6.5.1 Summary of Dynamic Runs
- Tabulation 6.5.2 Tilting Pad Journal Bearing Summary for
Single Bearing Operation
- Tabulation 6.5.3 Tilting Pad Thrust Bearing Summary for
Opposed Pair Bearing Operation

SYMBOLS

A	Cross-sectional area, in^2
A_a	Cross-sectional area of shroud, in^2
A_s	Cross-sectional area of blade, in^2
B	Rotor disk thickness, ft
b	Turbine blade axial length, in
C	Absolute gas velocity, ft/sec
C_f	Skin friction coefficient
C_p	Specific heat, BTU/lb - $^{\circ}\text{F}$
C_h	Blade chord, in
C_o	Isentropic spouting velocity, ft/sec
c	Radial clearance, in
D	Diameter, ft or in
D_h	Hydraulic diameter, ft
E	Young's Modulus, $\frac{\text{lb}}{\text{in}^2}$
E_A	Total available energy, $\frac{\text{ft-lb}}{\text{sec}}$
E_o	Ideal energy transferred to rotor, $\frac{\text{ft-lb}}{\text{sec}}$
F	Force, lb
f	Friction factor
f_s	Composite frequency of shroud, $\frac{\text{rev}}{\text{min}}$
g	Acceleration of gravity, ft/sec^2 or in/sec^2
H	Enthalpy, BTU/lb
H_{ad}	Overall adiabatic head, BTU/lb
h	Film heat transfer coefficient, $\text{BTU/hr-ft}^2\text{-}^{\circ}\text{F}$
h_B	Blade height, in

SYMBOLS

h_o	Minimum film thickness, in
I_A	Moment of inertia (axial), in ⁴
I_T	Moment of inertia (tangential), in ⁴
J	Conversion factor, 778 ft-lb/BTU
K	Spring constant, lb/in
K_w	Disk friction loss coefficient
L	Tube length, ft
ℓ	Length, in
M	Mach number
M_o	Unknown bending moment, in-lb
N	Disk rotational speed, rev/min
ND	Nodal diameter
N_s	Specific speed
N_{Pr}	Prandtl number
N_{Re}	Reynolds number
N_{St}	Stanton number
n	Blade number
P	pressure, psia
P_i	Internal pressure, psi
P_o	Inlet pressure, psia
P_{ex}	Exhaust pressure, psia
Q	Seal leakage flow, lb/sec
Q_o	Unknown shear force lb/in
Q_{DF}	Disk friction heat input BTU/sec

SYMBOLS

Q_{SF}	Heat due to seal friction, BTU/sec
R	Gas constant, in/ $^{\circ}R$ or ft/ $^{\circ}R$
ΔR_1	Exit end deflection at bearing cap, in
R_m	Mean radius of shroud, in
r	Radius, ft or in
r_i	Inner radius, in
r_o	Outer radius, in
S_p	Deflection of shroud, in
S_s	Seal clearance, in
s	Blade spacing, in
T	Temperature, $^{\circ}R$ or $^{\circ}F$
T_a	Maximum temperature shroud, $^{\circ}F$
T_L	Thrust bearing axial load, lb
$T_{^{\circ}R}$	Total temperature relative to blade, $^{\circ}R$
t_e	Trailing edge width, in
U	Rotor tip speed, ft/sec
U_s	Average free stream velocity, ft/sec
U_t	Growth of shroud due to temperature, in
U_w	Growth of shroud due to centrifugal force, in
V	Velocity, ft/sec
V_R	Relative velocity through blade, ft/sec
V_2	Exhaust volume flow, ft ³ /sec
ω_1	Relative gas velocity, ft/sec
W_1	Unknown force, lb
\dot{w}	Flow rate, lb/sec

SYMBOLS

χ	Unknown length, in
β	Rotor blade angle, degrees
β_g	Relative gas entering angle, degrees
γ	Ratio of specific heats
Δ	Deflection, in
ξ	Turbine loss factor
η_{cyc}	Cycle efficiency
η_H	Turbine hydraulic efficiency
η_i	Incidence loss coefficient
η_T	Actual turbine efficiency
θ	Slope, radians
k	Thermal conductivity, BTU/hr-ft-°F
μ	Viscosity, lb/ft - hr
ν	Specific volume, ft ³ /lb
ρ	Density, lb/ft ³
ρ_T	Degree of turbine reaction
σ_b	Bending stress, psi
σ_r	Radial stress, psi
σ_ϕ	Tangential stress, psi
τ	Specific torque, lb/ft ²
ν_k	Kinematic viscosity, $\frac{\text{lb-hr}}{\text{ft}^2}$ or $\frac{\text{lb-sec}}{\text{in}^2}$
ψ_N	Nozzle velocity coefficient
ψ_R	Rotor velocity coefficient

SYMBOLS

ω_N Natural frequency, rad/sec or rev/min

ω_c Critical speed of shaft, rev/min

Subscripts:

H_2O Water

\mathcal{S} Denotes fluid properties
in free stream

B Blade parameter

cond Condenser conditions

DF Disk friction

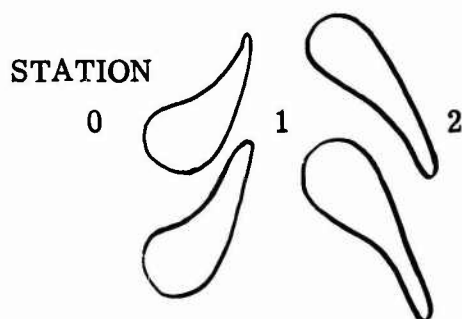
e Turbine exhaust
conditions

L Leakage

N Nozzle parameter

T Blade throat dimension

u Tangential component



1.0 INTRODUCTION

The report covers the preliminary design of a "Low Volumetric Flow Turbine Design". The turbine concept is based on a reaction design using close clearance gas bearing type seals to control leakage past the rotor blade passages. The turbine concept is an outgrowth of the turbine described in DDC Report AD831635L, titled "Low Volumetric Flow Turbine Performance Prediction and Analysis", dated March 1968.

A preliminary design analysis of a turbine unit that is to be used for test evaluation of the performance potential of the controlled leakage seals and aerodynamic passages was conducted and is covered by this report. The preliminary design effort included the following analyses and design:

1. Aero-thermodynamic analysis of the flow passages concerned with the energy transfer from working fluid to rotor.
2. Thermal analysis of rotor, housings, and seals in order to determine temperature levels and gradients.
3. Dynamic analysis of seals, rotors, and blades in order to determine stability of rotor system.
4. Mechanical design of rotor, bearings, seals, and system to insure proper stress loading of components.

A preliminary layout drawing of the turbine unit was completed and included in this report.

Following approval of the preliminary design by the government Project Engineer, the final design will proceed.

2.0 DESCRIPTION

The turbine concept covered by this report is a special design that was conceived by personnel at the U.S. Army Engineers Reactor Group, Research and Technology Department, Fort Belvoir, Virginia. The purpose of the concept is to improve the performance of turbines that operate in the low volumetric flow regime. A significant factor that must be considered in turbine efficiency is the leakage or bypass flow that does not pass through the rotor blades and therefore cannot contribute to useful output power. When low volumetric flow machines are considered, the conventional approach is to design impulse machines which reduce the bypass leakage because there is essentially no pressure drop across the rotor. Impulse machines, however, have considerable kinetic energy losses as the fluid enters the rotor because the relative velocities are high. Also, where low volumetric flow is considered, then the design may require partial admission to the rotor or a low blade height, either of which results in lowering the efficiency. If highly efficient sealing techniques were employed in the low volumetric flow turbine to control

bypass flow then reaction could be designed into the rotor which results in low rotor relative approach velocities and high rotor efficiency which helps to maintain high overall turbine performance. Another area where the controlled leakage seals contribute to improved performance is in reducing the rotor windage losses. When considering low volumetric flow machines, the rotor windage becomes a significant percentage of the output power as compared to large volume flow machines which have a corresponding increase in power output. If the highly efficient seals are utilized to prevent bypass flow around the blade passages, then these same seals control the leakage of working fluid into the clearance areas on the sides of the rotor. If these clearance areas around the rotor are then evacuated or maintained at lower pressure levels than normal stage exhaust, then the windage losses of that stage can be reduced significantly.

The turbine concept is shown schematically in Figure 2.0.1 and can be described further as follows: The working fluid, which is specified as steam for the turbine design under consideration, enters the turbine unit and passes into the nozzle inlet plenum. The steam then passes through the nozzles or stators in the housing where it is accelerated and discharged with a tangential whirl component equal to the rotor tangential velocity at design point speed. The steam then as it enters the rotor, has only a small axial component relative to the rotor. The steam in the rotor is then expanded further as it passes from the discharge nozzles or channels in the rotor and this resulting momentum change produces rotor torque and work. This process of energy transfer from the steam to the rotor is typical of an axial flow turbine utilizing reaction in the rotor blading and an axial relative inlet to the rotor results in the commonly referred to "50 percent reaction stage".

The high efficiency seals are required on the inlet side of the rotor to prevent excessive leakage of the steam from bypassing the rotor nozzles. These seals are shown in Figure 2.0.1 on either side of the stator nozzles and control the steam leakage from the rotor nozzle annulus.

With reaction turbines, since there is a large difference in pressure level across the rotor nozzles, seals are commonly used below the rotor nozzles so that the pressure level on either side of the rotor disk can be controlled to provide thrust balance. This, of course, is dependent upon rotor size and thrust bearing load capability and consideration of additional thrust loads from external sources or additional stages. For the design under consideration, the pressure unbalance across the rotor is approximately 40 psi and the rotor disk area is nearly 400 in² which would produce a thrust load of 16,000 pounds. The seal on the exit side of the rotor is therefore located at a diameter that will provide a balance of the pressure loading forces and eliminate excessive thrust loads from the bearings. The areas below these seals on either side of the rotor below the blading are vented to a low pressure condenser operating at 2 psia. This low side cavity pressure eliminates a significant portion of the rotor windage loss.

The rotor is supported by the output shaft which in turn is supported by water lubricated tilting pad journal and tilting pad thrust bearings.

SCHEMATIC OF TURBINE CONCEPT

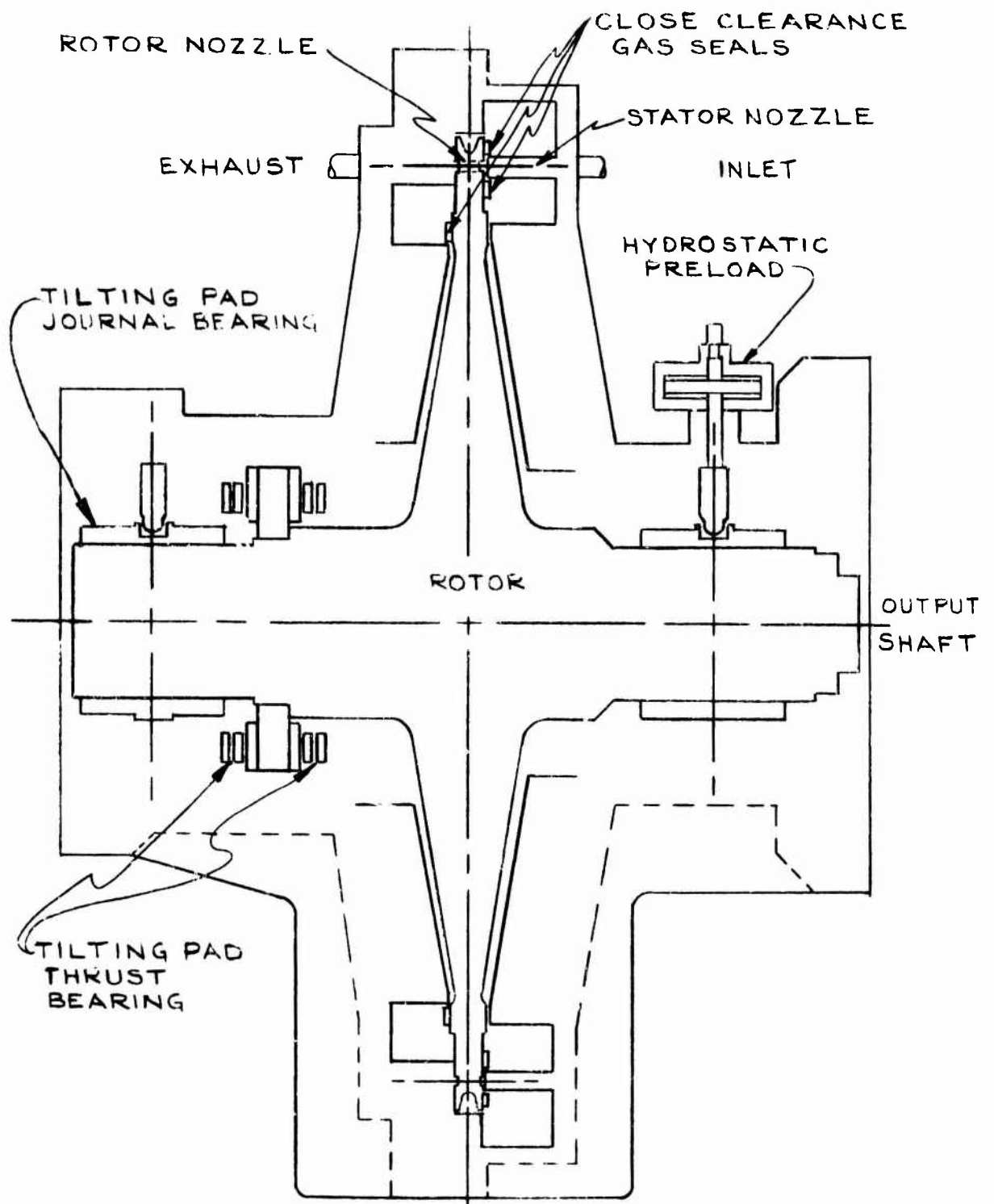


FIGURE 2.0.1

The tilting pad bearings are utilized for their self-aligning and stability characteristics which are essential when using low viscosity lubricants such as water. The water used for lubricating the journal and thrust bearings is returned to the steam generator. The journal bearings are operated under an induced preload which is applied by a piston which applies force to the pivot point of one pad of each bearing set. This preload maintains the rotor shaft position in the desired location and eliminates the possibility of the shaft moving around in a large bearing clearance. The preload is reduced to a low value at startup and shutdown which prevents damage to the bearing surfaces when the load capacity is low due to the low operating speed. The rotor thrust that was previously mentioned is adjusted to provide some load on the thrust bearing so that the shaft does not float across the thrust bearing clearance.

The seals located on either side of the rotor inlet annulus are the most critical components of this turbine concept and their performance has a very significant effect on turbine performance. In order for this turbine concept to achieve an improvement over conventional turbines in the low volumetric flow regime, these two seals must control the leakage of flow that would bypass the rotor blades to a small percentage of the total flow. If the percent bypass flow is controlled to 2 - 4 percent of the total flow, this turbine concept will provide an improvement over conventional machines in the low volume flow regime. This low volume flow regime can be more accurately defined by considering the dimensionless parameter, specific speed, which considers volume flow rate, rotative speed and energy available per unit mass of fluid passing through the machine. Low specific speed machines denote low volumetric flow per any given physical machine size. Low specific speed with reference to turbine efficiency indicates values less than approximately 40 when specific speed (N_s) is defined as shown on Figure 2.0.2. It can be seen in this figure that conventional turbine designs experience a decrease in turbine performance as the N_s value becomes lower than 40. Also shown in Figure 2.0.1 is the predicted performance of the subject turbine concept using highly efficient controlled leakage seals. This curve shows the area of turbine performance improvement that is felt to exist. The subject, "Low Volumetric Flow Turbine", is being designed for a N_s value of approximately 17.

The performance improvement previously discussed is dependent upon the adequacy of the controlled leakage seals and therefore, a special design approach has been used for these seals. Conventional labyrinth seals have approximately 5 to 10 times higher leakage rates than practical for this turbine concept, so therefore some design concept that provides a much closer sealing gap must be considered. The basic design approach for the seals consists of a gas bearing concept which provides for a very small gap across the sealing surface. Gas bearings can operate with film thickness values of 0.0005 to 0.001 inches which will then be the gas leakage passage width. This gas bearing-seal unit will follow the axial motions of the runner (side of the rotor disc) in order to maintain this close clearance. Fixed seals would not be practical due to the relative motion between the housings and rotor caused by pressure and temperature effects.

TURBINE EFFICIENCY vs SPECIFIC SPEED FOR OPTIMUM D_s

$$N_s = \frac{(RPM)(V_e)^{1/2}}{H_{ad}^{3/4}}$$

V_e = EXHAUST VOLUME FLOW - ft^3/SEC
 H_{ad} = ISENTROPIC HEAD DROP ACROSS STAGE - ft

— AXIAL INLET WITH CLOSE CLEARANCE SEALS
 - - - CONVENTIONAL TURBINE TECHNOLOGY

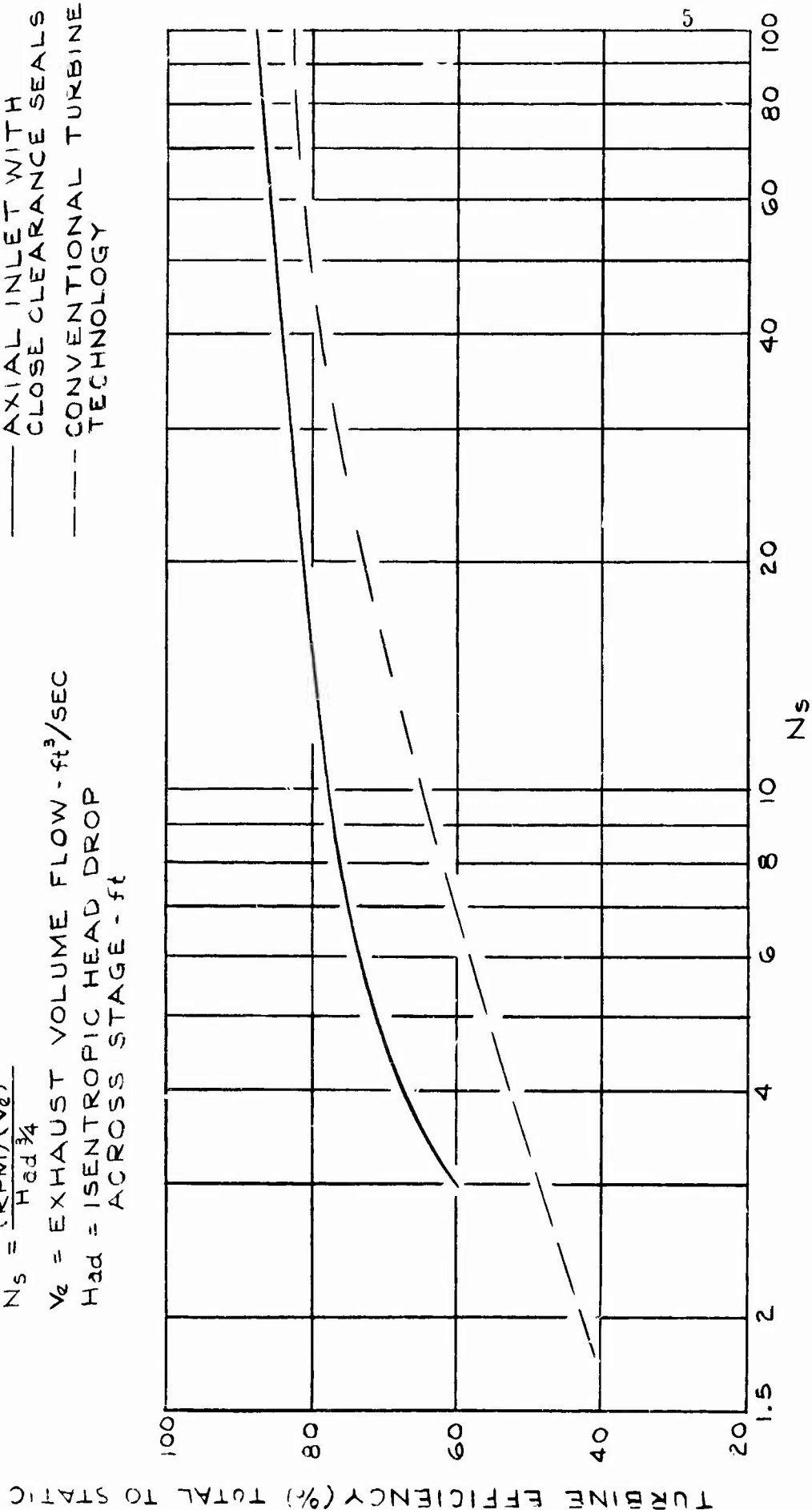


FIGURE 2.0.2

This section has presented a brief discussion of the turbine design in order to familiarize the reader with the design effort. Detailed discussion of the design of each component is included in the "Discussion" and "Design" section of the report.

3.0 DISCUSSION

The following section discusses the design concept of the LVF turbine and the necessary investigations and trade-offs involved in establishing the preliminary design. The turbine concept is based on a reaction design and depends on fluid film, positive stiffness face seals to control the leakage into the rotor cavity. The turbine design requires special considerations in the following areas:

1. Aero-thermodynamic analysis of the flow passages concerned with energy transfer from working fluid to rotor.
2. Thermal analysis of rotor housing and seals required to determine temperature levels and gradients.
3. Dynamic analysis of rotor, disk, and blades required to define the dynamic characteristics over the intended operating speed.
4. Mechanical design of the rotor, bearings, seals and system to establish proper loading and functional compatibility of components.

Included is the discussion of the selection, analysis, and preliminary design of the controlled-leakage seals and bearings submitted by Franklin Institute Research Laboratories (FIRL) in accordance with their sub-contract.

3.1 AERO-THERMODYNAMIC ANALYSIS

The aerodynamic portion of the design analysis was completed and is reported herein. The nozzle and rotor design geometry specified should provide excellent operating potential for the LVF turbine concept. The performance prediction completed and reported in Section 8 indicates that this design should yield performance exceeding that of a conventional turbine operating under similar design conditions. The following section will describe the design analysis used to define the aerodynamic performance of the turbine, including efficiency relationships and loss coefficients derived for the LVF turbine design.

3.1.1 Aerodynamic System Description

The LVF turbine concept is in operation somewhat similar to a conventional axial flow reaction turbine, in that a portion of the total energy available to the turbine is expended in the turbine nozzles and the remainder is taken in the turbine rotor. The degree of expansion taken in the turbine nozzles of a conventional turbine is optimized as a function of design operating conditions. For design conditions similar to the LVF turbine, operating at a low specific speed, the optimum degree of reaction is usually low, approaching impulse operation. The primary reason is that at low specific speeds the output power is low compared to the available energy, and low turbine flow rates are required. The leakage flow, however, is essentially fixed, dependent on design pressures, and the leakage flow becomes a larger percentage of total turbine flow thereby reducing the overall turbine efficiency. The use of impulse blading results in increased losses through the turbine stage, since typical rotor cascades for impulse turbines have blade efficiencies on the order of from 0.75 to 0.80. This is due to the large turning angles inherent with impulse blades and high viscous losses due to the high gas velocities entering the turbine rotor. The rotor blading efficiency for the LVF turbine, however, approaches that of efficient nozzles, and a design rotor velocity coefficient of 0.96 was used in the design analysis. Consequently, the efficiency potential of the LVF turbine is significantly greater than a standard impulse turbine. The leakage problem was approached by using limited leakage, hydrostatic gas seals which form an important component of the LVF turbine concept, and is examined in detail in the following sections.

3.1.2 Performance Evaluation

The predicted turbine performance for the LVF turbine was evaluated using methods and equations specified in the following sections. Appropriate equations were derived to yield efficiency relationships and loss factors such as seal leakage, seal friction, and disk friction associated with the LVF turbine.

3.1.2.1 Preliminary Evaluation of Seal Losses

Approximating expressions were used to estimate seal leakage and friction to provide a basis for evaluating the effect of seal clearance and seal height on turbine performance. The final performance evaluation reported in Section 8.0 was based on more exact values of leakage flow and seal friction specifically evaluated for the final seal design. The conceptual seal configuration analyzed in the following section is shown in Figure 3.1.1. The configuration has two seals on the inlet side of the turbine rotor and one on the exhaust side on a lower radius. Nomenclature, specifying pressures and seal radii in the figure, was used in the following design analysis and is reported here for reference.

The seal leakage flow was evaluated using preliminary equations obtained from the Franklin Institute Research Laboratories (FIRL) and are equivalent to the equations derived in Reference 5.0.1. The leakage flow for Seal 1 was evaluated by:

$$Q_1 = \frac{\pi S_1^3 (P_1^2 - P_{\text{CON}}^2)}{12 RT \gamma_K \ln(r_4/r_3)}, \text{ lbs/sec or } \xi_{L1} = \frac{Q_1}{W} \quad (3.1-1)$$

The leakage flow for Seals 2 and 3 was evaluated using the above equation with appropriate pressures and radii. Leakage flow from Seals 1 and 2 located at the turbine inlet affect the performance of the LVF turbine since leakage flow through these seals is not available to the turbine rotor. Leakage through Seal 3 occurs after the flow has passed through the turbine rotor and was not included in the performance analysis.

The preliminary expression used to evaluate the seal friction horsepower loss for Seal 1 was:

$$HP_{SF} = 2.61 \times 10^{-6} \frac{\gamma_K N^2}{S_1} (r_4^4 - r_3^4), \text{ horsepower} \quad (3.1-2)$$

where: $2.61 \times 10^{-6} = \frac{1}{550 (12)} \left[\left(\frac{2\pi}{60} \right)^2 \frac{\pi}{2} \right]$

As may be noted, the effect of running very close seal clearances is to minimize seal leakage at the expense of the frictional horsepower loss. Consequently, for a given seal height, or sealing radii, there exists an optimum seal clearance from the standpoint of turbine performance. The optimum operating seal clearance was subsequently evaluated as a function of seal height as shown in Figure 3.1.2. Strictly on the basis of performance, it is advantageous to use the smallest seal height possible and run with very close clearances. Since small seal heights typically lead to poor seal performance, the actual seal design chosen was the result of a compromise between turbine efficiency and a static and dynamic evaluation of seal response characteristics. Figure 3.1.2 can be used to determine any penalty incurred in performance by

CONCEPTUAL SEAL CONFIGURATION LVF TURBINE DESIGN

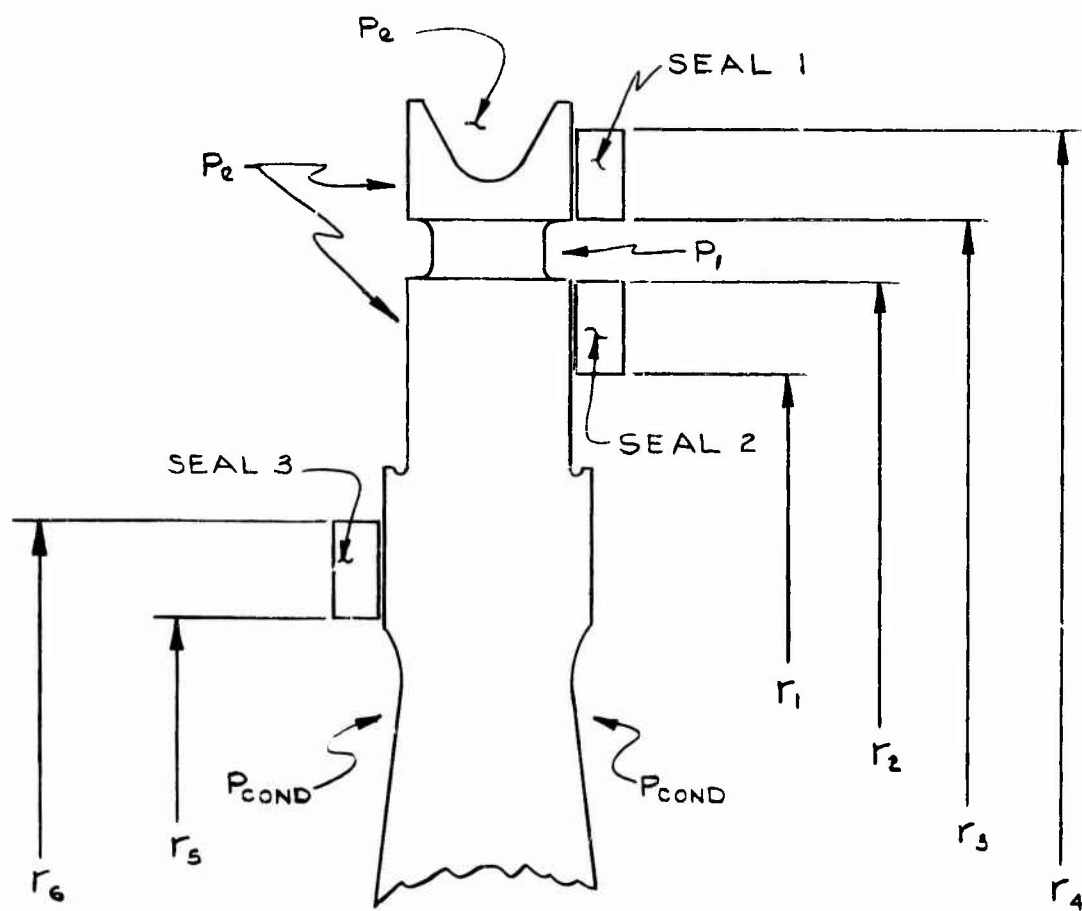


FIGURE 3.1.1

EFFECT OF SEAL CLEARANCE AND LENGTH ON TURBINE EFFICIENCY

COND. PRESSURE = 2.0 psia
 THRUST LOAD = 50 POUNDS
 $\alpha = \beta_2 = 15^\circ$
 TURBINE DIAMETER = 24 IN.

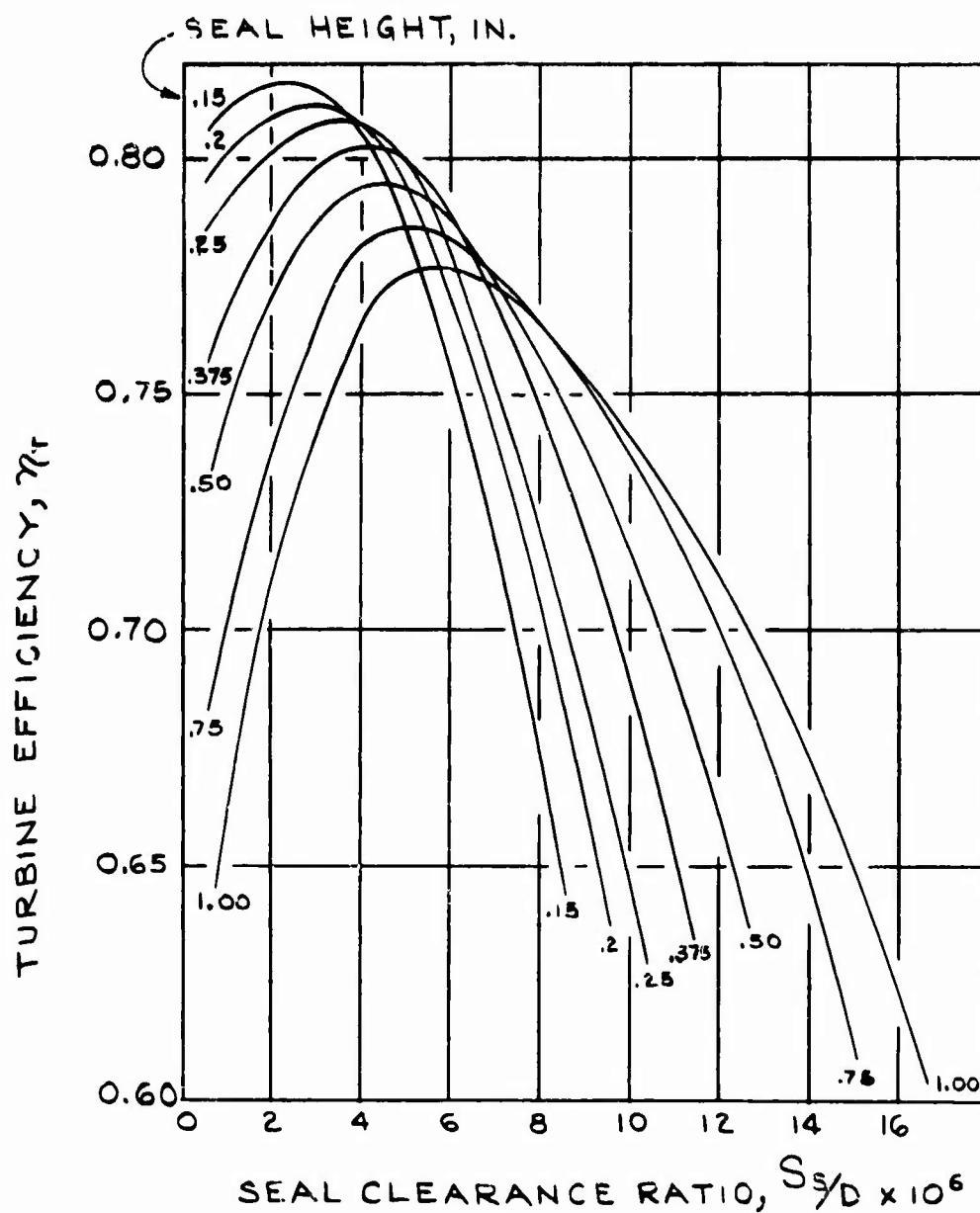


FIGURE 3.1.2

choosing a particular seal design with a non-optimum seal height, chosen to meet stability criteria.

A significant pressure load exists on the inlet side of the turbine rotor due to the rotor inlet pressure between the two front seals, condenser pressure below the lower seal and the thrust load due to pressure existing under each sealing pad. A balancing force exists due to the pressure load on the exit side of the turbine wheel, but since there exists a pressure differential across the turbine rotor, the forces exerted on the exit side of the turbine rotor do not precisely balance the forces exerted on the turbine inlet area. The following procedure was used to evaluate the force balance across the turbine rotor.

The total thrust load under the sealing pads was initially estimated by assuming that the average pressure under the seal is the mean pressure between each side of the sealing surfaces. The actual average pressure under the sealing pad was evaluated for the design seal by FIRL and is included in the design analysis covered in Section 6.5. Using average pressures, the total axial force exerted on the inlet side of the turbine rotor was evaluated for the preliminary design analysis and is given by the following expression:

$$F_1 = \pi \left[(r_4^2 - r_3^2) \left(\frac{P_1 + P_e}{2} \right) + (r_3^2 - r_2^2) P_1 + (r_2^2 - r_1^2) \left(\frac{P_1 + P_{con}}{2} \right) \right], \text{ lbs} \quad (3.1-3)$$

The forces tending to balance the above thrust load are dependent on the seal radius of the rear seal, since lowering this sealing radii increases the area on the exit side of the turbine wheel experiencing 50 psi exhaust pressure, thereby increasing the balancing force. In this analysis the thrust balance was adjusted to yield a net positive thrust on the turbine inlet which will be taken up in the thrust bearing used in the design. The total balancing force is then:

$$F_2 = \pi \left[(r_4^2 - r_6^2) P_e + (r_6^2 - r_5^2) \left(\frac{P_e + P_{con}}{2} \right) + \frac{T_L}{\pi} \right], \text{ lbs} \quad (3.1-4)$$

where T_L is the total thrust bearing load. The selection of the value T_L is explained in some detail in Section 6.5. With specified values for the sealing radii used on the inlet side of the turbine, design pressures established, and the thrust bearing load fixed, the sealing radii on the rear of the turbine necessary to balance the thrust load may be determined by equating the above expressions for axial force, and solving the resulting equation for r_6 . The lower seal radius is then determined by the seal height.

The relative position of the three sealing surfaces used to determine the thrust balance has an effect on turbine performance. For example, if the seal spacing on the front of the turbine rotor ($r_3 - r_2$) were increased, the pressure load existing on the inlet side of the turbine rotor would also increase. Pressure balance then requires the rear seal be lowered, exposing a larger portion of the wheel disk to exhaust pressure rather than condenser pressure. The greater gas density at exhaust pressure tends to increase the frictional loss of the rotating wheel disk, resulting in a net decrease in turbine performance. The overall effect on turbine performance of varying inlet seal spacing is shown in Figure 3.1.3 and the total disk friction loss shown in the curve is derived in the following section.

3.1.2.2 Wheel Disk Friction

A wheel frictional loss is incurred whenever a disk is rotated in a viscous medium. This loss typically varies directly with gas density surrounding the rotor, disk diameter squared, and turbine tip speed cubed. Since the tip speed is also a function of the turbine diameter, the frictional loss is then proportional to diameter to the fifth power. Turbine speed was established by the design specifications and the turbine diameter was chosen to provide optimum performance. With these values specified, the turbine disk friction for the LVF turbine was minimized by venting the turbine disk below the two lower seals on the inlet and exit sides of the turbine wheel to condenser pressure, thereby reducing the gas density next to the wheel.

The total frictional loss for the LVF turbine was evaluated by summing losses determined for four specific sections of the wheel disk. These are: (1) the inlet side of the turbine rotor; (2) exit side of turbine rotor below seal, (3) exit side of turbine rotor above rear seal, and, (4) top of turbine disk shroud.

The frictional loss evaluated for Section 1 was based on experimental data obtained by a number of investigators. For example, the work conducted by J. W. Daily and R. E. Nace (Reference 3.2.7) provided disk friction loss coefficients used in the following relationship. The disk friction loss for Section 1, expressed as a fraction of the available energy, is given by:

$$\xi_{DF_1} = \frac{1}{2} \left(\frac{K_{DF_1} \rho_{ex} D^2 U^3}{1449 W H_{ad}} \right) \quad (3.1-5)$$

For Section 2, the friction loss was expressed as a percentage of the loss obtained for Section 1, by:

$$\xi_{DF_2} = \xi_{DF_1} \left(\frac{r_2}{D} \right)^5 \quad (3.1-6)$$

VARIATION OF TURBINE EFFICIENCY WITH INLET SEAL SPACING

$$\beta_2 = 12^\circ$$

$$P_0 = 140 \text{ PSIA}$$

$$\alpha = 15^\circ$$

$$P = 50 \text{ PSIA}$$

$$S_5 = 0.001 \text{ IN.}$$

$$P_c = 2.0 \text{ PSIA}$$

$$\text{SEAL SPACING} = (r_3 - r_2)$$

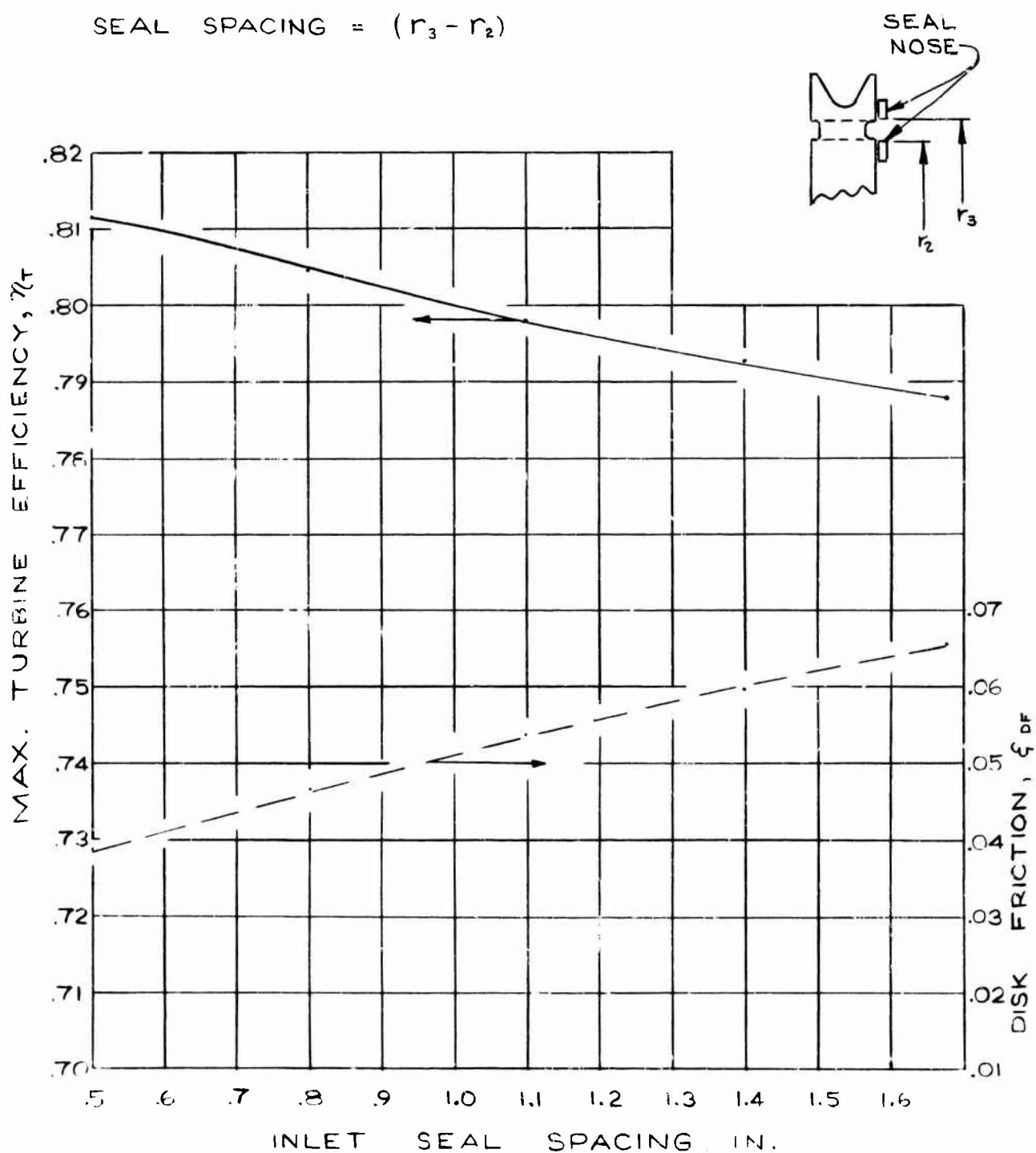


FIGURE 3.1.3

The frictional loss associated with Section 3 was obtained by evaluating the loss for one side of an entire disk of radius r_4 , and subtracting the loss obtained for a disk of radius r_6 at the same gas density. For the radius r_4 , the total disk friction loss is:

$$\xi_{DF-r_4} = \frac{1}{2} \left(\frac{K_w \rho_2 (2r_4)^2 (U_4)^3}{144 g W H_{ad}} \right)$$

where U_4 = turbine tip speed evaluated at radius r_4 . For the radius r_6 , and again using Equation 3.1-5, the disk friction loss is given by:

$$\xi_{DF-r_6} = \frac{1}{2} \left(\frac{K_w \rho_2 (2r_6)^2 (U_6)^3}{144 g W H_{ad}} \right)$$

For a given rotational speed, the turbine tip speed is seen to be proportional to the radius, or:

$$\frac{U_4}{U_6} = \frac{r_4}{r_6}$$

After manipulation, the frictional loss for Section 3 may be expressed as:

$$\xi_{DF3} = \frac{2 K_w \rho_2 U_4^3 (r_4^5 - r_6^5)}{144 g W H_{ad} r_4^3} \quad (3.1-7)$$

The loss factor associated with Section 4 was evaluated using friction factors and loss coefficients presented in Reference 3.1.1. A dimensionless friction factor was obtained in this report for typical disk Reynolds numbers and operating tip clearances for the LVF turbine. The coefficient obtained was 0.002. Using this factor, the frictional moment (M) of a disk of thickness (B) is given by:

$$M = .002 \left(\frac{\pi}{8} \right) \left(\frac{\rho}{g} \right) B D^2 U_4^2, \text{ ft-lbs} \quad (3.1-8)$$

This frictional moment may be expressed as a frictional power loss, or:

$$M_P = M \left(\frac{2U_4}{D} \right) \frac{\text{ft-lbs}}{\text{sec}}$$

The total frictional loss obtained for Section 4, as a percentage of available energy, is therefore:

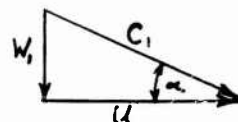
$$\xi_{DF4} = \frac{.002 \pi \rho B D U_4^3}{4 g W H_{ad}} \quad (3.1-9)$$

The seal friction and disk friction losses obtained above are directly subtractive from turbine efficiency, and these factors along with seal leakage constitute the primary geometrical loss factors associated with the LVF turbine design. Aerodynamic loss factors such as nozzle and rotor velocity coefficients are discussed in the following sections.

3.1.2.3 Turbine Efficiency

Relationships were derived defining turbine efficiency for the proposed LVF turbine design by examining the energy transfer between the working gas stream and the turbine rotor. In the proposed turbine concept, the gas stream enters the rotor axially with no relative tangential component of inlet velocity. Hence, the gas stream is accelerated through the stator section until the tangential component of the gas velocity matches wheel speed, eliminating the whirl component of wheel velocity relative to the rotor. The remainder of the expansion energy is taken across the rotor blades and the resulting change in gas angular momentum imparts torque to the turbine rotor. Turbine efficiency was predicted in terms of blade angles, velocity coefficients and relative velocity vectors in this section, using the following velocity diagrams.

Velocity vectors at rotor inlet:



The following relationships are applicable for the condition of axial inlet relative velocity. The absolute velocity at the rotor inlet, corrected for the stator velocity coefficient, is:

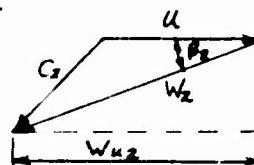
$$C_1 = \psi_n \sqrt{2g J (H_0 - H'_1)} \quad , \quad \text{ft/sec} \quad (3.1-10)$$

The relative rotor inlet velocity is then:

$$W_1 = C_1 \sin \alpha \quad , \quad \text{ft/sec} \quad (3.1-11)$$

This component of velocity adds to the total energy available to the turbine rotor, and after modification was included in the expression used to obtain the rotor exit relative velocity, as follows:

Velocity vectors at rotor exit:



Energy transfer from the working gas stream to the turbine rotor is evaluated by means of the change of angular momentum relative to the rotor. The change in angular momentum is given by the change in the tangential component of relative velocity (W_{u2}) and the

method shown in Reference 3.2.7 is used to evaluate the magnitude of the relative gas velocity leaving the rotor, or:

$$W_2 = \sqrt{\eta_2 W_1^2 + \eta_1 (2gJ)(H_1 - H_2')} \quad , \text{ ft/sec} \quad (3.1-12)$$

where η_1 , the recovery factor, is approximately equal to the square of the rotor velocity coefficient (ψ_R). Reference 3.2.7 indicates that a conservative value of η_2 is η_1^2 , and using these relationships, Equation 3.1-12 becomes:

$$W_2 = \psi_R \sqrt{\psi_R^2 W_1^2 + 2gJ(H_1 - H_2')} \quad , \text{ ft/sec} \quad (3.1-13)$$

At the design point, the relative inlet velocity has no tangential component, and the total change in angular momentum is given by the tangential component of W_2 . The ideal energy transfer to the rotor is then of the form.

$$E_o = \dot{W} \frac{W_2}{g} (\cos \beta_2) \quad , \text{ ft-lb/sec} \quad (3.1-14)$$

where \dot{W} is the total turbine flow. To obtain the actual energy transfer, the flow rate must be corrected due to leakage through the two seals located on the front of the turbine rotor. Also, the above is the total gas energy transferred to the rotor, and frictional losses in the turbine such as seal friction and disk friction must be subtracted from E_o to obtain the true shaft output power.

If the overall available energy is given as:

$$E_A = \frac{\dot{W} C_o^2}{2g} = \dot{W} J (H_o - H_2') \quad , \text{ ft-lb/sec} \quad (3.1-15)$$

then the turbine hydraulic efficiency may be expressed as:

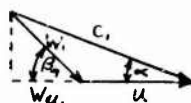
$$\eta_H = \frac{E_o}{E_A} = \frac{2U}{C_o^2} (W_2 \cos \beta_2) \quad (3.1-16)$$

Loss factors examined above, including seal friction, seal leakage, and disk friction, were expressed as a fraction of available energy. As such, they may be used directly to modify the turbine hydraulic efficiency into an actual turbine efficiency as follows:

$$\eta_T = \eta_H (1 - \xi_L) - (\xi_{DF} + \xi_{SF}) \quad (3.1-17)$$

Turbine efficiency as it is defined above is based on the total enthalpy at the turbine nozzle inlet and the enthalpy under static conditions at the rotor exhaust. No correction was made for the kinetic energy in the exhaust gas, and the total to static efficiency evaluated above is used in the remainder of this report to define the performance of the LVF turbine.

A similar analysis was performed for turbine operation under off design operating conditions. The following inlet vector diagram is typical of the turbine operating at less than design speed.



Under this operating condition, the tangential component of absolute inlet velocity is greater than the turbine tip speed, resulting in a whirl component of rotor inlet relative velocity, W_{u1} , defined by:

$$W_{u1} = C_1(\cos \alpha) - u, \text{ ft/sec} \quad (3.1-18)$$

If the off design condition were reversed, such that the tip speed were greater than the tangential component of absolute velocity, the above equation is still valid. W_{u1} would then be negative, and since the positive direction of W_{u1} is in the direction of wheel rotation, the indicated direction would be opposite to wheel rotation. In either case, the magnitude of the relative inlet gas velocity, W_1 , is given by:

$$W_1 = \left[(W_{u1})^2 + (C_1 \sin \alpha)^2 \right]^{1/2}, \text{ ft/sec} \quad (3.1-19)$$

furthermore, under these conditions, the rotor inlet relative velocity no longer enters the turbine axially, but enters at the angle, β_1 , shown in the above sketch.

Since the rotor blades were designed for axial entry, with a 90° blade entrance angle, the gas stream enters the turbine rotor with a certain amount of incidence. The incidence angle in degrees is given by $(90 - \beta_1)$, and Figure 7.1.4 in Section 7.0 was used to obtain the incidence loss coefficient, η_i . This coefficient was used to modify the axial inlet velocity in evaluating the rotor exit relative velocity, or:

$$W_2 = \psi_R \sqrt{\eta_i \psi_R^2 (W_1^2) + 2gJ(H_1 - H_2')}, \text{ ft/sec} \quad (3.1-20)$$

The total change in angular momentum used to evaluate the hydraulic efficiency is given by the change in whirl velocity. Assuming that W_{u2} is positive in a direction opposite to wheel rotation, and taking due regard for the sign of the tangential velocities,

$$\eta_H = \frac{2u}{C_o} (W_{u1} + \cos \beta_2 W_2) \quad (3.1-21)$$

Loss coefficients used in Equation 3.1-17 to obtain turbine efficiency η_T , were evaluated in the same manner as reported in the design point analysis.

3.1.3 Performance Optimization

Using the relationships reported in the preceding section, the performance of the LVF turbine was analyzed and optimized. Parameters optimized were rotor and stator blade angles, and turbine velocity ratio.

The optimum turbine diameter and nozzle angle was established by examining the variation of turbine efficiency with design velocity ratio (U/C_0) for various turbine nozzle angles, as shown in Figure 3.1.4. Variation of design velocity ratio has the effect of changing the degree of turbine reaction, defined as:

$$\rho_r = \frac{H_1' - H_2'}{H_0 - H_2'}$$

This quantity varies with tip speed, since the LVF turbine operates with axial relative inlet velocity at the design point and the portion of total head drop taken in the stator section must be modified so that the tangential component of inlet velocity matches the wheel speed. A similar effect is noted by varying turbine nozzle angle and the degree of turbine reaction is shown for various design velocity ratios, and nozzle angles, in the following table.

DEGREE OF TURBINE REACTION

		Design Velocity Ratio			
		.5	.55	.6	.65
Nozzle	10	.72	.66	.60	.53
Angle,	12	.72	.66	.59	.52
Degrees	15	.71	.65	.58	.51
	20	.69	.63	.56	.48

From Figure 3.1.4 the effect of changing the nozzle exit angle has a minimal effect on LVF turbine efficiency and this parameter was not considered critical in terms of turbine performance. The nozzle exit angle (10^0) specified for this design was based on flow considerations between the stator and rotor sections, explained in detail in Section 6.0. The optimum design velocity ratio as shown in this figure was about 0.62. The design velocity ratio chosen for the LVF turbine design, however, was 0.60 resulting in a turbine diameter of 24" and a tip speed of 1,250 fpm. This velocity ratio is slightly less than the absolute optimum; however, since very little change in turbine performance was observed, the lower velocity ratio was chosen which results in a slightly smaller turbine diameter.

VARIATION OF MAXIMUM TURBINE EFFICIENCY WITH VELOCITY RATIO AND NOZZLE ANGLE

$$\beta_1 = 90^\circ$$

$$\beta_2 = 15^\circ$$

$$\gamma_N = \gamma_R = 0.96$$

$$S_s = 0.001 \text{ IN.}$$

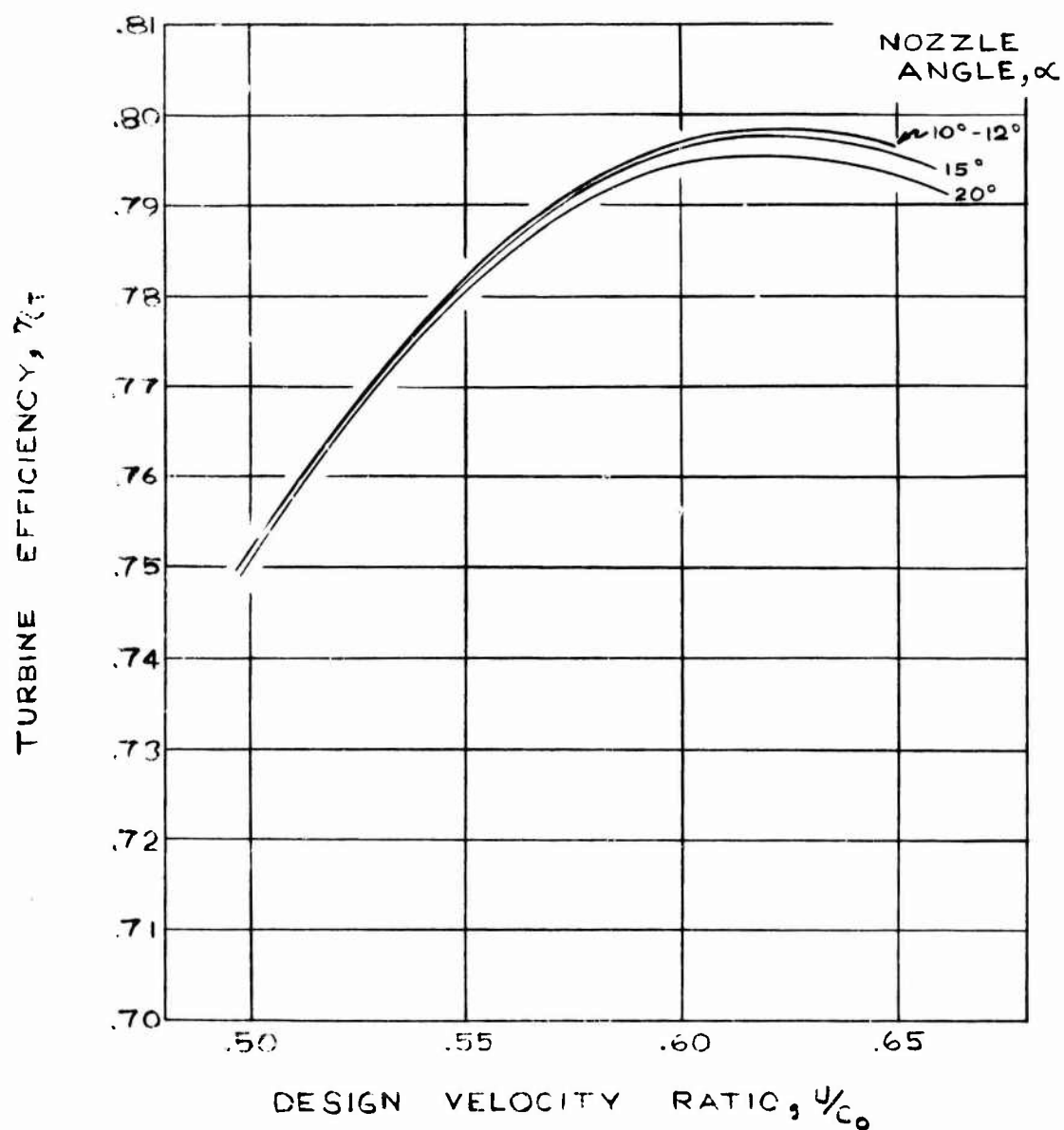


FIGURE 3.1.4

As shown in Figure 3.1.5, the rotor exit blade angle is much more critical in terms of turbine performance than is the nozzle angle. As should be expected, the turbine efficiency increases with decreasing nozzle angle for a fixed blading efficiency. The design blade angle (12°) was chosen on the basis of turbine performance and manufacturing considerations. From a performance standpoint, it is advantageous to use the smallest blade angle practical, and to facilitate a rotor blade channel integral with the turbine disk; a minimum blade angle of 12° was chosen.

VARIATION OF MAXIMUM EFFICIENCY WITH VELOCITY RATIO AND ROTOR EXIT ANGLE

$$\beta_1 = 20^\circ$$

$$\alpha = 15$$

$$\gamma_N = \gamma_b = 0.96$$

$$T_L = 50 \text{ LBS.}$$

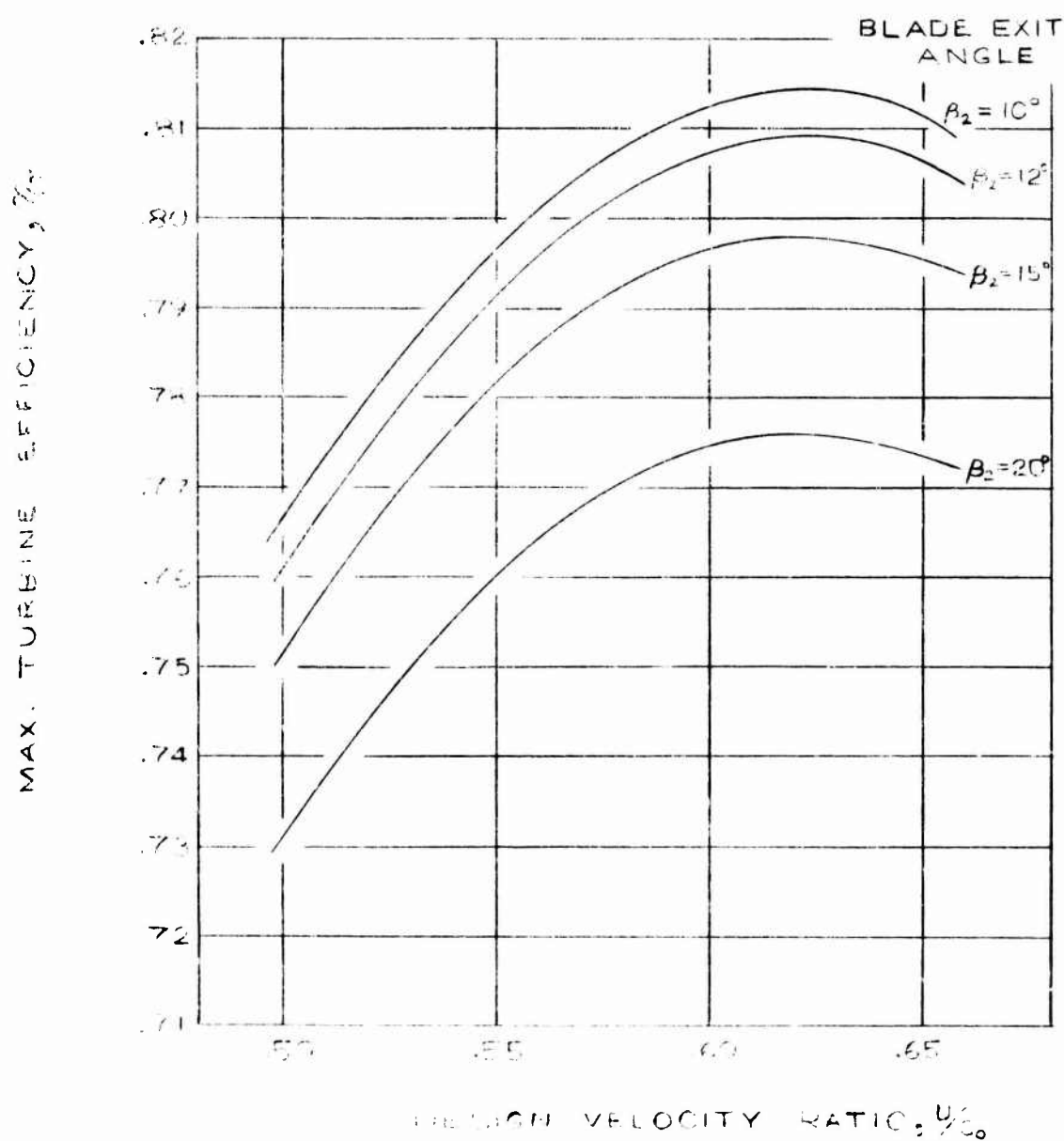


FIGURE 3.1.5

3.2 HEAT TRANSFER ANALYSIS

This discussion will include those means used to evaluate a temperature gradient throughout the turbine. This section will define the approaches used in obtaining local heat transfer coefficients in the various areas, the means of evaluating the disk friction (which is a heat added to the system), evaluation of the circulation flow around the disk, and finally, an evaluation of the means of calculating the temperature throughout the system. Several approaches were analyzed in an attempt to obtain the most applicable for this particular configuration. These approaches will be discussed in detail in the following sections.

3.2.1 Main Body of Disk

A cross section of the overall turbine configuration is shown in Figure 3.2.1. In evaluating the local temperature distribution throughout this system, it is important to obtain values of all areas of heat input and heat rejection to the system. The heat transfer coefficients are also very important in that they provide the means for the heat flow. This is a particularly difficult heat transfer problem, since a number of complex functions are occurring which add or subtract heat from the system. The initial heat source of the system is the high temperature (430°F) steam of the turbine inlet. Although the exhaust temperature is considerably lower (330°F), it is desirable to maintain the turbine wheel and most of the housing at an even lower temperature than this exhaust gas temperature to prevent thermal distortion. Considerable heat is also added to the system through the friction occurring at the seal faces and through disk friction around the disk. The magnitude of these heat additions is approximately 9 HP in the seal area and 1.3 HP due to disk friction on the low (2 psia) pressure area. Because of the centrifugal compressor action of the disk, there is considerable mixing of the flow between the disk root and the disk tip, hence, this mixing action must also be considered when evaluating the gas temperature adjacent to the disk.

3.2.1.1 Local Heat Transfer Coefficient

The local heat transfer coefficient along the disk surface is difficult to evaluate on a theoretical basis because of the large turbulence in mixing which occurs. However, several reports have data relating to these conditions. These include References 3.2.1 through 3.2.5. Calculations of the heat transfer coefficient for the disk were made using correlations presented in these references. Although none of these references represented exactly the conditions of the LVF turbine, they provided a basis for comparison and analysis to obtain heat transfer coefficients for the LVF turbine.

SKETCH OF TURBINE CROSS SECTION

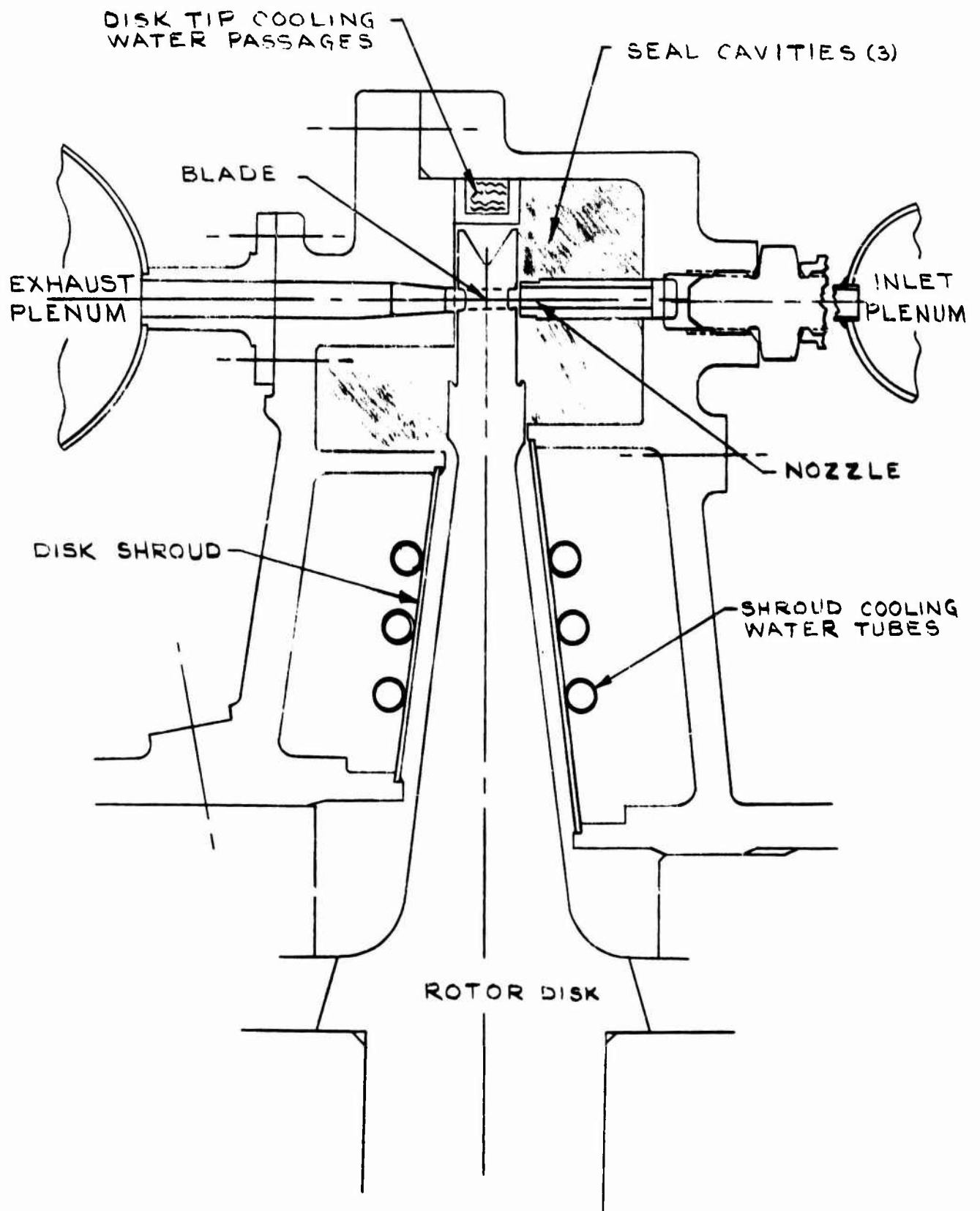


FIGURE 3.2.1

The basic considerations applicable to the LVF turbine are those associated with heat transfer, due to disk friction of the wheel and mass transfer into the gas surrounding the disk, due to the leakage flow from the seals at the periphery of the disk. Reference 3.2.1 presents data showing the heat transfer to a rotating disk including the effects of mass transfer. However, the dimensionless leakage flow rate parameters which are presented in Reference 3.2.1 are two orders of magnitude larger than those of the LVF turbine. Consequently, in obtaining the heat transfer coefficient from this reference, an extrapolation of the data was necessary. Using these data of Reference 3.2.1, the total disk heat transfer coefficient was obtained as 28 BTU/hr - ft² - °F on the nozzle side of the disk and 57 BTU/hr - ft² - °F on the exhaust side of the disk. The change of a factor of two in heat transfer coefficient results from the leakage rate being considerably different on each side. This variation due to leakage flow rate, of course, is not applicable to the actual case since the leakage flow rate is so small as to approach a situation of no leakage flow as far as heat transfer coefficient is concerned. Therefore, these heat transfer values can only be used as a guide and the correlation of this reference is judged not applicable to the LVFT situation.

The second reference, Reference 3.2.2 "Mass Transfer, Flow, and Heat Transfer by a Rotating Disk", has a very general correlation for the calculation of disk friction. This equation yields a heat transfer coefficient for the disk of 3.6 BTU/hr - ft² - °F. This value is felt to be the other extreme from that of Reference 3.2.1 and is quite low for forced convection considering the velocities of the disk.

Reference 3.2.3 "Analysis of Turbulent Flow and Heat Transfer on a Flat Plate at High Mach Numbers with Variable Fluid Properties" was then used to calculate the average disk friction of the wheel. This more general paper based on flat plate tests rather than rotating disks could be considered to be conservative in that the high turbulence to centrifugal mixing effects in the case of the rotating disk would not be considered; however, the heat transfer coefficients were felt to be reasonable and should be conservative for use in the LVFT configuration. Based on the correlation of Reference 3.2.3, an average heat transfer coefficient for the wheel was found to be 6.93 BTU/hr - ft² - °F.

When considering the three analytical approaches, it was judged that the approach of Reference 3.2.3 would be most applicable to the LVFT configuration, and would result in slightly lower than actual heat transfer coefficients and, hence, would be a conservative approach to use when calculating the temperatures throughout the turbine disk and the nearby housing. Consequently, this correlation was used for the analysis.

3.2.1.2 Disk Friction

A large number of references (References 3.2.6 through 3.2.13) concerning disk friction are available. These references include both theoretical and experimental data. A summary of data presented in many of these references is shown in Figure 3.2.2. It may be noted that there is a large variation in disk friction between the various authors. However, the majority of the data is similar and it includes six references, Reference 3.2.6 through 3.2.11. The other references which do not agree well are those of Buckingham and Stodola, which do not vary as a function of Reynold's number. These older references are probably valid for the conditions at which the data were taken, however, not applicable to a large range of Reynold's numbers. The recent data of Daly and Nece (Reference 3.2.7) and Mann and Marston (Reference 3.2.6) are felt to be the most accurate and were used in determining the disk friction coefficients.

The disk friction of a freely rotating disk is considerably higher than that of a shrouded disk. The reason for this difference is that a freely rotating disk will induce circulation of a large amount of gas thereby resulting in a large amount of work on the gas while a disk that is closely shrouded increases the friction between the gas and the disk, however, decreases the mass flow circulated and, hence, the disk friction is decreased. A decrease in disk friction as much as a factor of four is reported in References 3.2.12 and 3.2.7. As compared to an unshrouded disk, the shrouded disk can be expected to result in from one-third to one-fourth the disk friction of the unshrouded disk. The disk friction coefficients shown in Figure 3.2.2 have been modified; when the effect of shrouding was not shown it was assumed that the disk friction was decreased by one-third over that of the unshrouded disk. It may also be noted that Figure 3.2.2 includes the friction on both sides of the disk.

3.2.1.3 Circulation Flow

In evaluating the temperature gradient and heat transfer distribution of the LVF turbine, it is important to determine the amount of heat which is carried up the disk and down the shroud wall due to the pumping action of the disk. This pumping action, in effect, provides violent mixing and temperature equalization of the disk fluid. Several references are available concerning this recirculation flow. The references considered were References 3.2.2 and 3.2.5. However, these references proved to be of little value, since in the first reference flow was injected and in the second reference the amount of circulating flow was dependent upon the amount of naphthalene evaporated from the disk during the experimental test. Since these conditions are not consistent with the LVFT conditions, the information was not used for this application.

COMPARISON OF DISK FRICTION DATA (TWO SIDES IMMersed)

POWER = KW $\frac{\rho}{g} U^2 U^3 \frac{\text{ft-lb}}{\text{SEC}}$

- D TURBINE DIA ft
- U TIP SPEED ft/SEC
- ρ GAS DENSITY lb/ft³
- g 32.2 ft/SEC²

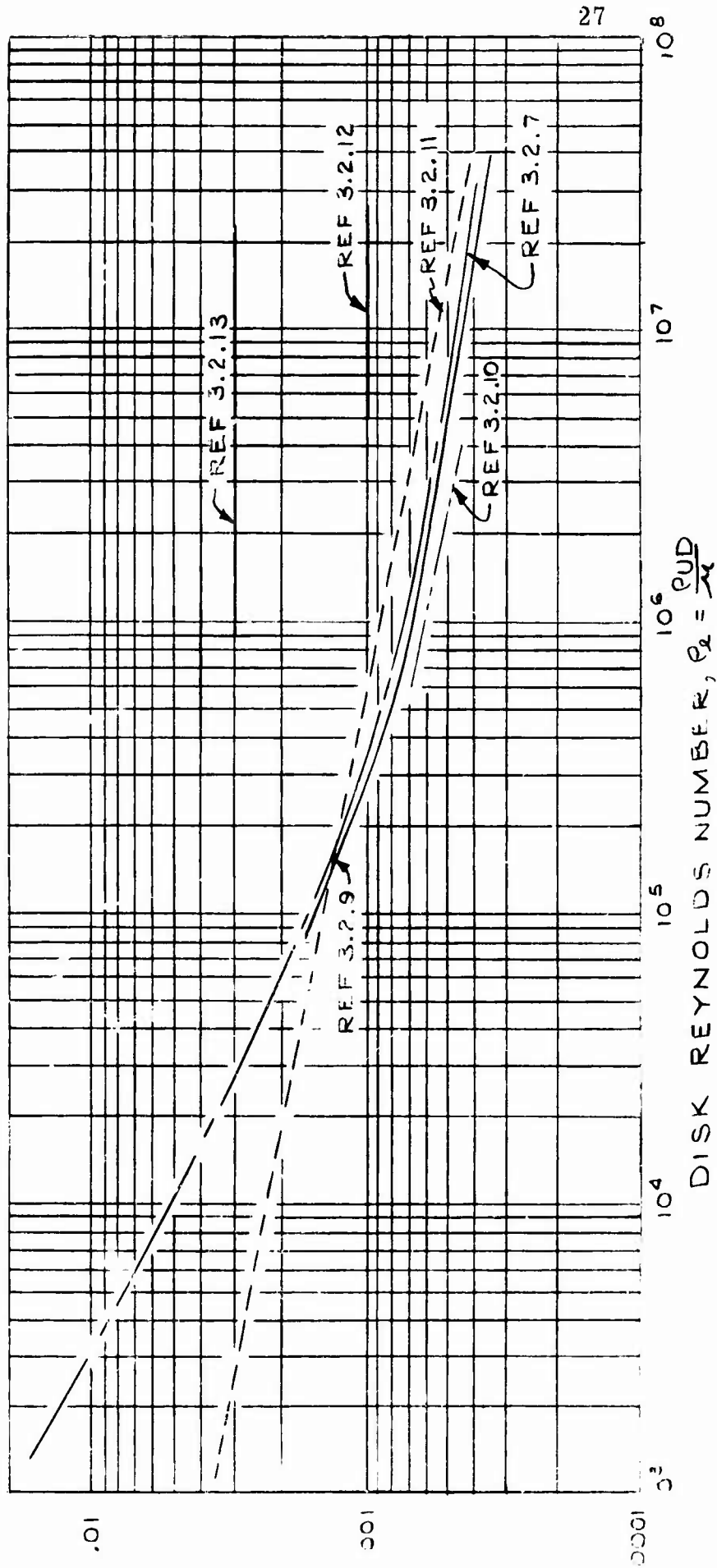


FIGURE 3.2.10 DISK FRICTION COEFF - KW

Unpublished experimental data obtained by the authors showed that the average velocity vector across a rotating disk was inclined at approximately 15° from the tangential velocity. In other words, a radial vector of approximately $\sin 15^\circ$ times the tangential vector is representative of the turbine configuration. Therefore, in the following heat transfer analysis, it was assumed that this radial vector described the mixing velocity in the gas.

3.2.1.4 Means of Cooling

Several means of cooling the disk were considered. These included rejecting the entire disk friction heat to the leakage flow through the peripheral seals, natural convection from the turbine housing to the surrounding air, and water cooling of the disk shroud.

Most turbines reject the disk friction heat by an open cycle heat rejection to the exhaust. That is, the relatively low temperature turbine exhaust gas flows into the disk cavity between the rotating disk and the shroud and here it is circulated by the pumping action of the disk and heated by the disk friction. Then the gas flows into the turbine exhaust at higher temperatures, carrying off the disk friction losses. In the LVFT concept, the leakage flow is greatly reduced over that of the conventional turbine, which circulates a large amount of flow in and out of the disk cavity. Hence, the disk friction is added to a relatively small amount of vapor and the vapor temperature would become unacceptably high. In fact, the leakage gas flow will become excessively hot just due to the seal friction that is partially absorbed by this leakage gas. Therefore, it is concluded that the disk friction heat could not be rejected to the leakage flow and other means of rejecting the heat would be required.

An examination was made to see if the disk friction heat could be rejected from the turbine housing by natural convection. Using the procedures presented in Reference 3.2.14 for natural convection, the natural convection heat transfer coefficient was found to be between 1 and 1.5 BTU/hr - ft² - °F. Assuming all disk friction heat must be rejected from the casing, then the temperature difference to reject the heat is approximately 600°F. Since this temperature is far in excess of any that could be tolerated, the natural convection approach was rejected. Another problem with natural convection would be that the turbine position in the associated machinery would have to be carefully located so that the natural convection air currents would not be prevented. Since this is difficult to assure in all cases, natural convection at best would be an awkward compromise.

The two more conventional and easily accommodated means of cooling the disk were rejected as inadequate. Therefore, it was felt that the disk must be water cooled in order to reject the disk friction heat.

3.2.1.5 Turbine Disk Heat Transfer Analysis

A thermal analysis of the turbine disk and surrounding area was made to determine the temperature and the gradients through these components. These temperatures were then used in the stress analysis of the disk.

A thermal model of the disk and its surroundings was set up with specified boundary conditions and the heat transfer was computed using a digital computer program described in Section 7.2.5.

The analysis used a 15° segment of the turbine disk which was divided into 28 temperature nodes. These temperature nodes are small elements of the system and are represented by a temperature at the center of the element. The heat transfer throughout the system is analagous to electrical current flow so that the problem can be solved using a resistance network. Each temperature node is connected to its adjoining nodes, which affects its temperature by a conductor. Conductors for heat transmission by conduction, convection and fluid flow conductors were used in this analysis. These conductors are defined in Section 6.2 of this report.

The boundary conditions established during the analysis are:

- 1 The cooling water temperature held constant at 130°F .
- 2 Temperatures of the upper portion of the disk at the edge and at the disk center held constant at 330°F and 380°F , respectively. These temperatures are assumed fixed because of their close proximity to the turbine nozzles.
- 3 The hub area of the disk is maintained at 130°F .
- 4 The vertical center line of the disk is assumed to be an adiabatic surface.
- 5 A one-half section of the disk was analyzed since it is assumed that the temperatures on the other side would be a mirror image.

The source of heat addition to the system is the disk friction in the annular space between the shroud and the turbine disk. This volume is vented to condenser pressure (2 psia) to minimize disk friction power losses by reducing the density of the steam in this space.

A recirculation flow pattern will be set up by the rotation of the disk and the frictional forces between the disk and the steam. The steam will flow upwards along the disk and then down along the shroud.

Disk friction was added to the ten fluid nodes in this annular space. In a fluid node the temperature of the upstream node affects the node downstream of it as a function of the flow velocity, density, and distance. In order to determine the magnitude of the fluid conductors, the mass flow or velocity of the recirculating steam must be determined.

Previous experience with steam and gas turbines shows that a circulation pattern of gas on the face of a rotating disk spirals outwardly from the disk center with a resultant velocity vector at 15° from the tangential velocity. Based on this observation, the radial velocity of the recirculation gas was determined. The steam circulation in the annular space between the shroud and the disk was then determined and the fluid conductors were calculated. Section 6.2 shows in more detail this calculation.

Disk friction heat is added to the fluid nodes and is transported through the annular space between the disk and the shroud by the fluid conductors. This heat is dissipated into the turbine disk and the shroud's water jacket by conduction and convection.

Heat is added to the system by the disk friction until the heat entering equals the heat leaving into the cooling water. At this point all the node temperatures will be in equilibrium.

The heat transfer computer program does have the capability of showing the transient temperature response of the system. However, transient temperatures were not computed in this analysis due to the extremely long computer time which would be necessary. The long computer time is necessary due to the large difference in the capacitance of the fluid and solid nodes. In order to achieve convergence in the calculations a minimum time step must be used which is a function of the nodes' capacitance. The smallest value of capacitance will determine the minimum time step. To achieve a reasonable compute time, a high value of capacitance was input for all the variable temperature nodes which will make the program converge more quickly but will invalidate transient temperatures.

The heat transfer coefficients discussed in paragraphs 3.2.1.1, 3.2.1.2, and 3.2.1.3 were used in the calculation of the disk temperatures.

The steady state temperature distribution of the disk, shroud and recirculating steam indicates reasonable temperature gradients along the disk for adequate mechanical design analysis. No problem is anticipated in the thermal control of this area. The stress analysis design section of this report discusses in detail the design of the disk based on the thermal gradients evaluated here.

3.2.2 Disk Shroud and Seal Area

The outer periphery of the turbine rotor is of particular interest in considering the temperature distribution since this area is the highest stressed area of the turbine. This area is also the most complex to analyze since the largest number of external factors are affecting the disk surface. These external factors include: the seal leakage flow around the disk; the seal friction; the disk friction; the heat conducted from the live steam flow through the turbine; and the effect of cooling due to the water flow through the tip shroud. Figure 3.2.1 schematically shows this configuration. Each of the items mentioned above will be described in detail in the following sections.

Heat is added to this area of the turbine by hot leakage gas, seal friction, and disk friction. The seal friction and the seal gas leakage flow rate were calculated from equations obtained from FIRL.

The leakage flow rate is quite important in that it provides a means of carrying off the seal friction heat in the leakage flow, thereby preventing excessive heating of the seal. It also is a heat source which is adding heat to the disk. The analysis shows that the largest diameter seal would reach excessively high temperatures without external cooling. Therefore, water cooling is provided to the casing at the disk tip as shown in the sketch of Figure 3.2.1. This water cools the gas around the disk tip shroud which in turn cools the seal face area and, hence, controls the seal face temperature to acceptable limits.

3.2.3 Nozzle and Blade Area

The heat transfer coefficient is evaluated for the nozzle flow passages based on conventional forced convection correlations presented in Reference 3.2.17.

The blade heat transfer coefficient determination is more complex as little published data are available. This coefficient was evaluated using an unpublished empirical procedure developed by the authors. The total temperature of the gas relative to the blade is lower than the steam inlet temperature due to the energy extracted to reach the rotational velocity of the disk. This temperature is used to evaluate the fluid properties of the steam in the rotor and is the temperature used for heat transfer analysis.

3.2.4 Turbine Housing

The heat transfer analysis used to determine the steady state temperatures of the turbine housing components is similar to that used for the turbine disk. The same computer program was used for both analyses.

The analysis of the turbine housing also contains solid and fluid nodes like the turbine disk area. The combination of the solid and fluid nodes gives the same problem as for the turbine disk in that the computer time would be too long to calculate the transient temperatures unless a much faster computer is used. Therefore, false values of capacitance were input for all the nodes other than the fixed temperature nodes in order to bring the calculation to convergence more quickly.

Heat is added to the turbine housing area by the high temperature steam passing through the inlet ducts, the turbine blades and the exhaust duct. The chief mechanism for this heat addition is convection from the steam to the passage walls. Other sources of heat addition are from the fluid friction in the seals and disk friction on the turbine wheel tip.

The outer rim of the turbine wheel has a 5" x .375" passage which carries cooling water flow at 130°F, maintaining this area at a constant temperature. The other boundary conditions are the temperatures of the inlet, leaving, and turbine blade steam which are held constant at 430°F, 281°F, and 354°F. The main part of the turbine disk is also held constant at 336°F.

The turbine housing rejects heat by natural convection to the surrounding air which is fixed at 100°F.

The temperature distribution as calculated by the program for the turbine housing and surrounding area shows that the only apparent problem area is the temperature difference between the components on the inlet side as compared with the exhaust side. From a thermal stress viewpoint it would be desirable if this axial temperature gradient could be reduced to zero and the radial temperature gradient on the inlet and outlet side be approximately the same. This can be done by extending the disk shroud cooling water jacket to the area which must be cooled. The temperature distribution is shown in Section 6.2. This area of the thermal control problem will be examined more thoroughly during the next phase of this program.

The thermal control of the turbine housing is not considered to be a significant problem and relatively minor design changes should be able to provide a temperature distribution suitable for a reliable mechanical design.

3.2.5 Shaft and Bearing Area

The design of the thrust and journal bearings require condenser water to be used as a cooling medium. This water will be 130°F and sufficient water will be supplied to maintain the temperature of the bearings and the adjacent shaft area at the water temperature.

Heat flow from the turbine disk into the disk center and the shaft is not considered to be a significant problem based on the results of the disk heat transfer analysis and extended into the disk center and shaft area. This analysis shows that 6.4 BTU/min flows into the shaft both in the forward and aft directions from the disk. This additional heat will require an additional 1.25% of water to be added to the bearing cooling system.

3.3 VIBRATION ANALYSIS

The turbine blade natural frequencies, disk and rotor critical speeds, critical modes and possible excitation sources were investigated for their importance and effect on the successful operation of the LVF turbine. The investigation revealed areas where the turbine was unique, determining where the analytical effort should be concentrated.

3.3.1 Blade and Shroud Vibration

Vibration investigation is important in the successful operation of all turbines, and is equally important to the LVF turbine. The normal frequencies considered for steam turbines are, in order of importance, the fundamental mode, the second bending mode, and the torsional mode. When the blades are in packets, the translation and pitching mode of the packet should be considered. These modes, for the most part, are non-existent in the LVF turbine concept. They are non-existent because the blades are short and because of the restraint provided by the continuous shroud, which only allows movement in the axial or tangential directions. The frequencies possible to excite with significant amplitude would be a mode in which all the blades would deflect in unison. The movement of the blades restrained by the shroud is only possible in this turbine concept in the axial direction and the tangential direction, called the axial and tangential mode. (Figure 3.3.1) These modes were analyzed and adjusted so that the resulting frequencies were not excitable from possible excitation frequencies. The excitation frequency sources in the LVF turbine are from running speed, seal segments, nozzles, and nozzle segments. The damping available is material damping, aerodynamic damping, and seal damping. The seal damping is considered to be insignificant.

3.3.2 Turbine Disk Vibration

The LVF turbine has close running clearance between the seal and disk, making the disk critical speeds of primary importance. With the disk sides being used as mating surfaces for the seal, any shape the disk assumes from operating at or near a diametral mode (Figure 3.3.2) can cause rubbing or excessive seal movement which may result in excessive leakage. The diametric modes are caused by operating at critical speeds where an integral number of waves fit exactly into the circumference of the disk. The criteria followed for any disk design given a mean diameter, blade type, and shroud design, is to establish a disk thickness in excess of that required to resist centrifugal and thermal stress, which will keep the disk's critical speed at a safe margin from operating speed and its harmonics.

TURBINE BLADE VIBRATION MODES³⁷

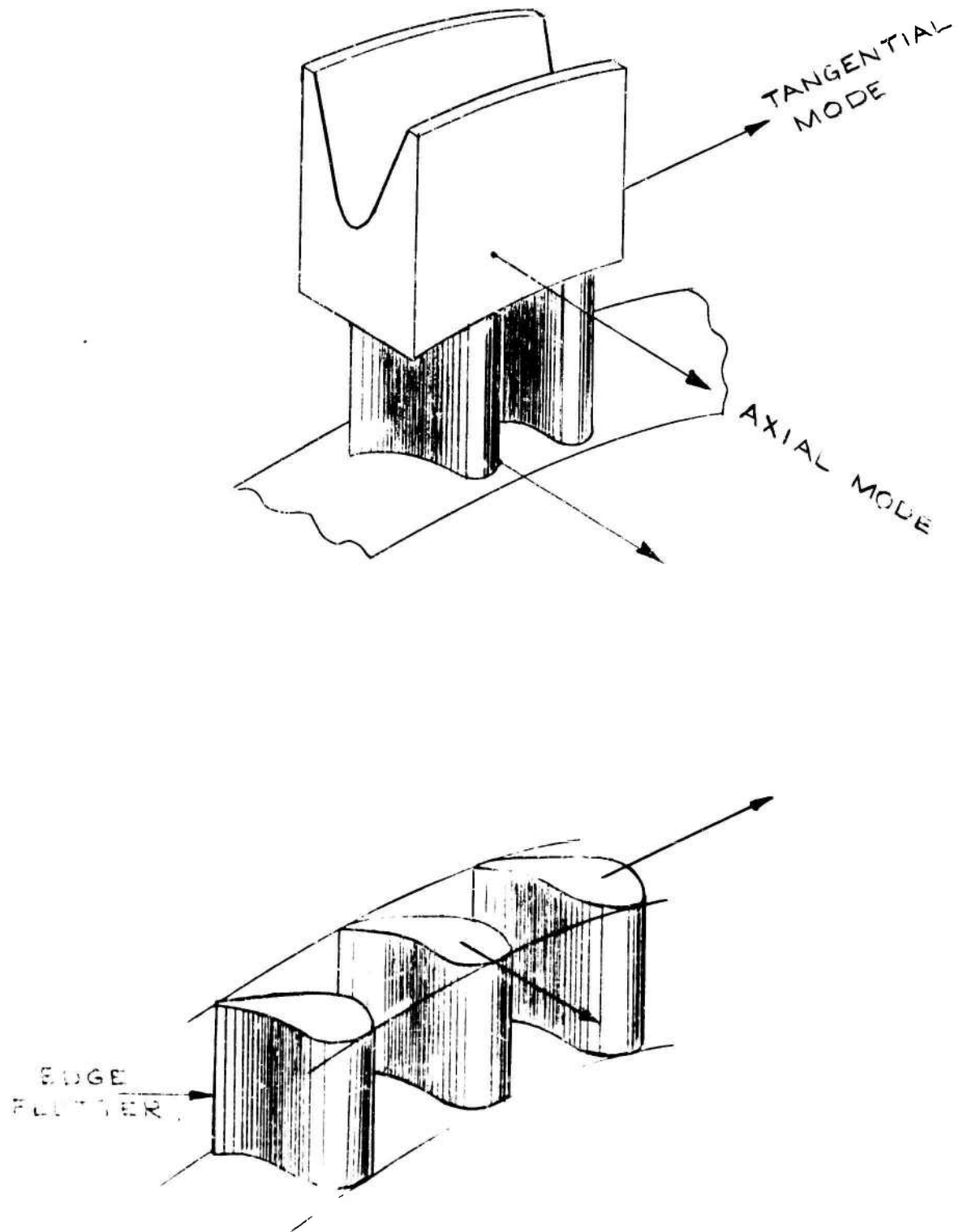


FIGURE 3.3.1

DIAMETRAL MODES

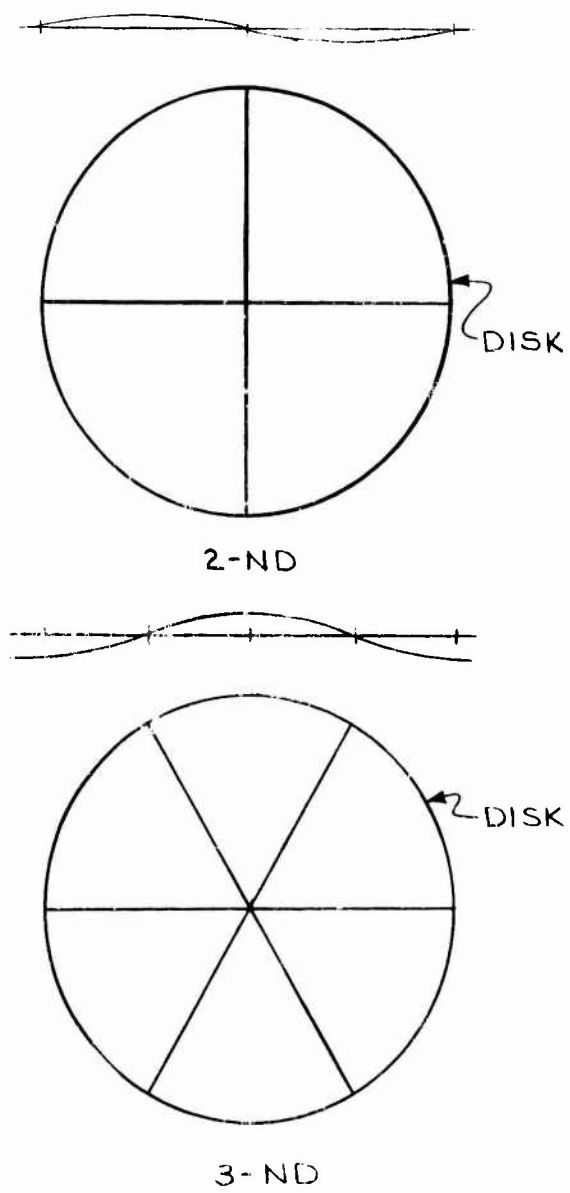


FIGURE 3.3.2

The analysis of the disk vibration is far from exact and the coupled modes are unpredictable. Therefore, it is considered good practice in a disk where vibration is critical to the performance of the disk to leave extra material on the disk that can be removed after manufacture. The disk is then tested, the nodal diameters defined, and if necessary, material machined away, detuning the disk frequencies from the excitation frequencies.

3.3.3 Rotor Dynamics

The L V F turbine requires a rotor system that will confidently operate from start to running speed without excessive vibration or significant axial excursions or radial movement from a co-axial position. The turbine requires close running clearances that make these requirements of importance beyond that of a normal turbine-disk relation. The minimization of misalignment and the 12,000 rpm operating speed dictated the size of bearings and bearing center distance. (Figure 3.3.3) These two criteria quite obviously result in a design concept which uses a stiff shaft which, fortunately, is the simplest to analyze, providing the most confidence in the mode shapes and dynamic characteristics. The first critical, called the cylindrical mode, assumes a linear system and is a function of rotor mass, bearing and shaft stiffness, and the flexibility of the supports. The L V F turbine rotor system requires the consideration of two additional modes of vibration; one, the conical mode and two, half-frequency whirl. (Figure 3.3.4) In addition, the load carrying capacity of the bearing is a function of both weight and dynamic unbalance and is established by the bearing film thickness.

BEARING SPACING DESIGN

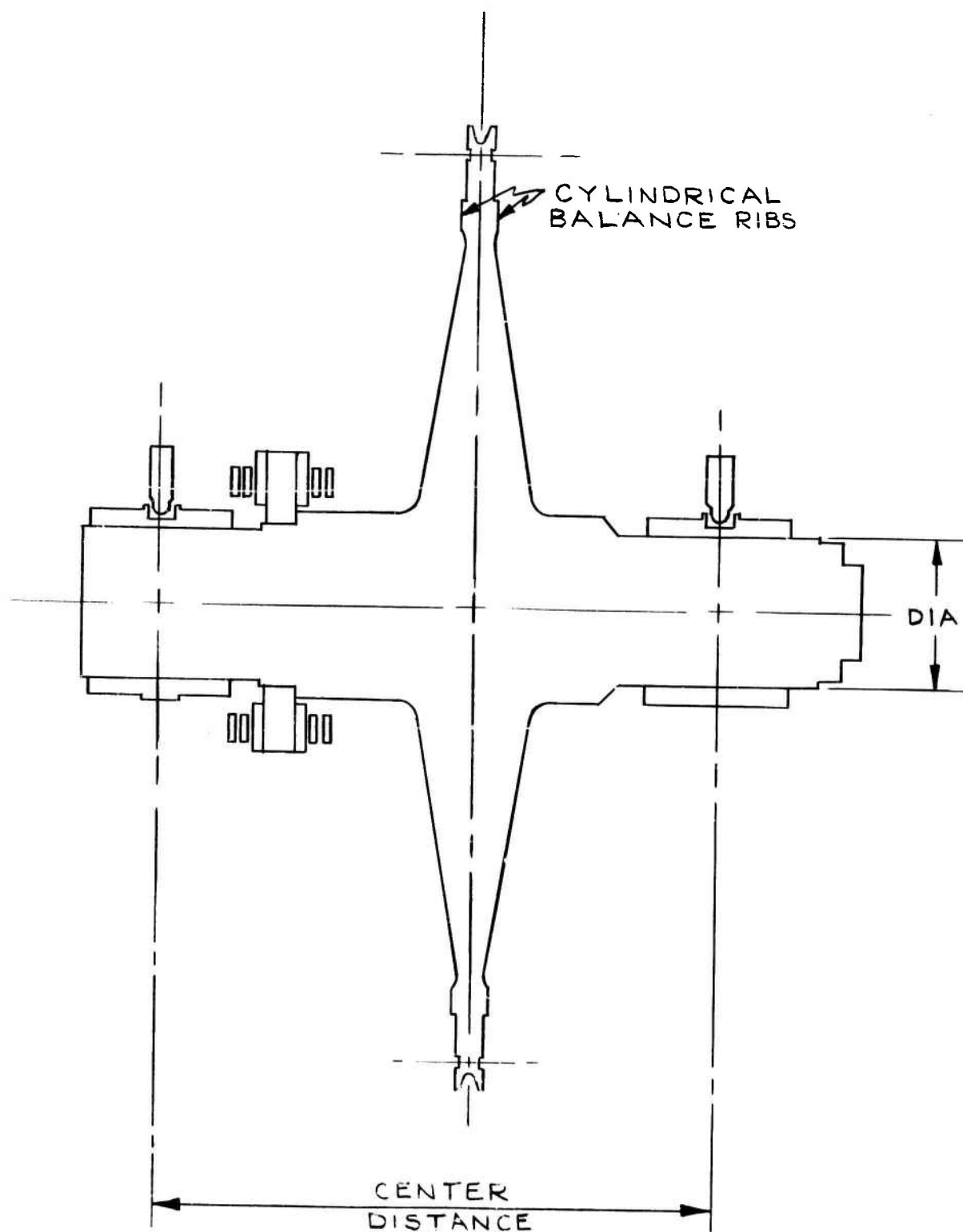


FIGURE 3.3.3

SHAFT VIBRATION MODE

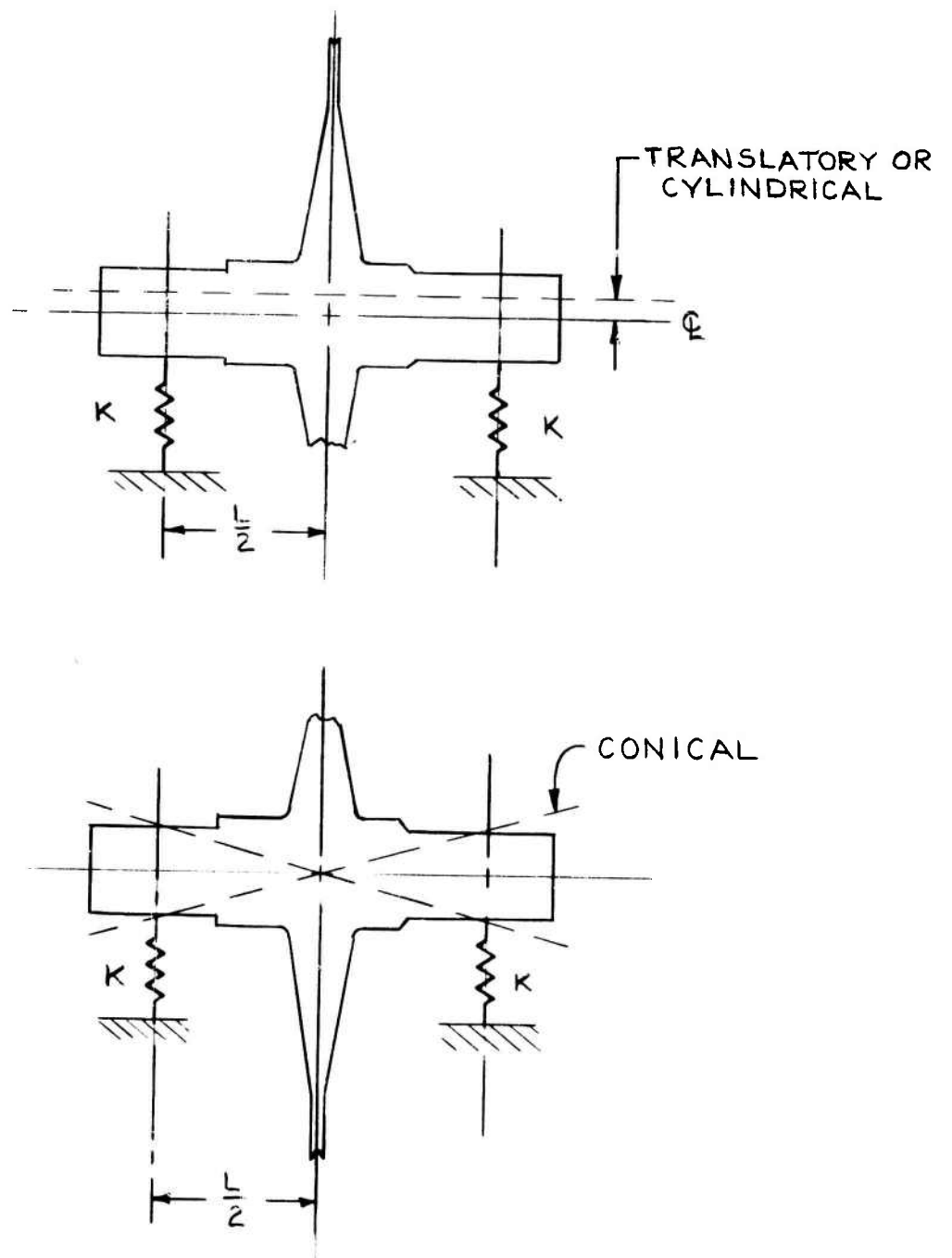


FIGURE 3.3.4

3.4 STRESS ANALYSIS

The preliminary design of the L V F turbine required substantial stress analysis in three primary areas. These areas are: (1) blades and shroud; (2) the disk; and (3) the casing. The increased importance of the stress analysis in these areas is due primarily to the use of controlled-leakage seals requiring exact alignment. This required alignment must be obtained with as little influence from structural distortions caused by mechanical or thermal loads as practical. The remaining areas of the mechanical design followed well-established design procedures. This section discusses the stress analysis performed and elastic investigations made necessary to establish the final preliminary design.

3.4.1 Turbine Blades and Shroud

The L V F turbine requires a shroud of considerable radial thickness to be attached to the tip of the blades in order to accommodate the seal running face. (Figure 3.4.1) This requirement is unusual in turbine design because the radial thickness of the continuous shroud is sufficiently thick that the shroud is acting as a ring that depends on the blades for continuity between the shroud and disk. Normally, in turbine design the shroud, in addition to being thin, is split into segments and cannot develop significant tangential stress. The shroud is not split in the L V F design because the seal face would have to run over radial discontinuities. These discontinuities, if present, would have provided axial leakage paths and also could cause deterioration of the seal.

The growth of the shroud is caused by the centrifugal force and thermogradient. The blades attached to the shroud and disk prevent the shroud from expanding as if it were a free rotating ring subjected to a thermogradient. The shroud being a thin ring and the disk being solid would result in differential growth if it was not prevented by the blades. The required restraint results in a tensile stress in the blades, additional radial stress in the disk, and local stress in the shroud. To decrease the growth of the shroud from centrifugal force, material was removed where it was not required for strength by adding a groove in the shroud. The thermal growth of the shroud was reduced by water cooling the housing that surrounds the shroud, thereby cooling the shroud and seals. (Figure 3.4.1) Additional bending moments are applied to the shroud from the seal and from the pressure differential between the inlet and exit side of the disk. These bending moments made it necessary to perform an elastic composite analysis of the shroud and blade.

The geometric shape of the shroud is designed to prevent bending moments from being applied to the blades and to minimize twisting of the shroud caused by centrifugal force and thermogadients. The shroud is designed with its center of gravity coinciding with the center of gravity of the blades and disk. The shroud has heat added on the inlet side from the seal and therefore has a significant local temperature increase of the surface and an increase in average temperature of the seal face side of the shroud. In order to cool the hot side of the shroud, minimizing the thermogradient, the inlet side of the shroud will have fins added. Without provision being made to obtain an equal average temperature of the two sides of the shroud, the difference in radial growth would apply bending moments to the blades and would result in the shroud twisting, causing excessive seal leakage. The analysis necessary in this area is not complete. The size and number of fins necessary to reduce the thermogradient will be established in the final phase of this report.

CRITICAL DIMENSIONS OF SHROUD AND BLADE USED IN STRESS ANALYSIS

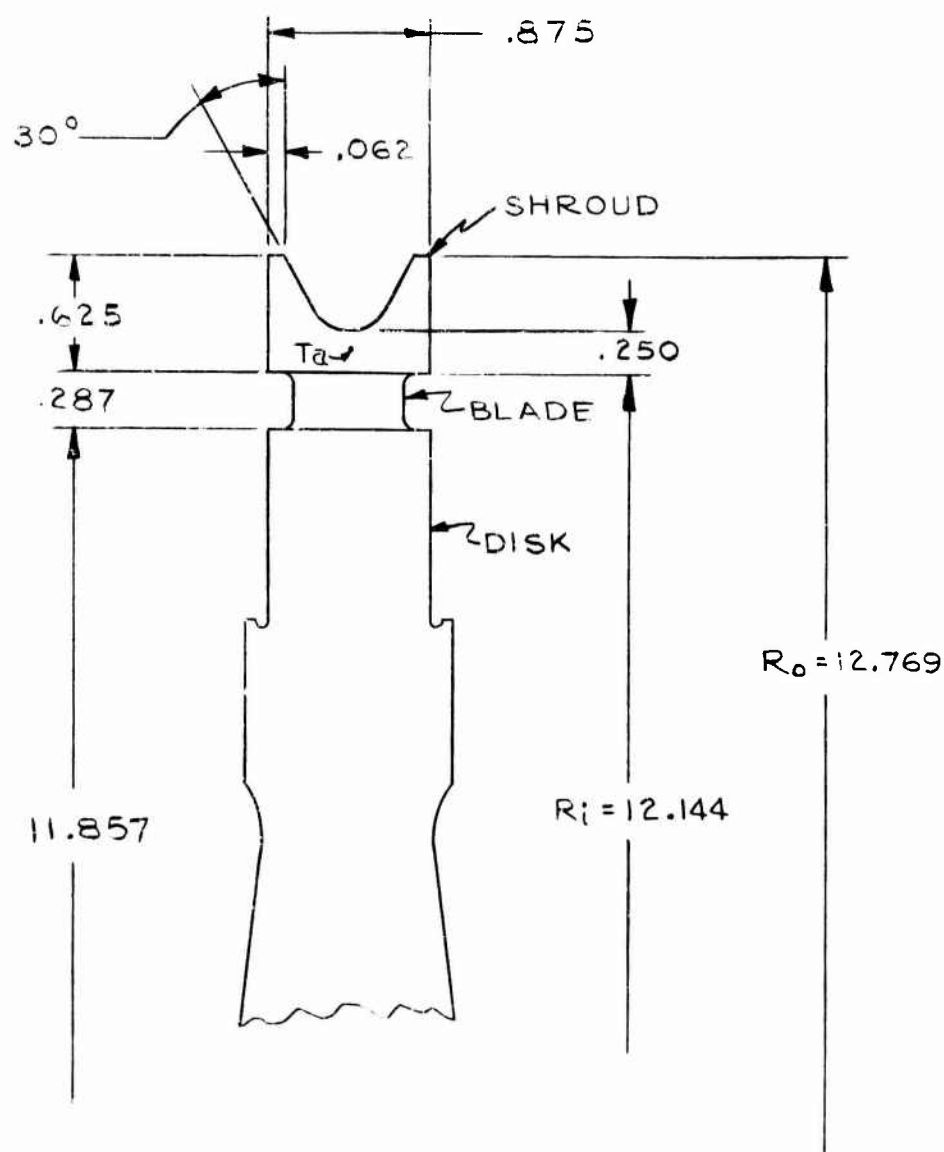


FIGURE 3.4.1

3.4.2 Disk Stress Analysis

The rotating disk carries the blades in a centrifugal force field while the disk is subjected to radial and axial thermogradients and external bending moments. The LVF turbine does not experience extreme radial thermogradients; however, the sides of the disk and shroud are used as sealing surfaces requiring the minimization of disk deflections to assure proper running clearances between the seal and disk. The seals apply bending moments to the disk and shroud. Also, bending moments can be experienced from axial thermogradients if the thermogradients are allowed to be extreme.

The disks reviewed for this application are: (1) the constant stress disk, (2) the hyperbolic disk, (3) the conical disk with a hole, and (4) the conical disk without a hole. These disks are all discussed in Reference 3.4.1, but a brief explanation is as follows.

The disk of uniform strength is defined as one in which the radial stress, σ_r , and the tangential stress, σ_θ , are equal and have the same value at all radii. This type disk has a thick hub and a thin rim. As a result the disk was not considered desirable in the LVFT concept because of the bending moments at the rim and the potential vibration problem at the rim because of diametral modes. The hyperbolic disk, which has a thick bore and a thin rim, could be designed to work in the LVFT application and is simplest to analyze.

The conical disk with a hole is similar to the hyperbolic disk with the exception that the rim is inherently thicker with conical sides being less costly to machine. The hole, however, would require a mechanical attachment to the shaft, such as a shrink fit. The disk design which has a continuous conical section with no hole in the bore was selected for the LVFT application because it retained the disk and the shaft centers coaxial. Also, the disk does not depend on a shrink fit nor require the alignment of a Gleason spline or a through-bolt. The use of a conical disk without a hole allows the shafts to be welded to the disk and machined with accurate normality and concentricity to each other and the seal rubbing surface.

The disk stress analysis provides the tangential and radial stress as well as the deflection as a function of radius. The average stress is computed for evaluation of rupture.

3.4.3 Turbine Casing

The LVF turbine operating conditions are not extreme. This allows the design procedures to follow standard steam turbine design practice. Therefore, the casing design is based on ASME pressure code recommendations where applicable, and in addition materials and fabrication techniques are chosen for their economy and reliability.

Where the turbine design is unique is the close running clearances between the seal face and disk, the exact normality relationship between the integral shaft and disk, and the required parallelism between the disk and the seal face. These features are more critical to the LVFT's function than in normal steam turbine design.

The casing includes ribs that reduce deflection and provide additional support stiffness. The casing is designed in an axially symmetric manner, providing the necessary normality between the walls that define the running clearance between seal and disk. The casing can be assembled conveniently, aligned, and shimmed, obtaining the required clearance in the critical areas.

The temperature of the inlet side of the casing is generally higher than the exit side. This could cause distortions of the casing because of the difference in radial thermal growth. In order to reduce this temperature difference to an acceptable level, water cooling will be added in the area of the inlet side below the lower seal, the object being to obtain equal radial expansion of inlet and exit casing. The final thermal investigation and design is to be determined later in the final analysis.

The ribs and symmetric design of the casing provide a structure that is not expected to distort from the predicted thermogradient of Section 6.2.5. The local skin temperatures in the hot gas areas, such as the inlet nozzles, are not expected to distort the casing because they are only applied in a local area.

The design condition was selected as 140 psi and 430°F, the maximum inlet pressure and temperature experienced in the system. The casing does not operate at this pressure in normal circumstances, but could inadvertently approach this value if the exhaust became restricted or the seals failed.

3.5 MECHANICAL DESIGN

The LVF turbine is designed to provide a reliable test unit with predictable aerodynamic characteristics and sufficient structural stability that critical clearances can be held with confidence. This goal is obtained using standard commercial hardware, when available, and commercial material and fabrication techniques. The preliminary design is shown in the included drawing entitled "LVF Turbine". The aero/thermal, heat transfer, vibration and stress considerations in the design have been discussed in Sections 3.0 and 6.0 of this report.

Franklin Institute Research Laboratories (FIRL) was subcontracted to design the three controlled-leakage seals and to specify the design criteria for the journal and thrust bearings necessary to provide the stability and alignment required for the successful operation of the proposed controlled-leakage seals. The preliminary design of the controlled-leakage seals and bearing design criteria is submitted in compliance with the subcontract agreements and is presented in Sections 3.5.1, 3.5.2 and 3.5.3 of this report.

Section 3.5.1 describes the analysis and design of steam-lubricated seals investigated for the LVFT test unit. The seals are subjected to surface speeds of approximately 75,000 fpm and up to 100 psi pressure differential. Proper performance of the seals is vital to overall turbine performance. A sectored fluid-film seal that uses a hydrostatic steam secondary seal was found to be the best configuration. A rolling diaphragm secondary seal arrangement was also considered promising for low temperature stages.

In addition to the seal analysis and design, FIRL sized the water lubricated journal and thrust bearings for support of the turbine rotor. Tilting pad bearings were selected for both radial and axial support of the rotor. They were selected because of proven performance and anti-whirl characteristics.

The thrust load on the thrust bearing is established by the radial position of the third seal and the pressure distribution under the seals. The thrust must be controlled to a specific value without reversal.

3.5.1 Discussion of Controlled Leakage Seal

A fluid-film seal consisting of individual circumferential sectors offered the best compromise of accomplishing an effective seal and simultaneously accommodating casing to rotor misalignment and dynamic motions of the rotor. Thermal distortions are also minimized with the sectored configuration.

Because fluid film stiffness on an individual sector is low, it is necessary that the secondary seal arrangement be nearly frictionless and be capable of compensating for force and moment unbalance.

The preferred secondary seal concept consists of supporting the individual sectors by hydrostatic bearings. Each sector is pre-loaded by the high pressure fluid against a steam lubricated hydrostatic bearing. The hydrostatic bearing film thickness can be adjusted to very small values by proper flow control. Thus, leakage is minimized and stiffness can be made very large while simultaneously accomplishing the necessary frictionless support. By utilizing steam (at ambient temperature) as the hydrostatic fluid the sector is in nearly perfect thermal equilibrium. The sectors are held together by a soft garter spring, which does not inhibit relative axial motion of the sectors with respect to one another.

The primary drawback with using steam as the hydrostatic fluid for the secondary seal is that the required supply pressure (upstream of the restriction) will be greater than the turbine inlet pressure. Thus, a separate source of pressurized steam is required. The flow however, is very small so that total losses to the steam cycle would probably not be significant. It is also possible to use water as the hydrostatic lubricant, but then thermal complications are introduced, because to maintain the water in the liquid state it must enter at a much lower temperature than the ambient steam.

Dynamic analysis determined that a 15 degree sector with a hydrostatic primary face configuration would operate with a runout of .001 TIR without difficulty. The limit of runout was not established. A 30 degree sector will not follow collar nutations. It is possible that a hydrodynamic profile on a 15 degree sector could operate, but this has not been analytically determined.

Tilting-Pad bearings were selected for both radial and axial support of the rotor. They were chosen because of proven performance and anti-whirl characteristics.

The primary accomplishment of the FTRL Program was to screen both primary and secondary seal candidates, and establish a basic configuration that shows excellent promise. To get to this stage required a considerable effort, and work remains in finalizing the design and establishing performance over the complete operating range. The ready availability of the basic configuration and analytical tools will allow final design to be expeditiously completed.

Performance Summary of Typical Seal (Seal 1)

film thickness, = 1 mil
 gap film thickness = 1 mil
 axial load, W_p = 99.5 lbs/sector
 primary leakage = 0.369 lbs/sec (total)
 gap leakage = 0.0081 lbs/sec (total)
 friction horsepower = 2.75 HP total
 film stiffness = 17,000 lbs/in. /sector
 sealed fluid pressure = 95 psia
 ambient pressure = 2 psia
 shaft speed = 12,000 rpm
 secondary film thickness = 0.0002 in
 secondary load = 387 lbs/sector
 secondary leakage = 0.020 lbs/sec (total)
 secondary supply pressure = 250 psia
 secondary stiffness = 103,000 lbs/in. /sector

3.5.1.1 Choice of Sectored Concept

The fluid-film seal employing hydrostatic or hydrodynamic interface geometries are finding acceptance in a variety of applications. Although the state of the art is very recent, much of the fundamentals are contained in well founded lubrication theory, and the advantages of the fluid film are very obvious. They can contain leakage and friction loss to very small and sometimes negligible values and the fluid film prevents rubbing contact, so that theoretically, infinite life is projected. The basic principle differs from that of an ordinary face seal in that the fluid film has positive stiffness. Closure of the film will increase fluid film capacity, while opening of the film will cause a reduction in load capacity. Then, seal rings of properly proportioned mass and inertia can track motions of the rotating member, so that the fluid film is always interposed between the opposed surfaces.

For the turbine application proper seal tracking is of prime importance since the large diameter high speed rotor, supported on fluid film bearings, could have relatively large excursions from the perfectly aligned system. In order to insure in-phase following of the rotor, sectored seals were selected because of their superior tracking capability.

3.5.1.2 Problem Areas

There are two major problems concerned with the sectored seal. These are:

- (1) to determine mass, inertia, and fluid film characteristics so that the seal will accomplish its primary mission of following the runner with a thin film between the opposed surfaces

- (2) to determine a sector support means that will allow free and independent movement of the sectors, while simultaneously maintaining initial alignment.

Problem 1 is complicated by the non-linear and time dependent characteristics of the primary fluid film. Computerized analysis that couples the governing gas lubrication equation with the dynamics of the system is the only accurate method available. Application of this technique to a variety of configurations established those that would prove acceptable in service.

The second problem (2 above) arises because the steam film interface has limited stiffness and to insure mobility, the sectors must be supported in a practically frictionless manner. In addition, thermal distortions of the sector must not be so great so as to deleteriously influence the primary film geometry, which will be .001 inch or less in magnitude. The use of a steam hydrostatic bearing as the secondary seal could best meet the requirements of frictionless support and thermal equilibrium.

A problem with many hydrostatic gas bearings is a phenomenon known as pneumatic hammer. It is a violent chattering of the opposed surfaces, and results from the compressibility of the fluid introducing out-of-phase responses. To avoid pneumatic hammer, it is necessary to resort to very shallow recesses, or else eliminate recesses altogether and feed directly into the film. The restrictor then becomes the curtain area surrounding the recess, with depth equal to the film thickness. The restrictor area changes with the film thickness in a manner that helps reduce compressibility effects. As the film reduces, inlet flow is reduced, and as the film increases, inlet flow is increased. Actually, the analytical model described above is somewhat simplistic; the entrance effects accompanying external flow into a boundary layer can become very complex and it has been only very recently that some true picture of the problem has been evolved. The situation has really not been properly handled in bearing theory, and some empirical development is usually required when applying inherently compensated hydrostatic bearings.

Another problem area remaining, with the hydrostatic secondary seal, is start-up. If the pre-load is applied prior to energizing the hydrostatic secondary seal, there is a strong possibility that the hydrostatic bearing will not lift. At start-up the high-pressure only acts at the inlet holes, and a heavy closing load will not permit the steam to escape throughout the bearing area. The high pressure throughout the relatively small area of the inlet holes will not provide the necessary balancing force. To overcome this problem, it will probably be necessary to energize the secondary seals prior to allowing turbine inlet steam to enter.

The hydrostatic geometry of the primary seal will not have any hydrodynamic capacity. Thus, if pressure is lost while rotating, fluid stiffness will be lost and there will be danger of contact. The solution to this problem lies in providing material combinations that can accept

momentary light-load, high speed rubs, or by installing an added hydrodynamic profile that will react at tight films

3.5 1.3 Interface Geometries Considered

The ideal geometry for the interface is the one that provides optimum stiffness at the operating condition. A number of configurations were examined including hydrostatic, hydrodynamic, and hybrid which is a combination of hydrodynamic and hydrostatic. The sector size, radii and pressure were fixed and performance evaluated as a function of the interface geometry. Figure 3.5.1 shows the various sector face configurations and operating conditions analytically examined. Figures 3.5.2, 3.5.3, and 3.5.4 show steady state performance as a function of film thickness. Based on a compromise of stiffness (slope of load vs film thickness curve, Figure 3.5.2), leakage and friction horsepower loss, the orifice fed hydrostatic sector seal is favored. The hydrostatic seal was the original selection and further studies were made to establish more detailed performance. Comprehensive performance of the hydrostatic seal was developed including the effects of angular tilts about the central axes. The studies proved that:

- (a) Fluid film stiffness is adequate to insure sector motion.
- (b) Angular tilts of the seal collar will reduce or increase loading on the individual sectors, sufficiently large to allow compensatory axial movements of the sector.

Dynamic studies indicated that the hydrostatic seal would accurately track motions of the collar if the sector size was limited to 15 degrees. The results of these studies are discussed in Section 6 5.1 3.

The reason for the superior performance of the hydrostatic seal can best be explained by examining the pressure distribution across the face. For the step configuration, high pressure acts across the step without significant pressure drop. Closure of the step does not materially increase the step pressure with the result that stiffness is small. A face seal, which merely incorporates a plain flat surface has zero stiffness. The pressure distribution for this configuration is shown on Figure 3.5.5. A properly designed orifice compensated seal will have a pressure distribution lying somewhere between the flat plate and step seal. The pressure at the orifice can approach the high pressure when the clearance is sealed.

SEAL SECTOR FACE CONFIGURATIONS

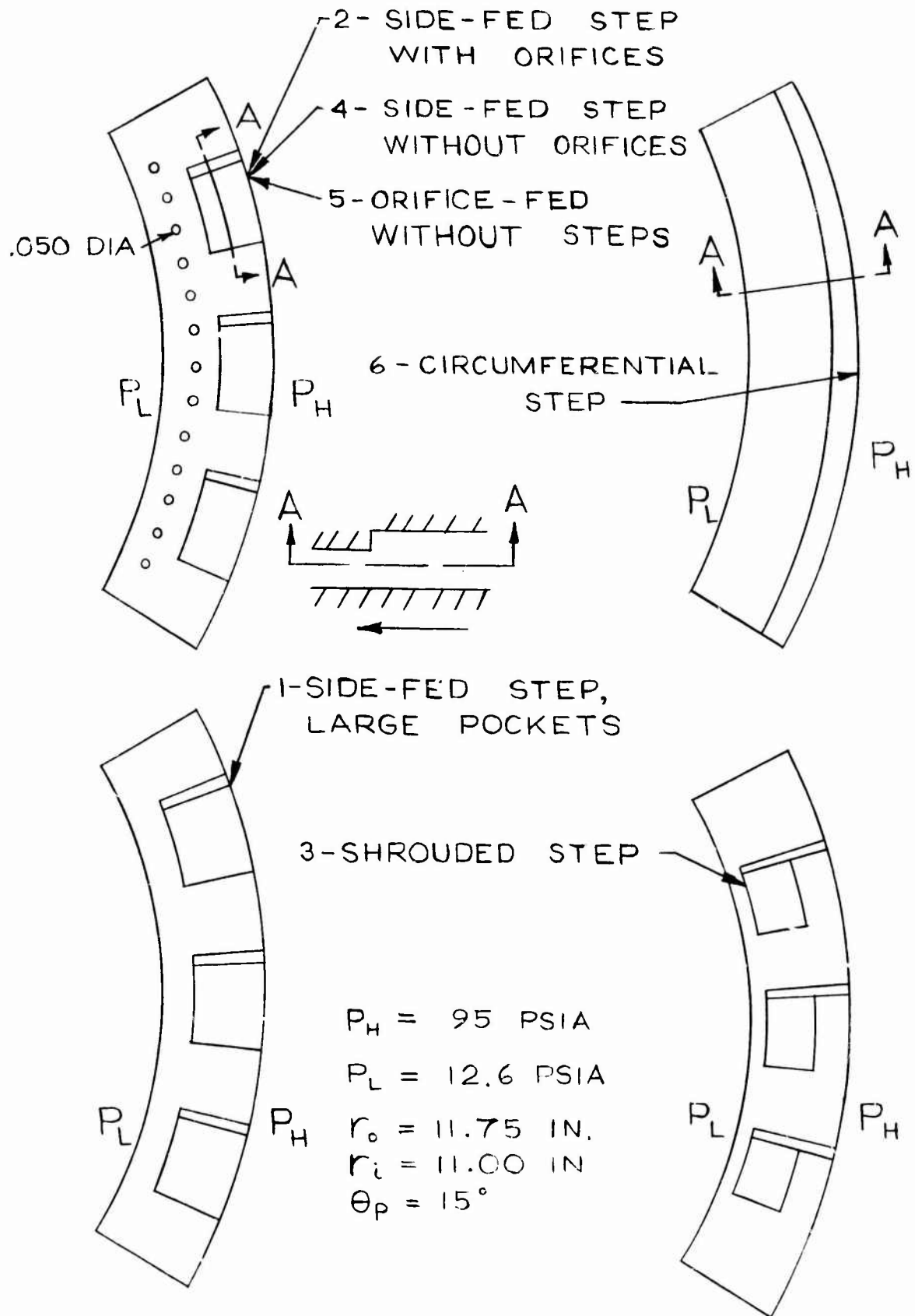


FIGURE 3.5.1

SECTORED SEAL CONFIGURATIONS
LOAD VS. FILM THICKNESS

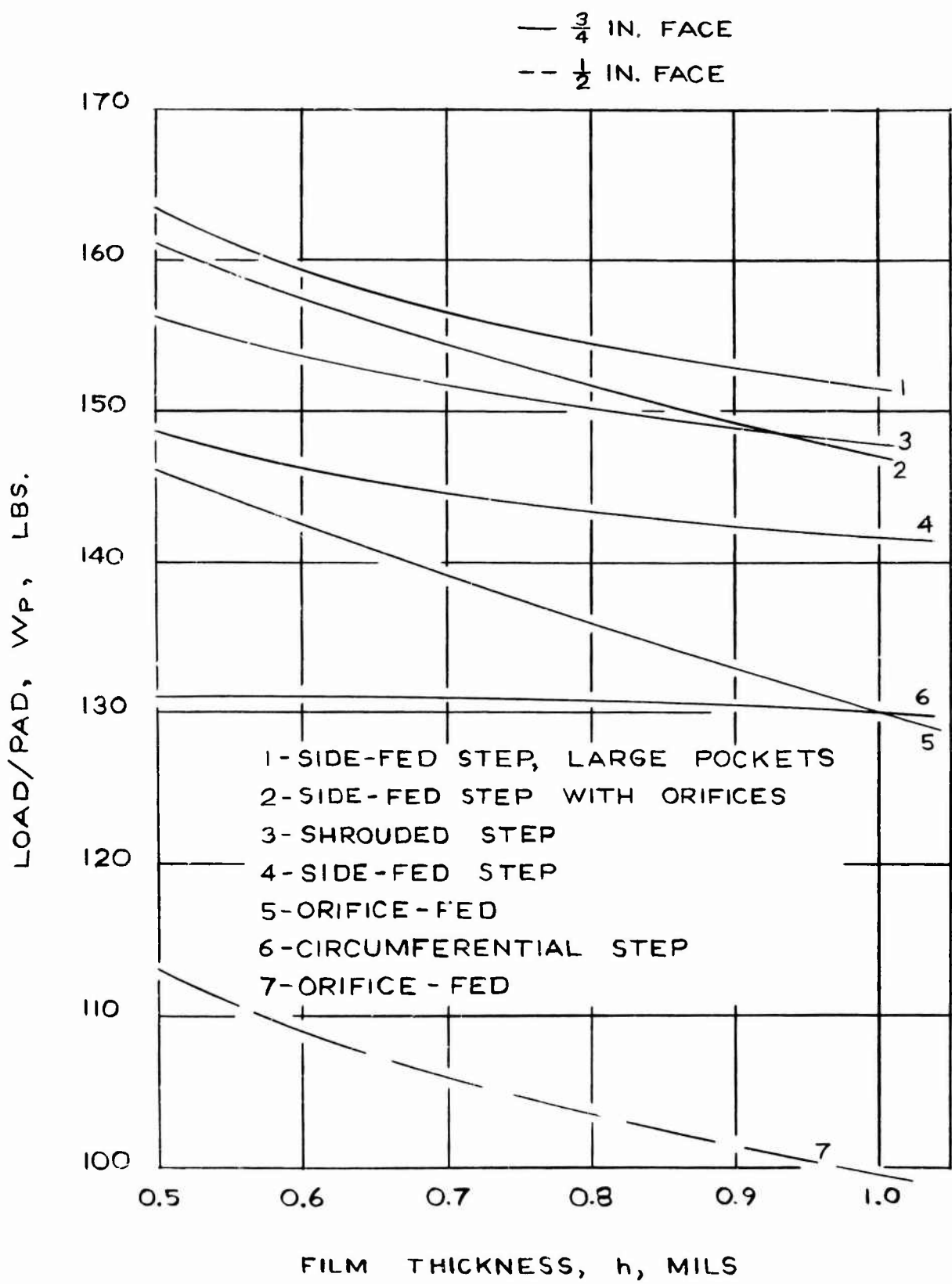


FIGURE 3.5.2

SECTORED SEAL CONFIGURATIONS FLOW VS. FILM THICKNESS

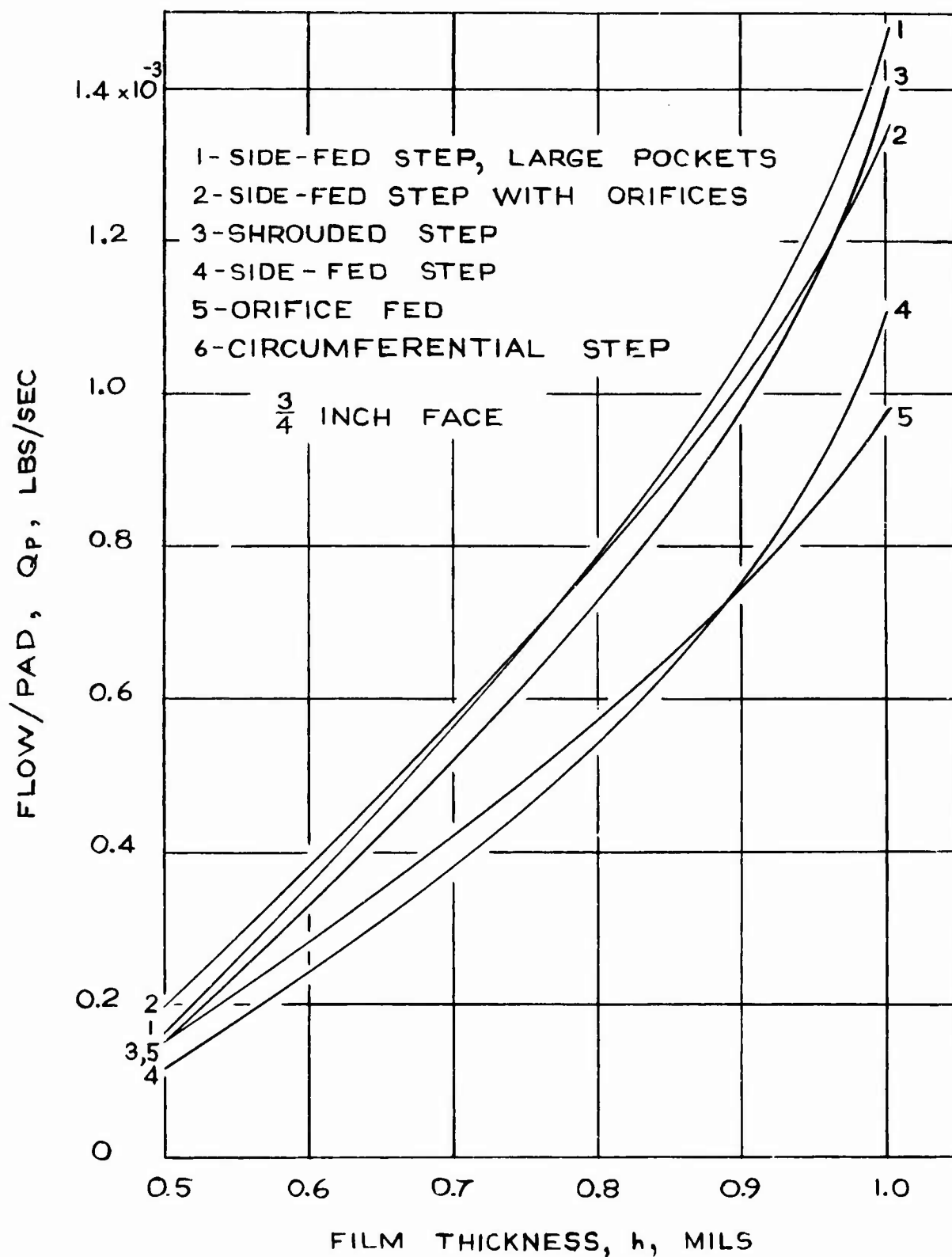


FIGURE 3.5.3

SECTORED SEAL CONFIGURATIONS HORSEPOWER LOSS VS. FILM THICKNESS

- 1- SIDE-FED STEP, LARGE POCKETS
- 2- SIDE-FED STEP WITH ORIFICES
- 3- SHROUDED STEP
- 4- SIDE-FED STEP
- 5- ORIFICE FED
- 6- CIRCUMFERENTIAL STEP
- $\frac{3}{4}$ INCH FACE

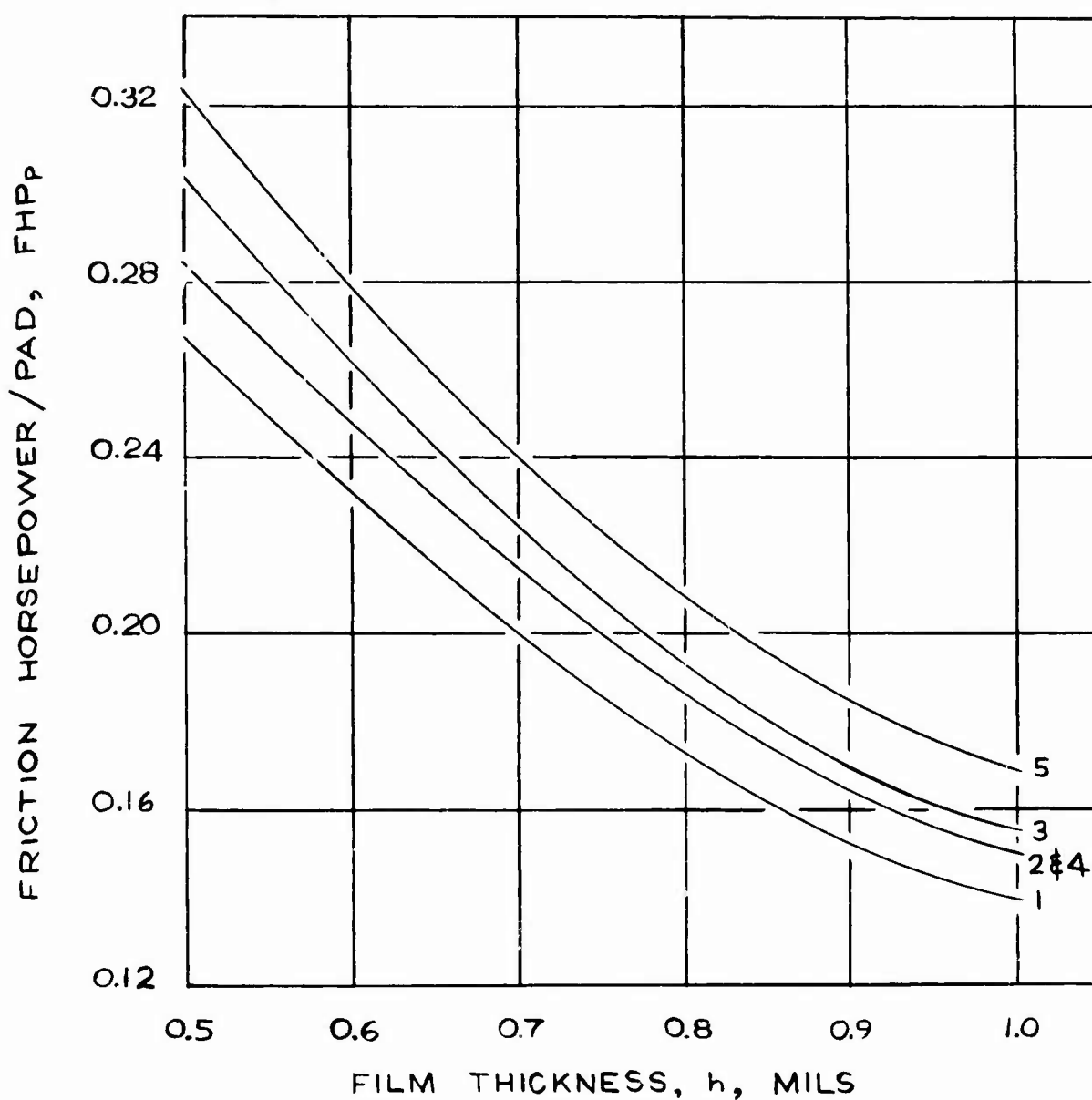


FIGURE 3.5.4

PRESSURE DISTRIBUTION ACROSS SEAL AT SECTOR MIDDLE

P_H = HIGH PRESSURE

P_L = LOW PRESSURE

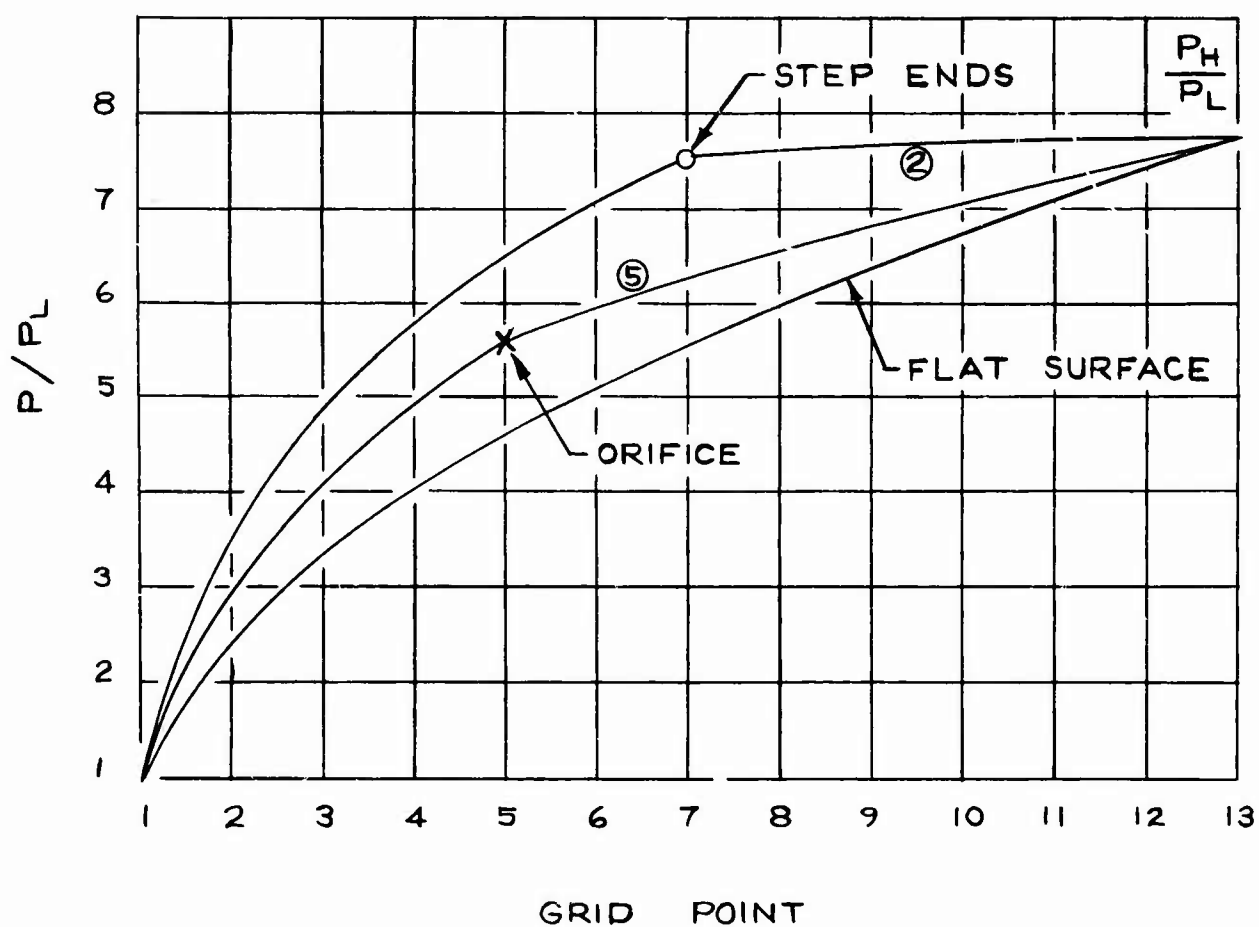


FIGURE 3.5.5

3.5.1.3.1 Hydrostatic

The preferred secondary seal consists of a steam hydrostatic bearing as shown on Sheet 5 of Section 10.0. It contains many small, shallow recesses interspersed throughout the bearing area. The individual recesses are fed through orifice restrictors to provide the necessary stiffness for the hydrostatic secondary seal. The high pressure side of the seal provides a strong pre-load that forces the sectors against the hydrostatic bearings. A garter spring also provides some pre-load and holds the sectors in position. An axial spring insures closure of the sectors at standstill, and prevents seal opening in the absence of hydraulic pressures. Since the circumferential area subjected to the high pressure is greater than the available area for the hydrostatic secondary seal, the average pressure in the secondary seal must be greater than the high pressure of the sealed fluid. Also, a pressure drop is required across the orifice restrictors to provide stiffness in the hydrostatic film. Thus, the supply pressure (upstream of the orifice) must be considerably greater than the pressure of the fluid being contained. In the normal operating condition, it was determined that this pressure must be greater than the turbine inlet pressure, and thus an auxiliary source of steam supply would be required.

The concept of employing a noncaptured, but pre-loaded hydrostatic bearing permits operating with very tight clearances, without the necessity to machine to tight tolerances, or be overly concerned about the effects of thermal expansions of the component members. The film thickness is self adjusting to load and inlet flow, and also can be externally adjusted by varying supply pressure. The hydrostatic film is extremely stiff and will not permit significant misalignment of the sectors due to force and moment unbalance.

3.5.1.3.2 Rolling Diaphragm

The basic configuration is shown on Figure 3.5.6.

L shaped sectors of 30° increments are held in place by non-interrupted rubber diaphragms that permit relative motion between adjacent sectors. The rolling diaphragms automatically compensate for sector movements that tend to upset the originally designed force and moment balance applied to the sector. For example, a radial movement of a sector causes the diaphragms to locally roll so that the area contained within the diaphragm in the displacement direction increases, while the opposite side decreases. A net restoring force is then applied to the sector. The same is true with respect to pitch movements (pitch axis normal to cross-section shown on Figure 3.5.6) and moments. A loose fitting guide pin also helps contain the sector and limits motions primarily to the axial direction.

The rolling diaphragm configuration was very seriously considered as a prime candidate, but the ability of the Viton rubber to withstand a 450°F steam environment was questionable. External cooling

ROLLING DIAPHRAGM SEAL

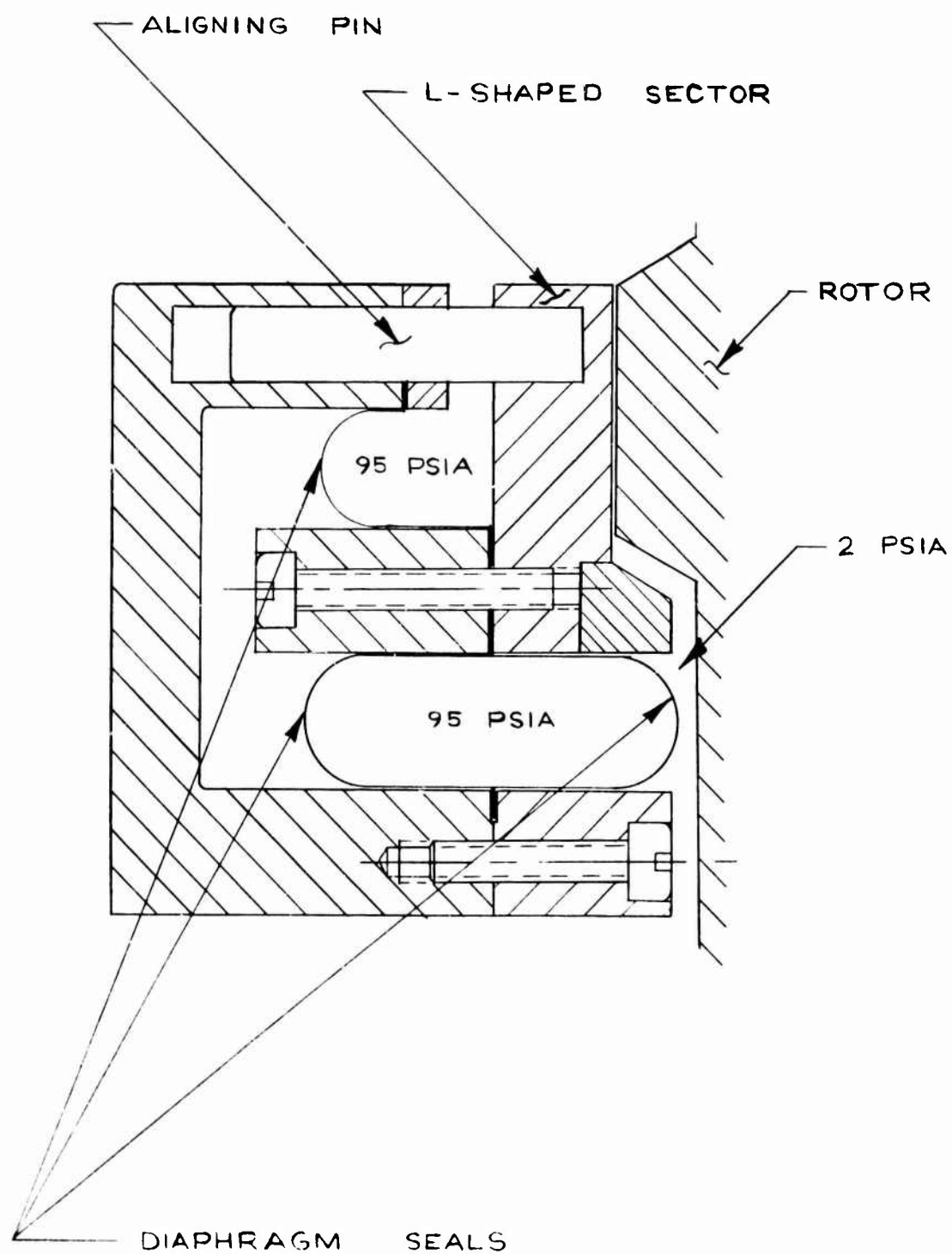


FIGURE 3.5.6

could be provided but this would unduly complicate the overall system, and destroy a prime advantage of simplicity of the original arrangement. It could still be applied to seals when the temperature levels are not excessive.

3.5.2 Journal Bearings

The journal bearings are the three-shoe, pivoted-pad type, with the top shoe spring-loaded to accommodate thermal and centrifugal expansion of the shaft. The 1,200 lb pre-load provides an adequate stiffness in all directions at the operating position. The pre-load is provided by a cylindrical piston which applies a pre-load gradually until the maximum load is obtained when the machine attains speed.

In conjunction with the pre-load cylinder, a monitoring pickup is installed in the bearing housing for measuring the movement of the cylinder. This measurement provides a continuous indication of the lubrication film thickness. The measurement is made with a Bently-Nevada pickup installed on the cylinder cap.

The journal bearing was analyzed on the basis of laminar theory and corrected for turbulence using information in the literature. Turbulent corrections were also made using FIRL's computer program. There is ample safety margin with respect to load capacity, and turbulence will further improve the load capacity.

3.5.3 Thrust Bearing

The thrust bearing is the pivoted-pad type. It is a completely captured bearing with eight pads on each bearing surface. No turbulent corrections were made to the thrust bearing load capacity because it was difficult to find reliable information. There is an ample safety margin with respect to load capacity and turbulence will further improve load capacity.

3.5.4 Thrust Load Balance

The LVFT design has three seals that exert forces on the disk, in addition to the force caused by the pressure differential across the blades and disk. These forces are balanced to within 50 to 400 pounds over the operating range of the machine. This thrust load established the capacity of the thrust bearing and insures against thrust reversal. The required balance and positioning of the third seal is based on the pressure distribution under the controlled-leakage seal face. The pressure distribution information was provided by FIRL and is discussed in Section 3.5.1.

3.5.5 Steam Wetness

The design point exhaust condition for the LVF turbine was chosen to allow a small amount of steam wetness at the exit of the turbine

rotor. The wetness, caused by an isentropic expansion, was reported in Section 5.0 as 2.5 per cent and the actual wetness at the turbine exit, including frictional effects, was calculated to be 0.73 per cent. This wetness could cause severe operational difficulties if it were to contact the sealing surface on the turbine exit. Analysis of the steam flow in the area of the rear seal was performed to evaluate the possibility of such an occurrence.

4.0 INVESTIGATION

Prior to this preliminary design phase, Barber-Nichols Engineering Company conducted a performance study program of this turbine concept. This study evaluated the performance potential for the LVF turbine and compared it to conventional or existing turbine performance values. This effort was performed under Contract No. DAAKO-2-67-C-0364 and the results are presented in detail in the final report, "Low Volumetric Flow Turbine Performance Prediction and Analysis", AD No. 831635L. The following conclusions were reached as a result of this study and are reiterated here for convenience.

1. The turbine concept using conventional labyrinth seals as shown in the LVFT patent disclosures does produce high efficiencies under high volumetric flow (high specific speed), but does not provide efficiencies higher than conventional turbines in the low volumetric flow regime (low specific speed) because of high leakage losses through the labyrinth seals.
2. The high efficiencies predicted for the LVFT concept in the high volumetric flow range can be extended to the low volumetric flow range by replacing the labyrinth seals with gas bearing type seals. The use of this controlled clearance type of seal will greatly reduce the bypass leakage which is the major reason why performance falls off at the low volumetric flows.

The tasks investigated under the current preliminary design effort are outlined as follows:

1. Parametric analysis of the steam inlet, exhaust, and power level of the turbine was performed in order to select the design conditions that would provide a test vehicle in the low volumetric flow range where the performance improvement of this turbine concept over conventional design should be apparent.
2. Perform preliminary evaluation of potential gas bearing seal concepts, review efforts of other investigators and select the most promising gas bearing seal design configuration. Analysis was then performed in seal concept to provide static and dynamic performance.
3. Design water lubricated bearing system to support turbine rotor covering radial and thrust loads.
4. Perform detail aerodynamic and performance analysis including detailed geometry of aerodynamic passages.

5. Perform thermal and stress analysis of complete turbine structure.
6. Complete the preliminary design layout including sections of critical components and areas needed to fully clarify the design concept.

5.0 DESIGN PARAMETERS

This section presents the basic design criteria and parameters upon which the design of the LVF turbine is based.

The aerodynamic design of the LVF turbine concept conforms to the criteria as set forth in the RFQ DAAK02-69-Q-0072 issued by the U. S. Army Engineer Reactors Group, Fort Belvoir, Virginia, in July, 1968. Barber-Nichols Engineering Company responded successfully to this RFQ after completing a preliminary design study of this low volumetric flow turbine design as presented in the report of Reference 5.0.1.

Two approaches to the design of the "Low Volumetric Flow Turbine" were considered. The first approach is a single stage turbine using the design concepts described in the LVFT report. (Reference 5.0.1) The second approach considered was a two stage turbine, the first stage design based on the LVFT concept and the second stage a conventional full admission axial turbine. The selected design is presented in the design section of this report.

The reason two design approaches were considered results from the total head drop available when expanding the steam from the conditions specified in RFQ DAAK02-69-Q-0072. If this expansion is taken in a single stage, the rotor tip velocity required for optimum efficiency will be approximately 1,800 ft/sec. This is a high value and results in highly stressed rotor parts due to centrifugal forces. However, it is well within the art for the temperatures involved and can be accomplished. Turbines have been designed that operate with tip velocities of 1,980 ft/sec at inlet gas temperatures of approximately 1,900°F. On the other hand, if a two stage machine is considered, where the head drop in each stage is approximately one-half the overall, the resulting tip velocity is on the order of 1,250 ft/sec which will result in much higher reliability and longer life. Also, at 12,000 rpm, the specified operating speed, the diameter of a two stage turbine will be 2.0 ft compared with 2.9 ft for the single stage. The two stage turbine will possibly be lighter than a single stage design because of the smaller diameter and lower stressed rotors. Since efficient sealing of the rotor is essential to achieve the desired efficiencies with the NPFO turbine concept, it should be noted that the two stage approach offers significant advantages for sealing. Because the diameters to be sealed are smaller, this results in smaller leakage areas and less chance for distortion of the rotor seal geometry.

Both designs are based on the performance requirements specified in RFQ DAAK02-69-Q-0072. These requirements are:

Turbine inlet steam temperature	= 430°F
Condenser pressure	= 12.3 psia

Turbine rotor speed, counterclockwise
when viewed from the shaft end = 12,000 rpm

Turbine net power output = 800 HP

The turbine inlet design point pressure was selected on the basis of a Rankine cycle efficiency analysis. Several values of steam superheat were evaluated at a constant steam temperature of 430°F. The purpose of this analysis is to show the effects of turbine nozzle exit steam quality on turbine efficiency. For each percent of condensed water at the nozzle exit, the turbine efficiency will be reduced by approximately 1-1/2%. It is important, therefore, when selecting the design point pressure that the expansion process does not enter too far into the wet region thereby significantly reducing turbine efficiency.

For a given inlet temperature, the amount of superheat cannot be increased significantly by reducing turbine inlet pressure because of the detrimental effects on overall cycle efficiency. To illustrate this point, several inlet pressure levels were evaluated and cycle efficiencies were calculated based on the effects of steam quality at the nozzle exit (rotor inlet). Figure 5.0.1 shows the results of this analysis. The shaded portion of the curve shows the range of inlet pressures which were investigated during the preliminary design phase of the contract. The turbine design was optimized at a design pressure level to give the maximum turbine and cycle efficiency at the design pressure and temperature while maintaining steam quality levels consistent with long life from erosion considerations.

The two turbine design approaches examined during this study effort are based on the specific design point shown in Figure 5.0.1, that is, an inlet pressure of 200 psia and an inlet temperature of 430°F, and 50°F of superheat.

Design Approach - 1

This design uses a single stage with partial admission. The basic concept will be the same as described in Reference 5.0.1. The turbine tip diameter is 34 inches with an overall turbine length of approximately six inches. The design uses three hydrostatic seals, two at the rotor inlet and one at the rotor exit. Due to the relatively high specific speed, $N_s = 19.7$, Figure 18 in Reference 5.0.1 shows that a larger seal clearance can be used without degrading turbine performance to any great extent. This greater seal clearance will still show improvement over a conventional partial admission turbine and allow for reduced seal manufacturing tolerances. The effective seal clearance could be as large as .00429 in. with a seal length of 0.25 in.

CYCLE EFFICIENCY
VS
TURBINE INLET PRESSURE

TURBINE INLET TEMP. = 430 °F

TURBINE EFFICIENCY ADJUSTED
FOR LOSSES DUE TO NOZZLE
EXIT QUALITY

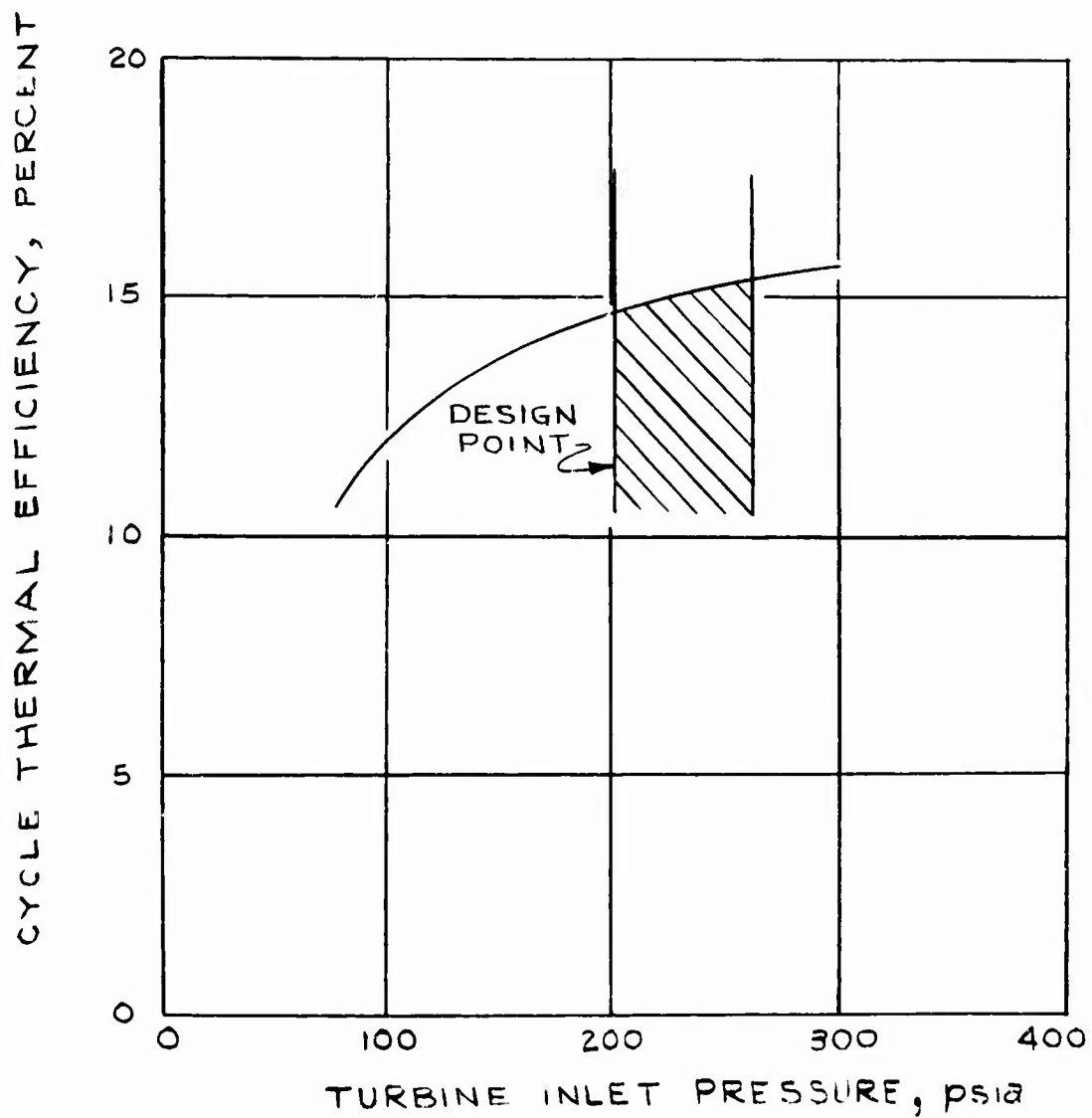


FIGURE 5.0.1

The turbine disk is vented to the condenser pressure to minimize disk friction losses by reducing the fluid density surrounding the disk.

Figure 18 in Reference 5.0.1 shows that a turbine efficiency of 82% can be expected for this design; however, correcting this efficiency for the losses due to expansion into the wet steam region, an actual efficiency at this design point is estimated to be 76%.

The tip speed of the turbine operating at 12,000 rpm is 1,790 ft/sec which is within the state of the art, but is on the high side. For this reason, a staged turbine design is considered.

Design Approach - 2

A two stage turbine design was evaluated. The two stage design will result in reduced tip speeds, simplified seal development due to reduced seal circumference and possible weight reductions over the single stage design.

The inlet design point for the two stage turbine is the same as for the single stage design. The first stage design will be similar to the single stage design discussed previously and will utilize the LVFT concept. The second stage design is a conventional full admission axial turbine because the higher specific speed of the second stage (30 to 40) shows that there will be only a small advantage in increased efficiency due to the LVFT concept. Conventional seals can be used on the second stage which reduces development and production costs.

A significant reduction in tip speed and diameters is obtained by the two stage design. The reduction in diameter lowers the tip speeds to a level where blade stress problems are insignificant. The table shown below gives the pertinent stage characteristics.

PRELIMINARY TWO STAGE DESIGN PERFORMANCE

Stage	N_s	η_T	Dia, in.	Tip speed ft/sec	Type
1	17.3	.81	23.6	1240	LVFT concept, partial admission
2	32.4	.75	20.4	1070	Conventional, full admission, axial flow

The effective overall efficiency of the two stages is .787.

Preliminary analysis of the two stage turbine design point selection was based on turbine wheel diameter, cycle efficiency, and exit steam quality and stage pressure drop split.

Figure 5.0.2 shows cycle efficiency versus turbine inlet pressure for three different pressure drop splits. The pressure drop split is defined as the fraction of the total turbine pressure drop ($P_{\text{inlet}} - P_{\text{exhaust}}$) taken in each stage. Figure 5.0.2 shows that cycle efficiency levels off at about 220 psia and only a three point increase in efficiency occurs when increasing inlet pressure from 100 to 220 psia.

Figure 5.0.3 shows the variation of turbine stage diameter with inlet pressure. This curve is based on a $U/C_0 = .65$ for Stage 1 and .48 for Stage 2 for optimum stage efficiency and a turbine speed of 12,000 rpm.

A major design criteria in the selection of the design point is the degree of wetness in the stage exhaust steam. The hydrostatic seals which will be used in Stage 1 of this design require dry steam as the sealing medium and condensation in this steam will cause serious seal problems. Therefore, in selecting the inlet pressure and pressure drop split, the wetness of the exhaust steam must be considered. For a pressure drop split of one-half in Stage 1 and one-half in Stage 2, and an inlet pressure of 140 psia, the exit steam will be in the superheat region. Higher inlet pressures result in wetness Stage 1 exit steam. Figure 5.0.4 shows the first stage nozzle exhaust steam quality as a function of inlet pressure.

In conclusion, the design point selection was based on consideration of the cycle efficiency, turbine diameter, stage pressure drop split and exhaust steam quality. Figure 5.0.5 shows the preliminary thermodynamic and performance data for the design point based on 800 IIP.

The low specific speed ($N_s = 22.4$) of Stage 2 was the cause of some concern of whether this stage could be full admission. Investigation of the Stage 2 nozzle configuration showed that the nozzle exit area would be 35.2 in², resulting in a nozzle height of 0.475" for a full admission stage. This nozzle height is considered to be reasonable for ease of manufacture and it was concluded that a full admission stage is practical.

A basic decision was made at the conclusion of the preliminary two stage turbine analysis that all future investigations and design on this program should be concentrated on Stage 1. The decision was based on the fact that the major objective of this program is to prove the validity and performance potential of the LVF turbine concept. Little gain would be realized from the design of the second stage conventional full admission turbine since no advancement in the state of the art is anticipated.

CYCLE EFFICIENCY VS TURBINE INLET PRESSURE

TWO STAGE TURBINE
EXHAUST PRESSURE = 12.3 psia
INLET TEMPERATURE = 430 °F

NOTE: TURBINE EFFICIENCY CORRECTED FOR
EXHAUST STEAM QUALITY

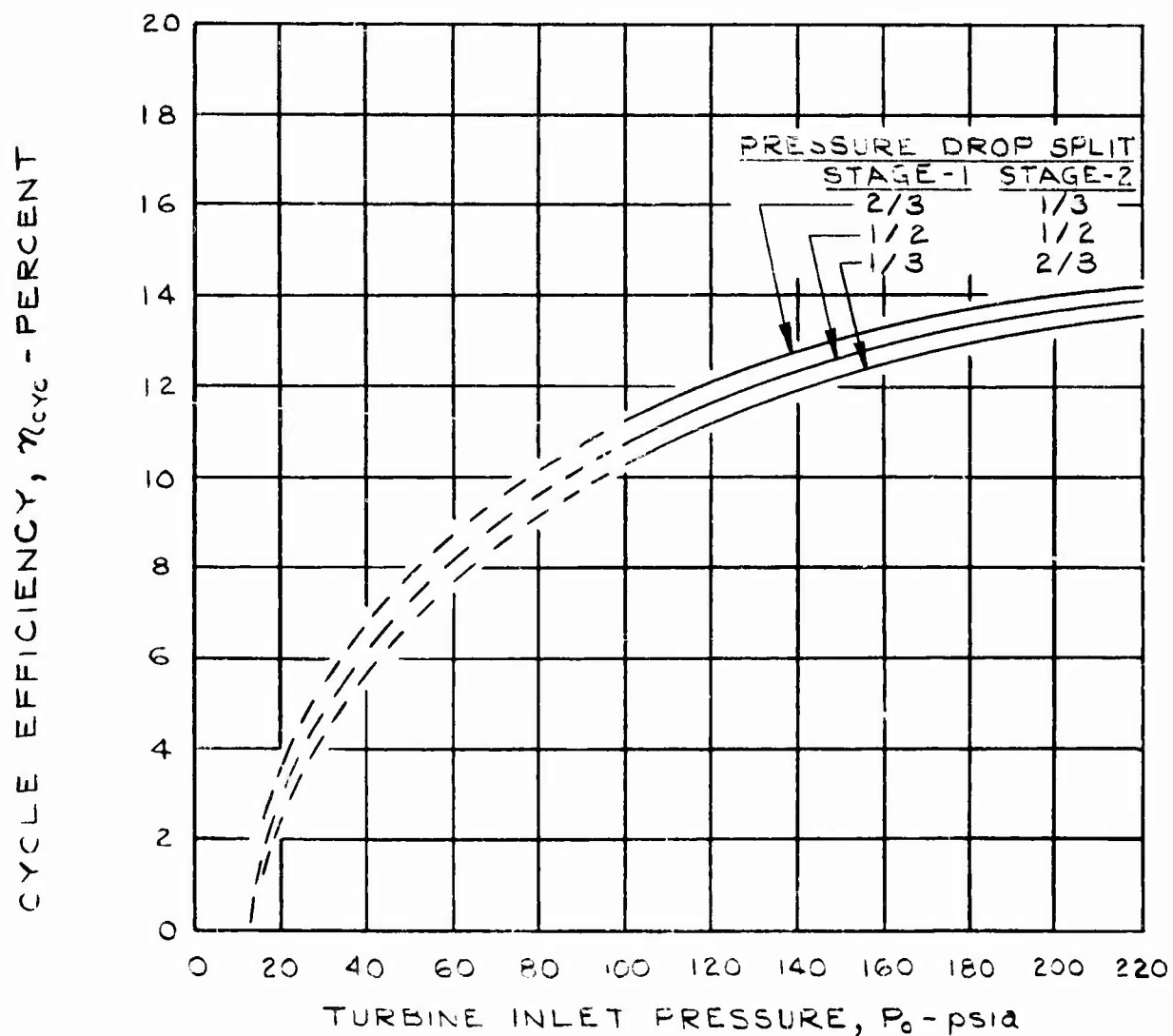


FIGURE 5.0.2

TURBINE WHEEL DIAMETER VS INLET PRESSURE

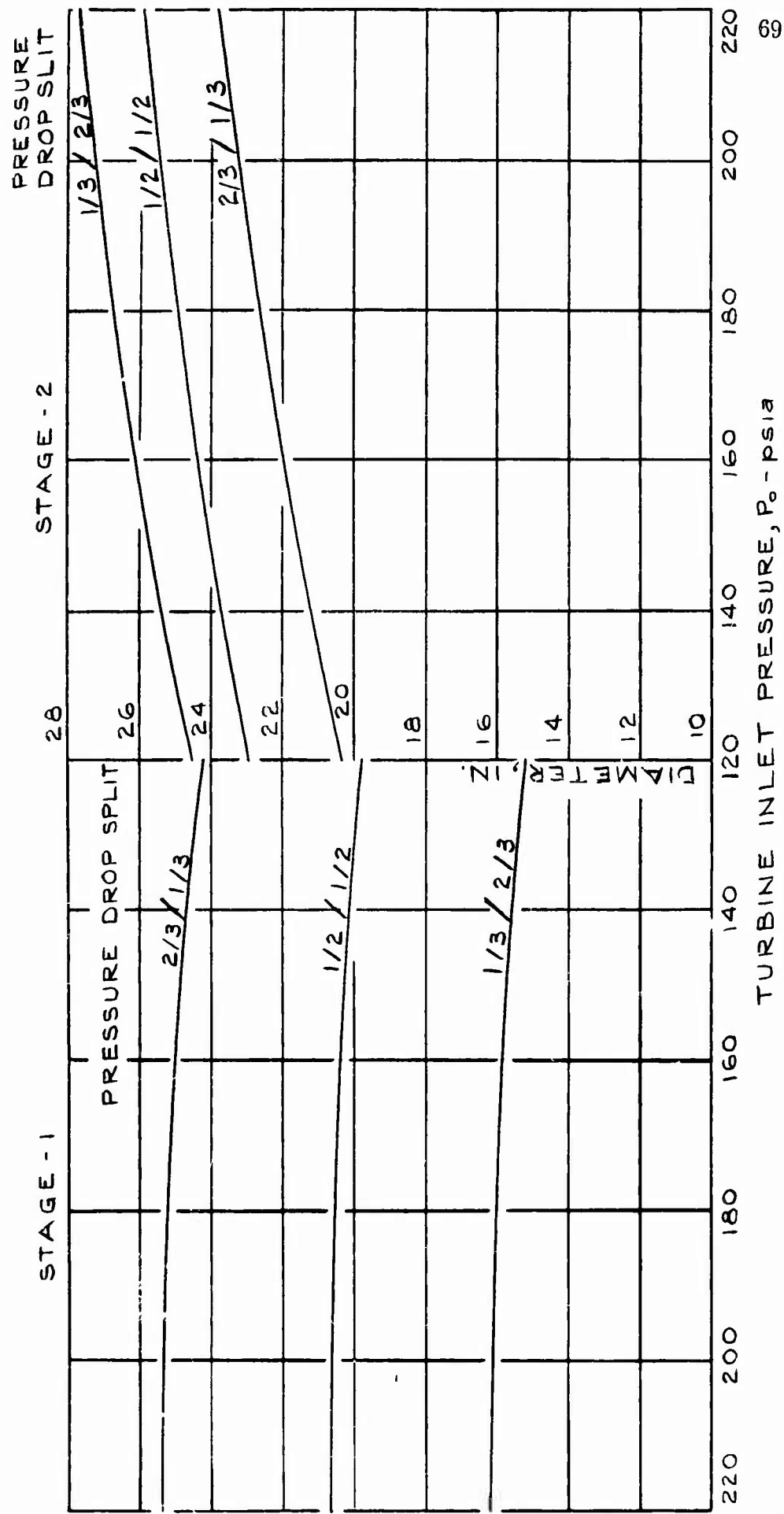


FIGURE 5.C.3

STAGE-1 NOZZLE EXIT STEAM WETNESS VS INLET PRESSURE

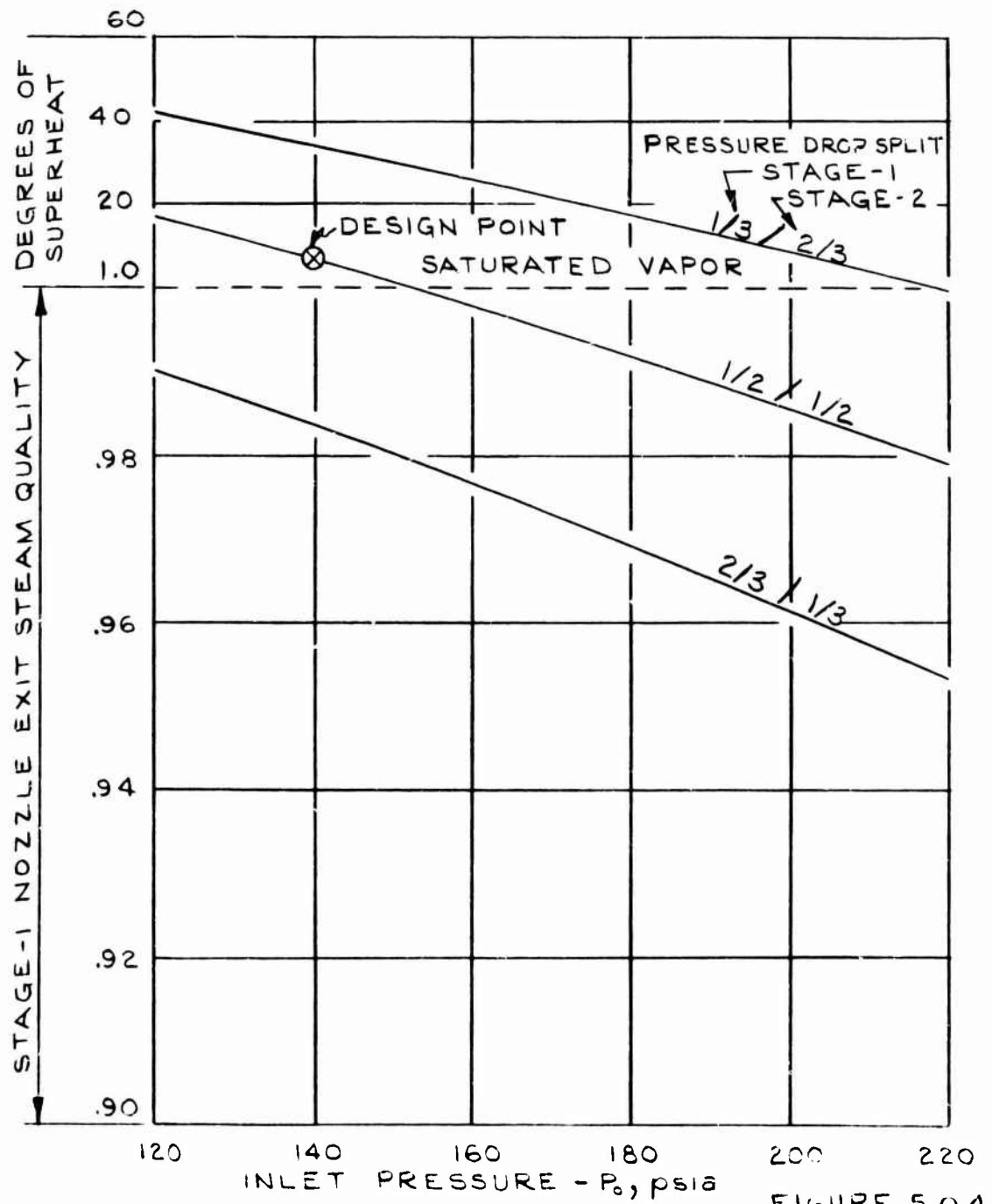


FIGURE 5.0.4

FIGURE 5.0.5

DESIGN POINT SELECTION PARAMETERS

PARAMETER	STAGE 1	STAGE 2
Inlet pressure, psia	140	76.2
Exit pressure, psia	76.2	12.3
Inlet temperature, °F	430	330
Exit temperature, °F	330	205
Exhaust steam quality, % for isentropic expansion	Superheated	91.5
Stage efficiency corrected for exhaust steam quality, %	81	69.8
Stage work, BTU/lb	43	93
Turbine speed, rpm	12000	12000
Wheel pitch diameter, in.	20.2	23.6
Velocity ratio, U/C_0	0.65	0.48
Specific speed, N_s	20.3	22.4
Turbine type	LVFT Config.	Full admission axial flow

A preliminary analysis on a single stage turbine was made to select the design point which would meet the following design criteria.

1. Turbine inlet temperature of 430°F maximum.
2. Specific speed of approximately 17 at 12,000 rpm.
3. No specific turbine inlet pressure.
4. Stage horsepower output approximately 450.
5. No restrictions on stage exhaust pressure.

Another requirement considered in selecting the design conditions is the quality of the steam in the turbine and particularly the quality of the steam that feeds the hydrostatic seals. It is desirable that this steam be superheated and contain no moisture. This is important because the hydrostatic seals are actually a special type of gas bearing. Gas bearing performance when operating on wet gases presents several unique problems. Therefore, it will be prudent to choose a design condition that provides dry steam if possible. The other consideration is erosion in the turbine passages as a result of water droplet impingement. This problem arises when droplets strike the leading edges of rotor or stator vanes. Moisture in the exhaust of any one stage is not detrimental, with respect to erosion, to that particular stage so the only concern is to maintain dry or nearly dry steam entering the rotor of the LVF turbine.

Since dry steam or at least low moisture content in the exhaust is a design goal, it was decided that the turbine inlet temperature selected should be the maximum of 430°F. The turbine specific speed was then selected to be 17.5 since this value is in the range where the LVF turbine concept can provide a significant improvement in performance over conventional turbines and yet the seal clearance and other parasitic losses are not as critical as when a lower specific speed is selected.

Using a turbine inlet temperature of 430°F and a specific speed of 17.5, output power, rotor tangential velocity and steam quality were analyzed as a function of turbine inlet and exhaust pressure. The results of this analysis are shown in Figures 5.0.6, 5.0.7, and 5.0.8. Figure 5.0.6 shows turbine output horsepower as a function of exhaust pressure for different inlet pressures. Figure 5.0.7 shows tangential velocity as a function of exhaust pressure for different inlet pressures. A design tangential velocity of 1,250 ft/sec was selected and appears as the dashed line of Figures 5.0.6 and 5.0.8. This tangential velocity of 1,250 ft/sec was selected on the basis of rotor stresses and strain under operating conditions. It is important in the LVF turbine concept that the hydrostatic seals perform properly. This will require that the sealing surface remain as true and flat as possible at the operating speed of the rotor, therefore a low stress wheel

LVFT STAGE PERFORMANCE
HORSEPOWER
VS
EXHAUST PRESSURE

$T_0 = 430^\circ\text{F}$
 $N_s = 17.5$
HP BASED ON $\eta_T = 80\%$

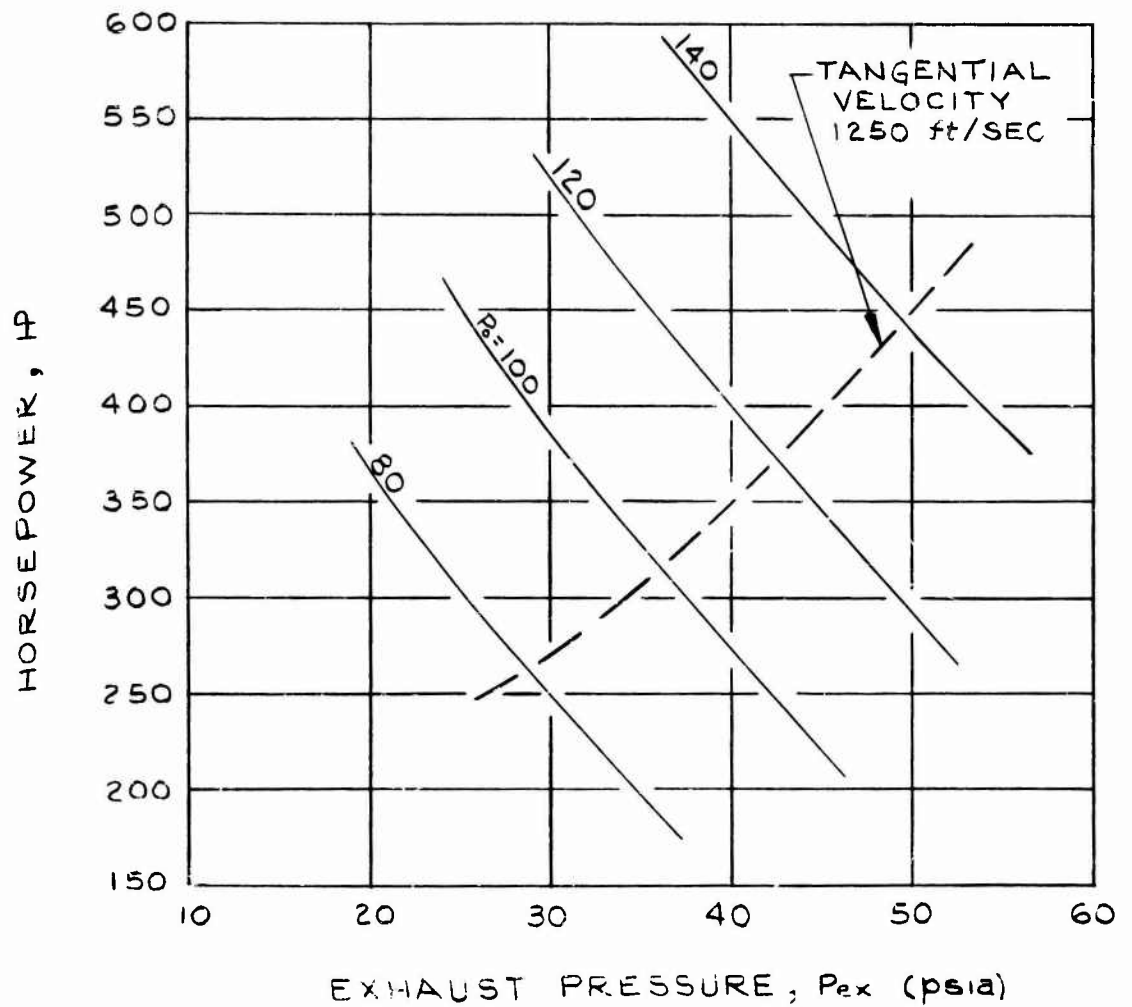


FIGURE 5.0.6

LVFT STAGE PERFORMANCE
TANGENTIAL VELOCITY
VS
EXHAUST PRESSURE

$$u/c_o = .60$$

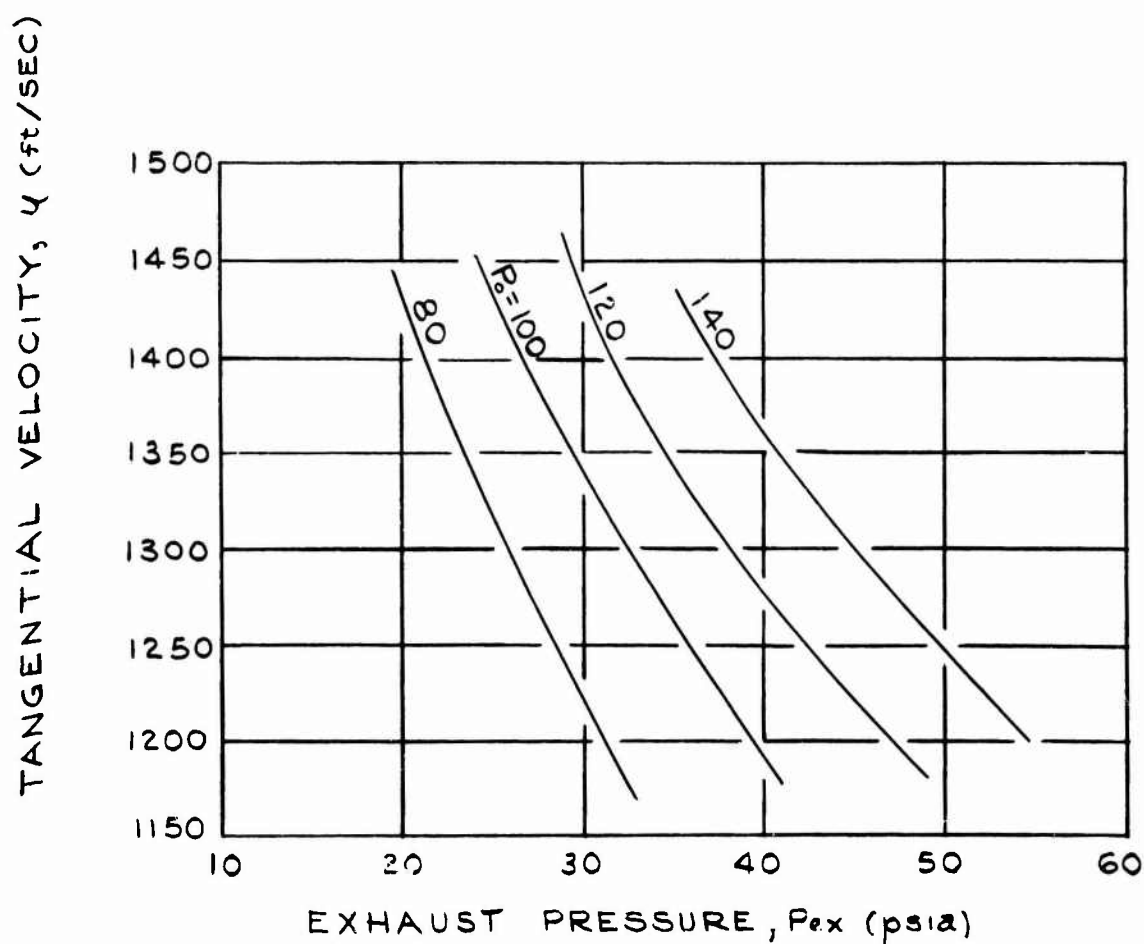


FIGURE 5.0.7

LVFT STAGE PERFORMANCE
EXHAUST WETNESS
VS
ISENTROPIC EXPANSION

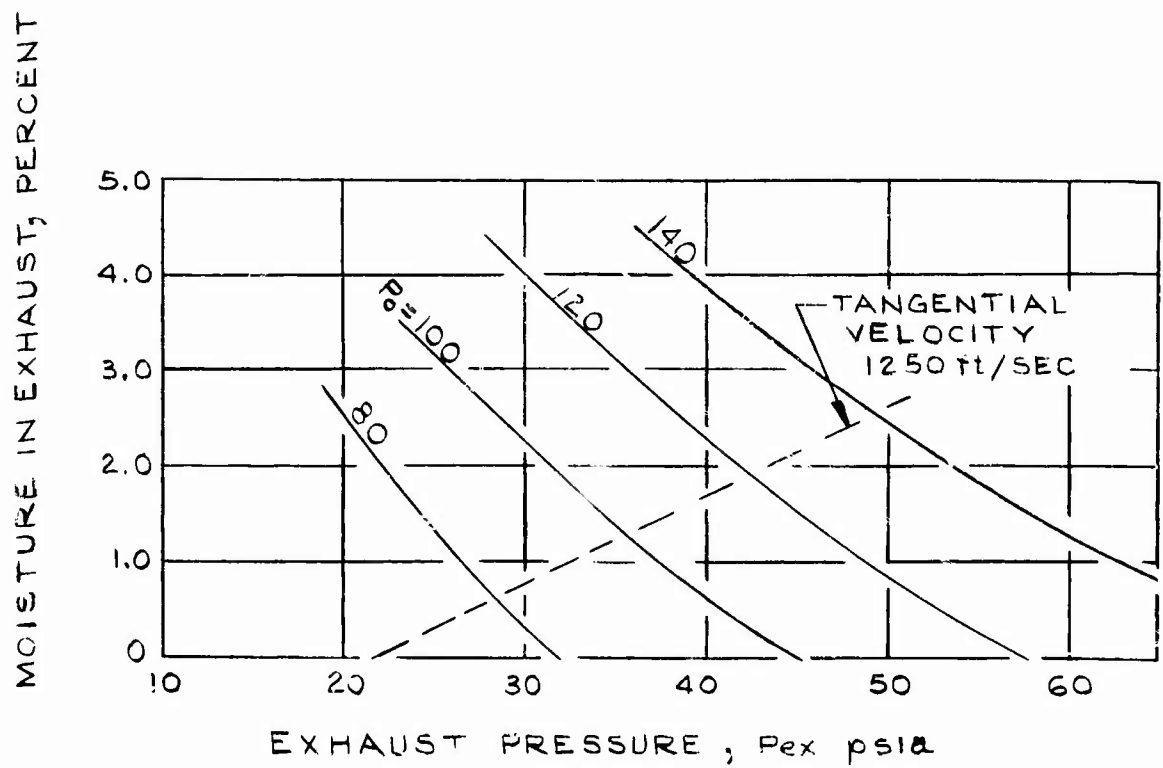


FIGURE 5.0.8

is desirable. It is felt that the 1,250 ft/sec design meets this goal. It can be seen in Figures 5.0.6 and 5.0.7 that if the 1,250 value is lowered further, this increases the exhaust pressure for any given inlet pressure which in turn lowers the output horsepower. Therefore, the selected value of 1,250 ft/sec is felt to be the most desirable value.

Figure 5.0.8 shows moisture or wetness in the exhaust steam as a function of exhaust pressure for several inlet pressures. The dashed line represents the 1,250 ft/sec tangential velocity. At inlet pressures up to 140 psia, the wetness is approximately 3% or less for the 1,250 ft/sec design and the moisture should not cause erosion damage. This wetness must be kept away from the one hydrostatic seal on the exhaust side of the rotor. Provisions will be incorporated in the design to ensure that the moisture does not come into contact with this seal. The steam condition in the inlet side of the rotor is superheated for all conditions along the dashed line so moisture in these seals or rotor vane erosion is not a problem.

The preliminary Stage 1 turbine design criteria selected at 140 psia inlet pressure and 1,250 ft/sec tangential velocity are summarized below:

Inlet temperature, T_o	= 430 °F
Inlet pressure, P_o	= 140 psia
Exhaust Pressure, P_{exh}	= 50 psia
Design speed, N	= 12 000 rpm
Tangential velocity, U	= 1,250 ft/sec
Velocity ratio, U/C_o	= .60
Horsepower	= 400 - 450

It should be noted that a turbine designed for this 140 psia inlet pressure will be at design all along the dashed line of Figure 5.0.6 and 5.0.8.

6.0 DESIGN

The preliminary design of the LVF turbine test unit used for an evaluation of the performance of the controlled-leakage seals and aerodynamic passages of the LVFT concept is presented in detail in this section. The equations necessary for the design analysis are included with justification substantiated by data where applicable. The preliminary design effort included the design analysis of the following areas:

1. Aero-thermodynamic analysis of the flow passages concerned with energy transfer from working fluid to rotor.
2. Thermal analysis of rotor housing and seals required to determine temperature levels and gradients.
3. Dynamic analysis of rotor and vibration analysis of disk and blades required to define the dynamic characteristics over the intended operating speed.
4. Mechanical design of the rotor, bearings, seals and system establishing proper loading and functional compatibility of components.

The sealing objectives are satisfied by fluid film, positive stiffness face seals that maintain a fluid film between opposing members and simultaneously inhibit leakage to an acceptable limit.

The preliminary layout, entitled "LVF Turbine", sheets one through five, provide the preliminary design and specify the critical dimensions and clearances.

6.1 AERO-THERMODYNAMIC DESIGN ANALYSIS

A number of components which are critical in terms of the aerodynamic operation of the LVF turbine were examined in detail to provide optimum performance characteristics while maintaining a structurally sound machine. Rotor and stator blade shapes were defined according to established practices, and the turbine rotor was designed to yield optimum performance while maintaining acceptable stress levels in the turbine blades and shroud. This section will be primarily concerned with those factors affecting the aerodynamic operation of the turbine. The mechanical design and stress evaluation are covered in Sections 6.4 and 6.5.

6.1.1 Turbine Rotor Design

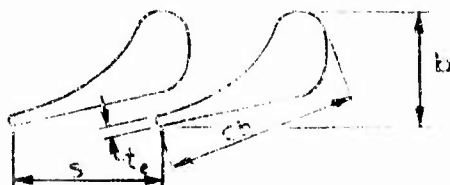
The maximum turbine efficiency for a given set of inlet gas conditions can be expressed as a function of the ratio of turbine tip speed, U , to isentropic spouting velocity, C_0 . The variation of turbine efficiency with velocity ratio was examined in Section 3.1, and for the design conditions the optimum turbine velocity ratio was 0.62. The value of this parameter was reduced to 0.60 for the design point as the lower tip speed results in a smaller turbine diameter, reducing the stress in the turbine rotor. The turbine rotative speed was fixed by the design specification at 12,000 rpm, and with the design velocity ratio of 0.60, the turbine diameter was evaluated to be 24.0 inches.

The width of the turbine rotor was established by the width of the turbine blade sections, plus a small toroidal section located on either side of the rotor blades. This passage was included in the rotor design since the flow issuing from the nozzle blades has inherent small wakes behind each stator vane due to the finite thickness of the stator trailing edge. The toroidal section in front of the turbine rotor allows a mixing or settling zone before the flow enters the rotor blades. The passage at the rear of the rotor was included to balance the rotor, and does not influence the aerodynamic operation of the turbine. The blade section width was evaluated as indicated in the next section as 0.625 inch, and with a toroidal section of 0.125 inch on either side of the turbine rotor, the total rotor width was established as 0.875 inch.

6.1.2 Rotor Blade Design

The rotor blade channels were designed using an established method of circular arcs and straight line segments, leaving a well defined throat at the rotor exit. This method allows the design of a smoothly convergent flow channel with no abrupt change in cross sectional area which would tend to add turbulence in the flow stream. The primary consideration in the blade design was to provide optimum performance defined in terms of the blade velocity coefficient (ψ_N). This parameter is defined as the ratio of actual exit velocity to the isentropic expansion

velocity, and is indicative of the operating efficiency of the blade section. The blade efficiency is usually specified in the literature as the square of the blade velocity coefficient. A secondary consideration influencing the rotor blade design was the requirement of providing a thick enough rotor trailing edge, t_e , (shown in the following sketch) to support the large rotor shroud.



The effect of the rotor trailing edge thickness on aerodynamic blade performance is covered in this section along with other factors influencing blade performance, such as blade aspect ratio and blade angle.

The design mass flow rate (4.32 lb/sec) for the LVF turbine was established by the required output horsepower, the overall turbine efficiency, and the available energy, or

$$\dot{W} = \frac{H_p \times 550}{\eta_t (H_{a1})} \quad \text{lbs/sec} \quad (6.1-1)$$

Turbine efficiency was established as indicated in Section 3.1 and the output power and available energy were specified in Section 5. The total throat area in the turbine rotor required to set the design operating pressure through the turbine stage was established using the above flow rate and the isentropic gas density. The throat area determined in this manner (3.32 in^2) is slightly smaller than actually required, due to nozzle friction increasing the gas temperature and decreasing the gas density at the rotor exit. This is desirable since the throat area will necessarily be adjusted after the machine is fabricated to provide the design degree of reaction in the turbine, and the throat area can be easily increased by honing the blade throats. The design throat area reported herein is consequently 3 or 4 per cent less than that actually required. The total rotor throat area is that area normal to the gas stream at the rotor exit, and is a function of blade angle, trailing edge thickness, total number of blades, blade height and turbine pitch diameter.

The rotor trailing edge thickness was required to be between .030 and .050 inch to provide adequate strength to support the rotor shroud. Information obtained from Reference 6.1.1 and shown in Figure 6.1.1 indicates that this requirement is detrimental to turbine performance; however, the magnitude of this loss amounts to about one per cent of the blade efficiency. Consequently, although a lesser edge thickness would be desirable, it is not felt that this requirement will significantly affect turbine performance.

EFFECT OF TRAILING EDGE THICKNESS ON BLADE PERFORMANCE

BLADE OUTLET ANGLE = 12°

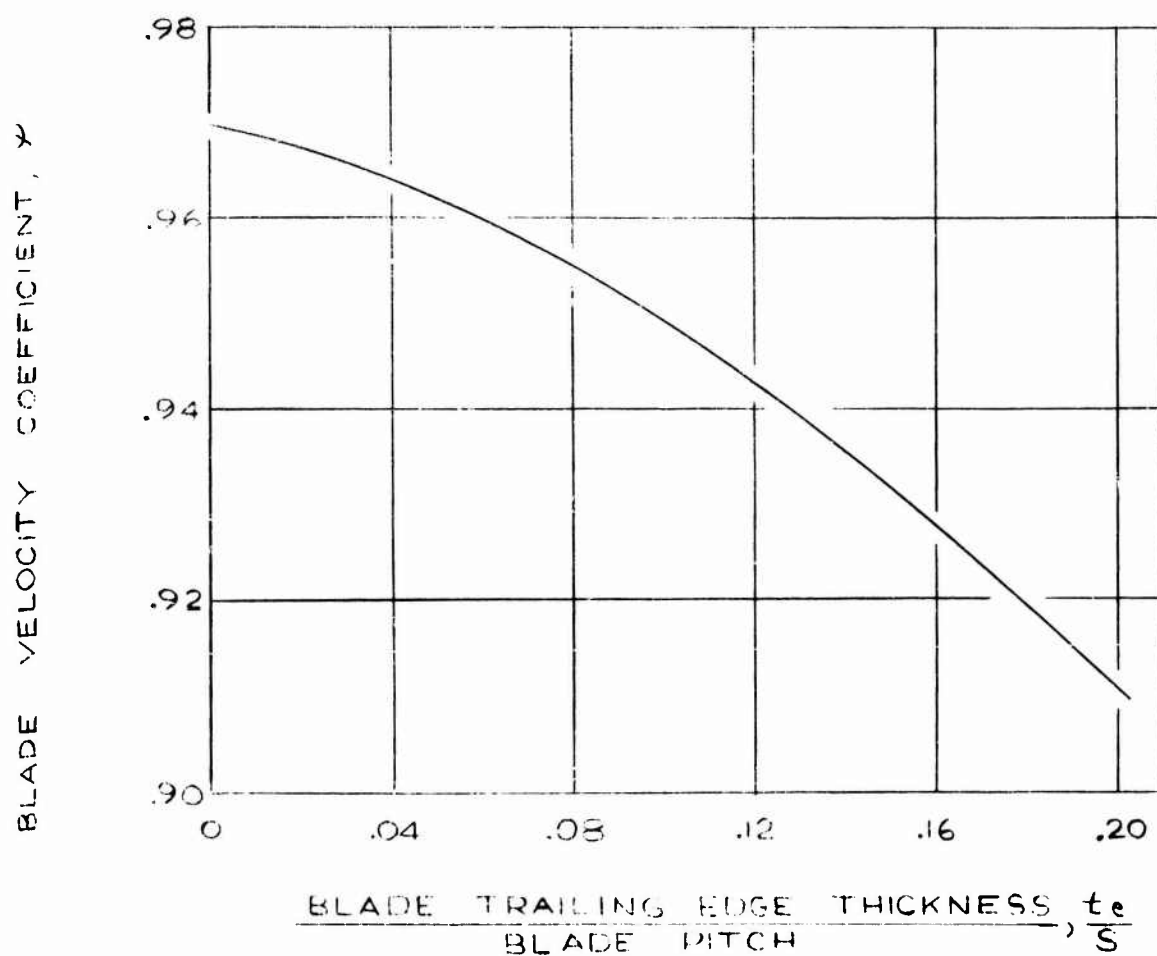


FIGURE 6.1.1

The optimum rotor blade height was established using information presented in Reference 6.1.2. In this report the optimum ratio of blade height to rotor diameter was presented as a function of turbine specific speed. For a specific speed of 17, appropriate to the LVF turbine design, the optimum blade height to diameter ratio was approximately 0.01, which for a turbine diameter of 24 inches yields a blade height of about 0.24 inch. This value was taken as a minimum for the LVF turbine design.

Test data for a number of turbine blade shapes was presented in Reference 6.1.3 and these results formed the basis for the final blade design. Of particular importance in this report was the blade aspect ratio, defined as the blade height divided by the minimum throat dimension. Typically, it is desirable to use the largest practical aspect ratio for a good blade design, assuming wall friction and edge losses are small, and in any case an aspect ratio of at least two is required to achieve good blade efficiency.

Since the trailing edge thickness, rotor pitch diameter, and blade angle were fixed or optimized for the LVF turbine, the minimum throat dimension at the pitch line was uniquely determined by the number of blades used in the turbine rotor. The blade height was then fixed by the total required throat area determined above. Consequently, a greater aspect ratio would require a larger number of rotor blades, increasing the complexity and cost of the turbine rotor. The final blade number chosen was 90, which was felt to be reasonable from a manufacturing standpoint. The throat dimension was 0.129, the blade height 0.287, and the resulting aspect ratio was 2.23. Nozzle velocity coefficients presented for similar nozzles in Reference 6.1.3 typically exceed 0.96, and this value was used in the design analysis to provide a slightly conservative estimate of turbine performance.

Another important design parameter discussed in Reference 6.1.1 was the design blade pitch to chord ratio. The blade pitch (s) was defined as the circumferential blade spacing, and the blade chord (C_h) the maximum blade length as shown in the above sketch. Optimum pitch to chord ratios for blade designs with a blade exit angle of 12° ranged from 0.62 reported by Ainley and Mathieson (Reference 6.1.1) to 0.76 (Zweifel, Reference 6.1.4), to 1.10 (Howell and Carter, Reference 6.1.5). Since the blade spacing was defined by the number of rotor blades and the rotor pitch diameter, the design pitch to chord ratio generally determines the blade axial length (b). A design value of 0.75 was used for the LVFT rotor blade design, resulting in a blade axial length of 0.625 inch.

The pitch line profile for the LVFT rotor blade is shown in Figure 6.1.2. Noted in this design is the blunt leading edge with an inlet blade angle of 90° . Since the design operating condition of this turbine is with a low axial inlet gas velocity, the 90° blade angle allows incidence free operation at the design point. The bluntness of the leading edge should minimize any incidence loss occurring under off design conditions. Figure 6.1.3 shows the gas stream velocity in terms of the isentropic mach number as a function of the developed length from the blade inlet.

PITCH LINE PROFILE ROTOR BLADES LVE TURBINE

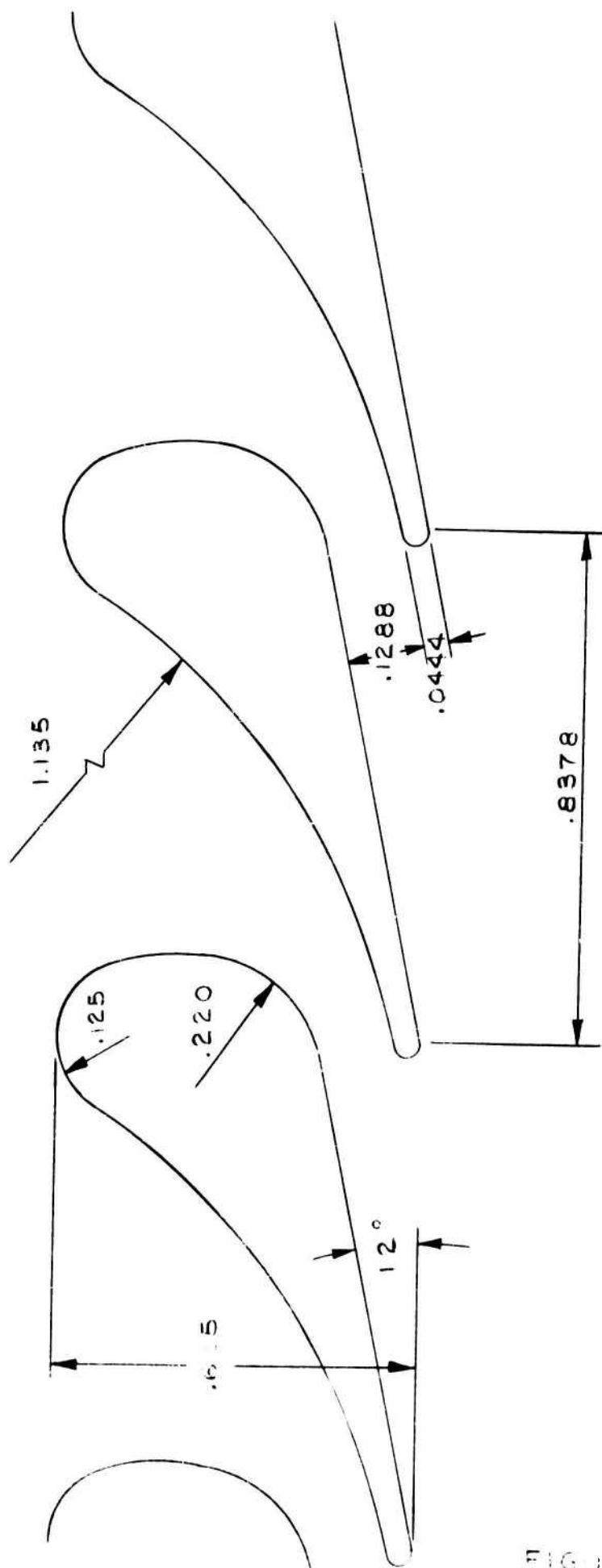
$$h^K = .287$$


FIGURE 61.2

ROTOR BLADE FLOW CHARACTERISTICS DEVELOPED ALONG PITCH LINE

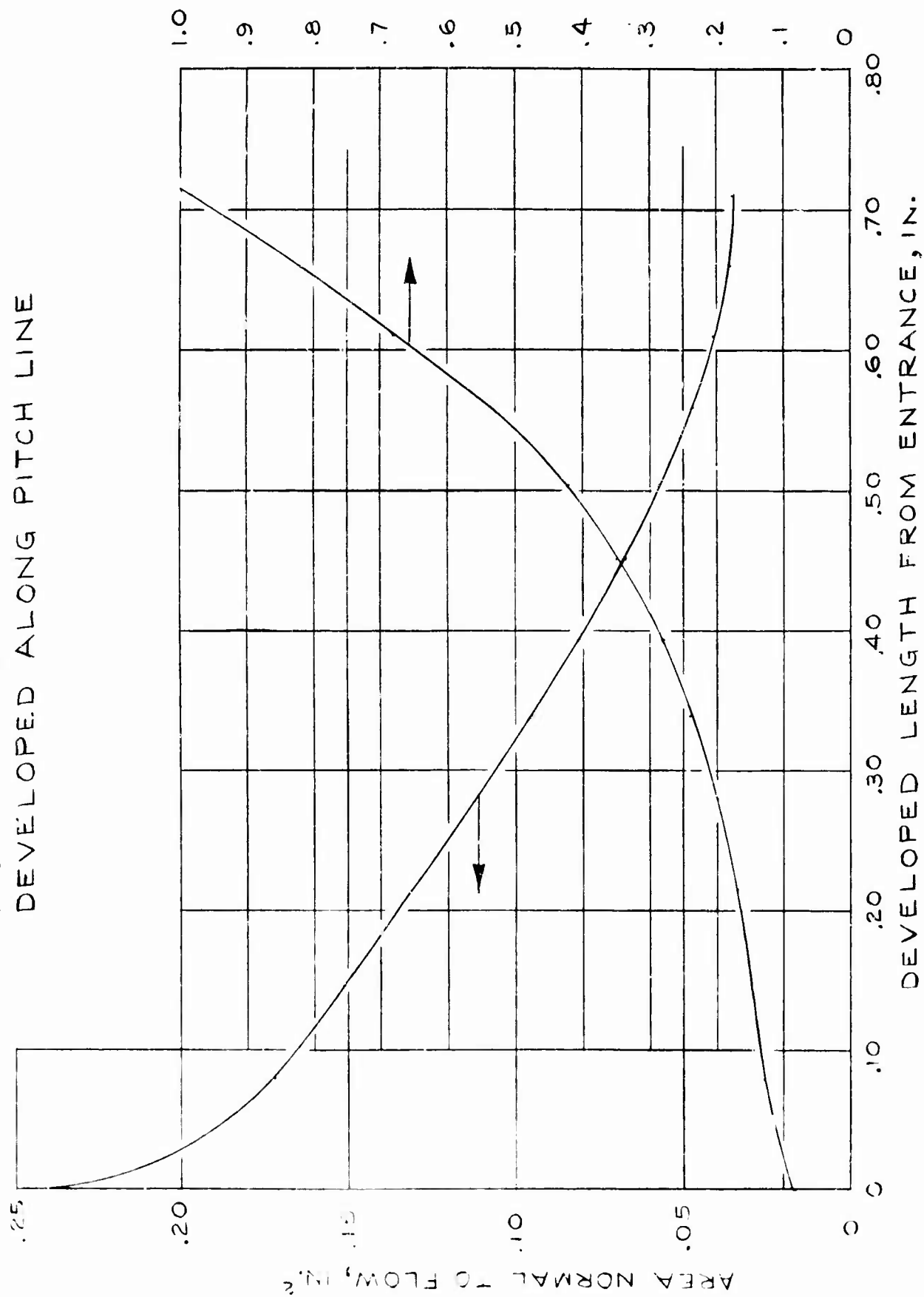


FIGURE 6.1.3

From this figure it is apparent that the design goal for the rotor blade design was achieved and the gas stream accelerates smoothly through the rotor blade emerging at celerity at the blade exit.

6.1.3 Turbine Nozzle Design

The requirement of achieving high efficiency in the stator blade design is not nearly as critical for good turbine efficiency as was the efficiency of the rotor blades. The effect of stator blade efficiency is of the same magnitude as the effect of the stator exit angle shown in Figure 3.1.4, and was not considered critical in terms of turbine performance. Generally, the same parameters were examined for the turbine nozzle design as were examined in the previous section and the same design philosophy was employed throughout. The primary design goals were to provide a smoothly converging flow passage and to maintain good flow characteristics entering the rotor.

The effect of the nozzle trailing edge thickness was felt to be of prime importance in this last regard, as wakes in the turbine flow leaving the stator section would be quite detrimental to the overall turbine performance. The magnitude of the edge thickness may be evaluated in terms of the blade number, nozzle angle and total throat area as follows

$$t_e = \frac{1}{n} \left(\pi D \sin \alpha - \frac{A_N}{H_N} \right) \quad \text{in} \quad (6.1-2)$$

The total throat area (2.40 in²) required for the stator section was derived using the isentropic gas density at the rotor inlet in the same manner as indicated in the previous section. As indicated above, the trailing edge thickness can be minimized by using the minimum blade height, minimum nozzle angle, or a large number of blades.

The nozzle blade height was chosen according to the relationship expressed in the previous section as 0.24 inch and the stator angle was chosen as the minimum acceptable according to Reference 6.1.3 as 10°. With a blade number of 72, the resulting trailing edge thickness was .0422 inch. This value is not excessive and the above dimensions were used in the stator blade design shown in Figure 6.1.4. The variation in gas velocity with developed length from the stator inlet is shown in Figure 6.1.5. Note in this figure that the gas velocity does not attain celerity at the stator exit, but is just adequate so that the tangential component of wheel velocity matches the turbine speed, and the gas stream enters the rotor axially.

PITCH LINE PROFILE
STATOR BLADE LVF TURBINE

$h_N = .240$
 $\eta = 72$
 $C_h = 1.287$

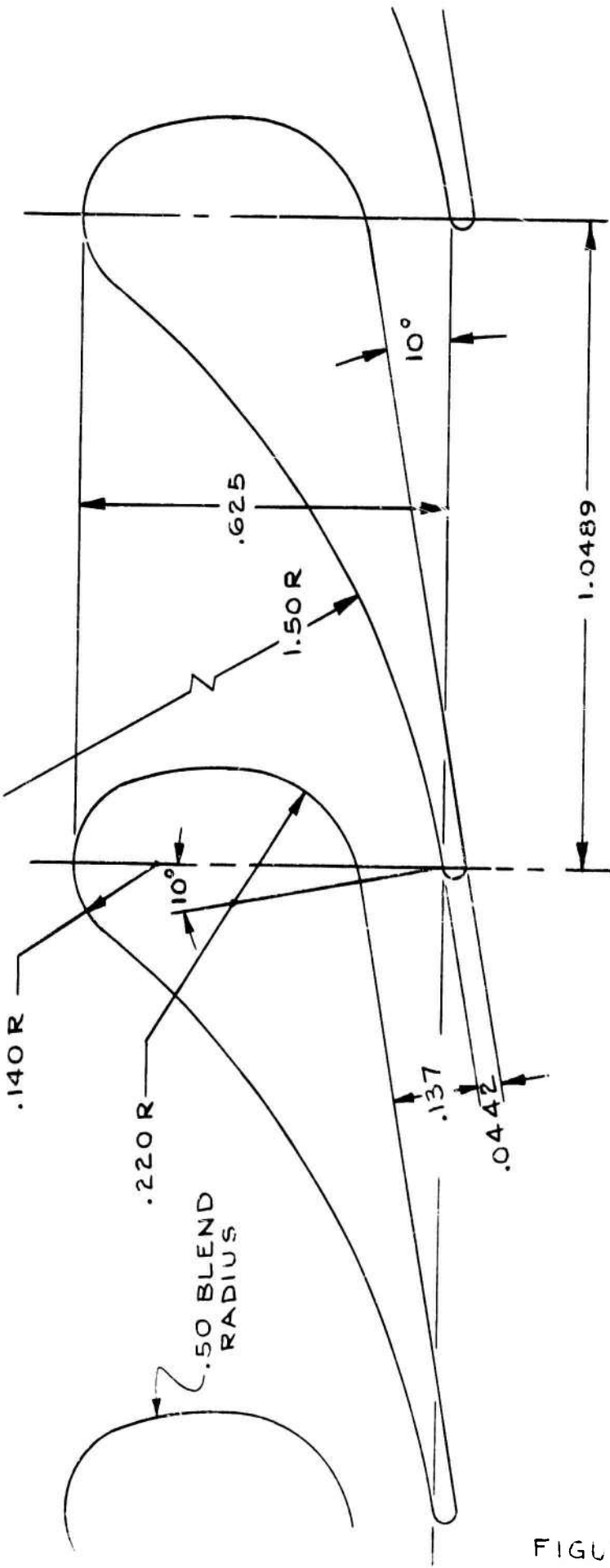


FIGURE 6.1.4

STATOR BLADE FLOW CHARACTERISTICS DEVELOPED ALONG PITCH LINE

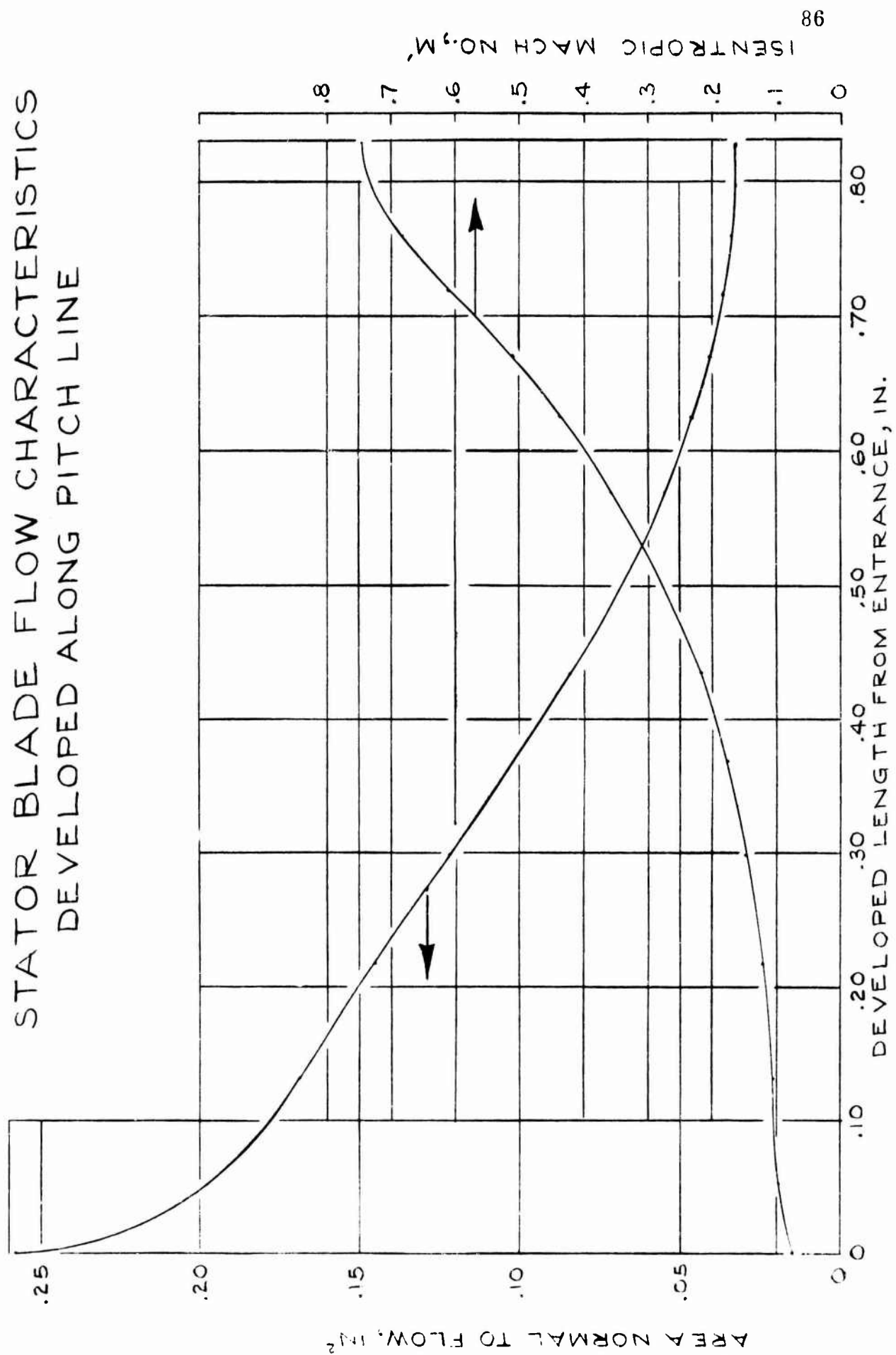


FIGURE 8.1.1

6.2 HEAT TRANSFER ANALYSIS

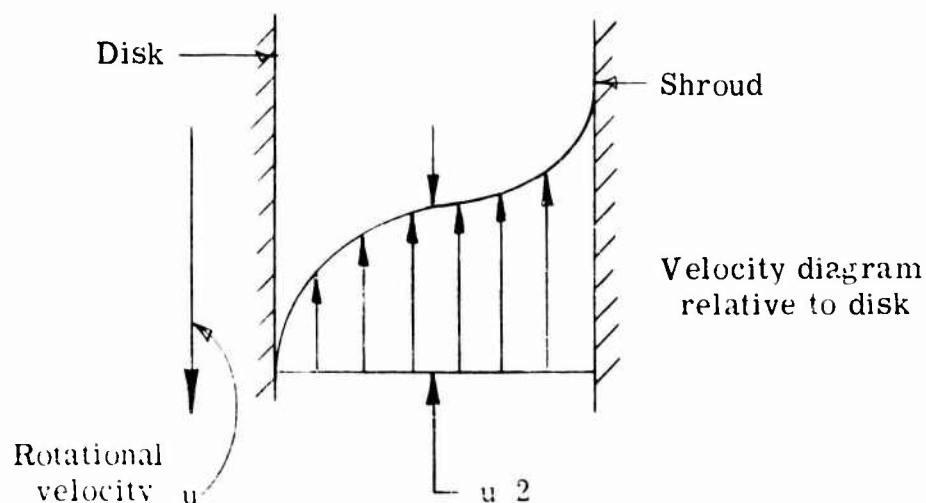
This discussion will include the design approach used to evaluate the temperature gradient throughout the turbine. In this section the approaches used to obtain local heat transfer coefficients, the local disk friction, the circulation flow around the disk, and the means of calculating the temperature throughout the system will be discussed.

6.2.1 Main Body of Disk

The main body of the disk is affected thermally by: (1) the local heat transfer coefficient; (2) the local disk friction; (3) the circulation flow rate; and (4) the cooling means. All these items are evaluated in order to calculate the temperature distribution throughout the turbine. The following sections describe the design approach used to evaluate these items as well as the approach used to calculate the turbine temperature distribution.

6.2.1.1 Local Heat Transfer Coefficient

The local heat transfer coefficient along the disk surface is difficult to evaluate on a theoretical basis because of the large turbulence in mixing which occurs, however, several reports have data relating to these conditions. These include References 3.2.1 through 3.2.5. Calculations of the heat transfer coefficient for the disk were made using correlations presented in these references. The procedure of Reference 3.2.3 was concluded to be the most applicable in Section 3.2.1.1. To use the approach of this reference, it was necessary to evaluate the local "free stream" velocity of the disk. The analysis was made assuming the velocity of the free stream was essentially one-half the disk velocity as shown in the sketch below.



The basic approach used in this reference was that of evaluating the heat transfer coefficient as a function of the friction coefficient of the wheel. Since the disk friction calculations are felt to be quite predictable due to the large amount of experimental data available, it was felt that a reasonable local skin friction coefficient could be derived from the local disk friction. This approach was used so that the skin friction coefficient was determined as a basis of the disk friction and hence, the local heat transfer coefficient was obtained as a function of the local disk friction. The equations and procedures used are shown in detail in Section 7.

The variation of the local heat transfer coefficient with turbine disk diameter is shown in Figure 6.2.1. It may be noted that the local film coefficient varies from 2 to 10 BTU/hr - ft² - °F as a function of radius over the disk surface which is of interest in the present calculation. This coefficient is quite low since the disk pressure and hence density is quite low. However, the disk friction is also low because of this low pressure and hence, a temperature difference of only 150°F is necessary to transfer the disk friction heat from the gas to the shroud.

6.2.1.2 Disk Friction

A large number of references (References 3.2.6 through 3.2.13) concerning disk friction are available. These references include both theoretical and experimental data. A summary of data presented in many of these references is shown in Figure 3.2.3. It may be noted that there is a large variation in disk friction between the various authors. However, the majority of the data is similar and it includes six references, References 3.2.6 through 3.2.11. As discussed in Section 3.2.1.2, the data of References 3.2.6 and 3.2.7 are most applicable.

In evaluating the disk friction it is first necessary to evaluate the disk Reynold's number:

$$N_{Re} = \frac{D U (3600)}{\nu \mu}$$

where: D = Disk tip diameter,

U = Disk tip speed, fps

ν = Specific volume, ft³ / lb

μ = Viscosity, lb ft - hr

For the inner portion of the disk the Reynolds number is 1.6×10^6 .

VARIATION OF LVF TURBINE
DISK AND SHROUD FILM COEFF.
AS A FUNCTION OF RADIUS

COEFF. BASED ON REF. 3.2.3

$$P_{\text{Disk}} = 2 \text{ psia}$$

$$T_{\text{gas}} = 255^\circ\text{F}$$

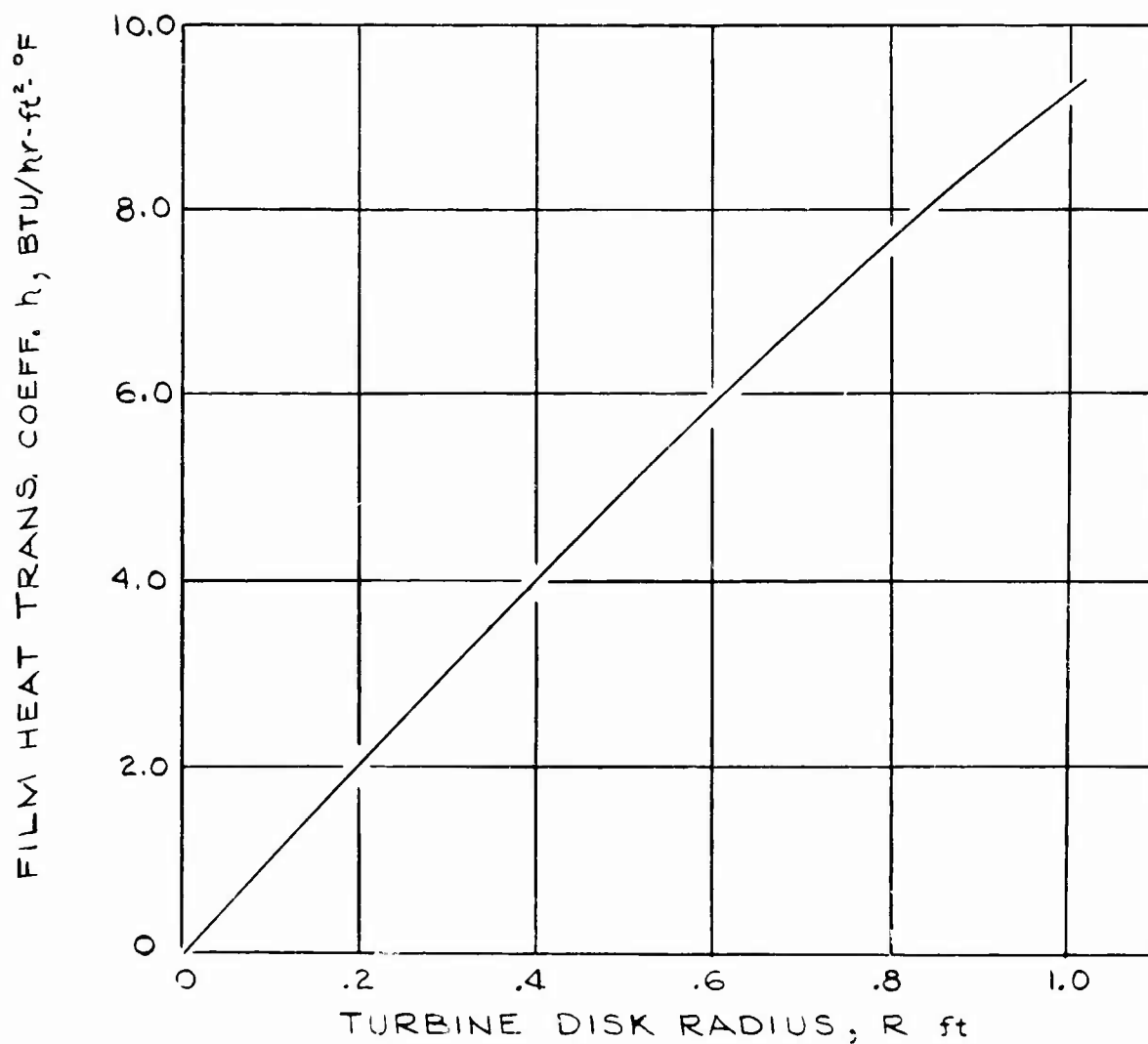


FIGURE 6.2.1

When using the correlation of Reference 3.2.6, this Reynold's number results in a disk friction coefficient of .00062, and hence, using the equation shown in Figure 3.2.2, the disk friction loss can be evaluated by:

$$W_{DF} = \frac{(0.00062) D^2 U^3}{g \nu} \quad \frac{ft-lb}{sec}$$

where: g acceleration of gravity, 32.2 ft/sec²

Based on the data of Reference 3.2.7, it is shown that in order to obtain the lower disk friction of the shrouded disk, the clearance should be 5% of the diameter or less. Therefore, the clearance in this case could be as great as 1.2 inch and still result in shrouded disk friction loss; however, since the disk is easily shrouded to 1/4 inch, the closer spacing is recommended.

It is desirable to obtain the local disk friction along the disk, therefore, it was assumed that the disk friction coefficient, K_W , is constant across the disk, and the disk friction for a local segment of the disk can be obtained by calculating the disk friction for the outer diameter of the area being considered and subtracting from it the disk friction of the inner diameter of the area being considered. Hence, as shown in Section 7.2.1, the local disk friction can be evaluated by:

$$W_{DF} = 711 (r_i^5 - r_o^5) \quad \frac{ft-lb}{sec}$$

where: r_i the outer radius of the area being considered, ft

r_o the inner radius of the area being considered, ft

This equation presents the friction for both sides of the disk, that resulting in four boundary layers. Therefore, when determining the heat balance and heat transfer situation of the LVF turbine, this amount of heat was divided equally and added to the disk in the location of the four boundary layers.

The results of the calculation of the disk friction as a function of turbine radius is shown in Figure 6.2.2. This figure is applicable to the portion of the disk that is below the seals on the outer edge of the disk, since the disk friction is higher at the periphery of the wheel due to much higher pressures than the 2 psia to which the main portion of the disk is vented. It should be noted that the values shown in Figure 6.2.2 are adjusted to include the disk friction on one side of the disk only.

DISTRIBUTION OF HEAT ADDED TO GAS DUE TO DISK FRICTION ONE SIDE OF DISK ONLY

$$P_{\text{disk}} = 2 \text{ psia}$$

$$T_{\text{gas}} = 255^{\circ}\text{F}$$

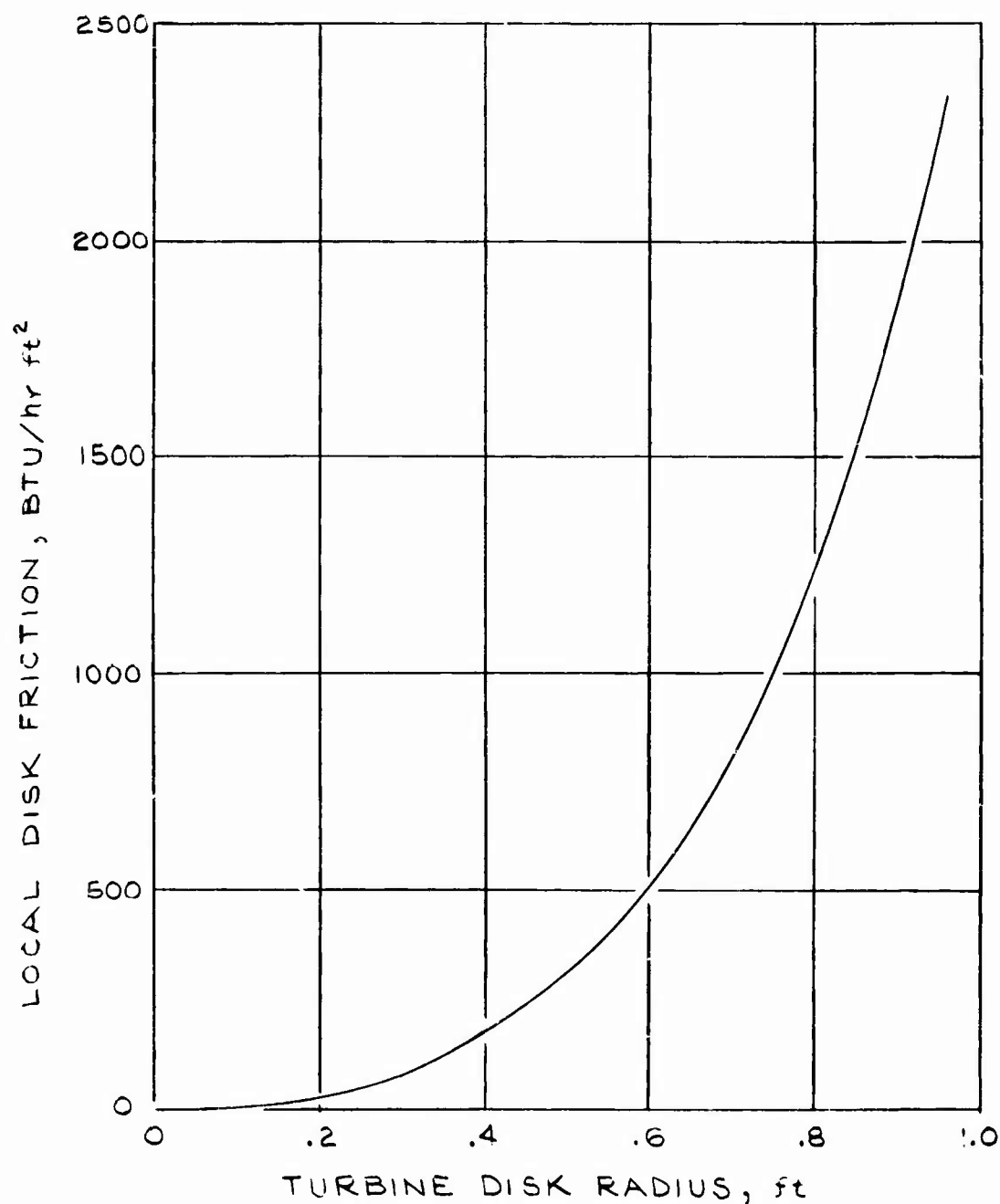


FIGURE 3.3.2

6.2.1.3 Circulation Flow

In evaluating the temperature gradient and heat transfer distribution of the LVF turbine, it is important to determine the amount of heat which is carried up the disk and down the shroud wall due to the pumping action of the disk. This pumping action, in effect, provides violent mixing and temperature equalization of the disk fluid. Several references are available concerning this recirculation flow. The references considered were References 3.2.2 and 3.2.5. However, these references proved to be of little value, since in the first reference flow was injected and in the second reference the amount of circulating flow was dependent upon the amount of naphthalene evaporated from the disk during the experimental test. Since these conditions are not consistent with the LVFT conditions, the information was not used for this application.

Unpublished experimental data obtained by the authors showed that the average velocity vector across a rotating disk was inclined at approximately 15° from the tangential velocity. In other words, a radial vector of approximately $\sin 15^\circ$ times the tangential vector is representative of the turbine configuration. Therefore, in the following heat transfer analysis, it was assumed that this radial vector described the mixing velocity in the gas.

6.2.1.4 Means of Cooling

Several means of cooling the disk were considered. These included rejecting the entire disk friction heat to the leakage flow through the peripheral seals, natural convection from the turbine housing to the surrounding air, and water cooling of the disk shroud. As presented in Section 3.2.1.4, the selected means of cooling was to water cool the disk shroud. This water cooling will be accomplished by taking the boiler feed water flow and passing it through a continuous tube which is soldered to the shroud of the disk, as shown in Figure 3.2.1. It is proposed that the feed water flow split evenly to each side of the disk housing. Because of the small amount of heat to be rejected to the water, the water temperature rise is less than 1°F when absorbing the entire disk friction heat. Therefore, it may be assumed that the water temperature throughout the tubes is equal to the condenser temperature of 130°F . Using the data of References 3.2.14 and 3.2.15, it is found that three turns of 0.45 inch ID tubing is adequate to transfer the heat necessary. It was assumed that the tube heat transfer area was equal to the tube diameter. A detailed description of this analysis is presented in Section 7.2.

6.2.1.5 Turbine Disk Heat Transfer Analysis

A thermal model of the disk and its surroundings was set up with specified boundary conditions and the heat transfer was computed using a digital computer program described in Section 7.2.5.

This analysis used a 15° segment of the turbine disk which was divided into 28 temperature nodes. These temperature nodes are small elements of the system and are represented by a temperature at the center of the element. The heat transfer throughout the system is analagous to electrical current flow so that the problem can be solved using a resistance network. Each temperature node is connected to its adjoining nodes, which affects its temperature by a conductor.

Conduction, convection, and fluid flow conductances were used in this analysis and are described as follows:

Conduction - These conductors are defined as:

$$R_{\text{CONDUCTION}} = \frac{K A}{\Delta X}, \text{ BTU/HR} - ^\circ\text{F}$$

where K = Thermal conductivity of the heat transfer medium

$$K_{\text{STEAM}} = .0145 \text{ BTU/hr} - \text{ft} - ^\circ\text{F}$$

$$K_{\text{TURBINE DISK}} = 22 \text{ BTU/hr} - \text{ft} - ^\circ\text{F}$$

$$K_{\text{WATER}} = 0.37 \text{ BTU/hr} - \text{ft} - ^\circ\text{F}$$

ΔX = Straight line distance between nodes, ft

A = Area of the common surface between two adjacent nodes, ft^2

Convection - The convection conductors are defined as:

$$R_{\text{CONVECTION}} = h A, \text{ BTU/HR} - ^\circ\text{F}$$

where h = Convection coefficient between the solid and fluid surface, $\text{BTU/hr} - \text{ft}^2 - ^\circ\text{F}$

A = Common surface between adjacent nodes over which the heat transfer occurs, ft^2

Fluid flow - The fluid flow conductors present a more complex problem than the other conductors. In this turbine disk problem ten fluid nodes are used. These nodes are located in the annular space between the disk and the shroud. When the disk is rotating, a re-circulation steam flow is set up in this annulus. Since the disk is

vented to the condenser to reduce disk friction, condenser steam is contained in this annulus and flows upward along the disk and then recirculates down along the shroud. These nodes are very important to the overall analysis since it is here that the disk friction heat is added to the system. A complete derivation of the fluid flow conductors is contained in the thermal analysis part of Section 7.0.

Based on the derivation in Section 7.2.5, the fluid flow conductor is

$$\bar{K}_f = \rho V A C_p \left(\frac{2 \Delta X_i}{\Delta X_i + \Delta X_{i-1}} \right)$$

where: ρ = Density of fluid, lb/ft³

V = Velocity of fluid, ft/hr

A = Fluid passage area, ft²

C_p = Fluid specific heat, BTU/lb - °F

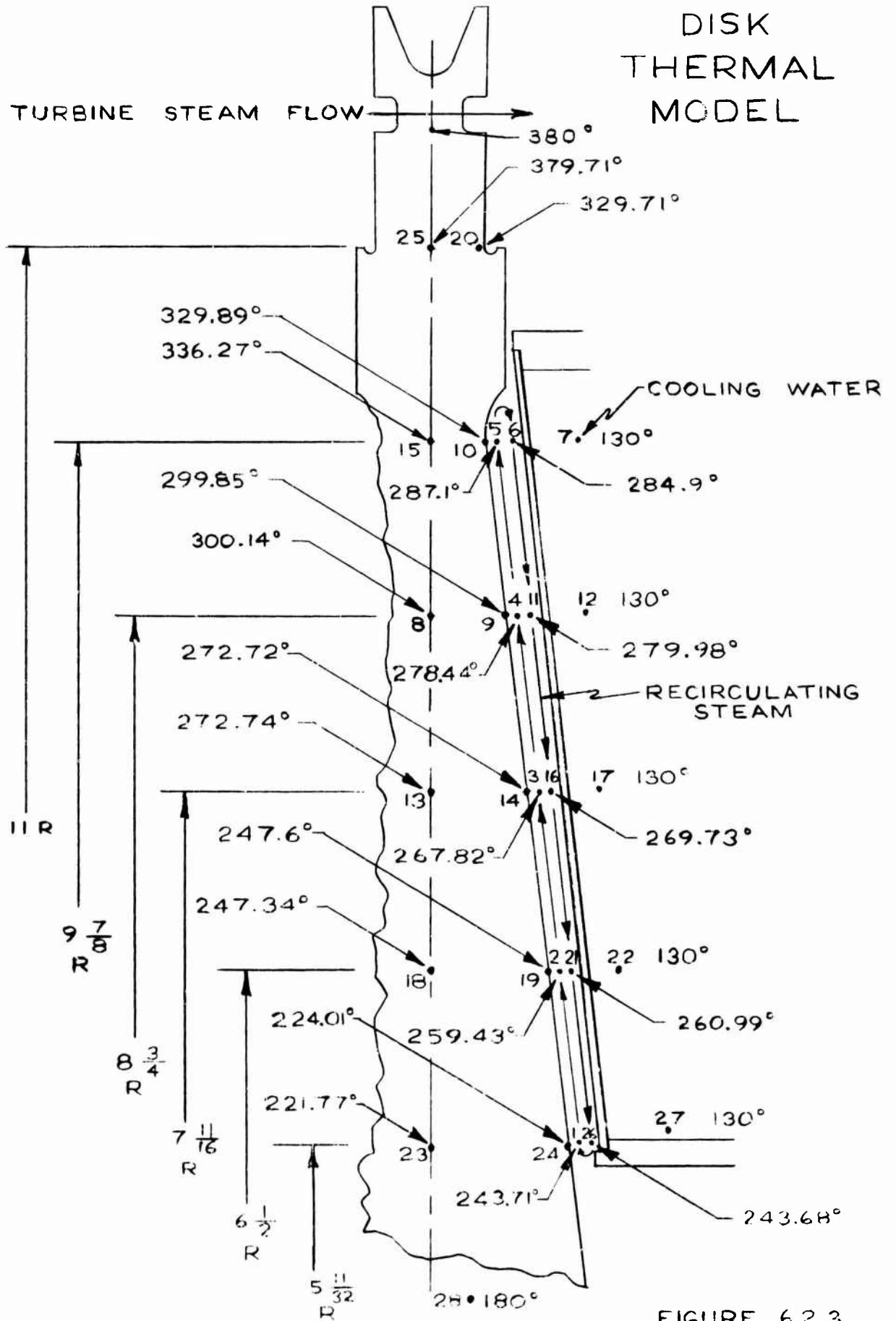
ΔX_i = Length of fluid node where temperature is being determined, ft

ΔX_{i-1} = Length of fluid node immediately upstream of node i , ft

The fluid conductors are one way conductors, in other words, a node is not affected in temperature by the node downstream of it but only by the upstream node.

Figure 6.2.3 shows the turbine disk thermal model with the node locations and the temperatures as calculated by the computer program. The boundary conditions established during the analysis are:

1. The cooling water temperature held constant at 130°F.
2. Temperatures of nodes 20 and 25 in the upper portion of the disk held constant at 330°F and 380°F, respectively. These temperatures are assumed fixed because of their close proximity to the turbine nozzles.
3. The hub area of the disk is maintained at 130°F.
4. The vertical center line of the disk is assumed to be an adiabatic surface.

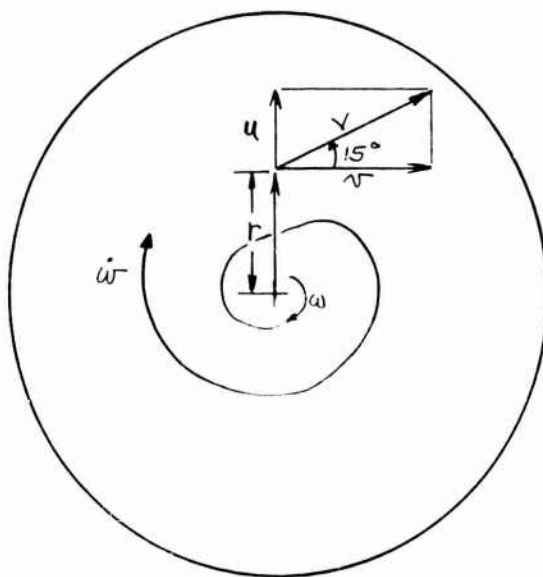


5. A one-half section of the disk was analyzed since it is assumed that the temperatures on the other side would be a mirror image.

The source of heat addition to the system is the disk friction in the annular space between the shroud and the turbine disk. This volume is vented to condenser pressure (2 psia) to minimize disk friction power losses by reducing the viscosity of the steam in this space.

A recirculation flow pattern will be set up by the rotation of the disk and the frictional forces between the disk and the steam. The steam will flow upwards along the disk and then down along the shroud. Disk friction was added to the ten fluid nodes in this annular space. In a fluid node, the temperature of the upstream node affects the node downstream of it as a function of the flow velocity, density, and distance. In order to determine the magnitude of the fluid conductors, the mass flow or velocity of the recirculating steam must be determined.

Previous Barber-Nichols Engineering Company experience with gas and steam turbines indicates that the outward flow along the face of a rotating disk proceeds in an outward spiraling direction from the disk center, with a resultant velocity (V) vector at 15° from the tangential velocity (v). The following diagram describes this observed flow pattern.



where \dot{w} = Mass flow rate
 ω = Rotational speed
 r = Radius
 u = Radial velocity of \dot{w}
 v = Tangential velocity of \dot{w}
 V_{WHEEL} = Rotational velocity at any r
 and $v = 1/2 V_{\text{wheel}} @ r$

The velocity (v) is deduced from considering the flow in the annular space between the rotating disk and the stationary wall. In this space the velocity of the gas on the face of the rotating disk will have a velocity equal to that of the disk. The gas on the face of the stationary shroud will have zero velocity. The average velocity in the passage is therefore one-half of the wheel velocity.

Based on this analysis, the radial velocities of the fluid nodes at 12,000 rpm are:

Node	r , in.	V_{wheel} , ft/sec	U , ft/sec
1,26	5.34	559	74.8
2,21	6.5	680	91.1
3,16	7.69	805	107.5
4,11	8.75	915	122.5
5,6	9.88	1035	138.5

The above values of radial velocity (U) were used to compute the fluid node conductors as described in the calculation section of this report.

Disk friction heat is added to the above fluid nodes and is transported through the annular space between the disk and the shroud by the fluid conductors. This heat is dissipated into the turbine disk and the shroud's water jacket by conduction and convection.

Figure 6.2.1 shows a plot of local disk friction heat in BTU/hr - ft² vs. turbine disk radii, in ft. for one side of the disk. This curve was used along with the local surface areas of the disk and shroud for a 15° wheel segment to determine the heat in BTU/hr added to each of the fluid nodes. The values of heat addition used in the disk heat transfer analysis are shown in the following table.

DISK FRICTION HEAT

Node No.	q , BTU/hr - ft ²	A , ft ²	Q , BTU/Min
1, 26	230	.01995	.0765
2, 21	390	.01320	.0858
3, 16	620	.0585	.1637
4, 11	950	.0180	.2800
5, 6	1350	.020	.4500

Heat is added to the system until the heat entering equals the heat leaving into the cooling water. At this point all the node temperatures will be in equilibrium. These temperatures are shown in Figure 6.2.3.

The heat transfer computer program does have the capability of showing the transient temperature response of the system. However, transient temperatures were not computed in this analysis due to the extremely long compute time which would be necessary.

As explained in the calculation section of this report, the program compute time interval for stable operation is a function of the sum of the conductors into a given node and the capacitance of the node as shown below.

Compute time step
$$\Delta T \leq \left(\frac{C}{\sum_N \bar{K}_N} \right)_{\text{MINIMUM}}$$

where C = Capacitance

$\sum_N \bar{K}_N$ = Sum of the conductors

ΔT = Compute time interval for stable operation

In order for the program calculations to converge, ΔT must be a minimum as determined by the above equation. The capacitance of the nodes are a function of the nodes density, volume, and specific heat. This problem contains solid, liquid and gaseous nodes. Obviously, the recirculating steam nodes will have the lowest density and also the smallest volume and therefore the lowest value of capacitance. Computing the capacitance of all the nodes shows that the recirculating steam fluid nodes have a value of capacitance many orders of magnitude less than the solid nodes. Based on the actual capacitance values of the nodes, the compute time interval will be very small resulting in prohibitively long IBM-1130 computer time requirements for the temperatures to go from their transient conditions to the steady state condition.

For this reason the node capacitances were input at a constant equal value, with the exception of the constant temperature nodes. The value selected was high enough to reduce the computer time to a reasonable value. This change therefore invalidates the transient temperature.

The capacitance of the constant temperature nodes is input as a very high value so that they will have essentially infinite heat capacity and their temperature remains constant.

The steady state temperature distribution of the disk, shroud and recirculating steam indicates reasonable temperature gradients along the disk for adequate mechanical design analysis. No problem is anticipated in the thermal control of this area. The mechanical design section of this report discusses in detail the design of the disk based on the thermal gradients evaluated here.

6.2.2 Disk Shroud and Seal Area

This area is the most complex to analyze since the largest number of external factors are affecting the disk surface. These external factors include: the seal leakage flow around the disk; the seal friction; the disk friction; the heat conducted from the live steam flow through the turbine; and the effect of cooling due to the water flow through the tip shroud. Figure 3.2.1 schematically shows this configuration. Each of the items mentioned above will be described in detail in the following sections.

Heat is added to this area of the turbine by hot leakage gas, seal friction, and disk friction. The seal friction is described by the following equation obtained from FIRL.

$$W_{SF} = 2.61 \times 10^{-6} \frac{\nu_K N^2}{h_B} (r_2^4 - r_1^4) \text{ HP}$$

where: ν_K Kinematic viscosity, lb-sec/in²

N Disk rotational speed, rev/min

h_B Blade height, in.

r_2 Outer radius of seal, in.

r_1 Inner radius of seal, in.

The leakage flow through the seals is obtained from the following equation, which was also obtained from FIRL:

$$Q_S = \frac{\pi S_S^3}{12 R T_1 \nu_K} \left[\frac{P_1^2 - P_2^2}{\ln(r_2/r_1)} \right] \frac{\text{lb}}{\text{Sec}}$$

where: S_S Seal clearance, in.

R Gas constant, in/^oR

T_1 Gas temperature entering seal, ^oR

ν_K Viscosity, lb-sec/in²

P_1 Seal high pressure, psia

P_2 Seal low pressure, psia

This leakage flow rate is quite important in that it provides a means of carrying off the seal friction heat in the leakage flow, thereby preventing excessive heating of the seal. It also is a heat source which is adding heat to the top of the shroud, in the case of Seal No. 1 (refer to Table 6.2.1 for seal number) or adding heat down around the disk to supplement the disk friction as in the case of Seal No. 2 and 3.

The values of the pressure, temperature, seal leakage, flow and frictional horsepower are shown in the table. Also shown in this table is the temperature rise in the seal leakage flow assuming all seal friction heat is absorbed by the leakage flow. This, of course, is not the actual case; however, it provides a measure of the temperature that the seal might reach in the event that supplemental cooling was not provided. As shown in this table, the temperature rise of Seal 1 and Seal 3 is quite high for a seal spacing of .001 inch. These temperatures indicate that Seal No. 1 will have to have supplemental cooling to control this temperature rise. This cooling is provided by water cooling of the shroud spacer above the wheel shroud as shown in Figure 3.2.1. In the case of Seal No. 3 it is shown in Table 6.2.1 that increasing the seal spacing decreases this temperature rise significantly. Therefore, it is recommended that Seal No. 3 have a seal spacing of .00125 inch. As previously discussed, this seal spacing is adjusted by suitable spring loadings on the seal.

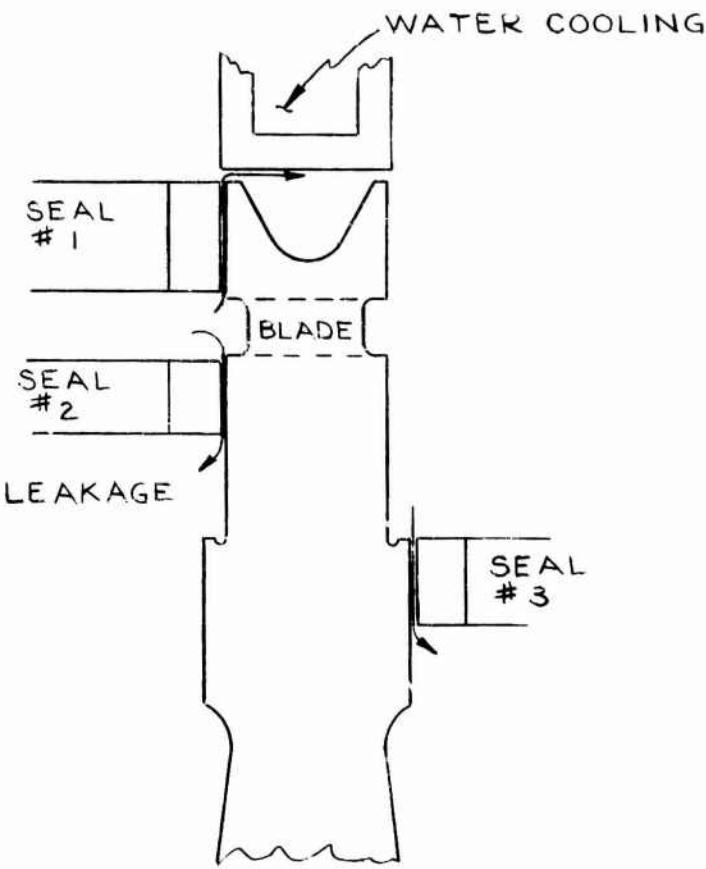
The gas heat transfer coefficient was evaluated at the rotor tip by the same means as that used for the main portion of the rotor as described in Section 3.2.1. This coefficient is approximately 411 BTU/hr - ft² - °F. This coefficient is much larger than that of the inner portion of the disk for two reasons. One is that the density is much higher since the pressure at this point is 50 psi rather than 2 psi, and the other is the much higher tip speed which increases the heat transfer coefficient.

6.2.3 Nozzle and Blade Area

The heat transfer coefficient of the hot steam entering the turbine is evaluated on the basis of forced convection equations as presented in Reference 3.2.17. This equation is as shown below:

$$\eta_f = 0.023 \frac{K}{D} (N_{Re})^{0.8} (N_{Pr})^{0.3} \quad \frac{\text{BTU}}{\text{hr-ft}^2\text{-}^\circ\text{F}}$$

SUMMARY OF SEAL FRICTION
AND LEAKAGE DATA



Seal No.	Seal Clearance, in.	Inlet Press psia	Exit Press. psia	Inlet Temp. °F	Leakage lb/sec	Friction HP	T °F Seal Flow
1	.001	93	50	430	.01613	3.97	347
2	.001	93	.2	430	.0223	2.93	186
3	.001	50	2	281	.00704	2.23	633
	.00125	50	2	281	.0137	1.78	260
	.00150	50	2	281	.0238	1.48	125

TABLE 6.2.1

where: K = Thermal conductivity, BTU/hr - ft - $^{\circ}\text{F}$

D_h = Hydraulic Dia., ft

N_{Re} = Reynolds No.

N_{Pr} = Prandtl No.

The resultant heat transfer coefficient was 270 BTU/hr - ft² - $^{\circ}\text{F}$ for the nozzle inlet area.

The effective gas temperature (T_{OR}) is important in evaluating the blade film coefficient and is defined by:

$$T_{OR} = T_s - \frac{(V_{R0})^2}{2gJc_p} \quad ^{\circ}\text{R}$$

where: T_{OR} = Total temperature relative to blade, $^{\circ}\text{R}$

T_s = Static temperature relative to blade, $^{\circ}\text{R}$

V_{R0} = Relative velocity entering blade, ft/sec

c_p = Specific heat, BTU/lb - $^{\circ}\text{F}$

J = Conversion factor, 778 ft - lb/BTU

Using the gas temperature relative to the blade to define the blade gas properties, the film heat transfer coefficient is evaluated by an unpublished empirical correlation of the authors. This equation is:

$$h = \frac{\bar{V}_R c_p N_{ST} (7610)}{\bar{v}} \quad \text{BTU/hr - ft}^2 - ^{\circ}\text{F}$$

where: \bar{V}_R = Average relative velocity through blade, ft/sec

\bar{v} = Specific volume, ft³/lb

c_p = Specific heat, BTU/lb - $^{\circ}\text{F}$

and

$$N_{ST} = \frac{C}{(N_{Re})^{.27} (N_{Pr})^{.667}}$$

where: C = 0.08 for typical turbine blade

N_{Re} = Reynolds number based on blade chord

N_{Pr} = Prandtl number

The results of the solution of this equation at the design point yield a heat transfer coefficient of 642 BTU/hr - ft² - °F for the gas flowing through the blade passages.

The heat transfer coefficient must be determined for the water passage which cools the gas above the tip of the turbine shroud. This film coefficient was evaluated based on the forced convection coefficients presented in Reference 3.2.14. All turbine feed water is passed through the housing at the shroud tip. The applicable equation for this film coefficient is:

$$h = \frac{K}{D} 0.023 (N_{Re})^{0.8} (N_{Pr})^{0.4} \cdot \frac{ETU}{hr - ft^2 - ^\circ F}$$

where: K = Thermal conductivity, BTU/hr - ft - °F

D = Hydraulic diameter, ft

N_{Re} = Reynolds number based on D

N_{Pr} = Prandtl number

Evaluation of this equation yields a film coefficient in the cooling water passage of 3780 BTU/hr - ft² - °F.

6.2.4 Turbine Housing

The heat transfer analysis used to determine the steady state temperatures of the turbine housing components is similar to that used for the turbine disk. The same computer program was used for both analyses.

The node system for the turbine housing is shown in Figure 6.2.4. This system also contains solid and fluid nodes like the turbine disk area. The combination of the solid and fluid nodes gives the same problem as for the turbine disk in that the computer time would be too long to calculate the transient temperatures unless a much faster computer is used. Therefore, false values of capacitance were input for all the nodes other than the fixed temperature nodes in order to bring the calculation to convergence more quickly.

Heat is added to the turbine housing area by the high temperature steam passing through the inlet ducts, the turbine blades and the exhaust duct. The chief mechanism for this heat addition is convection from the steam to the passage walls. Other sources of heat addition are from the fluid friction in the seals at nodes 3, 4, and 5 and disk friction at node 6.

TURBINE HOUSING
TEMPERATURE DISTRIBUTION

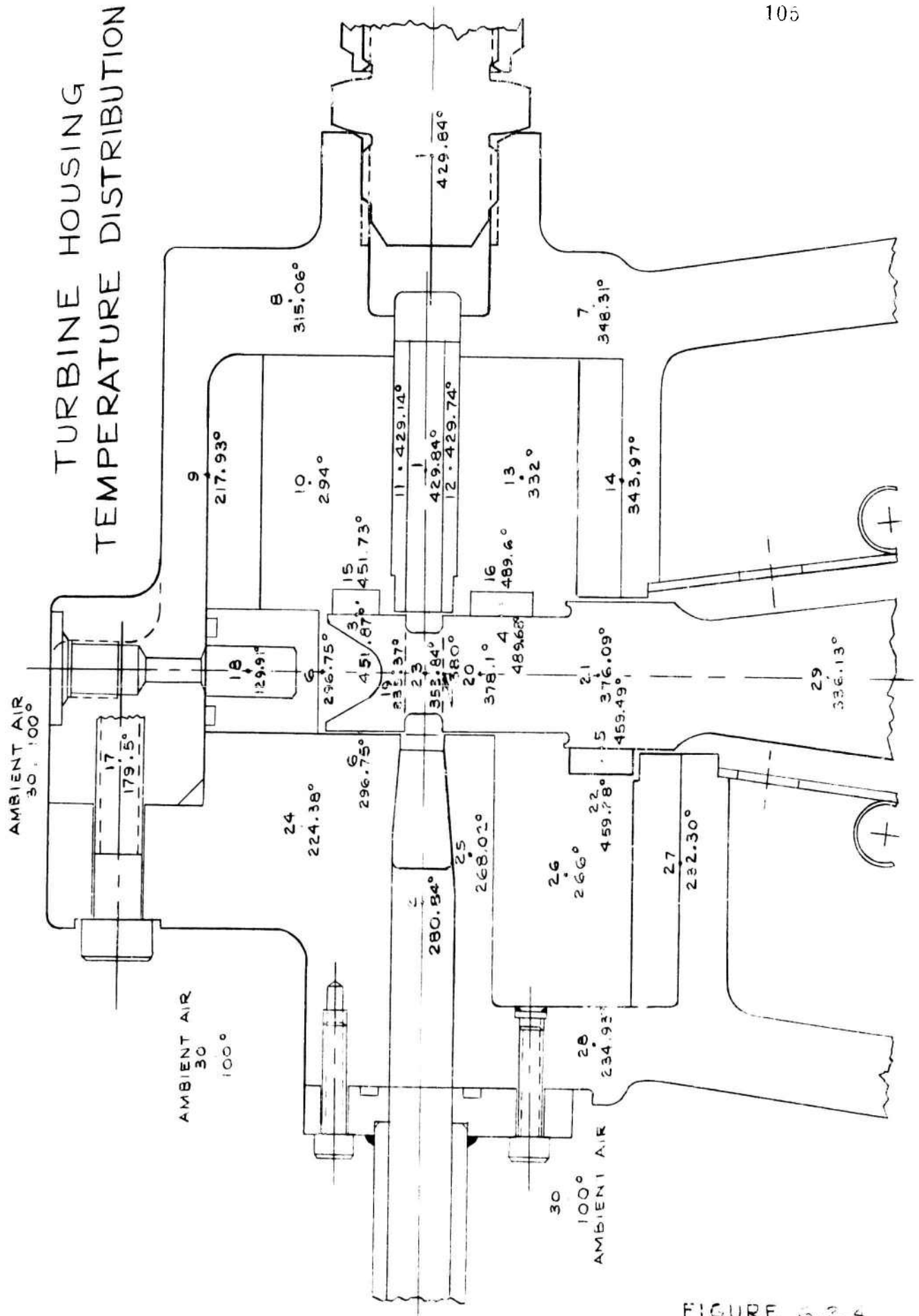


FIGURE 5.2.4

The heat addition due to seal friction at nodes 3, 4, and 5 is calculated and defined in Section 3.1 of this report. The values expressed in horsepower and converted to BTU/min over the 15° turbine housing segment are shown in the following table.

<u>Node</u>	<u>Seal Friction HP</u>	<u>Q BTU/min (15° Segment)</u>
3	3.97	7.0
4	2.93	5.18
5	1.78	3.14

The heat input due to disk friction at node 6 is calculated to be 4.04 BTU/min based on the disk friction data contained in Figure 6.2.2 for an average turbine tip radius of 1.06 ft.

In this analysis there is only one fluid conductor between nodes 3 and 6. The heat generated in node 3 will affect the temperature of node 6.

Node 18 has a .5" x 375" passage which carries cooling water flow at 130°F, maintaining this node at a constant temperature. The other boundary conditions are the temperatures of the inlet, leaving, and turbine blade steam which are held constant at 430°F, 281°F, and 354°F. The turbine disk, node 29, is also held constant at 336°F.

The outer nodes of the turbine housing reject heat by natural convection to the surrounding air which is fixed at 100°F. Nodes 7, 27 and 28 conduct into the turbine structure which is also held at 100°F.

The natural convection heat transfer coefficient from the turbine casing to the surrounding air is taken to be 1.0 BTU/hr - ft² - °F (Reference 3.2.14) which is a reasonable coefficient for the temperature difference anticipated between the casing and the ambient air.

The conduction between nodes was calculated as shown in Section 3.2.1 and consists of conduction, convection and the ore fluid conductor. The values of these conductors are shown in Section 7.2.5, Figure 7.2.5.

Mechanical joints between nodes include a joint resistance in the overall conductance value. The value of this joint resistance was taken from Reference 3.2.14. These values are 500 BTU/hr - ft² - °F at 6 gauge pressure on the joint and 11000 BTU/hr - ft² - °F at 3800 psia. For a bolt load of 4000 lbs bolt for 24 bolts in 360° or one bolt in 15°, a value of 4000 lbs load on the mechanical joints in the housing was used. The joint stress between the mechanical joints in the housing was calculated and based on these stresses and the connecting area in the joint, the joint resistance was calculated. This joint

resistance is based on a straight line interpolation between the resistance at 0 psi and 3800 psi. The following table gives the specific value of these resistances and the conductor at the joint.

JOINT RESISTANCE AND CONDUCTANCE

Connecting Nodes	Joint Stress, psi	Area, in ²	h_j , BTU/hr - ft ² - °F	\bar{K}_j , BTU/hr - °F
18 - 24	1630	2.45	4560	77.5
8 - 10	1680	2.38	4560	75.6
7 - 13	1930	2.072	5400	77.5
26 - 28	1980	2.02	5400	75.8
9 - 18	3870	1.032	11000	79.0

The temperature distribution in the turbine housing and surrounding area is shown in Figure 6.2.3. The only apparent problem area is the temperature difference between the components on the inlet side as compared with the exhaust side. From a thermal stress viewpoint it would be desirable if this axial temperature gradient could be reduced to zero and the radial temperature gradient on the inlet and outlet side be approximately the same. This can be done by bringing the shroud coolant water along the underside of node 14. This area of the thermal control problem will be examined more thoroughly during the next phase of this program.

The thermal control of the turbine housing is not considered to be a significant problem and relatively minor design changes should be able to provide a temperature distribution suitable for a reliable mechanical design.

6.2.5 Shaft and Bearing Area

The design of the thrust and journal bearings require condenser water to be used as a cooling medium. This water will be 130°F and sufficient water will be supplied to maintain the temperature of the bearings and the adjacent shaft area at the water temperature.

Heat flow from the turbine disk into the disk center and the shaft is not considered to be a significant problem based on the results of the disk heat transfer analysis and extended into the disk center and shaft area. This analysis shows that 6.4 BTU/min flows into the shaft both in the forward and aft directions from the disk. This additional heat will require an additional 1.25% of water to be added to the bearing cooling system.

This additional water is based on a bearing cooling requirement of 11.1 friction horsepower for the thrust bearing and 6.8 friction horsepower for each of the journal bearings. The heat equivalent of the frictional horsepower loss in the bearings is a total of 1046 BTU/min. The additional 6.4 BTU/min heat leak from the disk to the bearing area amounts to an almost insignificant quantity.

6.3 VIBRATION ANALYSIS

The preliminary design of the L V F turbine required substantial vibration analysis in three primary areas. These areas are: (1) blades and shroud; (2) the disk; and (3) the rotor. The turbine requires close running clearances between the disk and the controlled-leakage seal face. This requirement makes the disk, shaft, shroud and blades vibration important to the successful operation of the turbine. The blades in the L V F turbine are short and are reinforced by the shroud. This reinforcement makes the natural frequencies of the blades many times higher than running speed or nozzle passing frequency. Therefore, blade vibration should not be significant in the L V F turbine. The shaft vibration, or rotor dynamics, is important because of the close running clearances between the seal and the disk. The rotor was designed axially symmetric and designed for stiff shaft operation where the first critical is above operating speed. The following section provides the vibration aspects of the design in detail and includes the equations used in the analysis.

6.3.1 Turbine Blade Design

The turbine blades for the LVF turbine are shrouded and are short. These two requirements simplify the frequency analysis because it is only possible to excite the axial and tangential mode of the blade and shroud significantly. The other mode of interest, other than the diametric modes of disk and shroud, would be flutter of the trailing edges of the blades. (Figure 3.3.1) The natural frequencies of the axial and tangential mode are considered to be important because of the periodic force from the excitation sources tabulated in Figure 6.3.1.

These excitation forces are at frequencies of the fundamental speed of the machine and its harmonics. If the natural frequencies of the blade coincide or are sympathetic with the fundamental forcing frequency and, to a lesser degree harmonics of the forcing frequency, the blades and shroud could be excited. The deflection of the blades and shroud could possibly build up in amplitude such that the seal face and shroud could rub or distort, causing excessive leakage.

The design procedure followed was to calculate the natural frequency of the blade and shroud, both axial and tangential mode, then increase the blade moment of inertia until the natural frequencies are above any significant excitation frequency.

The equations that govern the axial and tangential mode of vibration are as follows:

Axial vibration

$$W_N = A \sqrt{\frac{EI_A}{UQ^4}}$$

Tangential vibration

$$W_N = A \sqrt{\frac{EI_T}{UQ^4}}$$

Where

A = Coefficient from Reference 6.3.1

Q = Length of blade, in.

$I_A \neq I_T$ = Moment of inertia in axial and tangential direction

E = Young's modulus #/in²

FIGURE 6.3.1

FREQUENCY OF EXCITATION FORCE

Source	Fundamental rpm	Significant Harmonic		
		2	3	4
Running speed	12,000	24,000	36,000	48,000
Nozzle passing	852,000*			
Seal segments	144,000**			
Vanes on ribs	108,000***			

*(Running speed) (Number of nozzles) = 12,000 X 71

** (Running speed) (Number of seal segments) = 12,000 X 12

*** (Running speed) (Number of vanes) = 12,000 X 18

The natural frequency of the axial mode, assuming a fixed-fixed beam, is 73.0×10^6 Rev/min and for the tangential mode 90×10^6 Rev/min, both of which are many times above the highest excitation frequency.

The detailed stress analysis of the shroud and blade in Section 6.3 provides the spring rate of the shroud and blade as a composite structure. A simple model of a spring and mass system was assumed and the natural frequency calculated.

$$f_s(\text{composite}) = \frac{1}{2\pi} \sqrt{\frac{K_A}{m}}$$

where f_s = Frequency of composite

K_A = Spring constant of shroud, blade system, lb/in

m = Total mass of shroud and blade

From the above $f_s = 190 \times 10^4$ Rev/min.

The above calculation indicates that a shroud mode of vibration exists of frequency f_s that has a natural frequency approximately ten times greater than the nozzle excitation source. The tenth harmonic of the nozzle passing frequency is usually considered to be insignificant and therefore is not expected to produce significant axial vibration of the shroud.

The trailing edge of the blades were thickened to decrease the stress in the thin edge and to allow rework if nicked when manufacturing. The resulting thicker edge is not susceptible to flutter.

6.3.2 Disk Vibration

Vibration of the turbine disk is critical in turbine design and even more important in the LVF turbine. This increased importance is because the sides of the disk are used as mating surfaces for the peripheral seals. Any shape assumed by the disk where the disk is deflected on a plane will affect the running clearance and could increase leakage and possibly cause rubbing. The deflection can come from mode shapes called the diametral modes which result from operating at speeds having an integral number of waves fitting exactly into the circumference. (Figure 3.3.2) The resulting disk displacement when running speed is tuned in close to a diametral mode can build up an intolerable amplitude. The criteria for a disk design given a mean diameter and a blade and shroud design is to establish a disk of a thickness in excess of that required to resist centrifugal stresses which would keep the disk's critical speeds at a safe margin from operating speed and also operating speed harmonics.

The disk has extra material on the sides that can be removed in order to detune the disk. The disk will be statically vibrated and the diametral modes determined and compared to possible excitation sources. Material will then be removed if detuning is necessary.

The equations governing the diametral modes of vibration are as follows: (Reference 6.3.2) Equating the kinetic energy to the sum of the potential energy and centrifugal work, this gives the following expression:

$$p^2 = \frac{E' h_0^2}{48 R^4} \frac{C_p}{C_k} + W^2 \frac{C_c}{C_k}$$

where $C_p = \int \psi_p(x) dx$

$$C_k = \int \psi_k(x) dx$$

and $C_c = \int \psi_c(x) dx$

The calculation is made in this report by using Tables 2 through 11 of Reference 6.3.2.

Using the equations, tables of Reference 6.3.2, and the disk shown in Figure 6.3.2, the critical speeds relative to the second and third diametral modes were calculated. These speeds are:

Third, 29,780 rpm (3ND)

Second, 21,500 rpm (2ND)

The second and third critical speeds are sufficiently removed from running speed that they will not be excited.

The first nodal diameter (1ND) is not excitable in a one disk system, and therefore was not calculated. (Reference 6.3.2)

Other types of disks were investigated; for example, the constant stress disk, not acceptable because of its thin outer diameters, which would be more accessible to these diametral modes. A disk with a hole was investigated, but the large radial growth at the bore was undesirable and the shaft with a disk with a hole would have required an attachment technique such as a through-bolt, a Gleason spline, a rabbit joint, or a shrink fit. Either of these designs would have ultimately required disassembly and assembly, which would change balance and relationship between shaft and disk. Also, balancing becomes more difficult. The design used on the LVFT

MODULE OF SOLID DISK ASSUMED FOR STRESS ANALYSIS

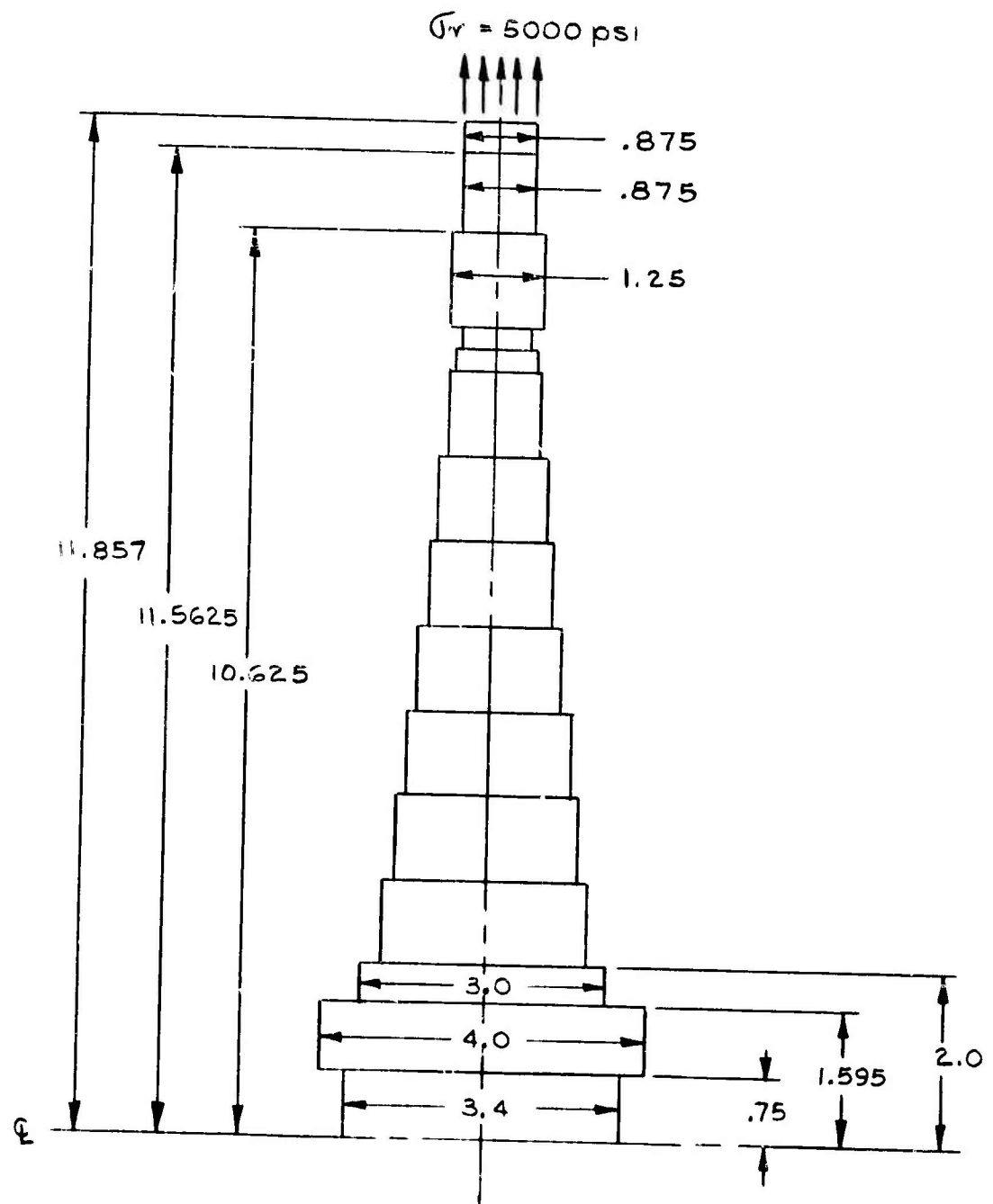


FIGURE 6.3.2

of a continuous disk and integral shaft will provide the most reliable design because of the inherent coaxial relationship of the shaft and disk and the normality between the sides of the disk and seal. This coaxial and normality relationship is obtained regardless of balance or growth from centrifugal force and can more easily be controlled in a symmetric disk.

6.3.3 Rotor Dynamics

The rotor dynamics of a rotating system include the forces caused by rotating unbalance, critical speeds, and instability. The close running clearance of the seal requires a rotor system that has predictable dynamic characteristics and a minimum of misalignment. Both of these criteria can best be accomplished in a stiff shaft design, that is, where the machine operates at approximately 15 to 20 per cent below first critical.

The first critical is one in which the shaft whirls between two nodes at the bearing. The calculation for the first critical frequency is done by considering the rotating mass to be supported on two springs of a constant spring rate. The spring rate has been defined in Tabulation 6.5.1. The first critical of the LVF turbine is 14,000 rpm, approximately 15 per cent above operating speed of 12,000 rpm. The calculation for the critical includes the stiffness of the shaft as well as bearing film stiffness. The analysis for the first critical was based on the Rayleigh-Ritz equation. (Reference 6.3.3) The equations for the critical speeds are:

$$W_c = \sqrt{9 \sum_{1}^j W_N \delta_N / \sum_{1}^j W_N \delta_N^2}$$

where W_N = Weight of Nth mass

δ_N = Static deflection of the Nth mass

j = Total number of masses

and the model assumed is shown in Figure 3.3.3.

Equally important as avoiding operation at or near the first critical is having sufficient balance so that excess forces are not applied to the bearings. This force, or mass unbalance, produces a radial force that rotates at shaft speed with a magnitude dependent upon both the amount of unbalanced mass in the system and the rotating speed. It is necessary to establish limits for rotating unbalance for the LVFT rotating mass. From Table 6.5.1 the following information is needed to make this calculation:

h_o = Minimum film thickness = .001175 in.

C = .003 radial clearance, in.

from Reference 6.3.4 the equation for h_o is:

$$h_o = C [1 - \epsilon] \text{ or } 1 - \frac{h_o}{C} = \epsilon$$

where ϵ = eccentricity ratio

The force per bearing is assumed to equal 200 pounds which includes 141.4 pounds static weight and 58.6 pounds unbalance force. The unbalance acceptable is .014 in/lb based on 58.6 pounds mass unbalance and ϵ of .608 obtained from the following equation:

$$\text{Force of unbalance} = \frac{W}{g} w^2 r$$

where W = Magnitude of unbalance

w = Rotational speed rad/sec

g = Gravitational constants, in/sec²

r = Effective radius of unbalance, in.

Cylindrical balance ribs are provided on the sides of the disk. (Figure 3.3.3) This is where material can be removed for balancing without penetrating the disk profile.

Because of the close running clearance of the disk, the conical mode of shaft vibration was considered to be important to the operation of seals. Therefore, criteria was followed in the design that best avoided this mode of vibration. This consisted primarily of using two identical bearings and putting the center of gravity of the rotating mass in the center between two journal bearings. (Figure 3.3.3)

The calculation for the conical mode provides the natural frequency of 18,917 rpm, approximately 58 per cent higher than maximum rotating speed, and between 1 and 2 harmonic. It is fair to assume that the conical mode will not be excited.

The occurrence of half frequency whirl, which is more associated with lightly loaded machines, is not expected in the LVF turbine. The turbine requires a 1,200 pound preload at 12,000 rpm, providing the bearing film stiffness required and establishing the critical speed at a safe margin. The large preload required will prevent half frequency whirl from occurring significantly. The provisions for the variable preloading devices allows the preload

to be varied as a function of speed while measuring the deflection or film thickness of the bearing. These parameters provide a monitoring technique that will indicate if half frequency whirl is present and when preload is sufficient to eliminate the phenomena.

6.4 STRESS ANALYSIS

The preliminary design of the L V F turbine required substantial stress analysis in three primary areas. These areas are: (1) blades and shroud; (2) the disk; and (3) the casing. The remaining areas of the mechanical design followed normal well-established design procedures.

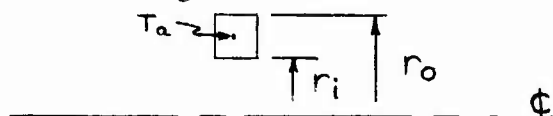
The stress analysis was directed to those areas where investigation and substantiation were necessary to provide a reliable test unit. The blades and shroud are subjected to loads that are unique to this turbine because of the radial thickness of the shroud. Because of this unique loading, it was necessary to derive equations for the elastic relationship between the shroud and blades and to establish procedures to calculate the stress in the blades from the force of the shroud.

The casing, subjected to a small external pressure, was designed to withstand the worst pressure loading that potentially could exist. It was concluded that the maximum operating pressure of the highest pressurized compartment was the design criteria. This was because if the seals failed, the pressure could inadvertently approach the design pressure. The following section discusses the stress analysis and detail and includes the derivation of equations and data for substantiation of the necessary equations.

6.4.1 Turbine Blade and Shroud Stress

The blades are subjected to forces which include centrifugal force of the blade, pressure differential across the blade, the tension from retaining the shroud, and bending moment caused by the seals (see Figure 6.4.1). The blades provide the continuity between the shroud and the disk. In order to provide the continuity the blades are stressed in tension, restraining the shroud from expansion as a free ring subjected to a centrifugal force field and thermal expansion. The forces are then transmitted to the disk through the blades, further expanding the disk.

Assume a free thick ring as shown of radius r_o and r_i subjected to both centrifugal and thermal growth.



From Reference 6.4.1 the equations for stress and deflection of a free rotating flat ring are:

$$\text{Deflection } U_w = \rho_w^2 \frac{r}{E} \frac{(3+\mu)(1-\mu)}{8} \left(r_o^2 + r_i^2 + \frac{1+\mu}{1-\mu} \frac{r_o^2 r_i^2}{r^2} - \frac{1+\mu}{3+\mu} r^2 \right)$$

$$\text{Radial stress } \sigma_r = \rho_w^2 \frac{3+\mu}{8} \left(r_o^2 + r_i^2 - \frac{r_o^2 r_i^2}{r^2} - r^2 \right)$$

$$\text{Tangential stress } \sigma_T = \rho_w^2 \frac{3+\mu}{8} \left(r_o^2 + r_i^2 + \frac{r_o^2 r_i^2}{r^2} - \frac{1+3\mu}{3+\mu} r^2 \right)$$

where: ρ = Density, lb/in³

ω = Angular speed, rad/sec

r = Radius in general, in.

r_i = Inner radius, in.

r_o = Outer radius, in.

μ = Poisson's ratio, .3 for steel

E = Modulus of elasticity, lb/in²

and from Reference 6.4.2 the equation for the expansion of a ring when raised in temperature is

$$U_T = (\Delta T)(\alpha)R, \quad \text{IN.}$$

LOADS ON BLADE AND SHROUD

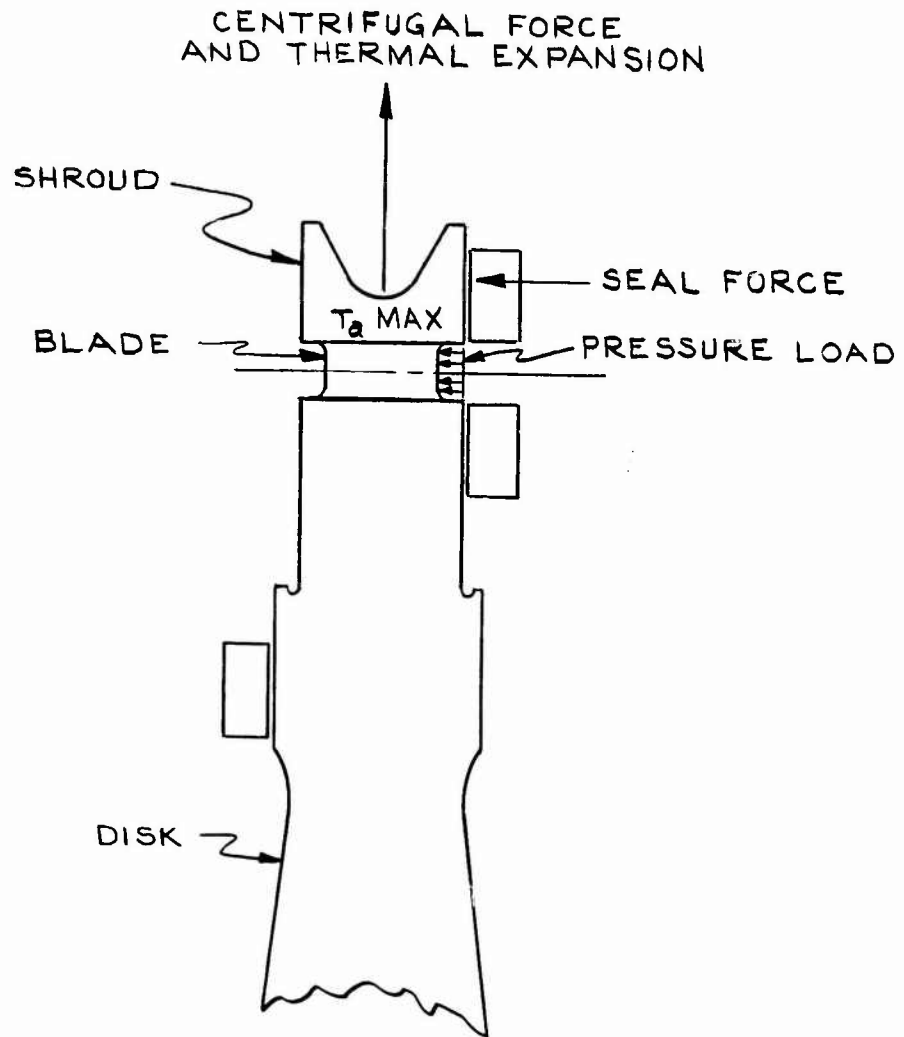


FIGURE 6.4.1

The resulting total free growth of the shroud is the summation of the thermal and centrifugal growth.

$$U_T + U_\omega = U$$

The growth of the disk has been defined in Section 6.4.2 with a temperature gradient which represents steady state operation. There are quite obviously two conditions to be considered: (1) condition at start where the disk is cold and the shroud is assumed to have reached the maximum temperature of $T_a(\max)$; and condition (2), the operation condition where in addition to the shroud being at $T_a(\max)$ the disk has warmed up, alleviating the stress. The blades provide the restraint necessary to retain continuity and are assumed to hold the shroud down to the required displacement. The force required to retain the ring to the required displacement for continuity is

$$\text{Force} = -P_i (A_s)$$

where: $-P_i$ = Internal pressure, psi

A_s = Internal area of shroud, in²

P_i is obtained from the following relationship (Reference 6.4.1)

$$\Delta P_i = P_i \frac{r}{E} \frac{r_i^2}{r_o^2 - r_i^2} [(1-\mu) + (1+\mu) \frac{r_o^2}{r^2}]$$

This equation represents a ring with a hole subjected to negative internal pressure. The pressure obtained in this manner is then distributed over the area of shroud equally and represents the total force straining the blades. The stress calculated in this manner is tabulated in Figure 6.4.2 under condition one and condition two, startup and operating.

In addition to these stresses, the shroud and blades are subjected to other local stresses. The shroud can be represented as a ring which, in addition to the blade, must react to the axial force and bending moment caused by pressure differential and seal face pressure. (Figure 6.4.3) The shroud provides the running surface for the upper seal. Excessive deflection or rotation can cause increased leakage. For the blades to deflect it is necessary for the shroud to twist through an angle ϕ ,

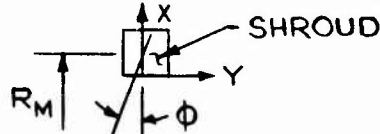


Figure 6.4.3 shows the elastic model of the shroud and blades. To retain continuity it is necessary for ϕ_1 and Δ_1 of the shroud and ϕ_2 and Δ_2 of the blade to be equal.

$$\phi_1 = \phi_2$$

Rotation of blade = rotation of shroud

$$\Delta_1 = \Delta_2$$

Deflection of blade = deflection of shroud

TABULATION OF STRESS IN BLADE AND SHROUD

(all stress in psi)

Location		CONDITION #1				CONDITION #2			
		Shroud Restraint	Shroud Bending	Centrifugal Force of Blade	Total Maximum Stress	Shroud Restraint	Shroud Bending	Centrifugal Force of Blade	Total Maximum Stress
Blade	Tip	21444.	630.	-	22074.	16971.	630.	-	17601.
	Root	21444.	2250.	3473.	27167.	16971.	2250.	3473.	22694.
Shroud	At point of blade attach- ment				93500.				74857.

Condition #1 startup

Condition #2 Normal operation

FIGURE 6.4.2

ELASTIC MODEL OF SHROUD AND BLADE

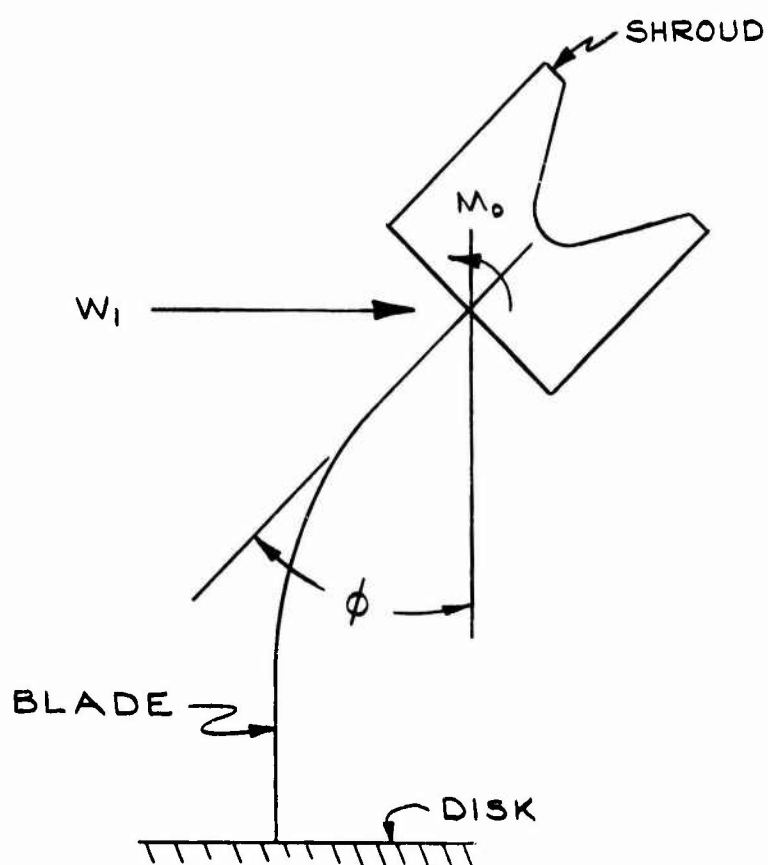


FIGURE 6.4.3

W_1 = Unknown shear force concentrated at end of blade

N_2 = Uniformly distributed load (total)

J = Inertia of beam section (total)

M_0 = Unknown moment at one end

(from Figure 6.4.3)

Moment at any value of X

$$\Sigma M_x = W_1(l-x) + \frac{W_2}{l} \frac{(l-x)^2}{2} - M_0 = EJ \frac{d^2 y}{dx^2}$$

$$\frac{dy}{dx} = \frac{1}{EJ} \left[W_1 \left(lx - \frac{x^2}{2} \right) + \frac{W_2}{2l} (l^2 x - lx^2 + \frac{x^3}{3}) - M_0 x + C_1 \right]$$

for $x=0, \frac{dy}{dx}=0, C_1=0$ for $x=l, \frac{dy}{dx} = \phi_1$

$$\phi_1 = \frac{1}{EJ} \left[\frac{W_1 l^2}{2} + \frac{W_2 l^2}{6} - M_0 l \right]$$

therefore $M_0 = (W_1 + \frac{W_2}{3}) \frac{l^2}{2} - \frac{EJ}{l} \phi_1$

$$Y = \frac{1}{EJ} \left[W_1 \left(\frac{lx^2}{2} - \frac{x^3}{6} \right) + \frac{W_2}{2l} \left(\frac{l^2 x^2}{2} - \frac{lx^3}{3} + \frac{x^4}{12} \right) - M_0 \frac{x^2}{2} + C_2 \right]$$

at $x=0, y=0$ and $C_2=0$ at $x=l, Y = \Delta_1$

where Δ_1 = deflection of beam

$$\Delta_1 = \frac{l^2}{EJ} \left[\frac{W_1 l}{3} + \frac{W_2 l}{8} - \frac{M_0}{2} \right]$$

from continuity the $\theta_{\text{BEAM \#1}} = \theta_{\text{SHROUD \#2}}$

$$\phi_1 = \phi_2$$

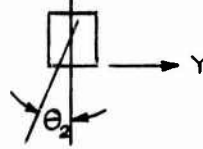
and $\Delta_{\text{BEAM}} = \Delta_{\text{SHROUD}}$

$$\Delta_1 = \Delta_2$$

deflection and rotation of shroud.

Assume shroud is narrow ring under distributed torque about its axis. Then from Reference 6.4.3 the ring is assumed to rotate about its centroid through an angle of $\frac{M R^2}{EI}$ where M = bending moment per linear inch, let M_0 = total moment

$$\phi = \frac{M_0 R}{EI}, \quad I = \text{MOMENT OF INERTIA}$$



let $\Delta_2 = r\theta_2$ for small angles

$$\theta_2 = \frac{\sum MR}{EI} \quad \Delta_2 = \frac{\sum MR}{EI} r$$

$$\Delta_1 = \Delta_2$$

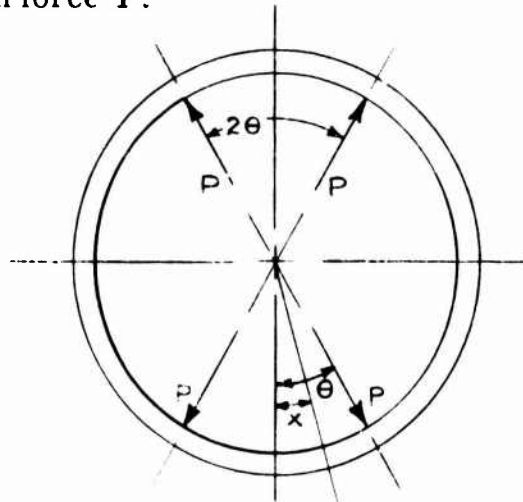
$$\theta_1 = \theta_2$$

$$\frac{l^2}{EI} \left[\frac{W_1 l}{3} + \frac{W_2 l}{8} - \frac{M_0}{2} \right] = \frac{\sum MR r}{EI}$$

$$\frac{1}{EI} \left[\frac{W_1 l^2}{2} + \frac{W_2 l^3}{6} - M_0 l \right] = \frac{\sum MR}{EI}$$

solving simultaneously provides the moments and shears that, when applied to the shroud and blade individually, determine the resulting stress, deflection, and rotation listed in Figure 6.4.2.

The preceding analysis conservatively defined the stress in the blades. The analysis, however, does not provide the local stress in the shroud or include the local deformation of the shroud from the multiple attachment points. The following analysis is a more detailed analysis of the shroud. For this analysis the shroud is assumed to be a ring having equally spaced radial supports (Reference 6.4.4). Each support (or blade) loads the ring with force P .



$$2\theta = \frac{360}{90} = 4^\circ$$

X = Angle measured from midway between adjacent radial forces

P = Magnitude of each radial load

T = Tension at any section X

M = Bending moment

U_t = Strain energy

σ = Stress

S_p = Radial outward deflection at point of application of force P

Q = Radial load

TQ = Tension from Q

SQ = Radial inward deflection

From the previous analysis the deflection required for continuity was calculated. Using this deflection, the required force necessary to retain continuity is calculated from the following equations.

$$\frac{S_p}{P} = K_3 \frac{R^3}{EI} + \frac{K_4 R}{EA}$$

$$\text{where: } K_3 = \left[\frac{1}{\sin^2 \theta} \left(\frac{\theta^5}{45} - \frac{\theta^7}{315} + \frac{3\theta^9}{14175} \right) \right]$$

$$K_4 = \left[\frac{1}{\sin^2 \theta} \left(\frac{\theta}{2} + \frac{\sin \theta \cos \theta}{2} \right) \right]$$

The above equations provide the force applied at the equally spaced supports. The stress in the shroud from force P is then calculated from the following relationship.

$$\frac{\sigma}{P} = K_1 \frac{R_L}{I} + \frac{K_2}{A}$$

$$\text{where } K_1 = \left[\frac{\theta^2}{6} - \frac{\theta^4}{60} + \frac{3}{5040} \theta^6 \right]$$

$$K_2 = \frac{\cot \theta}{2}$$

6.4.2 Turbine Disk Design

The turbine disk is of the solid (no hole at bore) conical profile type with shaft attached by welding. The disk design has continuous conical sides extended to the hub where the shaft is welded. The design inherently retains the centers of the disk and shaft coaxial and has the least effect on balance from external bending moments, thermal distortion, and mechanical attachment of the shaft. The shaft welded to the disk can be machined concentric and with the most exact normality, obtaining the necessary relationship between the centers of the shaft and the side of the disk. The rotor can be balanced more exactly without the loss of balance when disassembled.

Figure 6.4.4 shows the stress distribution in the disk from the centrifugal force at 12,000 rpm and the thermogradient assumed in Figure 6.4.5. The stress is also plotted, superimposed. Figure 6.4.6 provides the tabulation of deflection and stress as a function of radius. In the figure the average stress is indicated and is the most acceptable criteria used to establish burst strength of the disk. From Reference 6.4.5 it is specified that in disk design the average tangential stress should not exceed 50 to 60 per cent of the rupture strength.

The temperatures are not extreme in the LVFT design, allowing the use of the minimum ultimate strength as the rupture strength. The LVFT design average tangential stress is approximately 34.6 per cent of ultimate. The disk has sufficient margin that the disk can be detuned at a later date, if necessary, as discussed in Section 3.3.2 of this report. The magnitude of stress in the disk has little meaning until compared with the properties of the material selected for the prevailing conditions. Figure 6.4.7 shows material reviewed for the application.

The shroud and blades are machined integral from the disk forging. The stress in the shroud dictated the material finally selected for the disk because of their higher stress condition. The material selected is high strength (Cr-Ni-Mo) forging material, which has an ultimate strength of 150,000 psi and a yield strength of 125,000 psi. The material, therefore, has a strength without heat treating excessively, which provides material condition having the most ductility and highest material damping. The additional criteria normally used for the selection of disk material is the creep rate. The maximum temperature of the shroud is 451°F maximum, which is low enough that creep will not be significant.

Section 6.4.1 of this report describes condition one, the startup condition, and condition two, the normal operating condition. The startup condition when the disk is cold and the shroud is hot is the worst stressed condition. The use of the high strength material is necessary for this short time operation, assuming that no pre-heating of the disk is to be accomplished. Also, to meet the criteria established of not exceeding the rupture modulus by more than 50 to 60 per cent, it is necessary

ELASTIC STRESS IN TURBINE DISK AT 12000RPM

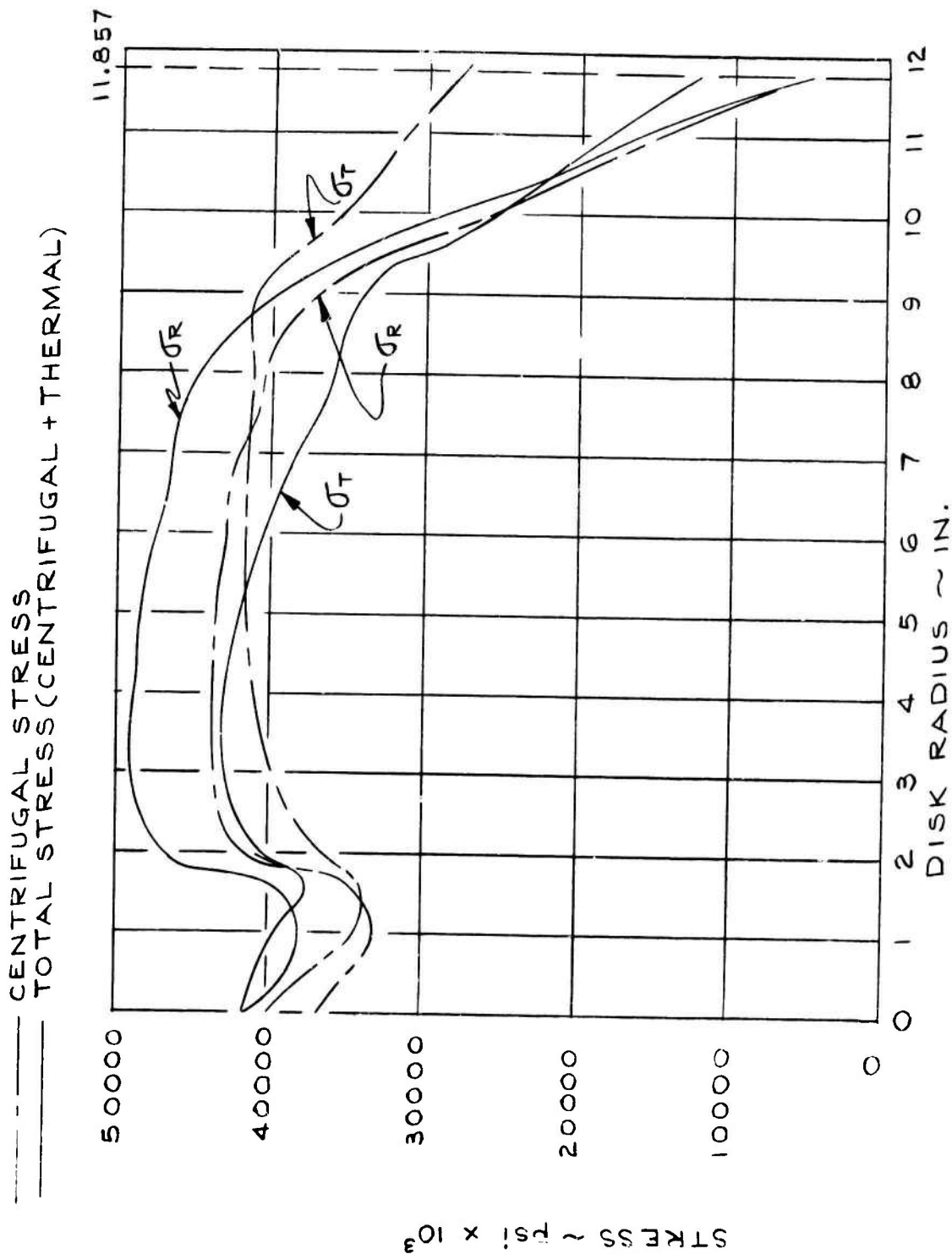


FIGURE 3.4.4

TEMPERATURE DISTRIBUTION IN TURBINE DISK

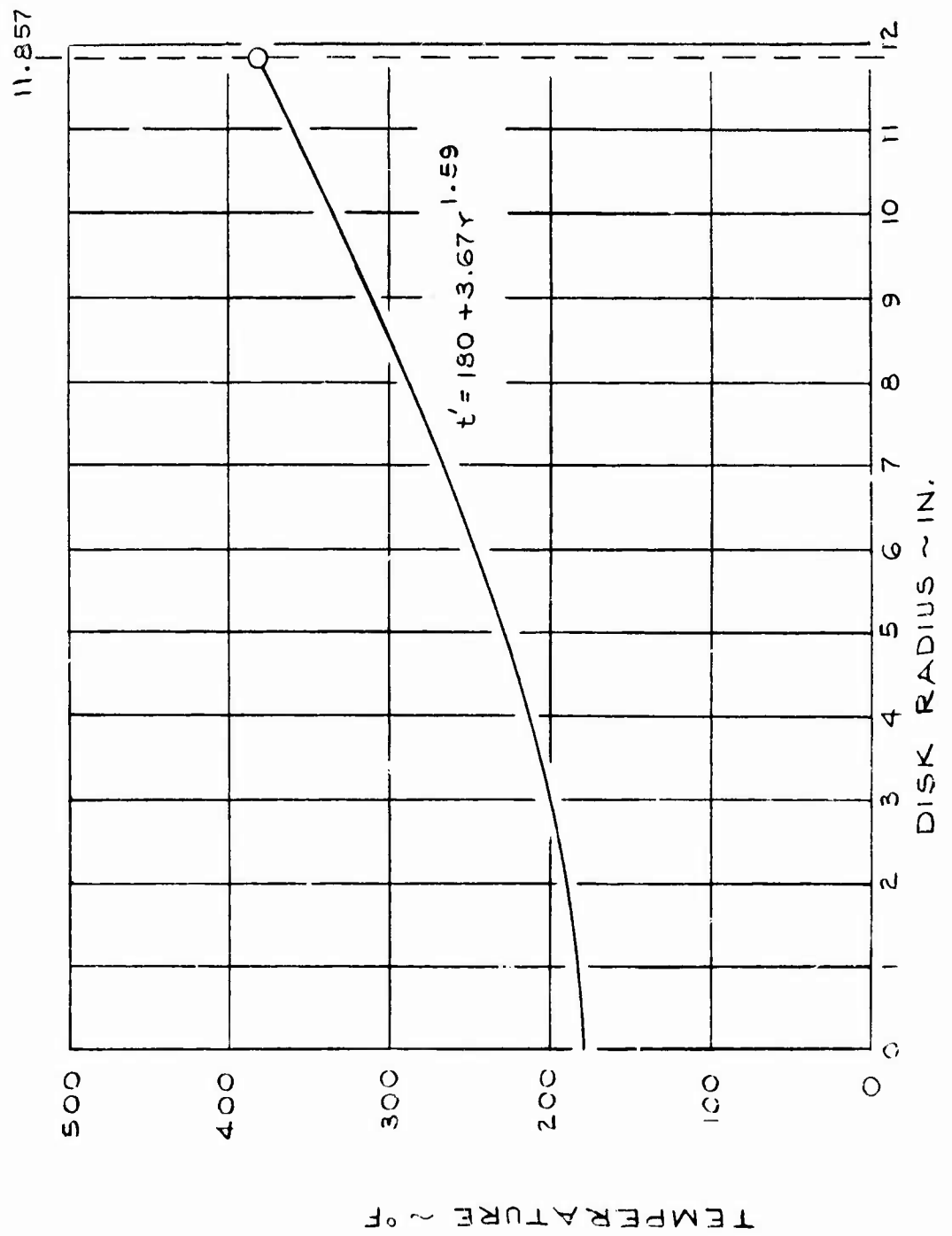


FIGURE 6.4.5

TABULATION OF DISK STRESS
AND DEFLECTION AT 12,000 RPM

130

$$t' = 180 + 3.67 \times 1.59 \text{ } ^\circ\text{F}$$

$$\rho = .28 \text{ lb/in}^3$$

Radius	No Thermal Gradient			With Thermal Gradient			Radial Growth Mils
	Disk Thick- ness at the Given Radius, Inches	∇_r	∇_t	Radial Growth Mils	∇_r	∇_t	
11.857	0.875	5000	27721	9.97	5000	12386	.0194
11.5625	0.875	8100	28771	9.96	8160	14017	
10.625	1.25	18741	32618	9.70	19967	20605	
9.5	0.90	32347	38592	9.24	39177	39830	
9.25	0.91	35200	40000	9.00	37500	32988	
9.0	1.00	37000	40800	8.75	39400	33725	
8.5	1.10	39300	41318	8.28	42700	35049	
8.0	1.18	40458	41115	7.84	44412	35893	
7.0	1.44	42131	41558	6.92	46489	38397	
6.0	1.70	42767	41665	5.75	47417	40373	
5.0	1.98	43531	41519	4.75	48478	41901	
4.0	2.20	43576	40900	3.63	48738	42723	
3.0	2.50	43581	39768	2.57	43950	42772	
2.0	3.00	41458	36504	1.52	46755	40196	
1.595	4.0	34754	33780	1.17	39264	37496	
0.75	3.4	33607	35628	.60	38116	40212	
0.0	3.4	36600	36600	0	41590	41591	

Average Tangential Stress = 38132 psi

FIGURE 6.4.6

STEAM TURBINE DISK MATERIALS

(In order of ascending cost)

No.	Material	Condition	Cost Base & Grade \$/p	Remarks
1	TriTen	Plate cross- rolled	7.20	Low alloy, hi strength steel plate suitable for flat-sided disks. Up to 3/4" thick. Ten. str. = 70,000 psi, Yield str. = 50,000 psi. 3/4" to 1-1/2" thick: ten. str. = 67,000 psi, Yield str. = 46,000 psi. Max. metal temp. = 600°F.
2	ConPac	Plate cross- rolled	10.80	Lo alloy, hi strength steel plate suitable for flat-sided disks. Up to 1-1/2" thick: Yield str. = 70,000 psi. Max. metal temp. = 600°F.
3	T-1 Type A	Plate cross- rolled	13.25	Lo alloy, hi strength steel plate suitable for flat-sided disks. Up to 1-1/4" thick: Ten. str. = 115-135,000 psi. Yield str. = 100,000 psi. Max. metal temp. = 750°F (600°F max. recommended)
4	T-1 Type B	Plate cross- rolled	14.15	Lo alloy, hi strength steel plate suitable for flat-sided disks, but some contouring may be possible. 1-1/2" to 2" thick: Ten. str. = 115-135,000 psi, Yield str. = 100,000 psi. Max. metal temp. = 750°F.
5	T-1	Plate cross- rolled	15.60	Lo alloy, hi strength steel plate suitable for flat-sided or contoured disks. Up to 3-1/2" thick: Ten. str. = 105-135,000 psi, Yield str. = 90,000 psi. Max. metal temp. = 800°F.
6	AISI 4147	Contour forgings	-	Lo alloy, contoured forgings by Bethlehem. Economical only for quantity orders (15). Ten. str. = 120,000 psi, Yield str. = 105,000 psi. Max. metal temp. = 900°F.

FIGURE 6.4.7
Page 1

STEAM TURBINE DISK MATERIALS (Cont'd)

(In order of ascending cost)

No.	Material	Condition	Cost Base & Grade ¢/p	Remarks
7	AISI 4140	Forgings	-	Lo alloy Cr-Mo steel, quenched and tempered. Sections up to 6" thick. Ten. str. = 100,000 psi, Yield str. = 80,000 psi. Max. metal temp = 900°F.
8	AISI 4340	Forgings	-	Lo alloy Cr-Ni-Mo steel, quenched and tempered. Up to 6" thick: Yield str. = 110,000 psi. Up to 14" thick: Yield str. = 80,000 psi. Max. metal temp. = 900-1000°F.
9	Cr-Ni-Mo	Forgings	-	Hi strength, low alloy metal, quenched and tempered. Up to 14" thick: Ten. str. = 150,000 psi, Yield str. = 125,000 psi. Max. metal temp. = 900-1000°F.

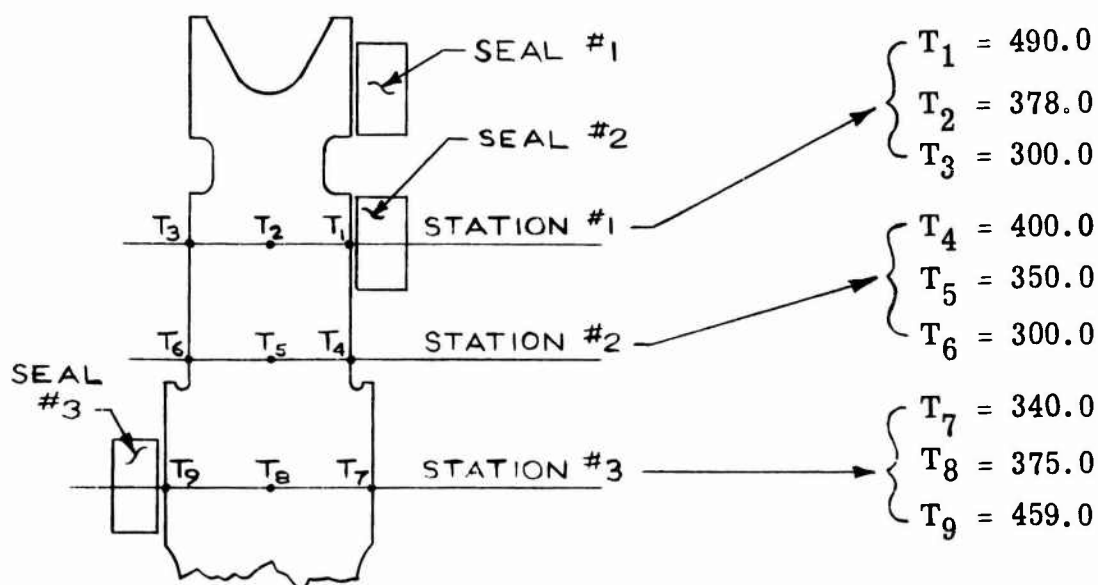
FIGURE 6.4.7
Page 2

to use the higher strength material in condition two, the normal operating condition.

It is possible to pre-heat the disk and reduce the stress in the shroud, thereby using a less expensive, more available material, such as 4340. The decision of whether to use the less expensive, more readily available material will be made in the final phase of this design after a more thorough thermal analysis is accomplished in the disk and shroud areas.

Thermal stress in the disk was investigated in areas where axial thermogradients exist.

The areas of concern are as shown and the temperatures assumed for the analysis are listed for condition one, normal condition.



The gradients are controlled by water cooling the sides of the disk below seal 3 and therefore the major portion of the disk is not subjected to axial thermogradients.

The areas above seal 3 will have axial thermogradients. The differential temperature across the disk is linear and will not exceed 100°F with the exception of the local areas under the seals. The equation for the thermal stress is:

$$\sigma_{z_T} = \frac{\alpha \Delta t E}{2(1-\mu)}$$

Using this equation and assuming a linear gradient, the stress was calculated to be 13,690 psi. The deflection, or dishing, of the disk and shroud from this thermogradient is approximately .0008 inch and the resulting slope is .00006 radians.

Under the seal face there is a local heating of the seal surface. The thermal map provides the thermal gradient and is expressed as a hyperbolic curve for this analysis. Assuming a hyperbolic distribution, the maximum thermal stress is 20,535 psi, based on the following equation.

$$\sigma_{zT} = \frac{3\alpha \Delta t E}{4(1-\mu)}$$

This stress is a local stress and will not appreciably increase the dishing of the disk.

The stress and deflections from the bending moments applied to the disk from the thrust load were calculated and found to be insignificant. The bending moments applied to the shroud were considered significant and have been calculated in Section 6.4.1.

The three seal mating surfaces are machined integral with the disk sides, requiring a lapped surface whose normality is held close to the growth journal diameters of the shaft. Excess material is available on the seal faces for refinishing if the seal faces become inadvertently scored or scratched. Also included in the profile of the disk are balance ribs where the balancing material is removed without penetrating the disk profile, jeopardizing the structural integrity of the disk.

6.4.3 Turbine Casing

The L V F turbine casing was designed as an ASME coded pressure vessel, where applicable. This procedure conveniently defined the cylindrical and end wall thicknesses, reinforcement, corrosion allowance, and fillet radii. The items thusly defined provide the basic configuration. The material was also selected at this point as ductile iron, grade 60/45. Ductile iron is universally used in castings of pumps and turbines and is readily available at many casting facilities. This material has high ductility and can be welded if necessary. The material properties are listed in the Figure 6.4.8.

The calculated stress and deflection values in cylinder, flat head, and ribs are listed in Figure 6.4.9.

Distortion due to thermal expansion was alleviated by designing the casing axially symmetric. In addition, the inlet and exit scrolls are attached by long thin wall tubes in order to reduce the bending moments applied to the casing from thermal growth of scrolls. The turbine is mounted by a standard 13.0 inch bolt circle flange and is further supported by a wobble foot that supports the weight of the turbine but does not restrain the free axial thermal growth.

The material of the seal cartridge was selected such that the resulting expansion of the seal cartridge and the casing that surrounds it would have equal thermal expansion. This was accomplished by determining the temperature distribution of the casing and the seal cartridge area and then selecting a material for the cartridge that would result in compatible thermal growth.

Figure 6.2.3 shows the thermal map of the seals, shroud, and inlet and exit area. The casing temperatures from the inlet side to the exhaust side are different and can cause distortion. It is intended to add cooling on the inlet side of the casing to reduce the thermal difference to a tolerable level. This further design and thermal analysis will be accomplished during the final design phase of this design effort.

The cooling baffles that surround the disk are secured at the bottom only, allowing free expansion of the baffles, thereby preventing bending moments from being applied to the support housing of the seal cartridge.

The ribs included in both the inlet casing and the exit cover are provided for three primary reasons: (1) as described in the vibration section, the ribs add support stiffness essential to the reliable prediction of the critical speed; (2) they reduce the deflection and resulting stress in the casing junctures; and (3) they prevent distortion of the casing from local thermogradients, such as the nozzle inlet.

PROPERTIES OF DUCTILE IRON 60-45

<u>Compression strength</u>	
Ratio of compression yield strength to tensile yield strength (approx.)	1.2
<u>Endurance Ratio (E. L./T.S.)</u>	
Unnotched	.45 to .55
Notched	.25 to .35
<u>Modulus of elasticity in tension, million psi</u>	23-26
<u>Modulus of elasticity in torsion, million psi</u>	9.2-9.5
<u>Shear strength</u>	
Ratio of shear strength (in torsion) to tensile strength (approx.)	0.90
<u>Proportional limit, in. psi</u>	31,000
<u>Poisson's Ratio</u>	0.28-0.29
<u>Thermal Expansion</u>	
Mean value in./in./°F x 10 ⁻⁶ over the temp. range	
68-212°F	6.2
68-392°F	6.8
68-572°F	7.1
<u>Damping Capacity</u>	
Intermediate between cast iron and steel	Approx. 1.8 to 2.0 times that of steel
<u>Density</u>	
lbs/cu. in.	0.245-0.26
lbs/cu. ft.	423-449

FIGURE 6.4.8

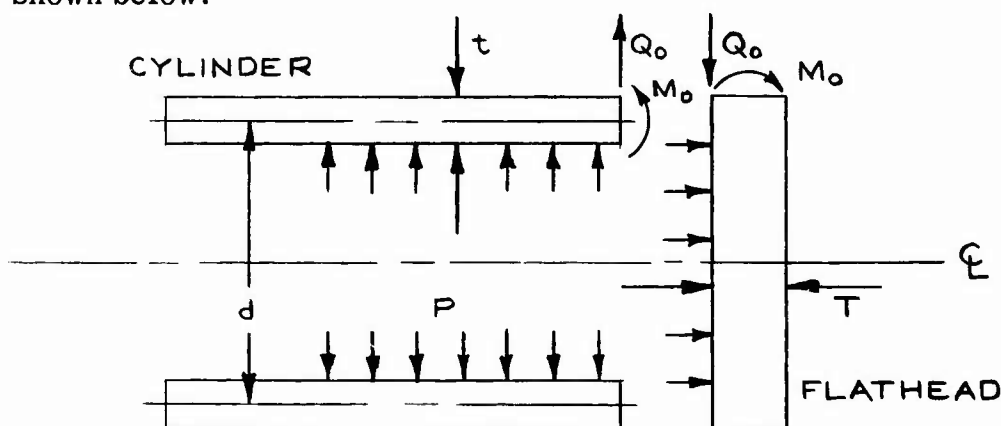
TABULATION OF STRESS AND DEFLECTION IN CASING
(all stress in psi)

Location	At 125 psi Inlet Pressure			At 12.4 psi External Pressure		
	Shear	Hoop	Longitudinal	Shear	Hoop	Longitudinal
Stress in cylinder of inlet juncture (see Section	2563.	14050.	41125.	256.	1405.	4112.
Deflection	.013 at OD of bearing cap			.0013 inch at OD of bearing cap		
Exit Cover: Bending stress in vanes	16350.			1635.		
Deflection of exit cover	.017 at OD of bearing cap			.0017 inch at OD of bearing cap		

FIGURE 6.4.9

6.4.3.1 Inlet Casing

The inlet side of the casing (Figure 6.4.10) for this analysis is treated as a cylindrical vessel with a flat head. With this model the approach is to calculate the discontinuity stresses at the juncture from the edge forces and bending moments. The model assumed for the analysis is shown below.



From Reference 6.4.6 the equations for the deflections and rotation are expressed in the forms:

$$\frac{M_o a_5}{P d^2} + \frac{Q_o a_6}{P d} + a_4 = \frac{M_o a_1}{P d^2} + \frac{Q_o a_2}{P d} + a_3$$

$$\frac{M_o b_5}{P d^2} + \frac{Q_o b_6}{P d} = \frac{M_o b_1}{P d^2} + \frac{Q_o b_2}{P d} + b_3$$

(FLATHEAD) (CYLINDER)

where quantities $a_1, a_2, a_3, b_1, b_2,$ and b_3 are influence numbers for the flathead and a_5, a_6, a_4, b_5 and b_6 are influence numbers for the cylinder. Solving the two equations simultaneously provides the bending moments M_o and shear force Q_o used to calculate the final stress at the junction. The stress ratios in the cylinder are:

$$\text{Shear} \quad I_{SJ} = 3 \left| \frac{Q_o}{P d} \right|$$

$$\text{Axial} \quad I_{AJ} = \frac{1}{2} + 12 \frac{d}{t} \left| \frac{M_o}{P d^2} \right|$$

Circumferential (hoop)

$$I_{CJ} = \left| 1 + 2 B d \left(\frac{Q_o}{P d} \right) (1 + \nu) \right| + 12 \mu \frac{b}{t} \left| \frac{M_o}{P d^2} \right|$$

STRESS ANALYSIS OF LVFT CASING

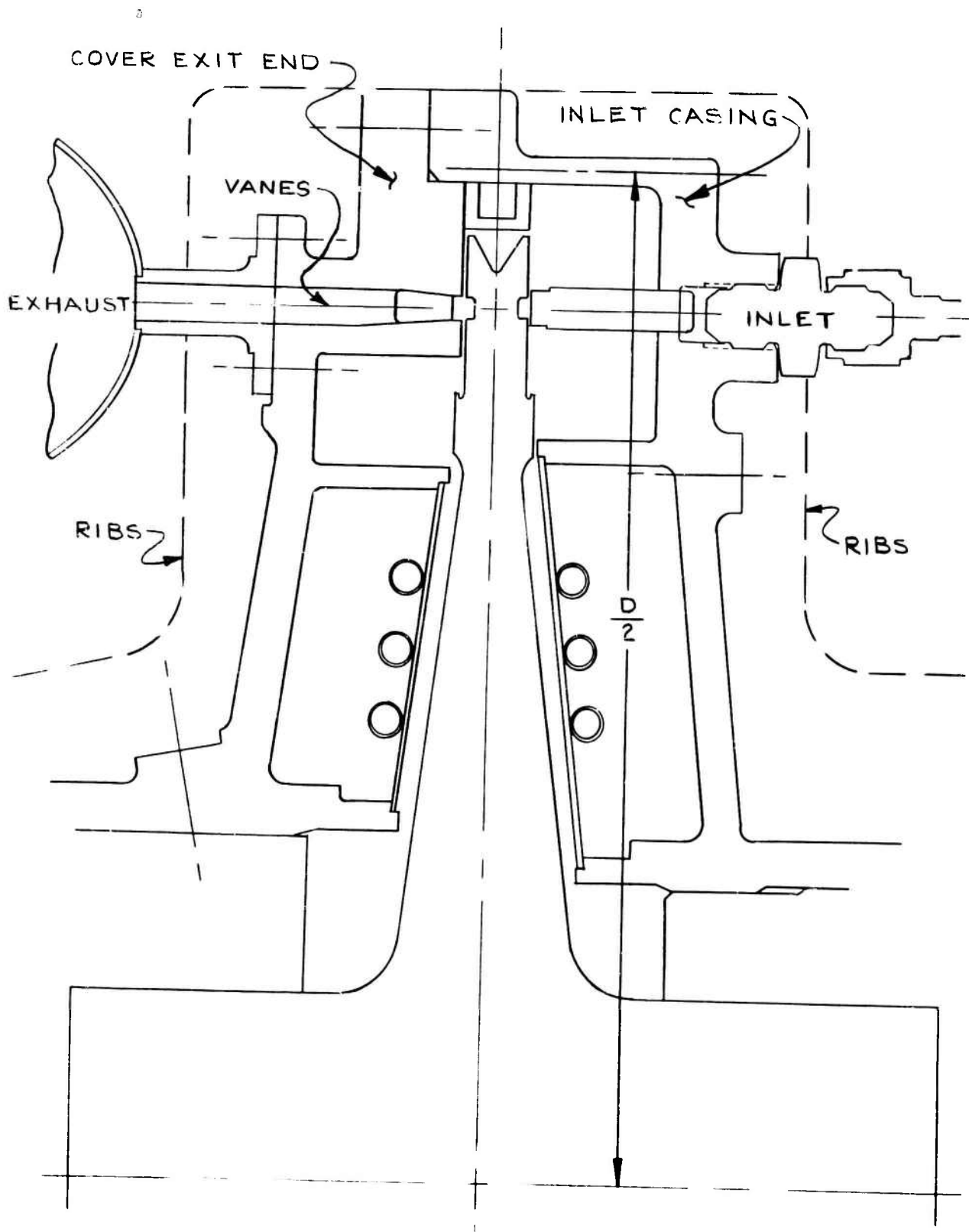


FIGURE 6.4.10

Stress ratios in the head:

$$\text{Shear} \quad I_{SJ} = \frac{3t}{4T}$$

$$\text{Axial} \quad I_{AJ} = \frac{2t}{T} \left| \frac{Q_o}{P_d} \right| + 12 \frac{d}{t} \left(\frac{t}{T} \right)^2 \left| \frac{M_o}{P_d^2} - \frac{Q_o}{P_d} \left(\frac{T}{2d} \right) \right|$$

$$\text{Hoop} \quad I_{CJ} = \frac{2t}{T} \left| \frac{Q_o}{P_d} \right| + 12 \frac{d}{t} \left(\frac{t}{T} \right)^2 \left| \frac{M_o}{P_d^2} - \frac{Q_o}{P_d} \left(\frac{T}{2d} \right) - \left(\frac{1-M}{32} \right) \right|$$

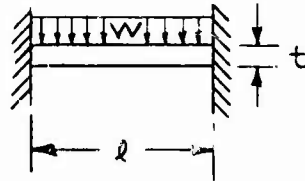
The ribs included in the inlet casing are designed to share 50 per cent of the pressure load. For this analysis they are assumed to be acting like fixed-fixed beams. From Reference 6.4.3 the equation for the deflection of one rib is:

$$Y_R = \frac{1}{24} \frac{W X^2}{E I l} (2 l x - l^2 - x^2)$$

W = total load, lb

t = thickness of rib

l = length of rib



The calculated stress and deflection in the ribs and head juncture are provided in Figure 6.4.9.

6.4.3.2 Cover Exit End

The exit end cover is required to contain the pressure, support the journal and thrust bearings, and provide access to the disk and seal assemblies. The cover has vanes for directing the flow and providing openings for the free flow of exhausted steam. The vanes supplement the ribs in providing attachment to the lower plate (see Figure 6.4.10).

Analysis of the stress and deflections required that a composite analysis be formulated which would provide the exit end deflections, yet provide the stress in the vanes. Equations 1 and 2 provide the information that is tabulated in Figure 6.4.9.

6.5 MECHANICAL DESIGN

The mechanical design requires strict attention to disk and seal face alignment; that is, the disk mating surface must run as parallel as possible to the seal face. This critical relationship is assured through five primary considerations.

1. Designing a sectored fluid film, positive stiffness face seal with a secondary seal that is nearly frictionless and capable of compensating for force and moment unbalance.
2. Designing the journal bearings to provide a minimum angular misalignment and adequate stiffness.
3. Designing the thrust bearing to provide the proper axial stability and to retain alignment of the disk and seal face.
4. Balancing the thrust load on the disk by establishing the radial position of the third seal.
5. Designing the casing to minimize distortion, deflection, and to include provision to obtain the necessary clearances and alignment.

This section presents the preliminary design based on the above considerations and includes FIRL's mechanical design of the controlled-leakage seals, journal bearings, and thrust bearings.

6.5.1 Design and Performance

Sheet 5 of Section 10 is a layout of the sectored seal with the hydrostatic secondary. The primary dimensions of the sector have been sized by accurately force and moment balancing the sector for normal operating conditions. Locations of the center of pressure of both the interface and sectored fluid films were obtained by computerized analysis which will be subsequently described.

Each sector has an angular extent of 15° and a series of 11 orifices of .012 inch in diameter are machined into the face of each sector. The fluid being sealed feeds the orifices. The orifice holes emanate into a .050 inch diameter recess, .001 in deep at the face. The recess insures that the major flow restriction occurs in the orifice and not in the film. True orifice compensation results in improved stiffness over the inherent type.

During normal operation the seals are held in place by the high pressure of the sealed fluid, which pre-loads the sectors against the secondary seal ring that contains the feed orifices. For seal No. 1, a garter spring holds the sectors in place when the system is depressurized.

An axial spring insures closure in the absence of hydraulic pressure.

The secondary hydrostatic seals are integral with the seal ring. A series of inlet holes are fed from a common steam inlet manifold. The holes do not terminate at a recess, because the higher supply pressures of the secondary seal could precipitate pneumatic hammer. The restriction is formed by the curtain area of the cylinder of steam in the clearance space. The clearance sensitivity of the restrictor produces inherent compensation which materially reduces chances of pneumatic hammer at the expense of film stiffness. The small film thickness associated with this seal however, insures adequate stiffness even though the compensation is inherent.

It is essential that the major seal components be of similar materials so that thermal expansion problems will not be encountered. The materials selected are the same as the turbine rotor, namely 4340 steel. An aluminum oxide coating on both the seal and rotor interfaces assures excellent protection from rubbing at start-up and shut-down and for momentary rubs at high-speed.

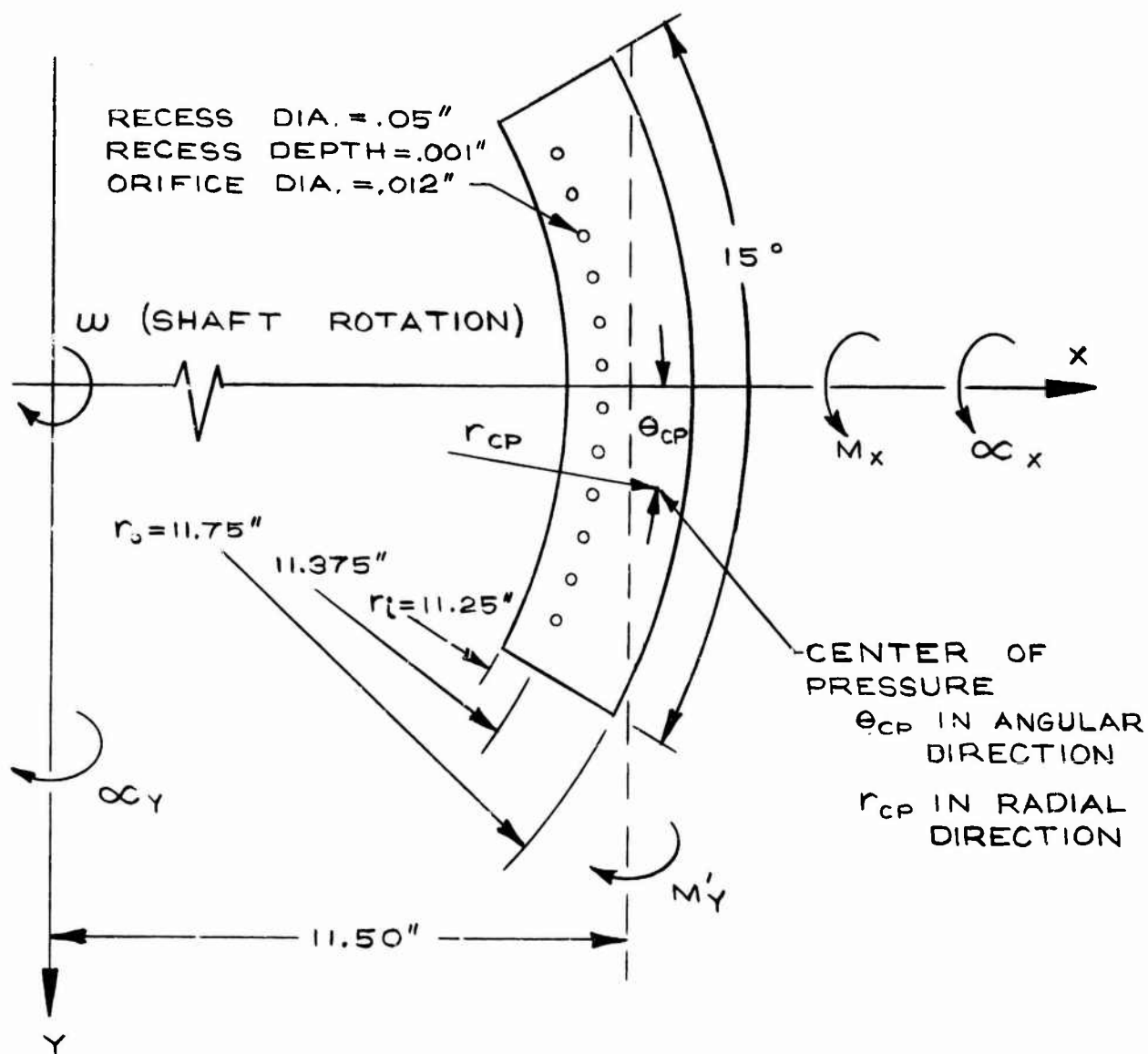
6.5 1.1 Steady-State Performance of the Hydrostatic Primary Seal

Extensive steady-state performance has been developed for primary seal 1. Figure 6.5.1 show appropriate nomenclature and dimensions. The performance curves shown on Figure 6.5.2 show load per sector, total friction horsepower loss and total leakage, as a function of the aligned film thickness. The leakage includes the estimated loss between sectors. At the design condition performance is as follows:

Film Thickness, $h = 1$ mil
 Total Leakage, $Q_T = 0.045$ lbs/sec
 Load Per Sector, $W_p = 99.5$ lbs.
 Total Friction Horsepower Loss, $FHP_T = 2.75$ HF
 Sector Film Stiffness, $K_a = 17,000$ lbs/in.
 Shaft-Speed, $N = 12,000$ rpm
 Sealed Fluid Pressure, $P_s = 95$ psia
 Ambient Pressure, $P_a = 2$ psia

Figure 6.5.3 provides additional performance as a function of the aligned film thickness, h . M_x is the moment of the fluid film thickness about the x axis, as shown in Figure 6.5.1. At the design film thickness of 1 mil, there is slight residual moment due to rotation of the turbine disk. The value of the moment is 0.28 in-lbs. This moment will produce a slight tilt of the sector. The M_y , about the y axis is much larger, but this moment is counterbalanced by hydraulic forces acting on other sections of the seal. The location of the center of pressure is identified by θ_{cp} and r_{cp} . Figure 6.5.4 indicates performance as a function of the angular tilt about the y axis. The maximum tilt at the design film thickness is 0.851×10^{-4} rad., so that the curves represent operation over a range of about half the maximum tilt allowable. Within the range indicated on Figure 6.5.4 performance is not materially affected. Figure 6.5.5 show

NOMENCLATURE AND DIMENSIONS OF HYDROSTATIC PRIMARY SEAL



α_x AND α_y ARE TURBINE DISK TILTS ABOUT ORTHOGONAL AXES THROUGH CENTER OF ROTATION

M_x AND M'_y ARE MOMENTS ACTING ON SEAL

FIGURE 6.5.1

ORIFICE - FED SECTORED SEAL PERFORMANCE VS. FILM THICKNESS AT DESIGN OPERATION

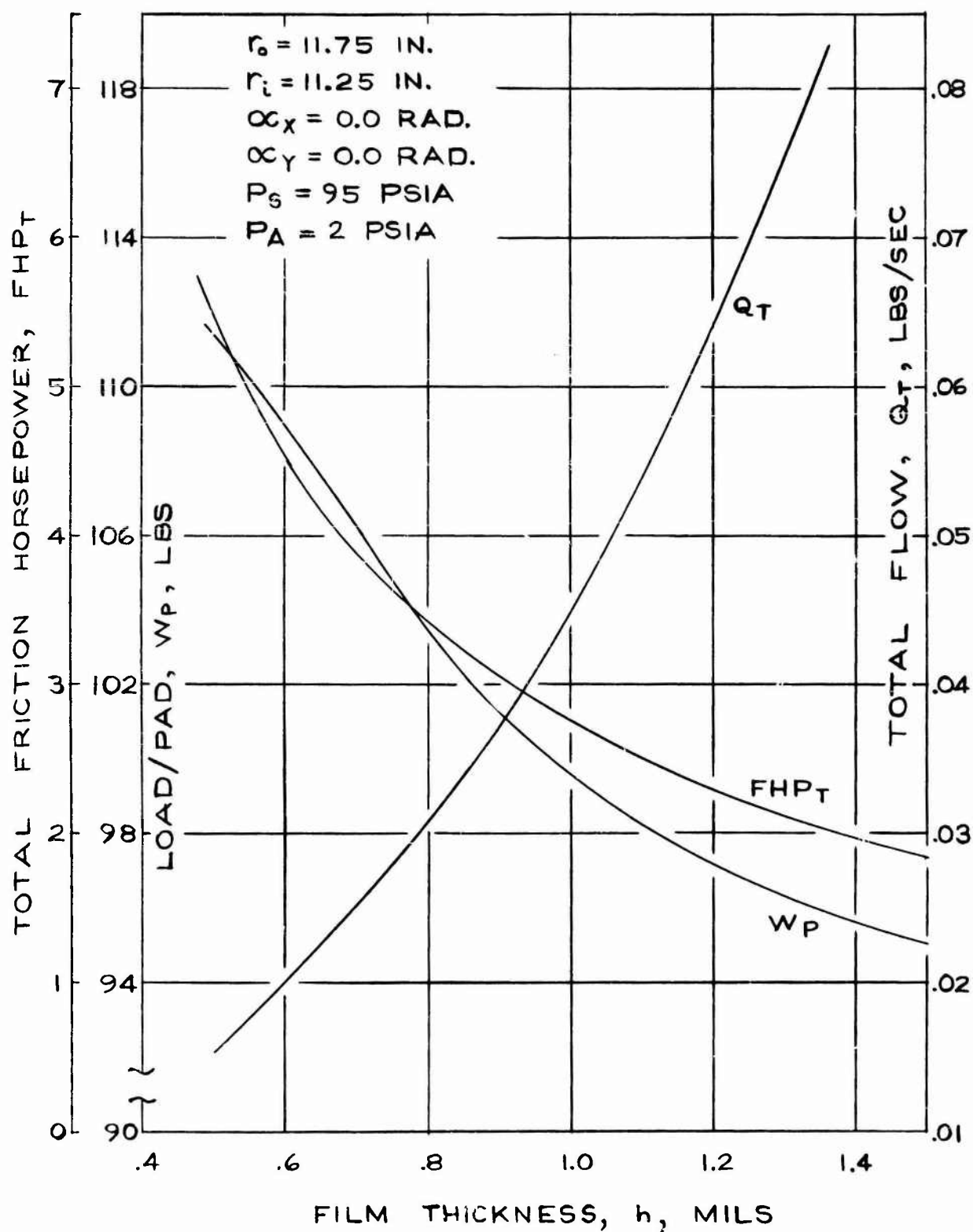


FIGURE 6.5.2

ORIFICE - FED SECTORED SEAL MOMENTS, CP VS. FILM THICKNESS AT DESIGN OPERATION

146

$r_o = 11.75$ IN.
 $r_i = 11.25$ IN.
 $\alpha_x = 0.0$ RAD.
 $\alpha_y = 0.0$ RAD.

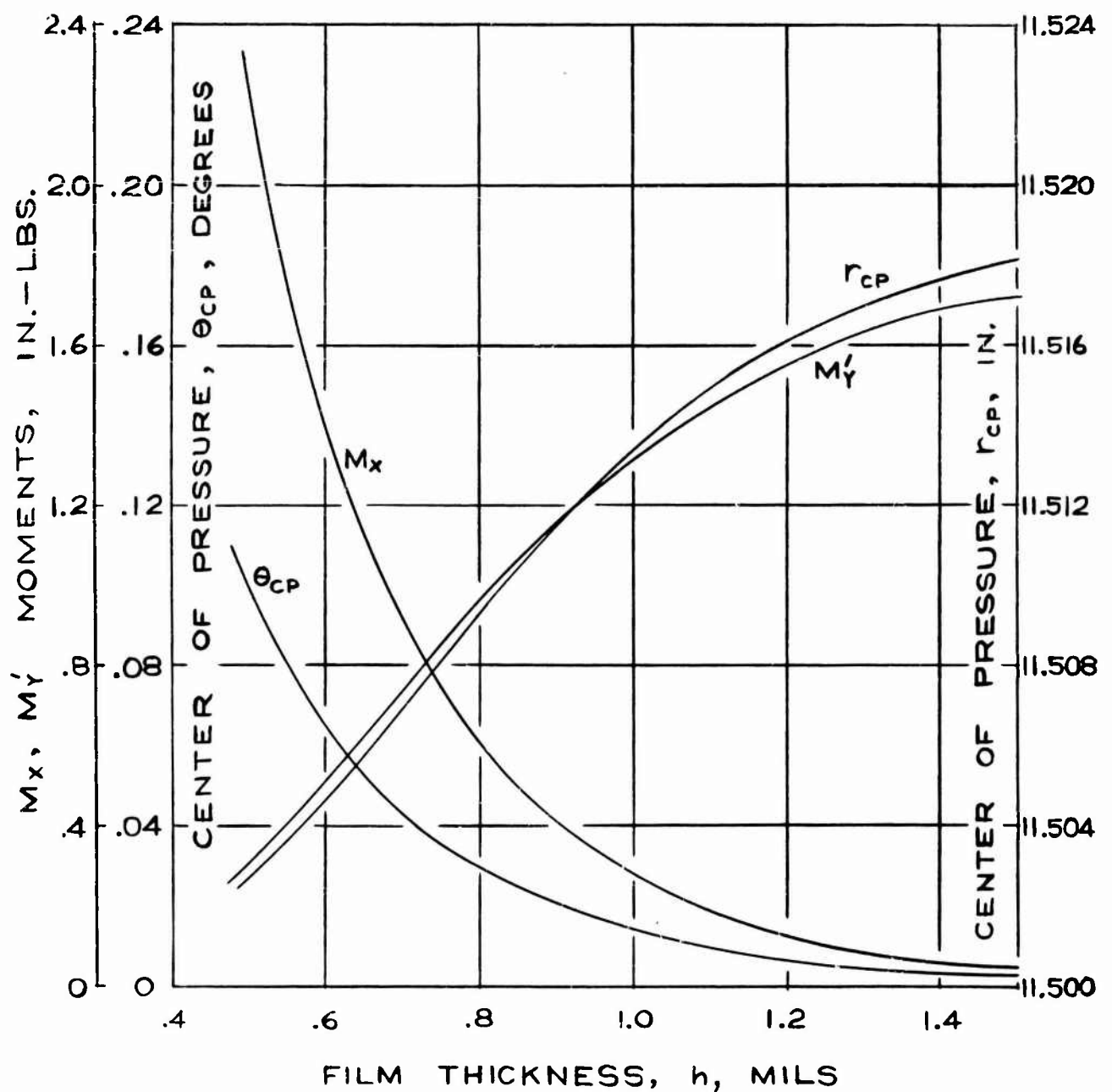
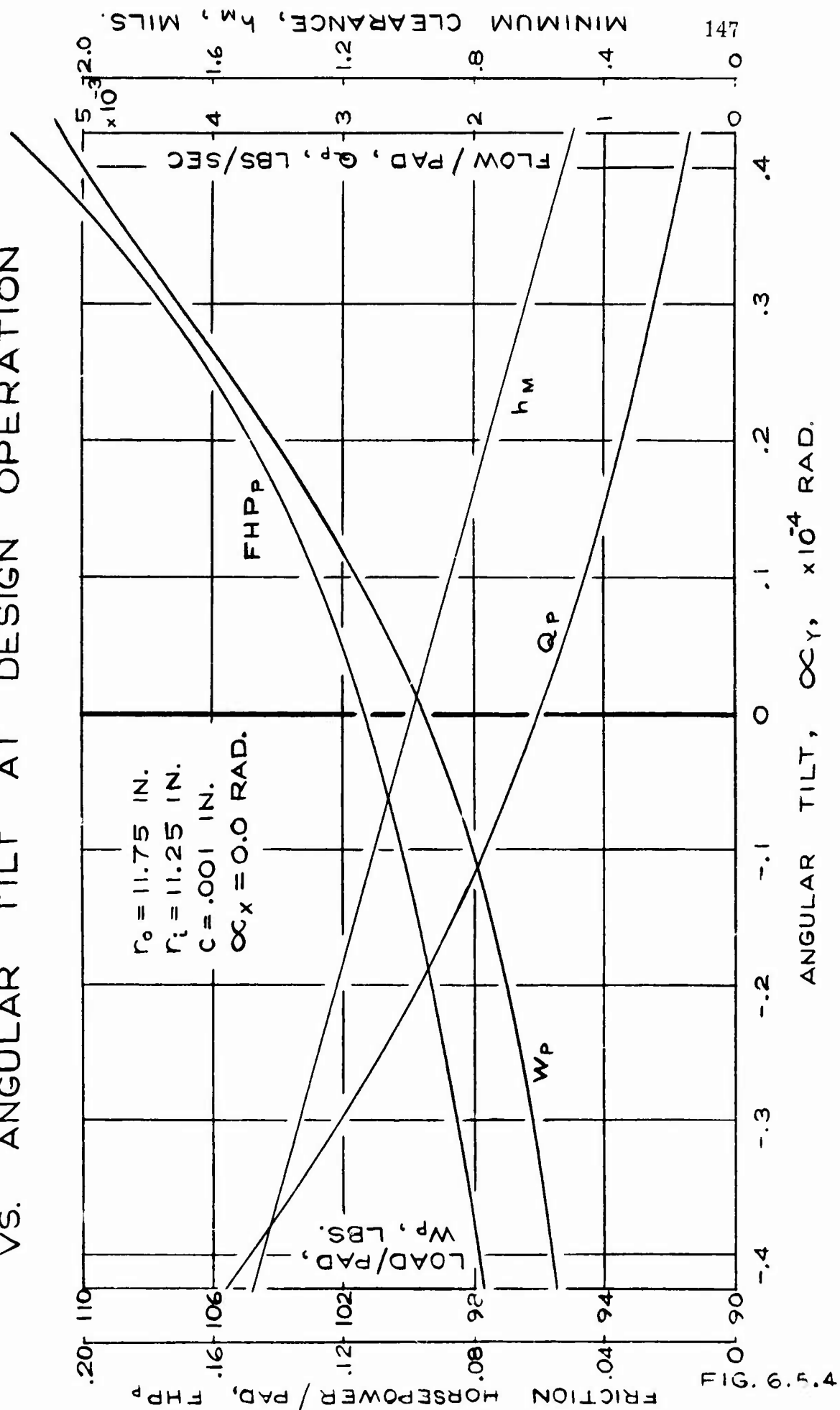
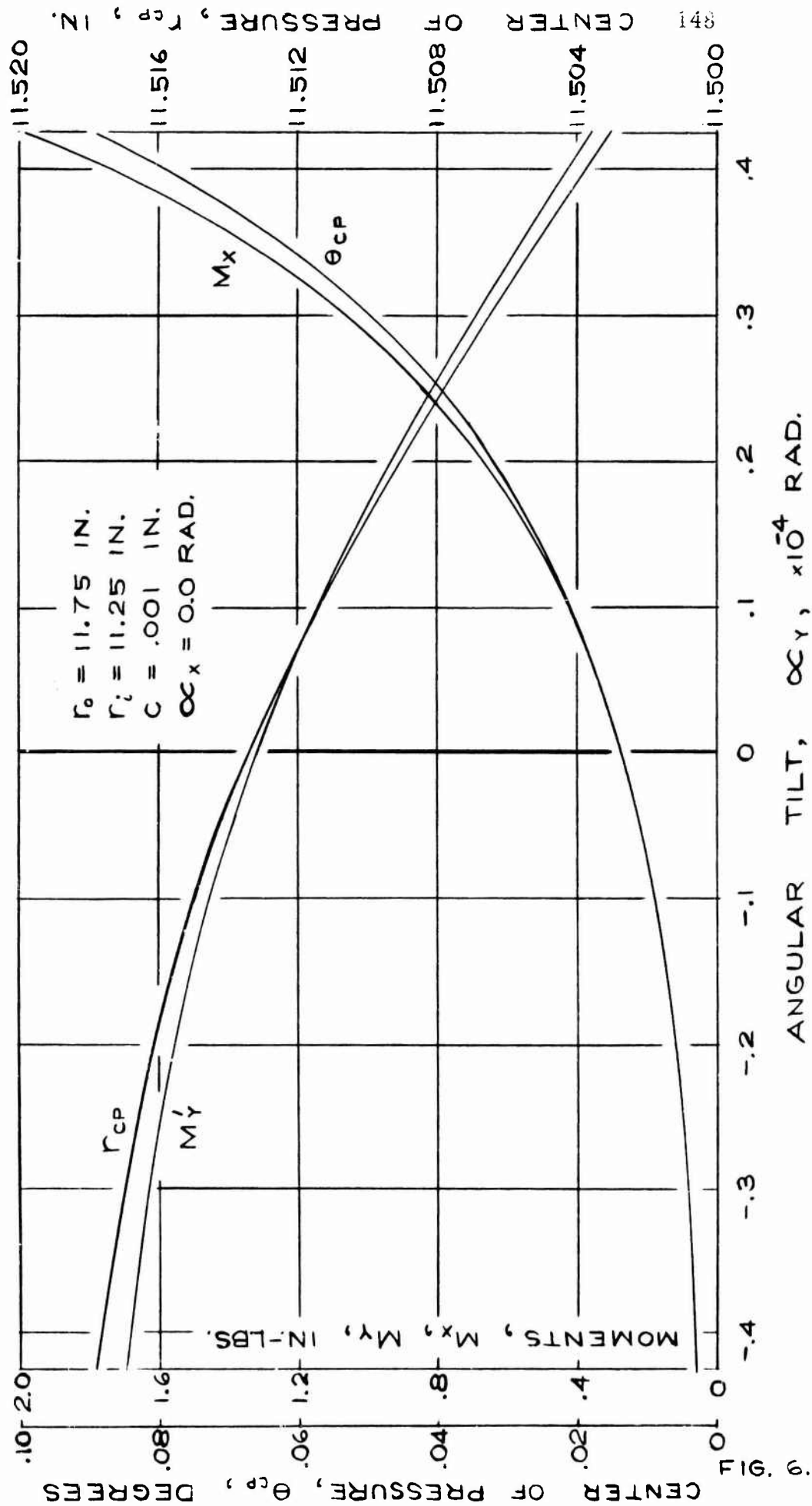


FIGURE 6.5.3

ORIFICE - FED SECTORED SEAL - PERFORMANCE VS. ANGULAR TILT AT DESIGN OPERATION



ORIFICE - FED SECTORED SEAL - MOMENTS, CP VS. ANGULAR TILT AT DESIGN OPERATION



variations in moments and center of pressure as a function of the angular tilt of the rotor α_y . Note that the moment about the x axis is considerably affected by an angular tilt about the y axis. However, thrust capacity also increases (Figure 6.5.4) and this insures axial displacement of the sector. The moment M_y will be counter-balanced by the righting capability of the hydrostatic secondary seal. Figures 6.5.6 and 6.5.7 show performance as a function of the yaw of the shoe α_x . Again, primary performance is not materially affected by yaw except for the tilt moment about the x axis as shown on Figure 6.5.7. This will cause motion of the shoe in the yaw mode. The degree to which angular motions affect sector motions were determined by dynamic studies.

Steady-state performance for a 30 degree Rayleigh-step sector seal was also established. Results are indicated in Section 12.1.

Section 12.2 contains derivations for leakage between sectors.

6.5.1.2 Steady-State Performance of Hydrostatic Secondary Seals

The same computer program used to analyze the primary seal was employed for analyzing the secondary seal. Although the program was designed for handling a thrust sector, input can be manipulated so that the cylindrical secondary seal could be simulated. By using large radii and uniform film thickness, a flat plate is approximated which closely resembles the secondary seal area. For purposes of the analysis, orifice compensation was employed since this is the only type of compensation that the computer program can handle.

The geometry of the secondary seal is shown on Sheet 5 of Section 10.0. Analytically, the first determination was the restrictor size. Figure 6.5.8 shows pertinent performance as a function of the orifice diameter. The primary consideration is determining what orifice size to use to produce reasonable stiffness. From Figure 6.5.8, an orifice diameter of 0.0025 in. was selected. This produced a compromise between minimum and maximum recess pressures so that adequate stiffness would be available, and also the leakage was very small. Note that the selected film thickness of 0.0002 in. is extremely tight, but since the sector is not captured and free to float in one direction, this small film thickness is easily realized. Figure 6.5.9 shows performance as a function of film thickness. Performance is excellent, as the tabulation below indicates.

A major deficiency of the concept analyzed is the small orifice size. In addition to manufacturing difficulties, the possibilities of clogging are prevalent. To offset this problem, it was decided to change the type of compensation from orifice to inherent. This is accomplished by equating the curtain area in the film to the hole area calculated on the basis of full orifice compensation. Thus,

$$A_o = A_i \quad (6.5-1)$$

ORIFICE - FED SECTORED SEAL - PERFORMANCE VS. ANGULAR TILT AT DESIGN OPERATION

$r_o = 11.75$ IN.
 $r_i = 11.25$ IN.
 $C = .001$ IN.
 $\alpha_Y = 0.0$ RAD.

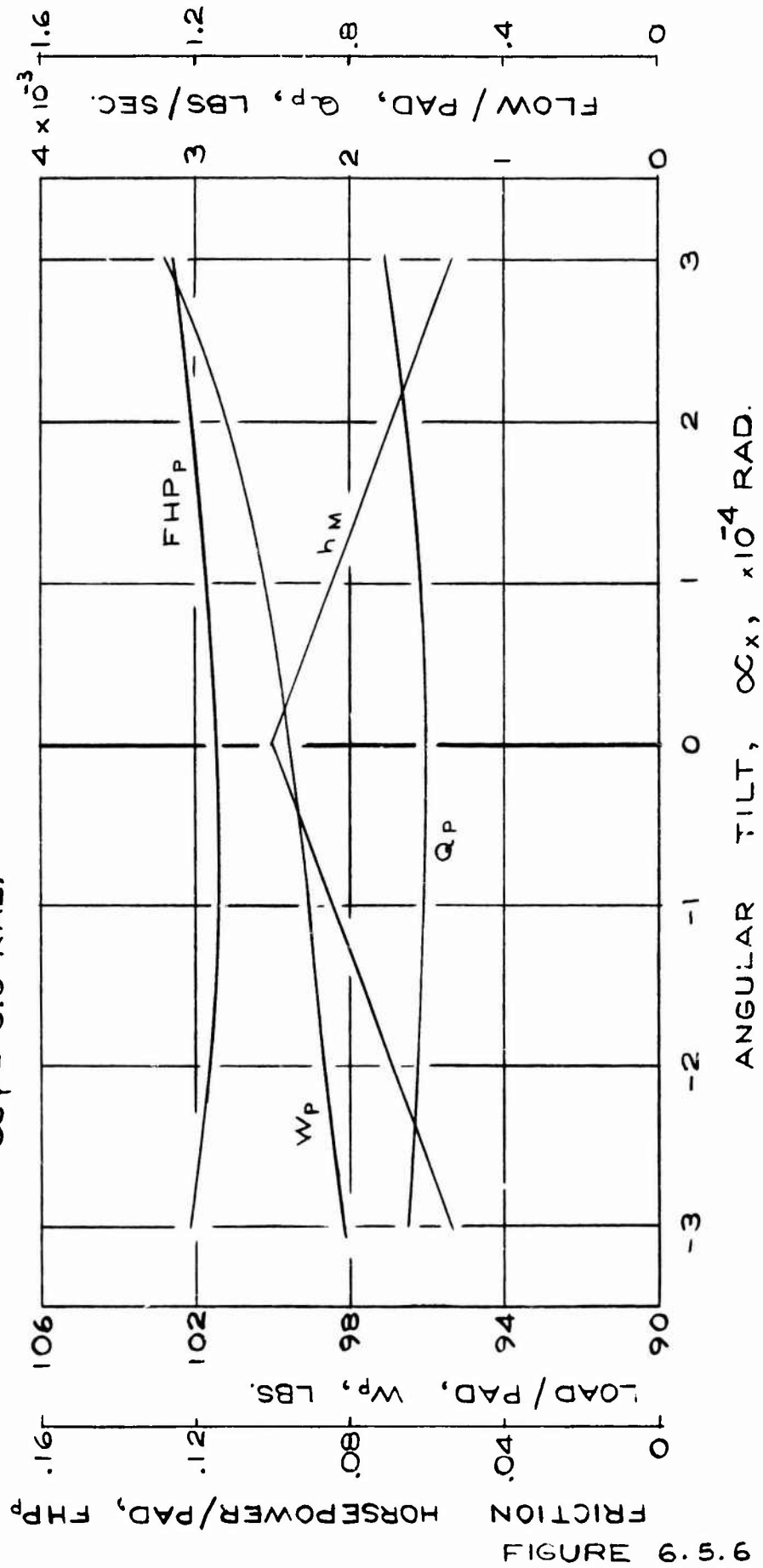


FIGURE 6.5.6

ORIFICE - FED SECTORED SEAL
MOMENTS, CP VS ANGULAR TILT
AT DESIGN OPERATION

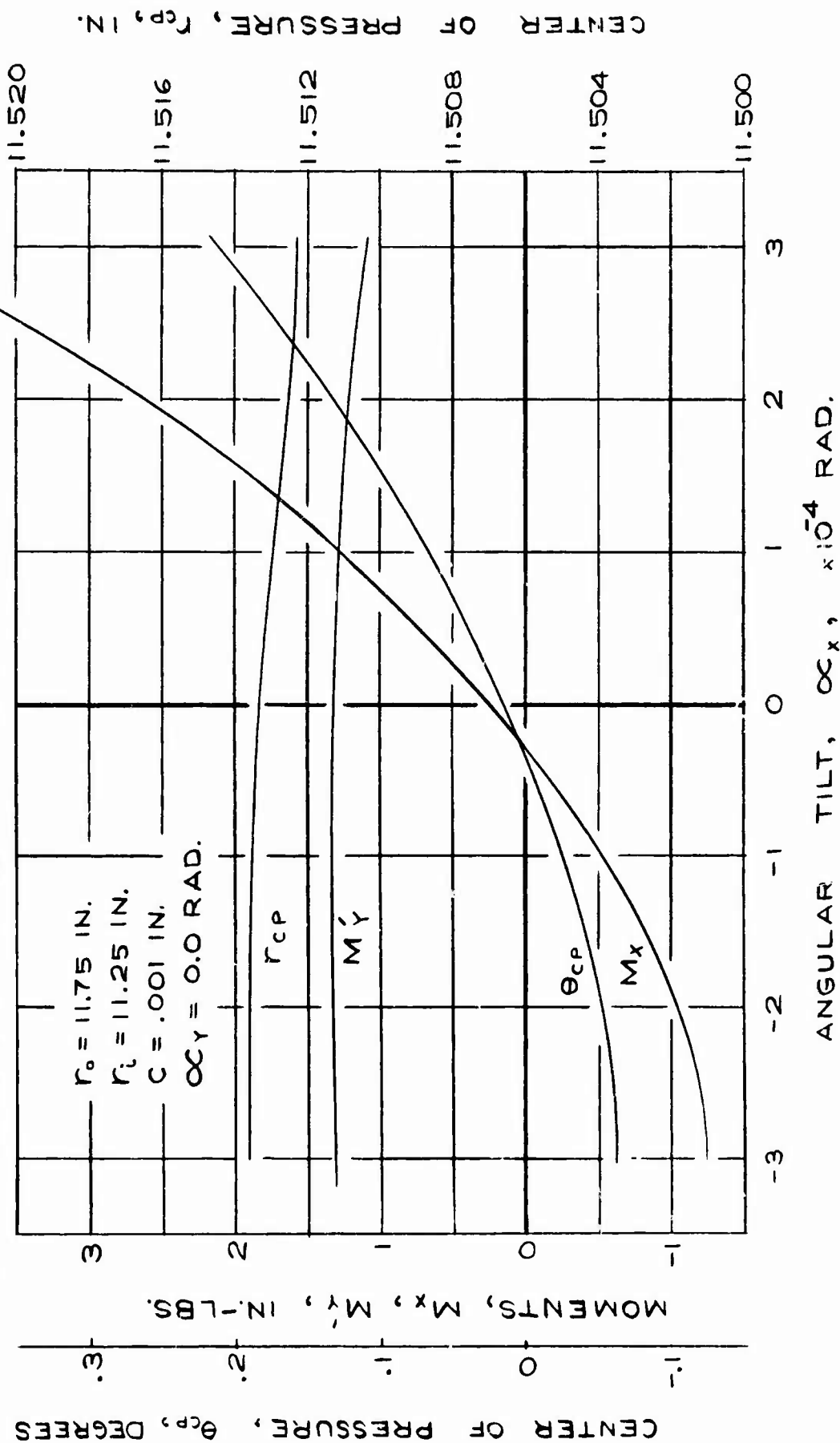


FIGURE 6.5.7

SIZING ORIFICE FOR STEAM SECONDARY SEAL¹⁵²

$r_o = 11.75$ IN.

$\theta_p = 15^\circ$

$P_s = 250$ PSI

$h = 0.0002$ IN.

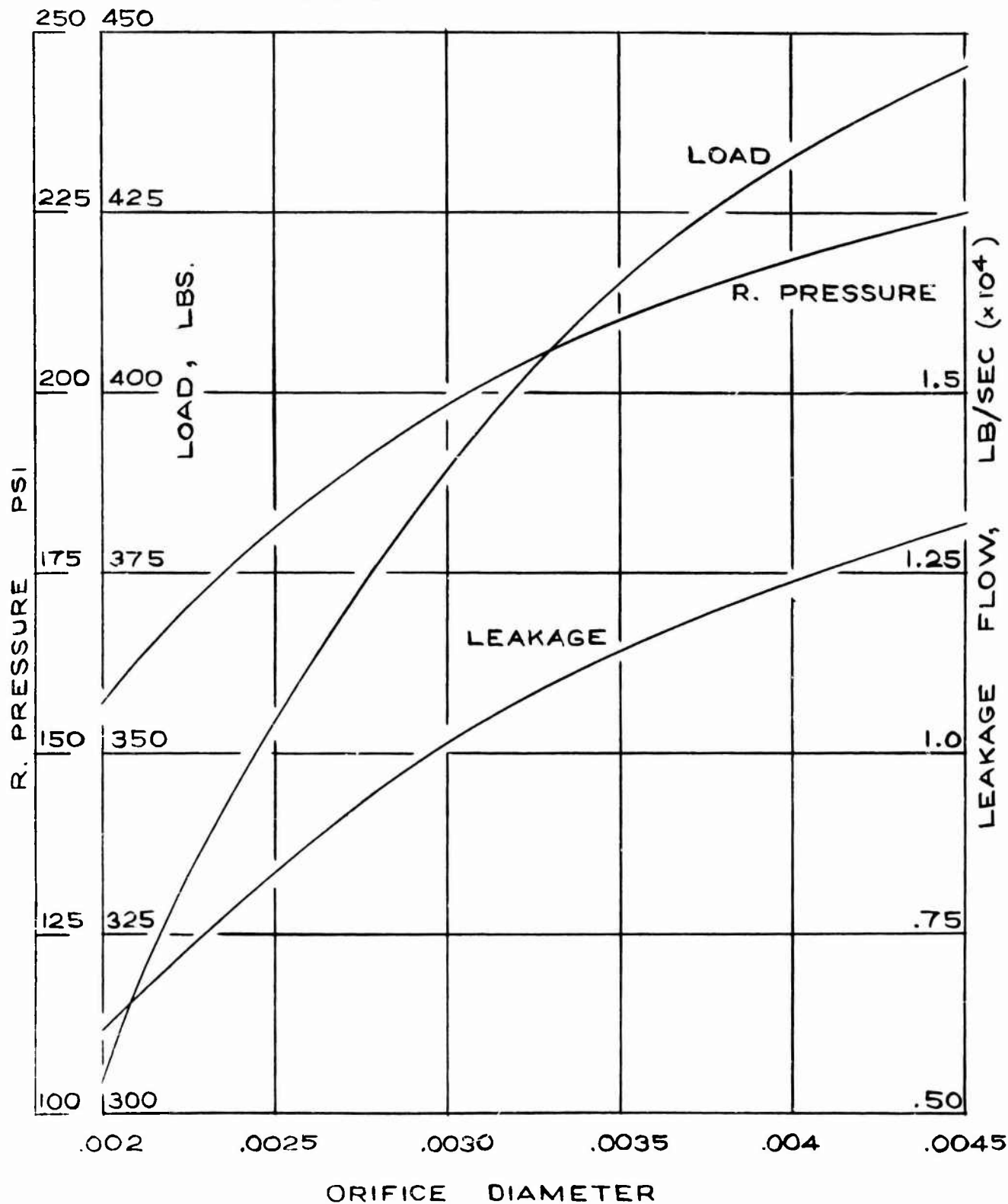


FIGURE 6.5.8

SECONDARY SEAL PERFORMANCE AS
A FUNCTION OF AXIAL CLEARANCE

$r_o = 11.75 \text{ IN.}$
 $\theta_p = 15^\circ$
 $d_o = .0025 \text{ IN.}$

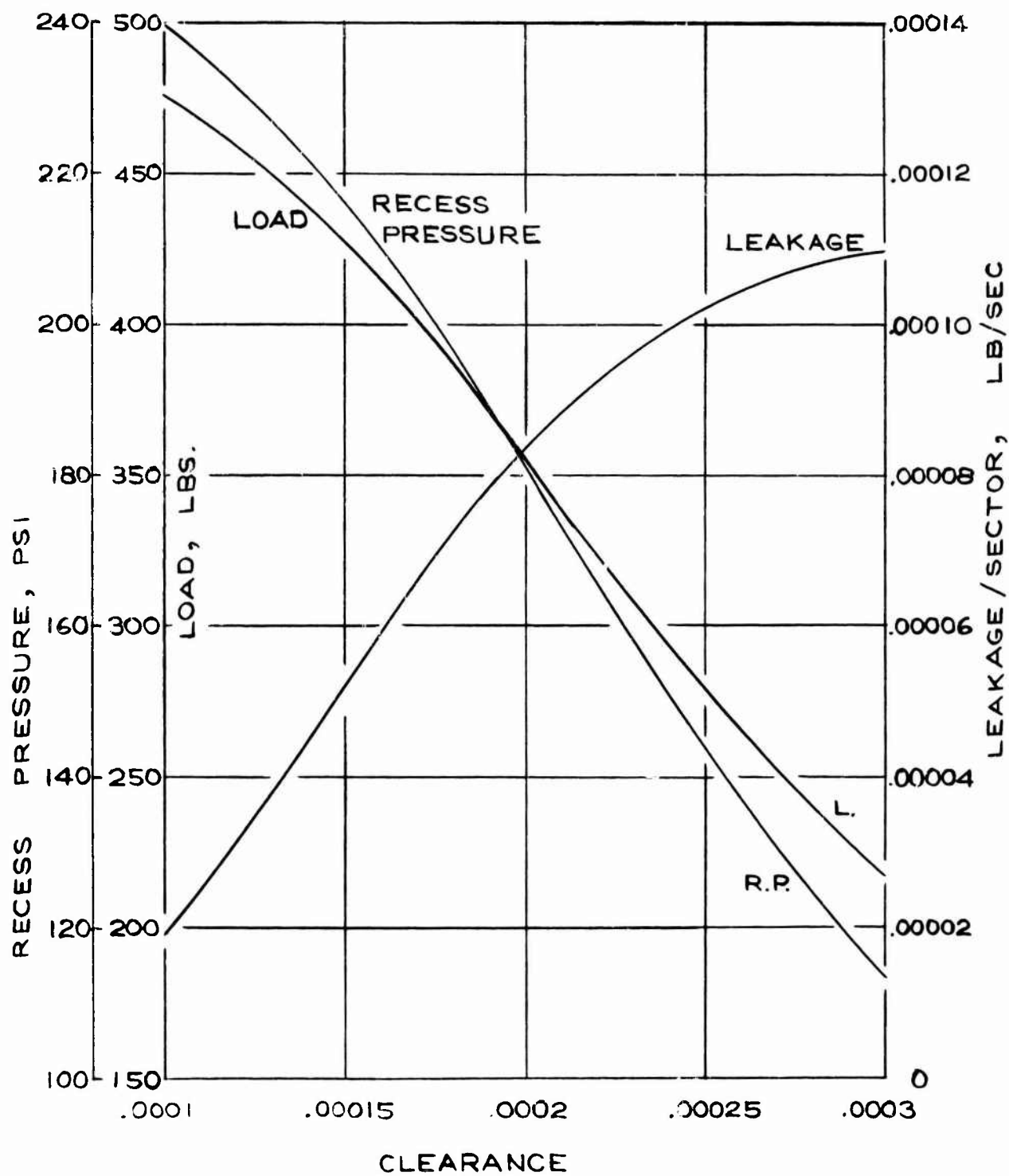


FIGURE 6.5.9

$$\frac{\pi d_o^2}{4} = \pi dh \quad (6.5-2)$$

where d_o = orifice diameter for full orifice compensation = .0025 in
 d = orifice diameter for inherent compensation
 A_o = restrictor area for orifice compensation
 A_i = restrictor area for inherent compensation
 h = film thickness = 0.0002 in

Solving for d in equation (6.5-2) yields

$$d = 0.00781 \text{ in.}$$

The conversion to inherent compensation is accomplished at a sacrifice in stiffness, but since there is a considerable excess of stiffness with the orifice seal, there is no significant penalty. Based on prior experience, the stiffness of the inherently compensated seal is about 2/3 of that of the orifice compensated type. Predicted performance for a 15 degree sector at design conditions is as follows:

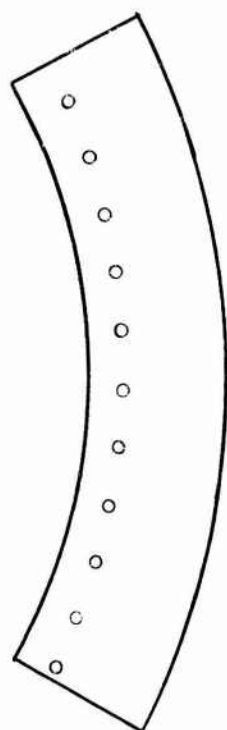
Film thickness, $h = 0.0002$ in.
 Supply pressure, $P_s = 250$ psia
 Orifice size, $d = 0.00781$ in.
 Sector load, $W = 386$ lbs.
 Leakage/Sector, $Q = 0.000084$ lbs/sec
 Recess pressure, $P_r = 184$ psi
 Sector stiffness, $K = 103,500$ lbs/in.

6.5.1.3 Dynamic Performance

The true test of the seal design is to establish whether its behavior is acceptable in the dynamic environment to which it is subjected. A 2 ft. rotor spinning at 12,000 rpm can certainly introduce difficult vibratory forcing functions. Using an accurate and proven computerized analysis, called the time-transient method, which is described in the analytical section of this report, the tracking capability of a single sector, in response to various nutations of the rotating runner was tested. The sector was considered to be supported by frictionless secondary seals. Operating speed was 12,000 rpm and steam conditions were at normal operations. Figure 6.5.10 shows the sectors analyzed and the principal axes of rotation about which the sectors could rotate. A maximum of two degrees of freedom were considered pertinent. These were axial motions of the sector and yaw rotations about the y axis (Figure 6.5.10).

A total of 10 computer cases were run, and it was as a result of the dynamic runs that some prime candidate configurations were eliminated.

CASE 1



$$\theta_p = 15^\circ$$

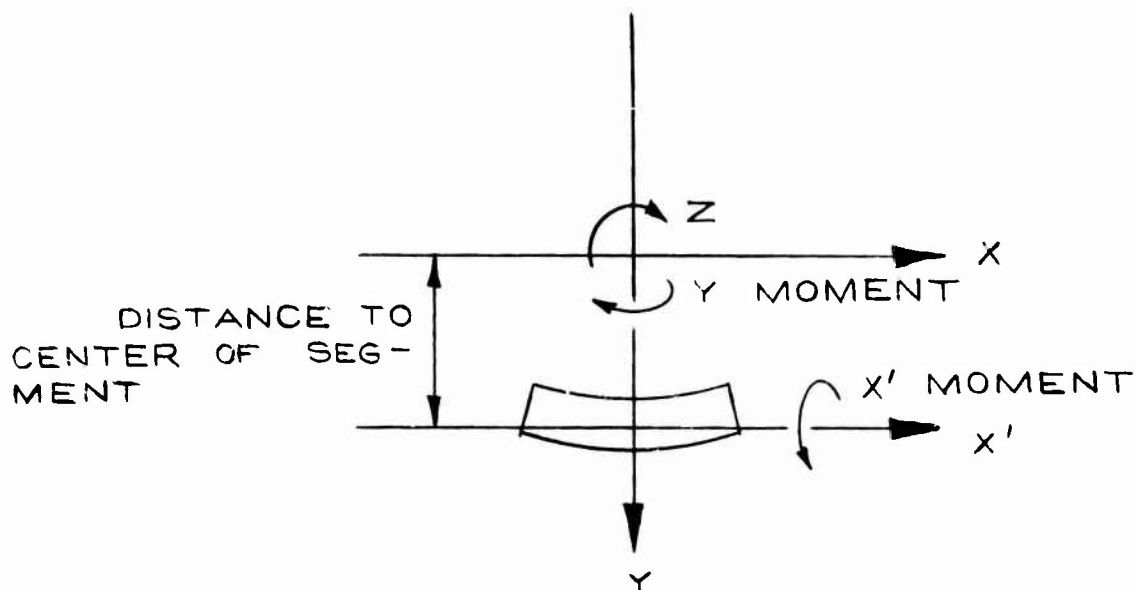
NO. OF ORIFICES = 11

CASE 2



$$\theta_p = 30^\circ$$

NO. OF STEPS = 3



THE FOLLOWING PLOTTED RESULTS ARE FOR ONE SEGMENT ONLY

FIGURE 6.5.10

The most important run was case 10 because it decided the final selection of the 15 degree hydrostatic sector. Seal No. 1 was analyzed with dimensions shown on Sheet 5 of Section 10 0. The following conditions apply.

Seal Fluid pressure = 95 psia
 Ambient pressure = 2 psia
 Collar nutations = .001 TIR
 Degrees of freedom = 2 (axial, yaw)
 Shaft Speed, N = 12,000 rpm

Figures 6.5.11 and 6.5.12 are wheel nutations about the y and x axes respectively. As expected, they are 90 degrees out of phase. Amplitudes in radians corresponds to .001 in. TIR. (The odd scale, for angular motions resulted because of an error in the automatic plotting routine in converting from non-dimensional values). Figure 6.5.13 shows sector response in the axial mode. Note the total amplitude of translation is 0.001 in, precisely equivalent to the wheel nutation. The motion is exactly in phase with rotation about the x axis. Thus the sector is following shaft movements extremely well. Further verification of the excellent tracking capability of the sector is afforded by the yaw of the sector about the y axis as shown on Figure 6.5.14. This mode is in-phase with that of the turbine rotor at a considerably smaller amplitude. Figure 6.5.15 shows sector leakage as a function of shaft revolutions. After initial transients (resulting from assumed starting conditions) die the sector leakage settles to a mean value of 0.0015 lbs/sec. This corresponds to a steady-state leakage of 0.00152 lbs/sec. at a one mil uniform film not including gap leakage. The fluid-film force on the sector oscillates about the 99.5 lb. level which is precisely the value computed on the basis of the steady-state analysis, and of course is equal to the hydraulic closing force acting on the seal. Figure 6.5.16 shows the fluid-film moment about the y axis. The y moments cause well-controlled motions about the y axis as was previously discussed.

In summary, the two degree of freedom dynamic analysis shows the 15 degree hydrostatic sector seal to behave extremely well, essentially in perfect unison with the forcing function.

A summary of dynamic cases is shown on Tabulation 6.5.1, and plotted results are included as Section 12.3. In the various cases a number of things were varied. First, two types of seals were investigated (1) the 15 degree sector hydrostatic orifice seal and (2) the tri-Rayleigh step sector of 30 degrees angular extent. For a number of cases mistaken inertial values were used, which contributed to the instability. These cases are appropriately asterisked in Tabulation 6.5.1. Another variable was the number of degrees of freedom. In some cases only the axial mode was permitted; in the others, yaw was included to more closely resemble the actual situation.

BN-SEAL DYNAMIC PERFORMANCE AT DESIGN OPERATION, 24-SEGMENT ORIFICE-FED STEP SEAL,
CASE 10. TWO DEGREES OF FREEDOM, WHEEL Y-NUTATION.

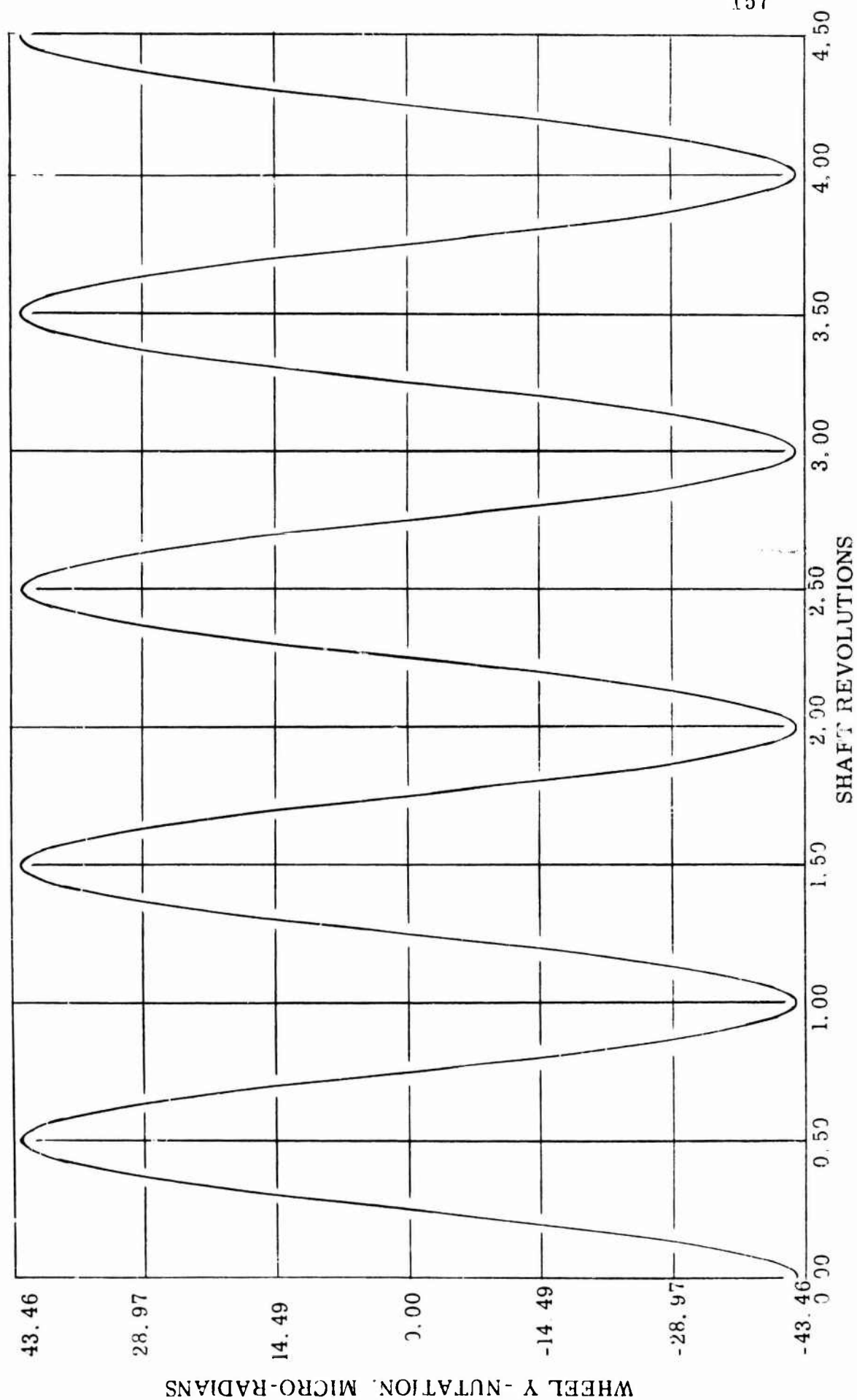


FIGURE 6.5.11

BN-SEAL DYNAMIC PERFORMANCE AT DESIGN OPERATION, 24-SEGMENT ORIFICE-FED STEP SEAL,
CASE 10, TWO DEGREES OF FREEDOM, WHEEL X-NUTATION

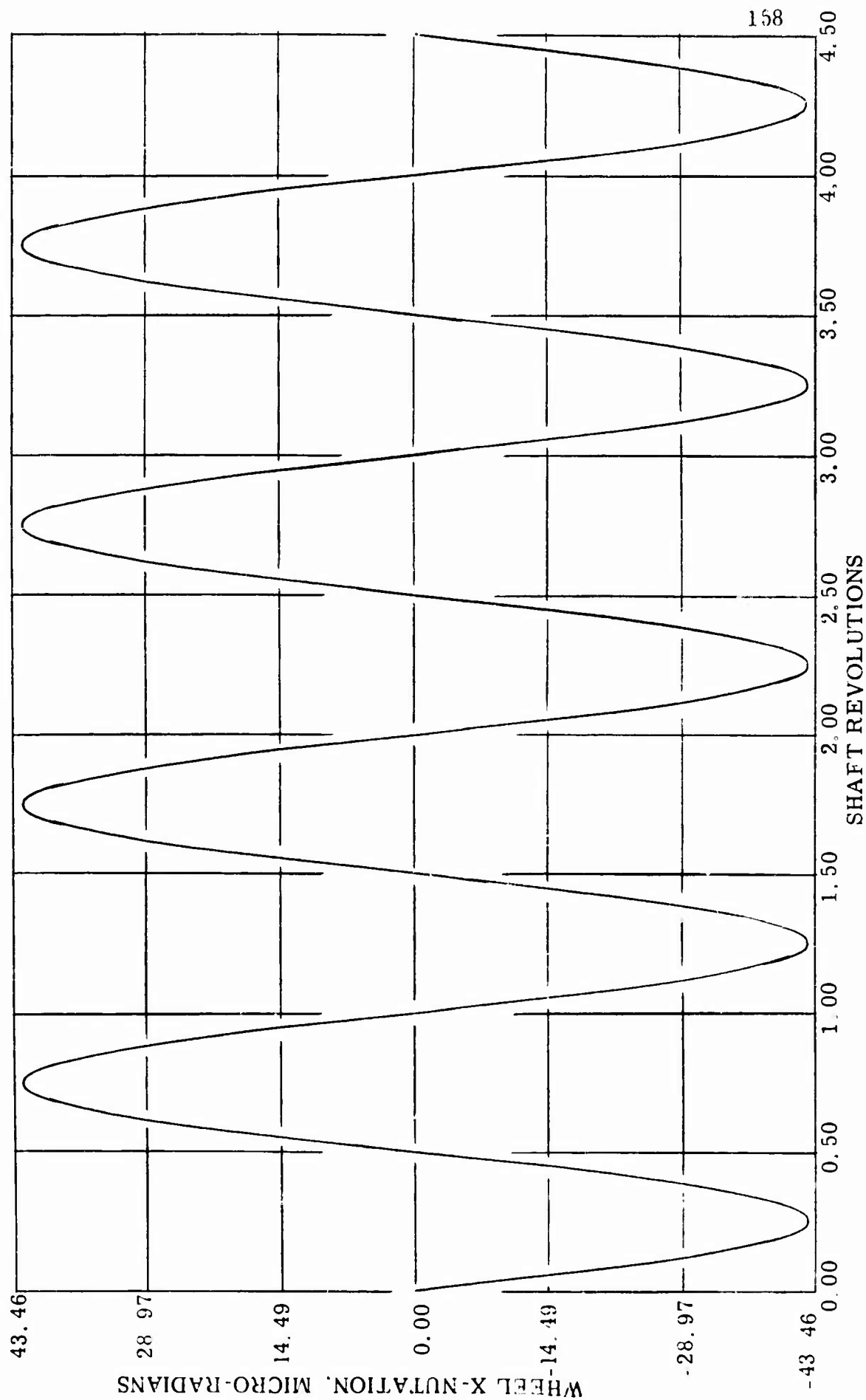


FIGURE 6. 5. 12

BN-SEAL DYNAMIC PERFORMANCE AT DESIGN OPERATION, 24-SEGMENT ORIFICE-FED STEP SEAL,
CASE 10, TWO DEGREES OF FREEDOM, SEAL TRANSLATION

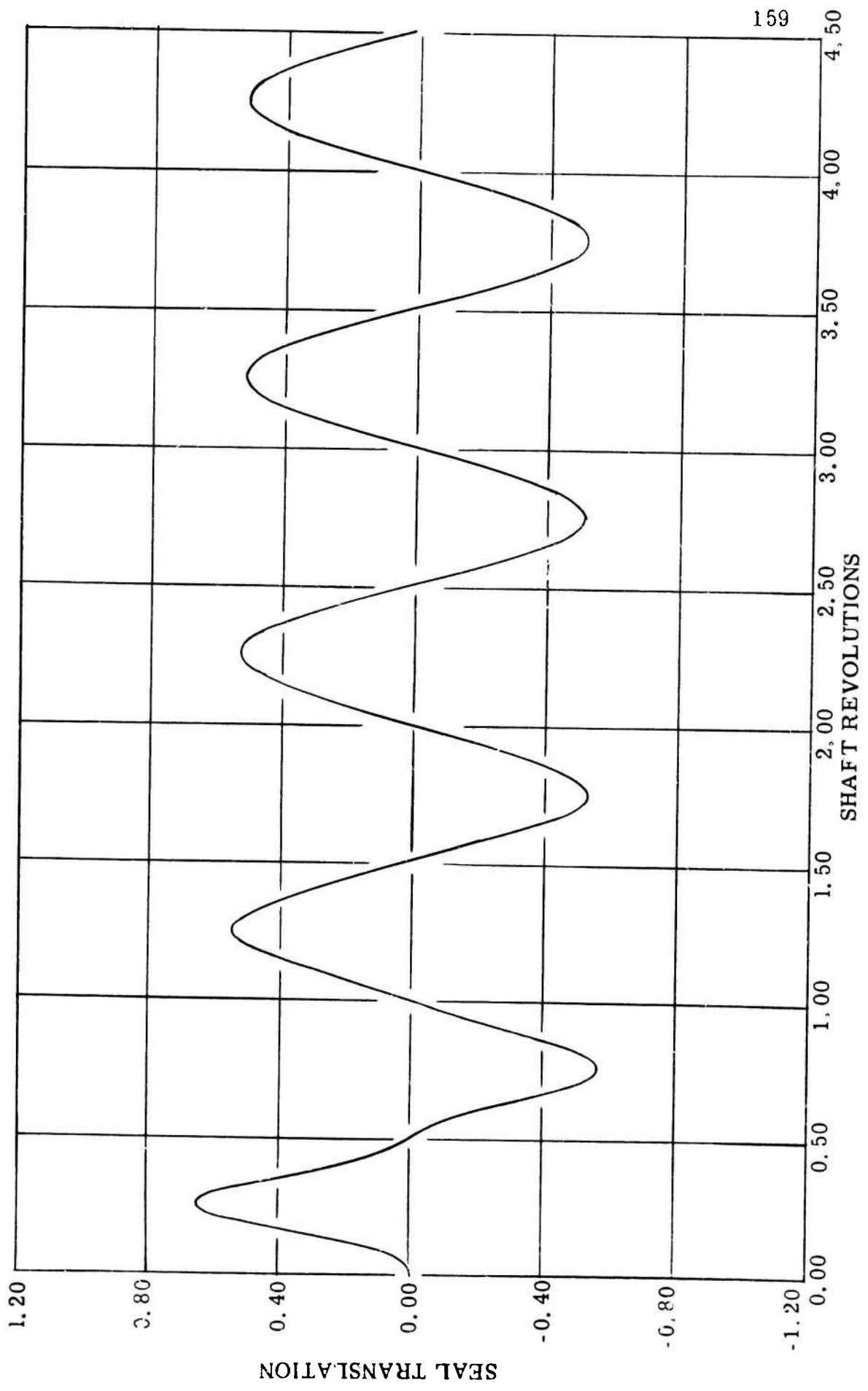


FIGURE 6.5.13

BN-SEAL DYNAMIC PERFORMANCE AT DESIGN OPERATION, 24-SEGMENT ORIFICE-FED STEP SEAL.
CASE 10, TWO DEGREES OF FREEDOM, SEAL Y-ROTATION

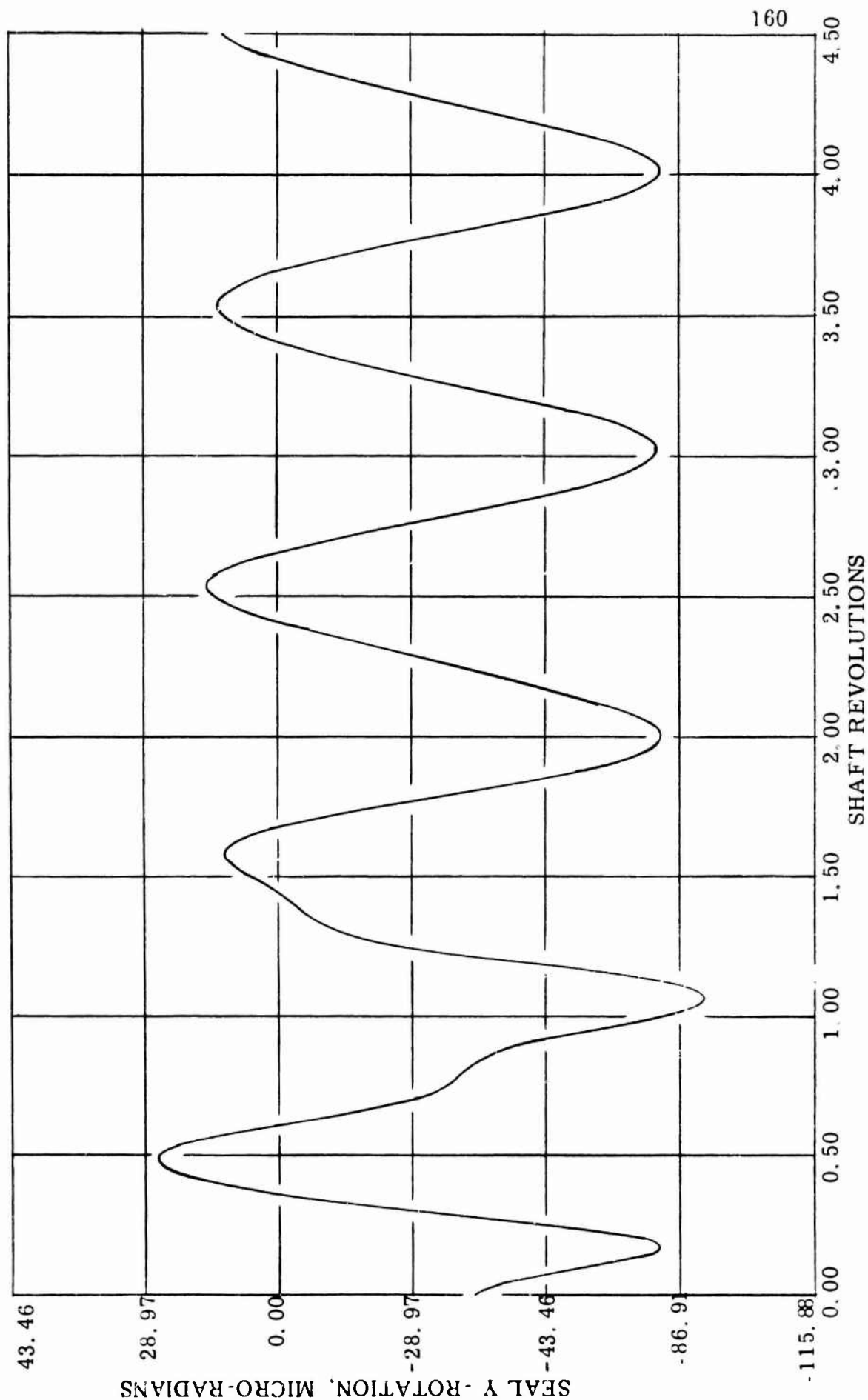


FIGURE 6. 5. 14

BN-SEAL DYNAMIC PERFORMANCE AT DESIGN OPERATION, 24-SEGMENT ORIFICE-FED STEP SEAL.
CASE 10, TWO DEGREES OF FREEDOM, SEAL LEAKAGE

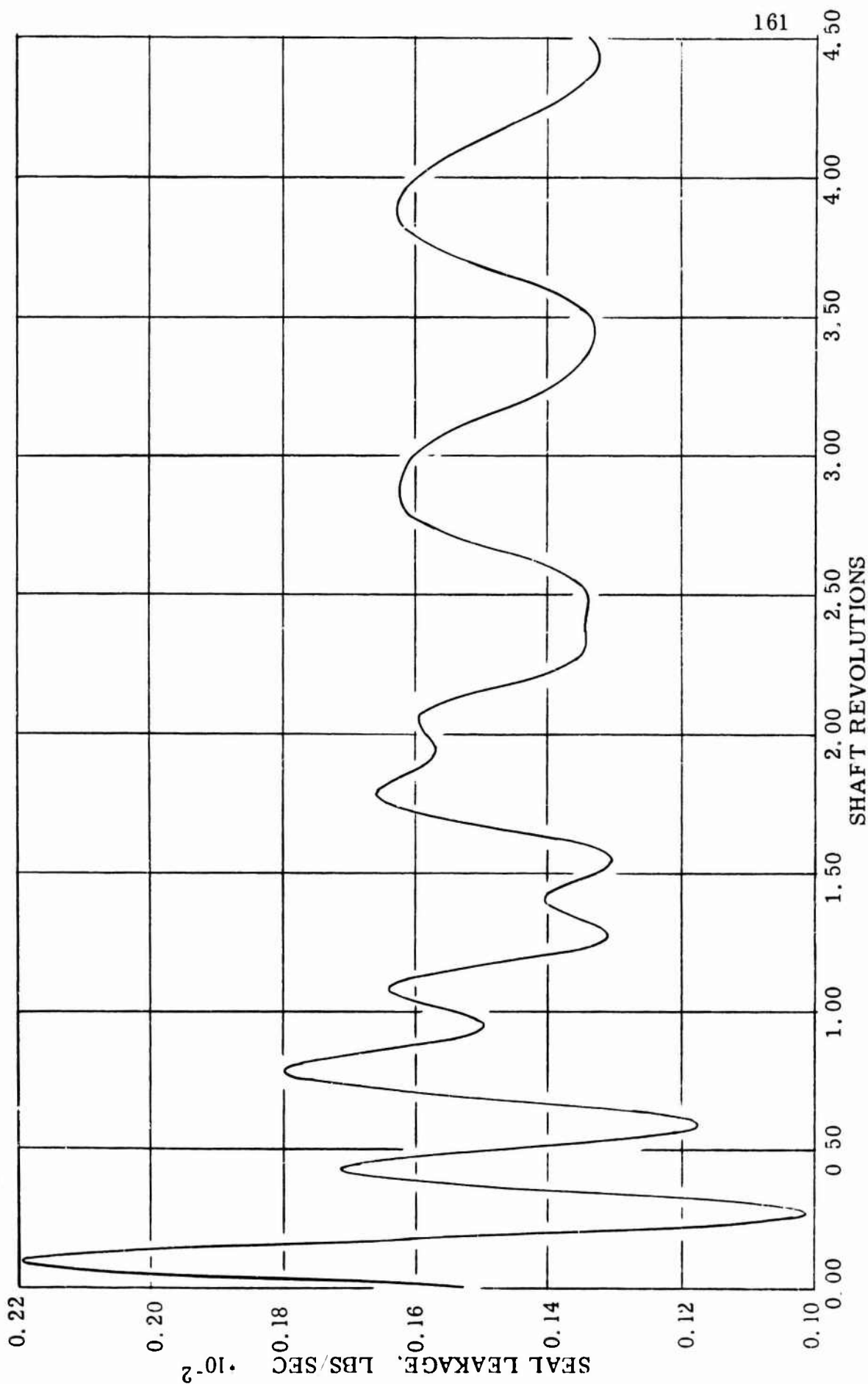


FIGURE 6.5.15

BN-SEAL DYNAMIC PERFORMANCE AT DESIGN OPERATION, 24-SEGMENT ORIFICE-FED STEP SEAL,
CASE 10, TWO DEGREES OF FREEDOM, SEAL Y-MOMENT

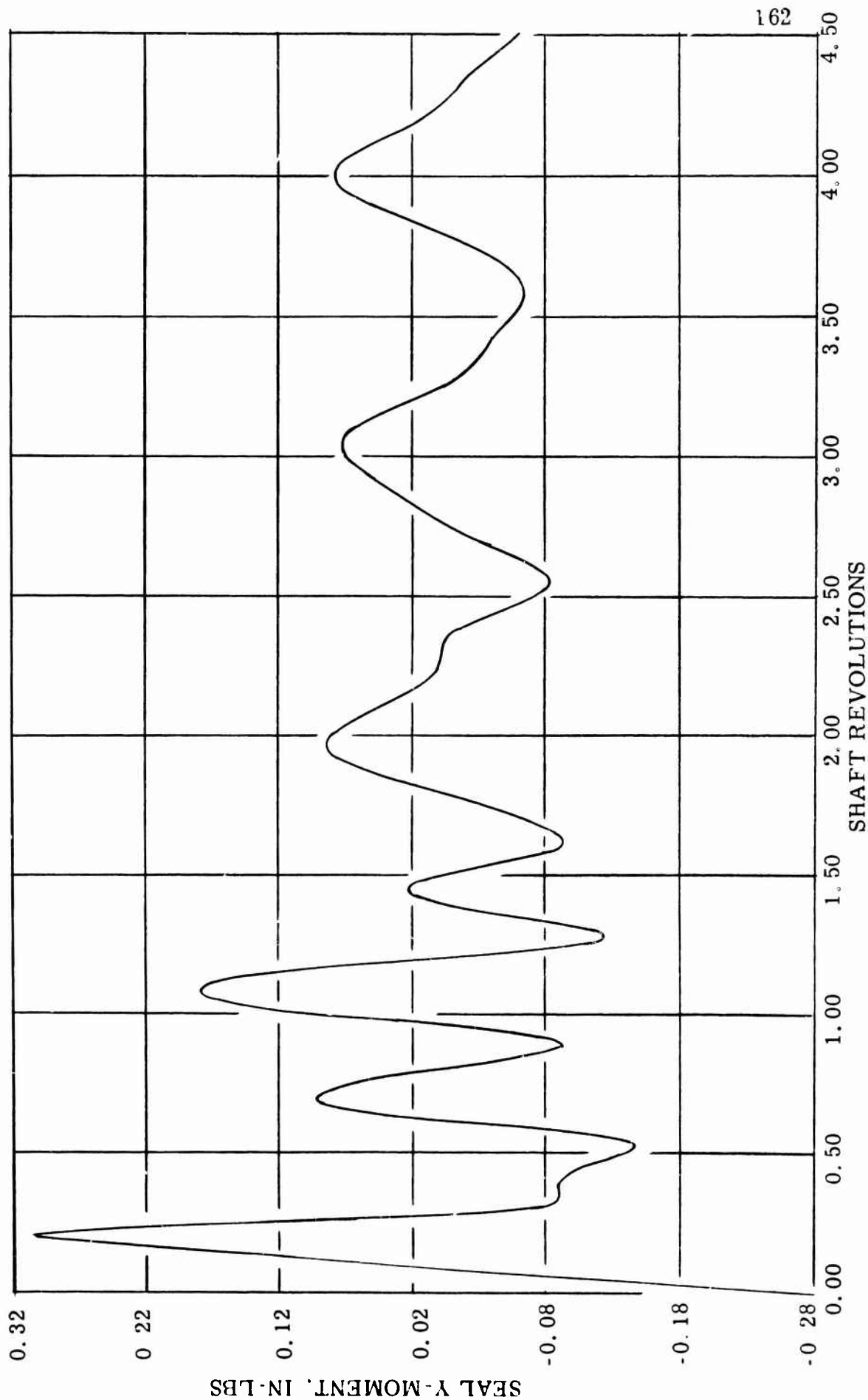


FIGURE 6 5.16

SUMMARY OF DYNAMIC RUNS

Case No.	Sector Geometry	TIR	Number of Degrees of Freedom	Time Step	Mass ² Lb-Sec ²	Inertia ² Lb-In-Sec ²	Results
1	Hydrostatic Orifice 15°	.001	1	$\pi/40$.00086	---	Stable
2	Large Step 30°	.001	1	$\pi/40$.00177	---	Stable
3	Large Step 30°	.005	2	$\pi/200$.00253	.00761	Unstable
4	Large Step 30°	.005	1	$\pi/200$.00253	.00761	Unstable
5	Large Step 30°	.0035	2	$\pi/200$.00253	.00761	Unstable
6	Large Step 30°	.005	2	$\pi/40$.00253	.00761	Unstable Coarse Time Step
7	Hydrostatic Secondary Seal	---	1	$\pi/20$.00253	---	Unstable, Numerical Problems
8	Hydrostatic Orifice 15°	.005	2	$\pi/200$.00115	.00385	*Unstable (inertia too large)
9	Large Step 30°	.001	2	$\pi/200$.00253	.00761	Unstable
10	Hydrostatic Orifice 15°	.001	2	$\pi/200$.00115	.00088	Stable

TABULATION 6.5.1

The variable DT is the non-dimensional time-step. A time step of $\pi/40$ means that there are 40 time intervals for each shaft revolution. The coarser time step of $\pi/40$ was acceptable in all cases that it was utilized except for case 7 which was run to determine the stability characteristics of the hydrostatic secondary seal. In this case, the unstable result was attributable to the coarseness of the time step. With regard to the complete set of dynamic runs, the following conclusions are formulated.

1. In no case could a large misalignment approaching 0.005 TIR be tolerated.
2. The 15° hydrostatic sector was found to be stable in two degrees of freedom with a 0.001 TIR run out.
3. The hydrodynamic geometry was not properly tested when reduced to 15°.
4. The 30° sector would not respond properly in two degrees of freedom.
5. Masses and inertias were computed on the basis of steel as the sector material.
6. The hydrostatic secondary seal was not properly analyzed for pneumatic hammer stability although it is felt that the use of inherently compensated orifices should avoid this problem.

6.5.1.4 Bearing Performance

The recommended journal bearings are the three shoe, pivoted-pad type, with the top shoe spring loaded to accommodate thermal and centrifugal expansions of the shaft. These bearings have adequate load capacity and will avoid whirl tendencies. Recommended pre-loads result in adequate stiffness in all directions at the operating position.

The thrust bearing is also of the pivoted-pad type. It is a completely captured bearing with eight pads on each bearing surface.

Analysis was accomplished on the basis of laminar theory, and corrections for turbulence made by using information in the literature. Also, for the journal bearing, a few computer runs were made with a turbulent bearing computer program, for load capacity only. No turbulent corrections were made to the thrust bearing load capacity, because it was difficult to find reliable information. Also, there is ample safety margin with respect to load capacity, and turbulence will further improve load capacity.

6.5.2 Journal Bearings

Both 3 x 3 and 4 x 4 (length x width) bearing pads were investigated.

Tabulation 6.5.2 is a summary of the journal bearing performance. Indicated are friction horsepower per bearing both at zero and full load conditions, stiffness at zero and full load, minimum film thickness at zero and full load, pivot film thickness, pre-load, first rigid body natural frequency, and required flow to limit the temperature rise due to viscous friction to 10°F .

Our recommendation is to use the 4 x 4 bearing. Stiffness and minimum films are very good. The friction horsepower per bearing is about 7 hp, and the required flow to the bearing cavity is 3.5 gpm. The first rigid body critical occurs at about 15,000 rpm. We are uncertain of the significance of this because without a complete dynamic analysis the effect of squeeze film damping is unknown. In any event, the critical frequency of the 4 x 4 bearing is furthest from the operating point than with the other bearings.

Note that the pre-load is fairly high and hydrostatic liftoff will probably be required.

Performance curves for each of the bearings investigated are attached. On one set of curves, Figures 6.5.17 through 6.5.19, friction horsepower, minimum film thickness and load are plotted against eccentricity ratio. Displacements were taken between pads and directly at the spring loaded shoe. The latter case is not applicable to the horizontal rotor, but is included for completeness. The second set of plots, Figures 6.5.20 through 6.5.22, shows temperature rise versus flow to the bearing cavities. We have assumed that the bearings will operate in flooded cavities and the heat of viscous friction is entirely convected by fluid flow.

6.5.3 Thrust Bearings

The thrust bearing geometrical data and operating condition performance is shown on Tabulation 6.5.3. The performance information is for the pre-loaded pair and not just for one side. Note that turbulent horsepower is estimated at 11. This plus 14 for the two journal bearings gives a total horsepower loss of 25, about 3 percent of the turbine output. Required flow for cooling is approximately 6 gpm. A total of 13 gpm is necessary for both journal and thrust bearings.

Complete performance curves are included for the pre-loaded pair, Figures 6.5.23 through 6.5.26. Individual performance of each bearing side is also included on all curves except flow versus temperature rise. The flow on this curve is the total flow for both sides. The following curves are included.

- a. Load vs. Pivot Film Thickness. Figure 6.5.23
- b. Friction Horsepower vs. Pivot Film Thickness. Figure 6.5.24
- c. Minimum Film Thickness vs. Pivot Film Thickness. Figure 6.5.25
- d. Total Flow vs. Temperature Rise. Figure 6.5.26

TILTING PAD JOURNAL BEARING SUMMARY
FOR SINGLE BEARING OPERATION

Operation conditions

Shaft speed = 12 000 rpm

Viscosity = $0.455 \times 10^{-6} \frac{\text{lb-sec}}{\text{in}^2}$ (water at 200°F)

Load = 134 lb

Geometric parameters

Number of pads = 3

Pad angle = 100°

Pivot position = 50° from leading edge
= 2 in. in length direction

Performance parameters

Dia. in.	Length in.	Friction Horsepower		Stiffness lb/in.		Minimum Clearance Mils		Machined Clearance Radial Mils	Pre- load lbs	Natural Frequency rpm	Flow for $\Delta = 10^\circ$ gpm
		Load 0 lb	Load 134 lb	Load 0 lb	Load 134 lb	Load 0 lb	Load 134 lb				
4	4	6.5	6.8	712,000	848,500	1.245	1.175	3.0	1255	14,937	3.5
3	3	1.83	2.05	272,000	470,600	1.04	.875	2.5	428.9	11,124	1.1
3	3	1.89	2.00	520,000	694,300	.83	.733	2.0	595.7	13,512	1.0

TABULATION
6.5.2

Note: Pivot clearance is one-half machined in clearance.

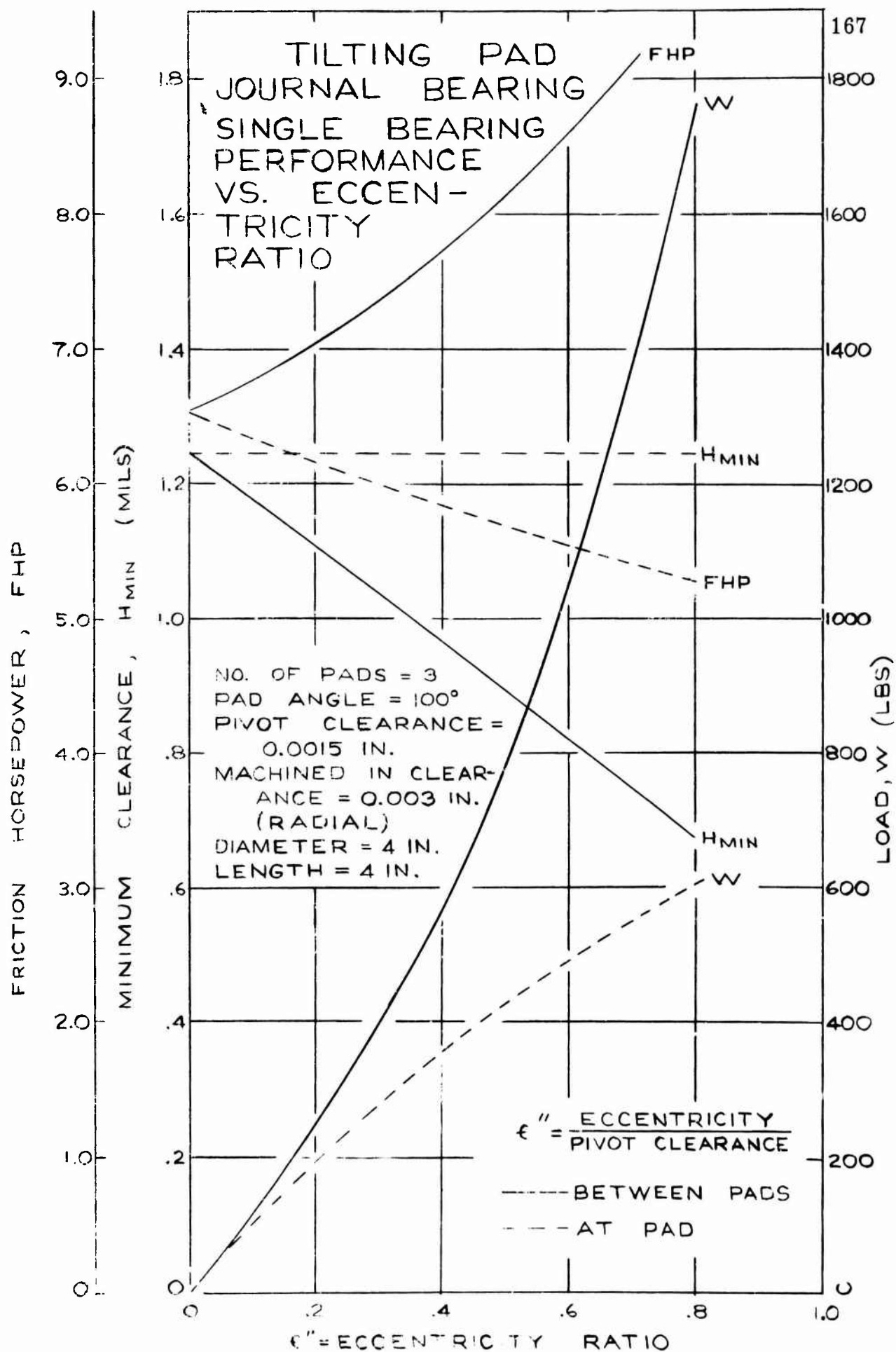


FIGURE 6.5.17

TILTING PAD JOURNAL BEARING ¹⁶⁸ SINGLE BEARING PERFORMANCE VS. ECCENTRICITY RATIO

NO. OF PADS = 3 $\epsilon'' = \frac{\text{ECCENTRICITY}}{\text{PIVOT CLEARANCE}}$
 DIAMETER = 3 IN.
 LENGTH = 3 IN.
 PAD ANGLE = 100°
 PIVOT CLEARANCE = .00125 IN.
 MACHINED-IN CLEARANCE = .0025 IN. (RADIAL)
 ——— BETWEEN PADS
 - - - - DIRECTLY AT PAD

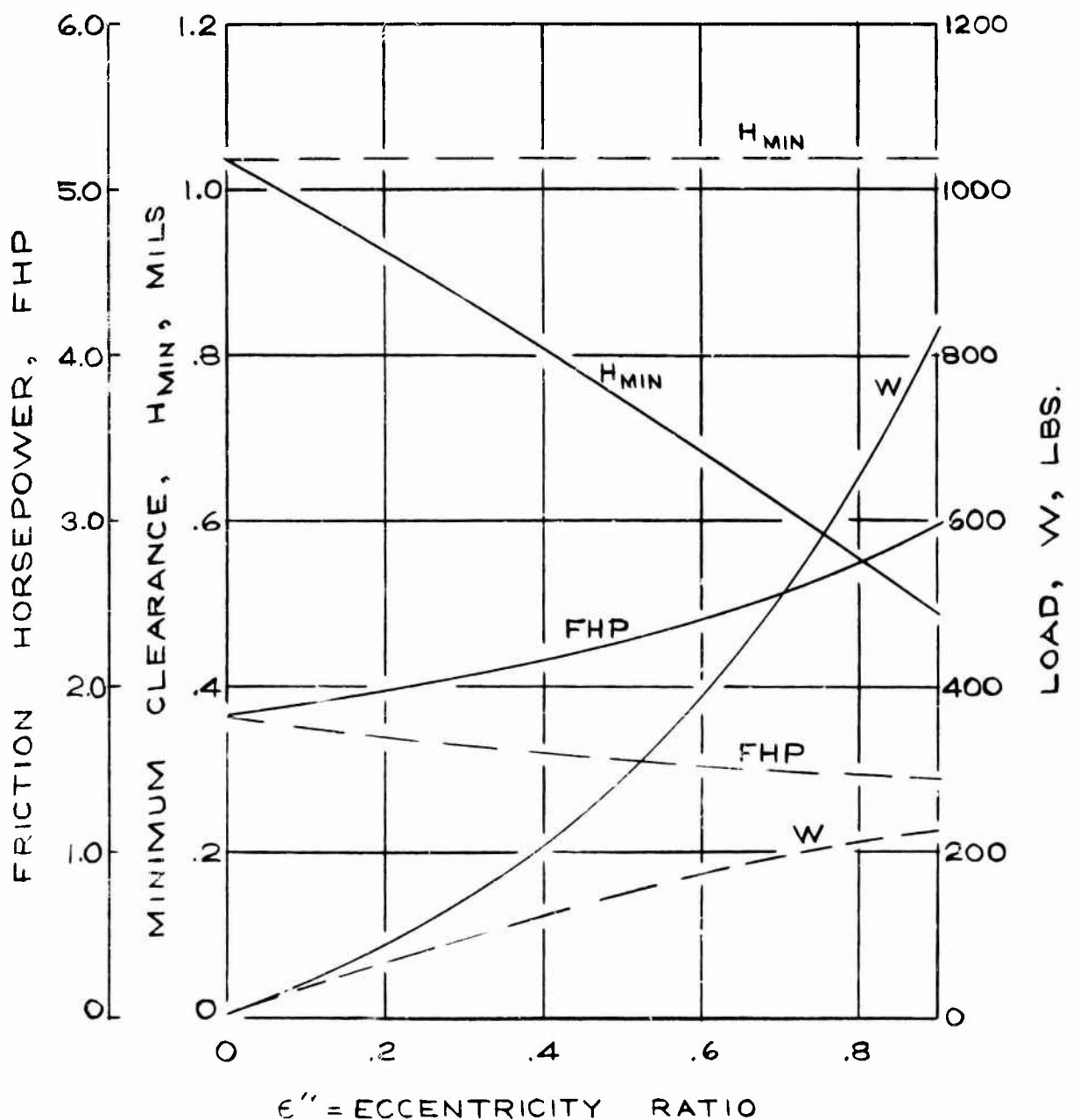


FIGURE 6.5.18

TILTING PAD JOURNAL BEARING- SINGLE BEARING PERFORMANCE VS. ECCENTRICITY RATIO

169

NO. OF PADS = 3

DIAMETER = 3 IN.

LENGTH = 3 IN.

PAD ANGLE = 100°

PIVOT CLEARANCE = .001 IN.

MACHINED-IN CLEARANCE = .002 IN. (RADIAL)

—— BETWEEN PADS

--- DIRECTLY AT PAD

$$\epsilon'' = \frac{\text{ECCENTRICITY}}{\text{PIVOT CLEARANCE}}$$

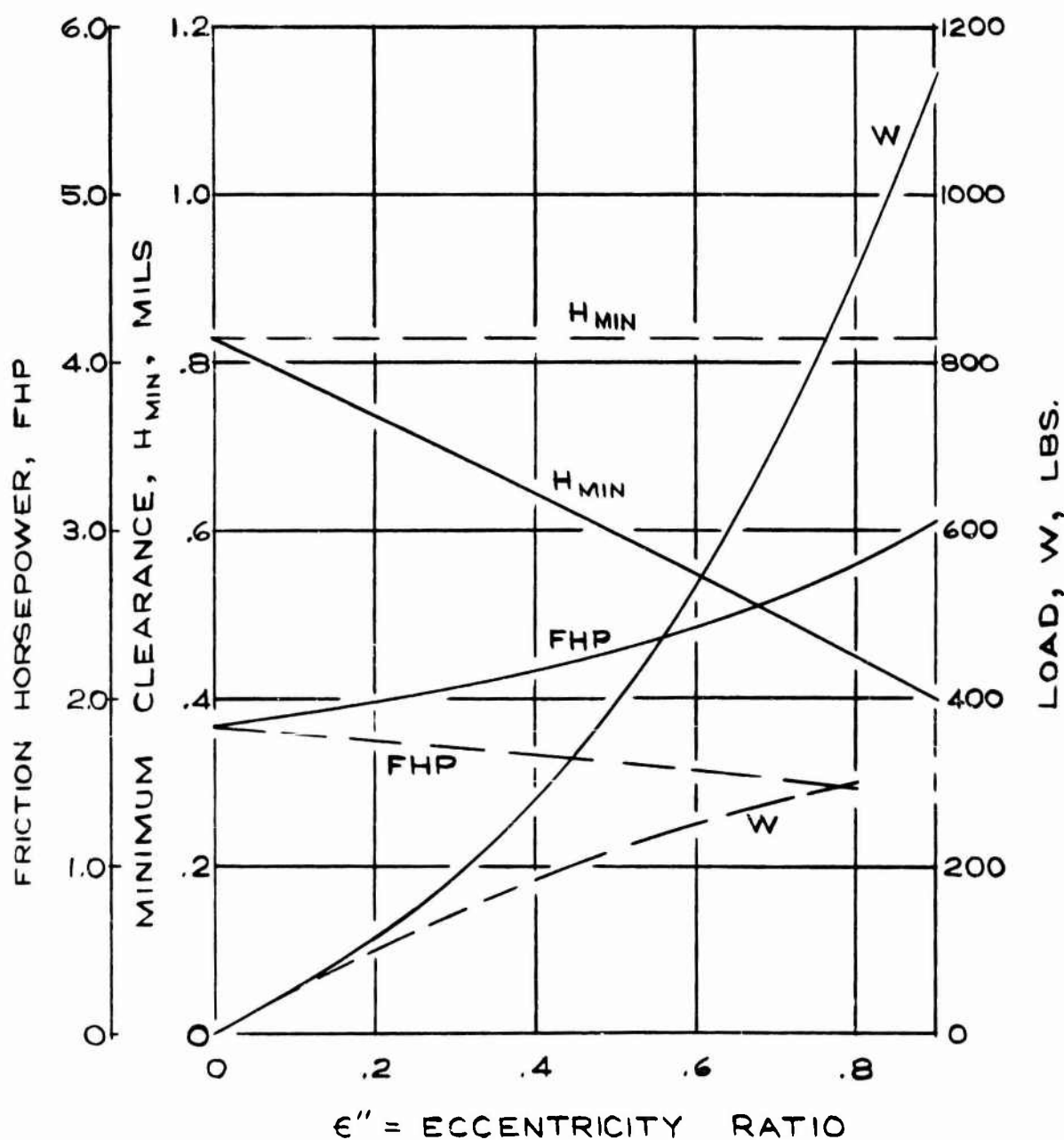


FIGURE 6.5.19

TILTING PAD JOURNAL BEARING SINGLE BEARING FLOW VS. CHANGE IN TEMPERATURE

NO. OF PADS = 3
DIAMETER = 4 IN.

LENGTH = 4 IN.

PAD ANGLE = 100°

PIVOT CLEARANCE = 0.0015 IN. HORSEPOWER.

MACHINED IN CLEARANCE =
0.003 IN. (RADIAL)

NOTE:
TEMPERATURE CHANGE
DUE ONLY TO SINGLE
BEARING FRICTION

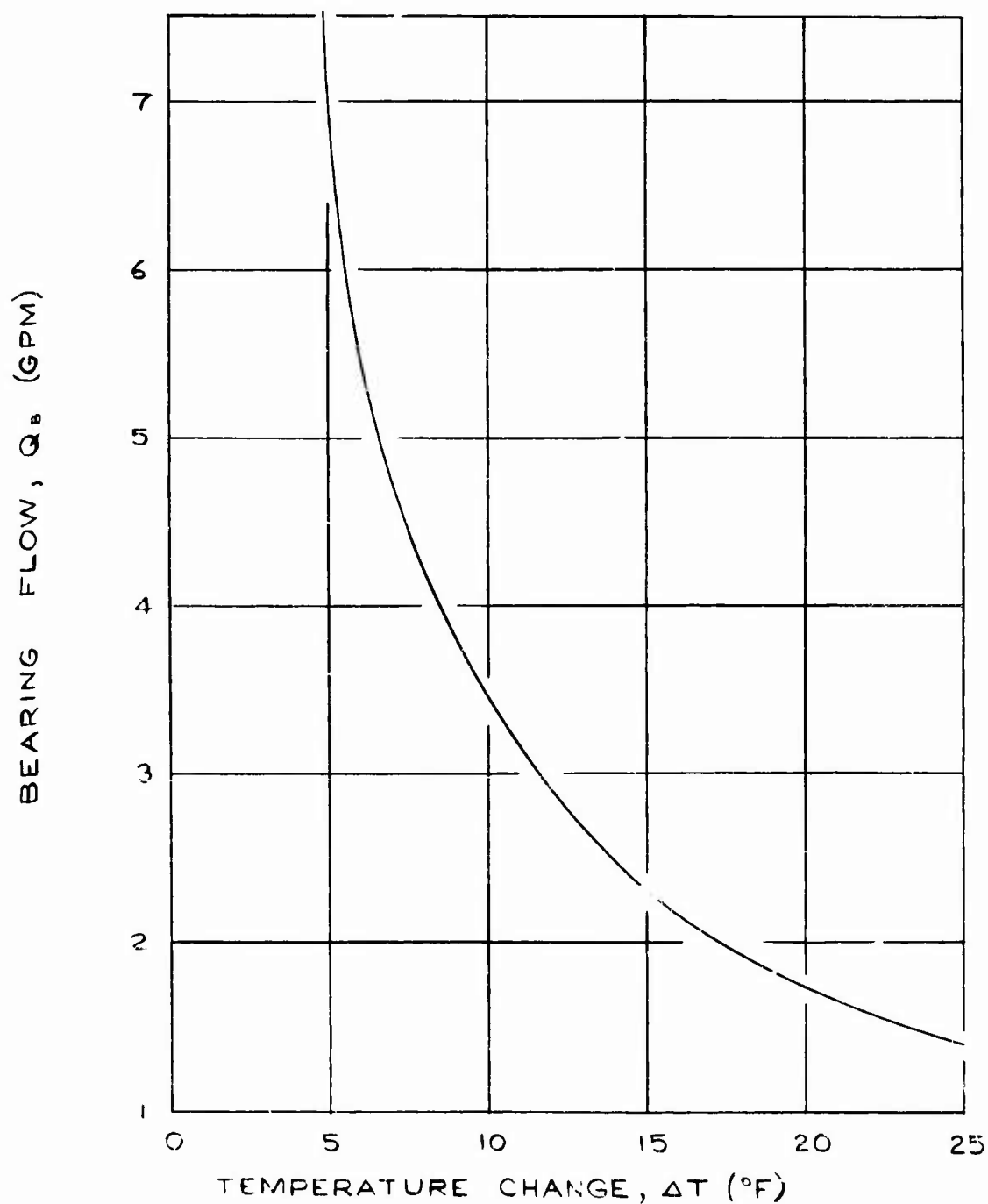


FIGURE 6.5.20

TILTING PAD JOURNAL BEARING - SINGLE BEARING FLOW VS. CHANGE IN TEMPERATURE 171

NO. OF PADS = 3
 DIAMETER = 3 IN.
 LENGTH = 3 IN.
 PAD ANGLE = 100°

NOTE: TEMPERATURE
 CHANGE DUE ONLY TO
 SINGLE BEARING FRIC-
 TION HORSEPOWER

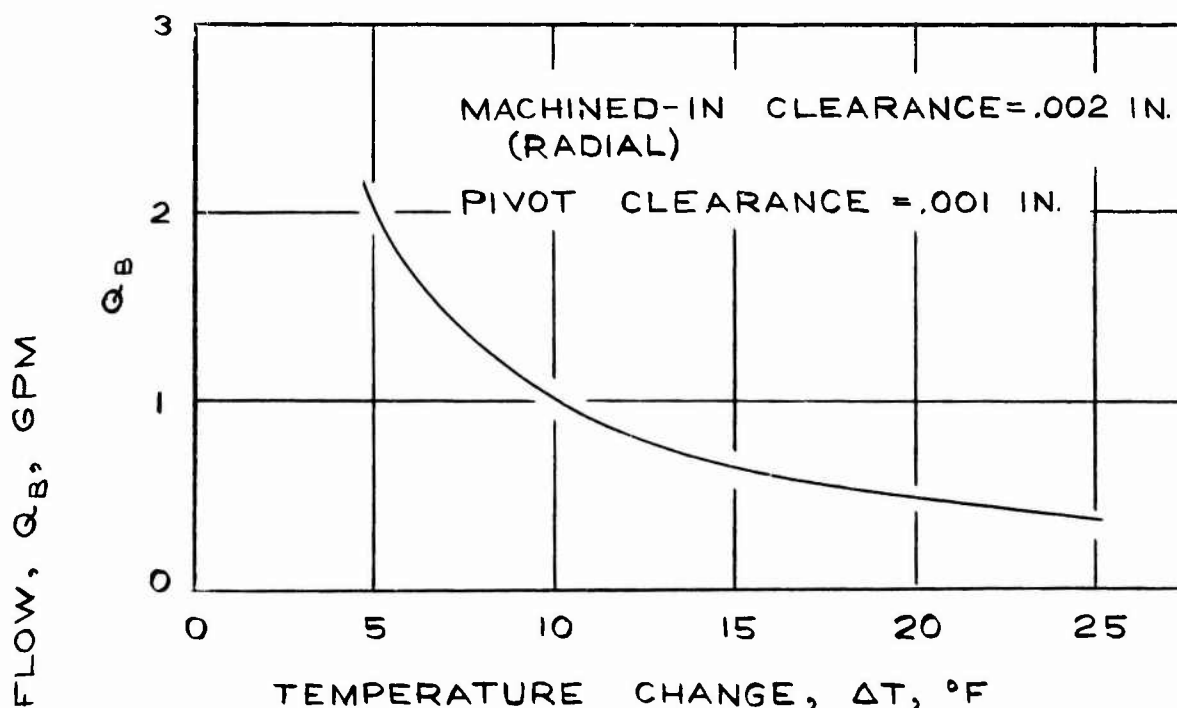


FIGURE 6.5.22

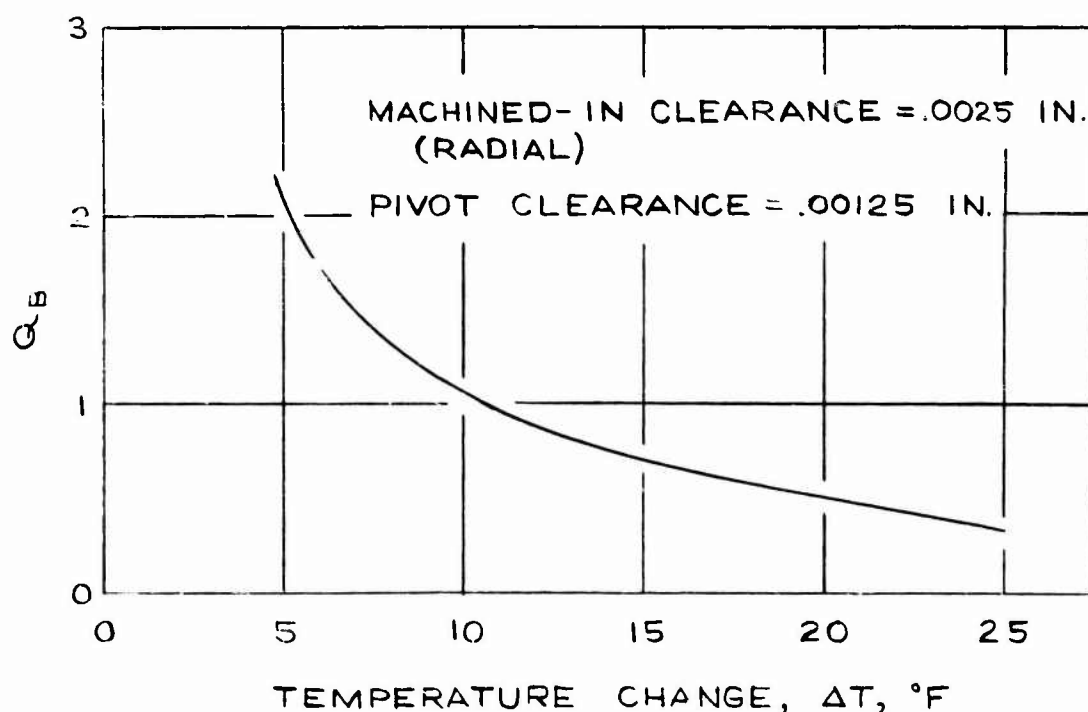


FIGURE 6.5.21

TILTING PAD THRUST BEARING SUMMARY
FOR OPPOSED PAIR BEARING OPERATION

Operating conditions

Shaft speed = 12,000 rpm

Viscosity = $0.455 \times 10^{-6} \frac{\text{lb-sec}}{\text{in}^2}$ (water at 200°F)

Load = 400 lbs

Geometric parameters

Number of pads = 8

Pad angle = 40°

Groove angle = 5°

Outside diameter = 8 in.

Inside diameter = 5-1/4 in.

Pivot position = 24° from leading edge

= 6-5/8 in. diameter

Performance parameters

(under load = 400 lb)

Friction horsepower = 12.7 HP

Film thickness = 0.00239 in.

Total inlet flow = 14.2 gpm ($\Delta T = 4.05^\circ\text{F}$)

Total inlet flow = 6.4 gpm ($\Delta T = 10^\circ\text{F}$)

TILTING PAD THRUST BEARING 173 OPPOSED PAIR BEARING LOAD VS PIVOT CLEARANCE

NO OF PADS = 8
OUTSIDE DIAMETER = 6 IN.
INSIDE DIAMETER = 3 IN.
PAD ANGLE = 40°
PIVOT CLEARANCE = .0015 IN. (CONCENTRIC)

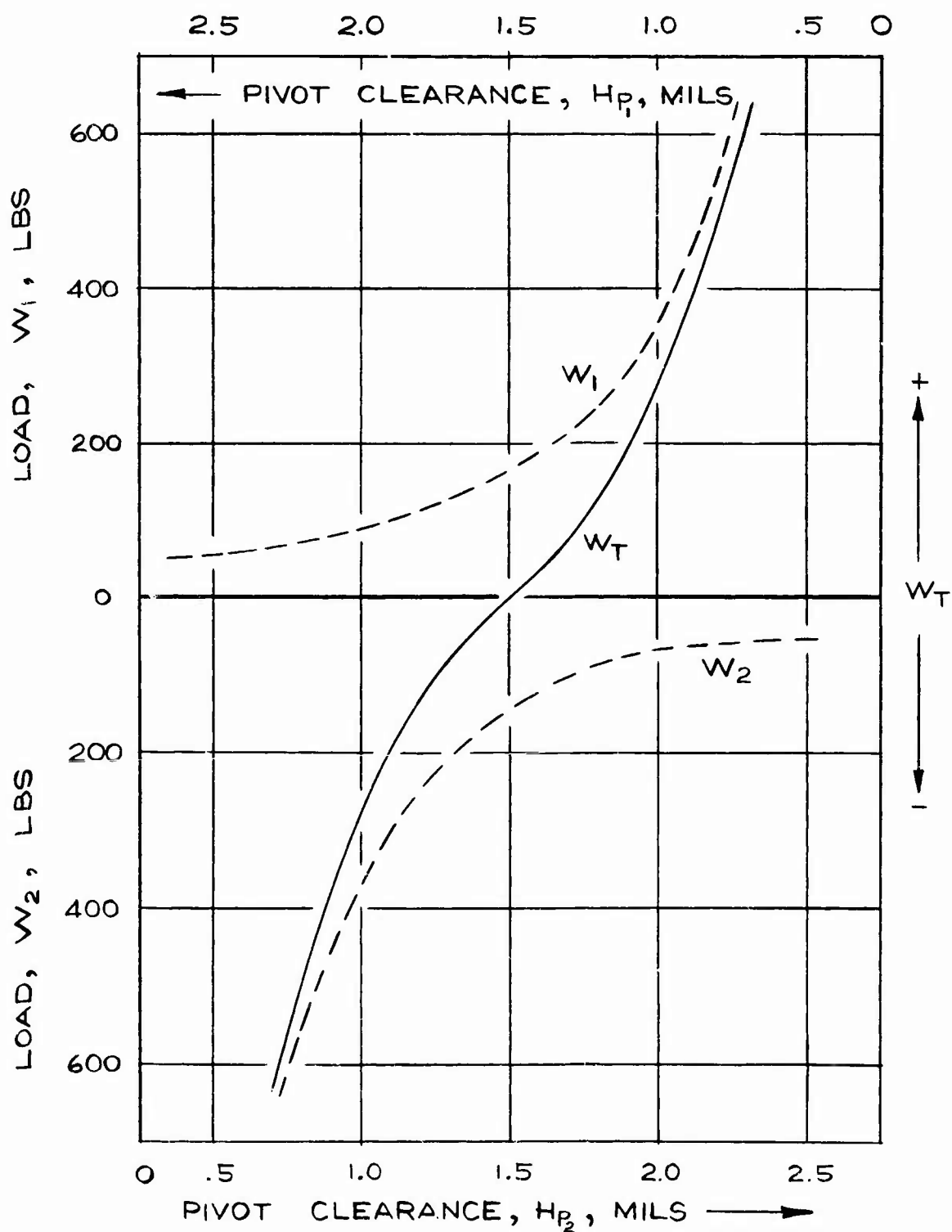


FIGURE 6.5.23

TILTING PAD THRUST BEARING 174 OPPOSED PAIR BEARING FHP VS PIVOT CLEARANCE

NO. OF PADS = 8

OUTSIDE DIAMETER = 6 IN.

INSIDE DIAMETER = 3 IN.

PAD ANGLE = 40°

PIVOT CLEARANCE = .0015 IN. (CONC. POS)

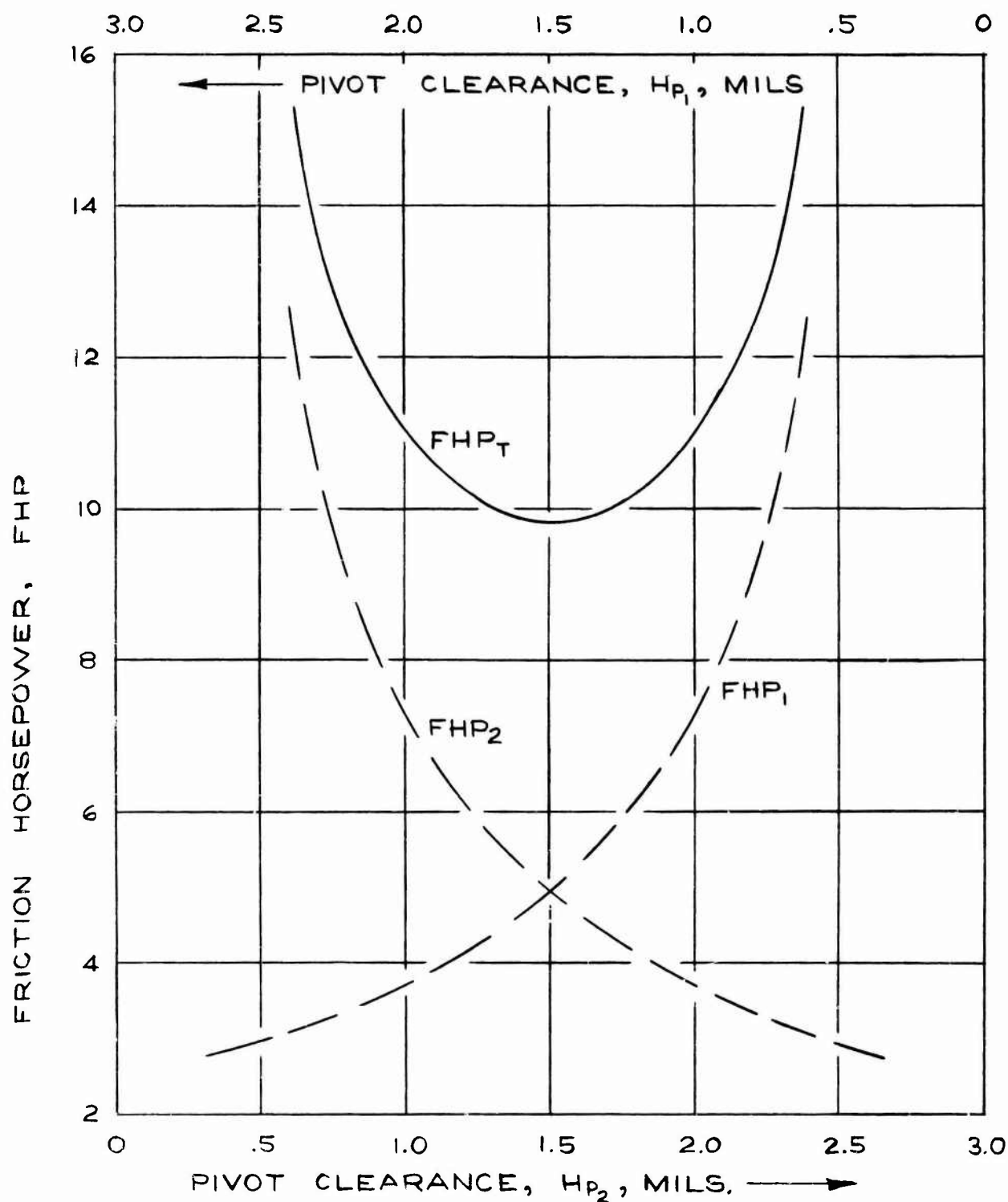


FIGURE 6.5.24

175

TILTING PAD THRUST BEARING - OPPOSED PAIR BEARING MINIMUM CLEARANCE VS. PIVOT CLEARANCE

NO. OF PADS = 8
OUTSIDE DIAMETER = 6 IN.
INSIDE DIAMETER = 3 IN.
PAD ANGLE = 40°
PIVOT CLEARANCE = .0015 IN. (CONC. POS.)

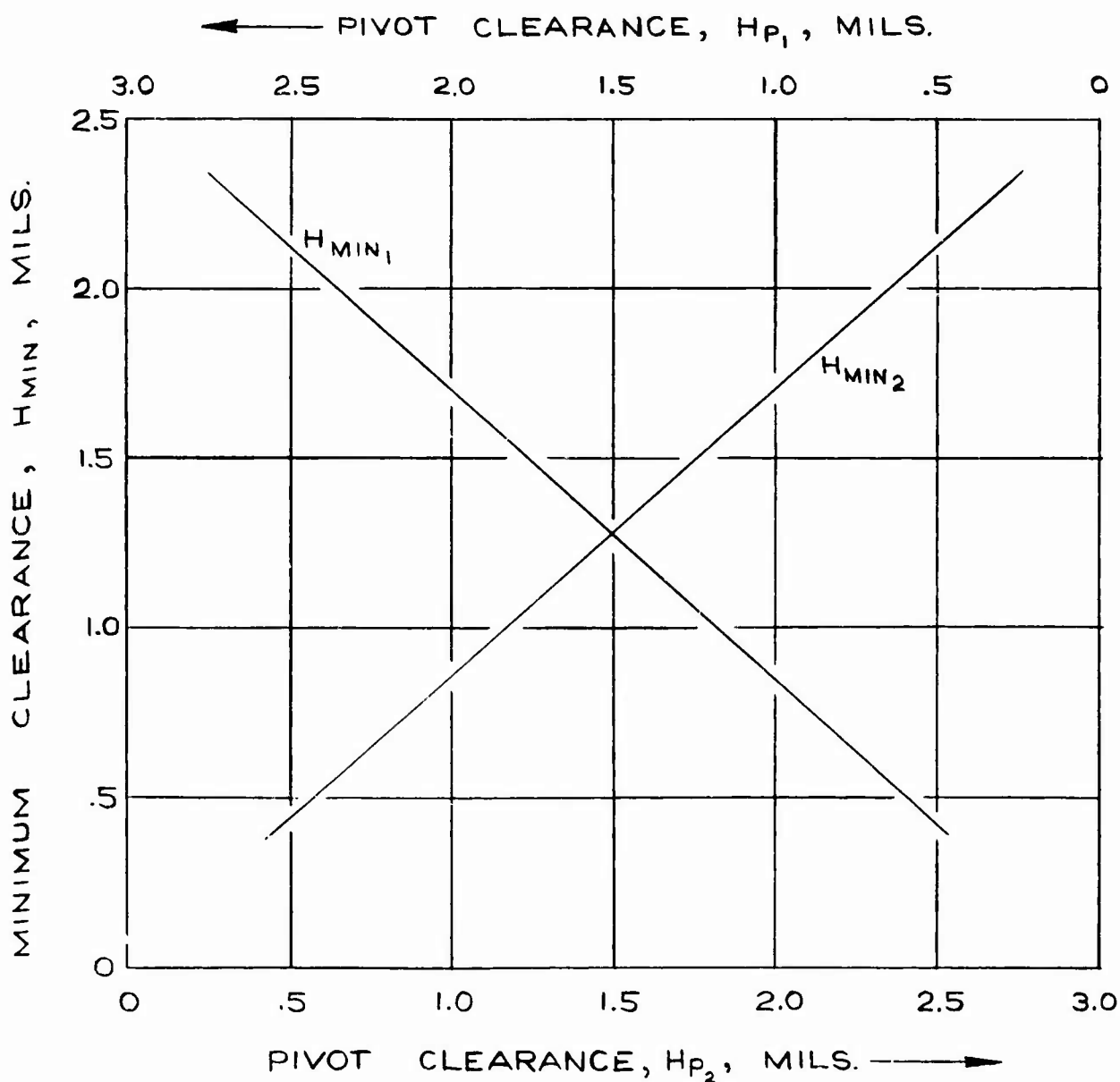


FIGURE 6.5.25

TILTING PAD THRUST BEARING OPPOSED PAIR BEARING FLOW VS CHANGE IN TEMPERATURE

NO. OF PADS = 8
PAD ANGLE = 40°
INSIDE DIAMETER = 3 IN.
OUTSIDE DIAMETER = 6 IN.
PIVOT CLEARANCE = .0015 IN.
(CONCENTRIC POSITION)

NOTE: TEMP. CHANGE
DUE ONLY TO OPPOSED
PAIR BEARING FRIC-
TION HORSEPOWER

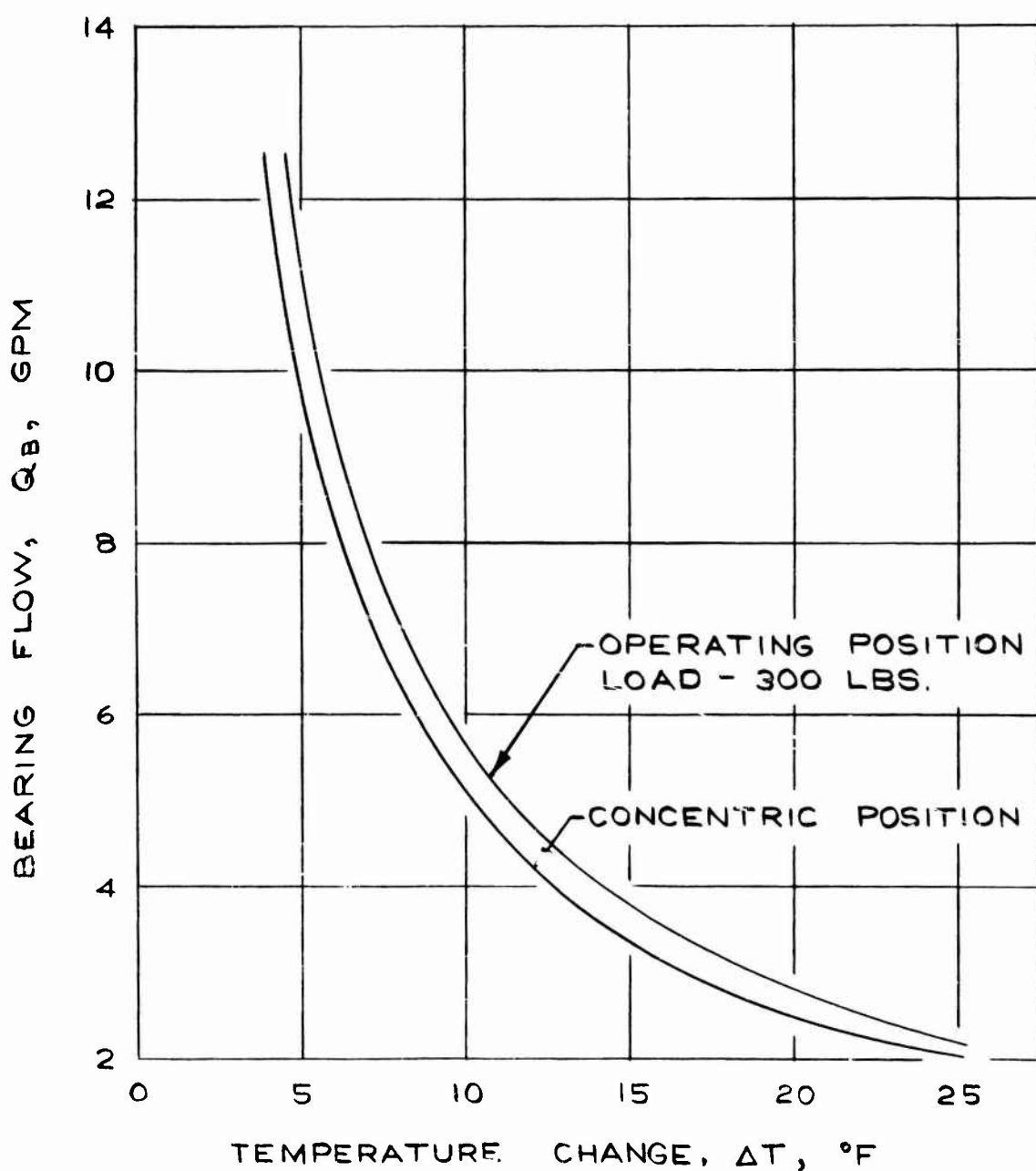


FIGURE 6.5.26

6.5.4 Thrust Load Balance

A significant force exists on the inlet side of the turbine disk that must be balanced by radially positioning the exit seal (Figure 3.1.1). This total force is caused by the pressure differential across the blades and disk, and the pressure distribution under the seal faces. A balancing force exists because of the pressure load on the exit side of the turbine disk. This balancing force is a function of the pressure on the exit side, the radial position of the third seal, and the pressure distribution under the seal face.

The differential thrust is sustained by the thrust bearing during operation. The thrust load during normal operation is 400 pounds downstream.

The equations for the force on the inlet side F_1 and the force on the exit side F_2 are as follows:

$$F_1 = \sum \text{force on inlet side, lb}$$

$$F_1 = \pi \left[\left(r_4^2 - r_3^2 \right) \left(\frac{P_1 + P_e}{2} \right) + \left(r_3^2 - r_2^2 \right) P_1 + \left(r_2^2 + r_1^2 \right) \left(\frac{P_1 + P_{\text{cond}}}{2} \right) \right]$$

$$\text{and } F_2 = \sum \text{force on exit side, lb}$$

$$F_2 = \pi \left[\left(r_4^2 - r_6^2 \right) P_e + \left(r_6^2 - r_5^2 \right) \left(\frac{P_e + P_{\text{cond}}}{2} \right) + \frac{T_L}{\pi} \right]$$

Force on thrust bearing is 400 lb

$$\text{Therefore } F_1 - F_2 = 400 \text{ lb}$$

Substituting the expression for F_1 and F_2 and the values of P_1 , P_e and P_{cond} into the above relationship provides the following equation for the unknown radius r_6 (Figure 3.1.1)

$$R_6^2 - .718 R_L - 105.503$$

$$R_6 = 10.637$$

Positioning the third seal at $R_6 = 10.637$ balances the force on the disk to within 400 pounds with a positive 50 pound load directed downstream in order to prevent thrust reversal.

6.5.5 Steam Wetness

The total heat addition necessary to vaporize the wetness in the exhaust steam was evaluated to be 6.7 BTU per pound of steam. Heat addition to the steam in the area between the rotor blades and the seal was evaluated by determining the turbine disk friction in this area by the equation given in Section 3.1.1. The magnitude of the disk friction was calculated to be 9.7 HP, or about 7 BTU/sec. This heat is added to the steam flow comprised of seal leakage and recirculation occurring at the rotor exit, and is adequate to vaporize all wetness in the exhaust steam reaching the seal as long as the total flow rate in this area is less than about one lb/sec. The conclusion reached as a result of the above analysis was that wetness occurring in the area of the rear seal can be eliminated by restricting recirculation at the exit of the turbine rotor, between the rotor blades and the rear seal. To this end, a reasonably close running clearance at the root of the rotor blades was included in the turbine design.

7.0 CALCULATIONS

This section includes examples of the calculations performed to obtain the results presented in Section 6.0 of this report. The symbols used are listed on pages x through xiv, and where the symbols were unique to the particular section, a more detailed list is provided in the individual section. The computer programs are included where the analysis was performed by computer and the necessary terminology included in the appropriate sections. The calculations were demonstrated in those areas where the LVF turbine was unique, where derivations of equations were required, and where the calculation was difficult enough that the procedure should be demonstrated.

The calculation procedure and computer program description for the controlled-leakage seal submitted by FIRL and the terminology unique to FIRL's analysis is included in Section 7.5.

7.1 AERO-THERMODYNAMIC ANALYSIS

This section presents the method of calculation used during the L V F turbine analysis and design. These calculations are used to determine the turbine's design and off design performance and to establish the design parameters of the turbine. The equations as presented in this section were programmed for digital computer operation and two IBM-1130 computer programs were developed.

One program requires that the seal diameters be a part of the input so that seal locations can be varied. This program is identified in the equations as B/N-6. The other program performs a force balance for any desired load on the thrust bearings and will then determine the diameters of the seal located on the exhaust side of the turbine. Seal length, thrust load, and rotor inlet seal spacing are required as inputs. This second program is identified as B/N-6-1.

These programs calculate the turbine design point performance as determined by the design point value of velocity ratio. The turbine diameter and basic nozzle dimensions are also calculated. Values of off design velocity ratio (U/C_0) can be input so that off design performance will be evaluated based on the turbine configuration determined from the design point calculation.

Parasitic losses such as disk friction, seal leakage, and seal friction are calculated so that a real turbine efficiency can be determined.

The seal leakage and seal friction losses are based on hydrostatic seal performance equations as supplied by Franklin Institute.

In both programs, the option of round nosed or sharp nosed blades can be selected. The nozzle loss coefficients used in the program are based on data from Reference 7.1.1 for round and sharp nosed blades at various incidence angles.

Following is a list of the equations used in the programs to calculate the turbine's performance. Figure 7.1.1 gives the symbols and nomenclature for these equations. Figure 7.1.2 shows the design point input and output data from the computer using the following equations.

Figure 7.1.3 shows the thermodynamic H-S diagram for the cycle and the velocity triangles through the turbine for the design and off design cases.

FIGURE 7.1.1
(page 1)
SYMBOLS AND NOMENCLATURES

Parameter	Symbol	FORTTRAN Symbol	Dimensions
Input Data			
1. Inlet pressure	P_0	PØ	psia
2. Inlet temperature	T_0	TØ	°F
3. Inlet enthalpy	H_0	HØ	BTU/lb
4. Rotor inlet pressure	P_1	P1	psia
5. Rotor inlet temperature	T_1	T1	°F
6. Rotor inlet enthalpy	H_1	H1P	BTU/lb
7. Rotor inlet specific volume	ν_1	V1P	ft ³ /lb
8. Rotor exit pressure	P_2	P2	psia
9. Rotor exit enthalpy	H_2	H2P	BTU/lb
10. Rotor exit specific volume	ν_2	V2P	ft ³ /lb
11. Rotor exit temperature	T_2	T2	°F
12. Condenser pressure	P_{cond}	PCOND	psia
13. Gas constant (steam)	R	R	ft/°F
14. Average steam viscosity (Seal 1)	μ_1	AMU1	lb/ft - hr
15. Average steam viscosity (Seal 2)	μ_2	AMU2	lb/ft - hr
16. Average steam viscosity (Seal 3)	μ_3	AMU3	lb/ft - hr
17. Condenser steam specific volume	ν_{cond}	VCOND	ft ³ /lb
18. Horsepower	HP	HP	-
19. Turbine speed	RPM	RPM	Rev/Min

FIGURE 7.1.1

(page 2)

SYMBOLS AND NOMENCLATURES

Parameter	Symbol	FORTRAN Symbol	Dimensions
Input Data			
20. Estimated turbine efficiency	η_E	EFFE	-
21. Nozzle coefficient	ψ_N	PSIN	-
22. Rotor coefficient	ψ_R	PSIR	-
23. Rotor blade exit angle	β_2	BETA2	Degrees
24. Rotor blade inlet angle	β_1	BETA1	Degrees
25. Disk friction coefficient	KW	AKW	-
26. Seal clearance	H	H	Inches
27. Seal radii (B/N-6 only)	R1, R2, R3, R4, R5, R6		Inches
28. Turbine tip thickness	B	B	Inches
29. Seal length	SL	SL	Inches
30. Seal spacing	SSP	SSP	Inches
31. Thrust load	TL	TL	Lbs
32. Blade shape option	OPT	OPT	Round nosed 0.0 Sharp nosed 1.0
33. Number of velocity ratio conditions	N	N	-
34. Velocity ratio	U/C_0	UCØ(I)	-

FIGURE 7.1.1
(page 3)

SYMBOLS AND NOMENCLATURES

Parameter	Symbol	FORTTRAN Symbol	Dimensions
Output Data			
35. Turbine tip velocity	U	U	ft/sec
36. Hydraulic efficiency	η_H	EFFH	-
37. Adiabatic head	H_{AD}	HAD	ft
38. Seal leakage	ξ_L	XISL	lb/sec
39. Turbine efficiency	η_T	EFFT	-
40. Nozzle arc of admission	ϵ_N	EPSIN	-
41. Rotor nozzle height	H_R	HR	Inches
42. Inlet nozzle angle	α	ALPHA	Degrees
43. Pitch diameter	D	D	Inches
44. Flow rate	\dot{w}	EMF	lb/sec
45. Disk friction loss	ξ_{DF}	XIDF	-
46. Seal friction loss	ξ_{SF}	XISF	-
47. Nozzle height in stator	H_N	HN	Inches
48. Nozzle area	A_N	AN	Inches
49. Arc of admission in rotor	ϵ_R	EPSIR	-

DESIGN POINT CALC. A = 10 X1 = .96

INPUT DATA

P0 = 140.0000 T0 = 890.0001 H0 = 1237.8 P = 95.0000 T1 = 818.001 HIP = 1202.8
 VIP = 4.9210 P2 = 50.0000 H2P = 1151.0 V2P = 8.3100 T2 = 741.0001
 PCOND = 2.000 R = 85.6000 AMU1 = 0.045300 AMU2 = 0.043300 AMU3 = 0.042500 VCON = 173.7300
 HP = 425.00 RPM = 12000.0 EFFE = 0.8145 PSIN = 0.9600 PSIR = 0.9600

BETA2 = 12.0000

BETA1 = 90.00 AKW = 0.000750 H = 0.0010 SL = 0.5000 SSP = 0.5000 TL = 400.00 B = 0.875

OPT = 0.0000

N = 10

OUTPUT DATA AT DESIGN POINT

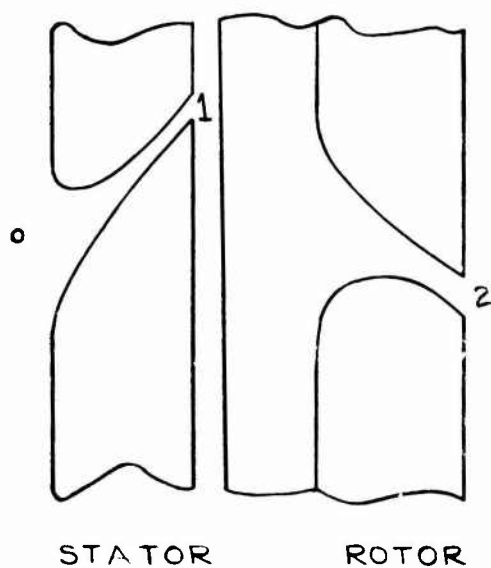
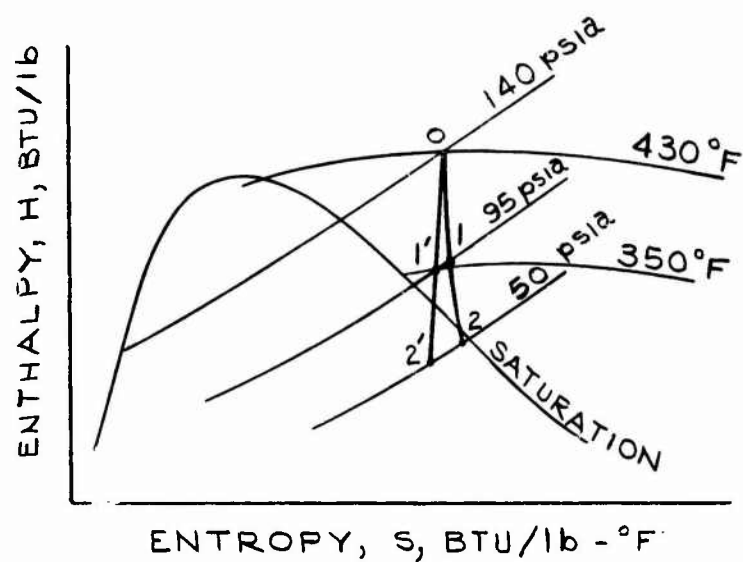
U = 1252.15	ALPHA = 10.18	XISF = 0.017407
EFFH = 0.8776	R1 = 11.197	HN = 0.2389
HAD = 67530.2	R3 = 12.197	AN = 3.2590
XISL = 0.010174	R5 = 10.336	EPSIR = 0.8740
EFFT = 0.8134	D = 23.8953	R2 = 11.697
EPSIN = 0.7464	EMF = 4.2495	R4 = 12.697
HR = 0.2389	XIDF = 0.037827	R6 = 10.836

OFF DESIGN OUTPUT DATA

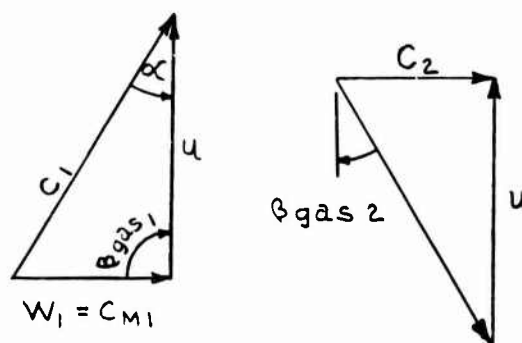
UC0	U	COEFF	EFFH	XIDF	XISL	XISF	EFFT	RGAS	RPM
0.600	1252.1	0.9999	0.8776	0.0380	0.0101	0.0174	0.81314	89.98	12025.2
0.100	208.6	0.3665	0.2553	0.0001	0.0101	0.0004	0.25209	12.16	2004.3
0.200	417.3	0.3888	0.4645	0.0014	0.0101	0.0019	0.45646	15.08	4008.7
0.300	626.0	0.4276	0.6292	0.0047	0.0101	0.0043	0.61376	19.76	6013.1
0.400	834.7	0.5087	0.7515	0.0112	0.0101	0.0077	0.72485	28.32	8017.4
0.500	1043.4	0.7453	0.8338	0.0220	0.0101	0.0121	0.79118	47.14	10021.8
0.650	1356.5	0.9095	0.8866	0.0483	0.0101	0.0205	0.80870	114.87	13028.3
0.700	1460.8	0.7453	0.8873	0.0604	0.0101	0.0237	0.79411	132.85	14030.5
0.800	1669.5	0.5087	0.8630	0.0902	0.0101	0.0310	0.73301	151.67	16034.9
0.900	1878.2	0.4276	0.8078	0.1284	0.0101	0.0393	0.63187	160.23	18039.3

FIGURE 7.1.2

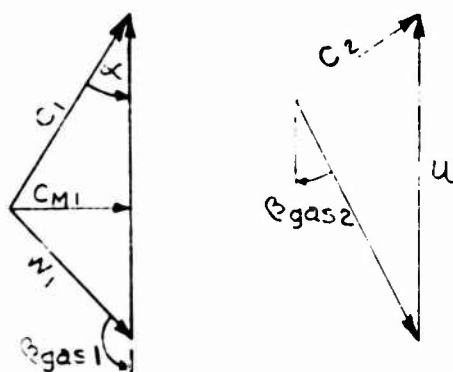
LVF TURBINE THERMODYNAMIC CYCLE AND VELOCITY DIAGRAMS



DESIGN POINT



$u/C_0 > \text{DESIGN VALUE}$



$u/C_0 < \text{DESIGN VALUE}$

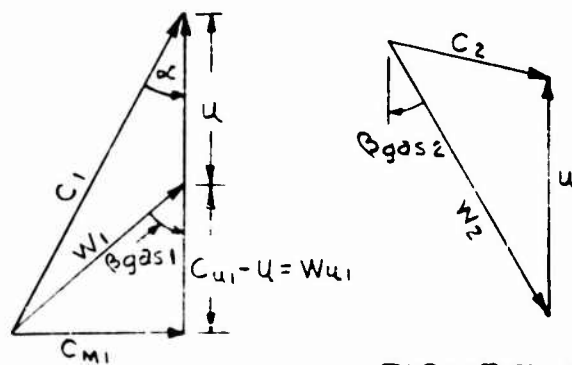


FIGURE 7.1.3

TURBINE PERFORMANCE EQUATIONS

Design Point Calculations

1. Nozzle spouting velocity

$$C_1 = \gamma_N \times 224 (H_0 - H_1')^{1/2}, \text{ FT./SEC.}$$

2. Stage spouting velocity

$$C_0 = 224 (H_0 - H_2'), \text{ FT./SEC.}$$

3. Tip speed

$$U = U/C_0 (C_0), \text{ FT./SEC.}$$

4. Inlet nozzle angle

$$\cos. \alpha = U/C_1$$

$$\alpha = \cos^{-1}(U/C_1), \text{ DEGREES}$$

5. Axial velocity into rotor

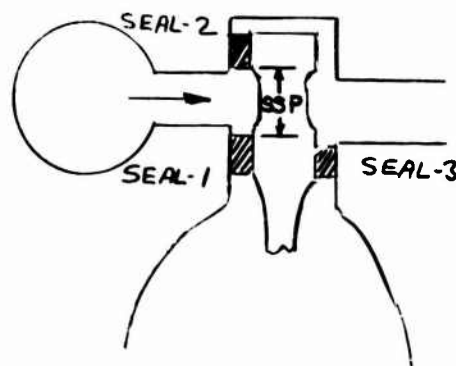
$$W_1 = C_{M1} = C_1 (1 - \cos^2 \alpha)^{1/2}, \text{ FT./SEC.}$$

6. Turbine pitch diameter

$$D = \frac{229 U}{\text{RPM}}, \text{ INCHES}$$

7. Inner radius of seal - 2 (B/N-6-1)

$$R_3 = \frac{(D + SSP)}{2}, \text{ INCHES}$$



8. Outer radius of seal - 2(B/N-6-1)

$$R_4 = R_3 + SL, \text{ INCHES}$$

9. Outer radius of seal - 1(B/N-6-1)

$$R_2 = R_3 - SSP, \text{ INCHES}$$

10. Inner radius of seal - 1(B/N-6-1)

$$R_1 = R_2 - SL, \text{ INCHES}$$

11. Outer radius of seal - 3(B/N-6-1)

$$CIP = \frac{(R_4^2 - R_3^2)(P_1 + P_2)}{2} + P_1(R_3^2 - R_2^2) + \frac{(R_2^2 - R_1^2)(P_1 + P_{COND})}{2}$$

$$C_2 = CIP - \left(\frac{TL}{3.1416} \right) + \frac{SL^2}{2(P_2 + P_{COND})} - P_2 R_4^2$$

$$C_3 = P_2 (SL) + P_{COND.} (SL)$$

$$R_6 = \frac{(C_3 + (C_3^2 - 4P_2C_2)^{1/2})}{2P_2}, \text{ INCHES}$$

12. Inner radius of seal - 3(B/N-6-1)

$$R_5 = R_6 - SL, \text{ INCHES}$$

13. Rotor hydraulic efficiency

$$W'_2 = (50100(H'_1 - H'_2) + \gamma_R^2 C_{M1}^2)^{1/2}$$

$$\eta_H = \frac{2U}{C_0^2} (\cos \beta_2 \gamma_R W'_2)$$

14. Flow rate

$$\dot{W} = \frac{HP (707)}{\eta_{TE} (H_0 - H'_2)}, \text{ LB/SEC}$$

15. Rotor exit density

$$\rho_{COND} = \rho'_2 = \frac{1}{\sqrt{C_{COND}}}, \text{ LB./FT.}^3$$

16. Adiabatic head

$$H_{AD} = (H_0 - H'_2) 778, \text{ FT.}$$

17. Disc friction loss

$$\xi_{DF1} = \left(\frac{2 K_w P_2 U^3}{144 \dot{w} H_{AD} 32.2 R_9^3} \right) (R_4^5 - R_6^5)$$

$$\xi_{DF2} = \left(\frac{.002 (3.1416) P_2 B D U^3}{18550 \dot{w} H_{AD}} \right)$$

$$\xi_{DF3} = \left(\frac{K_w P_{COND.} D^2 U^3}{4630 \dot{w} H_{AD}} \right)^{1/2}$$

$$\xi_{DF4} = (\xi_{DF3}) \left(\frac{2 R_5}{D} \right)^5$$

$$\xi_{DF \text{ TOTAL}} = \xi_{DF1} + \xi_{DF2} + \xi_{DF3} + \xi_{DF4}$$

18. Seal leakage

$$\Delta P_1 = (P_1^2 - P_{COND}^2)$$

$$\Delta P_2 = (P_1^2 - P_2^2)$$

$$CONST = \frac{3.1416 H^3}{144 R}$$

$$\dot{w}_{S.L.} = CONST \left[\left(\frac{\Delta P_1}{T_1 \gamma_1 \ln \frac{R_2}{R_1}} \right) + \left(\frac{\Delta P_2}{T_1 \gamma_2 \ln \frac{R_4}{R_3}} \right) \right] (16.7 \times 10^6)$$

LB/SEC.

$$\xi_{S.L.} = \frac{\dot{w}_{S.L.}}{\dot{w}}$$

19. Seal friction horsepower loss

$$A_1 = \pi(R_4^2 - R_3^2), \text{ IN.}^2$$

$$A_2 = \pi(R_2^2 - R_1^2), \text{ IN.}^2$$

$$A_3 = \pi(R_6^2 - R_5^2), \text{ IN.}^2$$

$$\tau_1 = \frac{\pi(R_4 + R_3) \text{ RPM } \mu_2}{60 H 16.7 \times 10^6}, \text{ LB.}$$

$$\tau_2 = \frac{\pi(R_2 + R_1) \text{ RPM } \mu_2}{60 H 16.7 \times 10^6}, \text{ LB.}$$

$$\tau_3 = \frac{\pi(R_5 + R_6) \text{ RPM } \mu_3}{60 H 16.7 \times 10^6}, \text{ LB.}$$

$$\text{TORQUE} = \frac{\tau_1 A_1 (R_4 + R_3)}{2} + \frac{\tau_2 A_2 (R_2 + R_1)}{2} + \frac{\tau_3 A_3 (R_5 + R_6)}{2}$$

$$\text{HP}_{S.F.} = \frac{6.28 \text{ TORQUE RPM}}{396000}$$

IN. - LBS.

$$\xi_{S.F.} = \frac{\text{HP}_{S.F.} 550}{\dot{W} \text{ HAD}}$$

20. Turbine efficiency

$$\eta_T = \eta_H (1 - \xi_{S.L.}) - (\xi_{DF} + \xi_{SF})$$

21. If $(\eta_{TE} - \eta_T) > .01$ then go back to Equation 14 and replace η_{TE} with η_T .

If $(\eta_{TE} - \eta_T) \leq .01$ then go to Equation 22.

22. Nozzle height

$$H_N = \frac{\dot{W} v_T' 144}{\pi D C_{M1}}, \text{ INCHES}$$

23. Arc of admission test

$$Y = H_N / D$$

IF $(Y - .01) > 0$ GO TO EQ. 25

IF $(Y - .01) \leq 0$ GO TO EQ. 24

24. Arc of admission

$$\epsilon_N = \frac{\dot{W} \sqrt{144}}{.01 D^2 \pi C_{M1}}$$

then $H_N = .01 D$, INCHES and go to Equation 25.

25. Rotor exit relative velocity

$$W_2 = \gamma_R W_2', \text{ FT/SEC.}$$

26. Rotor nozzle exit area

$$A_N = \frac{\dot{W} \sqrt{144}}{W_2}, \text{ IN.}^2$$

27. Rotor nozzle exit height

$$H_R = \frac{\dot{W} \sqrt{144}}{\pi D \sin \beta_2 W_2}, \text{ INCHES}$$

28. Rotor nozzle test

$$X = H_R / D$$

IF $(X - .01) \leq 0$

go to Equation 29

IF $(X - .01) > 0$

End of design point program

29. Rotor arc of admission

$$\epsilon_R = \frac{\dot{W} \sqrt{144}}{.01 D^2 \pi \sin \beta_2 W_2}$$

30. Rotor nozzle exit height

$$H_R = .01 D, \text{ INCHES}$$

(end of design point program)

Off Design Point Calculations

31. Tip speed at various off design velocity ratios

$$U = (U/C_0) C_0, \text{ FT/SEC.}$$

32. Tangential velocity relative to rotor tip speed

$$W_{U1} = C \cos \alpha C_1 - U, \text{ FT/SEC.}$$

33. Axial velocity into rotor

$$W_1 = (C_1^2 \sin^2 \alpha + W_{U1}^2)^{1/2}$$

34. Gas angle into rotor

$$\cos \beta_{GAS} = \frac{W_{U1}}{W_1}$$

35. Incidence angle of gas into rotor

$$\hat{U} = (\beta_1 - \beta_{GAS}), \text{ degrees}$$

36. Round and sharp nosed blades, incidence angle loss coefficient.

See Figure 7.1.4 for values of COEFF.

The computer program contains a curve fit for this function

37. Hydraulic efficiency

$$\eta_H = (2(U/C_0)^2) \left(W_{U1} \cos \beta_2 \psi_R (50100 (H'_1 - H'_2) + \psi_R^2 (\text{COEFF}(W_1^2))^{1/2} \right)$$

38. Disk friction loss

Same as Equation 17.

39. Seal leakage loss

Same as Equation 18

40. Seal friction horsepower loss

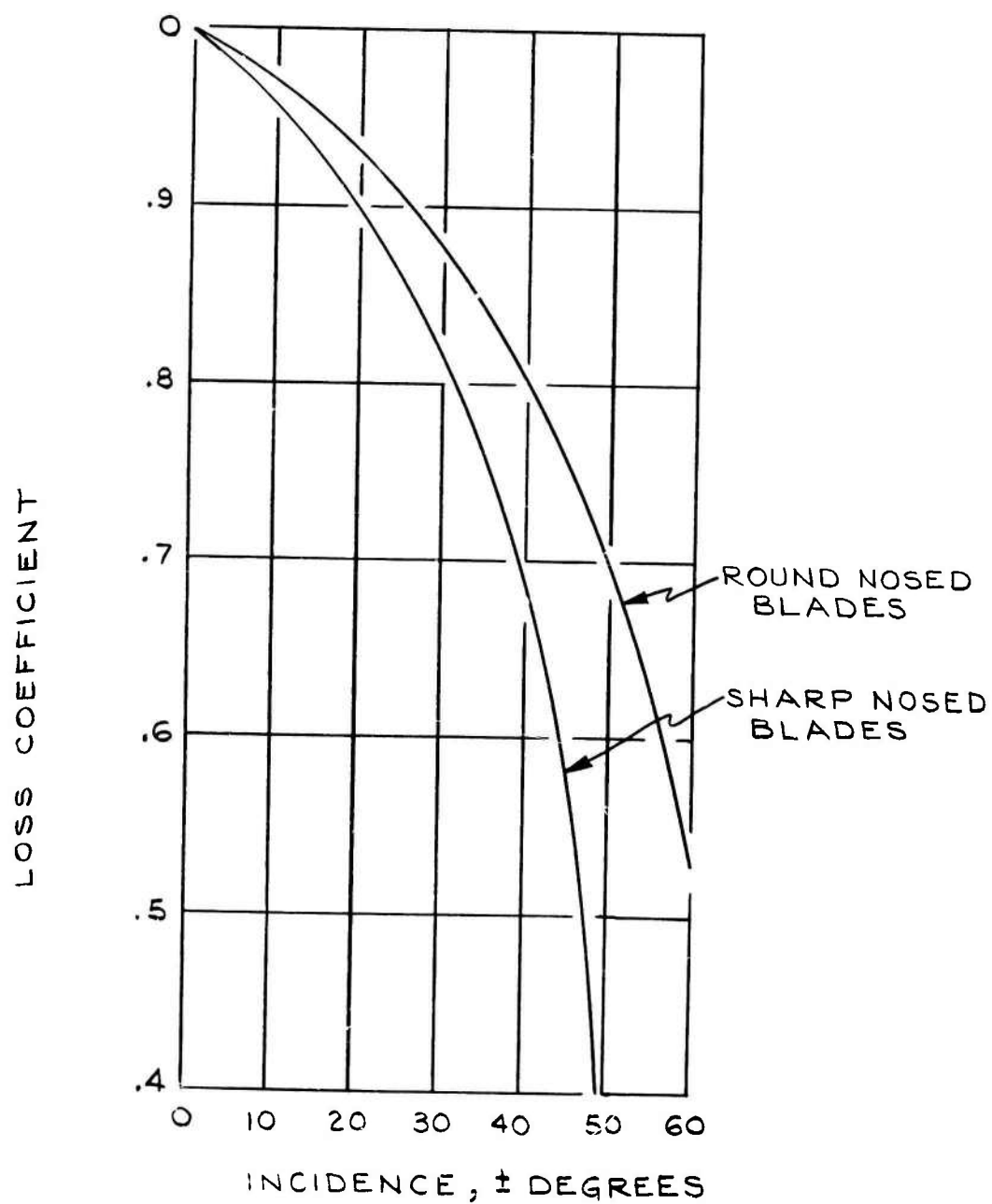
Same as Equation 19.

41. Turbine efficiency

$$\eta_T = \eta_H (1 - \xi_{SL}) - (\xi_{DF} + \xi_{SF})$$

End of off design program.

GAS INCIDENCE ANGLE
VS
LOSS COEFFICIENT
FOR ROUND AND SHARP NOSED
TURBINE BLADES



REF.: "PRINCIPLES OF TURBOMACHINERY" SHEPPARD
FIGURE 7.1.4

7.2 HEAT TRANSFER ANALYSIS

This section describes in detail the calculation procedures used to perform the heat transfer analysis on the LVF turbine. The methods of calculation of the heat transfer coefficients for the disk, cooling water and blades are described.

The derivation of the methods used to determine the disk and housing temperature gradients is presented along with the equations used in the digital computer program.

7.2.1 Disk Heat Transfer Coefficients

Based on the procedure of Reference 3.2.3, the local heat transfer coefficient, h , is a function of the local Reynolds number based on boundary layer momentum thickness, $N_{Re \theta}$, which is, in turn, a function of the local skin friction coefficient, C_f . To evaluate C_f , the local disk friction was calculated and then C_f was evaluated. This approach was used for the low pressure portion of the disk, and is described in detail below.

Conditions:

Pressure around disk - 2 psia

Estimated temperature around disk (based on previous calculation) - 255° F

Therefore, steam properties around disk: (Reference 3.2.15)

Specific volume, v	=	212 ft ³ /lb
Specific heat, C_p	=	.46 BTU/lb - °F
Conductivity, k	=	.015 BTU/ft - hr - °F
Viscosity, μ	=	.031 lb/ft - hr
Prandtl No. N_{pr}	=	0.94

7.2.1.1 Evaluate Disk Friction (Refer to Figure 3.2.3)

Disk Reynold No.

$$N_{Re} = \frac{D U}{v \mu} \frac{3600}{\pi}$$

where: D disk tip diameter, ft
 u disk tip speed, fps
 v specific volume, ft³/lb
 μ viscosity, lb/ft - hr

For the NPFO conditions:

$$D = 26 \text{ in.} = 2.16 \text{ ft.}$$

$$u = \frac{\pi N D}{60} = \frac{(12,000)(2.16)(\pi)}{60} = 1352 \text{ fps}$$

$$N_{Re} = \frac{(2.16)(1352)(3600)}{(212)(.031)} = 1.6 \times 10^6$$

using this Reynolds number, the disk friction coefficient, K_w , is found from the data of Reference 3.2.6 and Figure 3.2.3 as:

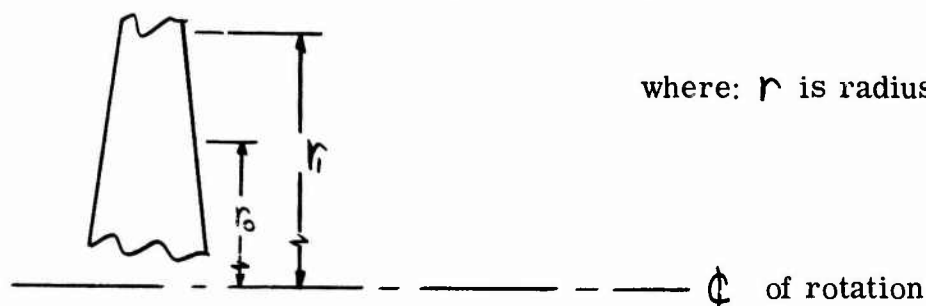
$$K_w = 0.00062$$

In the following calculations it is assumed that this disk friction coefficient applies regardless of the diameter of the segment being considered.

To obtain the disk friction, the following equation applies,

$$W_{DF} = \frac{K_w D^2 U^3}{g \nu} \quad (\text{Reference Figure 3.2.3})$$

Since the local disk friction is required, the symbols shown below are used:



where: r is radius, ft

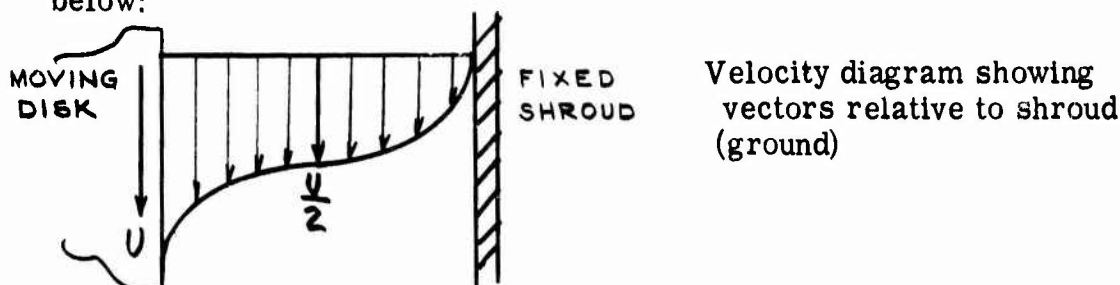
since: $D = 2r, \text{ FT.}$

$$U = \frac{N \pi 2r}{60}, \text{ FT./SEC.}$$

substituting this into the equation above yields:

$$\begin{aligned} W_{DF} &= \frac{K_w}{g \nu} 4 \left(\frac{N \pi 2}{60} \right)^3 (r_1^5 - r_0^5), \frac{\text{FT-LB}}{\text{SEC}} \\ &= \frac{(0.00062)(4)}{(32.2)(212)} \left[\frac{12000 \pi 2}{60} \right]^3 (r_1^5 - r_0^5) \\ &= 711 (r_1^5 - r_0^5), \frac{\text{FT-LB.}}{\text{SEC.}} \end{aligned}$$

This equation includes friction for both sides of a shrouded disk. This loss occurs in four boundary layers (two on disk and two on shroud) as shown below:



Therefore, when considering the disk or the shroud on the basis of a flat plate and a free stream, the local free stream velocity is equal to $U/2$. The results of these calculations are shown in Figure 3.2.3.

Using the approach of Reference 3.2.3 to obtain local heat transfer coefficients, first the local skin friction coefficient must be evaluated.

7.2.1.2 Evaluate Local Skin Friction

As defined in Reference 3.2.3: $C_f = \frac{2\tau_s v}{\bar{U}_s^2}$

where:

τ is the specific torque, lb/ft²
 \bar{U}_s is the average free stream velocity, fps

since: $U_s = U/2$, then:

$$\begin{aligned}\bar{U}_s^2 &= \frac{U_{s1}^2 + U_{s2}^2}{2} = \frac{U_1^2 + U_0^2}{8} \\ &= \frac{1}{8} \left(\frac{N\pi 2}{60} \right)^2 (r_1^2 + r_0^2) \\ &= 1.97 \times 10^{-5} (r_1^2 + r_0^2), \text{ FT./SEC.}\end{aligned}$$

To evaluate τ

$$\tau = \frac{F}{A}$$

$$A = \pi(r_1^2 - r_0^2), \text{ FT.}^2$$

and:

$$\frac{W_{DF}}{4} = F \left(\frac{2\pi N}{60} \right) \left(\frac{r_1 + r_0}{2} \right), \frac{\text{FT-LB}}{\text{SEC.}}$$

therefore:

$$F = \frac{W_{DF} (60)}{(4)(2) \pi N \left(\frac{r_1 + r_0}{2} \right)} = 1.99 \times 10^{-4} \frac{W_{DF}}{\left(\frac{r_1 + r_0}{2} \right)}, \text{ LB.}$$

then:

$$\tau = \frac{1.99 \times 10^{-4} W_{DF}}{\pi (r_1^2 - r_0^2) \left(\frac{r_1 + r_0}{2} \right)}, \text{ LB./FT.}^2$$

Substituting these equations into the skin friction coefficient equation yields:

$$\begin{aligned} C_f &= \frac{(2)(1.99 \times 10^{-4}) W_{DF} (32.2) (212)}{\pi (r_1^2 - r_0^2) \left(\frac{r_1 + r_0}{2} \right) 1.92 \times 10^5 (r_1^2 + r_0^2)} \\ &= \frac{418 W_{DF}}{(r_1^2 - r_0^2) \left(\frac{r_1 + r_0}{2} \right) (r_1^2 + r_0^2)} \end{aligned}$$

7.2.1.3 Evaluation of Film Coefficient

After calculation of the local C_f , the local Reynolds number based on boundary layer momentum thickness, $N_{Re\theta}$, is evaluated from Figure 6 of Reference 3.2.3 as a function of C_f , then from Figure 8 of Reference 3.2.3, the local Stanton number, N_{ST} , is evaluated as a function of $N_{Re\theta}$.

The Stanton number is:

$$N_{ST} = \frac{h \sqrt{\delta}}{C_{P\delta} \bar{U}_\delta}$$

where:

h = film coefficient, BTU/hr - ft² - °F

δ = denotes fluid properties in the free stream

then:

$$h = \frac{N_{ST} C_{P\delta} \bar{U}_\delta}{\sqrt{\delta}}$$

substituting known values and previous equations yields:

$$\begin{aligned} h &= \frac{(46)(1.92 \times 10^5)(r_1^2 + r_0^2) N_{ST}}{212} \\ &= 427(r_1^2 + r_0^2) N_{ST}, \text{ BTU/HR.-FT.}^2 \text{ °F} \end{aligned}$$

The results of these calculations are shown in Figure 3.2.2.

7.2.2 Cooling Water Heat Transfer Coefficient

The disk shroud and the turbine tip is cooled by water flow through these areas. The water conditions are: temperature 130°F, and flow rate 4.3 lb/sec.

7.2.2.1 Disk Shroud Cooling

The configuration selected is shown in Figure 3.2.1. One-half of the total flow is directed to each side of the turbine through three coils of 0.45 in. I.D. tubing.

Overall temperature rise of water:

$$\Delta T_{H_2O} = \frac{Q_{DF}}{(\dot{W} C_P)_{H_2O}}$$

where:

Q_{DF} = is disk friction heat input, BTU/sec

\dot{W}_{H_2O} = is water flow rate, lb/sec.

$C_{P_{H_2O}}$ = is water specific heat, BTU/lb - °F

Then:

$$\Delta T_{H_2O} = \frac{.593}{(4.3)(1.0)} = 0.138^\circ F$$

This temperature rise is insignificant, therefore, all water properties are evaluated at 130°F. Therefore, from Reference 3.2.15, for 255°F water:

Density, $\rho = 49 \text{ lb/ft}^3$

Thermal conductivity $K = .4 \text{ BTU/hr - ft - }^\circ F$

Specific heat $C_P = 1.0 \text{ BTU/lb - }^\circ F$

Viscosity $\mu = 0.5 \text{ lb/hr - ft}$

Prandtl No $N_{PR} = 1.3$

Tube Reynolds number is:

$$N_{Re} = \frac{D G}{\mu}$$

where:

$$G = \frac{\dot{W}}{A} = \frac{(4.3)(3600)(4)(144)}{(2)(\pi)(.45)^2} = 2.58 \times 10^6 \text{ LB/HR-FT}^2$$

then:
$$N_R = \frac{(0.45)(2.58 \times 10^6)}{(12)(0.5)} = 1.935 \times 10^5$$

the film coefficient can be obtained from Reference 3.2.14 for Prandtl numbers from 0.7 to 120 and L/D greater than 60 as:

$$\begin{aligned} h &= \frac{K}{D} 0.023 (N_{Re})^{0.8} (N_{Pr})^{0.4} \text{ BTU/HR-FT}^2 \text{ } ^\circ\text{F} \\ &= \frac{(0.4)(12)(0.023)(1.935 \times 10^5)^{0.8} (1.3)^{0.4}}{(0.45)} \\ &= 4610 \text{ BTU/HR-FT}^2 \text{ } ^\circ\text{F} \end{aligned}$$

Pressure drop in the tube, using the procedure of Reference 3.2.14:

$$\Delta P = \frac{f G^2 L}{2g(D/2) \rho 3600^2}$$

where:

f is the friction factor

L is the tube length, ft

$f = .00475$ as function of N_R (Figure 6 - 11 of Reference 3.2.14), then:

$$\begin{aligned} \Delta P &= \frac{(.00475)(2.58 \times 10^6)^2 (21)(12)(2)}{(2)(32.2)(.45)(59)(3600)^2} \\ &= 718 \frac{\text{LB.}}{\text{FT}^2} = 5.0 \text{ PSI} \end{aligned}$$

7.2.2.2 Tip Cooling

The flow passage for the disk tip cooling water has cross sectional dimensions of 0.375 by 0.50 inch. The water is introduced to the chamber where the flow splits and flows to the opposite side of the turbine and is collected for passage to the boiler. Therefore, one-half of the total flow passes through each half of the turbine housing.

The heat transfer analysis was identical to that for the shroud cooling situation above. Using the approach presented above, the following results were obtained:

$$\Delta T_{H_2O} = \frac{Q_{DF} + Q_{SF} + Q_L}{(\dot{W} C_p)_{H_2O}}$$

where:

Q_{SF} = heat due to seal friction BTU/sec

Q_L = heat due to leakage flow BTU/sec

$$\Delta T_{H_2O} = \frac{2.8 + 2.77 + .8}{(4.3)(1)} = 1.8^\circ F$$

$$G = 2.18 \times 10^6 \text{ LB/HR-FT}^2$$

$$N_R = \frac{(.534)(2.18 \times 10^6)}{(12)(0.5)} = 1.95 \times 10^5$$

$$h = \frac{(0.4)(12)}{(.534)} (.023)(1.95 \times 10^5)^{.8} (1.3)^{.4}$$

$$= 3780 \text{ BTU/HR-FT}^2 \cdot ^\circ F$$

$$\Delta P = \frac{(.00474)(2.18 \times 10^6)^2 (1.9)(12)(2)}{(2)(32.2)(.534)(59)(3600)^2}$$

$$= 38.9 \text{ LB/FT}^2 = 0.27 \text{ PSI}$$

7.2.3 Blade and Nozzle Heat Transfer Coefficients

The blade heat transfer coefficients were calculated based on an unpublished empirical relationship developed by the authors. This calculation must be made using fluid properties which are relative to the rotor. That is, the temperature and pressure which is affecting the rotor is not the same as that affecting the nozzle because of the velocity of the rotor. Therefore, all values are calculated on the basis of the rotor being fixed and the housing rotating; these values are termed relative values.

The relative total pressure entering the rotor is equal to the static pressure of the nozzle exit, 95 psia. The relative total temperature is defined by the total energy equation as:

$$T_{OR} = T_s + \frac{V_{R0}^2}{2gJc_p}, \text{ } ^\circ R$$

where:

T_{OR} = total temperature relative to blade, $^\circ R$

T_s = static temperature relative to blade, $^\circ R$

V_{R0} = relative velocity entering blade, fps

c_p = specific heat, BTU/lb - $^\circ F$

J = conversion factor, 778 ft - lb/BTU

The static temperature relative to the blade is equal to the static temperature leaving the nozzle assuming an adiabatic process. Therefore, the nozzle exit static temperature is evaluated using Mach number functions of Reference 3.2.16 based on the nozzle pressure ratio:

Since the nozzle pressure ratio is:

$$PR = \frac{140}{95} = 1.472$$

which yields:

$$\left. \begin{array}{l} M = 0.79 \\ T_0/T_s = 0.914 \end{array} \right\} @ \gamma = 1.3$$

where:

M = Mach number

T_0 = total temperature entering nozzle, $^\circ R$

γ = ratio of specific heats.

Since the nozzle function is to reach wheel velocity only and neglecting the axial component, then:

$$V_{R0} = 0$$

and

$$T_{0R} = (.914)(430 + 460) = 814^{\circ}R = 354^{\circ}F$$

This temperature is used to evaluate the fluid properties: (from Reference 3.2.15)

$$\nu = 4.86 \text{ ft}^3/\text{lb}$$

$$\mu = .037 \text{ lb/ft} \cdot \text{hr}$$

$$K = .0175 \text{ BTU/hr} \cdot \text{ft} \cdot ^{\circ}F$$

$$C_p = .48 \text{ BTU/lb} \cdot ^{\circ}F$$

$$N_{PR} = .9?$$

Based on unpublished empirical data of the authors:

$$h = \frac{\bar{V}_R C_p N_{ST} 3600}{\nu}$$

where:

\bar{V}_R = average relative velocity through blade, fps

N_{ST} = Stanton number

and

$$N_{ST} = \frac{C}{N_{Re}^{.27} N_{PR}^{.667}}$$

Where:

$C = 0.08$ for typical turbine blades

N_{Re} = Reynolds number based on chord,

and

$$N_{Re} = \frac{\bar{V}_R Ch 3600}{\nu \mu}$$

where Ch blade chord, ft.

The blade exit relative velocity is calculated in a manner based on Mach number functions. These functions are presented in Reference 3.2.16. The basic known parameters are:

$$\text{Inlet relative total pressure} \quad P = 95 \text{ psia}$$

$$\text{Exit static pressure} \quad P = 50 \text{ psia}$$

$$\text{Ratio of specific heats} \quad \gamma = 1.3$$

$$\text{Inlet relative total temperature} \quad T = 354^{\circ}\text{F}$$

Therefore, $PR_R = \frac{95}{50} = 1.9$, which yields a pressure ratio slightly greater than critical (1.83); therefore, assume sonic exit velocity so that:

$$V_{R\text{EXIT}} = \sqrt{\gamma g R T} = \sqrt{(1.3)(32.2)\left(\frac{1545}{78}\right)(814)} \\ = 1710 \text{ FT./SEC.}$$

since:

$$\bar{V}_R = \frac{V_{R\text{INLET}} + V_{R\text{EXIT}}}{2} = \frac{0 + 1710}{2} \\ = 855 \text{ FT./SEC.}$$

$$N_{Re} = \frac{(855)(3600)(0.625)}{(4.86)(.037)(12)} = 8.88 \times 10^5$$

then

$$N_{ST} = \frac{0.08}{(8.88 \times 10^5)^{.27} (.92)^{.667}} = .00211$$

and

$$h = \frac{(855)(.48)(.00211)(3600)}{4.86} = 642 \text{ BTU/HR-FT}^2\text{-}^{\circ}\text{F}$$

7.2.4 Seal Analysis

The seals were analyzed to evaluate the seal temperature, friction, and leakage flow rate. The seal friction and leakage flow rate were evaluated from equations presented in a previous section and the values pertinent to the seal temperature analysis are presented in Table 6.2.1.

To obtain an idea of the maximum temperature that the seal could ultimately approach (uncooled), a calculation was made assuming that all the seal friction loss was added to the seal leakage flow. The heat balance is:

$$W_{SF} = 2545 = Q_S C_{PS} \Delta T_S 3600$$

or

$$\Delta T_S = \frac{W_{SF} 2545}{Q_S C_{PS} 3600}, \text{ } ^\circ\text{F}$$

Where:

W_{SF} = seal friction loss, HP

Q_S = seal leakage, lb/sec

C_{PS} = specific heat, BTU/lb - $^\circ\text{F}$

An example calculation for Seal #1 and the information presented in Table 6.2.1 is:

$$\Delta T_S = \frac{(3.97)(2545)}{(.01613)(.5)(3600)} = 347^\circ\text{F}$$

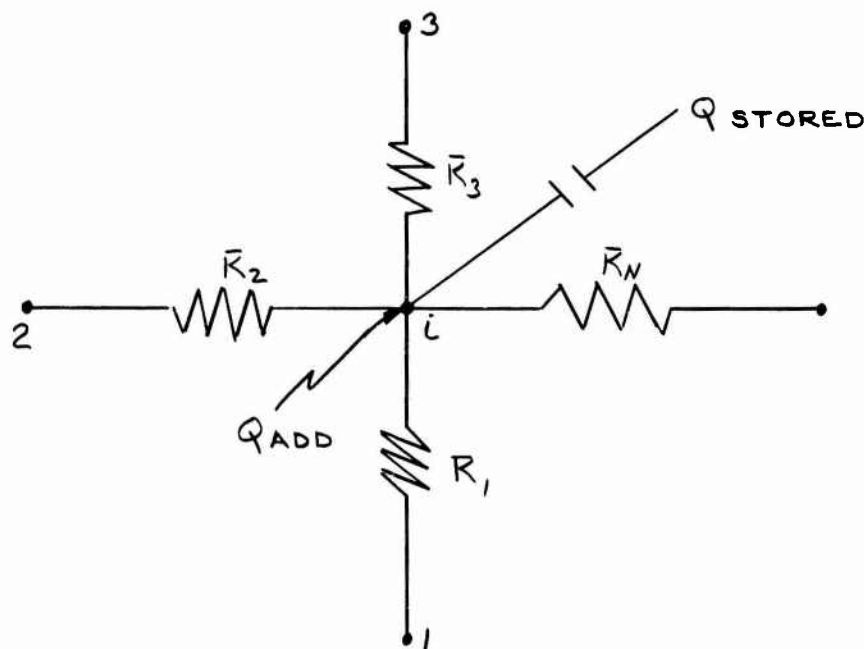
This temperature rise is much greater than will actually occur, as will be shown later, since much of the heat will be carried off from the seal area to cooled areas of the turbine.

7.2.5 Temperature Calculations

The heat transfer analysis of the turbine disk and shroud area and the turbine housing nozzle and disk tip area, due to the complexity of the geometry, used a numerical analysis technique to determine the steady state temperature gradients through these components.

The first step in the analysis is to divide the section to be analyzed into small elements. The smaller the element, the more accurate the results; however, more computer time and capacity will be used.

An energy balance was made on a single element, assuming that the average temperature of the element can be represented by a temperature at the center of the element. The element can also be thought of as a point surrounded by adjacent elements connected to the element of interest by conductances so that the total system is analogous to an electrical network. The sketch shown below shows the network about one given node or element.



The energy balance on i

$$Q_{\text{add}} = Q_{\text{stored}} + Q_{\text{out}}$$

$$Q_{\text{STORED}} = \rho C_p A (\Delta x) \frac{dT_i}{dt} = C_i \frac{dT_i}{dt}$$

C_i = Heat capacity or capacitance of i

ρ = Density

C_p = Specific heat

$$A(\Delta x) = \text{Volume}$$

$$\frac{\Delta T_i}{\Delta \tau} = \text{Change of temperature with respect to time.}$$

The heat leaving node i (Q_{out}) is expressed as the conductance multiplied by the temperature difference between node i and its adjacent node as shown below.

$$Q_{\text{out}} = \bar{K}_N (T_i - T_N)$$

The conductance (\bar{K}_N) can represent either conduction, convection, or radiation heat transfer. For this analysis, radiation was neglected so that only conduction and convection were used to transfer heat in the system. These conductances are defined as follows:

$$\bar{K}_{\text{conduction}} = \frac{KA}{\Delta x}, \text{ BTU/HR-}^\circ\text{F}$$

$$\bar{K}_{\text{convection}} = hA, \text{ BTU/HR-}^\circ\text{F}$$

where:

K = thermal conductivity of the connecting material

A = heat transfer area

Δx = distance between two nodes

h = convection heat transfer coefficient

An approximation of the derivative of temperature with respect to time can be made with a finite difference equivalent.

$$\frac{\Delta T}{\Delta \tau} \cong \frac{T_i^{\tau+\Delta\tau} - T_i^{\tau}}{\Delta \tau}$$

The superscripts in the above equation refer to time where $(\tau + \Delta\tau)$ will be used as the "new" time and (τ) will be used as the "old" time.

In this analysis, the following assumptions are made:

1. The system temperatures are known at the "old" time.
2. The conductance values (\bar{K}_N) are based on the old temperature.
3. The capacitor values are based on the "old" temperatures.

The energy balance on node i can now be rewritten:

$$\begin{aligned} Q_{ADD} &= Q_{STORED} + Q_{OUT} \\ &= C_i \frac{dT_i}{dt} + \sum_N \bar{K}_N (T_i^T - T_N^T) \\ &= C_i \frac{T_i^{T+\Delta T} - T_i^T}{\Delta T} + \sum_N \bar{K}_N (T_i^T - T_N^T) \end{aligned}$$

where: $\sum_N \bar{K}_N (T_i^T - T_N^T)$ = sum of the conductances times the temperature difference about node (i).

Rearranging

$$\begin{aligned} T_i^{T+\Delta T} - T_i^T &= \frac{\Delta T}{C_i} (Q_{ADD} - \sum_N \bar{K}_N (T_i^T - T_N^T)) \\ &= \frac{\Delta T}{C_i} Q_{ADD} - \frac{\Delta T}{C_i} \sum_N \bar{K}_N T_i^T + \frac{\Delta T}{C_i} \sum_N \bar{K}_N T_N^T \end{aligned}$$

$$(1) \quad T_i^{T+\Delta T} = T_i^T \left(1 - \frac{\Delta T \sum_N \bar{K}_N}{C_i} \right) + \frac{\Delta T}{C_i} \left(Q_{ADD} + \frac{\sum_N \bar{K}_N T_N^T}{60} \right)$$

where: $T_i^{T+\Delta T}$ = Temperature of node i at the "new" time, $^{\circ}\text{F}$

T_i^T = Temperature of node i at the "old" time, $^{\circ}\text{F}$

ΔT = Time increment, minutes

C_i = Capacitance of node i , $\text{BTU}/^{\circ}\text{F}$

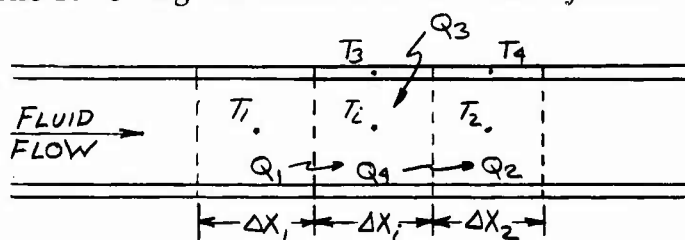
$\sum_N \bar{K}_N$ = Sum of the conductances into node i , $\text{BTU}/\text{hr} - ^{\circ}\text{F}$

Q_{ADD} = Heat addition to node i , BTU/min

This is the equation used in the digital computer program to compute the temperature of each node in order of input at the "new" time.

As mentioned in Section 3.2.1, there are several nodes in the systems analyzed where the conductances between the nodes represent a fluid flow situation. For this case it is assumed that there is no axial conduction in the fluid and that the film coefficient between the fluid and the passage wall is known.

The following sketch shows the fluid system.



A heat balance on node i gives:

$$Q_1 - Q_2 + Q_3 = Q_4$$

$$Q_1 = \rho V_{\text{VELOCITY}} A C_P \frac{T_1 + T_i}{2} = \text{Energy flow into the control volume due to the fluid flow.}$$

$$Q_2 = \rho V_{\text{VELOCITY}} A C_P \frac{T_i + T_2}{2} = \text{Energy flow out of the control volume due to the fluid flow.}$$

$$Q_3 = h P \Delta X (T_3 - T_i) = \text{Convective heat transfer.}$$

$$Q_4 = \rho A \Delta X C_v \frac{dT_i}{dt} = \text{Internal energy change.}$$

where: A = cross sectional area of tube passage

P = perimeter of inside of tube

For simplification let

$$\bar{K}_f = \rho V_{\text{VELOCITY}} A C_P$$

$$\bar{K}_{\text{CONVECTION}} = h P \Delta X$$

$$C = \rho A \Delta X C_v$$

The equation is therefore

$$\bar{K}_f \frac{(T_1 + T_i)}{2} - \bar{K}_f \frac{(T_i + T_2)}{2} + \bar{K}_{\text{CONVECTION}} (T_3 - T_i) = C_i \frac{dT_i}{dt}$$

$$(2) \quad \bar{K}_f \left(\frac{1}{2} \right) (T_1 - T_2) + \bar{K}_{\text{CONVECTION}} (T_3 - T_i) = C_i \frac{dT_i}{dt}$$

This equation shows that T_i is a function of downstream temperature (2). Since conduction in the fluid stream was neglected, T_i should be insensitive to downstream temperatures. This problem can be overcome by assuming the axial temperature gradient along the fluid is linear between nodes 1 and 2. This allows the following substitution.

$$\frac{T_1 - T_2}{2 \Delta X} = \frac{T_1 - T_i}{\Delta X}$$

$$\frac{1}{2}(T_1 - T_2) = (T_1 - T_i)$$

Therefore, Equation (2) can be rewritten

$$(3) \quad \bar{K}_f (T_1 - T_i) + \bar{K}_{CONVECTION} (T_3 - T_i) = C_i \frac{\partial T_i}{\partial \tau}$$

Equation (3) is now independent of downstream temperatures. This equation shows that the heat exchange between nodes i and 2 is one way. In other words the temperature of node 2 is affected by the temperature of node i but node i's temperature is unaffected by node 2. This must be taken into account in the program when handling the conductances of the fluid nodes.

So far it has been assumed that the spacing (ΔX), between the fluid nodes has been equal. In the real case this may not be necessarily so. Referring back to the previous sketch, let the fluid temperature entering node (i) be $T_{i,1}$ and the temperature leaving node (i) be $T_{i,2}$. These temperatures are at the nodes interfaces. Then applying a heat balance on node (i), we have

$$\rho V_{ELOCITY} A C_P (T_{i,1} - T_{i,2}) + h P \Delta X_i (T_3 - T_i) = \rho A \Delta X_i C_P \frac{\partial T_i}{\partial \tau}$$

or

$$\rho V_{ELOCITY} A C_P \left(\frac{T_{i,1} - T_{i,2}}{\Delta X_i} \right) + h P (T_3 - T_i) = \rho A C_P \frac{\partial T_i}{\partial \tau}$$

It was assumed that the axial temperature gradient is linear in the range T_1 to $T_{i,2}$ so that the following approximation can be made:

$$\frac{T_{i,1} - T_{i,2}}{\Delta X_i} \simeq \frac{T_1 - T_i}{\frac{\Delta X_1}{2} + \frac{\Delta X_i}{2}}$$

Substituting back into Equation (3) and multiplying by ΔX_i

$$\rho V_{ELOCITY} A C_P \left(\frac{2 \Delta X_i}{\Delta X_i + \Delta X_1} \right) (T_1 - T_i) + h P \Delta X_i (T_3 - T_i) = \rho A \Delta X_i C_P \frac{\partial T_i}{\partial \tau}$$

and therefore
$$\bar{K}_f = \rho_{\text{Velocity}} A C_p \left(\frac{2 \Delta X_i}{\Delta X_i + \Delta X_1} \right)$$

The value of \bar{K}_f is evaluated as a one way conductor for all the fluid nodes in the system.

Equation (1) was programmed using Fortran-4, for use in an available IBM-1130 digital computer. The program was set up for a maximum capability of 30 nodes. Figure 7.2.1 gives a list of the input-output symbols and dimensions with their Fortran equivalents. Figure 7.2.1 also contains the input data for the disk and shroud heat transfer analysis.

Figures 7.2.2 and 7.2.3 give the conductances used for the disk and housing analyses, respectively.

The program operates on a forward differencing technique where an initial set of temperatures are input at time zero. The computer increments time by a fixed input value and calculates the temperatures at the new time. The program then stores these temperatures and uses them as "old" temperatures for the calculation at the next time increment. The calculation will proceed to the limits of the program (30,000 sets of calculations) or until steady state temperature is reached and the operator stops the program.

Data printout can be obtained by switching data switch 10 to the ON position. Data is printed out as time versus temperature.

Figure 7.2.4 shows a flow diagram of the program. As mentioned previously, the capacitance values used in the analysis are not the real values, so that transient data will be invalid. If the real values were used the computer time would be excessive when the time increment is set according to the stability criteria of:

$$\Delta \tau \leq \left(\frac{C}{\sum_N \bar{K}_N} \right)_{\text{minimum}}$$

If this criteria is exceeded, the computation will oscillate or diverge.

FIGURE 7.2.1

HEAT TRANSFER PROGRAM

LIST OF SYMBOLS

Item	SYMBOLS		Units	Disk Analysis Input Data
	Derivation	FORTRAN		
Input Data				
1. Total no. of conduc- tor chords	-	KONT	-	
2. Number of nodes	-	M	-	28
3. Time increment	$\Delta \tau$	DTAU	Min.	1.0
4. Heat added	Q_{Add}	Q(I)	BTU/Min	(see text)
5. Initial tempera- tures	T_i	T(I)	$^{\circ}\text{F}$	130 $^{\circ}\text{F}$ except for fixed temp. nodes
6. Sum of the conductors about node i	$\sum_N \bar{K}_N$	SUMK(I)	BTU/hr- $^{\circ}\text{F}$	As determined from Figure 7.2.2
7. Capaci- tance of node i	C_i	CAP(I)	BTU/ $^{\circ}\text{F}$	1.0 except for fixed temp. nodes
8. Conduc- tance between nodes	$\bar{K}_f, \bar{K}_{Cond.}$	CONDI(IX, JND)	BTU/hr- $^{\circ}\text{F}$	See Figure 7.2.2
9. Node adjacent to node i	-	KADJ(IY, L)	-	See Figure 7.2.2

FIGURE 7.2.2
(page 1)
DISK HEAT TRANSFER ANALYSIS
NODE CONDUCTANCES

Node Connector	ΔX in.	Area in. ²	Conductance, \bar{K} , BTU/Hr - °F			
			Convection	Conduction	Fluid	Total
1 - 24	.023	1.6	.0896	8.4	-	.0885
1 - 26	.031	1.6	-	6.25	0.356	.337
2 - 1	.031	1.6	-	-	0.356	.356
2 - 19	.039	1.9	0.0712	5.74	-	.070
2 - 21	.093	1.9	-	2.47	-	2.47
3 - 2	1.133	.184	-	-	1.089	1.089
3 - 14	.062	2.28	.0985	5.34	-	.097
3 - 16	.109	2.28	-	2.53	-	2.53
4 - 3	1.125	.206	-	-	1.445	1.445
4 - 9	.070	2.59	.126	5.38	-	.123
4 - 11	.133	2.59	-	2.83	-	2.83
5 - 4	1.14	.264	-	-	2.08	2.08
5 - 10	.096	2.88	.182	3.62	-	.174
5 - 6	.156	1.43	-	1.33	-	1.33
6 - 5	.156	1.43	-	1.33	4.16	1.01
6 - 7	.554	3.0	.167	16.78	-	.165
7 - 6	.554	3.0	.167	16.78	-	.165
7 - 12	1.133	.64	-	1.745	-	1.745
8 - 9	.594	2.55	-	7.88	-	7.88
8 - 13	1.109	.736	-	1.22	-	1.22
8 - 15	1.125	.605	-	.99	-	.99
9 - 4	.070	2.59	.126	5.38	-	.123
9 - 8	.594	2.55	-	7.88	-	7.88
9 - 10	1.14	.715	-	1.152	-	1.152
9 - 14	1.125	.806	-	1.315	-	1.315
10 - 5	.096	2.88	.182	3.62	-	.174
10 - 9	1.14	.715	-	1.152	-	1.152
10 - 15	.843	2.96	-	6.45	-	6.45
10 - 20	1.156	1.54	-	2.44	-	2.44
11 - 4	.133	2.59	-	2.83	-	2.83
11 - 6	1.133	.363	-	-	3.24	3.24
11 - 12	.266	2.59	.126	30.1	-	.126
12 - 7	1.133	.64	-	1.745	-	1.745
12 - 11	.266	2.59	.126	30.1	-	.126
12 - 17	1.117	.57	-	1.575	-	1.575
13 - 8	1.109	.736	-	1.22	-	1.22
13 - 14	.781	2.25	-	5.28	-	5.28
13 - 18	1.125	.80	-	1.305	-	1.305
14 - 3	.062	2.28	.0985	5.34	-	.097
14 - 9	1.125	.806	-	1.315	-	1.315
14 - 13	.731	2.25	-	5.28	-	5.28

FIGURE 7.2.2
(page 2)
DISK HEAT TRANSFER ANALYSIS
NODE CONDUCTANCES

Node Connector	ΔX in	Area in. ²	Conductance, \bar{K} , BTU/Hr - °F			
			Convection	Conduction	Fluid	Total
14 - 19	1.14	.86	-	1.383	-	1.383
15 - 8	1.125	.605	-	.99	-	.99
15 - 10	.843	2.96	-	6.45	-	6.45
15 - 25	1.156	1.115	-	1.77	-	1.77
16 - 3	.109	2.28	-	2.53	-	2.53
16 - 11	1.125	.226	-	-	1.83	1.83
16 - 17	.515	2.7	.126	16.2	-	.125
17 - 12	1.117	.57	-	1.575	-	1.575
17 - 16	.515	2.70	.126	16.20	-	.125
18 - 13	1.125	.80	-	1.305	-	1.305
18 - 19	.757	1.9	-	4.62	-	4.62
18 - 23	1.14	.838	-	1.35	-	1.35
19 - 2	.039	1.9	.0712	5.74	-	.070
19 - 14	1.14	.86	-	1.383	-	1.383
19 - 18	.757	1.9	-	4.62	-	4.62
20 - 10	1.156	1.54	-	2.44	-	2.44
20 - 25	.406	3.27	-	14.78	-	14.78
21 - 2	.093	1.9	-	2.47	-	2.47
21 - 16	1.125	.156	-	-	1.093	1.093
21 - 22	.50	1.9	.0713	11.75	-	.071
22 - 17	1.125	.46	-	1.263	-	1.263
22 - 21	.50	1.9	.0713	11.75	-	.071
22 - 27	1.14	.395	-	1.07	-	1.07
23 - 18	1.14	.838	-	1.35	-	1.35
23 - 24	1.15	1.6	-	2.55	-	2.55
23 - 28	3.218	.662	-	.378	-	.378
24 - 1	.023	1.6	.0896	8.4	-	.0885
24 - 19	1.156	.86	-	1.367	-	1.367
24 - 23	1.15	1.6	-	2.55	-	2.55
24 - 28	3.062	.65	-	.389	-	.389
25 - 15	1.156	1.115	-	1.77	-	1.77
25 - 20	.406	3.27	-	14.78	-	14.78
26 - 1	.031	1.6	-	6.25	-	6.25
26 - 21	1.14	.079	-	-	.469	.469
26 - 27	.492	1.6	.0896	11.0	-	.0888
27 - 22	1.14	.395	-	1.07	-	1.07
27 - 26	.492	1.6	.0896	11.0	-	.0888
28 - 24	3.062	.65	-	.389	-	.389
28 - 23	3.218	.662	-	.378	-	.378

FIGURE 7.2.3

(page 1)

TURBINE HOUSING HEAT TRANSFER ANALYSIS
CONDUCTOR VALUES

Node Connector	ΔX in.	Area in ²	Conductance, \bar{K} , BTU/hr - °F					Total
			Convection	Conduction Solid	Conduction Steam	Fluid	Joint	
1-8	1.7	2.58	4.85	9.759	-	-	-	3.24
1-7	1.7	2.4	4.5	5.4	-	-	-	2.46
1-11	0.2	6.4	4.19	288	-	-	-	4.13
1-12	0.2	5.64	3.69	253.8	-	-	-	3.63
2-24	1.1	8.4	6.54	23.63	-	-	-	5.12
2-25	0.6	8.1	6.3	91.13	-	-	-	5.88
3-19	0.4	1.93	5.37	10.87	-	-	-	3.6
3-15	0.1	1.61	4.47	36.23	-	-	-	3.98
4-16	0.1	1.5	4.16	33.75	-	-	-	3.69
4-20	0.4	1.5	4.16	8.44	-	-	-	2.78
5-21	0.6	1.41	3.92	5.29	-	-	-	2.25
5-22	0.1	1.41	3.92	31.73	-	-	-	3.49
6-18	0.4	3.0	47.72	16.91	-	-	-	4.88
6-19	0.6	6.68	18.5	312.6	-	-	-	17.45
6-24	0.9	1.93	5.35	4.83	-	-	-	2.54
6-3	1.3	-	-	-	-	0.4338	-	0.4338
7-1	1.7	2.4	4.5	4.15	-	-	-	2.16
7-13	1.6	2.07	-	5.83	.00314	-	77.5	.0031
7-14	1.4	1.92	-	3.09	-	-	-	3.09
7-30	6.0	4.2	0.103	0.55	-	-	-	0.654
8-1	1.7	2.58	4.85	9.76	-	-	-	3.24
8-9	1.5	2.48	-	3.72	-	-	-	3.72
8-10	1.6	2.38	-	13.39	.00359	-	75.6	.00359
8-30	-	7.1	.0485	-	-	-	-	.0485
9-8	1.5	2.48	-	3.72	-	-	-	3.72
9-10	0.7	6.88	-	51.6	.0238	-	-	.0238
9-17	1.9	1.44	-	5.71	-	-	-	5.71
9-18	1.5	1.03	-	1.59	-	-	79.0	1.55
9-30	-	7.2	.050	-	-	-	-	.05
10-9	0.7	6.88	-	51.6	.0238	-	-	.0238
10-8	1.6	2.38	-	13.39	.00359	-	75.6	.00359
10-11	0.7	6.44	-	48.3	.0193	-	-	.01925
10-18	1.4	1.36	28.8	6.12	.00183	-	-	.00183
10-15	0.9	1.92	-	43.2	.0029	-	-	.0029
11-10	0.7	6.44	-	48.3	.0193	-	-	.01925
11-1	0.2	6.4	4.19	288	-	-	-	4.13
12-1	0.2	6.82	3.69	253.8	-	-	-	3.63
12-13	0.7	5.7	-	42.75	.002115	-	-	.002115
13-7	1.6	2.08	-	5.83	.003142	-	77.5	.00314
13-12	0.7	5.7	-	42.75	.002115	-	-	.002115
13-14	0.7	5.36	-	40.2	.0162	-	-	.0162
13-16	1.0	1.8	-	40.5	.00242	-	-	.00242
13-21	1.5	3.36	-	10.27	.00451	-	-	.00451

FIGURE 7.2.3 (page 2)
 TURBINE HOUSING HEAT TRANSFER ANALYSIS
 CONDUCTOR VALUES

215

Node Connector	ΔX in.	Area in ²	Conductance, \bar{K} , BTU/hr - °F					Total
			Convection	Conduction Solid	Conduction Steam	Fluid	Joint	
14-7	1.4	2.52	-	3.086	-	-	-	3.086
14-13	0.7	5.35	-	40.2	.0162	-	-	.0162
14-30	-	5.0	.0347	-	-	-	-	.0347
15-3	0.1	1.61	4.47	36.23	-	-	-	3.98
15-10	0.9	1.92	-	43.2	.0029	-	-	.00289
16-4	0.1	1.5	4.47	33.75	-	-	-	3.69
16-13	1.0	1.8	-	40.50	.00242	-	-	.00242
17-18	1.0	3.4	44.6	7.65	-	-	-	6.52
17-24	1.6	1.79	-	2.52	-	-	-	2.52
17-9	1.9	1.46	-	5.71	-	-	-	5.71
17-30	-	16.0	0.111	-	-	-	-	0.111
18-17	1.0	3.4	44.6	7.65	-	-	-	6.52
18-24	1.3	2.45	64.3	4.24	-	-	77.5	3.77
18-6	0.4	3.01	47.72	16.91	-	-	-	4.88
18-9	1.5	1.03	-	1.59	-	-	79.0	1.55
18-10	1.4	1.36	28.8	6.12	.00183	-	-	.00183
19-23	-	2.88	12.85	-	-	-	-	12.85
19-6	0.6	6.68	18.5	312.6	-	-	-	17.45
19-3	0.4	1.93	-	10.37	-	-	-	10.87
20-23	-	2.79	12.45	-	-	-	-	12.45
20-4	0.4	1.5	4.16	8.44	-	-	-	2.78
20-21	1.0	2.66	-	4.88	-	-	-	4.88
21-5	0.6	1.41	3.92	5.29	-	-	-	2.25
21-13	1.5	3.36	-	10.27	.00451	-	-	.00451
21-20	1.0	2.66	-	4.88	-	-	-	4.88
21-29	1.8	2.86	-	4.91	-	-	-	4.91
22-5	0.1	1.41	3.92	31.73	-	-	-	3.49
22-26	0.8	1.68	-	37.8	.0029	-	-	.0029
23-19	-	2.88	12.85	-	-	-	-	12.85
23-20	-	2.79	12.45	-	-	-	-	12.45
24-30	-	4.4	.0306	-	-	-	-	0.0306
24-17	1.6	5.25	-	2.517	-	-	-	2.517
24-18	1.3	2.45	64.3	4.24	-	-	77.5	3.77
24-6	0.9	1.93	5.35	4.83	-	-	-	2.54
24-2	1.1	8.36	6.54	23.63	-	-	-	5.12
25-2	0.6	8.05	6.30	91.13	-	-	-	5.88
25-26	0.7	6.3	-	35.44	.019	-	-	.019
25-28	1.5	1.5	-	2.25	-	-	-	2.25
26-22	0.8	1.68	-	37.8	.0029	-	-	.029
26-25	0.7	6.3	-	35.44	.019	-	-	.019
26-28	1.3	2.02	-	11.36	.0027	-	75.8	.0027
26-27	0.7	5.56	-	41.7	.0168	-	-	.0167
27-26	0.7	5.56	-	41.7	.0168	-	-	.0167
27-30	-	5.0	.0347	-	-	-	-	.0347
27-28	1.4	1.88	-	3.02	-	-	-	3.02

TURBINE HOUSING HEAT TRANSFER ANALYSIS
CONDUCTOR VALUES

Node Connector	ΔX in.	Area in ²	Conductance, \bar{K} , BTU/hr - °F					Total
			Convection	Conduction Solid	Conduction Steam	Fluid	Joint	
28-25	1.5	1.5	-	2.25	-	-	-	2.25
28-26	1.3	2.02	-	11.36	.00271	-	75.8	.0027
28-27	1.4	1.88	-	3.02	-	-	-	3.02
28-30	6.0	15.36	0.107	0.385	-	-	-	.492
29-21	1.8	2.86	-	4.91	-	-	-	4.91
30-28	6.0	15.36	0.107	0.385	-	-	-	.492
30-24	-	4.4	.0306	-	-	-	-	.0306
30-17	-	8	.0555	-	-	-	-	.0555
30-9	-	7.2	.050	-	-	-	-	.050
30-8	-	7.1	.0493	-	-	-	-	.0493
30-7	-	15.73	.103	.551	-	-	-	.654
30-14	-	5.0	.0347	-	-	-	-	.0347
30-27	-	5.0	.0347	-	-	-	-	.0347

Thermal Conductivity

Housing $K = 27 \text{ BTU/hr} - \text{ft} - ^\circ\text{F}$

Disk $K = 22 \text{ BTU/hr} - \text{ft} - ^\circ\text{F}$

Steam $K = 0.0145 \text{ BTU/hr} - \text{ft} - ^\circ\text{F}$

Water $K = 0.37 \text{ BTU/hr} - \text{ft} - ^\circ\text{F}$

For series connection
$$\bar{K}_{\text{total}} = \frac{1}{\frac{1}{\bar{K}_{\text{convection}}} + \frac{1}{\bar{K}_{\text{conduction}}} + \dots}$$

For parallel connection
$$\bar{K}_{\text{total}} = \bar{K}_{\text{convection}} + \bar{K}_{\text{conduction}} + \dots$$

HEAT TRANSFER ANALYSIS
COMPUTER PROGRAM FLOW DIAGRAM

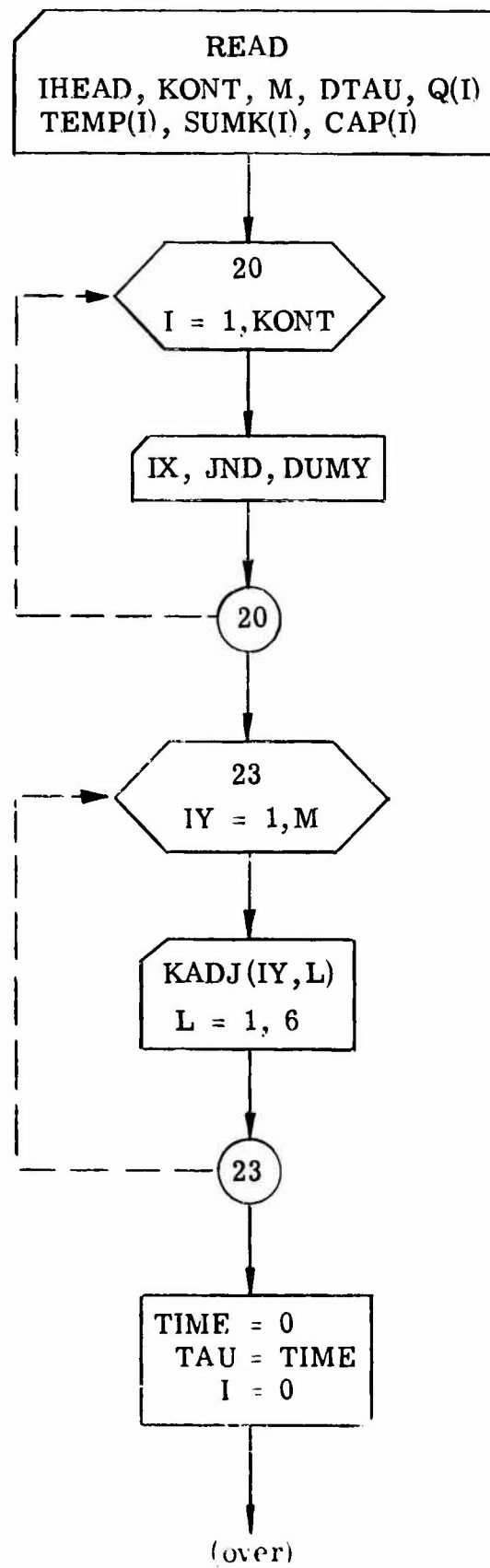


FIGURE 7.2.4

Page 1

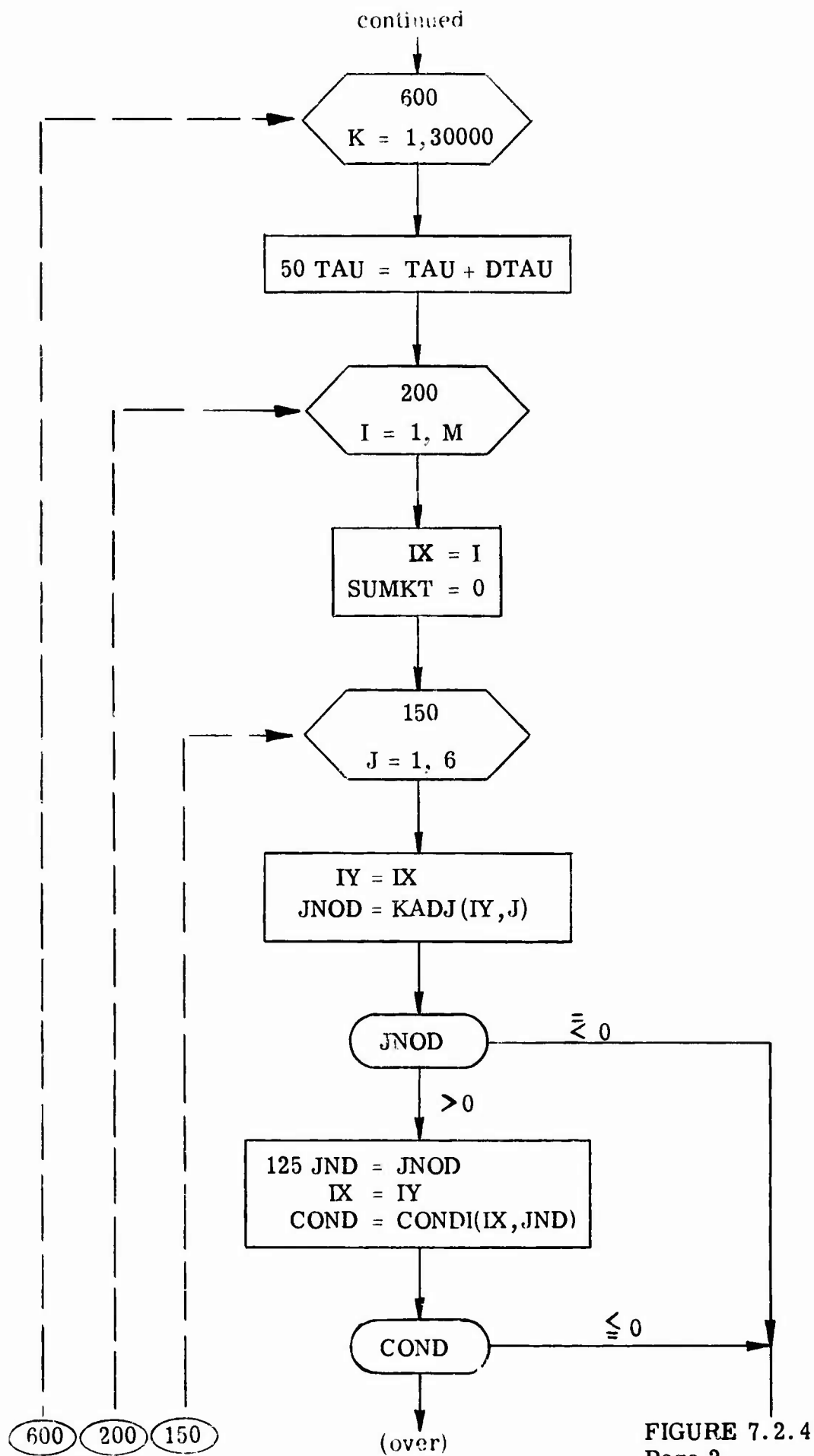


FIGURE 7.2.4
Page 2

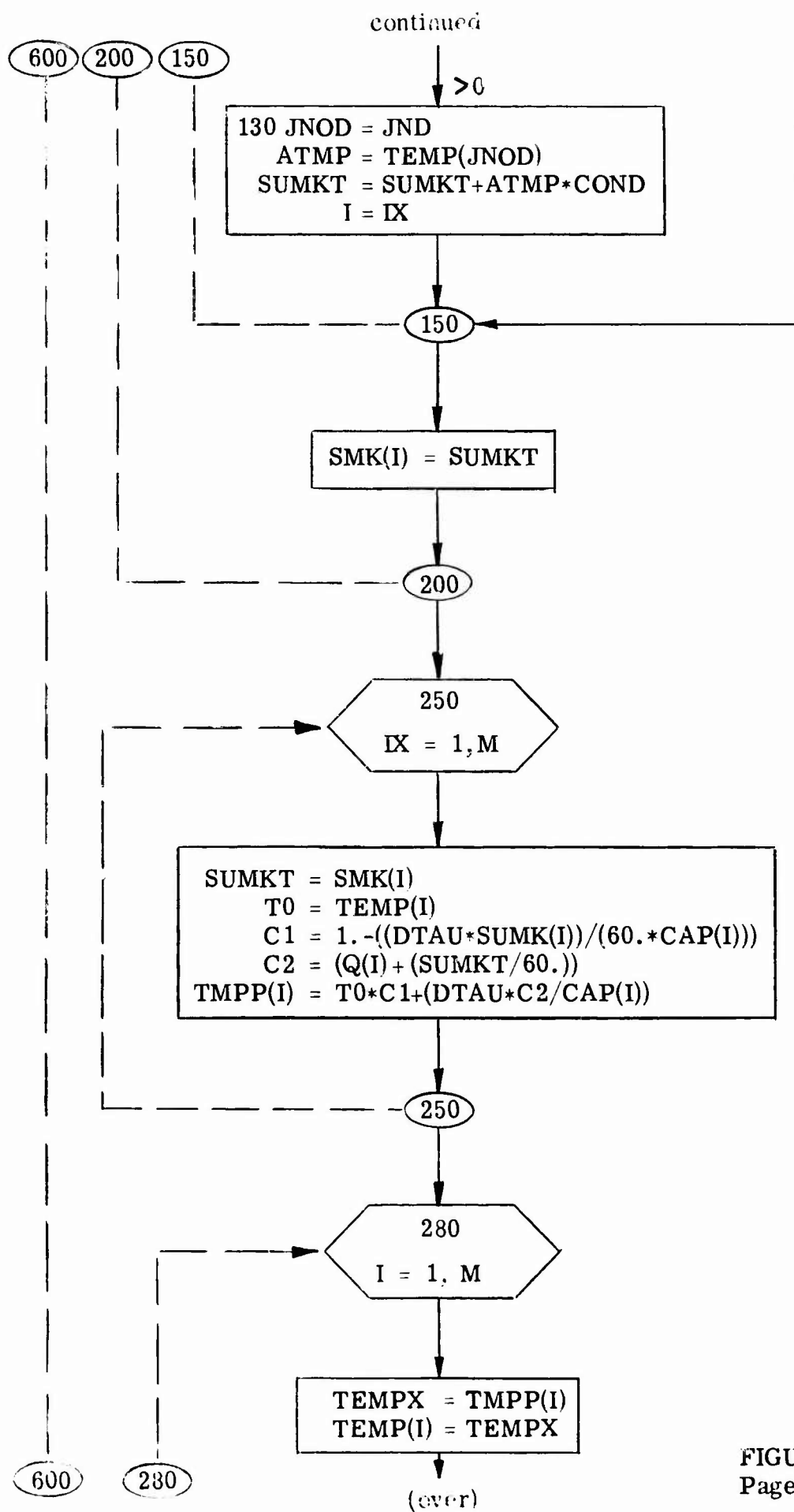


FIGURE 7.2.4
Page 3

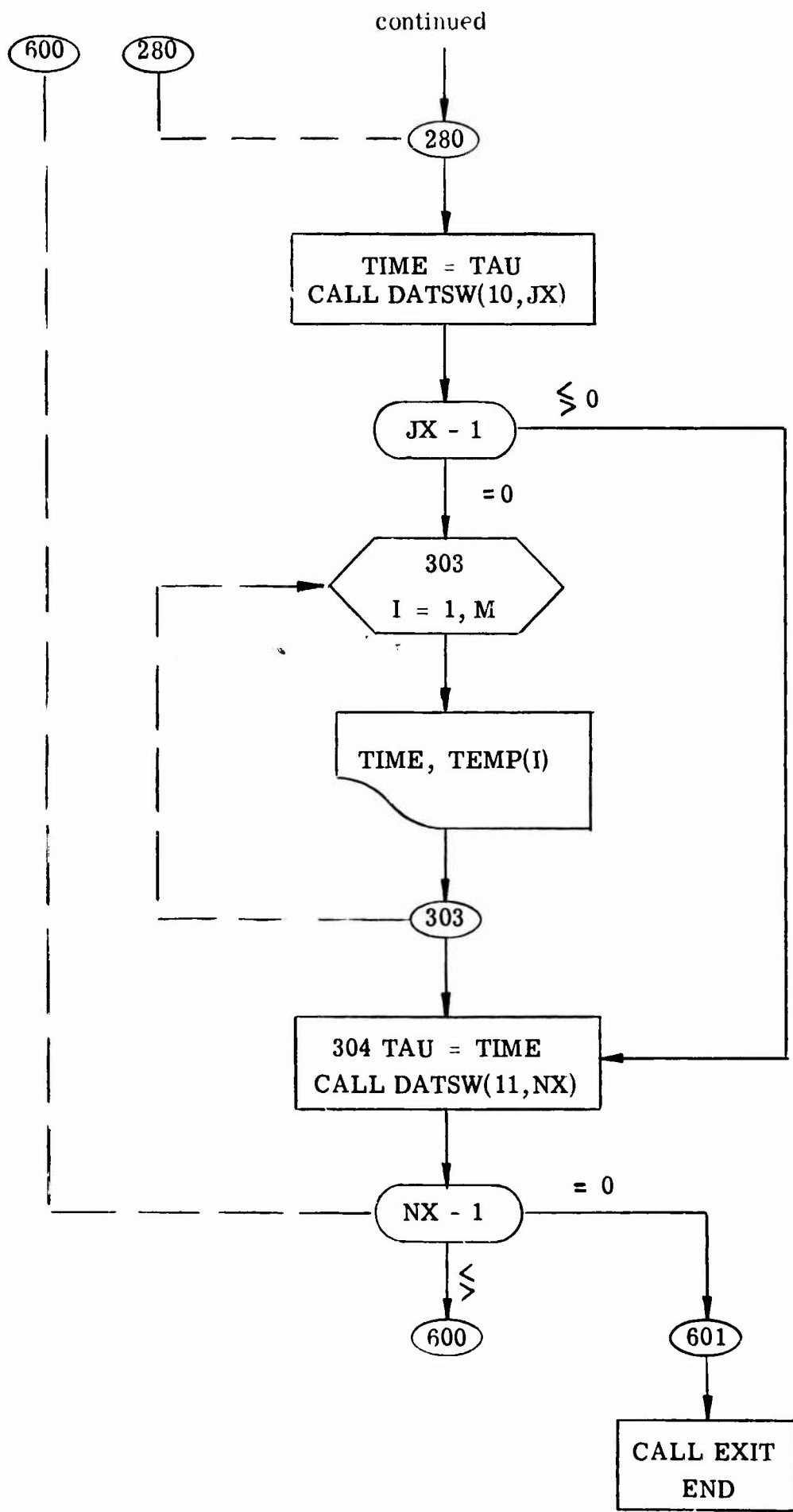


FIGURE 7.2.4
Page 4

7.3 VIBRATION CALCULATIONS

This section demonstrates the calculations performed in the vibration analysis of the LVF turbine. The symbols used are listed on pages x through xiv, and where the symbols are unique to the particular section, a more detailed list is provided in the individual section.

7.3.1 Turbine Blade Vibration Calculations

The calculation for the axial and tangential turbine blade and shroud natural frequency is as follows: (Reference 6.3.1)

Axial vibration:

$$\omega_N = A \sqrt{\frac{EI_A}{\mu l^4}} \quad \text{rad/sec}$$

where $A = 22.4$

$$E = 29.5 \times 10^6 \text{ lb/in}^2$$

$$I_A = .004 \text{ in}^4 \text{ (Figure 7.3.1)}$$

$$\mu = \text{Mass per unit length, lb - sec}^2/\text{in}^2$$

$$l = .287 \text{ inch}$$

$$\rho = \text{Density} = .28 \text{ for steel, lb/in}^3$$

from Figure 7.3.1 the area of blade $A_a = .207 \text{ in}^2$

$$\mu = \frac{A_a}{g} = \frac{.207}{386} (.287) = .00015 \frac{\text{lb-sec}^2}{\text{in}^2}$$

$$\text{Axial: } \omega_N = 22.4 \sqrt{\frac{(29.5 \times 10^6)(.004)}{(.00015)(.0067)}} = 77.6 \times 10^4 \text{ rad/sec}$$

or $739 \times 10^4 \text{ cps}$

$$\text{Tangential: } \omega_N = 22.4 \sqrt{\frac{(29.5 \times 10^6)(.006)}{(.00015)(.0067)}} = 134 \text{ rad/sec}$$

or $1,280 \times 10^4 \text{ cps}$

The composite mode of the shroud and blades acting together should be considered.

From section 7.4.1 the deflection per pound force of the blades

in the axial direction is $K_A = \frac{W_1}{\delta_p}$

$$K_A = \frac{7241.5}{.780 \times 10^5} = 9275 \times 10^5 \text{ lb/in}$$

W_1 = Total force on end of blades, lb

δ_p = Deflection of blade tip, in.

K_A = Spring constant of shroud blade system, lb/in

m = Total mass of shroud and blades

PITCH LINE PROFILE ROTOR BLADE LVF TURBINE

$$\text{AREA} = .207 \text{ IN}^2$$

$$I = .004 \text{ IN}^4$$

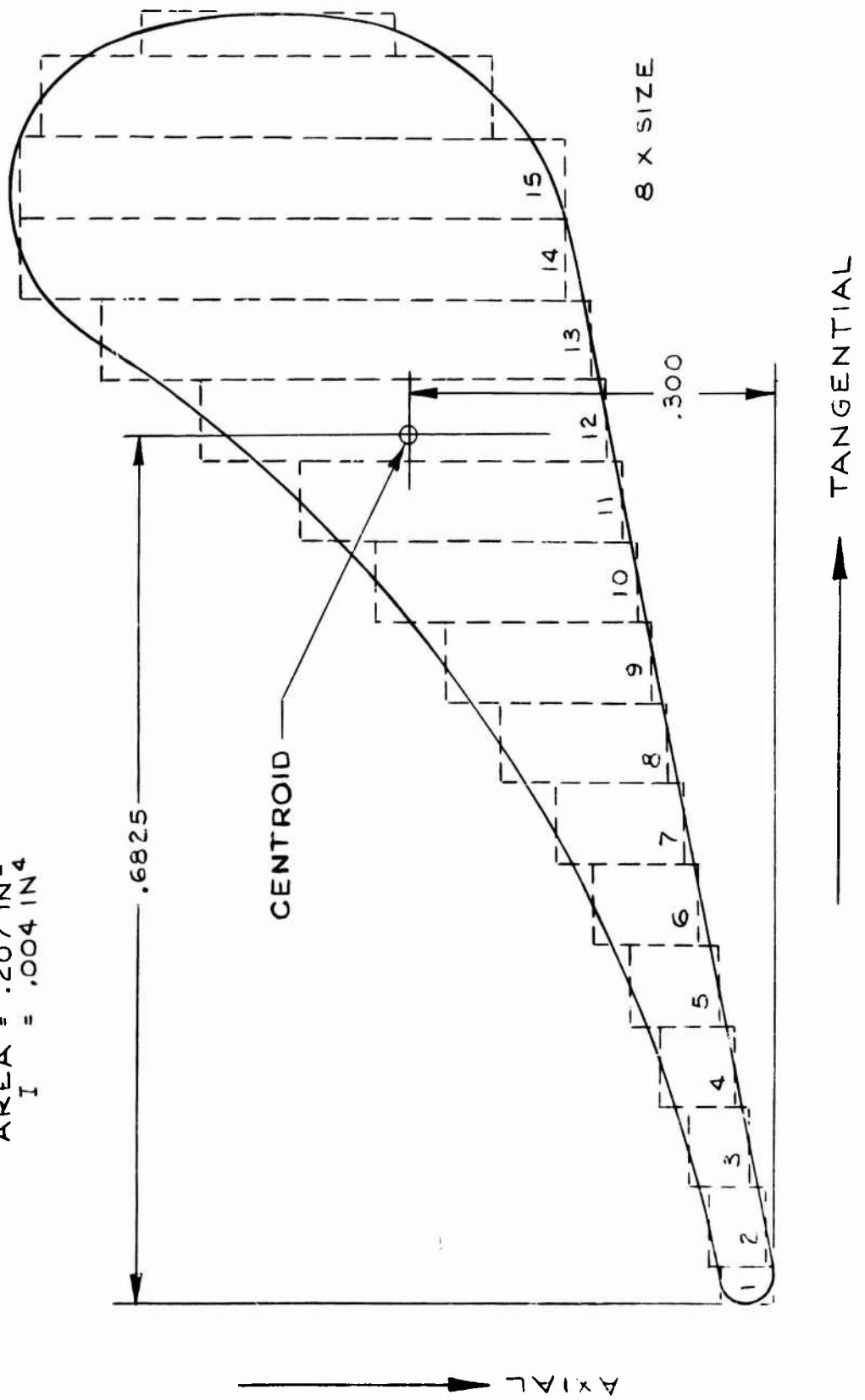


FIGURE 7.3.1

$$m = \text{Mass of blades} + \text{mass of shroud} = \frac{.207(.289)(.28)(90)}{386} + \frac{(.330)(\pi)(2)(12.456)}{386} \times .289$$

$$m = .00388 + .01956 = .023 \frac{\text{lb-sec}^2}{\text{in.}}$$

$$f_s = \frac{1}{2\pi} \sqrt{\frac{K_A}{m}}$$

$$f_s = \frac{1}{2\pi} \sqrt{\frac{927.5 \times 10^6}{.023}} = 3.17 \times 10^4 \text{ cps or } 190.5 \times 10^4 \text{ rev/min}$$

7.3.2 Disk Vibration Calculation

The procedure for calculating the second nodal diameter (2ND) is shown in Figure 7.3.2 and follows the method described in Reference 6.3.2.

7.3.3 Rotor Dynamics Calculation

The natural frequency of vibration, considering the shaft rotor system as a simple rigid body is:

$$f_N = \frac{60}{2\pi} \sqrt{\frac{2K}{m_s}}$$

where K = Film stiffness of one bearing, lb/in (assuming translation only)

m_s = Total mass of rotating system

f_N = Natural frequency, rev/min

$$m_s = \frac{\text{Rotor weight}}{g} = \frac{282.8}{386} = .752 \frac{\text{lb-sec}^2}{\text{in}}$$

For two bearing system

$$K_B = 848,000 \text{ lb/in} \times 2 = \text{stiffness of two bearings (Figure 6.5.1)}$$

$$f_N = \frac{60}{2\pi} \sqrt{\frac{2(848000)}{.752}} = 14380 \text{ rev/min}$$

For conical whirl, the springs develop a restoring moment, and for two springs this becomes $\frac{KL^2}{2}$ (in - lb/radius). (Figure 3.3.4)

AXIAL VIBRATION OF TURBINE DISKS
LVFT
TWO NODAL DIAMETERS K = 2

1	2	3	4	5	6	7	8	N = 3			
r	x	h	$\frac{h}{h_o}$	$\frac{h^3}{h_o}$	$\frac{X - X_o}{X}$	4 x 6	5 x 6	A	A x 8	B	B x 7
	.01685	-	-	-	-	-	-				
1.2525	.1	5.25	6.05	222.0	1	6.05	222.0	.0558	12.4	$.1 \times 10^{-6}$	605×10^{-6}
2.525	.2	3.6	4.12	69.75	1	4.12	69.75	.446	31.1	$.0128 \times 10^{-3}$	$.05275 \times 10^{-3}$
3.790	.3	2.35	2.69	19.50	1	2.69	19.50	1.507	29.4	$.219 \times 10^{-3}$	4.27×10^{-3}
5.05	.4	2.00	2.29	12.01	1	2.29	12.01	3.57	42.9	1.638×10^{-3}	19.7×10^{-3}
6.32	.5	1.68	1.92	7.09	1	1.92	7.09	6.975	49.4	7.81^{-3}	55.4
7.59	.6	1.38	1.575	3.91	1	1.575	3.91	12.05	47.1	.0280	.1095
8.84	.7	1.08	1.235	1.881	1	1.235	1.881	19.14	36.1	.0824	.1551
10.1	.8	1.08	1.235	1.881	1	1.235	1.881	28.6	53.8	.210	.397
11.37	.9	.875	1.000	1.000	1	1.000	1.00	40.7	40.7	.478	.478
12.625	1.0	.875	1.000	1.000	1	1.000	1.00	55.8	55.8	1.00	1.000

$$P^2 = 1.125 \times 10^5 \frac{398.7}{2.3186} = 194.1 \times 10^5$$

$$P = 19.41 \times 10^6 = 4410.$$

$$4410 \frac{60}{2} = 42100.$$

$$\frac{42100}{2} = 21500 \text{ rev/min}$$

FIGURE 7.3.2

Then the restoring spring moment equals the inertial moment, or

$$f_{\text{conical shaft}} = \frac{1}{2\pi} \sqrt{\frac{KL^2}{2I_{ts}}} \text{ cycles/sec}$$

where I_{ts} is the transverse moment of inertia of the shaft rotor system about a diameter (lb in sec²).

$$f_{\text{conical shaft}} = \frac{60}{2\pi} \sqrt{\frac{(848000)(17.4)^2}{2(32.5)}} = 18,917 \text{ rev/min}$$

$$I_{ts} = \sum \frac{1}{2} \rho \pi r^4 h$$

where: h = length of shaft, in

R = diameter of shaft, in.

7.4 STRESS CALCULATIONS

This section demonstrates the calculations performed in the stress analysis of the L V F turbine. The symbols used are listed in Section iv, and where the symbols are unique to the particular section, a more detailed list is provided in the individual section.

7.4.1 Shroud and Blade Stress Calculation

The following calculation gives the stress analysis of shroud and blade subjected to radial load of centrifugal force and thermal expansion, Assume shroud, blade and disk can be represented as shown in Figure 6.4.1.

Centrifugal growth U_w (assume rotating flat disk with hole in center (Reference 6.4.1)

$$U_w = \frac{\rho w^2 r (3+\mu)(1-\mu)}{E} \left[r_o^2 + r_i^2 + \frac{1+\mu}{1-\mu} \frac{r_o^2 r_i^2}{r^2} - \frac{1+\mu}{3+\mu} r^2 \right]$$

where ρ = Density .283 lb/in³

w = Angular velocity of rotation, rad/sec = 400π at 12,000 rpm

r = Radial distance of a point from the axis, in.

E = Modulus of elasticity, psi

μ = Poisson's ratio, 0.3 for steel

r_o = Rim radius, in.

r_i = Bore radius, in.

Assume the shroud should act like a flat disk with a reduced density because of the groove in rim.

$$\rho' = \text{Reduced density} = \frac{A'}{A} \rho$$

where A = Area of shroud with groove

A' = Area of shroud without groove

Area of shroud = A = width x height

$$A = .875 \times .625 = .547 \text{ in}^2$$

$$\text{Area of shroud with groove} = A' = .330 \text{ in}^2$$

$$\rho' = \frac{A'}{A} \rho = \frac{.330}{.547} (.283) = .171 \text{ lb/in}^3$$

@ $r = r_i$

$$U_w = \frac{.171(400\pi)^2(12.144)(3.3)(.7)}{29.5 \times 10^6 (8) (386)} \left[163.05 + 147.48 \frac{1.3}{7} (163.05) \right.$$

$$\left. - \frac{1.3}{3.3} (147.48) \right]$$

$$r_o = 12.769 \text{ in} \quad r_o^2 = 163.05 \text{ in}^2$$

$$r_i = 12.144 \text{ in} \quad r_i^2 = 147.48 \text{ in}^2$$

$$U_w = \frac{26.98 \times 10^4 (28.053)}{236 \times 10^6 (386)} [555.24] = \frac{756.87 \times 10^4}{91096 \times 10^6} [555.24]$$

$$U_w = .046 \text{ in.}$$

Deflection from thermal growth (assume ring of radius r_o & r_i):

$$U_T = \Delta T \alpha r_i, \text{ in.}$$

$$\alpha = 6.3 \times 10^{-6} \quad r_i = 12.144$$

$$\Delta T = T_a(\text{max}) - T_o \quad \text{Temperature change from zero stress state } T_o$$

$$T_a(\text{max}) \text{ for condition one and two is } T_a = 350 \text{ and } T_o = 183.$$

$$U_T = (350 - 183)(6.3 \times 10^{-6}) 12.144 = 13129.4 \times 10^{-6}$$

$$U_T = .0131 \text{ in.}$$

Total growth of shroud assuming free ring:

$$U = U_w + U_T = .046 + .0131 = .0591 \text{ in.}$$

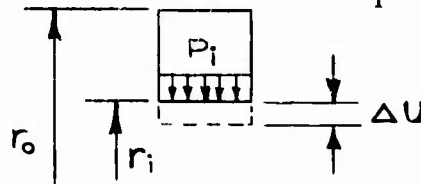
From tabulation of disk growth (Figure 6.4.6) the centrifugal growth at the disk rim radius 11.857 is $U_c = .0091$ condition one
 $= .0194$ condition two

Differential growth between shroud and disk ΔU is:

$$(\text{Condition one}) \Delta U_1 = U - U_{c1} = .0591 - .0091 = .0500 \text{ in.}$$

$$(\text{Condition two}) \Delta U_2 = U - U_{c2} = .0591 - .0194 = .0397 \text{ in.}$$

Calculate pressure required to contract shroud ΔU_1 & ΔU_2 , the amount required to retain compatibility. (Assume disk with hole in center with negative internal pressure) ($-P_i$ Reference 6.4.1)



$$\text{at } r_i, \Delta U = -P_i \frac{r_i}{E} \frac{r_i^2}{r_o^2 - r_i^2} \left[(1 - \mu) + (1 + \mu) \frac{r_o^2}{r_i^2} \right]$$

$$\text{Condition one } .0500 = -P_i \frac{12.144}{29.5 \times 10^6} \left[\frac{147.48}{163.05 - 147.48} \right] \left[.7 + 1.3 \frac{163.05}{147.48} \right]$$

(Let $\Delta U = .0500$ in)

$$.0500 = -P_i (.412) \times 10^{-6} (9.47) [.7 + 1.437]$$

$$.0500 = -P_i (8.338) \times 10^{-6}$$

$$\text{Condition one } -P_i = \frac{.0500}{8.338 \times 10^{-6}} = 5990. \text{ lb/in}^2$$

$$\text{Condition two } -P_i = \frac{.0397}{8.338 \times 10^{-6}} = 4761. \text{ lb/in}^2$$

Force in each blade required to provide pressure:

$$\frac{F}{\text{No. of blades}} = P_i (A_s)$$

where A_s = surface area of ID of shroud

Number of blades = 90

$$\text{Condition one } \frac{F_1}{\text{No. Blades}} = \frac{(.875)(12.144)(2\pi)(5990)}{90} = .118(3761.72) = 4439.0 \text{ lb}$$

$$\text{Condition two } \frac{F_2}{\text{No. Blades}} = \frac{(.875)(12.144)(2\pi)4761}{90} = .118(29773.5) = 3513 \text{ lb}$$

From Figure 7.3.1, the area and moment of inertia of blade are:

$$A_b = .207 \text{ in}^2$$

$$I_a = .004 \text{ in}^4 \text{ axial direction}$$

Tensile stress in blade:

$$\text{Condition one } \sigma T_1 = \frac{4439}{.207} = 21444. \text{ psi}$$

$$\text{Condition two } \sigma T_2 = \frac{3513}{.207} = 16971. \text{ psi}$$

The blades provide the attachment between the disk and shroud in the radial and axial direction. This portion of the analysis deals with the rotation and deflection of the shroud caused by bending moments applied from the seals. The blades deflect from the axial loads which are caused from the pressure differential across the blades and from the force from the upper seal face. For the blades to deflect it is necessary for the shroud to be twisted (see Figure 6.4.3).

$$\frac{\ell^2}{EJ} \left[\frac{W_1 \ell}{3} + \frac{W_2 \ell}{8} - \frac{M_O}{2} \right] = \sum \frac{MR r}{EI_p}$$

$$\frac{1}{EJ} \left[\frac{W_1 \ell^2}{2} + \frac{W_2 \ell^3}{6} - M_O \ell \right] = \sum \frac{MR}{EI_p}$$

$$\ell = .287 \text{ in.}$$

$$E = 29.5 \times 10^6, \text{ psi}$$

$$J = (\text{number of blades}) (\text{moment of inertia}) = (90)(.004) = .36 \text{ in}^4$$

$$W_1 = 3299.8 \text{ lb}$$

$$\sum M = [632.7 + M_O]$$

$$I_p = \text{Torsional moment of inertia of shroud} = I_x + I_y$$

$$I_p = .01008 + .07 = .08 \text{ in}^4$$

$$W_2 = 2076.17 \text{ lb}$$

$$(1) \quad \frac{.0824}{.36} \left[\frac{(3299.8 + W_1)(.287)}{3} + \frac{(2076.17)(.287)}{8} - \frac{M_O}{2} \right] = \frac{[632.7 + M_O](.312)}{.08}$$

$$(2) \quad \frac{1}{.36} = \left[\frac{(3299.8 + W_1)(.0824)}{2} + \frac{2076.17(.024)}{6} - M_O(.287) \right] = \frac{(632.7 + M_O)(12.457)}{.08}$$

$$(1) \quad .222 [315 + .0957 W_1 + 74.483 - .5 M_O] = 2467.5 + 3.9 M_O$$

$$(1) \quad 69.93 + .02125 W_1 + 16.54 - .111 M_O = 2467.5 + 3.9 M_O$$

$$.02125 W_1 - 4.011 M_O = 2381.03$$

$$(2) \quad 135.95 + .0412 W_1 + 8.305 - M_O(.287) = 35469.1 + 56.06 M_O$$

$$.0412 W_1 - 35324.8 - M_O(56.347)$$

$$(1) \quad W_1 - 188.75 M_O = 112048.5$$

$$-W_1 + 1367.65 M_O = -857378.64$$

$$1178.9 M_O = -745330.14$$

$$M_O = -632 \text{ in-lb}$$

$$W_1 - (188.75)(-632.0) = 112048.5$$

$$W_1 = 7241.5 \text{ lb}$$

$$y = -\frac{1}{3} \frac{Wl^3}{EI} = \frac{-(7241.5)(.287)^3}{(3)(29.5 \times 10^6)(.360)} = \frac{170.9 \times 10^{-6}}{31.86} = 5.36 \times 10^{-6}$$

$$\Theta = \frac{1}{2} \frac{Wl^2}{EI} = \frac{7241.5(.287)^2}{(2)(29.5 \times 10^6)(.360)} = \frac{593.89 \times 10^{-6}}{21.24} = 27.96 \times 10^{-6}$$

$$\left. \begin{array}{l} y = .00000536 \text{ inch} \\ \phi = .00002796 \text{ rad} \end{array} \right\} \text{ due to } W_1$$

$$y = \frac{1}{2} \frac{M_O l^2}{EI} = \frac{632 (.082)}{(2)(29.5 \times 10^6)(.36)} = \frac{51.82 \times 10^{-6}}{21.24} = 2.44 \times 10^{-6}$$

$$\phi = \frac{632 (.287)}{29.5 \times 10^6 (.36)} = \frac{181.38}{192 \times 10^5} = .944 \times 10^{-6} \text{ rad}$$

} due to M_O

Deflection and rotation of blade tip:

$$\text{Total } y_1 = .0536 \times 10^{-4} + .0244 \times 10^{-4} = .780 \times 10^{-5} \text{ in.}$$

$$\phi_1 = .2796 \times 10^{-4} + .0944 \times 10^{-5} = .289 \times 10^{-4} \text{ rad}$$

$$\sigma_{\text{Blade}} = \frac{M_c}{I} = \frac{632 (.3)}{90 (.004)} = \frac{189}{.360} = 630 \text{ psi} \quad \text{TIP}$$

$$\sigma_{\text{Blade}} = \frac{[632 + 7241.5 (.287)] (.3)}{.360} = \frac{2710.3 (.3)}{360} = 2258 \text{ psi} \quad \text{ROOT}$$

The following analysis calculates the stress in the shroud assuming a ring of equally spaced radial supports (Reference 6.4.4) (see Section 6.4.1).

$$S_p = \frac{PR^3}{2EI} \frac{1}{\sin^2 \Theta} \left[\frac{\Theta^5}{45} - \frac{\Theta^7}{315} + \frac{3\Theta^9}{14,175} \right] + \frac{PR}{2EA} \frac{1}{\sin^2 \Theta} \left[\frac{\Theta}{2} + \frac{\sin \Theta \cos \Theta}{2} \right]$$

$$\sin \Theta = .034899, \sin \Theta^2 = .0012179$$

$$2^\circ \text{ in rad} = .034907 \text{ rad}$$

$$R = 12.144 \text{ in} \quad R^2 = 147.477 \text{ in}^2 \quad R^3 = 1790.961 \text{ in}^3$$

$$E = 29.5 \times 10^6 \text{ psi}$$

$$I = .07 \text{ in}^4$$

$$\Theta^2 = .001218499 \text{ rad}$$

$$\Theta^3 = .0042537 \times 10^{-2} \text{ rad}$$

$$\Theta^4 = .00148484 \times 10^{-3} \text{ rad}$$

$$\Theta^5 = .00518 \times 10^{-5} \text{ rad}$$

$$\Theta^6 = .00284439 \times 10^{-6} \text{ rad}$$

$$\Theta^7 = .0099 \times 10^{-8} \text{ rad}$$

$$S_p = \frac{P(1470531.2)}{4.13 \times 10^6} \left[.01151 \times 10^{-7} \right] + \frac{P(9971.3)}{19.47 \times 10^6} \left[.03489 \right]$$

$$S_p = P \frac{.00169 \times 10^{-6}}{4.13} + P(17.87) \times 10^{-6}$$

$$S_p = P(.00409) \times 10^{-6} + P(17.87) \times 10^{-6}$$

$$\text{let } S_p = .0397 = P(17.87) \times 10^{-6}$$

$$P = \frac{.0397 \times 10^6}{17.87} = 2221.6 \text{ lb}$$

$$\sigma_s = 33.695 \times 2221.6 = 74856.81 \text{ psi}$$

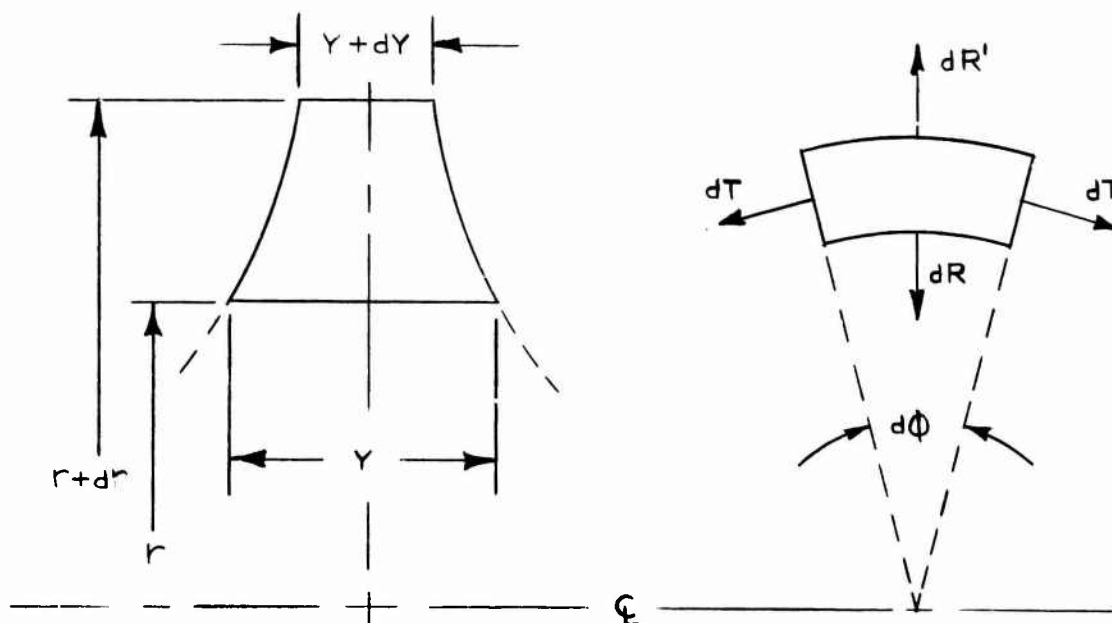
Maximum stress in shroud at operating condition.

where $S_p = .0397$ in
for Condition #2

7.4.2 Turbine Disk Stress Analysis

For the purpose of the analysis the disk was divided into a large number of parallel-sided rings and the Grannell method applied (Reference 7.4.1) Figure 6.3.2 shows the number and thickness of rings, assumed for the stress analysis. It is necessary to assume that the portion of the disk beyond the blade roots are not capable of carrying tangential stress. The blades are considered to be dead load and the disk is also required to retain the shroud, which is assumed to be a ring being restrained by the disk.

The equilibrium forces on an element of the disk are:



r = Radial distance of a point from the axis, in.

y = Thickness of the disk element at the distance r , in.

σ_r = Radial stress, psi

σ_t = Tangential stress, psi

$\mu = \gamma/g$ = density of the material of the disk, lb/in³

ω = Angular velocity of rotation, rad/sec

γ = Poisson's ratio, 0.3 for steel

α = Coefficient of linear expansion, in/in/⁰F

dr = Increment in the radius, in.

dy = Increment in the thickness, in.

dF = Centrifugal force on the mass, lb

dT = Tangential force, lb

dR = Radial force on the inner surface, dR' = outer surface

$d\sigma_r$ = Change in radial stress due to change in radius

Derivation of the relation:

Volume of the disk element

$$dV = yrd\phi dr$$

and the mass

$$dm = \mu dV = \mu yrd\phi dr$$

centrifugal force due to rotation on this mass,

$$\begin{aligned} dF &= dmr\omega^2 \\ &= \mu yr^2\omega^2 d\phi dr \end{aligned}$$

Forces acting on the sides of the element because of tangential stress σ_t ,

$$dT = ydr\sigma_t$$

Radial force on the inner face surface due to σ_r ,

$$dR = yrd\phi\sigma_r$$

and the similar force on the outer face surface

$$dR' = (y + dy)(r + dr)(\sigma_r + d\sigma_r) d\phi$$

where dy and dr are used algebraically.

For equilibrium of forces, we have

$$dR' - dR - dTd\phi + dF = 0$$

From above

$$dR' - dR = (yr + ydr + rdy + dydr) (\sigma_r + d\sigma_r) d\phi - yr \sigma_r d\phi$$

Simplifying and neglecting the terms of higher order,

$$dR' - dR = d\phi(yr\sigma_r dr + r\sigma_r dy + yrd\sigma_r)$$

$$= d(yr\sigma_r) d\phi$$

$$d(yr\sigma_r) d\phi - y\sigma_t dr d\phi + \mu yr^2 \omega^2 d\phi dr = 0$$

Simplifying and rearranging,

$$\frac{d(yr\sigma_r)}{dr} - y\sigma_t + \mu yr^2 \omega^2 = 0$$

This equation will be combined with the fundamental law of elasticity and relations for stresses due to thermal gradient.

With the operation condition and material specified, the effect of thermal gradient on the disk can be determined and superimposed on the elastic stresses.

Assuming a parallel sided solid disk, the following rigorous expression is used (Reference 7.4.1)

$$\sigma_r = \alpha E \left(\frac{1}{b^2} \int_0^b tr dr - \frac{1}{r^2} \int_0^r tr dr \right)$$

$$\sigma_t = \alpha E \left(-t + \frac{1}{b^2} \int_0^b tr dr + \frac{1}{r^2} \int_0^r tr dr \right)$$

where α = Coefficient of thermal expansion in/in/ $^{\circ}$ F

E = Modulus of elasticity - psi

b = Radius at rim, in.

It is necessary that the temperature t' be written as a function of radius r so that $tr dr$ can be integrated. For this case $t' = T + Ar^n$ and from Figure 6.4.5 $t' = 180 + 3.67 \times r^{1.59}$ where T is temperature of disk at zero thermal stress level (at disk center).

7.4.3 Casing Calculations

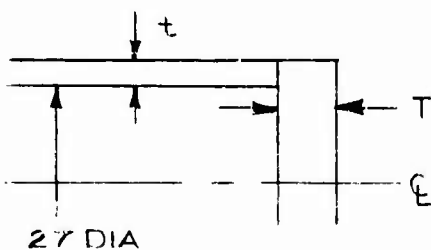
The following assumptions were made in order that a solution could be achieved using presently available mathematical theory.

1. The casing can be treated as a thin shell of revolution loaded symmetrically about its axis.
2. The deformations are small and the elastic material properties are homogeneous and isotropic with no plastic deformations to be considered.
3. The casing is pressurized by a uniform hydrostatic pressure with the shaft holes closed, which approximates the situation that would be experienced in a normal hydrostatic test of the casing.

Based on these assumptions, the philosophy of the analysis is to analyze the turbine casing by treating it as a shell of revolution under internal pressure, using the general theory and notes presented in Reference 7.4.1. The basic procedure involves dividing the casing into sections: flat end plates, short cylindrical shells, and rings. Pressurizing each of these sections separately produces differences in their edge deflections and rotations which, when the casing is put together, must be brought into equality. To produce this equality requires the application of edge shear forces and edge moments which give rise to discontinuity stress at the junctures. Once these edge forces and moments on each section are known, the stresses, strains, and deflections within the sections can be computed.

7.4.3.1 Inlet Casing Stress Calculations

For the stress analysis of the inlet side of the casing it is necessary to assume the model shown below constructed of a cylinder and a circular flat plate. The equations defined in Section 6.4.3 provide the deflection and rotation and are solved simultaneously for the discontinuity force shown in Section 6.4.3.1.



where

$$t = \frac{3}{8} \quad \frac{d}{t} = 72$$

$$T = \frac{5}{8} \quad \frac{d}{T} = 42.5$$

$$\mu = .3 \quad \frac{T}{t} = \frac{5/8}{3/8} = 1.66$$

$$P = 140$$

$$Bd = \sqrt[4]{12(.91) \sqrt{\frac{27}{.375}}} \quad Bd = 15.4 \quad (Bd)^2 = 237.$$

$$Bd = 1.819(8.48) = 15.4 \quad B = .571$$

$$a_1 = -3(1 - \mu) \frac{d}{T} = -3(.7)(42.5) = -89.25$$

$$a_2 = 2(1 - \mu) = 1.4$$

$$a_3 = \frac{3}{32} (1 - \mu) \frac{d}{T} = \frac{3}{32} (.7)(42.5) = 2.79$$

$$b_1 = \frac{6(1 - \mu) d d}{(Bd)^2 t T} = \frac{6(.7) 72(42.5)}{237} = 54.3$$

$$b_2 = \frac{-3(1 - \mu) d}{(Bd)^2 t} = \frac{-3(.7) 72}{237} = -.638$$

$$b_3 = -\frac{3(.7)(72) 42.5}{16(237)} = -1.693$$

$$a_4 = -\frac{T}{t} \left(\frac{2 - \mu}{8} \right) = \frac{-1.66(1.7)}{8} = -.353$$

$$a_5 = -\frac{1}{2} \frac{T}{t} (Bd)^2 = -\frac{1}{2} (1.66)(237) = -197.$$

$$a_6 = -\frac{1}{2} \frac{T}{t} (Bd) = -\frac{1}{2} (1.66)(15.4) = -12.79$$

$$b_4 = 0$$

$$b_5 = -\left(\frac{T}{t}\right)^2 (Bd) = -(1.66)^2(15.4) = -42.49$$

$$b_6 = -\frac{1}{2} \left(\frac{T}{t}\right)^2 = -\frac{1}{2} (1.66)^2 = -1.379$$

$$\frac{M_o}{Pd^2} a_5 + \frac{Q_o}{Pd} a_6 + a_4 = \frac{M_o}{Pd^2} a_1 + \frac{Q_o}{Pd} a_2 + a_3$$

$$\frac{M_o}{Pd^2} (-197) + \frac{Q_o}{Pd} (-12.79) - .353 = \frac{M_o}{Pd^2} (-89.25) + \frac{Q_o}{Pd} (1.4) + 2.79$$

$$\frac{M_o}{Pd^2} (-42.49) + \frac{Q_o}{Pd} (-1.379) = \frac{M_o}{Pd^2} (54.3) + \frac{Q_o}{Pd} (-.638) - 1.693$$

$$\frac{Q_o}{Pd} = -.378$$

$$\frac{M_o}{Pd^2} = .02048$$

$$I_{cj} = \left| 1 + 2Bd \left(\frac{Q_0}{Pd} \right) (1 + \lambda) \right| + 12 \mu \frac{d}{t} \left| \frac{M_0}{Pd^2} \right|$$

$$I_{cj} = \left| 1 + 2(15.4)(-.378)(.164) \right| + 3.6 \frac{27}{.375} \left| .02048 \right|$$

$$\lambda = B \frac{M_0}{Q_0} = .571 \frac{.02048}{-.378} (27) = -.836$$

$$I_{cj} = \left| 1 - 1.91 \right| + 5.31 \quad I_{cj} = 6.22$$

The casing end plate is assumed to share the pressure load equally with the ribs, therefore the pressure used to calculate the discontinuity stress is one-half of the design pressure or 125.3/2 psi.

$$\text{then } \frac{Pd}{2t} = \frac{125.3}{2} \frac{(27)}{.750(2)} = 2275 \text{ psi}$$

$$\sigma_{ct} = I_{cj}(2275) = 14050 \text{ psi}$$

$$I_{sj} = 3 \left| \frac{Q_0}{Pd} \right| = 3(.378) = 1.133$$

$$\sigma_{sj} = 2275(1.133) = 2563 \text{ psi}$$

$$I_{aj} = \frac{1}{2} + 12 \frac{27}{.375} \left| .02048 \right| = .5 + 1.77 = 18.2$$

$$\sigma_{aj} = 18.2(2275) = 41,125 \text{ psi}$$

7.4.3.2 Exit Casing Stress Calculations

The calculations for stress and deflection in the exit casing require the analysis of two specific areas. One, the ribs, are designed to assume one-half the pressure force and the end plate is assumed to withstand one-half of the pressure force. This is accomplished by designing the fixed-fixed ribs and the fixed-fixed blade such that they each have the same deflection under the same force. Two, the end plate is analyzed as a composite structure using the vanes to retain the continuity.

Total load on one beam.

$$\text{Force} = \Delta P(\text{area}) = 125.3(\pi R^2) = 125.3\pi(13.75)^2$$

$$\text{Force} = 74376.2 \text{ lb}$$

$$\frac{\text{Force}}{\text{Rib}} = \frac{74376.2}{9} = 8264 \text{ lb}$$

$$\text{Deflection of fixed-fixed beam is } y = \frac{1}{24} \frac{W_x^2}{EI_\ell} (2\ell x - \ell^2 - x^2)$$

at $x = 9.375$

$$y = \frac{1}{24} \left[\frac{8264 (x^2)}{26 \times 10^6 (1.16)(27.5)} \right] (2(27.5)x - 27.5^2 - x^2)$$

$$y = .030 \text{ in.}$$

The deflection of the circular plate of 20 inch diameter and 5/8 inch thickness is .032 inch. The deflection of plate and ribs is approximately equal, making the assumption of each carrying 50% of the pressure load valid.

The next step is to calculate the deflection in the composite structure shown in Figure 7.4.1. The equation for Y_1 & Y_3 , when solved simultaneously, provides the bending moment M_o at the interface.

$$Y_3 = \left[\left(\frac{W_2 + W_3}{2} + W_1 \right) L_3 - M_o \right] \frac{R_4}{2\pi E} \left[\frac{\pi}{4I_3} + \frac{2}{\pi} \left(\frac{2.5}{I_{p1}} + \frac{1}{I_3} \right) \right]$$

$$Y_1 = \left[\frac{W_1}{3} \left(R_2 - 2R_1 + \frac{2R_2 R_1}{R_2 + R_1} \right) + M_o \right] \frac{(R_2 + R_1)}{4\pi E}$$

$$\left[\frac{\pi}{4I_1} + \frac{2}{\pi} \left(\frac{2.5}{I_{p1}} + \frac{1}{I_1} \right) \right]$$

$$\text{Bending moment } M_o = \left(W_1 + \frac{W_2}{3} \right) \frac{L_2}{2} + \frac{EJ}{L_2} [Y_3 - Y_1]$$

EXIT CASING ELASTIC MODEL

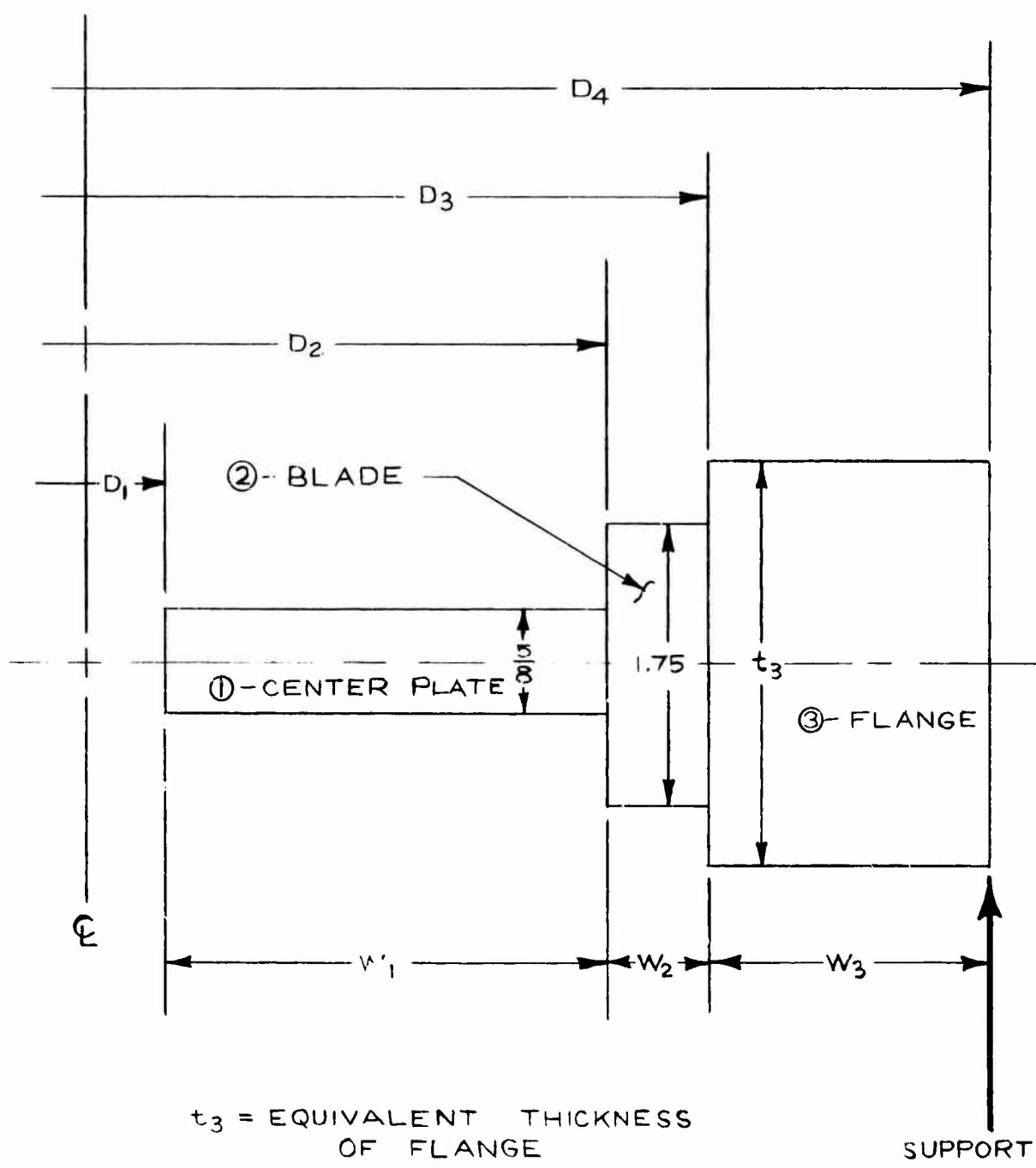


FIGURE 7.4.1

The maximum stress for the vanes

$$\sigma_N = \frac{M_O h}{J} \quad \text{where } J = NI$$

N = Number of vanes

I = Moment of inertia of one vane

(from Figure 7.4.1)

Diameter, in.

Force

$$D_2 = 23.50$$

$$W_1 = 20667. \text{ lb}$$

$$D_1 = 8.00$$

$$D_3 = 24.50$$

$$W_2 = 2034. \text{ lb}$$

$$D_2 = 23.50$$

$$D_4 = 30.00$$

$$D_3 = 24.50$$

$$W_3 = 50825.0 \text{ lb}$$

$$L_3 = 30.0 - 23.50 = 3.25 \text{ in}$$

$$L_2 = 24.5 - 23.50 = .50 \text{ in}$$

$$I_{y3} \approx .844$$

$$\left. \begin{array}{l} I_{y3} \approx .844 \\ I_{x3} \approx 3.38 \end{array} \right\} I_P = I_y + I_x = 4.224 \text{ in}^4$$

$$Y_3 = \left[\left(\frac{2034 + 50825}{2} + 20667 \right) 3.25 - M_O \right] \frac{15}{2\pi 26 \times 10^6} \left[\frac{\pi}{4(.844)} + \frac{2}{\pi} \left(\frac{2.5}{3.38} + \frac{1}{.844} \right) \right]$$

$$Y_3 = [85897.5 - M_O] .36$$

$$Y_1 = [6889 (9.72) + M_O] .048 [2.336 + 1.90]$$

$$M_O = \left(W_1 + \frac{W_2}{3} \right) \frac{l_2}{2} \frac{EJ}{l_2} (Y_3 - Y_1)$$

$$M_O = \left(20667 + \frac{2034}{3} \right) \frac{.5}{2} + \frac{26 \times 10^6 (5.94)}{(.50)} [30923 - .36 M_O - 13593 - .203 M_O]$$

$$M_O = 30607.4 \text{ in-lb}$$

$$\frac{M_O}{\text{Blade}} = \frac{30607.4}{9} = 3400 \text{ in-lb}$$

$$\sigma_{\text{MAX in vane}} = \frac{3400 (.750)}{.156} = 16350 \text{ psi}$$

$$\Delta R_1 = \frac{M_1 (r_2^2 - r_1^2)}{4\pi E} \left(\frac{\pi}{2I_1} + \frac{5}{2I_{p_1}} \right)$$

$$\Delta R_1 = 97568.4 \frac{(11.75^2 - 16)}{4 (26 \times 10^6)} \left[\frac{\pi}{.336(2)} + \frac{2.5}{233.8} \right]$$

$$\Delta R_1 = .01708 \text{ inch}$$

7.5 ANALYTICAL METHODS

The fundamental analytical problems are:

1. determining steady-state fluid film forces and moments
2. establishing dynamic response of sector considering fluid film and other applied forces.

To obtain the fluid-film characteristics requires solution of the time-dependent, compressible lubrication equation. This is a non-linear, second order differential equation with variable coefficients. In order to solve this equation, FIRL has utilized numerical techniques applied to the digital computer. The computerized analysis not only provides the most practical means for solving the equation, but allows considerable generality so that a wide variety of practical problems can be handled with a single program. The program descriptions are presented in Section 7.5.7. Following is the basic theory used for developing the computer programs.

7.5.1 Pad Configuration

A general thrust pad configuration for which the program was designed consists of multiple Rayleigh steps, with the option of including orifice fed recesses in the land region. The step may be bounded circumferentially as well as radially to inhibit side leakage and increase load capacity.

7.5.2 Pressure Distribution

For isothermal films, the compressible Reynolds' equation in polar coordinates is

$$\frac{\partial}{\partial r} \left(\frac{r \mu h^3}{\mu} \frac{\partial p}{\partial r} \right) + \frac{1}{r} \frac{\partial}{\partial \theta} \left(\frac{\mu h^3}{\mu} \frac{\partial p}{\partial \theta} \right) = 6r\omega \frac{\partial(\mu h)}{\partial \theta} + 12r \frac{\partial(\mu h)}{\partial t} \quad (7.5-1)$$

By changing the independent variable and non-dimensionalizing, the following equation results:

$$\frac{\partial}{\partial R} \left(\frac{R H^3}{2} \frac{\partial Q}{\partial R} \right) + \frac{1}{R} \frac{\partial}{\partial \theta} \left(\frac{H^3}{2} \frac{\partial Q}{\partial \theta} \right) = \lambda R \left[\frac{\omega}{\omega_1} \left(\sqrt{Q} \frac{\partial H}{\partial \theta} + \frac{H}{2\sqrt{Q}} \frac{\partial Q}{\partial \theta} \right) + \sqrt{Q} \frac{\partial H}{\partial T} + \frac{H}{2\sqrt{Q}} \frac{\partial Q}{\partial T} \right] \quad (7.5-2)$$

The choice of the independent variable $Q = p^2$ rather than the usual $p^2 H^2$ is selected because it is a more convenient variable at the Rayleigh step. Also note that T is non-dimensionalized with respect to an arbitrary speed ω_1 rather than the shaft speed, ω , so that hydrostatic performance at zero speed could be determined without introducing singularities in the analysis.

To solve for Q at the step, the continuity equation is applied about a unit grid sector surrounding each internal grid point along the step. The resulting equation becomes:

$$\begin{aligned} \frac{\lambda}{2} \left\{ \frac{2Q}{\sqrt{Q}} \frac{\partial H}{\partial T} + \frac{(H_- + H_+)}{2\sqrt{Q}} \frac{\partial Q}{\partial T} \right\} R dR d\theta + \frac{d\theta}{2} \left\{ \frac{1}{2} \frac{\partial Q}{\partial R} \right\}_- R_- \left(H_-^3 + H_+^3 \right) \\ - \frac{1}{2} \frac{\partial Q}{\partial R} \right\}_+ R_+ \left(H_-^3 + H_+^3 \right) + dR \left\{ \frac{H_-^3}{2R} \frac{\partial Q}{\partial R} \right\}_- \frac{H_+^3}{2R} \frac{\partial Q}{\partial \theta} \right\}_+ \\ + \lambda \frac{\omega}{\omega_1} dR \left\{ \frac{Q}{\sqrt{Q}} R \left(H_+ - H_- \right) \right\} = 0 \end{aligned} \quad (7.5-3)$$

The minus sign refers to conditions on the upstream side of the step, and the plus sign refers to conditions on the downstream side. A similar equation can be obtained for a step parallel to a circumferential line.

When expanding (7.5-2) and (7.5-3) in finite difference, both equations can be put into the same general matrix form, namely,

$$[C_j] + \{Q_j\} + [D_j] \{Q_{j-1}\} + [E_j] \{Q_{j+1}\} = \{F_j\} \leftarrow \quad (7.5-4)$$

$j = 1, N$

The coefficients $[C_j]$, $[D_j]$, and $[E_j]$ depend upon whether the grid point is at a boundary, step, or normal field point.

For interior points, the $[C_j]$ matrix is tri-diagonal and $[D_j]$ and $[E_j]$ are diagonal. The non-linearities occur because the coefficient matrices and the right hand side vector are functions of the \sqrt{Q} .

The boundary conditions are satisfied by manipulation of the coefficients and the right hand side of equation (7.5-3). Thus, for ambient pressures on the boundary:

$$[D] = [E] = 0$$

$$\{F\} = \{1\}$$

$$\text{and } C_{ik} = \delta_{ik} \quad (\text{kronocher delta})$$

The coefficient matrices of equation (7.5-4) are also functions of the clearance distributions.

It is noted that the time-transient Reynolds equation is applied. When solving a steady-state problem, the solution is a diffusion process (eliminating the equations of motion) that progresses in time until desired

convergence between successive iterations is achieved.

When solving a dynamics problem, a transient scheme as subsequently described is utilized. The column matrix solution of equation (7.5-4) proceeds as follows:

$$\text{Let } \{Q_{j+1}\} = [A_j] \{Q_j\} + \{B_j\} \quad (7.5-5)$$

$$j = N+2$$

Substituting (7.5-5) into (7.5-4) and solving for $\{Q_j\}$ produces

$$\begin{aligned} \{Q_j\} &= - \left[[C_j] + [D_j] [A_j] \right]^{-1} [E_j] \{Q_{j+1}\} \\ &= - [T]^{-1} \left[[D_j] \{B_j\} - \{F_j\} \right] \end{aligned} \quad (7.5-6)$$

where

$$[T] = [C_j] + [D_j] [A_j]$$

Comparing equations (7.5-5) and (7.5-6)

$$\begin{aligned} [A_{j+1}] &= - [T]^{-1} [E_j] \\ [B_{j+1}] &= - [T]^{-1} \left[[D_j] \{B_j\} - \{F_j\} \right] \end{aligned} \quad (7.5-7)$$

Note from the boundary conditions $\{Q_1\} = \{1\}$ which implies that

$$[A_2] = 0, \{B_2\} = 1 \quad (7.5-8)$$

Equation (7.5-8) is the starting point for the recursion relation of equation (7.5-7), and subsequent formation of the matrices $[A]$ and $[B]$.

For each time step, the non-linearity introduced by the parameter \sqrt{Q} in the coefficient matrices and right hand side is removed by computing its value from the previous iteration, and then solving the resultant linear equation

7.5.3 Film Thickness

In order to evaluate the coefficients of equation (7.5-4) the film thickness distribution must be determined from

$$H = 1 + Z_s - A_x R \sin \theta - A_y R \cos \theta - Z_b - B_x R \sin \theta + B_y R \cos \theta \quad (7.5-9)$$

When inside the stepped region, the step height is added, and when considering an opposed pair, the opposed bearing film thickness is obtained by subtracting H from the total axial clearance.

7.5.4 Hydrostatic and Hybrid Analysis

The effects of external pressure are handled by separate means depending on whether the recess can be considered a small source or not. If the recess is not a source and extends beyond the boundaries of one grid sector, the continuity equation can be applied to a closed path surrounding the recess. The resulting equation for the recess pressure becomes

$$\frac{dP_r}{dT} = \frac{F_0 - F_L}{AH_r A_r} - \frac{1}{H_r} \frac{dH_r}{dT} P_r - \frac{1}{H_r A_r} \int_A \frac{\partial}{\partial T} (PH) R dR d\theta \quad (7.5-10)$$

where the integral is taken over A, the area between the recess and the flow boundary

where

$$F_0 = OFC \left\{ (X)^{2/\alpha} \left[1 - X^{\alpha-1/\alpha} \right] \right\}^{1/2} \quad (7.5-11)$$

if P_r/P_s is less than critical, the ratio is set equal to the critical for determining mass flow.

$$F_L = - \int \frac{H^3 P}{R} \frac{\partial P}{\partial \theta} dR - \int H^3 P R \frac{\partial P}{\partial R} d\theta + \lambda \frac{\omega}{\omega_1} \int H P R dR \quad (7.5-12)$$

The integrals in equation (7.5-12) are taken along the selected closed path surrounding the recess. The procedure for obtaining a solution to equation (7.5-10) is to determine all quantities on the right hand side at the current time step and solve for the new recess pressures P_r . This approach does not solve the recess and field point pressures concurrently but at successive time intervals. If the recess is small, the pressure response can be very large unless very small time increments are chosen. When solving a steady-state problem, a small time step is not of serious consequence, but for a dynamic situation a small time step multiplies the number of solutions exorbitantly and this approach becomes impractical.

The solution to the problem posed by a source recess uses a scheme that solves for the recess and surrounding pressures simultaneously. By approximating the orifice flow F_0 by

$$F_0 = F_{\max} \left(1 - \frac{Q_r}{P_s^2} \right) \left(1 + \frac{P_r^2}{P_s^2} \right) \quad (7.5-13)$$

where P_r is from the previous time instant, the equation is thus linear in Q and the expression (7.5-10) (with dependent variable changed to Q_r) can now be put into a normal grid point format (equation 7.5-4) permitting simultaneous solution. This approach requires single grid point representation of the source, and an increase in the coefficient of discharge of the orifice to correct for the approximation imposed by

equation (7.5-13).

7.5.5 Bearing Forces and Moments

Solution of the Reynolds' equation for the pressure distribution immediately permits solution of the fluid film forces and moments.

$$T_f = \int_{r_i/r_o}^1 \int_0^\gamma (P-1) R d\theta dR \quad (7.5-14)$$

$$M_x = \int_{r_i/r_o}^1 \int_0^\gamma (P-1) R^2 \sin \theta d\theta dR \quad (7.5-15)$$

$$M_y = \int_{r_i/r_o}^1 \int_0^\gamma (P-1) R^2 \cos \theta d\theta dR \quad (7.5-16)$$

The effect of the viscous drag on the shaft is evaluated from

$$M_f = \int_{r_i/r_o}^1 \int_0^\gamma \frac{H}{2} \frac{\partial P}{\partial \theta} R d\theta dR + \frac{\lambda \omega}{6\omega_1} \int_{r_i/r_o}^1 \int_0^\gamma \frac{R^3}{H} d\theta dR \quad (7.5-17)$$

The above equations are for one pad. When multiple pads are considered, each pad is handled separately and the results consecutively added

7.5.6 Dynamics

As shown on Figure 6.5.10, the sector has two primary degrees of freedom. These are (1) axial motions (in z direction), (2) angular motions about the y axis. With the assumption of small displacements, the resulting non-dimensional dynamic equations are:

$$\ddot{Z}_s = \frac{1}{M_s} \left[T_f + W_{ae} \right] \quad (7.5-18)$$

$$\ddot{\gamma} = \frac{1}{I_y} \left[M_y - \frac{r_o}{c} \right] \quad (7.5-19)$$

In addition to the usual dynamic movements of the sector, the hydrostatic secondary seals must be examined for pneumatic hammer.

By treating a thrust sector of large radii, with uniform clearance, the cylindrical, hydrostatic secondary seal is approximated and equation (7.5-18) with the addition of sector weight can be applied

$$\dot{Z}_s = \frac{1}{M_s} [T_f + W_{ae} + W_s] \quad (7.5-20)$$

7.5.7 Solution Procedure

The general solution procedure for the steady-state analysis is as follows:

1. Read input quantities (geometry, λ , initial tilts, etc.).
2. Compute film thickness (equation 7.5-9).
3. Initialize Q throughout the grid ($Q = 1$).
4. Subdivide time into finite increments and for each time increment
 - a. Form coefficient matrices $[C]$, $[D]$ and $[E]$ of equation (7.5-4).
 - b. Form matrices $[A]$ and $[B]$, (equations 7.5-7 and 7.5-8)
 - c. Compute Q 's and $\sqrt{Q_s}$ (equation 7.5-5).
 - d. Test to see if newly computed Q 's are same as previous time step. If not, increment time step and with new \sqrt{Q} go back to (a) and continue. If new and old Q 's are identical within specified truncation go to (5)
5. Compute loads, moments, flows and viscous friction.

.. The dynamics are handled similarly, except after each time step, Z_s and \dot{Y} are computed from equations (7.5-18), (7.5-19), and (7.5-20). Then

$$\dot{Z}_s(t+\Delta t) = \dot{Z}_s(t+\Delta t)\Delta t + \dot{Z}_s(t) \quad (7.5-21)$$

and
$$Z_s(t+\Delta t) = Z_s(t+\Delta t)\Delta t + Z_s(t) \quad (7.5-22)$$

and similarly for $Y(t+\Delta t)$

The new displacements are then inserted into the film thickness expression for the next time increment. The process continues and the net results are displacements, flows, loads, etc. as a function of time.

7 5 8 Program Descriptions

This section describes the computer programs used in the analysis. Slight modifications were made to accomodate the particular problems associated with the sector seals.



Center for Computer-Aided Analysis

Program Description

7.5.8.1 BEARING AND SEAL SYSTEMS

PROGRAM:

GST-S, GAS LUBRICATED SECTORED THRUST
BEARINGS, STEADY STATE
PROGRAM NO. 32-19

PURPOSE:

To determine steady-state performance characteristics of gas lubricated sectored thrust bearings of various configurations.

APPLICATIONS:

Gas and air compressors, gas circulators, aerospace Brayton-cycle turbomachinery, cryogenic compressors and turboexpanders, machine tool spindles and slideways, pneumatic tools, instrument bearings, gyroscopes, textile spindles, gas turbines.

CAPABILITIES:

Sectored thrust pads, (polar coordinates)
Rayleigh steps in either direction
Hydrostatic, hybrid or hydrodynamic mode
Crown profiles: cylindrical, parabolic, spherical
Pivoted pads
Straight sliders
Orifice compensated recess, 1 per sector
Deformation
Misalignment
Up to 12 sectors per bearing
Dimensional or dimensionless input/output

METHOD:

The bearing is subdivided into a grid of finite spacing and Reynolds' equation is solved at the interior points by the column-matrix inversion⁽¹⁾ method until the pressure satisfies an externally specified truncation constant. For externally pressurized bearings continuity of flow through the restrictor and bearing film is simultaneously satisfied along with the Reynolds' equation for the interior points.

INPUT/OUTPUT

Input

Geometry
Type of bearing
Deformation*
Time step
Compressibility parameter
Misalignment
Origin of misalignment
Number of pads
External supply conditions*
Orifice size

Output

Individual pad forces
Fluid film moments
Friction moments
Center of pressure
Pivot film thickness
Minimum film thickness
Total forces
Total moments
Total friction moments
Total flow *
Minimum film thickness
Pressure distributions

*If applicable

SAMPLE PROBLEM:

One of the many uses of the steady-state program was to generate design data for a crowned profile tilting-pad thrust bearing. Geometric parameters are shown on Figure 1. Figure 2 shows field map data of friction moment factor, and pivot film thickness as a

(1) "Equilibrium Characteristics of Axial-Groove Gas-Lubricated Bearings", V. Castelli, J. Pirviks, Trans. of ASME, Journal of Lubrication Technology, Vol. 89, Series F, No. 2, April 1967, pp. 177-196.

function of pivot position. The family parameters are pad tilt and film thickness C . This particular field map was done for a pad with a cylindrical profile. Figure 3 shows the variation of load coefficient as a function of the compressibility parameter Λ .

NOMENCLATURE:

- C_L = dimensionless load coefficient = $W/P_a R_o^2$
 F = friction moment factor = $\frac{M_f}{P_a r_o^2 \delta}$
 h_{min} = minimum clearance, in.
 M_f = friction moments, in.-lbs
 μ = absolute gas viscosity, $\frac{\text{lb-sec}}{\text{in}^2}$
 ω = shaft speed, rad/sec
 Λ = compressibility parameter = $\frac{6\mu\omega R^2}{P_a C^2}$

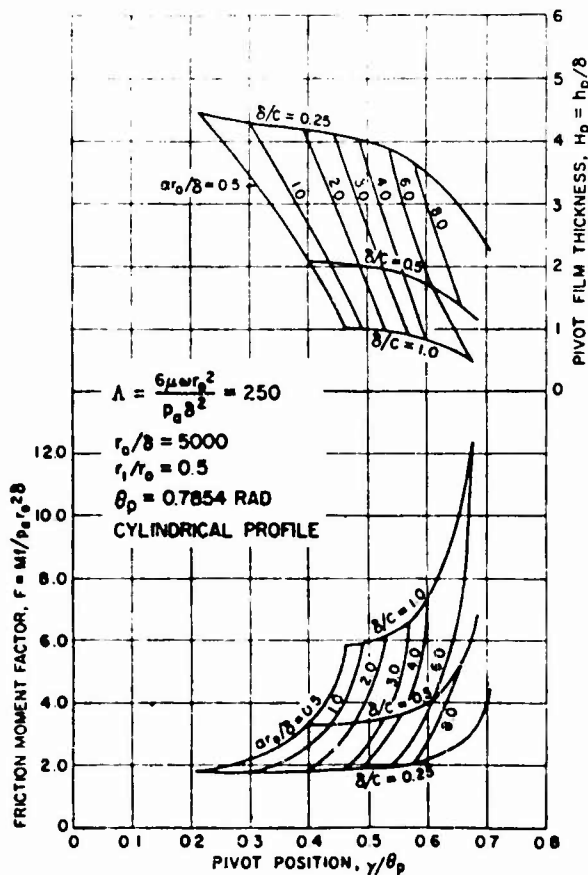


FIGURE 2 TILTING PAD THRUST BEARING FIELD PLOT FOR CONSTANT CROWN HEIGHT AND VARYING FILM THICKNESS

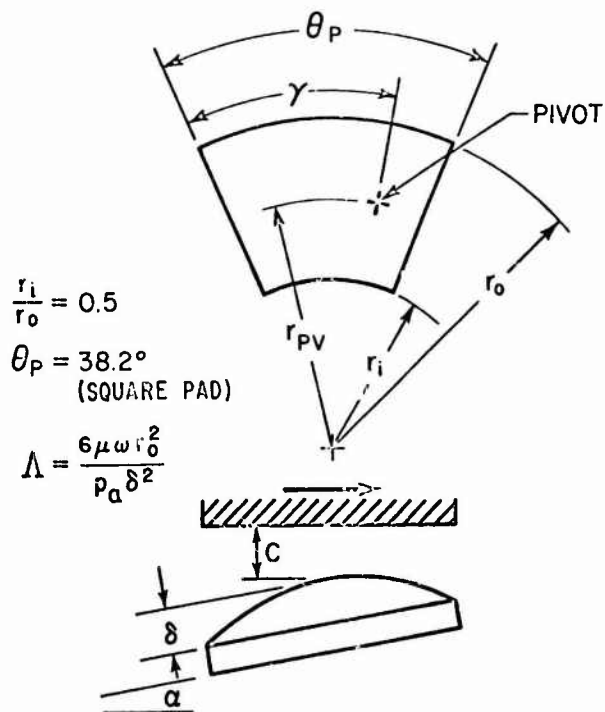


FIGURE 1 TILTING PAD THRUST BEARING GEOMETRY

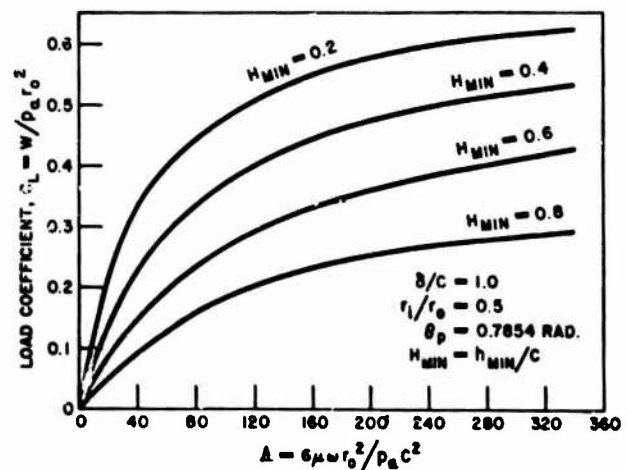


FIGURE 3 TILTING PAD THRUST BEARING—EFFECT OF VARYING COMPRESSIBILITY PARAMETER

**Center for Computer-Aided Analysis****Program Description****7.5.8.2 BEARING AND SEAL SYSTEMS****PROGRAM:**

GST-D, GAS LUBRICATED SECTORED THRUST
BEARINGS, DYNAMIC
PROGRAM NO. 32-20

PURPOSE:

To determine dynamic performance characteristics of gas lubricated sector pad thrust bearing configurations supported on a gimbal mount.

APPLICATIONS:

Gas and air compressors, gas circulators, aerospace Brayton-cycle turbomachinery, cryogenic compressors and turboexpanders, machine tool spindles and slideways, pneumatic tools, instrument bearings, gyroscopes, textile spindles, gas turbines.

CAPABILITIES:

Five degrees of freedom produced as a function of time
 shaft axial translation (1)
 gimbal translations (2)
 gimbal rotations (2)
Hydraulic parameters produced as a function of time
Rayleigh steps in both directions
Inclined slider
Crown profiles, cylindrical, parabolic, spherical
Orifice compensated recess, one per sector
Hydrostatic, hybrid or hydrodynamic mode
Opposed bearing pair or single surface
Up to twelve pads
Dimensionless or dimensional input/output
Off center gimbal axes
Case continuation
Pin joint (friction) gimbals
Elastic or flexure gimbal

METHOD:

The time-dependent lubrication equations are used to establish the bearing pressure distribution from which fluid film forces and moments are obtained. These are inserted into the equations of motion governing movements of the shaft and gimbal system, and reposition the components for the next time interval. If a hybrid bearing is employed the new recess pressures are determined by satisfying continuity through the restrictor and bearing film.

Large recesses as well as multiple sources can be treated. The new film thickness distribution and recess pressures are used as the initial conditions for the next interval. The process is repeated until bounded cyclic motions are evident, or instability is noted by exponential amplitude growth. The exciting force is misalignment of the thrust collar. The programs can treat either pin type gimbal bearings, or flexure gimbal mounts.

INPUT/OUTPUT**Input**

Pad geometry and type
Number of pads
Number of time steps
Value of time step
Initial displacements
Inertia and mass parameters
Friction moment, if pin gimbal
Torsional stiffness, if flexure gimbal
Lubricant parameters
External pressure system conditions
Thrust collar misalignment

Output per time step

Time step
Shaft axial displacement
Inner and outer gimbal axial displacements
Inner and outer gimbal angular displacements
Bearing flow
Fluid film force
Fluid film moments
Minimum film thickness

SAMPLE PROBLEM:

Figure 1 shows a central axis gimbal mounted thrust bearing. There are nine Rayleigh step pads. Both the inner and outer gimbal axes are pin joints. The case included friction in the joint and a misaligned thrust collar. Figure 2 shows the angular response of the gimbal about the X axis. After initial transients are dissipated the gimbal oscillates at an exponentially increasing amplitude as time progresses. Consequently this system under the given operating conditions is unstable. The swashing frequency of once per revolution is noted as an harmonic superimposed upon the natural frequency of the mount

NOMENCLATURE:

- BX = non-dimensional bearing displacement about inner gimbal axis = $\beta_x r_o / C$
 BY = non-dimensional bearing displacement about outer gimbal axis = $\beta_y r_o / C$
 C = reference film thickness, in.
 ZB = non-dimensional axial displacement of inner-bearing = displacement/C
 ZC = non-dimensional axial displacement of outer-bearing = displacement/C
 r_o = outside bearing radius, in.
 $\beta_{x,y}$ = angular displacement about x and y axis respectively, radians

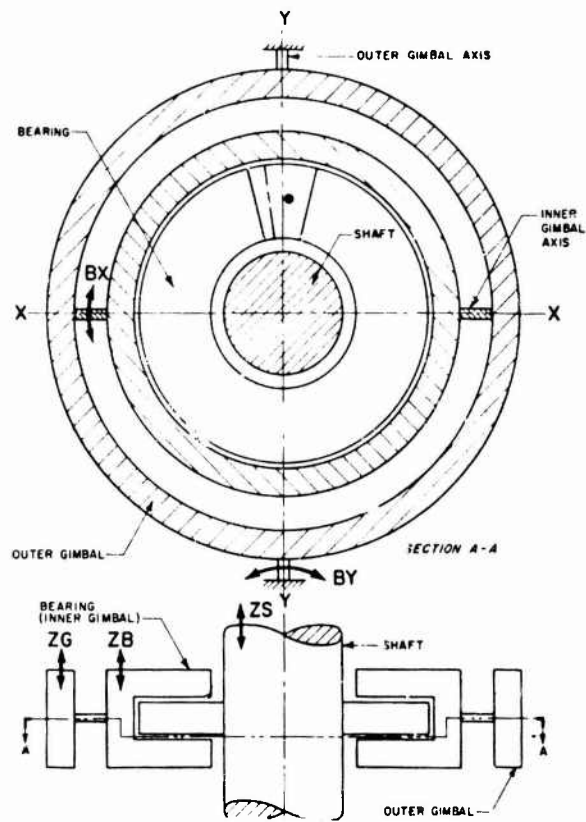


FIGURE 1 STEP THRUST BEARING AND MOUNT

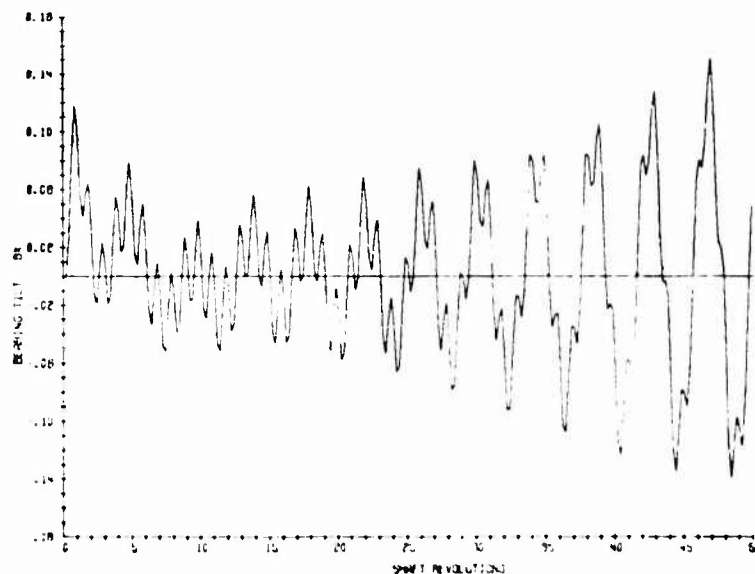


FIGURE 2 STEP THRUST BEARING PERFORMANCE—BEARING TILT VS. SHAFT REVOLUTIONS

7 5.9 Nomenclature

- A_i = orifice area, inherent compensation, in.²
 A_o = orifice area, in.²
 A_r = non-dimensional recess area = recess area / r_o^2
 A_x = non-dimensional shaft angular displacement about x axis
 = angle $\frac{r_o}{c}$
 A_y = non-dimensional shaft angular displacement about y axis
 = angle $\frac{r_o}{c}$
 B_x = non-dimensional sector displacement about x axis
 = $\frac{\alpha_x r_o}{c}$
 B_y = non-dimensional sector displacement about y axis
 = $\frac{\alpha_y r_o}{c}$
 C_d = orifice coefficient of discharge
 c = reference clearance, in.
 d = orifice diameter, inherent compensation, in.
 d_o = orifice diameter, in.
 FHP_P = sector friction loss, HP
 FHP_T = total seal friction loss, HP
 F_L = non-dimensional flow out of closed path surrounding recess
 = $\frac{12\mu f_L R'\theta}{c^3 p_a}$
 F_{max} = maximum non-dimensional orifice flow
 F_o = non-dimensional orifice flow = $\frac{12\mu f_o R'\theta}{c^3 p_a}$

- t_L = flow out of closed path surrounding recess, lb-sec/in.
 f_o = orifice flow, lb-sec/in.
 H = non-dimensional film thickness = h/c
 H_r = non-dimensional recess film thickness = h_r/c
 h = film thickness, in. or mils
 h_r = recess film thickness, in.
 I_x = non-dimensional sector moment of inertia about x axis

$$= \frac{\omega_1^2}{4p_a r_o^3} \times \{\text{moment of inertia}\}$$

 I_y = non-dimensional sector moment of inertia about y axis

$$= \frac{\omega_1^2}{4p_a r_o^3} \times \{\text{moment of inertia}\}$$

 K_a = axial film stiffness, lbs/in.
 M_i = non-dimensional viscous friction moment = $\frac{\text{moment}}{p_a r_o^2 c}$
 M_s = non-dimensional sector mass = $\frac{c \omega_1^2}{4p_a r_o^2} \times (\text{sector mass})$
 M_x = non-dimensional fluid film righting moment about x axis

$$= \frac{\text{Moment}}{p_a r_o^3}$$

 M_y = non-dimensional fluid film righting moment about y axis

$$= \frac{\text{Moment}}{p_a r_o^3}$$

 OFC = orifice flow coefficient = $\frac{12\mu A_o C_d P_s}{c^3 p_a^2} \frac{2dR'\Theta'}{(\alpha - 1)}$
 P = non-dimensional local pressure = pressure p_a
 P_a = ambient pressure, psia

P_H	= high pressure, psia
P_L	= low pressure, psia
P_r	= non-dimensional recess pressure = recess pressure/ p_a
p_s	= external supply pressure, psia
P_s	= non-dimensional supply pressure = p_s/p_a
p	= local pressure, psia
Q	= dependent variable = p^2
Q_p	= flow per pad or sector, lbs/sec.
Q_r	= dependent variable in recess = p^2
Q_T	= total seal leakage, lbs/sec.
R	= non-dimensional radius = r/r_o
R^*	= universal gas constant, $\frac{\text{in.}^2}{\text{sec}^2 \cdot ^\circ\text{R}}$
r	= radius, in.
r_{cp}	= radius to center of pressure, in.
r_1	= inside radius of bearing, in.
r_o	= outside radius of bearing, in.
T	= non-dimensional time = $t\omega_1/2$
T_f	= non-dimensional fluid film thrust force = $\frac{\text{force}}{p_a r_o^2} = \text{Total force}$
t	= time, sec.
W_{de}	= non-dimensional aerodynamic load = $\text{Load}/p_a r_p^2$
W_p	= pad load, lbs.

W_S	= non-dimensional sector weight = weight $\cdot p_a r_o^2$
X	= pressure ratio = p_r/p_s
X	= non-dimensional angular displacement about X axis = $\beta_x r_o/c$
Y	= non-dimensional angular displacement about Y axis = $\beta_y r_o/c$
Z_S	= non-dimensional sector axial displacement from equilibrium position = $\frac{\text{displacement}}{c}$
α	= ratio of specific heats
α_x	= sector angular displacement about x axis, rad.
α_y	= sector angular displacement about outer y axis, rad.
Δ	= step height, in
θ	= angular grid coordinate, radians
θ'	= absolute temperature, $^{\circ}\text{R}$
θ_{cp}	= angle to center of pressure, degrees
θ_p	= angular extent of sector, degrees
λ	= compressibility parameter = $\frac{6\mu\omega r_o^2}{p_a c^2}$
μ	= absolute viscosity, lb-sec/in. ²
ω	= angular shaft speed, rad/sec.
ω_1	= reference angular speed, rad/sec.

8.0 PREDICTED PERFORMANCE

The aerodynamic performance of the LVF turbine, with design geometry and seal locations specified in Section 6.0, was predicted using efficiency relationships discussed in Section 3.1. Actual loss parameters such as seal leakage and friction were evaluated by FIRL for the particular sealing configuration reported herein. The turbine efficiency obtained by the methods indicated in Section 3.1 was modified by these parameters to provide a realistic estimate of operating turbine efficiency.

The performance of the LVF turbine was evaluated under design and off design operating conditions and is reported in the following section. The predicted design point efficiency for the LVF turbine was 0.802. This performance may be compared favorably with the turbine efficiency predicted for a conventional partial admission impulse turbine. As indicated in Reference 5.1.1, a conventional turbine operating at a specific speed of 17 has an efficiency potential of 0.72. On this basis the performance potential of the LVF turbine offers a significant advantage over conventional turbines operating in this range of specific speed.

8.1 DESIGN POINT PERFORMANCE

Turbine hydraulic efficiency, evaluated using Equation 3.1-16), for the design blade angles and velocity ratio, chosen for the LVF turbine, is 0.8776. The design rotor and stator velocity coefficients used in this analysis to define gas velocities through the turbine were evaluated to be 0.96 at the design point. Data examined in Section 6.0 was used to verify this figure.

The following table summarizes the seal leakage and friction loss evaluated for each sealing surface. The friction loss parameters shown are expressed as a fraction of the total available energy, and as such, these losses are directly subtracted from the turbine hydraulic efficiency. Seal leakage is given as a fraction of the total flow rate and the correction on turbine efficiency was given in Section 3.1.

SEAL LEAKAGE AND FRICTION		
Seal Location	Individual Seal Leakage, ξ_2	Individual Seal Friction, ξ_{sf}
Front. OD Seal	.0106	.00407
Front ID Seal	.0104	.00516
Rear	-	.00383
Total	.0210	.01306

Seal leakage is not shown for the rear seal, as leakage here does not detract from turbine performance.

The turbine disk friction was evaluated for each of the four sections indicated in Section 3.1. This loss is reported in the following table in the same form as the seal friction loss above, and also is directly subtractive from turbine efficiency.

Location	Turbine Disk Friction ξ_{DF}
Turbine rotor rear Above rear seal	.0336
Turbine rotor rear Below rear seal	.0007
Turbine rotor front	.0018
Turbine rotor OD	.0073
Total	.0434

Using the turbine hydraulic efficiency and loss parameters reported above, the actual turbine efficiency was evaluated to be 0.802. This performance was predicted for the LVF turbine configuration using data from tested nozzle and rotor blade designs and no advancements are required to achieve the predicted performance. The total turbine flow rate necessary to produce an output power of 425 HP was evaluated from the available energy and the above turbine efficiency as 4.32 lb/sec, resulting in a turbine specific speed of 17.2. These values are well within the design goals established for the LVF turbine and the performance evaluation as given above for the design point was felt to be acceptable.

8.2 OFF DESIGN PERFORMANCE

The predicted off design performance of the LVF turbine is shown in Figure 8.1.1 as a function of turbine velocity ratio. Loss factors such as disk friction, seal friction and leakage were included in the performance evaluation. Also included was the loss factor associated with the gas incidence angle. The magnitude of the incidence angle was obtained by the method indicated in Section 2.1 and the loss coefficient was presented in Section 7.1. The resulting turbine efficiency shown in the figure is the actual turbine efficiency obtainable by the LVF turbine under various operating conditions.

VARIATION OF TURBINE EFFICIENCY WITH VELOCITY RATIO

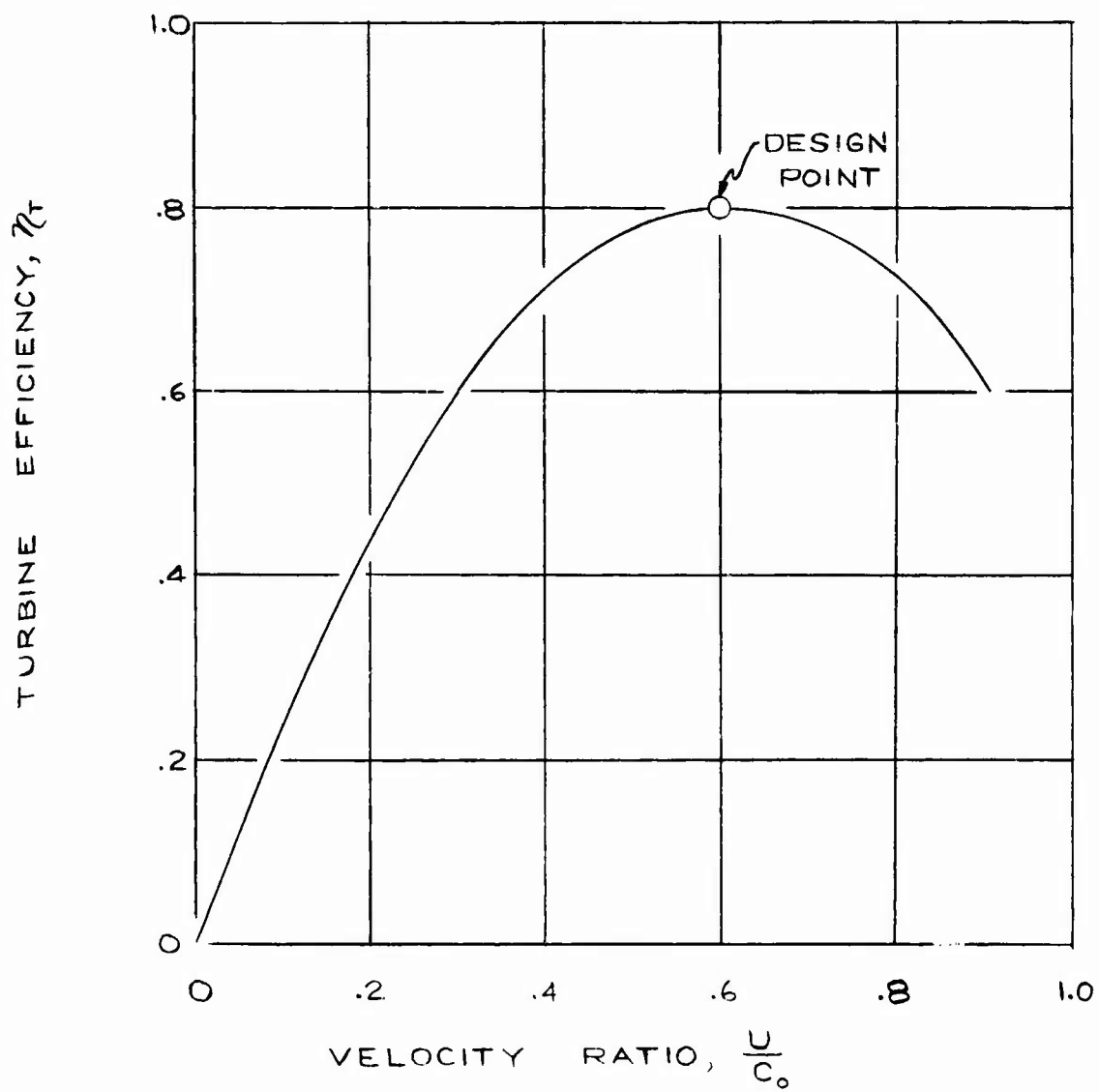


FIGURE 8.1.1

Turbine velocity ratio (U/C_0) was chosen as the independent variable used to present the off design performance of the LVF turbine. For a given turbine diameter, the turbine rotative speed will determine the tip speed U . The isentropic spouting velocity C_0 is determined by operating steam conditions and variation in design steam temperatures and pressures are felt in this parameter. Therefore, the dimensionless velocity ratio allows the evaluation of the actual turbine efficiency during start up, when turbine speed has not reached design, or part load conditions when the inlet pressure and temperature may be significantly different than design. Variations in turbine efficiency with pressure ratio is accounted for in Figure 8.11, since the spouting velocity is dependent on pressure ratio. According to data presented in Reference 6.1.3, turbine blade efficiencies remain essentially constant with leaving Mach number below a mach number of one, and during this analysis the nozzle and rotor velocity coefficients were assumed constant at the indicated value of 0.96.

9.0 RECOMMENDATIONS

9.1 GENERAL RECOMMENDATIONS

1. Further thermal analysis should be made in the seal areas after the controlled-leakage seals are finalized by FIRL.
2. Further thermal analysis should be made in the shroud area of the disk to determine in more detail the axial and radial temperature gradients and to determine if fins on the shroud are necessary.
3. A design study and analysis should be made to determine the additional cooling water necessary to reduce the axial temperature gradients in the turbine housing.
4. The thermal stress analysis of the disk should be updated with the information obtained from Recommendations 1, 2, and 3.
5. A proof of performance test should be conducted to demonstrate and substantiate the performance of the primary seal, secondary seal, and bearings, and to investigate the dynamic characteristics of the seal and rotor system before the construction of the LVF turbine.
6. The testing of the LVF turbine test unit should include temperature measurements in the critical areas of turbine housing, bearing sections, and cooling water passages, and measurements should be made of shaft, seal, and rotor response.

9.2 FIRL'S RECOMMENDATIONS

1. Since the seals' tracking capability is limited by the maximum runout of the rotor, it is recommended that the rotor-bearing system be dynamically analyzed to establish accurate rotor motions at the seal interface. This can be accomplished by FIRL using time transient analyses similar to the ones described in Sections 6.5.1 and 7.5 of this report.
2. Further effort is required to finalize the seal designs. Included are the following:
 - a. determining if a hydrostatic and/or hydrodynamic 15 degree sector can accurately track the total runouts determined from 1. above.

- b. including hydrodynamic backup for the hydrostatic seal to provide emergency reserve in case pressure is lost while the rotor is running
 - c. establishing the effect of lighter materials than steel (titanium and carbon)
 - d. conducting further dynamic studies of the secondary seal to aid in preventing pneumatic hammer
 - e. completing the designs of Seals 2 and 3.
- 3. Because seals are critical to turbine performance, turbine production should be deferred until seal performance has been substantiated
 - 4. The principle of the seals should be qualified on simplified test rigs. For example, a simple sector can be produced and tested for establishing performance of the hydrostatic secondary seal. It will probably be necessary to produce one complete seal for determining dynamic performance of the primary seal.
 - 5. Based on the combination of comprehensive analyses and qualification testing the seal configurations should be finalized and produced.
 - 6. FIRM should actively participate on a continuing subcontract basis to lend the necessary engineering support for further efforts related to seal development.

10.0 DRAWINGS

The preliminary design of the L V F turbine is presented in drawings entitled, "L V F Turbine Layout". The layout consists of sheets one through four.

Sheet one shows the full size cross-section of the turbine and an end projection viewed from the output shaft end.

Sheet two shows the necessary views and sections defining the journal bearings, water injectors, and water inlets of the output end.

Sheet three shows views and sections defining the journal and thrust bearing, water injectors, exhaust and seal housing, and left-hand end view of the turbine.

Sheet four shows the developed section through the stators and rotor nozzles, blade dimensions, and profiles.

Sheet five shows the hydrostatic seal segment assembly.

11.0 REFERENCES

- Reference 3.1.1 Hamm, H. W., "DETERMINING FLUID FRICTION OR WINDAGE OF ROTATING DISCS", Allis-Chalmers Electrical Review, Fourth Quarter, 1962.
- Reference 3.2.1 Mitchell, J. W. & Metzger, D.E., "HEAT TRANSFER FROM A SHROUDED ROTATING DISK TO A SINGLE FLUID STREAM", ASME Journal of Heat Transfer, Nov. 1965.
- Reference 3.2.2 Sparrow & Gregg, J. L., "MASS TRANSFER, FLOW, AND HEAT TRANSFER ABOUT A ROTATING DISK", ASME Paper 59-A-107, 1959.
- Reference 3.2.3 Deissler, R.G. & Loeffler, A.L., "ANALYSIS OF TURBULENT FLOW AND HEAT TRANSFER ON A FLAT PLATE AT HIGH MACH NUMBERS WITH VARIABLE FLUID PROPERTIES", NASA TR R-17, 1959.
- Reference 3.2.4 Ostrach, S. & Thorton, P.R., "COMPRESSIBLE FLOW AND HEAT TRANSFER ABOUT A ROTATING ISOTHERMAL DISK", NACA TN 4320, 1958.
- Reference 3.2.5 Kreith, F. et al, "MASS AND HEAT TRANSFER FROM AN ENCLOSED ROTATING DISK WITH AND WITHOUT SOURCE FLOW", ASME Journal of Heat Transfer, May 1963.
- Reference 3.2.6 Mann, R. W. & Marston, C. H., "FRICTION DRAG ON BLADED DISKS IN HOUSINGS AS A FUNCTION OF REYNOLDS NUMBER, AXIAL AND RADIAL CLEARANCE, AND BLADE ASPECT RATIO AND SOLIDITY", ASME Paper No. 61-Hyd-5, 1961.
- Reference 3.2.7 Daily, J. W. & Nece, R. E., "CHAMBER DIMENSION EFFECTS ON INDUCED FLOW AND FRICTIONAL RESISTANCE OF ENCLOSED ROTATING DISKS", ASME Journal of Basic Engineering, March 1960.
- Reference 3.2.8 Nece, R. E. & Daily, J. W., "ROUGHNESS EFFECTS ON FRICTIONAL RESISTANCE OF ENCLOSED ROTATING DISKS", ASME Paper 59-A-55, 1959.
- Reference 3.2.9 Pfleiderer, "DIE KREISELPUMPEN", Springer, Berlin, 1949.
- Reference 3.2.10 Schultz-Grunow, "DER REIBUNGSWIDERSTAND ROTIRENDER SCHEIBEN IN GEHAUSEN", Z. Angew. Math. Mech. Vol. 15, Bull. 4, July 1935, V.D.I. Berlin 1937.
- Reference 3.2.11 Ribary, F., "THE FRICTION LOSSES OF STEAM TURBINE DISCS", Brown-Boveri Review, Vol. 21, 1934.

- Reference 3.2.12 Stodola, A., "STEAM AND GAS TURBINES", Peter Smith, 1945.
- Reference 3.2.13 Buckingham, "WINDAGE RESISTANCE OF STEAM TURBINE WHEELS", Bureau of Standards, Washington, Vol. 10, 1914.
- Reference 3.2.14 McAdams, W. H., "HEAT TRANSMISSION", Third Edition, McGraw-Hill, 1954.
- Reference 3.2.15 Kays, W. & London, A.L., "COMPACT HEAT EXCHANGERS", Second Edition, McGraw-Hill, 1964.
- Reference 3.2.16 "TABLES OF COMPRESSIBLE FLOW FUNCTIONS", Pratt & Whitney Aircraft, 1963.
- Reference 3.2.17 "HOW TO EVALUATE FILM COEFFICIENTS FOR HEAT TRANSFER CALCULATIONS", The Oil & Gas Journal, 1953.
- Reference 3.4.1 Den Hartog, J. P., "ADVANCED STRENGTH OF MATERIALS".
- Reference 5.0.1 Nichols, K. E., "LVFT PERFORMANCE PREDICTION AND ANALYSIS, FINAL REPORT", Barber-Nichols/Engineering Co.
- Reference 6.1.1 Ainley, D. G. & Mathieson, G.C.R., "AN EXAMINATION OF THE FLOW AND PRESSURE LOSSES IN BLADE ROWS OF AXIAL-FLOW TURBINES", NGTE Report R86, Sept. 1951.
- Reference 6.1.2 Balje, Dr. O.E. & Binsley, R.L., "TURBINE PERFORMANCE PREDICTION: OPTIMIZATION USING FLUID DYNAMIC CRITERIA", Final Report Nonr 4507(00), Report No. R-6805, Dec. 1966.
- Reference 6.1.3 Kraft, H., "REACTION TESTS OF TURBINE NOZZLES FOR SUBSONIC VELOCITIES", Trans. of the ASME, Oct. 1949.
- Reference 6.1.4 Zweifel, O., "THE SPACING OF TURBO-MACHINE BLADING ESPECIALLY WITH LARGE ANGULAR DEFLECTION", The Brown-Boveri Review, Vol. 32, No. 12, 1945.
- Reference 6.1.5 Howell, A.R., & Carter, A D.S., "FLUID FLOW THROUGH CASCADES OF AERO FOILS", published in Proc. of Congress of Applied Mechanics, 1946.
- Reference 6.3.1 Den Hartog, J. P., "MECHANICAL VIBRATIONS", Third Edition.
- Reference 6.3.2 Moody, A.M.G., "THE AXIAL VIBRATION OF TURBINE DISKS", ASME Paper No. 44-A-24.
- Reference 6.3.3 Timoshenko, S., "VIBRATION PROBLEMS IN ENGINEERING", Third Edition.

- Reference 6.4.2 "STRENGTH AND DEFORMATION IN NON-UNIFORM TEMPERATURE FIELDS", authorized translation from the Russian, edited by Prof. Ya. B. Fridman.
- Reference 6.4.3 Roark, R. J., "FORMULAS FOR STRESS AND STRAIN".
- Reference 6.4.4 Alford, J. S., "DESIGN CRITERIA AND CONFIGURATION FOR LONG-LIFE AIRCRAFT GAS TURBINES".
- Reference 6.4.5 "BURST STRENGTH OF ROTATING DISCS", Institution of Mechanical Engineering.
- Reference 6.4.6 Watts, G.W. & Lang, H. A., "THE STRESS IN A PRESSURE VESSEL WITH A FLAT HEAD CLOSURE", ASME Paper No. 51-A-146.
- Reference 7.1.1 Sheppard, D. G., "PRINCIPLES OF TURBO-MACHINERY", The Macmillan Co., N.Y. 1965.
- Reference 7.4.1 Timoshenko, S., "STRENGTH OF MATERIALS, PART II".
- Reference 7.5.1 Castelli, V. & Pirvics, J., Jr., "EQUILIBRIUM CHARACTERISTICS OF AXIAL GROOVE GAS LUBRICATED BEARINGS", Columbia Univ., Dept. of Mech. Eng., Lubrication Research Lab. Report No. 1, 1965.
- Reference 7.5.2 Castelli, V. & McCabe, J.T., "TRANSIENT DYNAMICS OF A TILTING PAD GAS BEARING SYSTEM", ASME, June 1966, LubS-3.

12.0 APPENDIX

12.1 STEADY-STATE PERFORMANCE OF THE RAYLEIGH-STEP PRIMARY SEAL

Figures 12.1.1 and 12.1.2 show steady-state performance of the side-fed Rayleigh-Step seal as a function of the film thickness. The information is for both of the seals on the high pressure side, Seals 1 and 2. The slope of the load versus clearance curve is the fluid film stiffness. Note that the stiffness is not exceptionally large for either seal at the normal 1 mil operating condition. The 12.5 inch outside radius seal has relatively poor stiffness since the seal width is limited to 3/8 inch. The table below lists pertinent steady-state performance.

	SEAL 2	SEAL 1
Seal Outside Radius, in.	12.5	11.75
Seal Width, in.	0.375	0.50
Sector Flow, lb/sec.	0.0038	0.0037
Sector Load, lbs	76	218.5
Sector Stiffness, lb/in.	5,000	10,000
Viscous Power Loss, HP	0.18	0.19
Operating Film Thickness, in.	0.001	0.001

Figure 12.1.3 shows similar results for a 15 degree sector.

12.2 FLOW CALCULATION BETWEEN SEGMENTS

Laminar Flow Through Slot

$$\begin{aligned}
 f_L &= \frac{h^3 L}{24 RT \mu} \frac{P_H^2 - P_L^2}{b} \\
 &= \frac{95^2 - 2^2}{(24)(1029.35)(890)(2.43 \times 10^{-9})} \frac{h^3 L}{b} \\
 &= 168.84 \times 10^3 \frac{R^3 L}{b} \quad (P_a = 2)
 \end{aligned}$$

Orifice Flow Through Slot

$$\begin{aligned}
 f_o &= \frac{h L C_b P_h}{RT} \sqrt{\frac{2\gamma R}{\gamma-1}} \left\{ (P_c)^{2/\gamma} \left[1 - (P_c)^{\frac{\gamma-1}{\gamma}} \right] \right\}^{1/2} \\
 C_b &= .8 \\
 \gamma &= 1.315 \\
 T &= 430^{\circ} + 460^{\circ} = 890^{\circ}R \\
 \mu &= 2.43 \times 10^{-9} \text{ lb-sec/in}^2
 \end{aligned}$$

270

SIDE - FED RAYLEIGH-STEP SECTORED SEAL STEADY-STATE PERFORMANCE

30° PAD
 $r_o - r_i = .5$ IN.
 $r_o = 11.875$ IN.
 $P_A = 2.0$ PSIA
 $N = 12000$ RPM

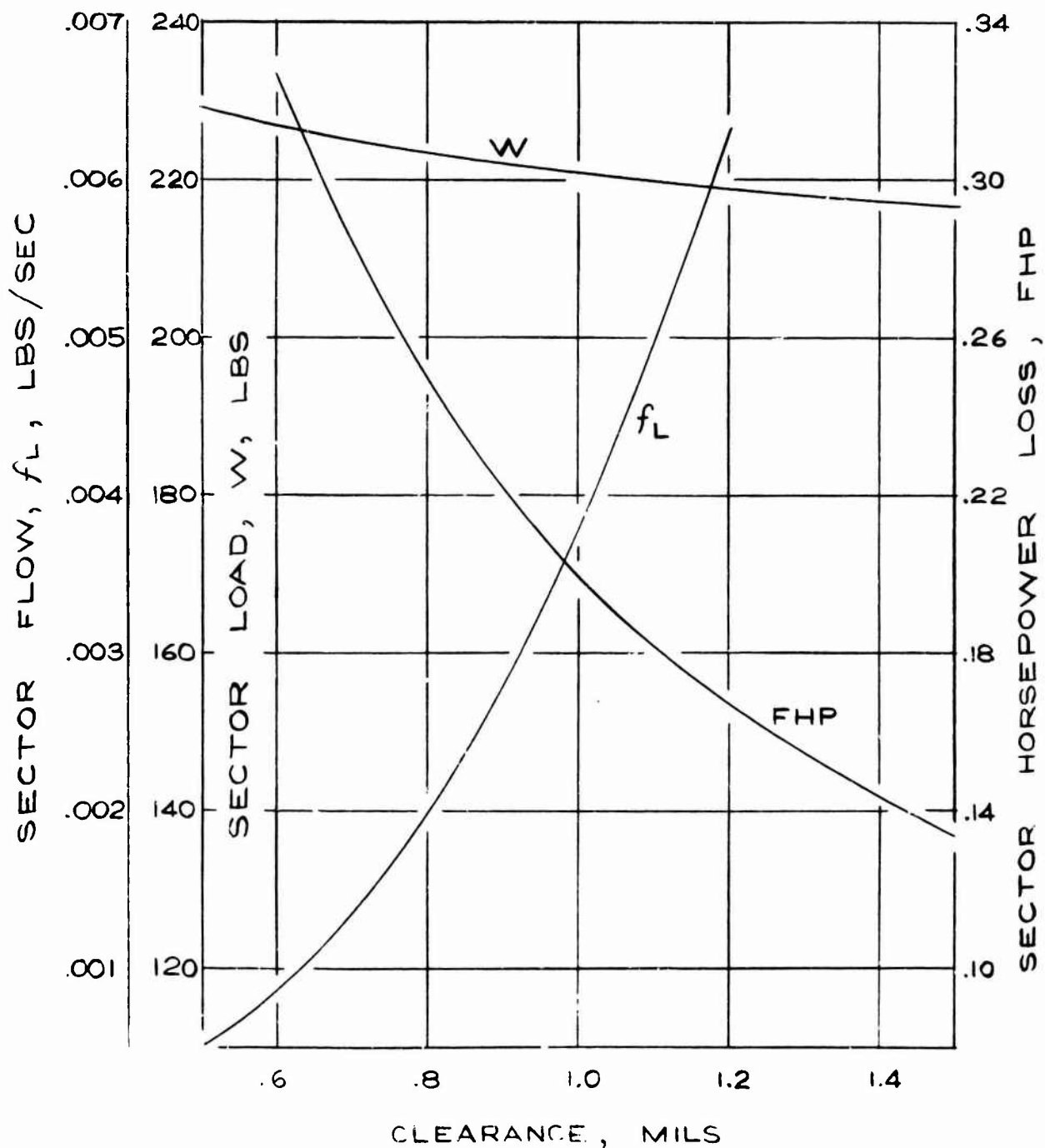


FIGURE '2.1.1

271 SIDE-FED RAYLEIGH-STEP SECTORED SEAL STEADY-STATE PERFORMANCE

30° PAD

$r_o - r_i = .375$ IN.

$r_o = 12.5$ IN.

$P_A = 50$ PSIA

$N = 12000$ RPM

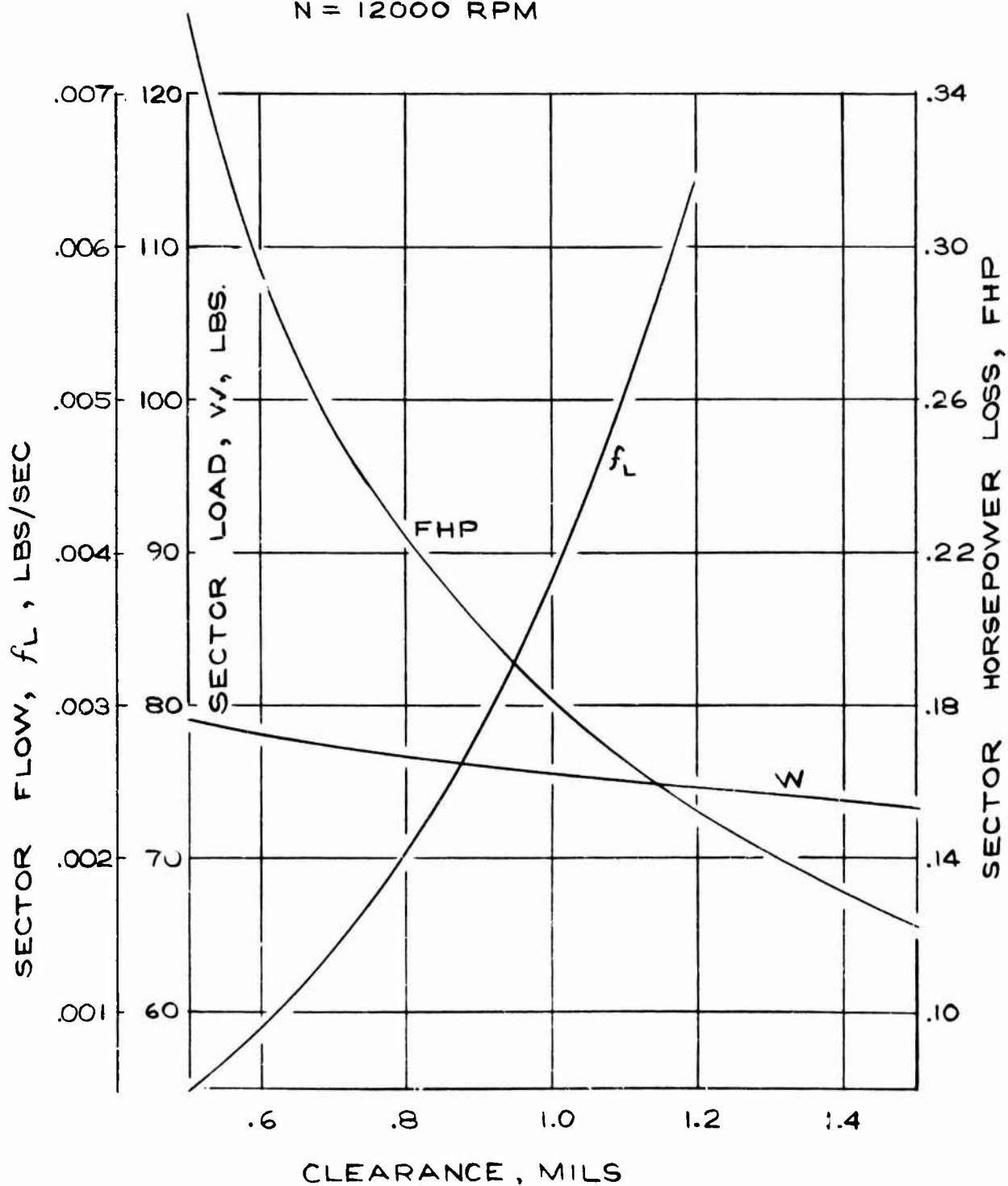


FIGURE 12.1.2

SIDE-FED RAYLEIGH-STEP SECTORED SEAL STEADY-STATE PERFORMANCE

15° PAD
 $r_o - r_i = .5$ IN.
 $r_o = 11.875$ IN.
 $P_A = 2.0$ PSIA
 $N = 12000$ RPM

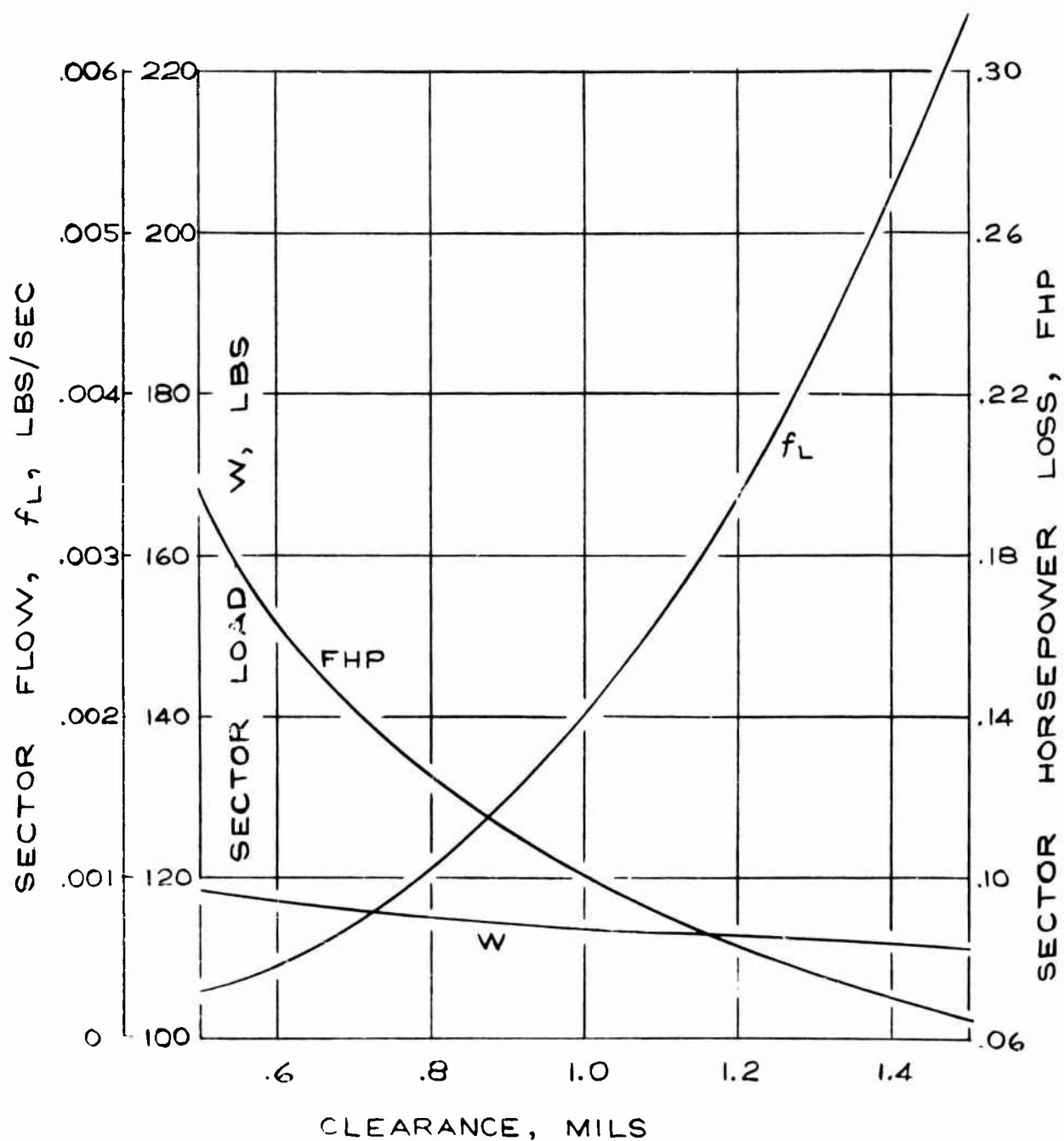


FIGURE 12.1.3

R = 397,741 in²/sec²

γ = 1.315

P_c = (2/1.315)^{1.315/1.315} = .543

f_o = $\frac{h L (.8) (95)}{(397,741) (890)} \sqrt{\frac{(2) (1.315) (397,741) (890)}{1.315 - 1.0}}$

f_o = $\left\{ (.543)^{\frac{2.0}{1.315}} \left[1 - (.543)^{\frac{.315}{1.315}} \right]^{1/2} \right\}$

f_o = .2147 x 10⁻⁶ (54.365 x 10³) {(.39505) (.1361)}^{1/2} hL

f_o = .0027 hL

In Weight Units , f_o = (386.4) (.0027) hL = 1.0457 hL (lbs/sec)

Let b = .5 (Primary Seal Width)

and h = .001

L in.	f _L lb/sec	f _o lb/sec
.5	.000169	.000523
1.0	.000338	.001046
1.5	.000506	.001568

Make gap size between segments h_g ≤ .001. Therefore laminar flow will be considered through the gap.

12.3 DYNAMIC PLOTS

BN-SEAL DYNAMIC PERFORMANCE AT DESIGN OPERATION, 24 SEGMENT ORIFICE-FED SEAL,
CASE 1, ONE DEGREE OF FREEDOM, WHEEL Y-NUTATION

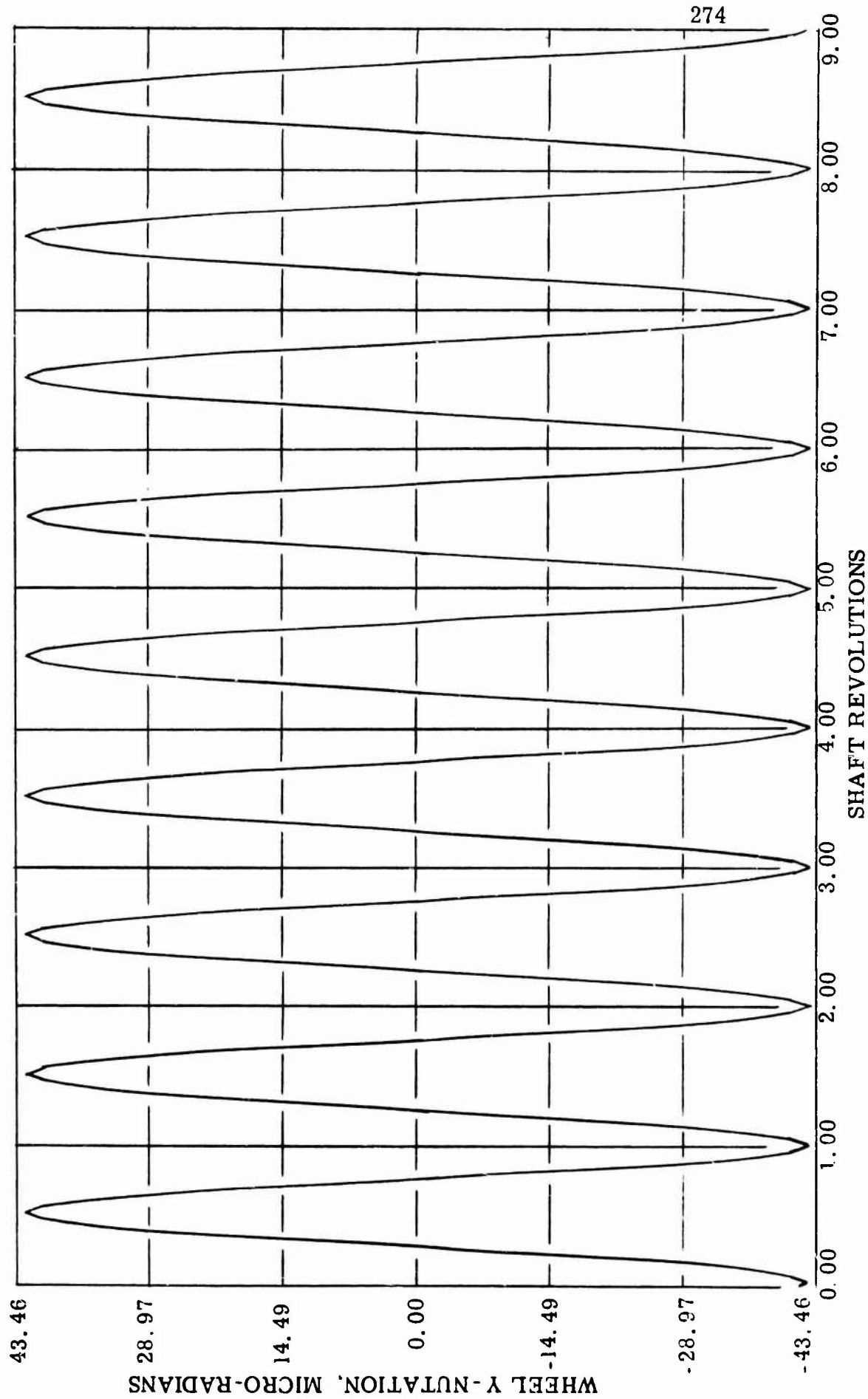


FIGURE 12.3.1

BN-SEAL DYNAMIC PERFORMANCE AT DESIGN OPERATION, 24 SEGMENT ORIFICE-FED SEAL,
CASE 1, ONE DEGREE OF FREEDOM, WHEEL X-NUTATION

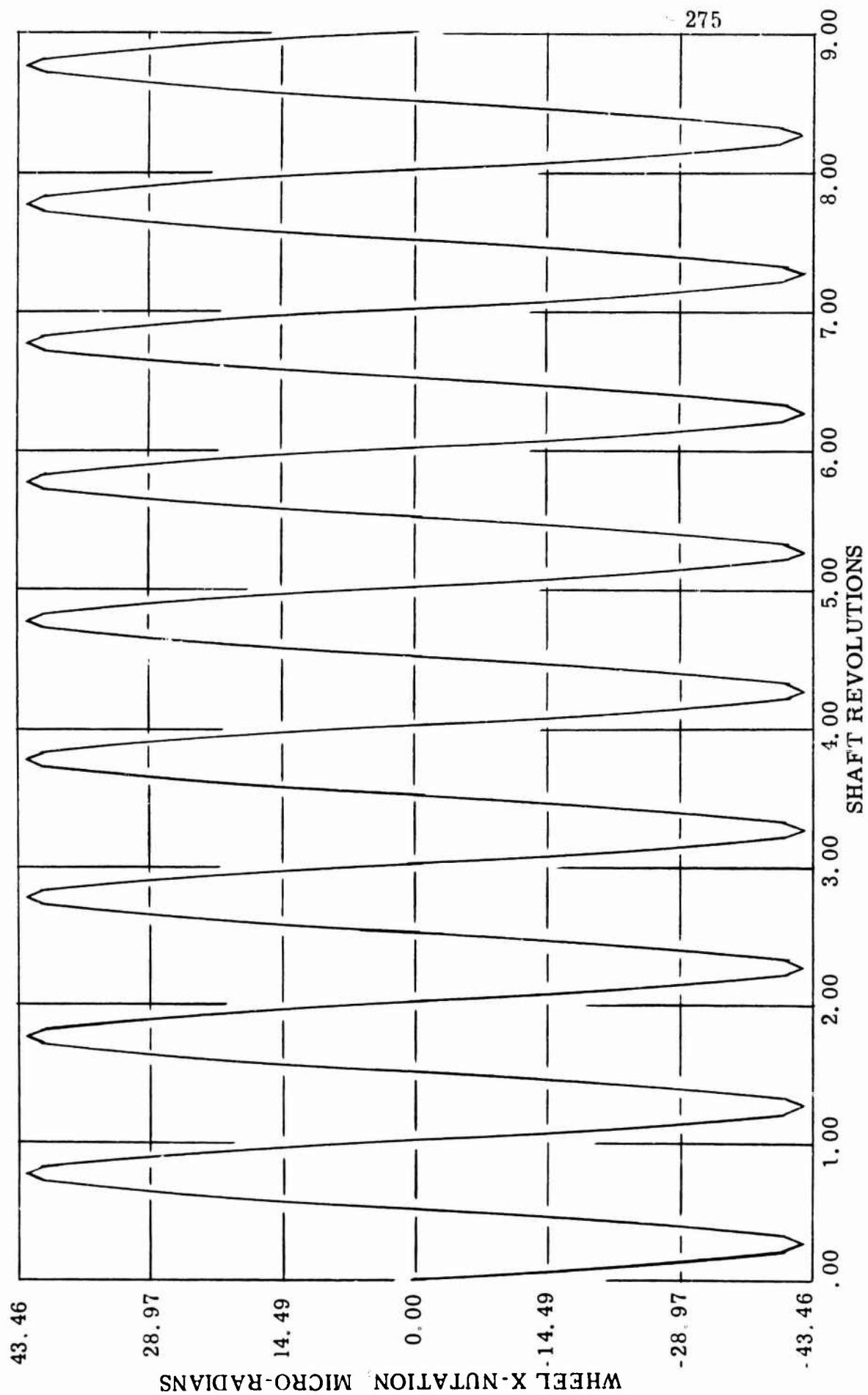


FIGURE 12.3.2

BN-SEAL DYNAMIC PERFORMANCE AT DESIGN OPERATION, 24 SEGMENT ORIFICE-FED SEAL,
CASE 1, ONE DEGREE OF FREEDOM, SEAL TRANSLATION

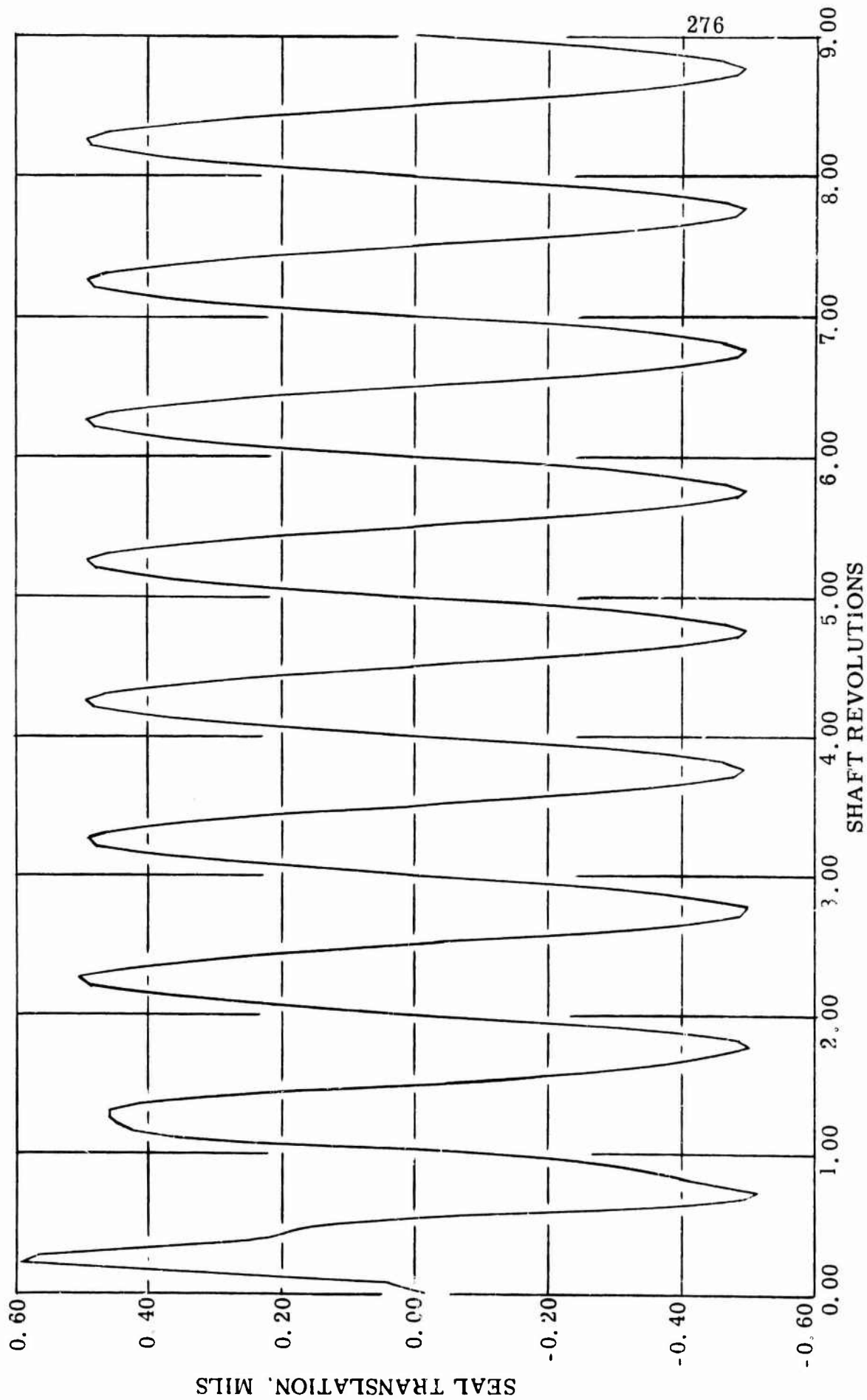


FIGURE 12.3.3

BN-SEAL DYNAMIC PERFORMANCE AT DESIGN OPERATION, 24 SEGMENT ORIFICE-FED SEAL
CASE 1, ONE DEGREE OF FREEDOM, SEAL LEAKAGE

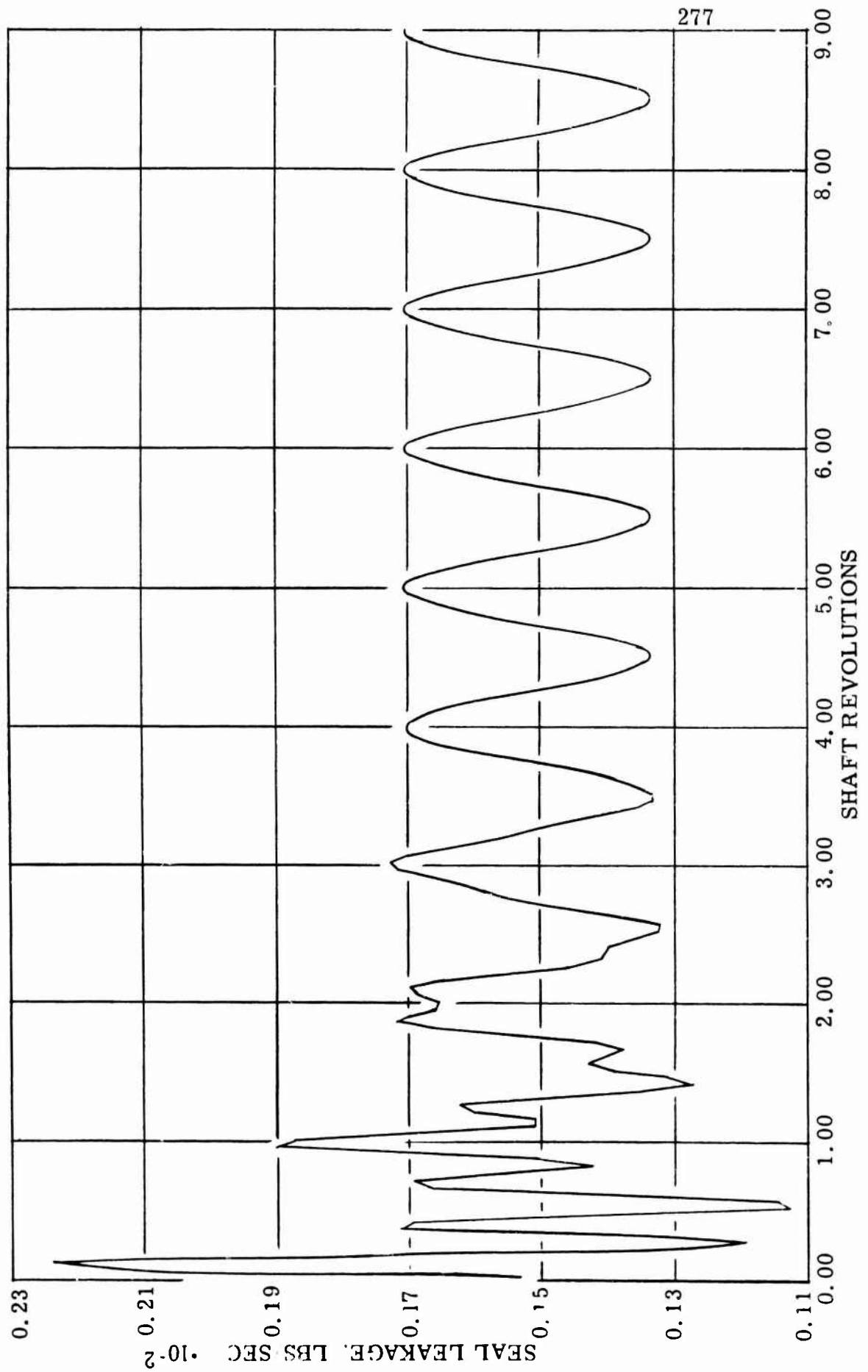


FIGURE 12.3.4

BN-SEAL DYNAMIC PERFORMANCE AT DESIGN OPERATION, 24 SEGMENT ORIFICE-FED SEAL,
CASE 1, ONE DEGREE OF FREEDOM, MINIMUM CLEARANCE

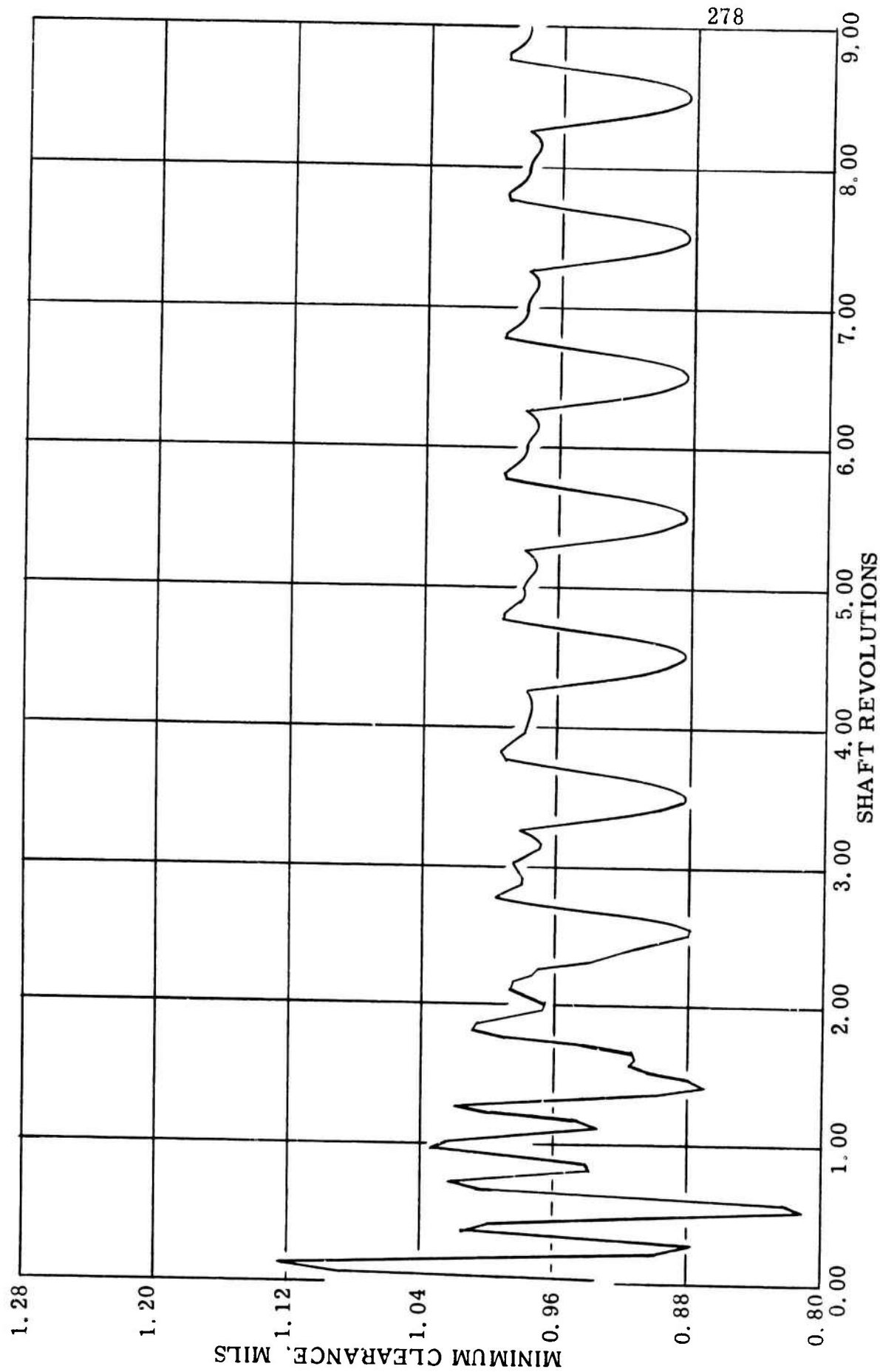


FIGURE 12.3.5

BN-SEAL DYNAMIC PERFORMANCE AT DESIGN OPERATION, 24 SEGMENT ORIFICE-FED SEAL,
CASE 1, ONE DEGREE OF FREEDOM, FLUID FILM FORCE

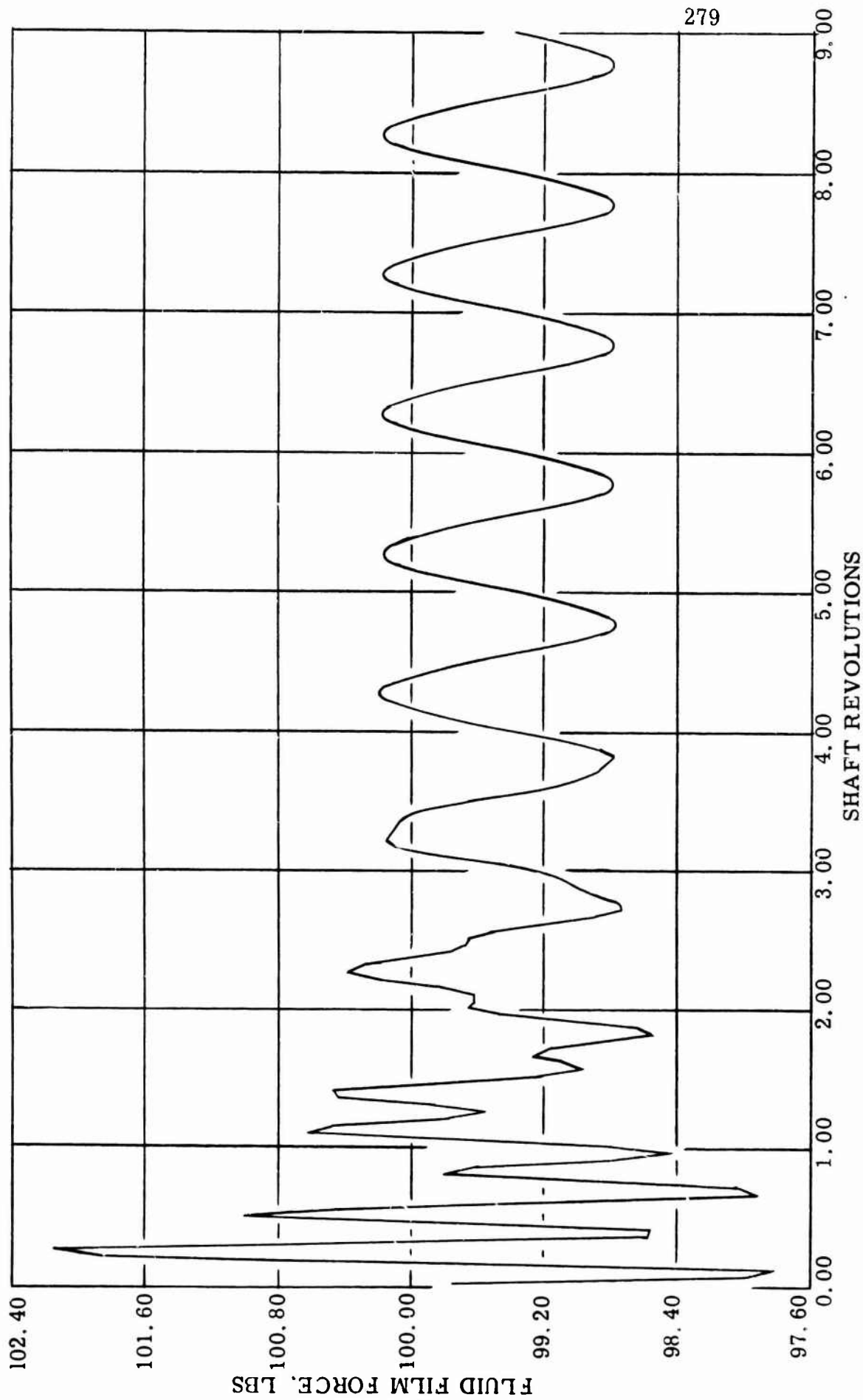


FIGURE 12.3.6

BN-SEAL DYNAMIC PERFORMANCE AT DESIGN OPERATION, 24 SEGMENT ORIFICE-FED SEAL
CASE 1, ONE DEGREE OF FREEDOM, SEAL Y - MOMENT

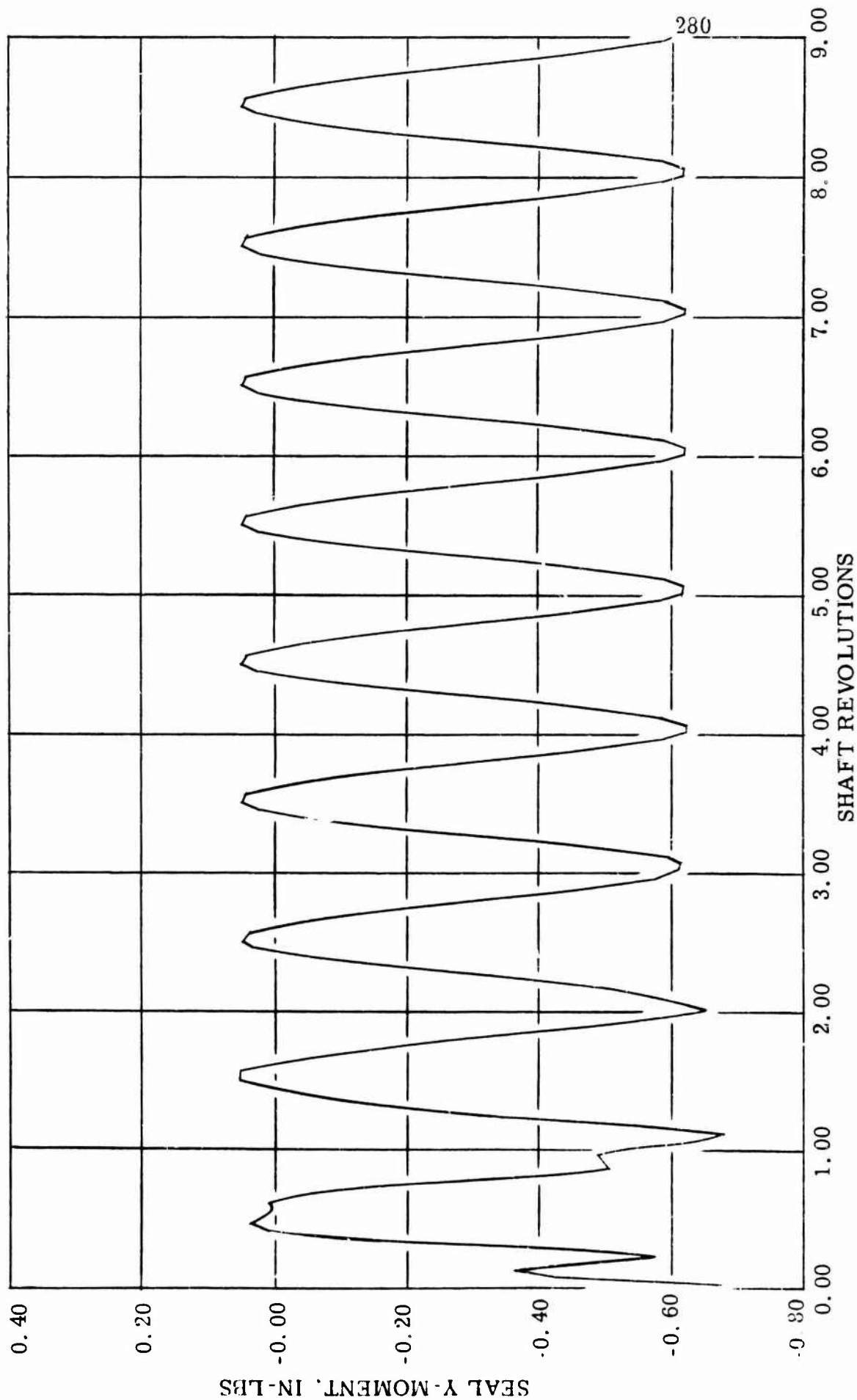


FIGURE 12.3.7

BN-SEAL DYNAMIC PERFORMANCE AT DESIGN OPERATION, 12-SEGMENT SIDE-FED STEP SEAL,
CASE 2, ONE DEGREE OF FREEDOM, WHEEL X-NUTATION.

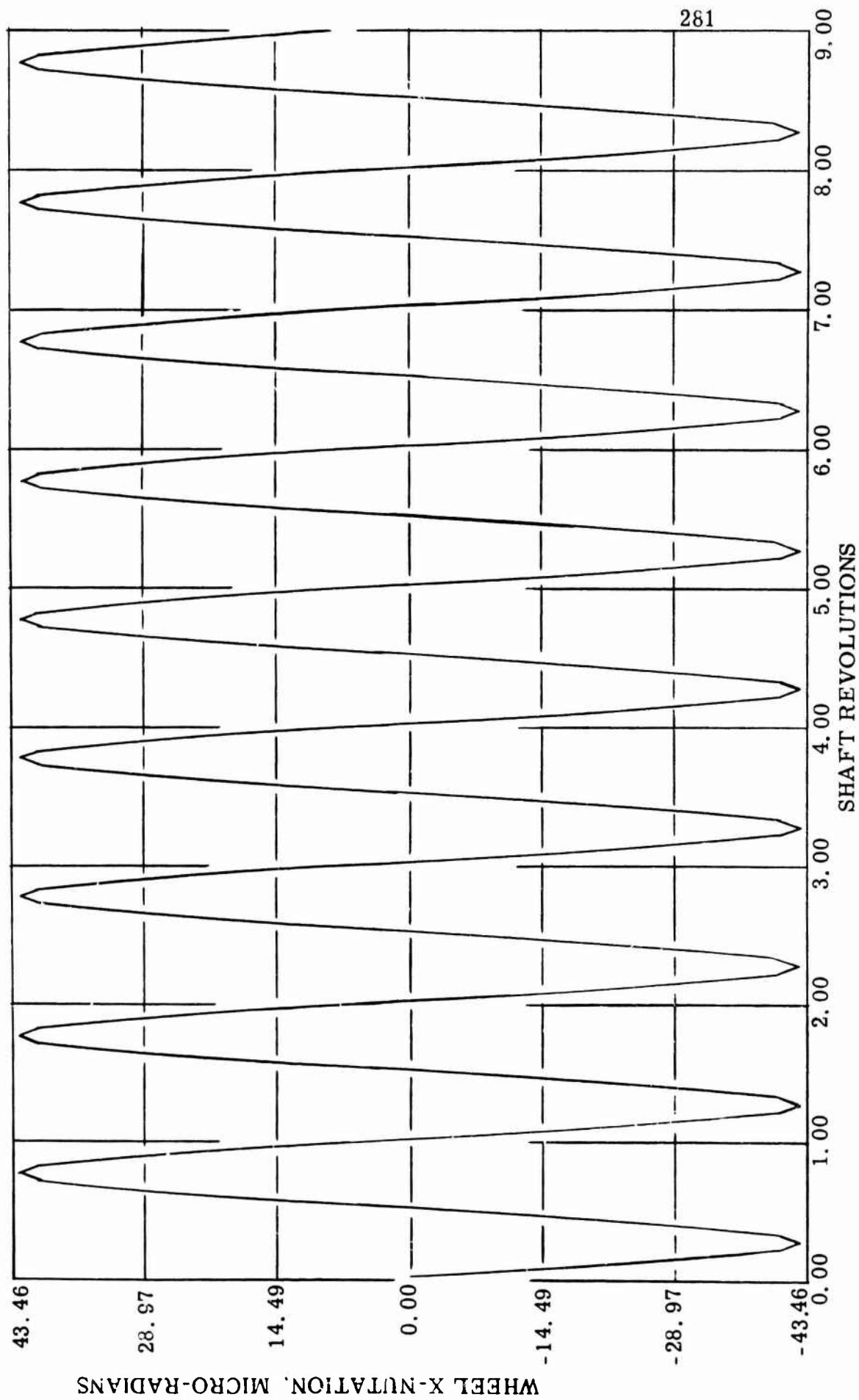


FIGURE 12.3.8

BN-SEAL DYNAMIC PERFORMANCE AT DESIGN OPERATION, 12-SEGMENT SIDE-FED STEP SEAL,
CASE 2, ONE DEGREE OF FREEDOM, WHEEL Y - NUTATION

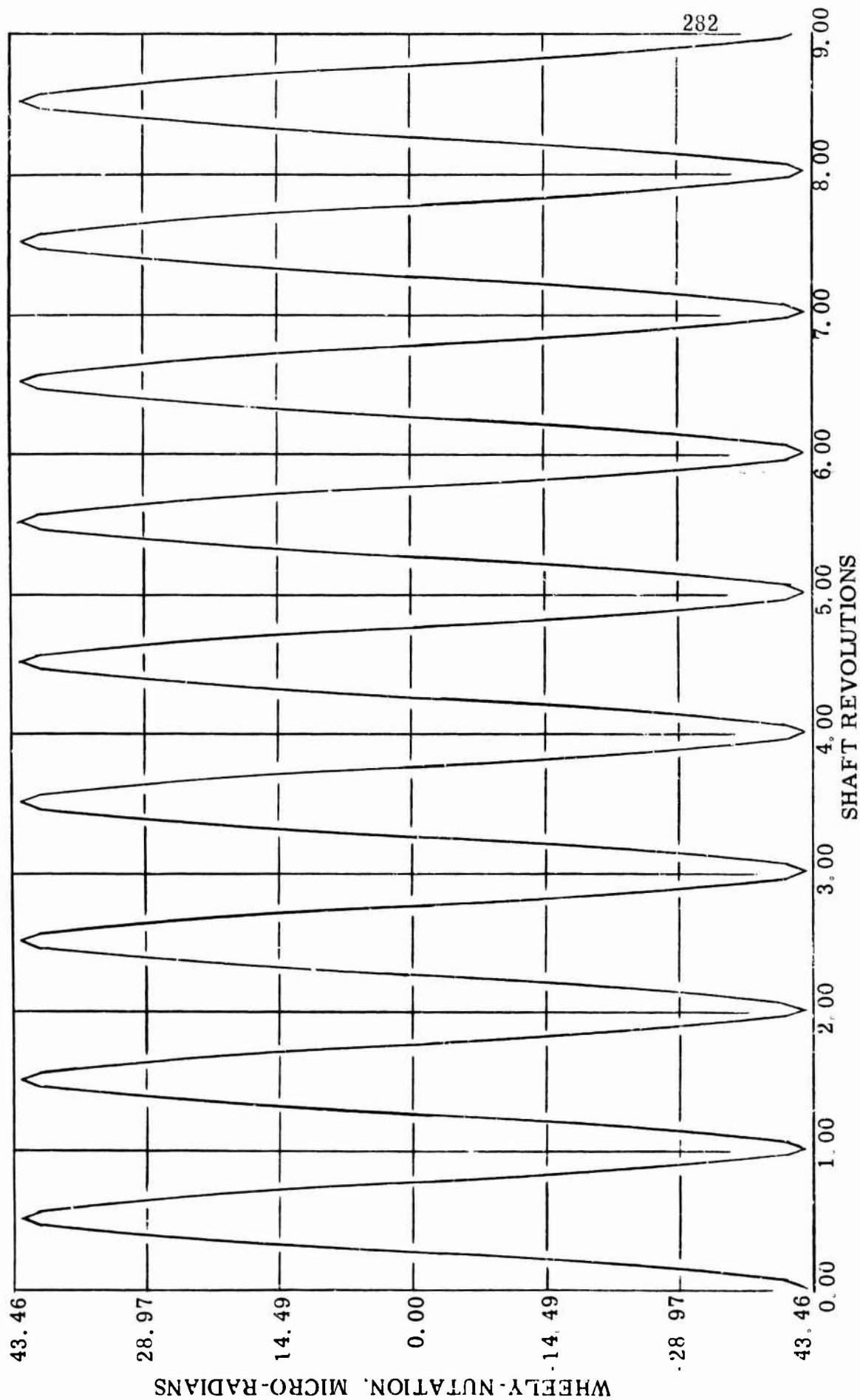


FIGURE 12.3.9

BN-SEAL DYNAMIC PERFORMANCE AT DESIGN OPERATION, 12-SEGMENT SIDE-FED STEP SEAL,
CASE 2, ONE DEGREE OF FREEDOM, SEAL TRANSLATION

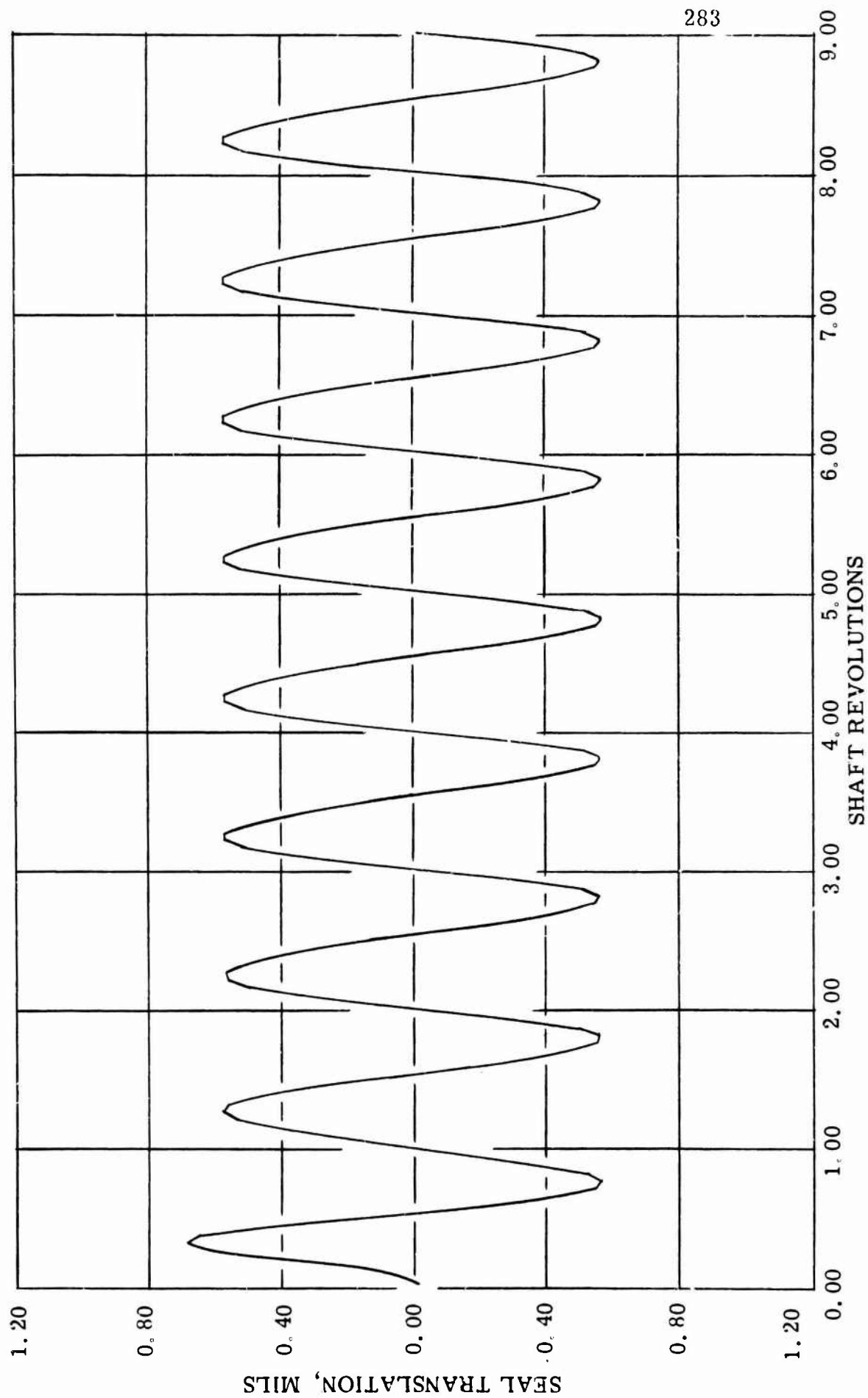


FIGURE 12.3.10

BN-SEAL DYNAMIC PERFORMANCE AT DESIGN OPERATION, 12-SEGMENT SIDE-FED STEP SEAL,
CASE 2, ONE DEGREE OF FREEDOM, MINIMUM CLEARANCE

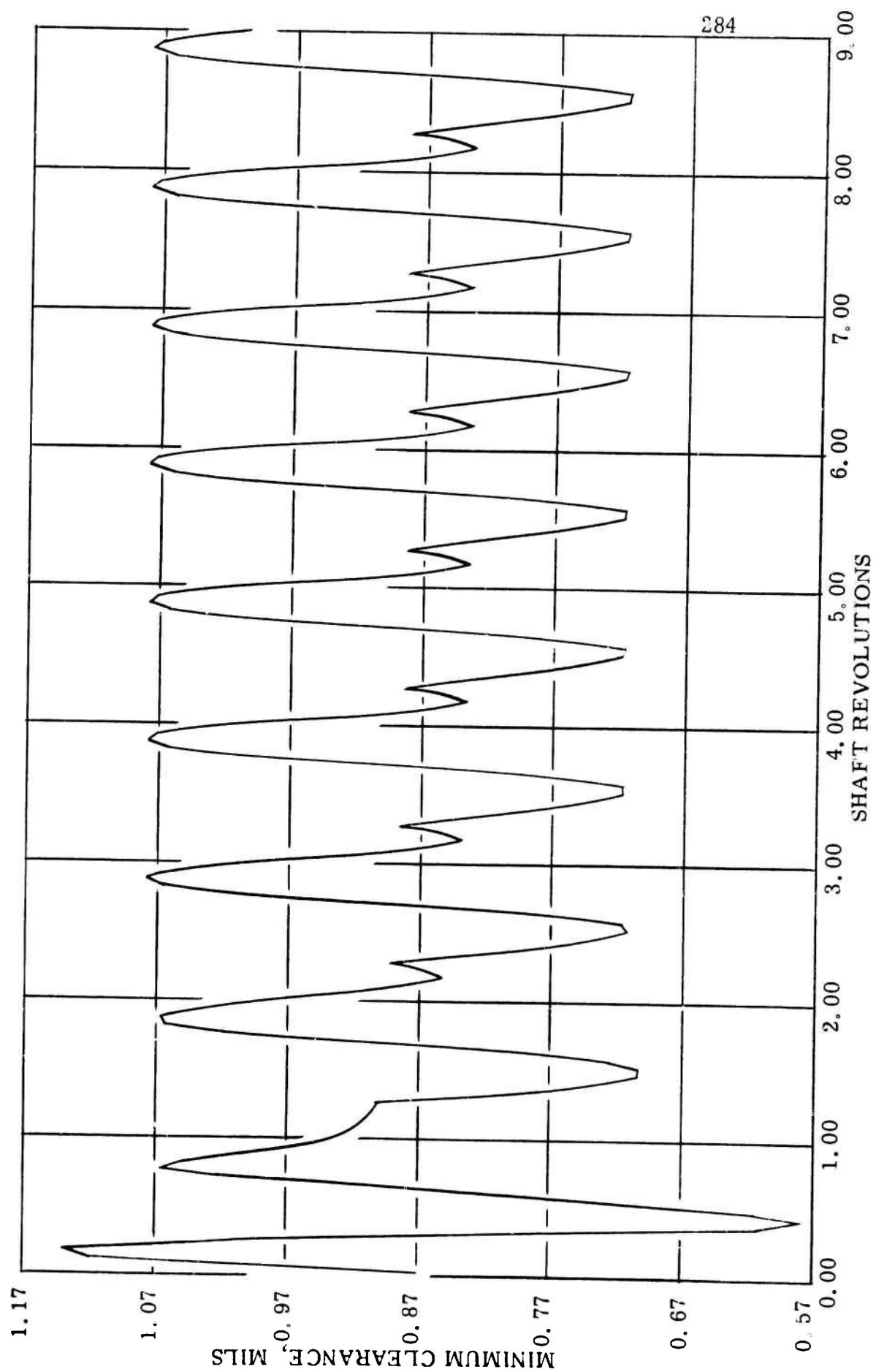


FIGURE 12.3 11

BN-SEAL DYNAMIC PERFORMANCE AT DESIGN OPERATION, 12-SEGMENT SIDE-FED STEP SEAL,
CASE 2, ONE DEGREE OF FREEDOM, SEAL LEAKAGE

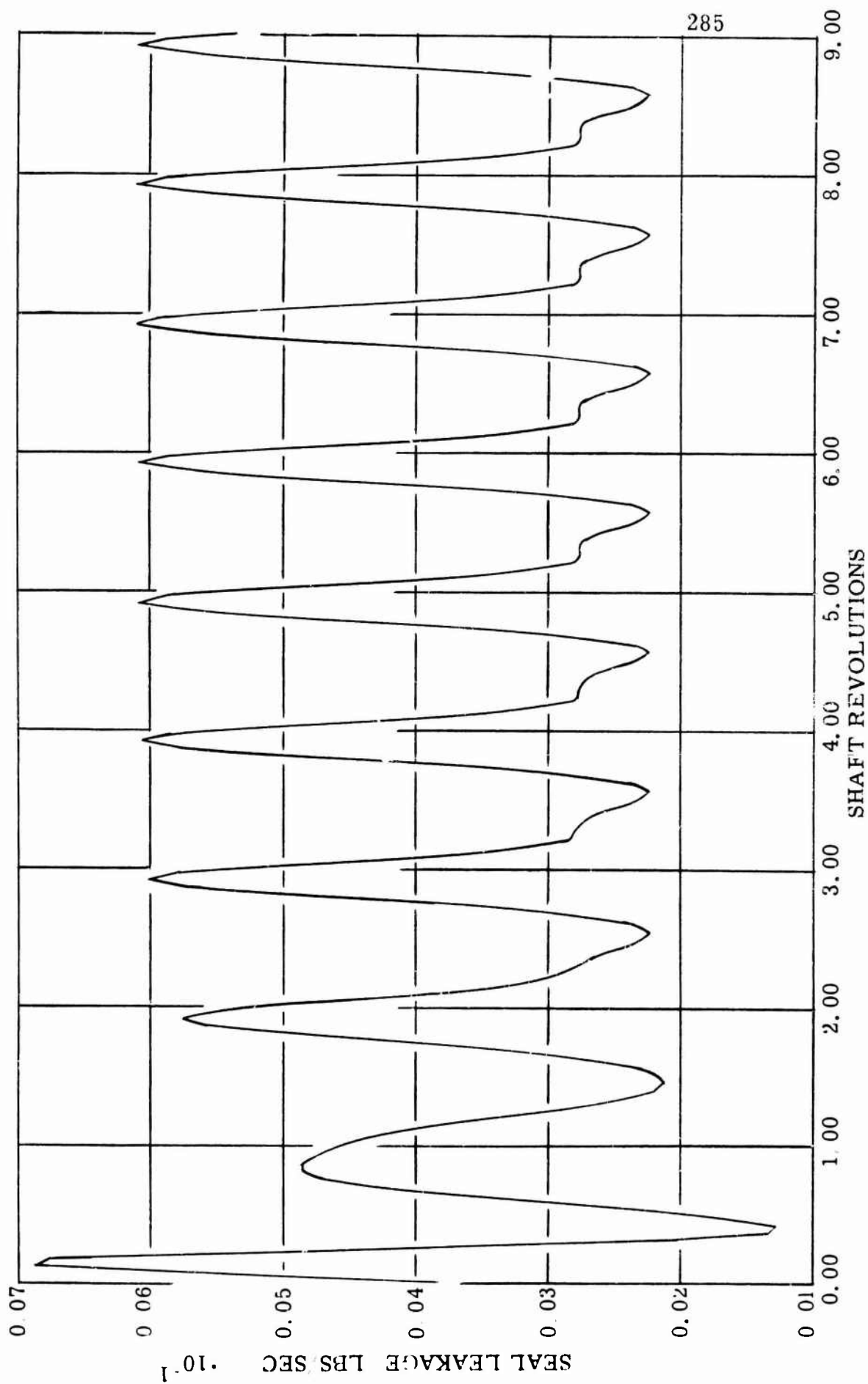


FIGURE 12.3.12

BN-SEAL DYNAMIC PERFORMANCE AT DESIGN OPERATION, 12-SEGMENT SIDE-FED STEP SEAL,
CASE 2, ONE DEGREE OF FREEDOM, FLUID FILM FORCE

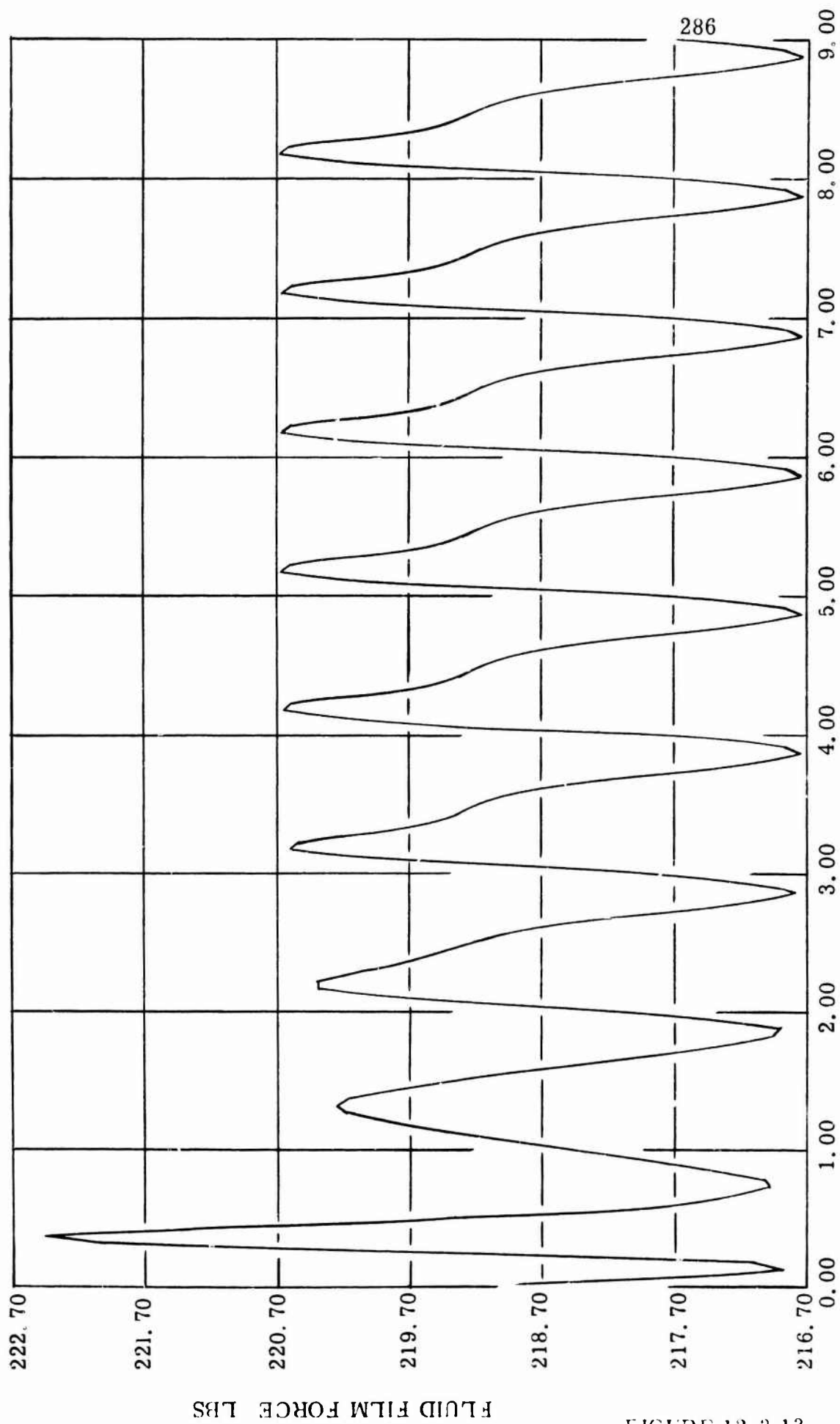


FIGURE 12.3.13

BN-SEAL DYNAMIC PERFORMANCE AT DESIGN OPERATION, 12-SEGMENT SIDE-FED STEP SEAL,
CASE 2, ONE DEGREE OF FREEDOM, SEAL Y-MOMENT

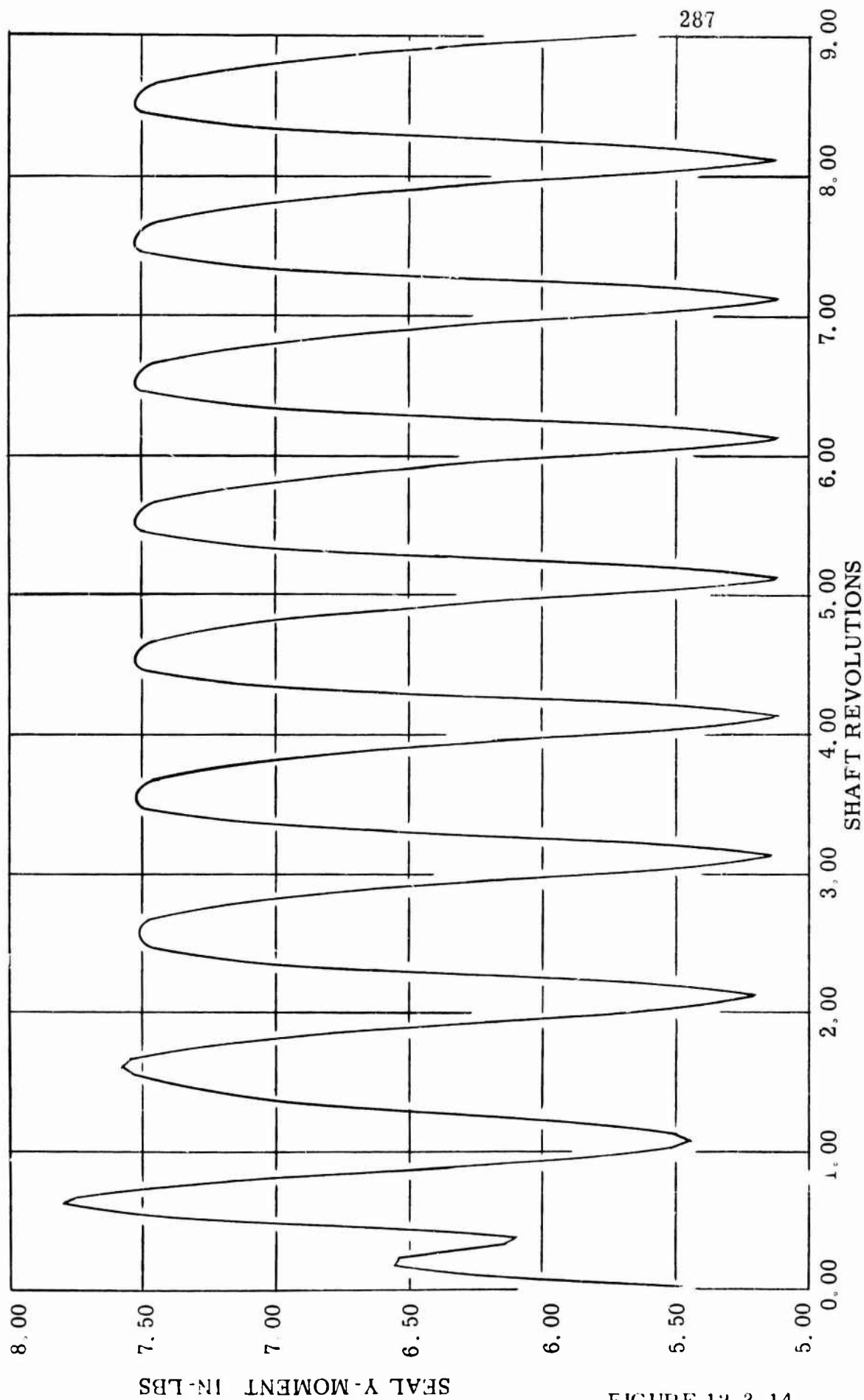


FIGURE 12.3.14

BN SEAL DYNAMIC PERFORMANCE
CASE 3, ROTATION

288

30° STEP SECTOR
.005 TIR
2 DEGREES

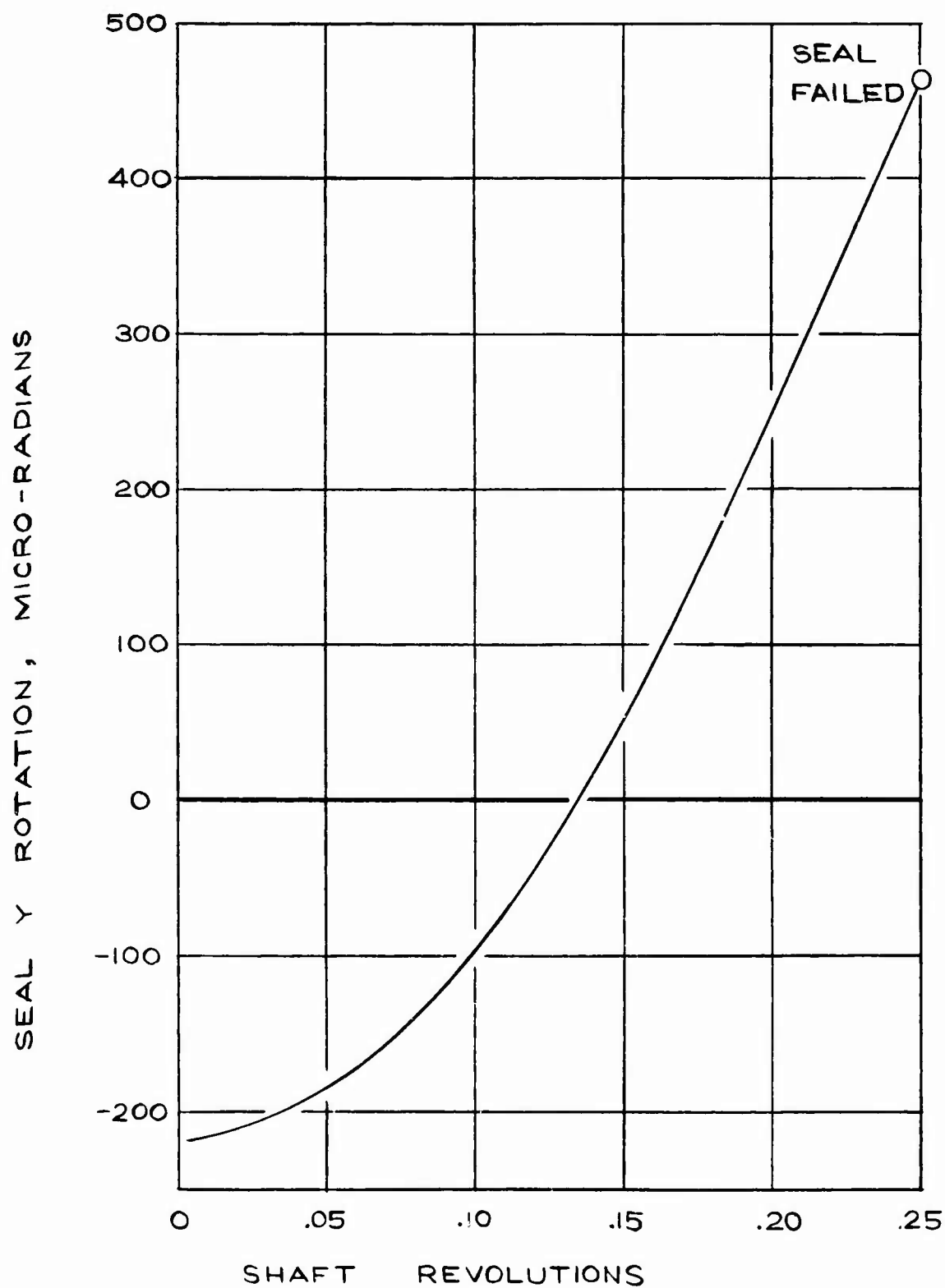


FIGURE 12.3.15

BN SEAL DYNAMIC PERFORMANCE²⁸⁹
CASE 3, TRANSLATION

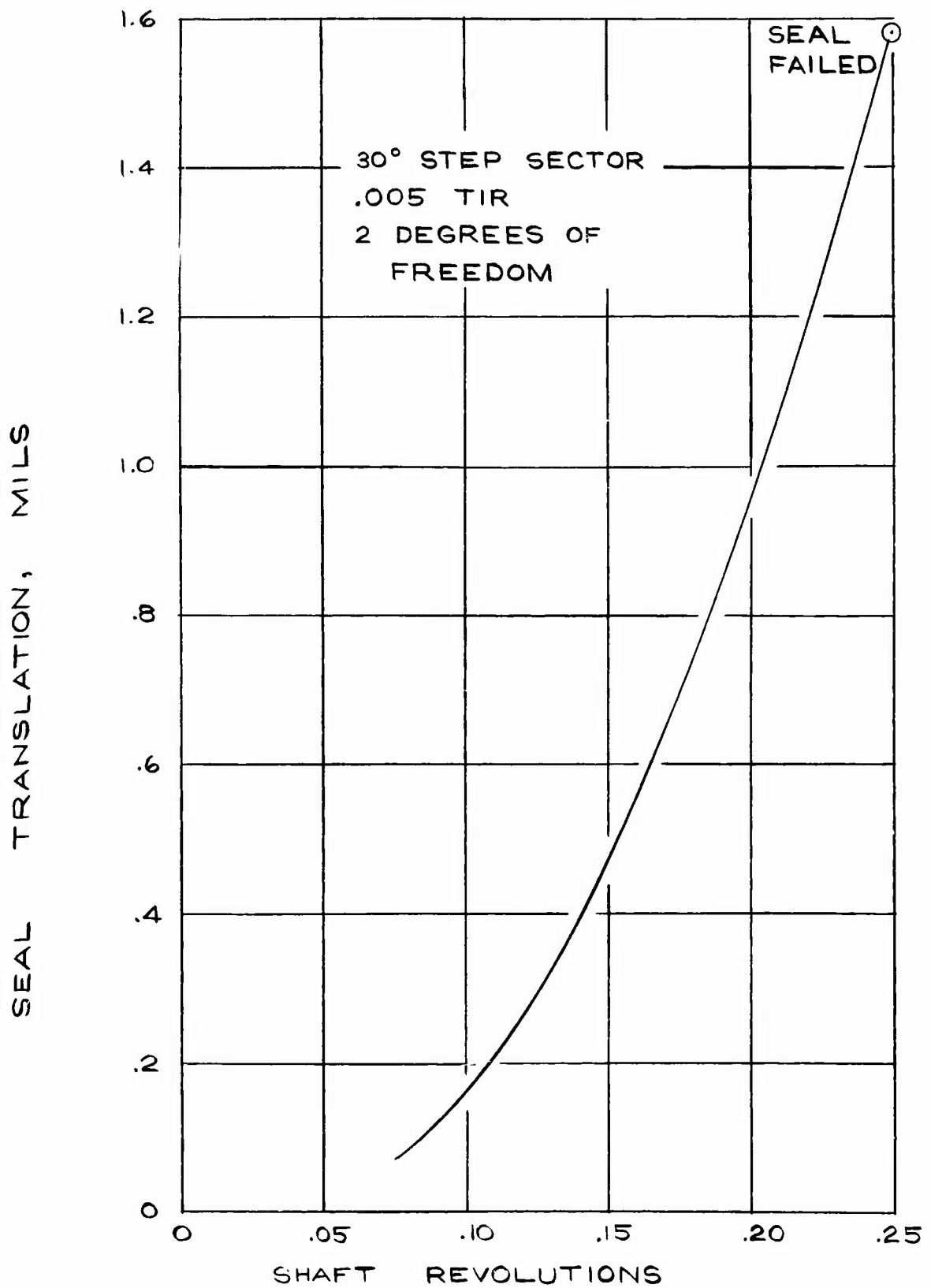


FIGURE 12.3.16

BN SEAL DYNAMIC PERFORMANCE ²⁹⁰
CASE 4, TRANSLATION

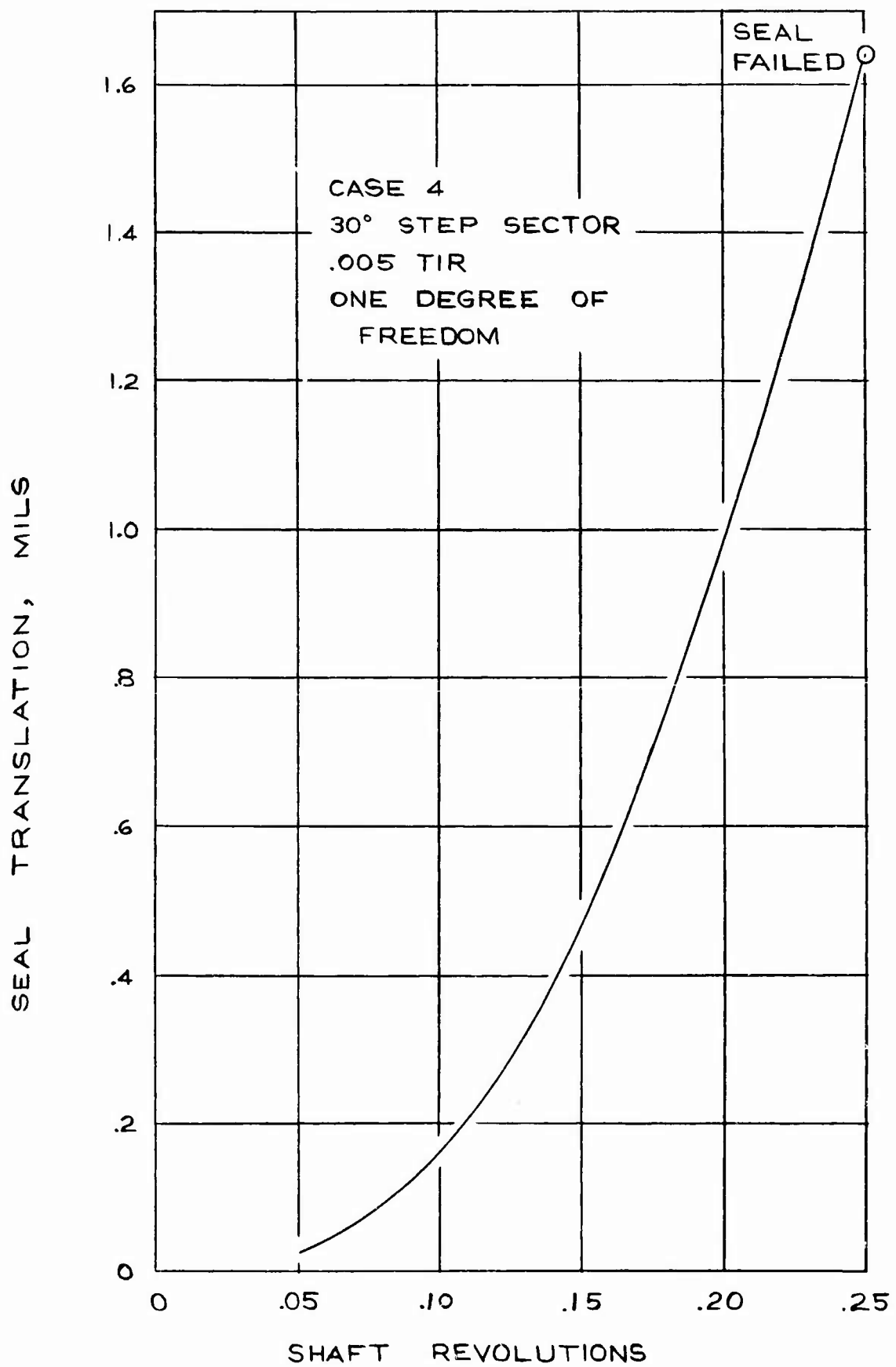


FIGURE 12.3.17

BN SEAL DYNAMIC PERFORMANCE
CASE 5, ROTATION

30° SIDE STEP BEARING
.00352 TIR
2 DEGREES OF FREEDOM

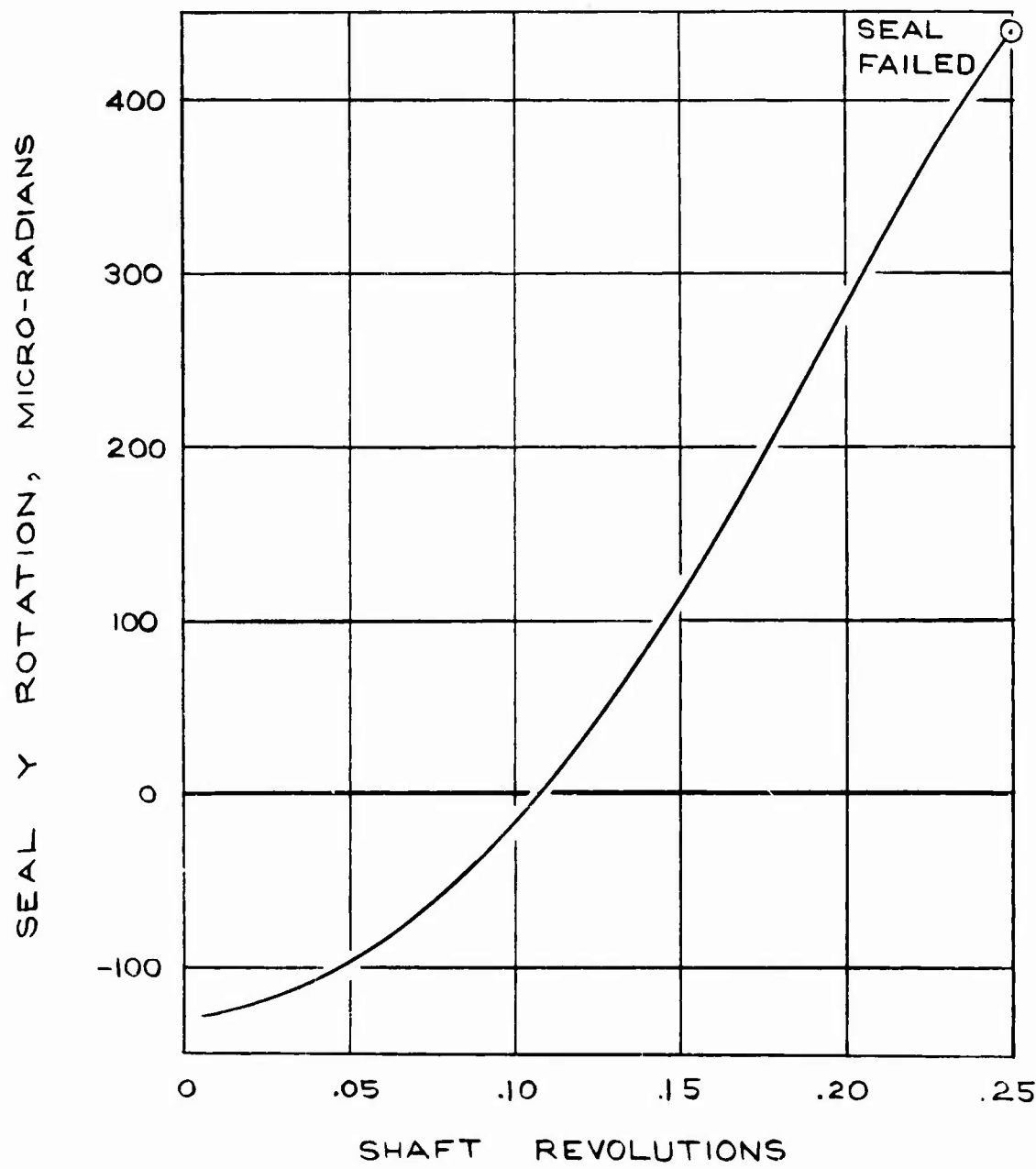


FIGURE 12.3.18

BN SEAL DYNAMIC PERFORMANCE CASE 5, TRANSLATION

30° SIDE STEP BEARING
.00352 TIR
2 DEGREES OF FREEDOM

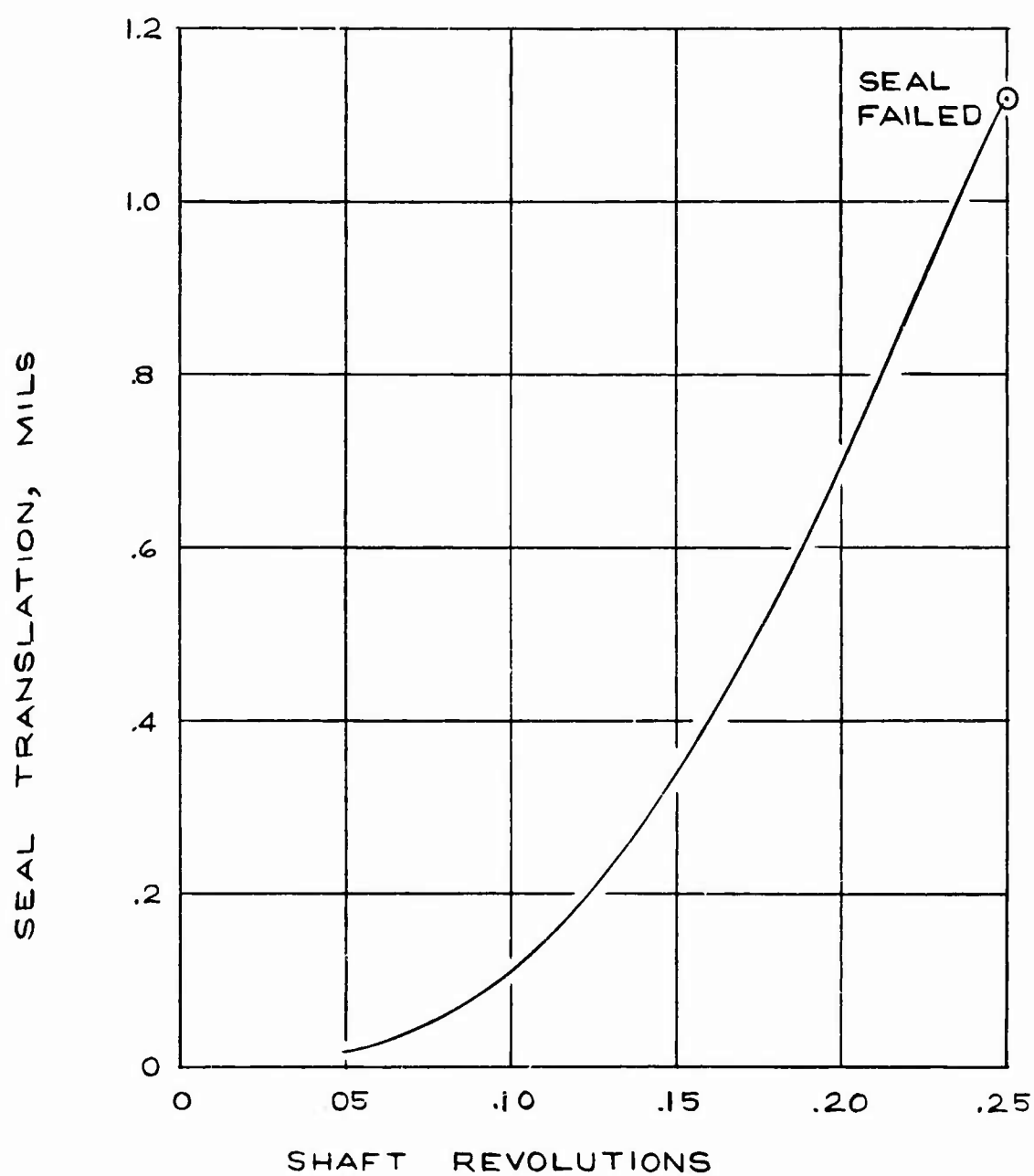


FIGURE 12.3.19

BN-SEAL DYNAMIC PERFORMANCE AT DESIGN OPERATION,
12-SEGMENT SIDE-FED STEP SEAL, CASE 9, TWO DEGREES
OF FREEDOM, WHEEL X-NUTATION

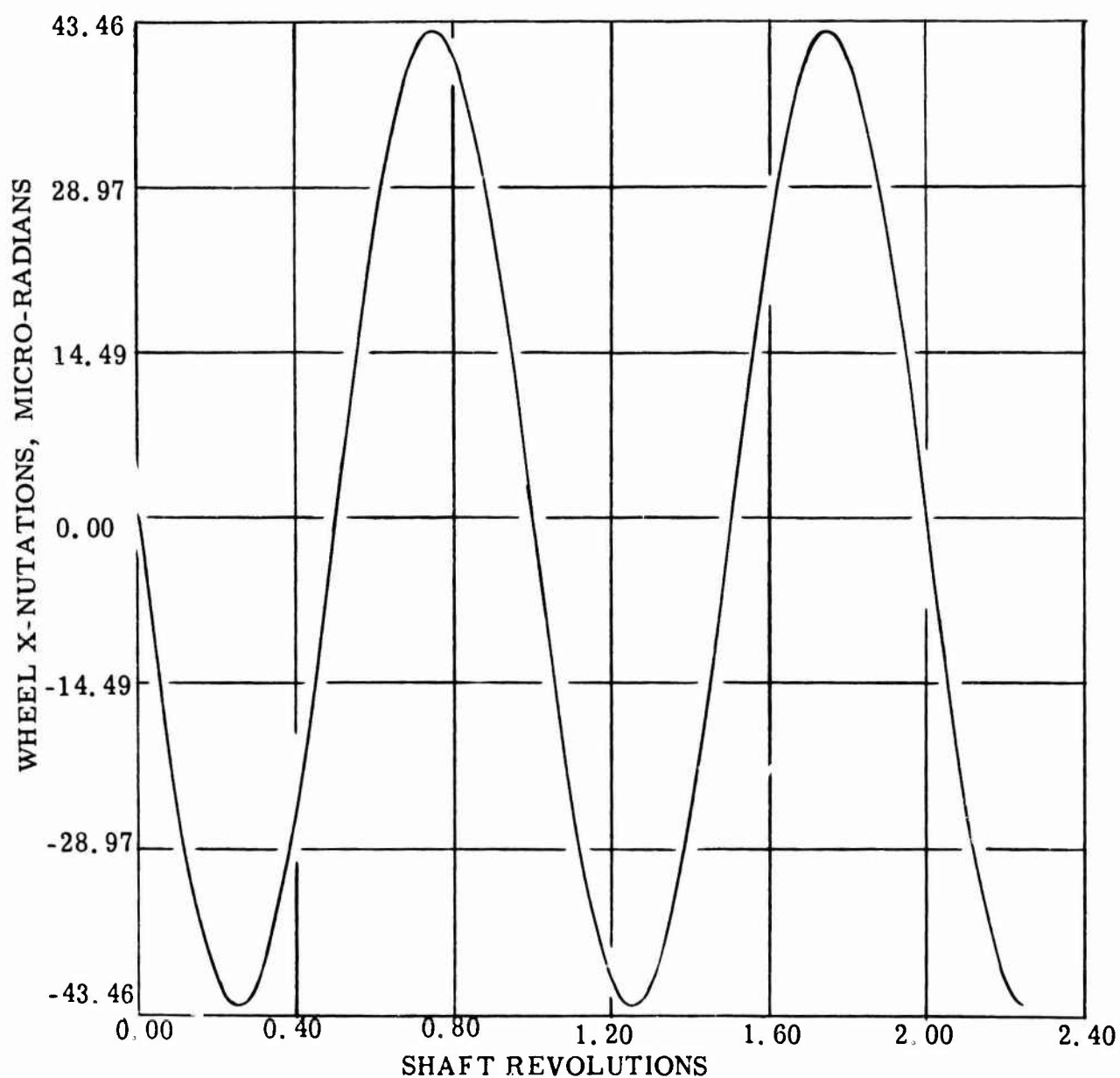


FIGURE 12.3.20

BN-SEAL DYNAMIC PERFORMANCE AT DESIGN OPERATION,
12-SEGMENT SIDE-FED STEP SEAL. CASE 9, TWO DEGREES
OF FREEDOM, WHEEL Y-NUTATION

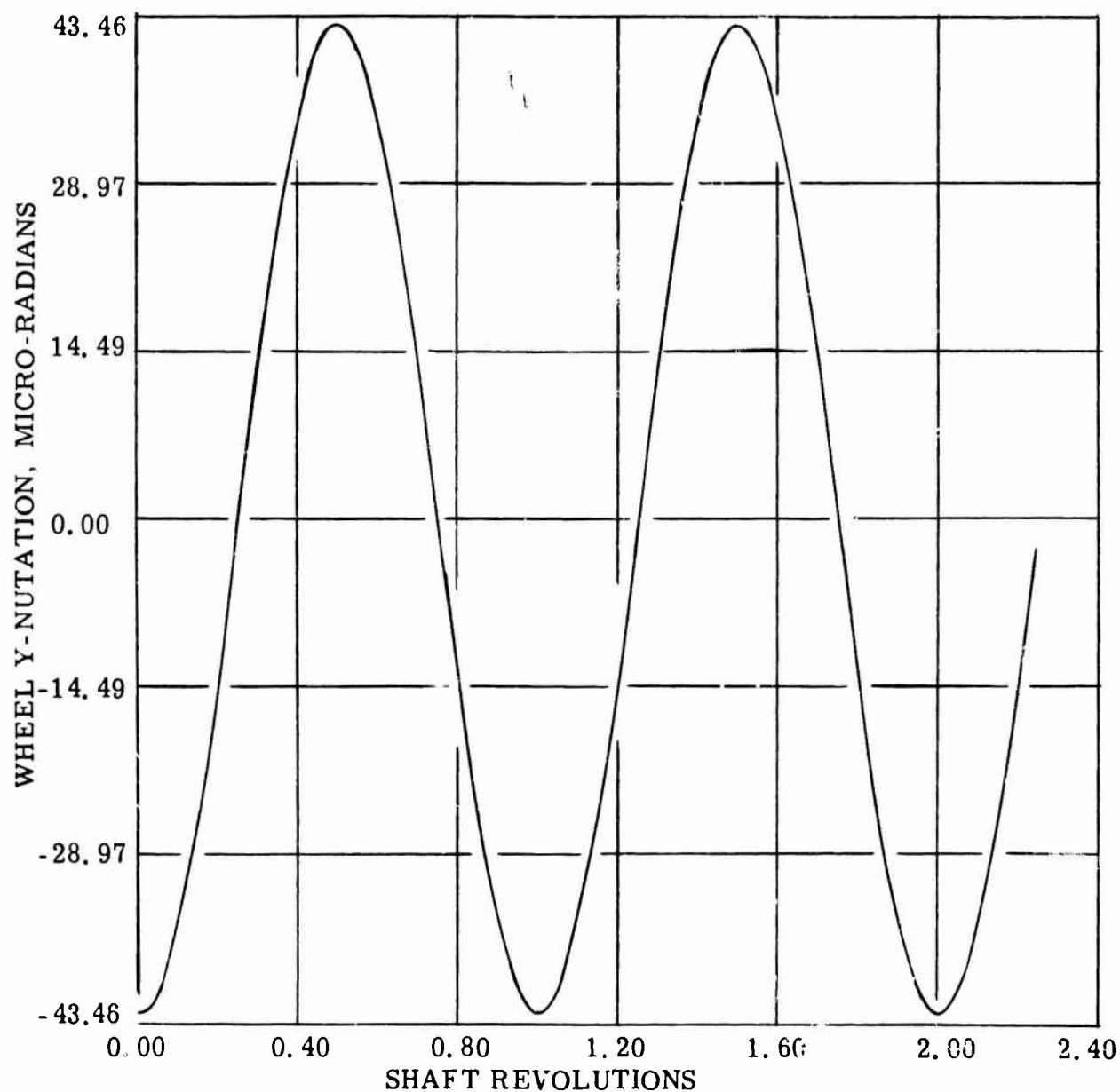


FIGURE 12.3.21

BN-SEAL DYNAMIC PERFORMANCE AT DESIGN OPERATION,
12-SEGMENT SIDE-FED STEP SEAL. CASE 9, TWO DEGREES
OF FREEDOM, SEAL TRANSLATION

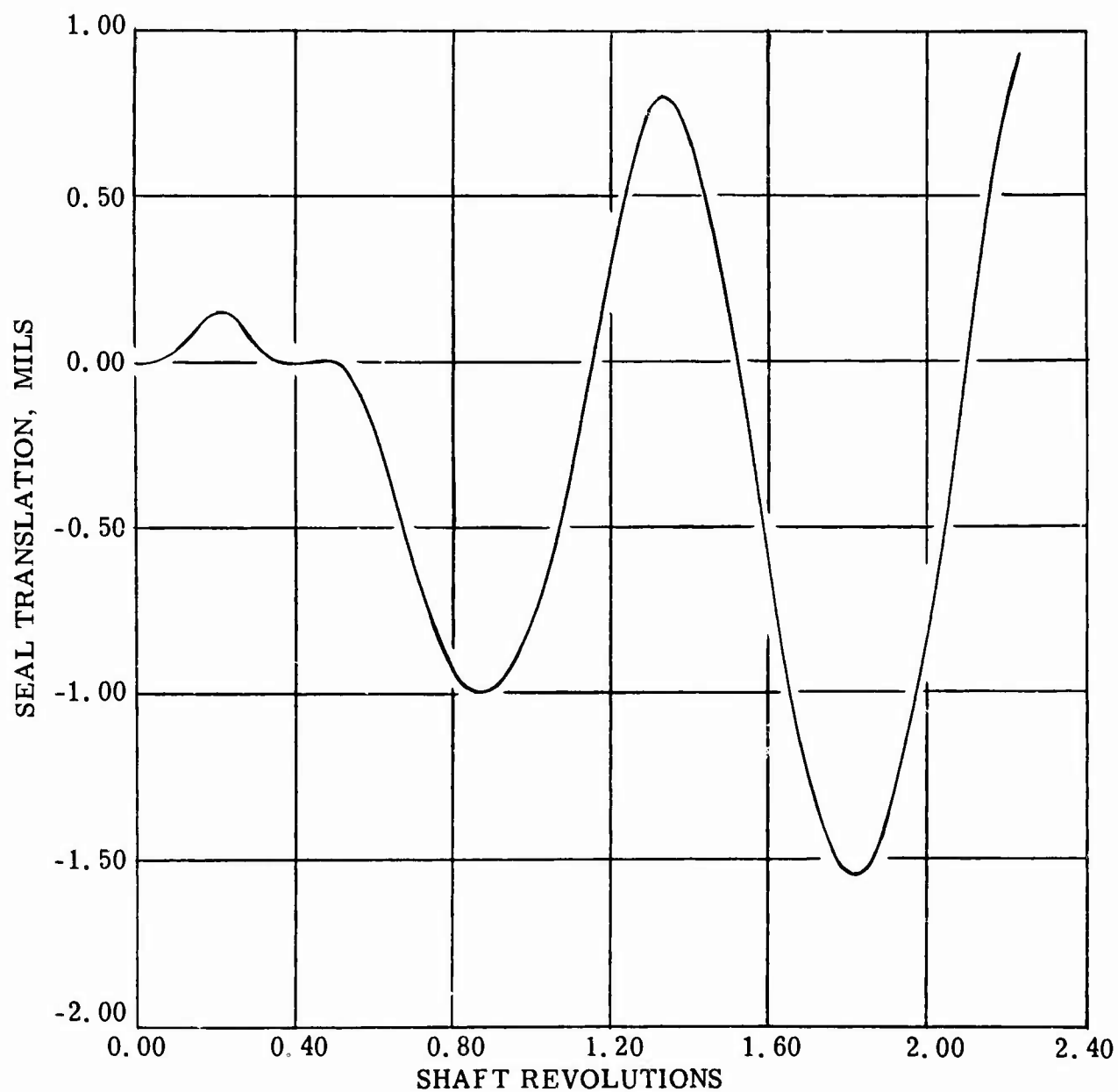


FIGURE 12.3.22

BN-SEAL DYNAMIC PERFORMANCE AT DESIGN OPERATION,
12-SEGMENT SIDE-FED STEP SEAL, CASE 9, TWO DEGREES
OF FREEDOM, SEAL Y-ROTATION

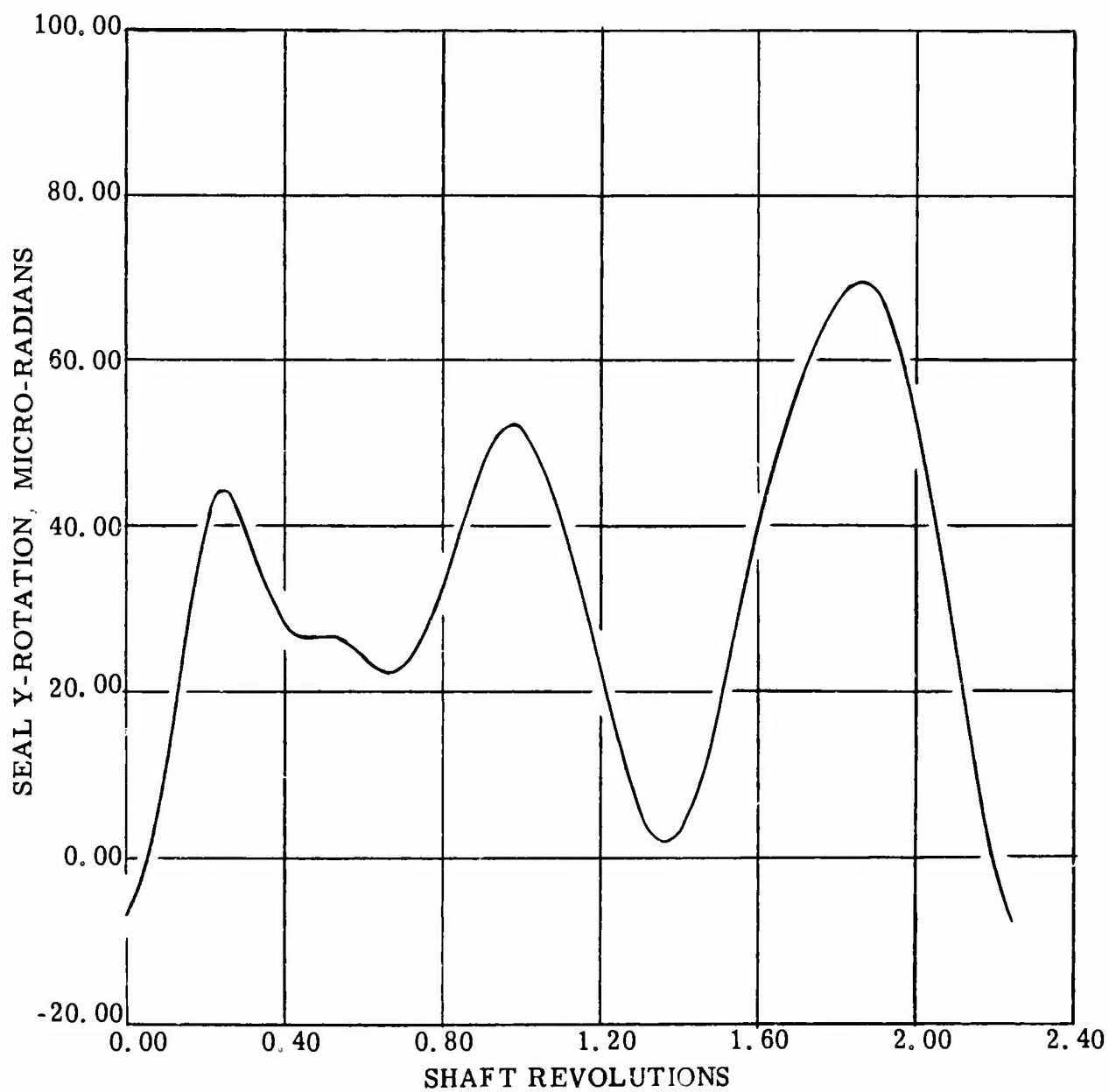


FIGURE 12. 3. 23

BN-SEAL DYNAMIC PERFORMANCE AT DESIGN OPERATION,
12-SEGMENT SIDE-FED STEP SEAL, CASE 9, TWO DEGREES
OF FREEDOM, SEAL LEAKAGE

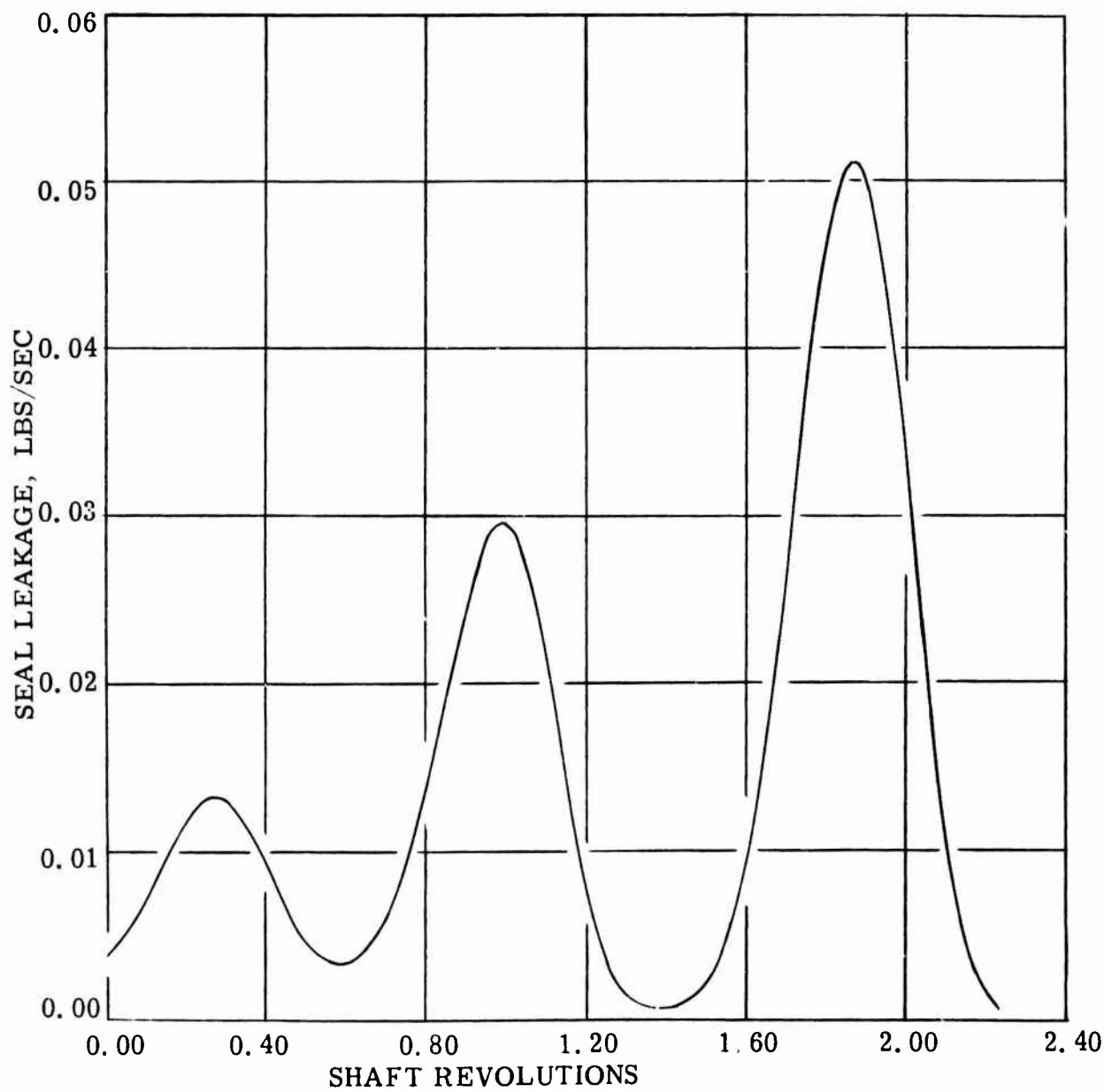


FIGURE 12.3.24

BN-SEAL DYNAMIC PERFORMANCE AT DESIGN OPERATION,
12-SEGMENT SIDE-FED STEP SEAL, CASE 9, TWO DEGREES
OF FREEDOM, MINIMUM CLEARANCE

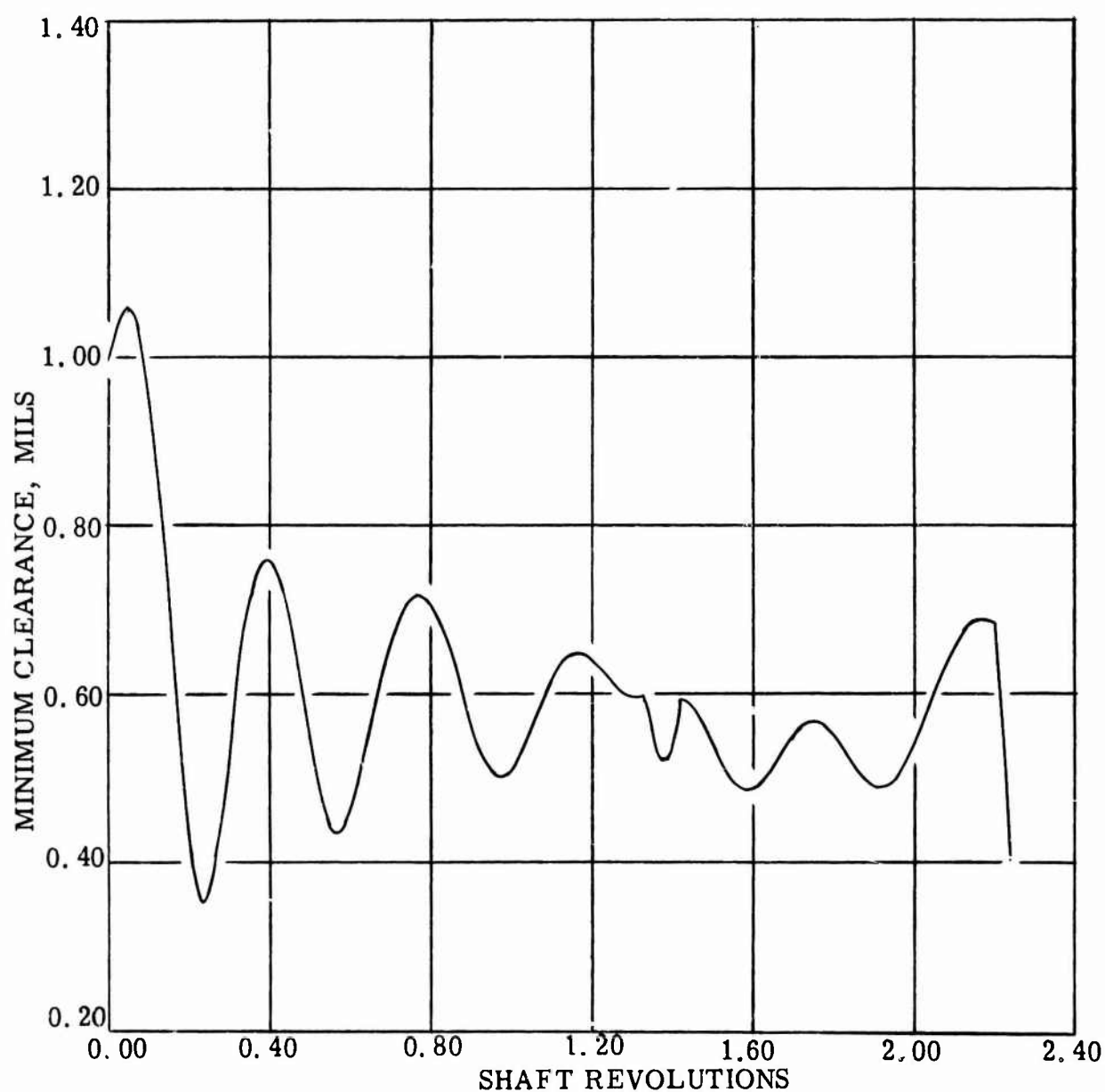


FIGURE 12.3.25

BN-SEAL DYNAMIC PERFORMANCE AT DESIGN OPERATION,
12-SEGMENT SIDE-FED STEP SEAL, CASE 9 TWO DEGREES
OF FREEDOM, FLUID FILM FORCE

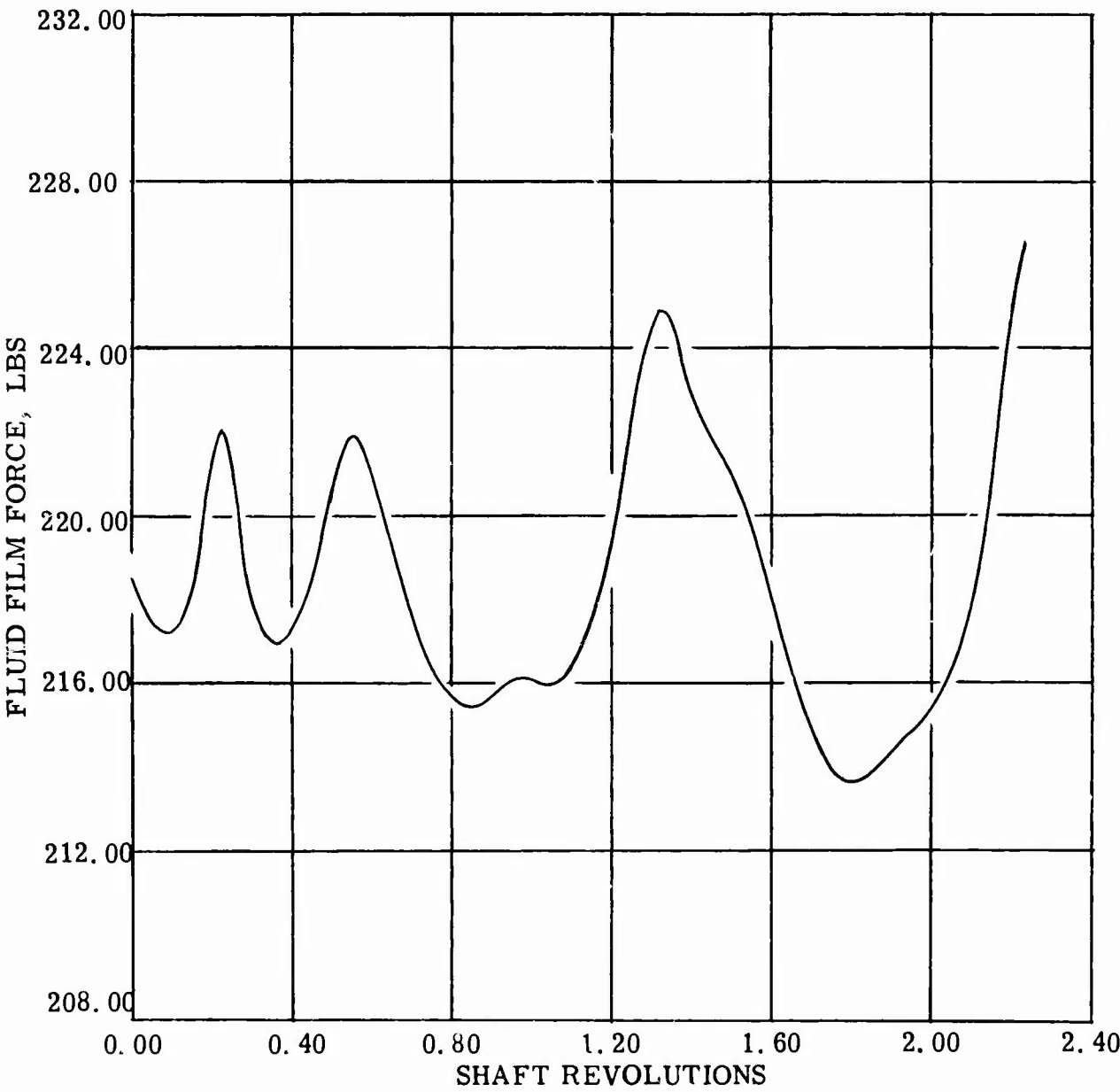


FIGURE 12.3.26

BN-SEAL DYNAMIC PERFORMANCE AT DESIGN OPERATION,
12-SEGMENT SIDE-FED STEP SEAL, CASE 9. TWO DEGREES
OF FREEDOM, SEAL Y-MOMENT

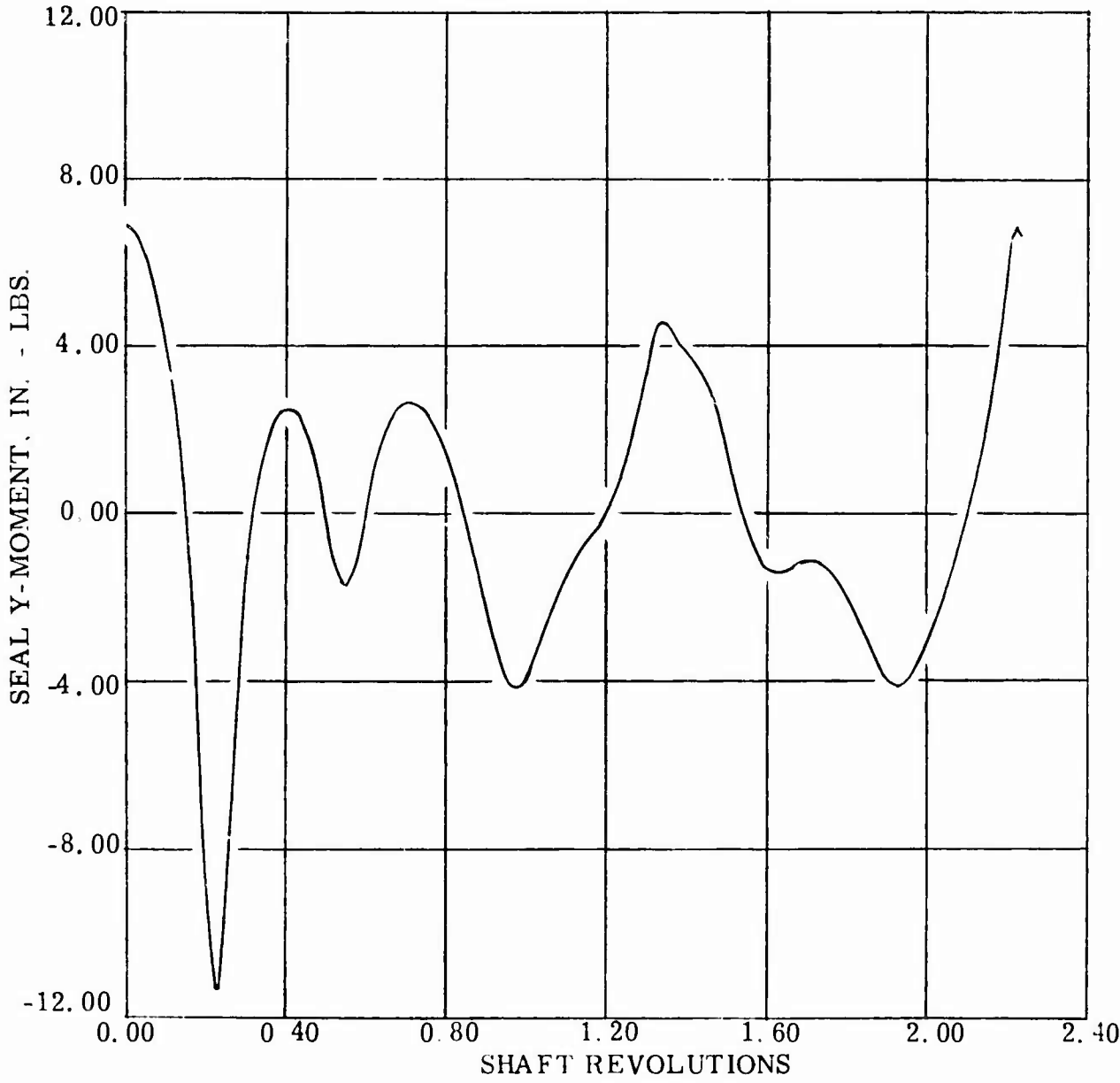
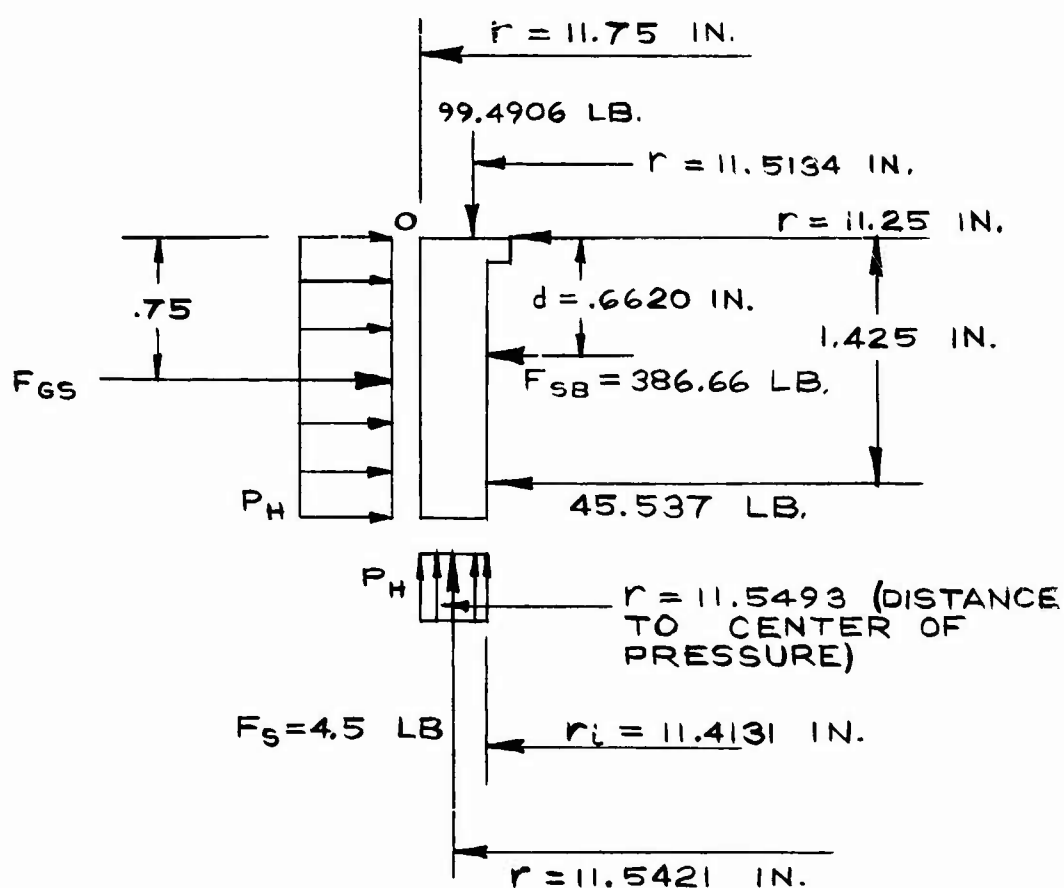


FIGURE 12.3.27

12.4 FORCE BALANCE AND INERTIA COMPUTATIONS

Geometry



$$P_H = 95 \text{ psia}$$

$$F_{GS} = 1\#/in. \cdot r \cdot \theta_p = (1\#/in.) (11.75 \text{ in.}) (.2618 \text{ rad.}) = 3.0761 \text{ lb.}$$

Vertical Load

$$(P_H - P_a) \text{ Area} + F_S = 99.4906$$

$$\text{Area} = (r_o^2 - r_i^2) \frac{\theta_p}{2}$$

$$r_o = 11.75 \text{ in.}$$

$$\theta_p = 15^\circ = .2618 \text{ rad.}$$

$$(95 - 2) \left[11.75^2 - r_i^2 \right] \frac{.2618}{2} + 4.5 = 99.4906$$

$$11.75^2 - r_i^2 = \frac{(94.9906) 2}{(.2618)(93)}$$

$$r_i^2 = 138.0625 - 7.80294$$

$$r_i^2 = 130.25956$$

$$r_i = 11.41313 \text{ in.}$$

Horizontal Load

$$(P_H - P_a) \text{ Area} + F_{GS} = F_{SB} + 45.537$$

$$\text{Area} = r_o \Theta_p L = (11.75) (.2618) (1.5) = 4.6142$$

$$(95-2) 4.61 + 3.0761 - 45.537 = F_{SB}$$

$$(429.123)$$

$$F_{SB} = 386.66 \text{ lbs.}$$

Center of Pressure

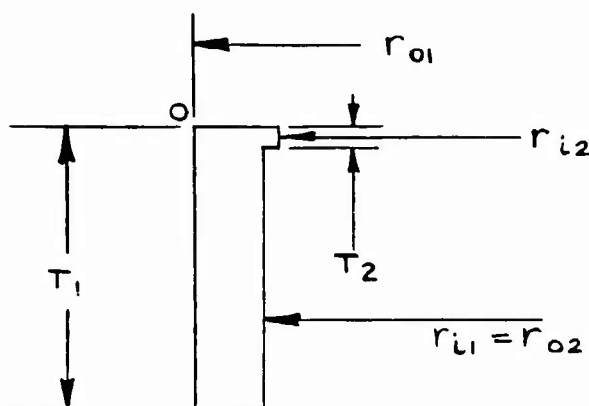
$$r_c = \frac{2}{3} \frac{\sin(\Theta_p/2)}{\Theta_p/2} \left[\frac{r_o^3 - r_i^3}{r_o^2 - r_i^2} \right]$$

$$= .66667 \left(\frac{.130526}{.1309} \right) \left[\frac{11.75^3 - 11.41313^3}{11.75^2 - 11.41313^2} \right]$$

$$= 11.5493 \text{ in.}$$

Center of Mass (Radial Direction)

$$r_m = \frac{2}{3} \frac{[T_1 (r_{o1}^3 - r_{i1}^3) + T_2 (r_{o2}^3 - r_{i2}^3)] \sin(\Theta_p/2)}{[T_1 (r_{o1}^2 - r_{i1}^2) + T_2 (r_{o2}^2 - r_{i2}^2)] \Theta_p/2}$$



$$\begin{aligned}
 &= .66667 \left[\frac{1.5 (11.75^3 - 11.4131^3) + .09375 (11.4131^3 - 11.25^3)}{1.5 (11.75^2 - 11.4131^2) + .09375 (11.4131^2 - 11.25^2)} \right] \frac{.130526}{.1309} \\
 &= .66476 \left[\frac{203.3656 + 5.8902}{11.7055 + .3465} \right]
 \end{aligned}$$

$$r_m = 11.5421 \text{ in.}$$

Moment Balance

$$\begin{aligned}
 \Sigma M_o \curvearrowright &= 0 \\
 &- (3.0761) (.75) - (429.474) (.75) - 4.5 (11.75 - 11.5421) \\
 &- (94.9906) (11.75 - 11.5493) + 45.537 (1.425) \\
 &+ (99.4906) (11.75 - 11.5134) + 386.66 d = 0 \\
 &-255.983 + 386.66 d = 0 \\
 &d = .6620 \text{ in.}
 \end{aligned}$$

Mass

$$\text{Weight} = \text{Volume} \times \text{Density}$$

$$\begin{aligned}
 \text{Volume} &= T_1 (r_{o1}^2 - r_{i1}^2) \frac{\theta_p}{2} + T_2 (r_{o2}^2 - r_{i2}^2) \frac{\theta_p}{2} \\
 &= 1.5 (11.75^2 - 11.4131^2) (.1309) + (.09375) \\
 &\quad (11.4131^2 - 11.25^2) (.1309) \\
 &= 1.5776 \text{ in.}^3
 \end{aligned}$$

$$\text{Weight} = (1.5776) (.283) = .44646 \text{ lb}$$

$$\text{Mass} = (.44646) / (386.4) = .00115 \text{ lb-sec}^2/\text{in.}$$

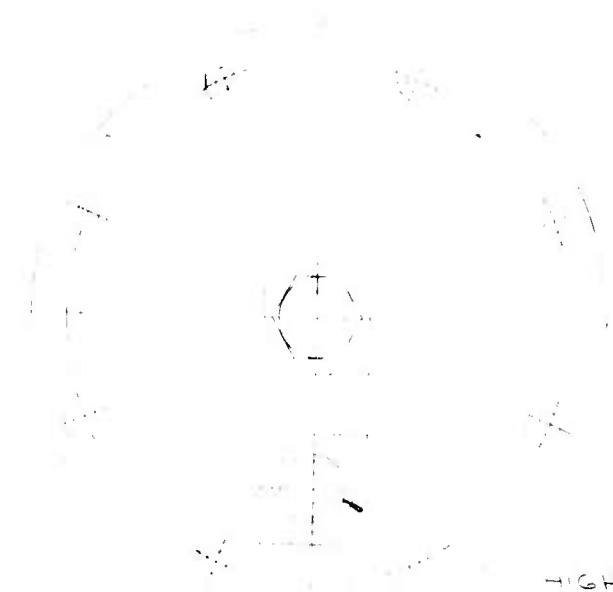
Inertia

$$\begin{aligned}
 I_{YY} &= \frac{\rho}{4} \left[\left(\frac{\theta_p}{4} - \frac{\sin \theta_p}{4} \right) - \left(\frac{-\theta_p}{4} - \frac{\sin \theta_p}{4} \right) \right] * \\
 &\quad \left[T_1 (r_{o1}^4 - r_{i1}^4) + T_2 (r_{o2}^4 - r_{i2}^4) \right] \\
 &= \frac{.283}{4} \left[\left(\frac{.2618}{4} - \frac{\sin .2618}{4} \right) - \left(\frac{-.2618}{4} - \frac{\sin -.2618}{4} \right) \right]
 \end{aligned}$$

$$\begin{aligned} I_{YY} &= \frac{\left[1.5 (11.75^4 - 11.4131^4) + .09375 (11.4131^4 - 11.25^4) \right]}{386.4} \\ I_{YY} &= .00088 \text{ lb-sec}^2\text{-in.} \end{aligned}$$

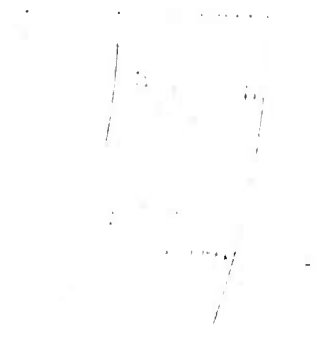
A

B



HIGH PR
TO BEAR
CYLINDE

SECTION **AC-AC**



C

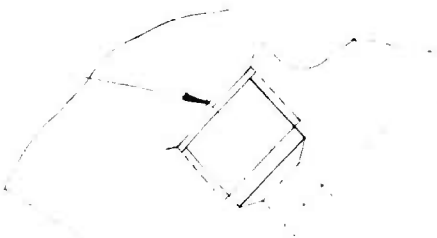
JOURNAL BEARING
WATER IN
AND 10050-8

PRESSURE IN
BEARING PRELOAD
DER AND 10050-4

SECTION **Z-Z**

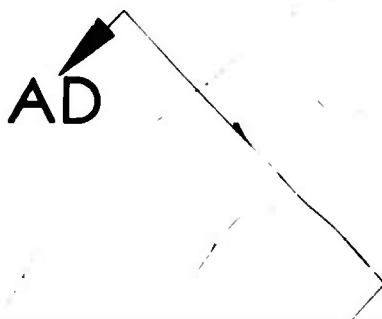
D

RING —



SECTION U-U

JOURNAL BEARINGS
WATER IN
AND 10050-8



AD

E

JOURNAL BEARING
WATER IN
AND 10050-8

SECTION **AD-AD**
WATER SUPPLY JETS

HYDROSTATIC STEAM IN
TO SECONDARY SEAL

THRUST BEARING
WATER IN
AND 10050-8

F

G

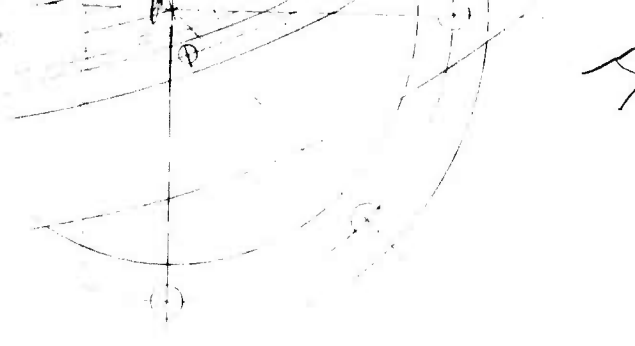
4

DISC COOLING
WATER OUT
AND 10050-8

DISC COOLING
WATER IN
AND 10050-8

SECTION **T-T**
EXHAUST DUCT

HYDROSTATIC STEAM IN
TO SECONDARY SEAL
AND 10050-6

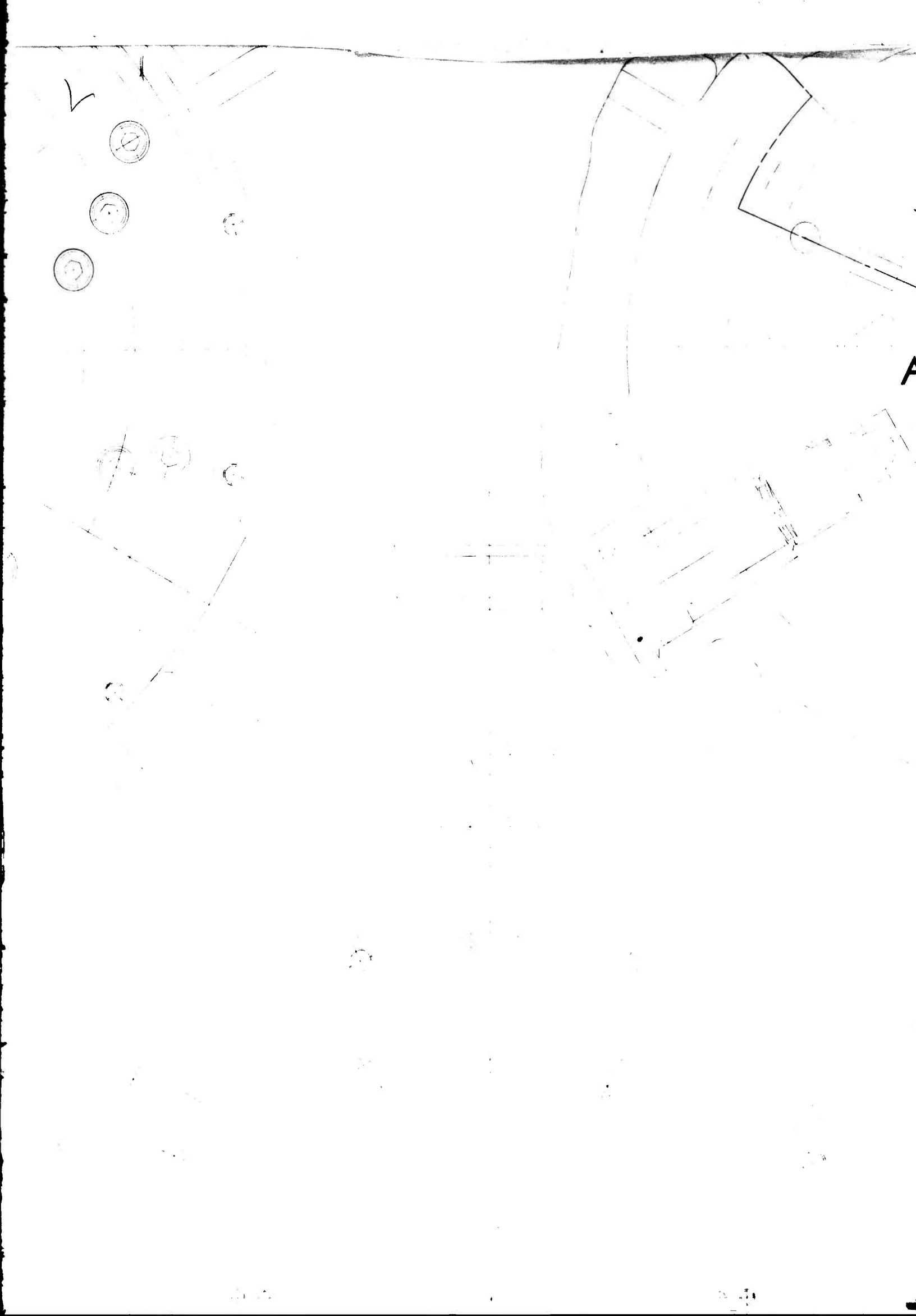


DISC COOLING
WATER OUT
AND 10050-8

REMOVED VIEW OF
LIMITED LEAKAGE SEAL

DISC COOLING
WATER IN
AND 10050-8

SECTION **Y-Y**



AD

SECTION **V-V**

N

(1/2)

2

1

1

0

1

2

3

4

5

6

7

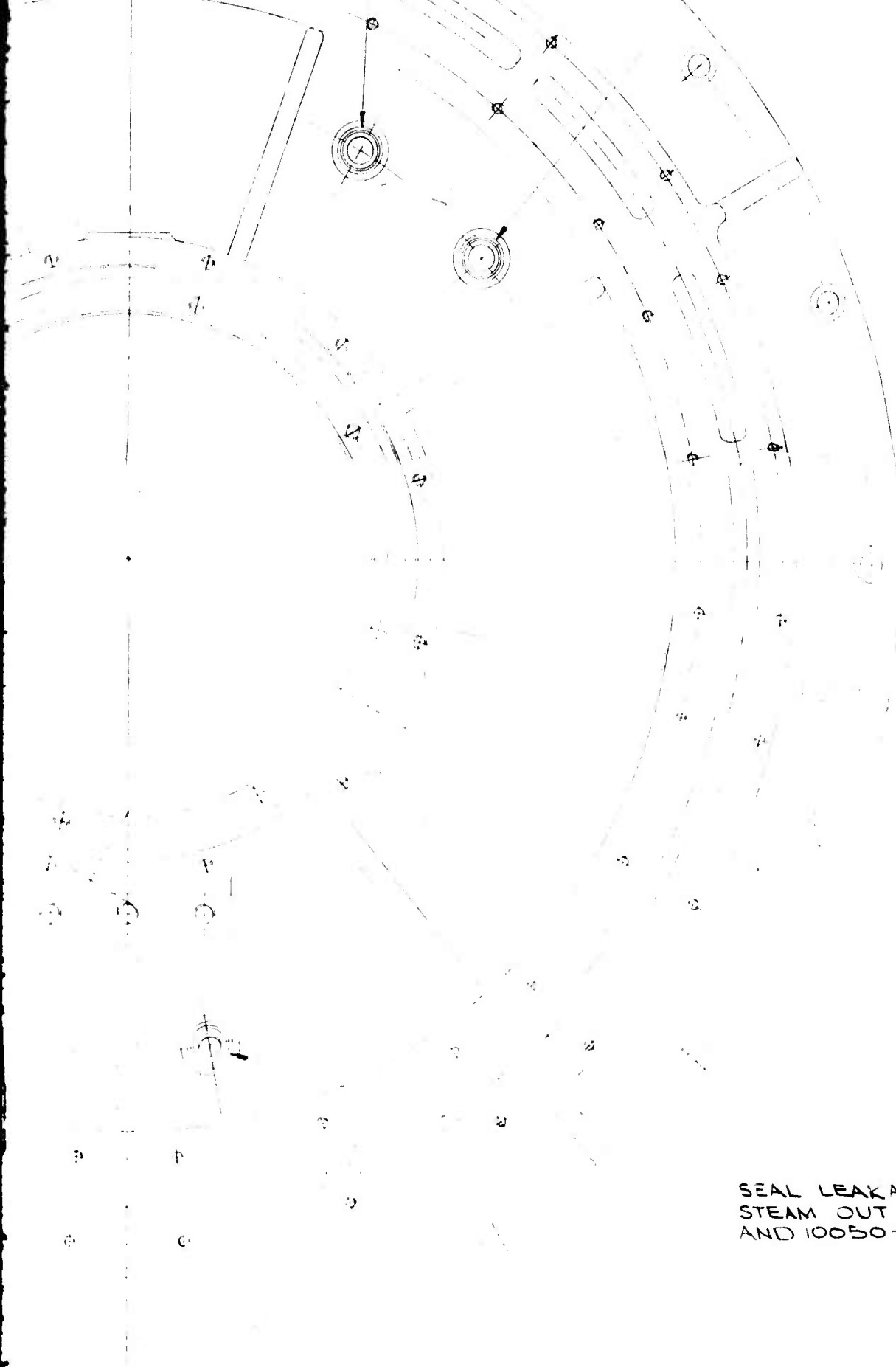
D

(10)



HYDROSTATIC STEAM IN
TO SECONDARY SEAL
AND 10050-6

REMO
EXHA
SIMIL



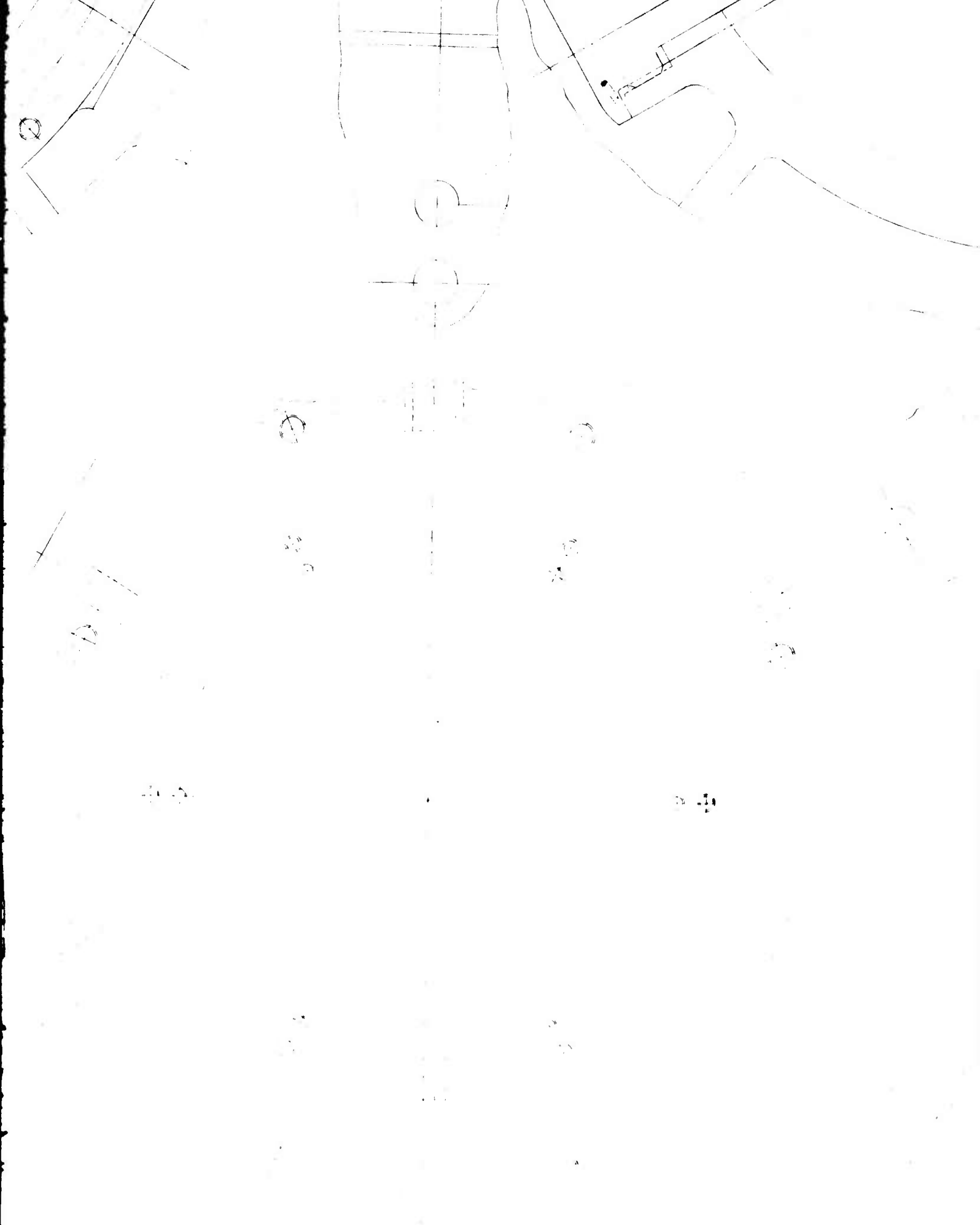
SEAL LEAKAGE
STEAM OUT
AND 10050-8

REMOVED VIEW OF
EXHAUST HOUSING
SIMILAR TO VIEW S-S



SECTION **Y-Y**

SECTION **AA-AA**



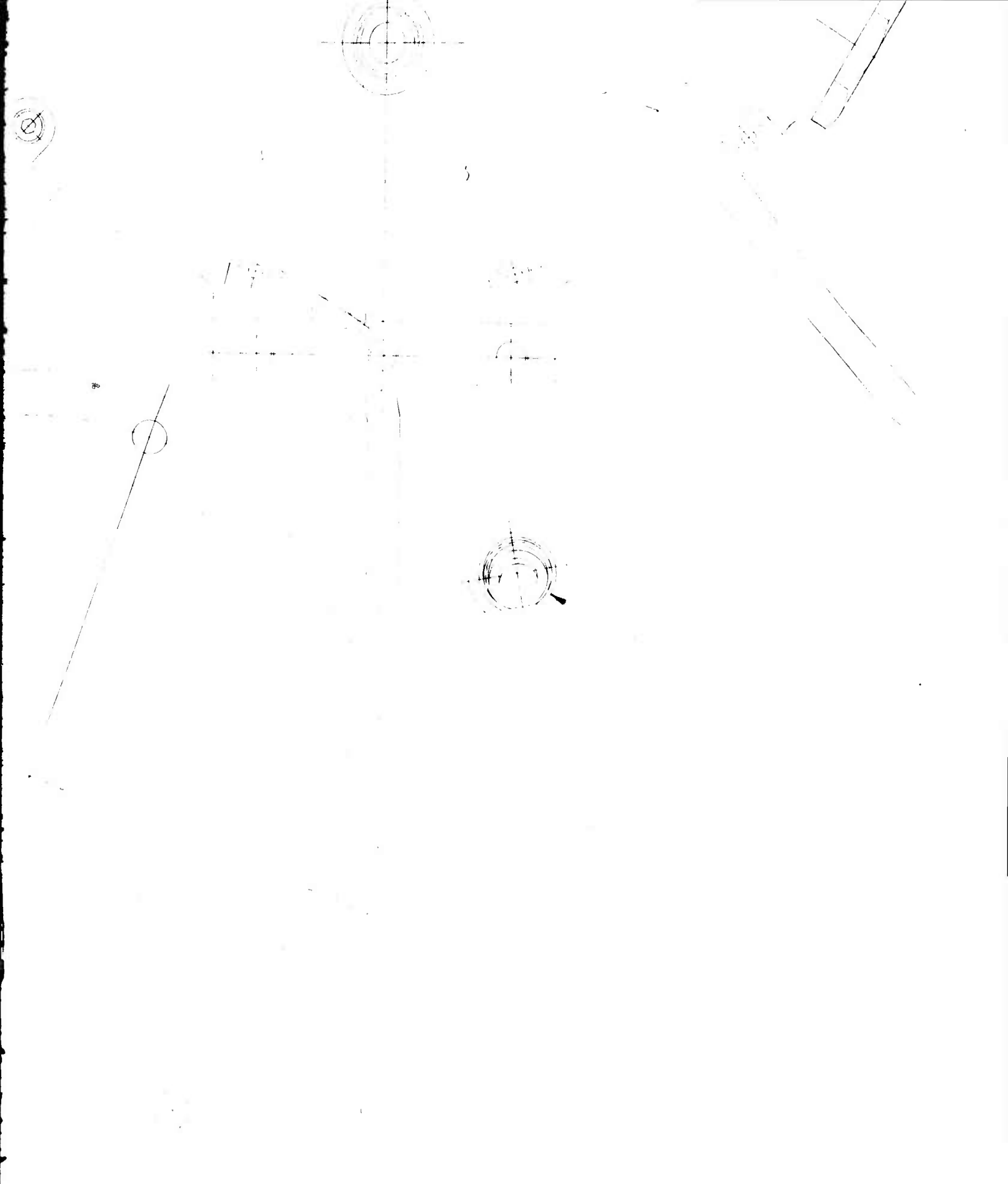
SECTION **W-W**

T



SECTION **V-V**

SECTION **AB-AB**



VIEW **S-S**

W

SEAL LEAKAGE
STEAM OUT
AND 10050-8

APPROVED		DATE	b n		BARBER-NICHOLS ENGINEERING CO. DENVER, COLORADO	
CHIEF			LOW VOLUMETRIC FLOW TURBINE LAYOUT			
PROJECT						
MFG						
TEST						
CHECKED						
DRAWN	WV		SIZE	CODE IDENT. NO.	DWG NO.	REV
			SCALE FULL & NOTED		SHEET 3 OF 4	

~~A~~

Q
Q
Q
Q

Q
Q
Q
Q

Q
Q
Q

B

EXHA

INLET D

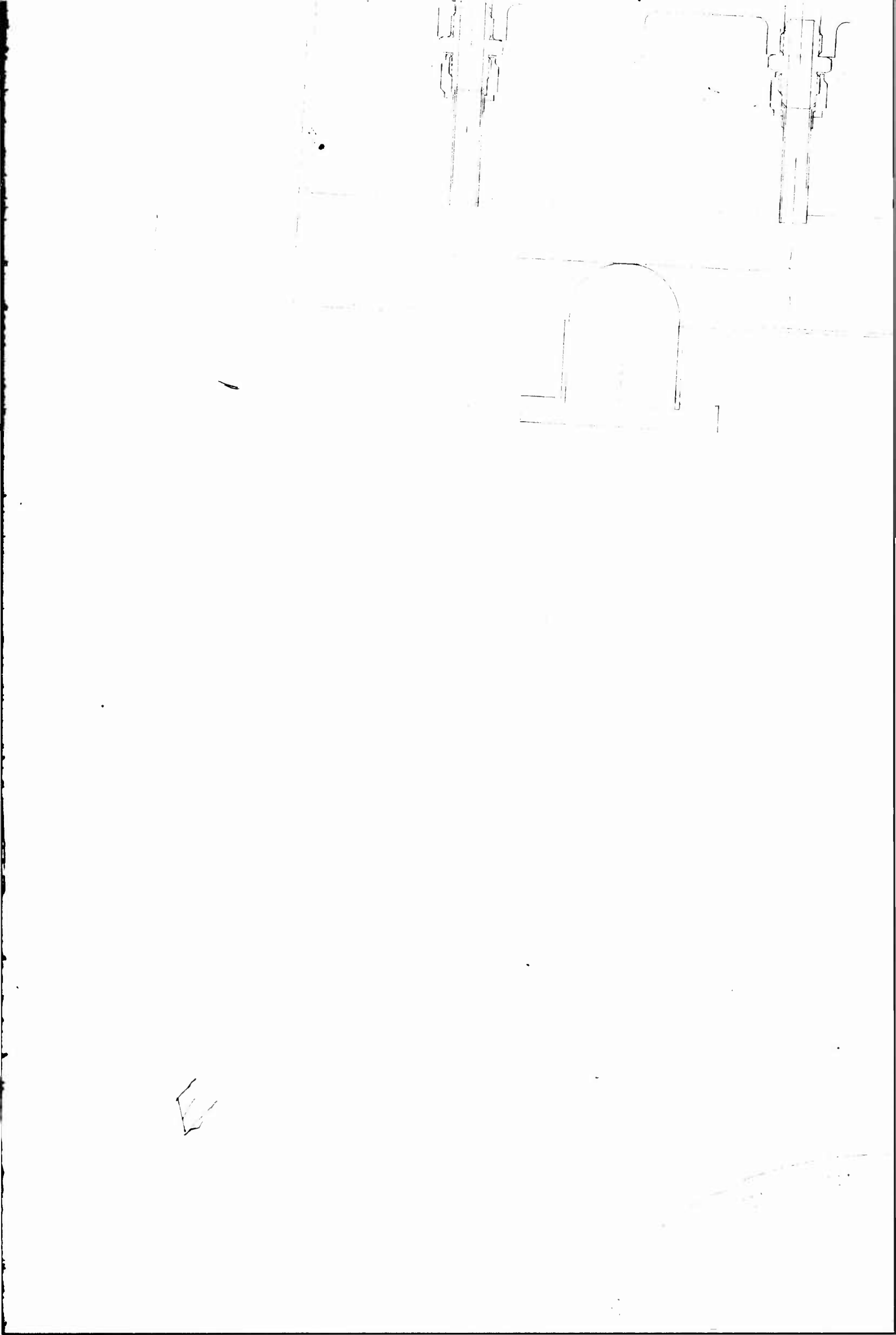
Q

EXHAUST DUCT

INLET DUCT

D





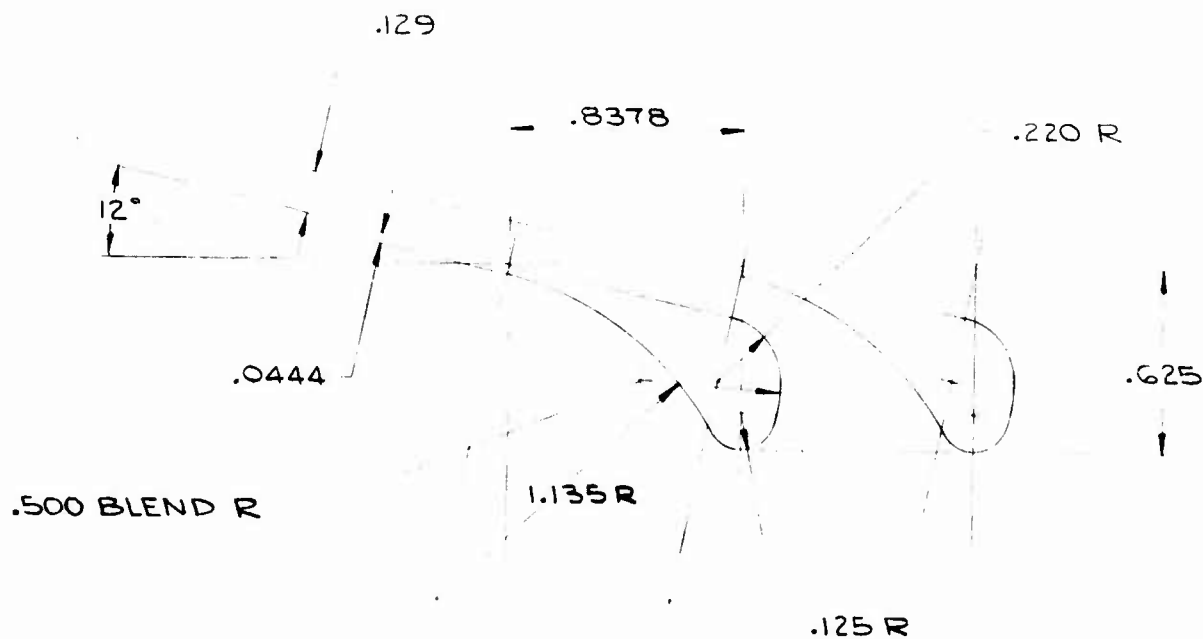
SEC
DEV
24.0
H

K

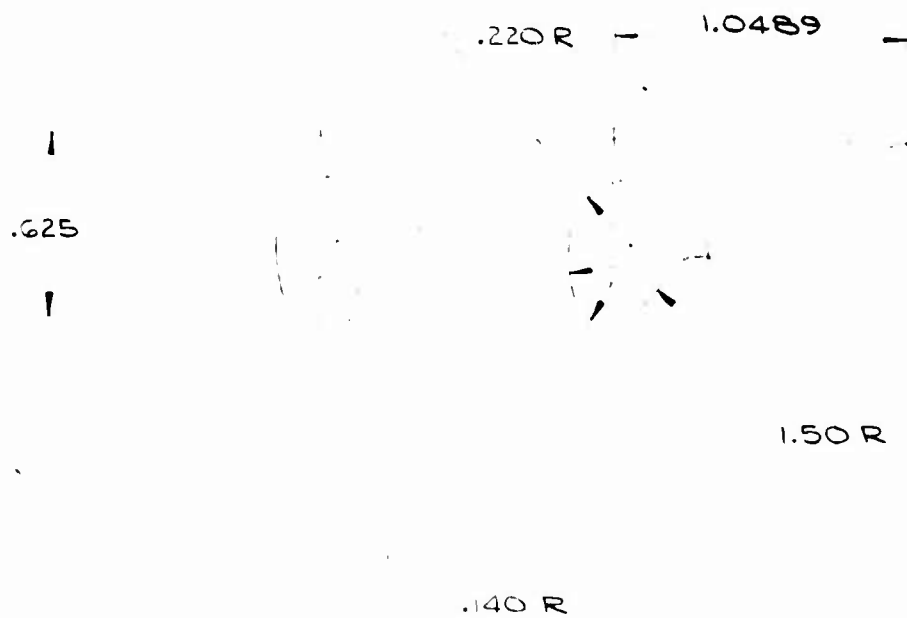
1

SECTION **B-B**
DEVELOPED ON
24.00" PITCH DIA
HALF SCALE

11



ROTOR BLADE PROFILE
TYP 90 BLADES
SCALE 2-1



STATOR BLADE PROFILE
TYP 72 BLADES
SCALE 2-1

H₁

OR

.625

.137

10°

.0422

50 R

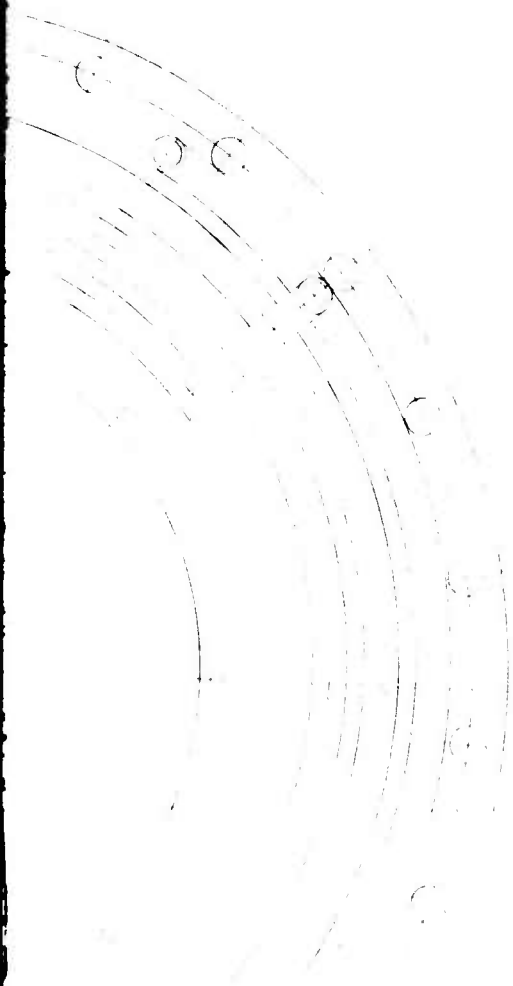
.500 BLEND R

FILE

I



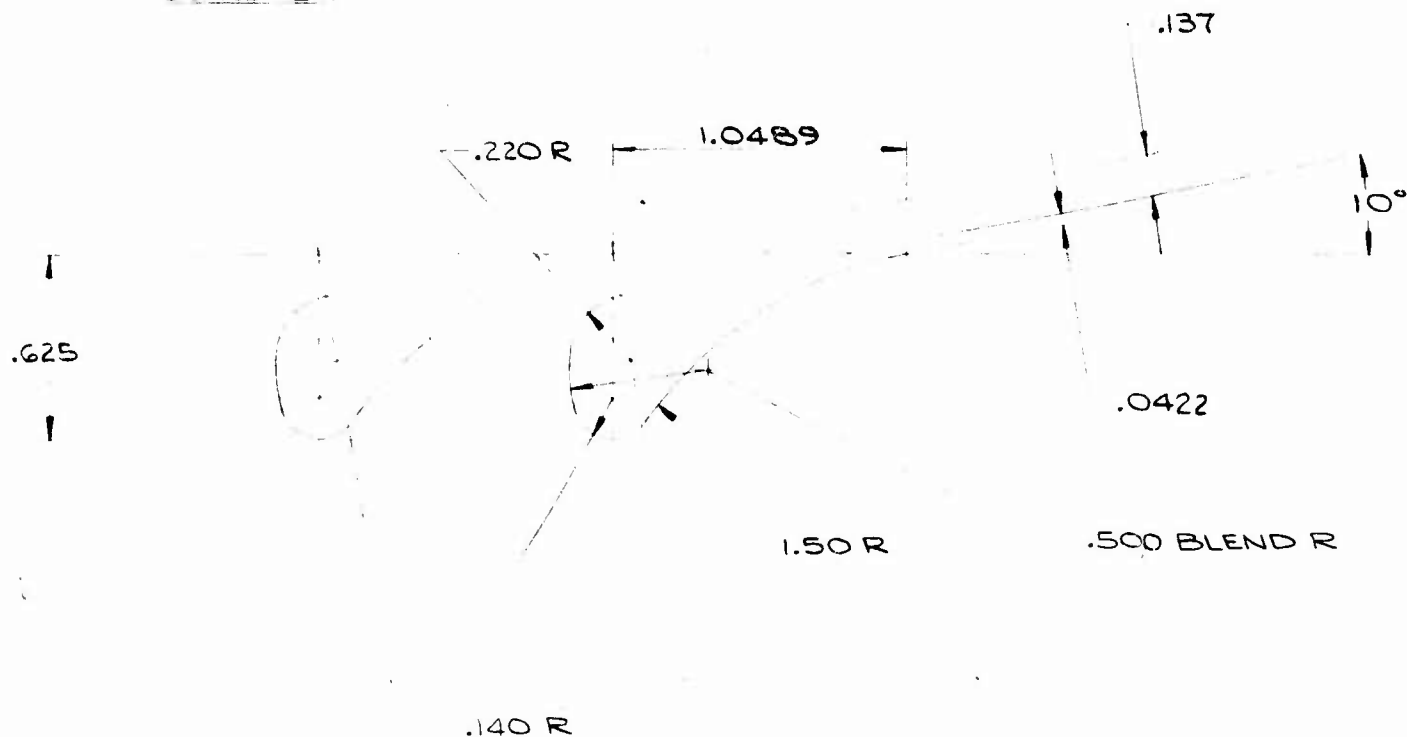
SECTION **AG-AG**
DISC COOLING PLATE



10

SECTION **AF-AF**
DISC COOLING PLATE

ROTOR BLADE PROFILE
TYP 90 BLADES
 SCALE 2-1



STATOR BLADE PROFILE
TYP 72 BLADES
 SCALE 2-1

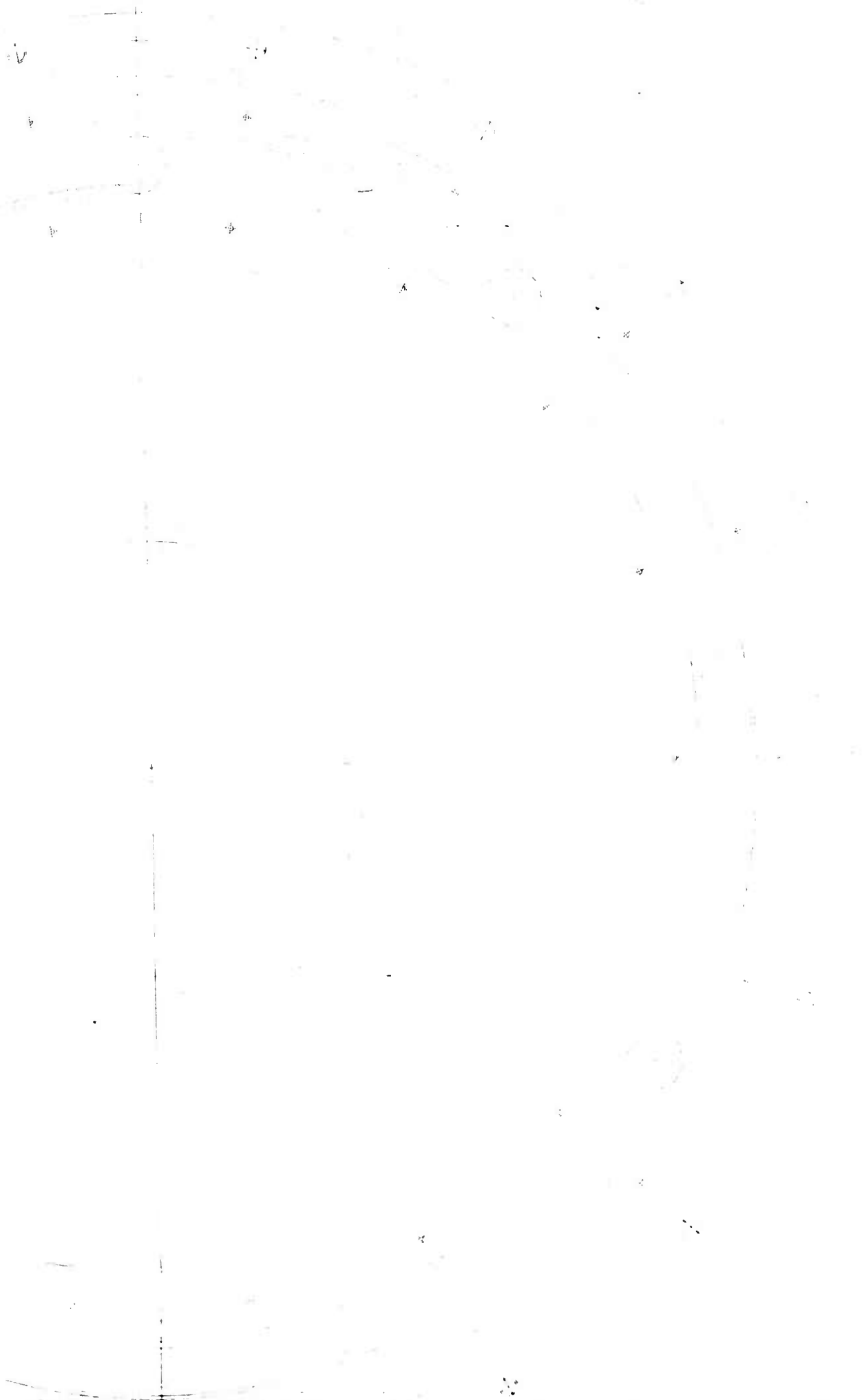
1
 2
 3
 4
 5
 6
 7
 8
 9
 10
 11
 12
 13
 14
 15
 16
 17
 18
 19
 20
 21
 22
 23
 24
 25
 26
 27
 28
 29
 30
 31
 32
 33
 34
 35
 36
 37
 38
 39
 40
 41
 42
 43
 44
 45
 46
 47
 48
 49
 50
 51
 52
 53
 54
 55
 56
 57
 58
 59
 60
 61
 62
 63
 64
 65
 66
 67
 68
 69
 70
 71
 72
 73
 74
 75
 76
 77
 78
 79
 80
 81
 82
 83
 84
 85
 86
 87
 88
 89
 90
 91
 92
 93
 94
 95
 96
 97
 98
 99
 100

N

APPROVED		DATE	b n		BARBER - NICHOLS ENGINEERING CO. DENVER, COLORADO	
CHIEF			LOW VOLUMETRIC FLOW TURBINE LAYOUT			
PROJECT						
MPG						
TEST						
CHECKED						
DRAWN	W.V.		SIZE	CODE IDENT. NO.	DWG NO.	REV
			SCALE FULL & NOTED		SHEET 4 OF 4	

A

8



C

JOURNAL BEAR
WATER IN
AND 10050-8

SECTION **R-R**
WATER SUPPLY JETS

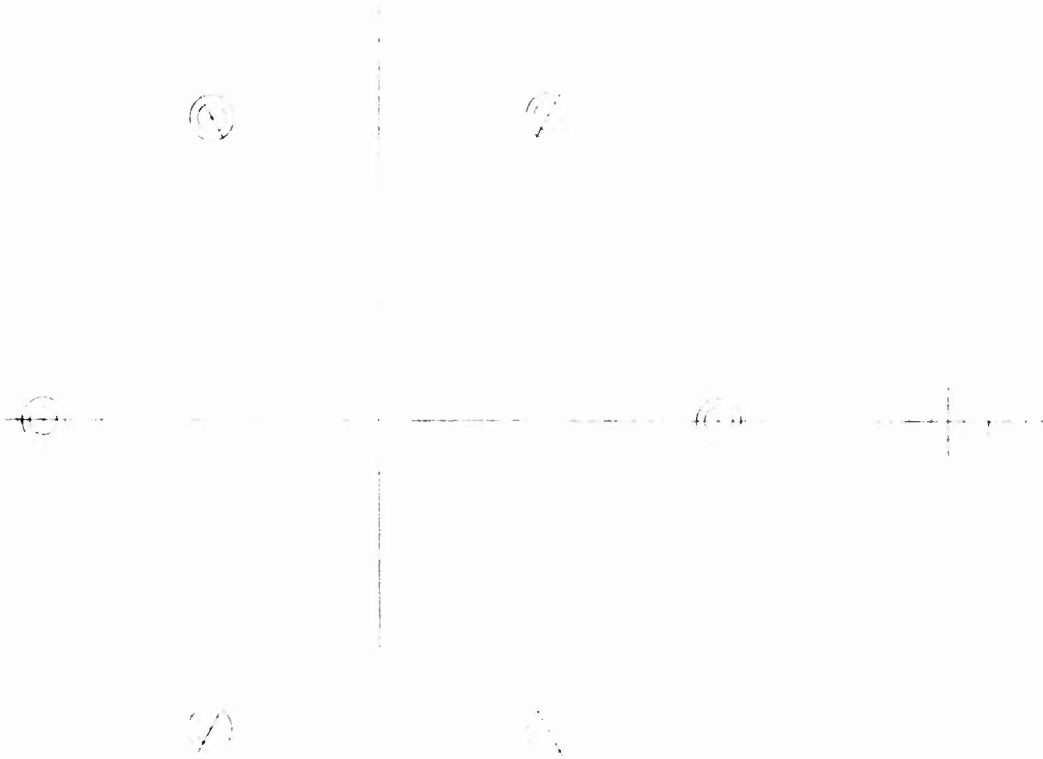
BEARING
IN
050-8

REMOVED VIEW OF SEAL HOUSING

SECTION **E-E**



E

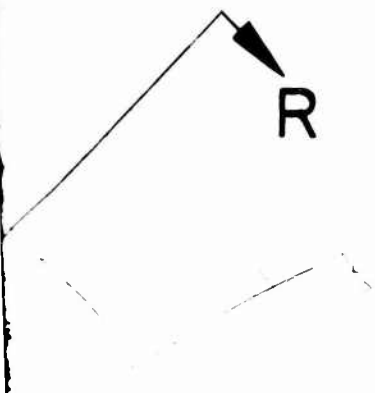


REMOVED VIEW OF SEAL RETAINER

E-E

SECTION H

JOURNNAL BEARING
WATER IN
AND 10050-8



F

Ø

(C)

(C)

Ø

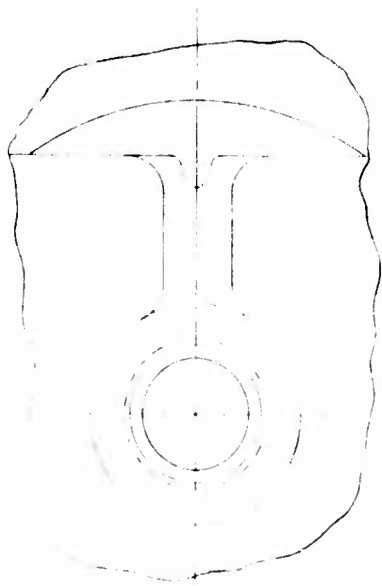
H-H

(C)

G



5

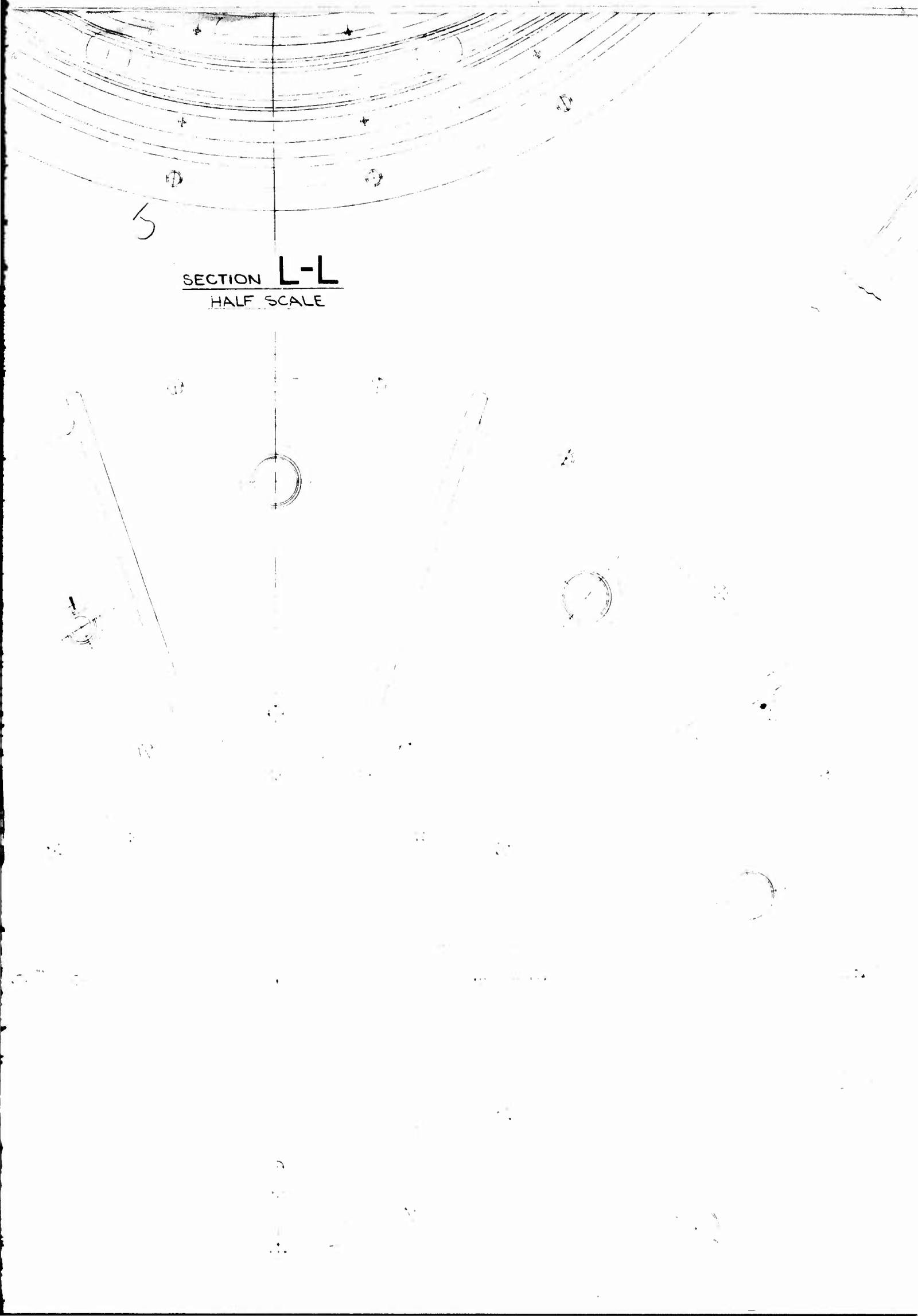


SECTION **AE-AE**

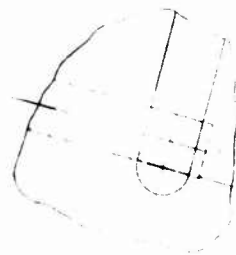
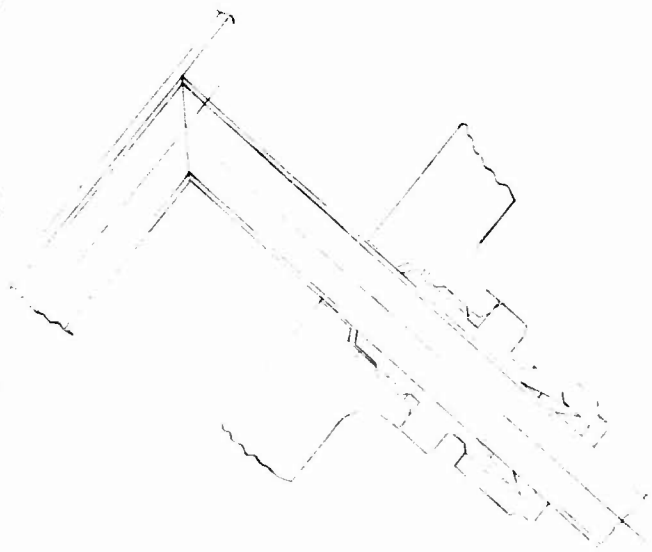
DISC COOLING -
WATER OUT
AND 10050-8

DISC COOLING -
WATER IN
AND 10050-8

SECTION **L-L**
HALF SCALE

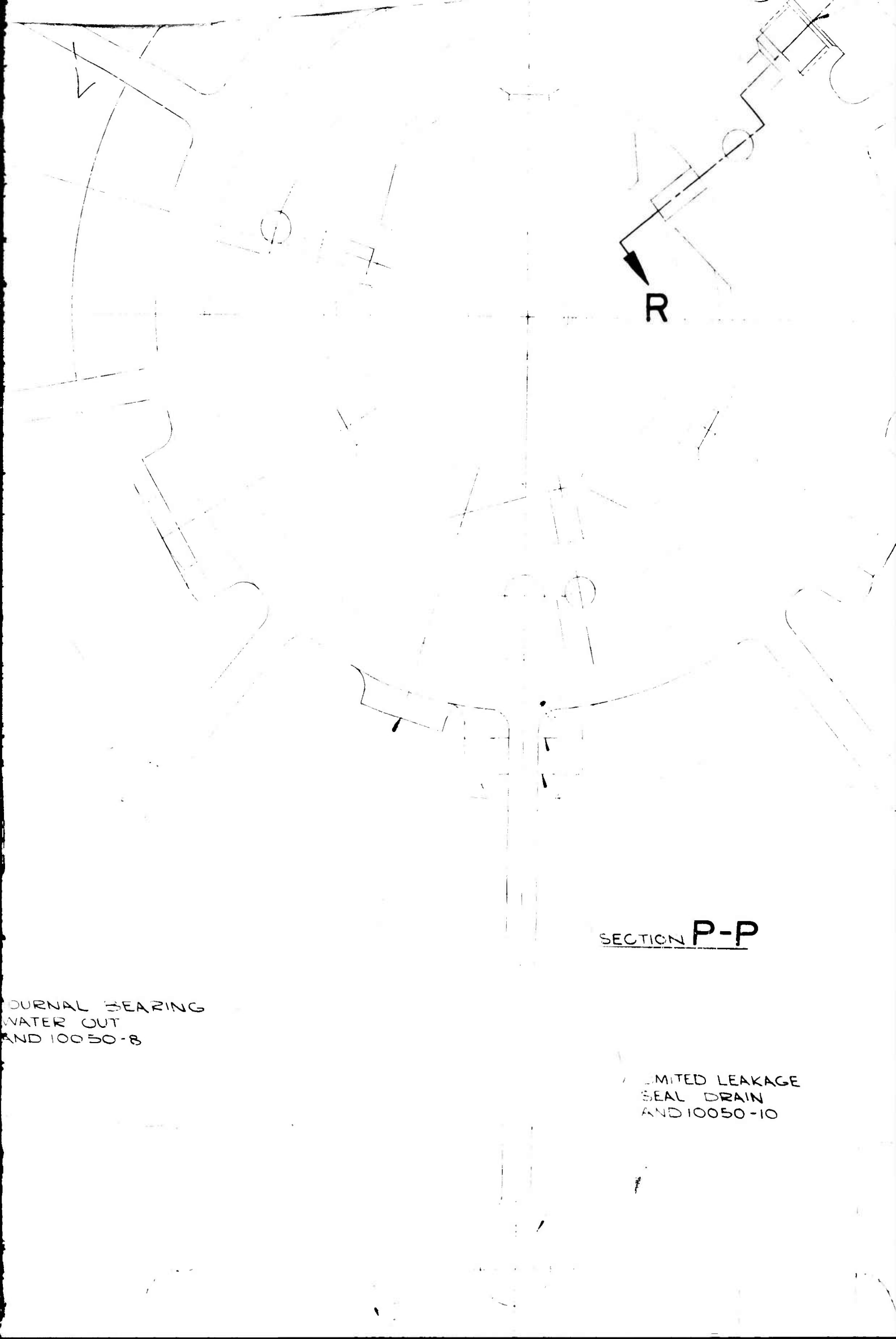


k



SECTION **N-N**

JOU
WA
AN



R

SECTION P-P

JOURNAL BEARING
WATER OUT
AND 10050-8

LIMITED LEAKAGE
SEAL DRAIN
AND 10050-10



LIMITED LEAGAGE -
SEAL DRAIN
AND 10050-10

SECTION



SECTION F-F

JOURNAL BEARING
WATER OUT
AND 10050-8

SECTION **K-K**
INLET DUCT



K-K
CT

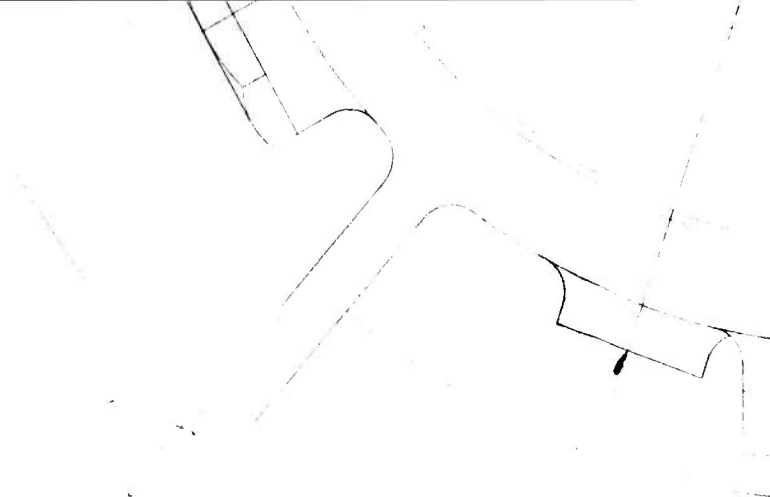
P



VIEW **G-G**
INLET HOUSING
SHOWN
HALF SCALE

VIEW J-J

R



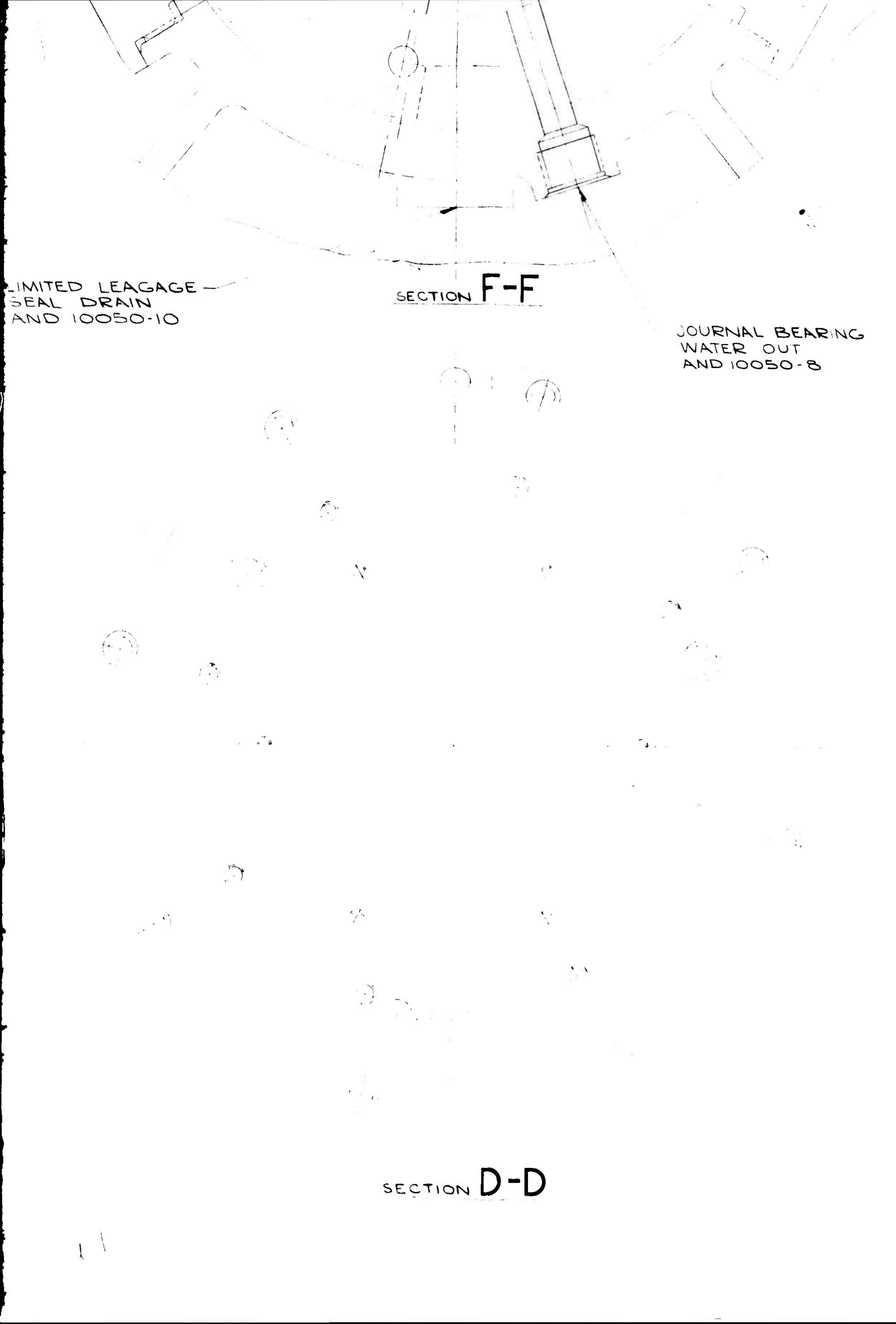
JOURNAL BEARING
WATER OUT
AND 10050-8

J-J

LIMITE
SEAL
AND

SECTION P-P

LIMITED LEAKAGE
SEAL DRAIN
AND 10050-10



LIMITED LEAGAGE —
SEAL DRAIN
AND 10050-10

SECTION **F-F**

JOURNAL BEARING
WATER OUT
AND 10050-8

SECTION **D-D**

SECTION **M-M**
SHROUD COOLING RING

P

M-M
POOLING KING

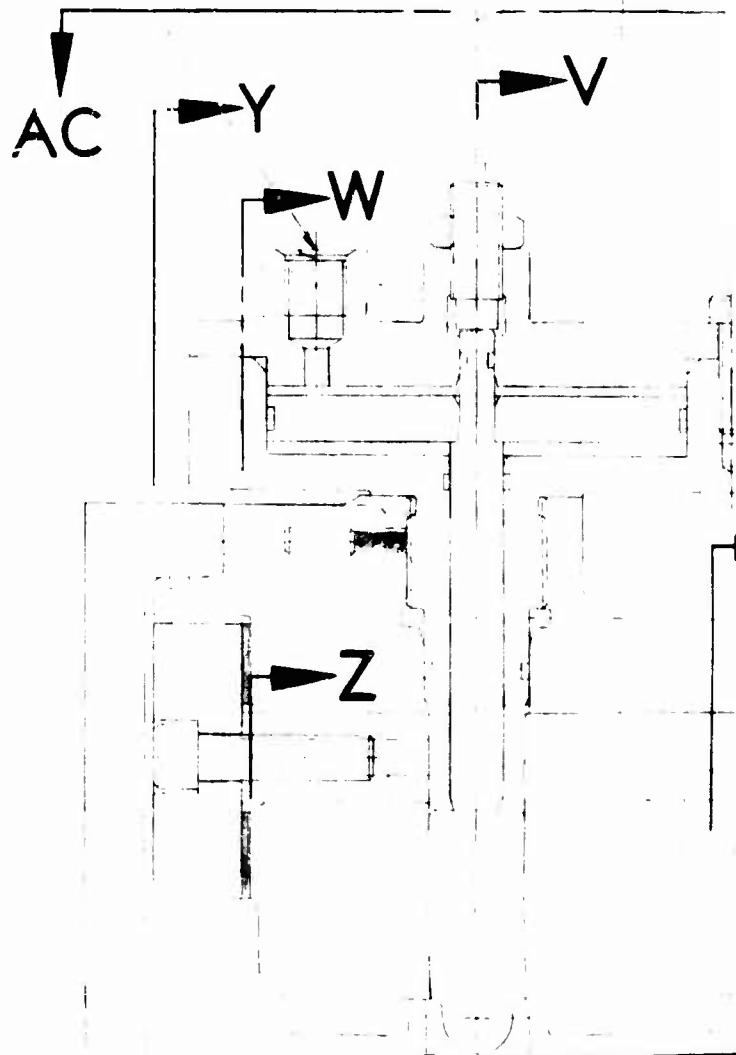
APPROVED		DATE	b n		HARBER - NICHOLS ENGINEERING CO. DENVER, COLORADO	
CHIEF			LOW VOLUMETRIC FLOW TURBINE LAYOUT			
PROJECT						
MFG						
TEST						
CHECKED						
DRAWN	WV		SIZE	CODE IDENT. NO.	DWG NO.	REV
			SCALE FULL & NOTED		SHEET	2 OF 4

A

→ S

EXHAUST
DUCT

HIGH PRESSURE IN
TO BEARING PRELOAD
CYLINDER
AND 10050-4



MAGNETIC SPEED

B

SHROUD COOLING
WATER OUT
AND 10050-4

T

L

M

AC

THRUST BEARING
WATER IN
ROTATED 45° CW
AND 10050-8

AG

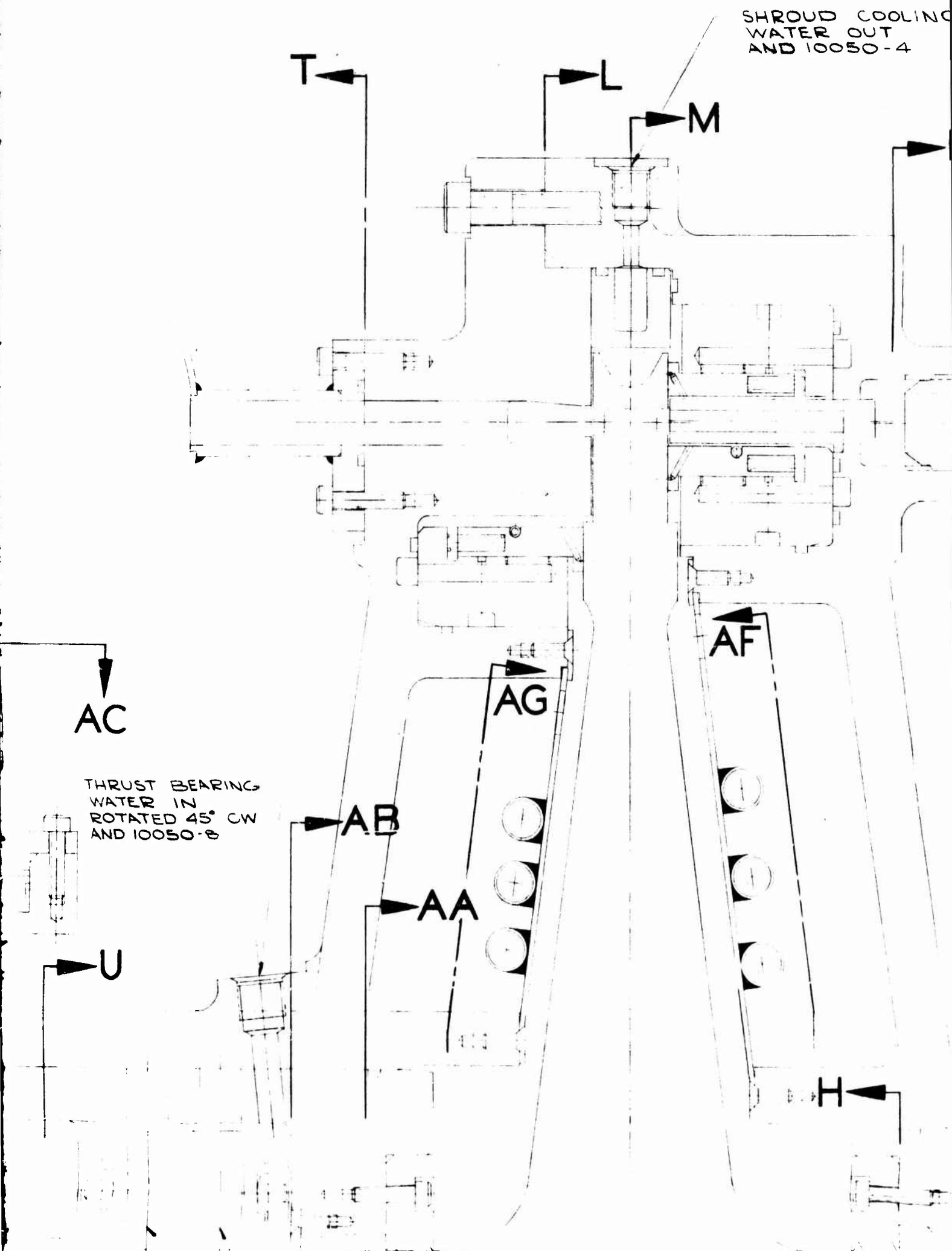
AB

AA

AF

U

H



C

COOLING
OUT
50-4

G

K

INLET
DUCT

HIGH PRESSURE IN
TO BEARING PRELOAD
CYLINDER
AND 10050-4

F

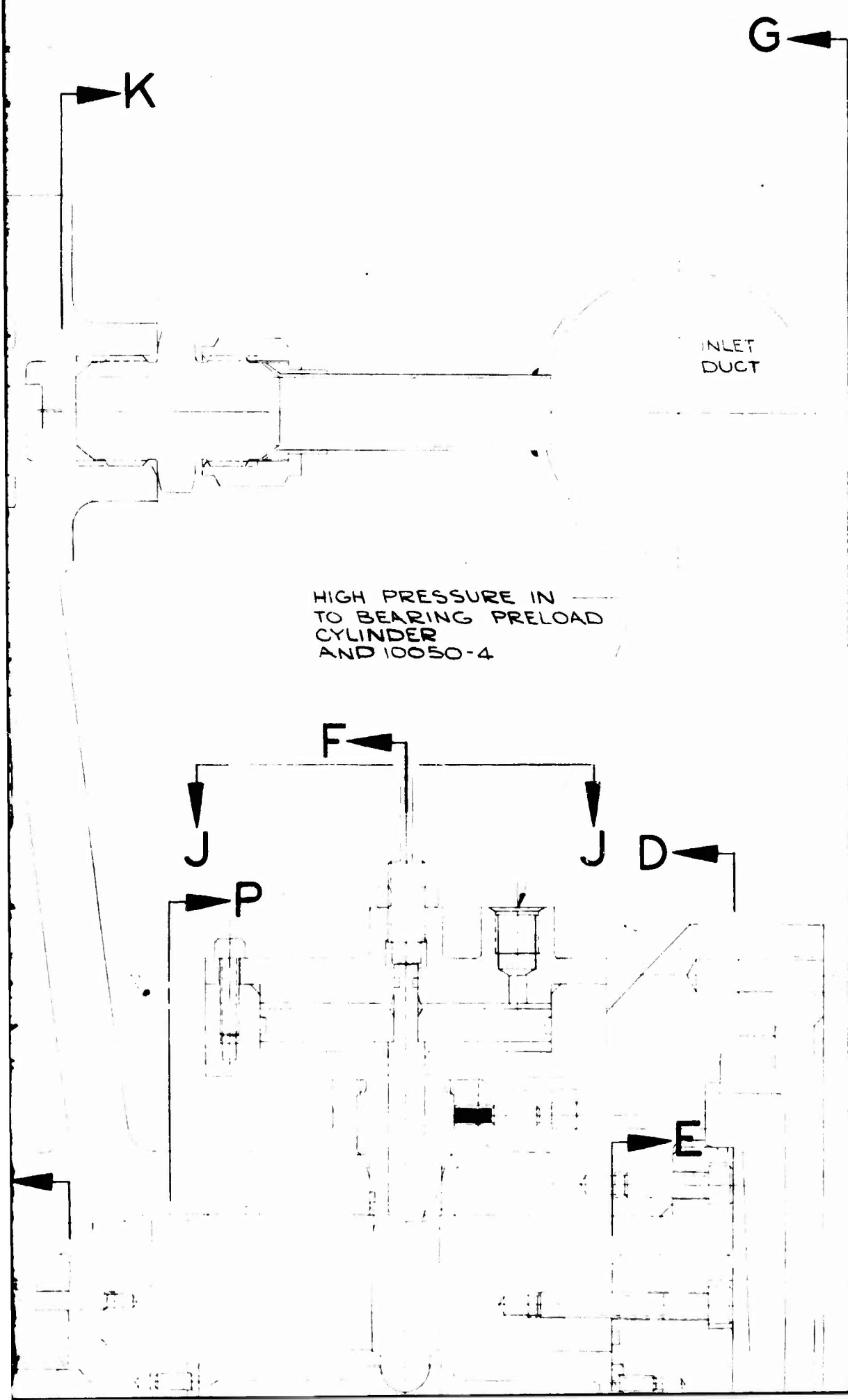
J

J

D

P

E



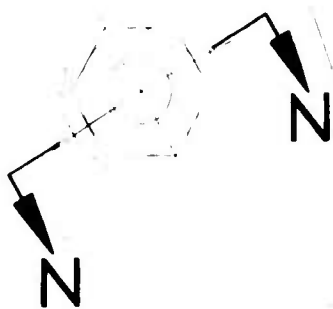
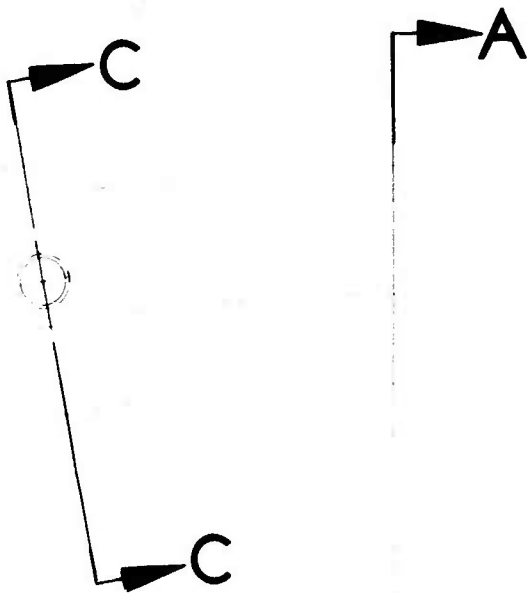
D

SECTION C-C

E.

24.00 ROTOR
PITCH DIA

F



G

11-1

11-1

11-1

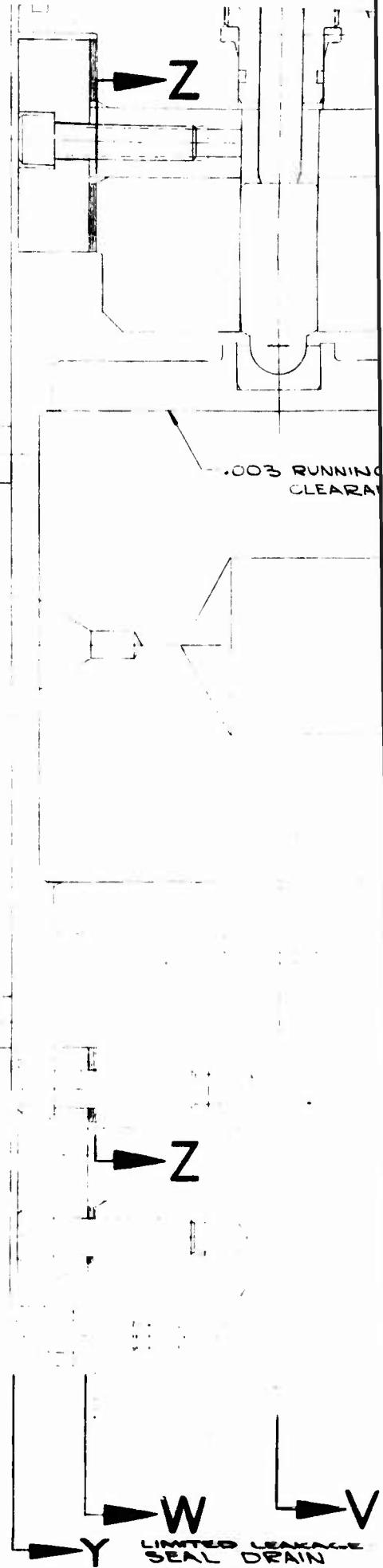
I

MAGNETIC SPEED
PICKUP BOSS
AND 10050-6

THRUST AND JOURNAL
BEARING WATER OUT
AND 10050-8

.003 RUNNING
CLEARANCE

LIMITED LEAKAGE
SEAL DRAIN
AND 10050-6
ROTATED 30° CW



3

CE

003 RUNNING
CLEARANCE

.00239 RUNNING
CLEARANCE

LEAKAGE
DRAIN
1050-6
D 30° CN

SEAL LEAKAGE
STEAM OUTLET
AND 10050-10
ROTATED 10°

V

U

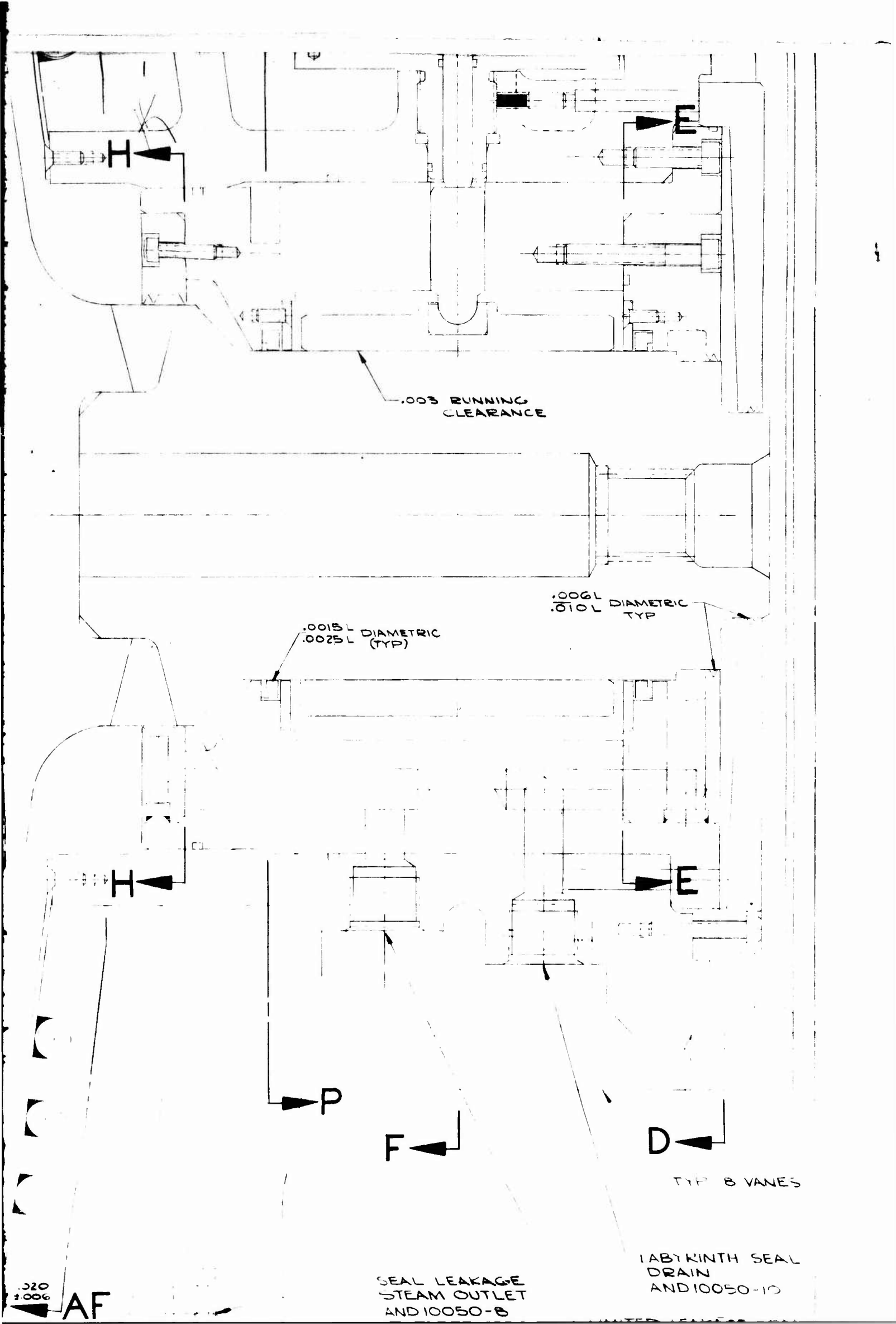
AB

AA

AG

020
1006

AF



.003 RUNNING
CLEARANCE

.0015 L DIAMETRIC
.0025 L (TYP)

.006 L DIAMETRIC
.010 L TYP

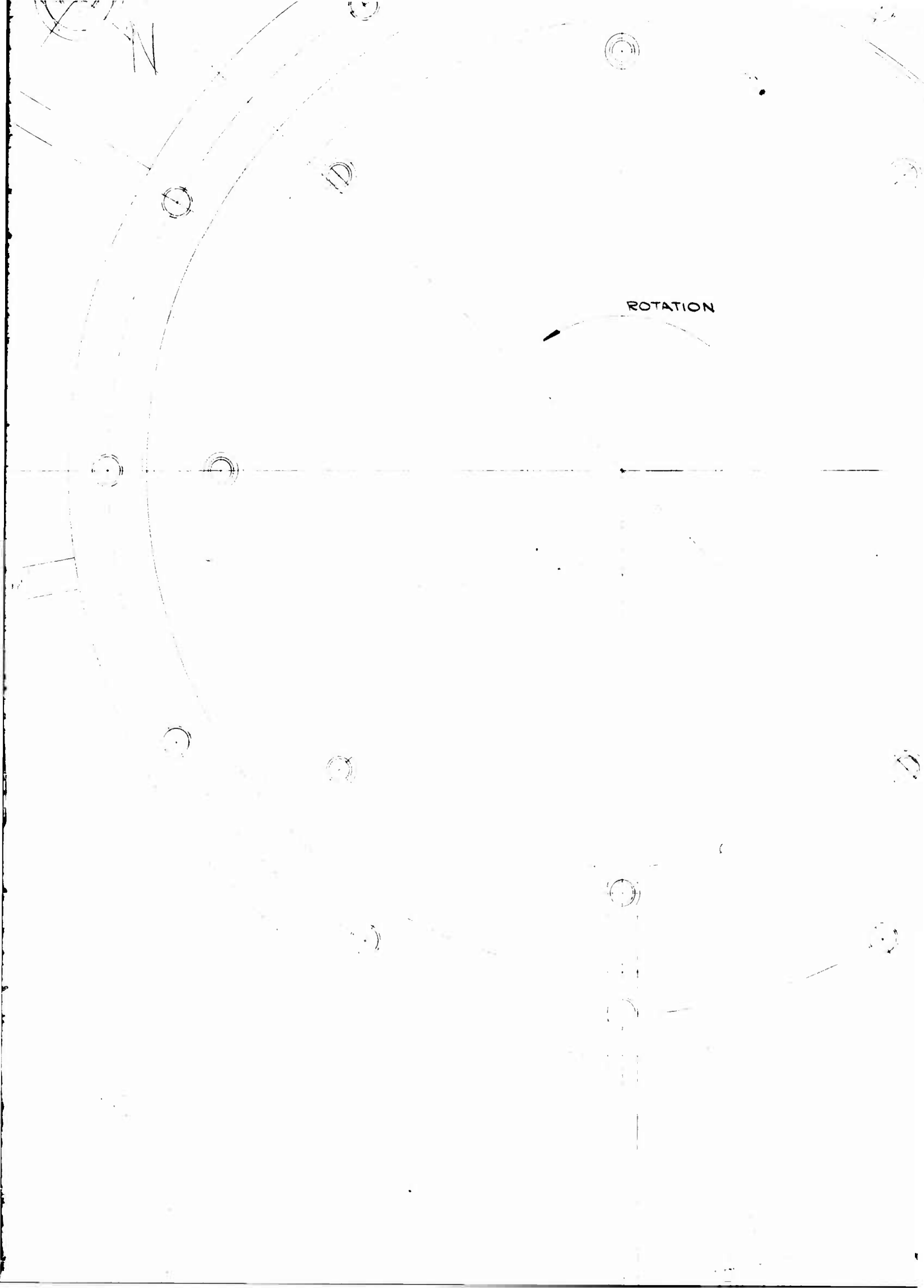
SEAL LEAKAGE
STEAM OUTLET
AND 10050-8

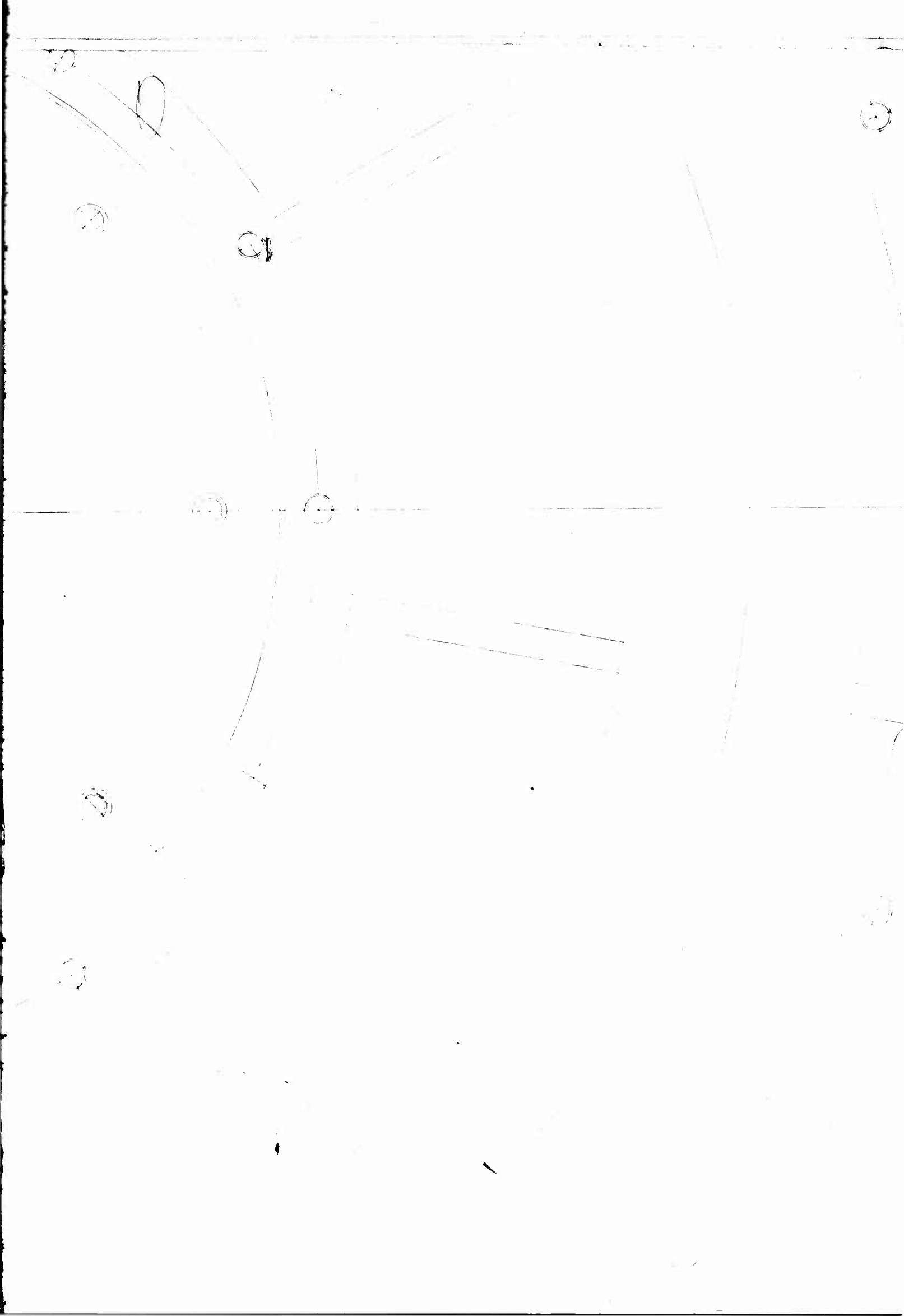
LABYRINTH SEAL
DRAIN
AND 10050-10

TYP B VANES

AF

30.000



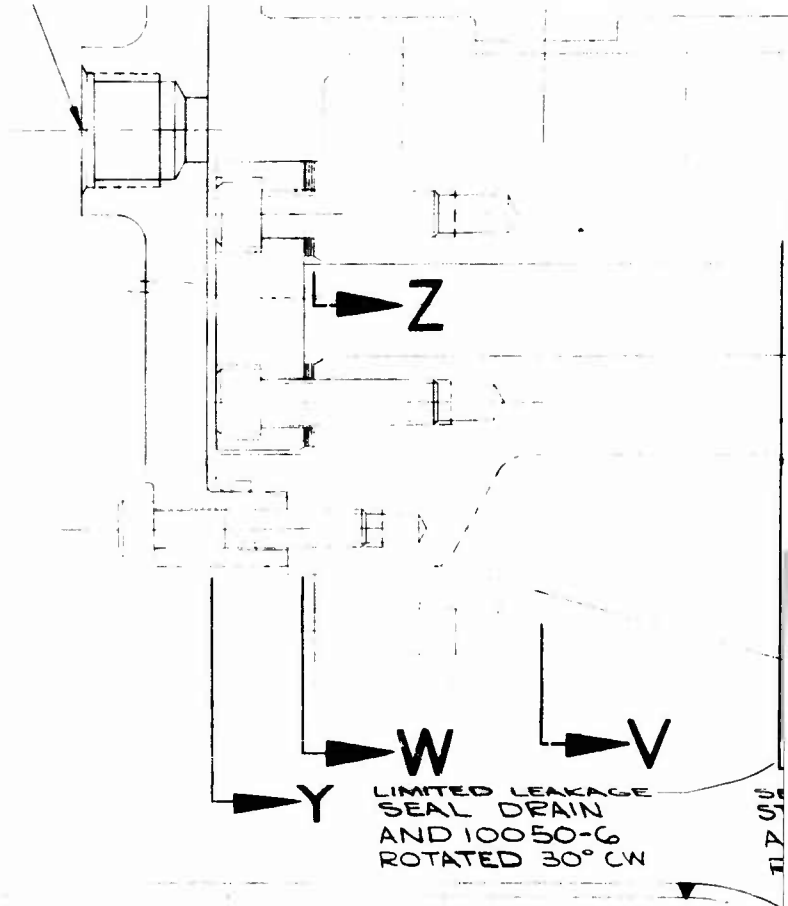




12



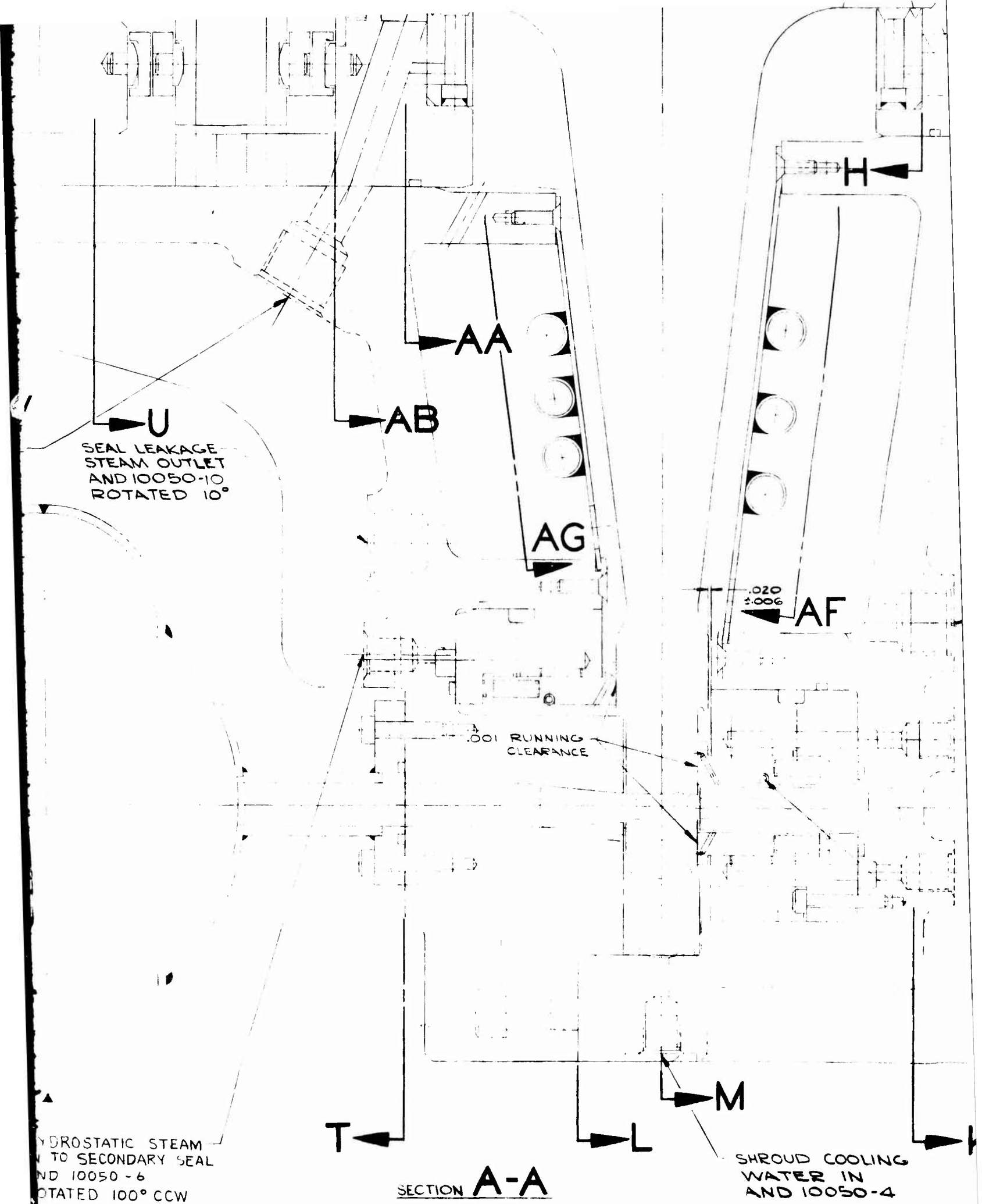
12

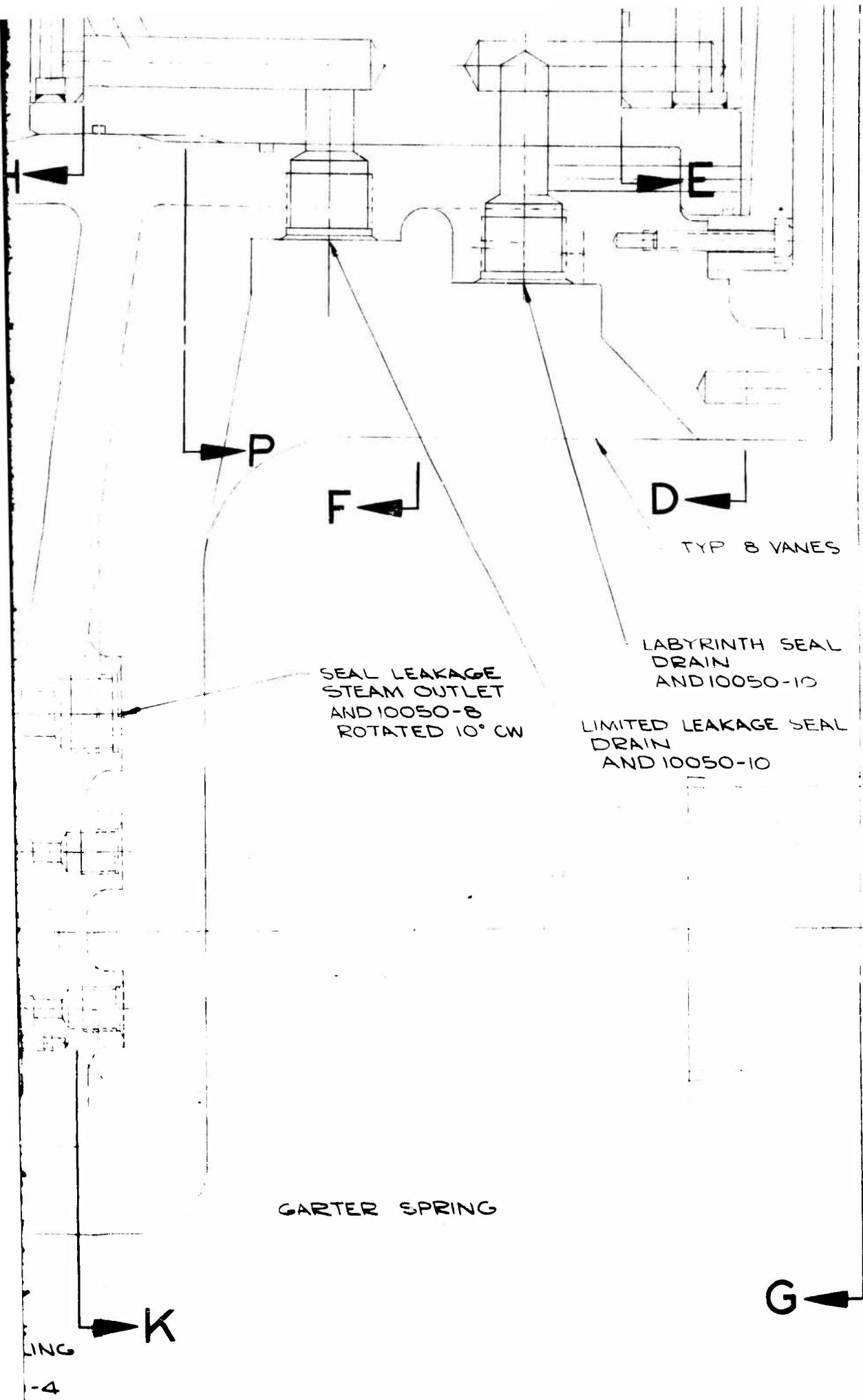


STEAM OUTLET -
TO CONDENSER
ROTATED 20° CCW

S

HYDROSTA
IN TC SEC
AND 1005
ROTATED

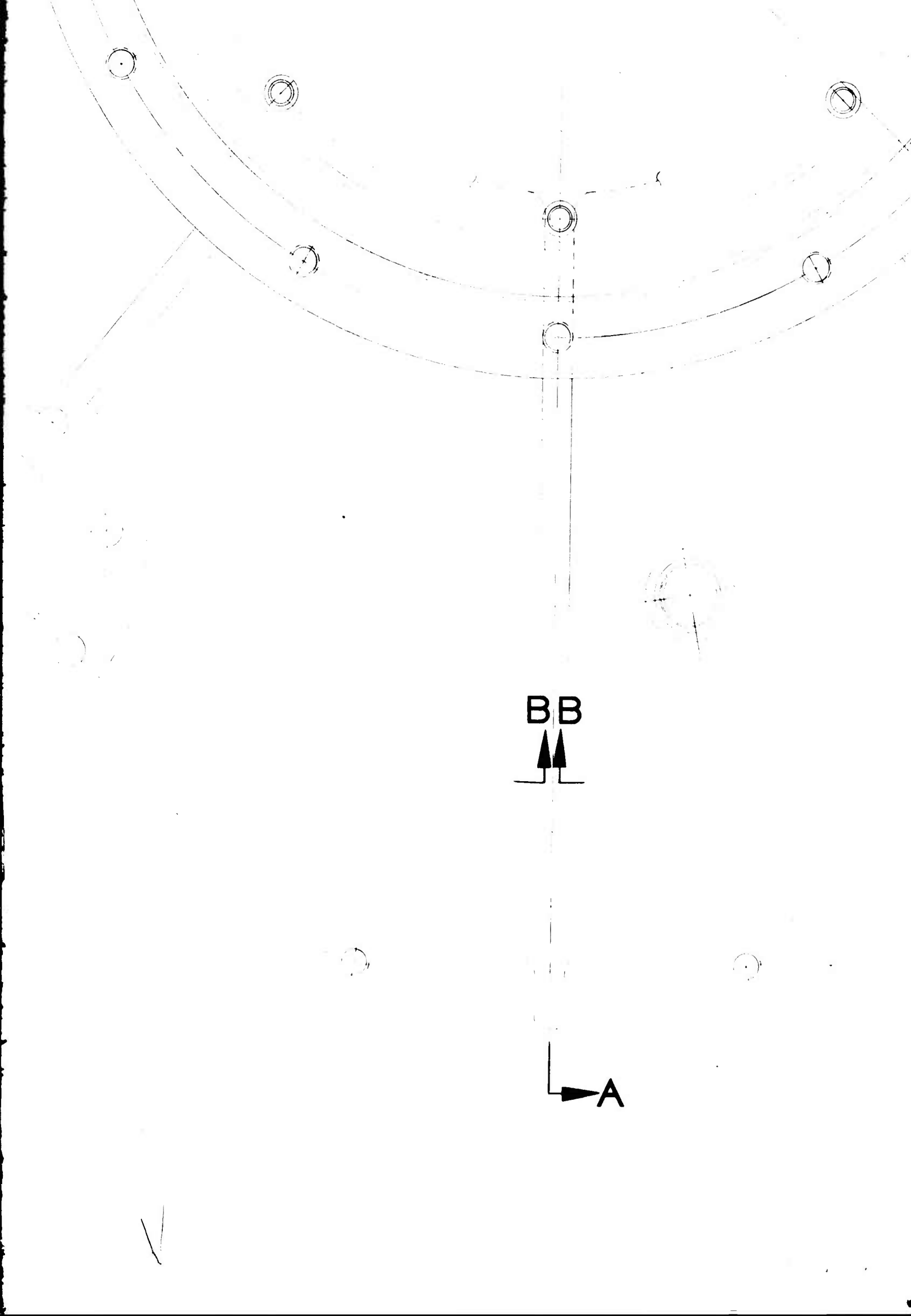


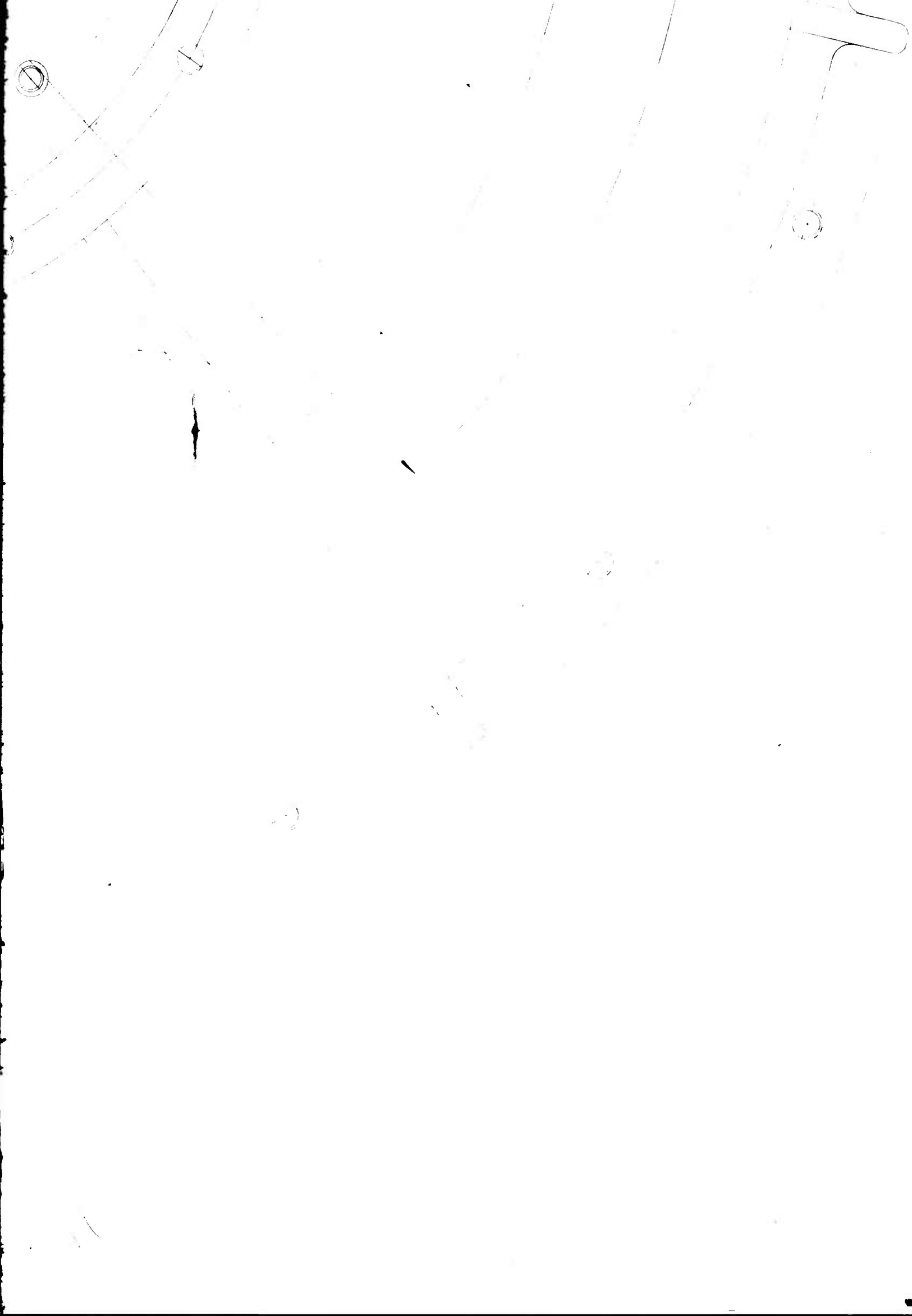


30.000

T

30.000





APPROVED		DATE	b n		BARBER - NICHOLS ENGINEERING CO. DENVER, COLORADO		
CHIEF			LOW VOLUMETRIC FLOW TURBINE LAYOUT				
PROJECT							
MFG							
TEST			SIZE	CODE IDENT. NO.	DWG NO.		REV
CHECKED							
DRAWN	W.V.		SCALE FULL & NOTED		SHEET 1 OF 4		